Nanomaterials for the Life Sciences

Edited by Challa Kumar

WILEY-VCH

Metallic Nanomaterials

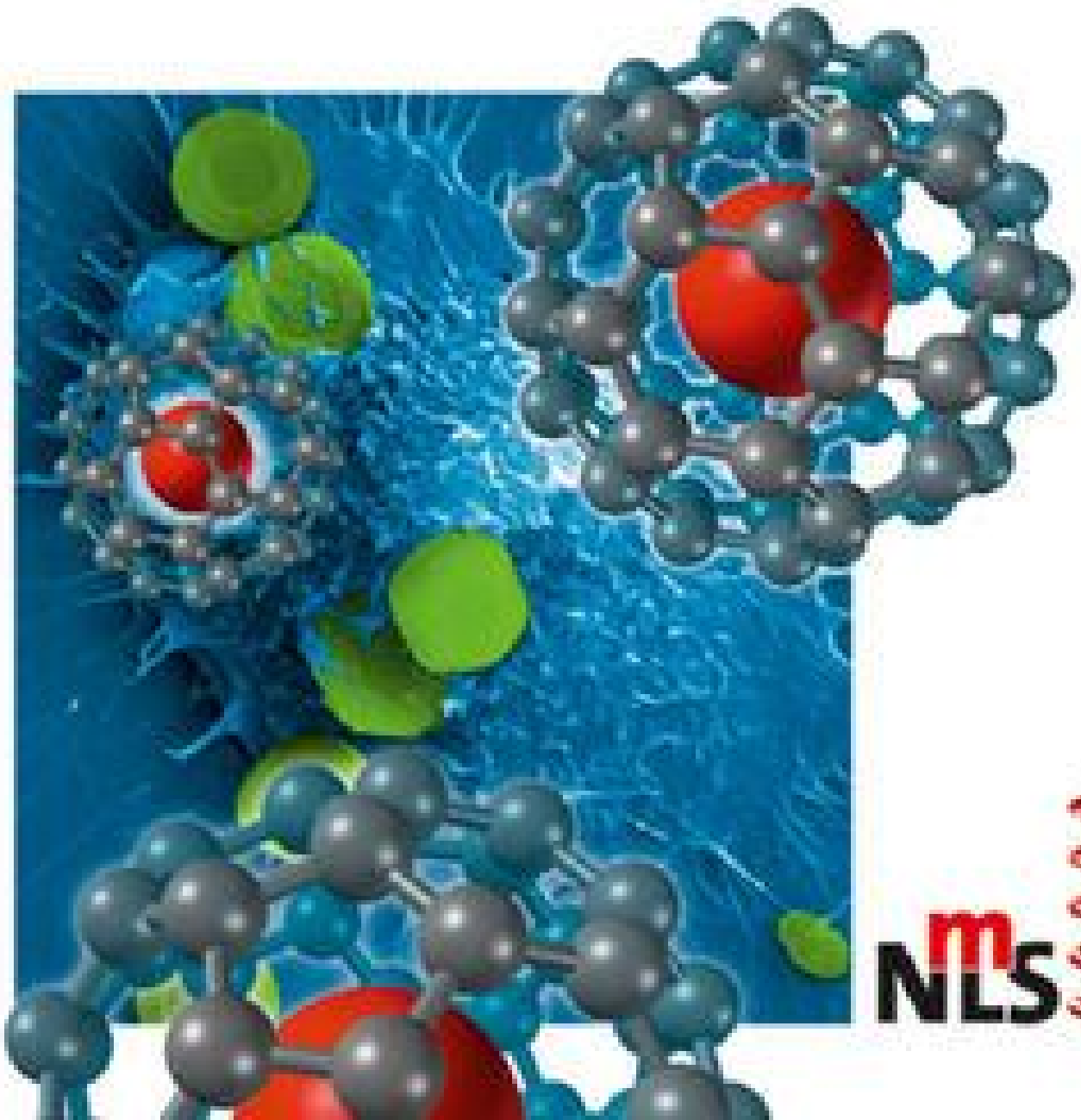

Contents

Metallic Nanomaterials Vol. 1. Edited by Challa S. S. R. Kumar

ISBN: 978-3-527-32151-3

1
Approaches to Synthesis and Characterization of Spherical and Anisotropic Copper Nanomaterials

Nicola Cioffi, Nicoletta Ditaranto, Luisa Torsi and Luigia Sabbatini

1.1
Introduction

Those familiar with the literature in the field of metal nanoparticles have, for sure, many times read a sentence such as: '. . . in recent years metal nanoparticles have attracted a great interest because of their unique size-dependent properties that can be different from those of the corresponding bulk material'. At the outset of this chapter, we promise the reader that we will carefully avoid any further use of this terminology! Indeed, we must specify that, when talking about nanoparticles synthesis, characterization and key properties, it is today mandatory to assess issues related to a tight control over size, shape, crystal structure and morphological purity. Obviously, chemical composition is also critical, but important aspects in the (nano)materials science have been widely demonstrated to correlate with the aforementioned morphological/structural parameters.

One of the most challenging goals in nanoparticle (NP) research is to develop successful protocols for the large-scale, simple and (possibly) low-cost preparation of morphologically pure NPs with identical properties. Additionally, NPs should be easily stored and manipulated without losing their properties. In this context, we will try to describe comprehensively the literature which exists on the preparation of copper nanosized materials, paying attention to all of these key characteristics.

The present chapter cites more than 350 papers, and focuses specifically on nonoxidized, nonsupported $Cu^{(0)}$ nanosized particles and structures. Unlike the situation in the recent literature, we will not use the adjective 'metallic' to qualify these nanophases. Attributing the metallic character to a novel copper nanomaterial should necessarily imply an assessment of its electron energy distribution. The chemical bond connecting a limited number of copper atoms clustered in the core of a NP and stabilized by an outer shell composed of other substances, can hardly be regarded as a *metallic* bond.

Metallic Nanomaterials Vol. 1. Edited by Challa S. S. R. Kumar

ISBN: 978-3-527-32151-3

Obtaining stable nanomaterials that consist exclusively of chemically pure (elemental) transition metals, without using any stabilizing agent, is an unresolved issue that remains the subject of contrasting opinions [1]. In the case of physical preparation techniques, traces of hydrocarbons deriving from the vacuum systems, gases present in the deposition environment, or other contaminants which come into contact with the NP during real-world applications (e.g. atmospheric oxygen), always give rise to an outer shell – even of submonolayer thickness – which stabilizes the elemental NP core. In solution-based approaches, even when stabilizers are not added intentionally, either the solvent itself or dissolved oxygen can be responsible for interactions with the NP surface, leading to a stabilizing zone that surrounds the particle and has its own composition, which differs from that of the NP core.

In this chapter, when reporting on copper nanomaterials, we will implicitly focus on the nanostructure main part – the core. The existence of a *relatively* thin stabilizing shell (composed of organic stabilizers, copper oxide or hydroxide, chemi- or physisorbed solvent molecules, etc.) surrounding the NP core will be accepted as a natural consequence of both the size and the chemical reactivity of the copper phase.

More complex core-shell structures in which the copper core has been intentionally modified by a *thick* layer of another material (polymer, oxide, other metals, inorganic compounds, etc.) will not be reviewed in this chapter, as they often imply brand-different synthesis approaches. In fact, most of these will form the subjects of other contributions in this textbook series.

As a consequence of all these premises, composite nanostructured materials (including Cu NPs in polymer or silica glass dispersing matrices), Cu_2O and CuO nanoparticles, Cu/Cu oxide core-shell materials, copper-containing compounds and alloys (including magnetic particles), multimetal NPs and supported nanophases (including electrochemically, lithographically or physically deposited nanophases that cannot be easily removed from the substrate without losing their properties), will not be described herein.

The number of studies published on the synthesis and characterization of copper nanomaterials has been growing exponentially in recent years; indeed, a literature search over the period 1991–2007 returned more than 5000 papers and patents [2].

In particular, we based our database search on a combined use of the keyword 'copper' with another one, chosen among the following terms: 'nanoparticle', 'nanocluster', 'nanowire' or 'nanorod'. The results were then analyzed, by publication year and document type. The latter classification was based on two groups – namely patents and academic studies (reviews, commentaries, papers, conferences, etc.) – that we have generically indicated as 'papers'. Histograms relevant to the different classes are reported in Figures 1.1 and 1.2; the former figure shows the distribution of the total number of patents (panel c), papers (panel b), and their sum (panel a), as a function of the publication year. The year-distribution of papers and patents as a function of the single keyword is described in Figure 1.2. A general increase in the publication frequency can be noted in all cases; however,

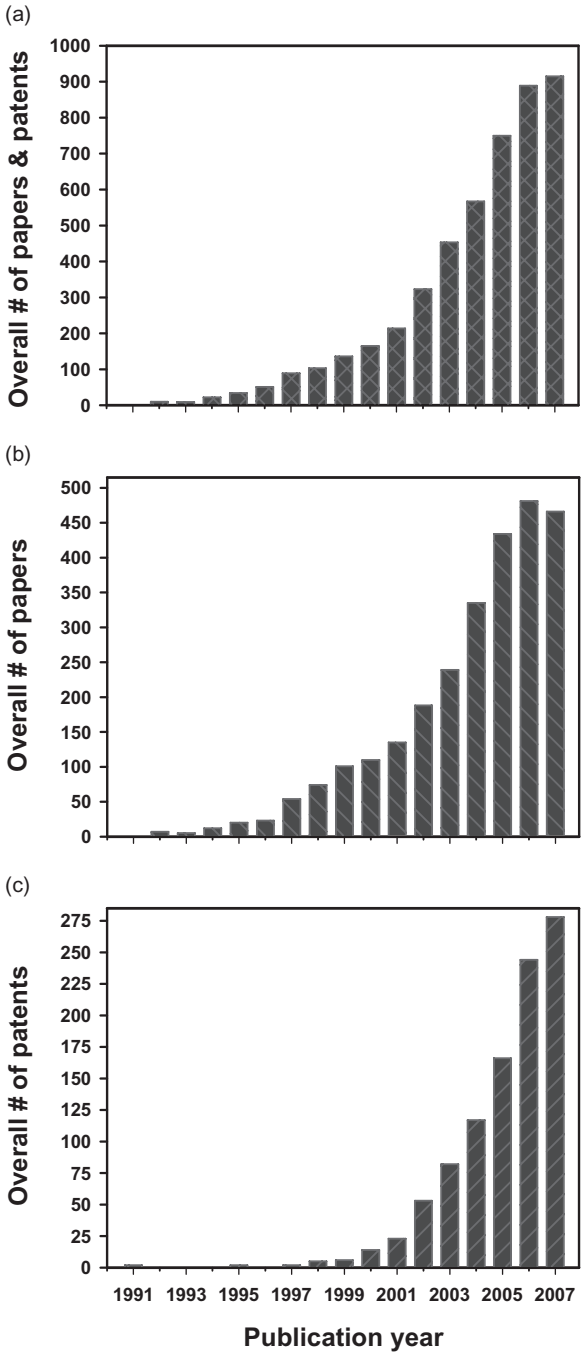

Figure 1.1 Histograms showing the distribution of the total number of patents (c), papers (b), and their sum (a), as a function of the publication year.

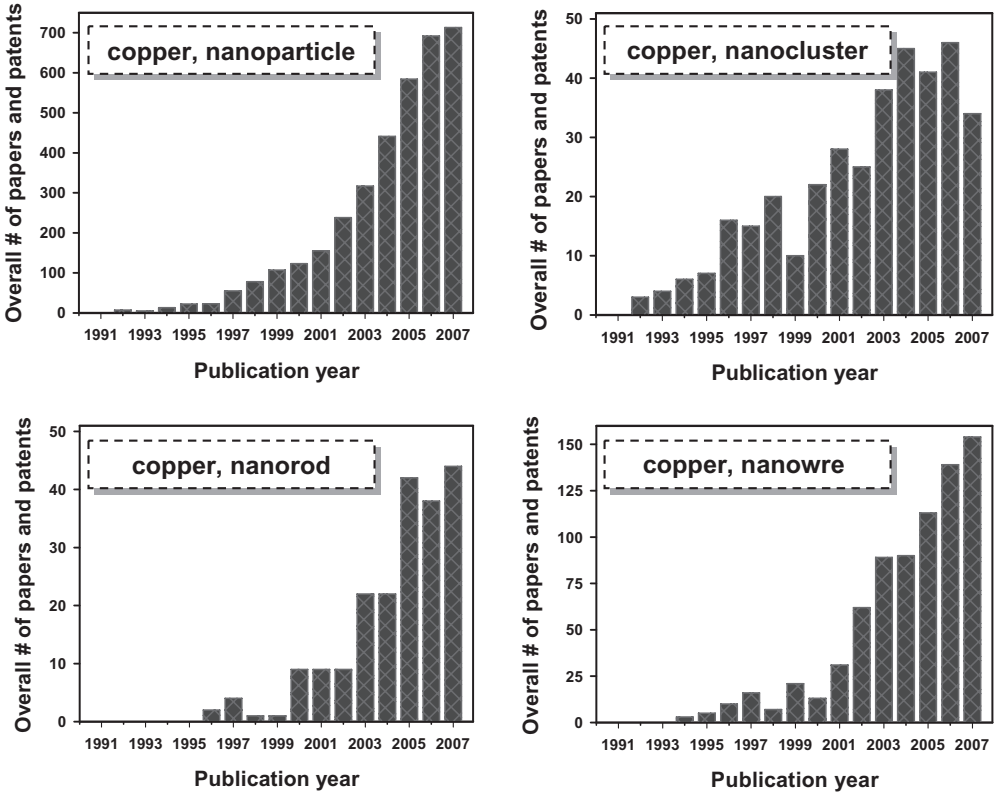

Figure 1.2 Histograms showing the year-distribution of papers and patents as a function of the single keyword.

the number of papers and patents relevant to the keywords 'nanoparticle' and 'nanowire' is markedly higher, as compared with the other two classes; moreover, their trends show a steeper increase in recent years.

Despite the large number of studies and their exponential increase, very few reviews have been issued on the synthesis and characterization of $Cu^{(0)}$ nanostructures, all of them dealing with specific approaches, limited periods or selected morphologies [3–13]. At present, there is therefore the need for a comprehensive review, providing a 'bird's eye view' of all the possible routes for the preparation of nanosized copper materials, and their characterization. Aiming at this purpose, in the present chapter we reported on all the main approaches, and have provided a brief commentary on each of these, following its historical evolution and the key aspects/findings of outstanding studies. As guideline to the classification of the different studies, we chose the type of synthesis approach, while characterization results were cited, in support of the description of specific nanomaterials and/or methods. Consequently, the present chapter is divided into four subsections, respectively devoted to physical, wet-chemical, photochemical and electrochemical methods for the synthesis of copper nanomaterials.

We clearly admit that such a classification is not perfect, and that some interesting studies may have been omitted, due not only to the high number of publications existing but also to the organization chosen for the chapter. Nevertheless, the chapter presents a critical selection of citations taken from the greatest number of studies on Cu NPs referenced to date. It is the authors' intention that the chapter should be considered as a basic aid for the reader who wishes to approach the 'microcosm' of the synthesis and characterization of copper nanomaterials in a concise and schematic manner.

1.2
Physical/Mechanical and Vapor-Phase Approaches

The reader will note that the sections of this chapter which describe chemical (and related) approaches are longer than the present paragraph, dealing with physical/mechanical and vapor-phase approaches. This choice is due basically to a recent remarkable development in the research fields corresponding to chemical approaches, determining a greater literature expansion, as compared to barely physical routes to unsupported $Cu^{(0)}$ NPs. In this section, a technique with great historical and applicative relevance – such as mechanical milling – has been cited concisely, as we believed there to be only a partial overlap between research on metal powders of industrial interest and the main topic of this chapter, namely, the controlled synthesis of Cu NPs with well-defined and uniform properties.

Some infrequent routes to Cu NPs – such as electrical wire explosion, electrospinning and spray pyrolysis – are cited for the sake of completeness, along with more widespread vapor-phase approaches, such as arc discharge, metal vapor and metal–organic vapor condensations.

Due to the aforementioned focus on unsupported $Cu^{(0)}$ NPs, several very important techniques – which lead principally to the deposition of supported or composite nanomaterials (including many plasma approaches, ion-beam sputtering deposition, lithography, etc.) – have not been included in this section.

1.2.1
Mechanical and Mechanochemical Milling

Mechanical techniques, such as ball milling (BM), represent one of the earlier examples of the so-called 'top-down' approaches to nanostructures, involving the controlled erosion of precursors to produce finer structures. Originally, the BM of powders was developed in metallurgy to produce finely dispersed alloys [14, 15], but subsequently it has been used to produce several metastable materials. First examples of the BM preparation of nanocrystalline materials dates back to the early 1990s [16]. The BM of powders is also known as 'mechanical attrition', and can be divided in two categories, as a function of the composition of the starting powder. The milling of elemental powders is indicated as mechanical

milling, whereas in the case of powders having different compositions it is indicated as mechanical alloying [17–19]. Although the minimum grain size achieved by mechanical attrition depends on several parameters, the size distribution of ball milled-particles can be quite broad when compared to that of NPs produced by chemical methods [14]. In general, mechanical erosion routes for the preparation of Cu NPs have been frequently outperformed by chemical approaches, due mainly to the less-tight control over NP size, shape and crystallinity.

Several studies were reported during the 1990s on the fundamental aspects of the BM-preparation of Cu NPs [20–26]. More recently, however, an improved version of the method has been proposed, leading to Cu nanograins with a narrower size distribution and good crystallinity [27]. During the 1990s a number of investigations were also conducted on the use of mechanical milling to induce solid-state displacement reactions and to obtain Cu NPs from $Cu^{(II)}$ precursors, such as dichloride [28–30]. Unfortunately, however, this process – which was named *mechanochemical* – showed certain weak points, such as the occurrence of combustion side-reactions, and has not undergone remarkable developments.

1.2.2 Electrical Wire Explosion and Electrospinning Approaches

The technique of electrical wire (EW) explosion has been studied since the 1950s [31–37], and the EW production of Cu nanoclusters and nanopowders has been investigated widely during the past 50 years [32, 33, 38]. In this method, the average particle size can be controlled by the ambient gas pressure, with the particle size usually increasing in line with pressure increases [39, 40]. Other parameters that may influence the final nanopowder include the chemical reactivity of the ambient gas and the initial radius of the wire [41, 42]. Although a number of studies have been reported on the EW production of Cu NPs, it should be noted that the final product of EW synthesis shows very poor stability towards storage or heating in air, due to severe oxidative degradation [43].

Electrospinning (ES) is another high-energy approach to Cu nanostructures, and is based on the application of high voltages. In recent years, this technique has attracted much interest for the preparation of nanofibers and other elongated nanostructures. In the ES process, a high voltage is applied to a polymer solution that is ejected from a conductive capillary. This results in fibers that are collected at a counterelectrode in the form of aligned bundles [44–46]. It is possible to modify the process by adding small-sized Cu NPs to the polymer solution, and to use this mixed precursor to obtain composite metal–polymer nanofibers [47]. Recently, such an approach was applied to the preparation of Cu nanocables capped by poly(vinyl alcohol) from Cu NPs having the same capping agent [48], while a solution of $Cu(NO_3)_2$ and poly(vinyl butyral) was used to produce long, electrospun copper fibers [49].

1.2.3
Spray and Flame-Spray Pyrolysis

Spray pyrolysis (SP) has been used to produce micro-and nanosized particles since the 1990s [50]. In a typical SP synthesis of Cu NPs, an aqueous solution of the correct precursor is atomized and the resultant droplets are transferred by a carrier gas into a tubular furnace (a possible instrumental set-up is shown in Figure 1.3), where the precursor is converted into spherical Cu NPs (see Figure 1.4) [51]. The

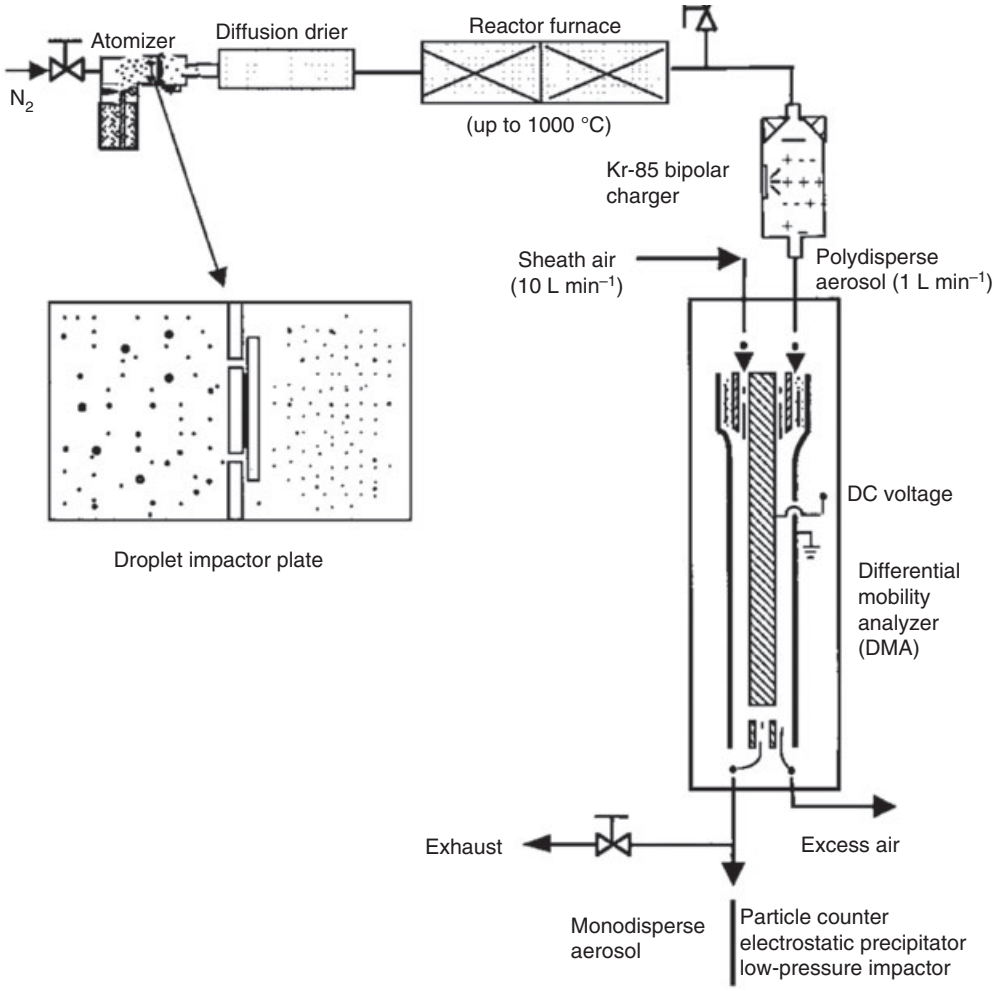

Figure 1.3 Spray pyrolysis system for particle generation and classification. Reprinted with permission from *Advanced Materials* **2002**, *14*(7), 518–21; © 2002 Wiley-VCH Verlag GmbH &Co.

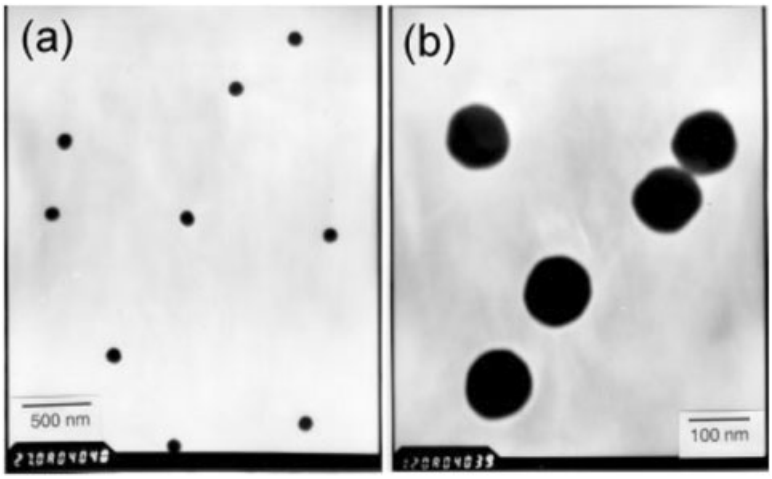

Figure 1.4 TEM images of copper particles produced at 600 °C. (a) original magnification ×27 000; (b) original magnification ×120 000. Reprinted with permission from *Advanced Materials* **2002**, *14*(7), 518–21; © 2002 Wiley-VCH Verlag GmbH &Co.

process is frequently based on the use of relatively high concentrations of H_2, mixed with the carrier gas, to promote reduction of the copper precursor [52, 53], although this procedure may increase potential safety hazards. In an alternative approach, low-molecular-weight alcohols are used as both cosolvent and reducing agent [51]. The key role of alcohols and polyols in the reduction of the copper precursor is discussed in Section 1.3.2. Here, it will simply be noted that the alcohol concentration can be used in SP processes to tune the NP chemical status. Changes in the Cu NP chemical composition induced by adding 10% ethanol to the precursor solution are shown in Figure 1.5 [51].

The application of *flame spray pyrolysis* to NP synthesis generally resulted in the production of metal oxides and salts [54–57]. Recently, Athanassiou *et al.* proposed the use of a flame-SP apparatus which operated in continuous fashion in a nitrogen-filled glovebox to produce carbon-coated Cu NPs with a good size uniformity [58].

1.2.4
Arc-Discharge Approaches

The use of arc discharges under an inert and/or reactive gas, or in liquid phase, implies the generation of a plasma jet inducing the formation of copper atoms and their condensation into particles of different structure and composition [59, 60]. Early investigations into application of the arc-discharge technique to the synthesis of Cu NPs were proposed during the 1990s [61–63], when mixtures of

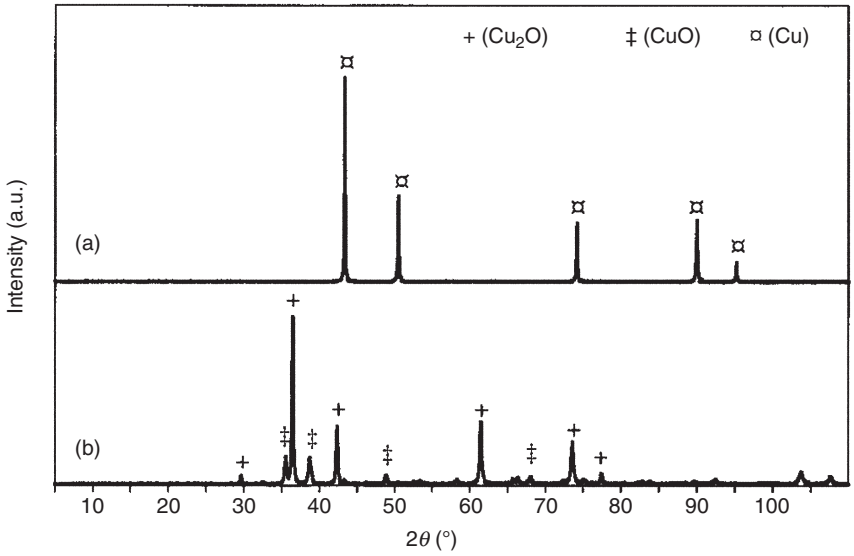

Figure 1.5 X-ray diffraction (XRD) pattern of copper particles prepared at 600 °C from 0.30 mol l^{-1} $Cu(NO_3)_2$ in (a) 10 vol.% ethanol and (b) pure aqueous solutions. Reprinted with permission from *Advanced Materials* **2002**, *14*(7), 518–21; © 2002 Wiley-VCH Verlag GmbH &Co.

an inert gas and hydrogen or methane reactive gases were respectively used to prepare aggregated copper powders [61] or carbon-encapsulated Cu NPs [62]. This is an example of what generally happens in this approach: when preparing Cu nanopowders without additional stabilizing agent, they inevitably tended to aggregate [61] or generate more complex structures [64]. Consequently, in recent years the approach has mainly focused on the encapsulation of Cu nanograins into carbonaceous [65] or polymeric [66, 67] protecting shells. The first class of NPs is basically a development of what was found in 1998 by Jao *et al.* [62], whereas in the second approach arc evaporation/condensation and plasma polymerization techniques were combined in a dual plasma process, leading to polymer-stabilized copper nanoparticles.

More recently, arc-discharge routes have been used in the liquid phase. This method, which is referred to as solid–liquid phase arc discharge (SLPAD), comprises polarizing copper electrodes that are maintained at high voltages and then momentarily short-circuited through an appropriate medium, such as an aqueous electrolyte solution [68], ethylene glycol [69], or an aqueous solution containing antioxidants and surfactants [e.g. ascorbic acid and cetyltrimethylammonium bromide (CTAB)] [70]. The high electrical power generates an arc of high temperatures (10^3–10^4 °C) that induces Cu melting and vaporization such that, close to the electrode surface the liquid is also vaporized and removes the Cu aerosol from the arc zone. The as-formed Cu particles are cooled immediately, preventing their further growth and/or aggregation [69], and then directly dispersed in the liquid

phase. By using this method, spindle-like or spherical structures may be obtained in pure solvents such as water [70] or ethylene glycol [69], respectively. The use of additional capping agents was found to increase the stability of spherical NPs in the low-dimensional range [70].

1.2.5
Metal Vapor Condensation

The term inert gas condensation (IGC) indicates a general approach based on the high-energy evaporation of metal atoms and on their subsequent condensation under inert conditions, leading to metal particles [71]. Most frequently, IGC has been performed by thermally evaporating metal atoms, although arc-discharge approaches and sputter-assisted methods [72] can also be considered as IGC processes. The IGC preparation of Cu nanopowders, which dates back to the 1980s, has often suffered from problems associated with unstabilized particles, including polydispersion and air instability, due to oxidation phenomena [73–76]. Many reports published during the 1990s sought to produce nanocrystalline macroscopic materials (by means of compaction or other techniques) [77] or were focused on the study of specific fundamental aspects [78–80]. In 1996, an alternative method was proposed, based on the rapid condensation of metal vapors by contacting them with the vapors of a cryogenic liquid [81, 82]. More recently, the method was modified by collecting metal vapors in a conventional liquid phase (e.g. acetone [83]) or other solvents such as toluene, diglyme and tetrahydrofuran [84].

1.2.6
Metal–Organic Chemical Vapor Condensation

In recent years, organometallic copper species have been employed as precursors for the preparation of Cu NPs via a controlled thermal decomposition process, known as metal–organic chemical vapor deposition (MOCVD). Copper$^{(II)}$-acetylacetonate ($Cu(acac)_2$) and its derivatives have gained wide popularity as precursor compounds for MOCVD routes [85–87], and many of the investigations on this topic have been recently reviewed by the group of E.I. Kauppinen [6]. Basically, the method is based on a controlled decomposition of the organometallic precursor in the vapor phase. In a laminar flow reactor, additional gases were tested as modifiers capable of tuning the nanostructure chemical composition, and elemental, oxide and composite copper NPs have all been obtained using this approach [6]. More recently, ensembles of Cu nanowires were also obtained by thermal decomposition of the same precursor; this had been sealed under vacuum in ampoules and then thermally treated at 300–400 °C [88]. The wire surface was shown to be protected by a thin carbonaceous layer that stabilized the elongated structure. The hexafluoro- derivative of $Cu(acac)_2$ has been also employed in MOCVD routes by the group of Wang [89, 90], who obtained Cu nanowires either by exploiting carbon nanotubes as the templating agent [89] or with controlled crystallization conditions for the growth of Cu structures [90].

Copper (oleate)$_2$ and Cu(II) phthalocyanine compounds were also investigated in similar MOCVD approaches, based respectively on the precursor decomposition in a sealed tube [91–93] or in a tubular reactor [94]. During the period between 2002 and 2004, a quite different approach was used by Bunge *et al.* [95] and Fischer and coworkers [96, 97]. These groups applied a modified version of the procedure developed by Floriani and colleagues [98], and rapidly injected an octylamine solution of a $Cu^{(I)}$-mesityl complex [95] or $Cu(OCH(Me)CH_2NMe_2)_2$ [96, 97] into a hot hexadecylamine solution (at 300 °C). This led to the production of high-quality nanoparticles, namely monodisperse spherical and crystalline $Cu^{(0)}$ NPs (of ca. 10 nm) that were passivated by amino groups.

1.3 Chemical Approaches

Transition-metal nanophases are intrinsically *unstable materials* (the thermodynamic minimum appears always to correspond to the bulk metal) that we can handle, store and use for technological applications exclusively in case the kinetics of their undesired degradation reactions are sufficiently slow. In aiming to slow down the rate of NP side reactions, a large number of investigations have been conducted to determine how the correct *stabilization* of metal NPs can be achieved.

As outlined by R.G. Finke and L.S. Ott in a recent review [1], those species capable of stabilizing a nanosized metal phase can be allocated to three classes, based on their mechanisms of action: (i) *electrostatic*, based on the classical theory of electrostatic colloidal stabilization, as developed by Derjaugin, Landau, Verwey and Overbeek (often referred to by the acronym DLVO); (ii) *steric*; and (iii) *electrosteric*, which is a combination of the electrostatic and steric modes.

Interestingly, the same authors provided a critical viewpoint of how to discriminate among different modes and attribute the role of *stabilizer* to a specific agent. It is a fact that the attribution of a stabilizing effect to a single surfactant/polymer/additive can be misleading: in many systems, there are often multiple possible stabilizers, and frequently the solvent itself, or dissolved counterions, may take part in the NP stabilization. Even the amount of dissolved oxygen can be critical (this is especially true in the case of copper), as the formation of an oxide shell may contribute to either the stabilization or aggregation of NPs.

However, it should also be noted that the choice of a specific stabilizer is presently driving the bibliographic classifications: many papers are specifically titled in terms of the leading stabilizer chosen for the NP preparation, and the number of agents that have been successfully applied to the synthesis of well-dispersed Cu NPs has undergone a vast increase, thus evidencing the need for a comprehensive examination of this field.

These critical issues have concurred to the organization of the following paragraphs, where attention has been paid both to the overall synthetic method (including the reaction medium) and to the stabilizer type. Consequently, the

red-ox approaches to Cu nanomaterials (in some cases indicated as wet-chemical processes) have been classified in terms of the stabilizer structure (Sections 1.3.1–1.3.4), the possible use of specific reaction media, such as compressed and supercritical fluids (Section 1.3.5) or ionic liquids (Section 1.3.6), and finally of specific reaction conditions, as in the case of ultrasonic-chemical processes (Section 1.3.7).

1.3.1 Wet-Chemical Routes without Surfactants

Apparently, the simplest solution-based approach to produce copper colloids is the direct reduction of a precursor in an appropriate aqueous solution. Most frequently, an alkaline medium and complexing additives are employed; this is necessary in order to sequester Cu ions and to prevent the undesired formation of insoluble $Cu^{(II)}$ hydroxides, eventually evolving into Cu_2O or CuO NPs. In contrast, the formation of cuprate ions or other soluble $Cu^{(II)}$ complexes makes possible the synthesis of $Cu^{(0)}$ NPs, due to the following reaction scheme [99]:

$$Cu^{2+} + 4OH^- \rightarrow Cu(OH)_4^{2-}$$

$$Cu(OH)_4^{2-} + BH_4^- \rightarrow Cu^{(0)} + BO_2^- + 2OH^- + 3H_2$$

Many studies have used a modified version of this aqueous route to Cu NPs [100–111]; the key aspects of the different approaches are shown schematically in Table 1.1.

During the early stages of research into this approach, submicron powders [101, 109, 112] or irregular smaller powders [103] were obtained; subsequently, the correct choice of the complexing agent and of the operating conditions led to the synthesis of several morphologies, including compact or hollow nanocubes and nanospheres (Figure 1.6) [104, 107], nanorods (Figure 1.7) [110] and ultralong nanowires (Figure 1.8) [105].

During the early 1990s, Tsai and Dye reported on the homogeneous reduction of metals salts with alkalides and electrides in aprotic (nonreducible) solvents, leading to nanoscale metal particles [113, 114]. The approach required some degree of experimental skills and was based on the use of solvated M^- and e^- species, that are among the strongest reducing agents in existence. Subsequently, by using $CuCl_2$ as a precursor, the method was successfully applied to the preparation of Cu NPs.

1.3.2 Wet-Chemical Routes Based on Surfactants and Low-Molecular-Weight Capping Agents

1.3.2.1 Aerosol OT (AOT)-Capped Cu Nanomaterials

The controlled preparation of metal colloids by the chemical reduction of copper salts in the presence of a micellar stabilizing environment was the subject of many

Table 1.1 Overview of different approaches to the synthesis of Cu NPs by means of direct reduction in aqueous solution.

Precursor	Reducing agent	Alkaline pH?	Ligand and/or addition of additives	NP type and mean size	Reference (year)
CuCl	Borohydride	Information not available	Information not available	Information not available	[100] (1996)
CuCl	Ethylene-diamine	Yes	KCl	Spherical, submicron ($0.8 \pm 0.3\,\mu m$)	[101] (1997)
CuCl	NaH_2PO_2 H_2O	Yes	No, but process carried out in autoclave @ 200 °C for 1 day	Micron-sized sponges, nanowalls inside the porous structure	[102] (2006)
$CuBr_2$	Borohydride	n.r.	The solvent itself? (several solvents were tested: water, alcohols, THF, acetonitrile, diethyl-ether, etc.)	Irregular; 10–50 nm	[103] (1999)
$CuCl_2$	Hydrazine	–	No	Low reactant conc. gave compact cubic or spherical NPs; high reactant conc. produced hollow NPs; in both cases, NP size was 100–200 nm	[104] (2005)
$Cu(NO_3)_2$	Hydrazine	Yes	Ethylene-diamine (probably, it also concurred to $Cu^{(II)}$ reduction)	Ultralong nanowires (diameter 100–200 nm) or nanodisks	[105] (2005)
$CuSO_4$	Borohydride	Yes	Trisodium citrate	Spherical; 10–30 nm	[106] (2007)
$CuSO_4$	Borohydride	Yes	EDTA	Elliptical; 20 nm	[99] (2005)
$CuSO_4$	Formaldehyde	Yes	Sodium tartrate; silica or polymer nanospheres were used as template	Hollow spherical aggregates; 200–300 nm	[107] (2005)
$CuSO_4$	Borohydride	Yes	I^- or SCN^-	Spherical; 10 nm	[108] (2002)
$CuSO_4$	Borohydride	No, but it increased during the process	No	Submicron powders; 200 nm	[109] (1999)

Table 1.1 *Continued*

Precursor	Reducing agent	Alkaline pH?	Ligand and/or addition of additives	NP type and mean size	Reference (year)
$CuSO_4$	Glucose	Yes	Glucose itself (optimization of its conc. proved to show an effect on the Cu NP morphology)	Spherical (~5 or 20 nm), rod-like (diameter ~50 nm, aspect ratio ~2.5)	[110] (2006)
$CuSO_4$	Hydrazine	n.r.	Hexanol, dimethyl oxalate. First step was the precipitation of spherical $Cu^{(II)}$-oxalate aggregates, acting as a template	Flower-like microcrystals	[111] (2006)

n.r. = not relevant for comparison.

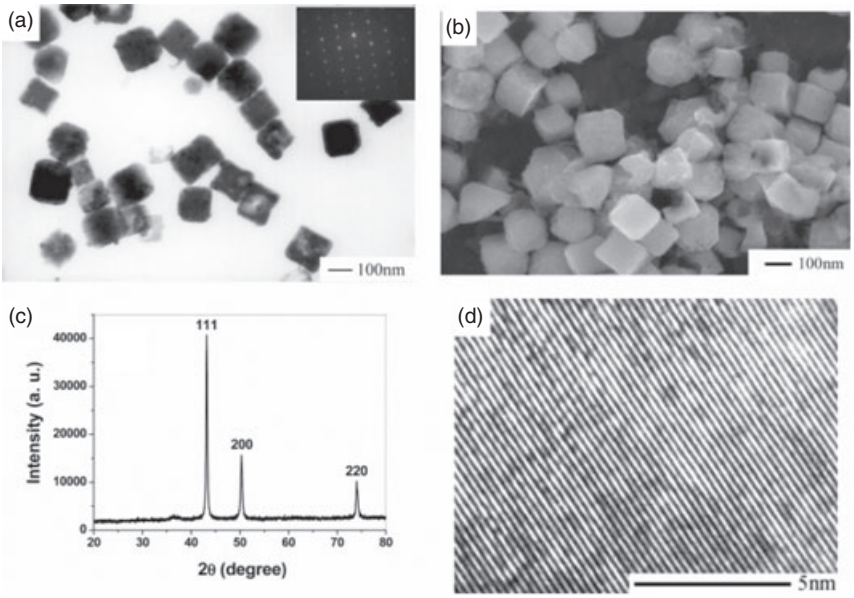

Figure 1.6 (a) TEM and (b) SEM images of cubic copper particles. The inset in (a) shows the selected-area electron diffraction (SAED) pattern obtained by focusing the electron beam on a cubic copper particle; (c) An XRD pattern of copper particles; (d) a high-resolution TEM image of one part of a cubic particle, showing its crystal structure. Reprinted with permission from *Journal of Physical Chemistry B* **2005**, *109*, 15803–7; © 2005 American Chemical Society.

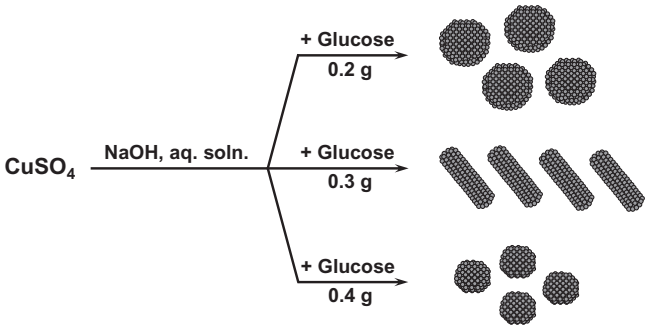

Figure 1.7 Schematic representation of the synthetic procedure proposed by T. Pal and colleagues [110] for the preparation of glucose-capped spherical and rod-shaped copper nanoparticles.

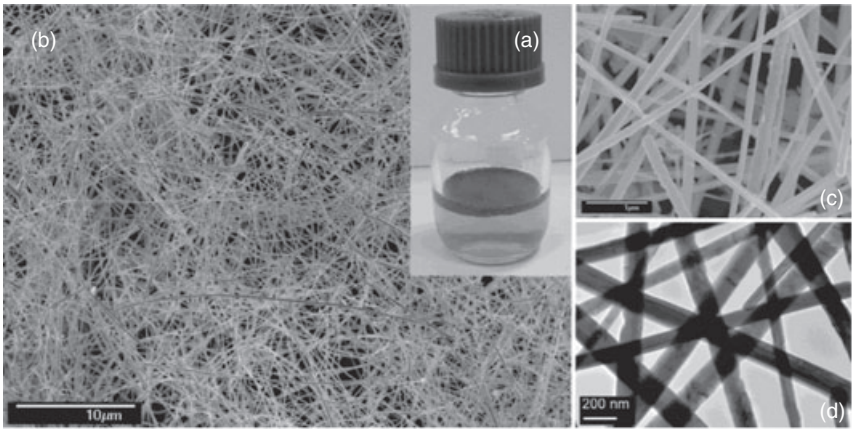

Figure 1.8 (a) As-prepared copper nanowires in mother liquor; (b, c) Field emission SEM images of general and detailed views of copper nanowires; (d) TEM image of copper nanowires. Reprinted with permission from *Langmuir* **2005**, *21*, 3746–8; © 2005 American Chemical Society.

studies during the 1990s, and has continued to develop tremendously during the past decade. This approach, which is often referred to as 'soft-wet-chemical', 'soft colloidal template' or 'microemulsion-based', is based on the use of reducing agents such as hydrazine and sodium borohydride, and has been successfully applied to the preparation of NPs composed not only of transition metals but also other compounds, salts and multimetal particles.

In this respect, many single-chained surfactants have been investigated, including sodium alkyl- or aryl-sulfates [sodium dodecyl sulfate (SDS), sodium benzyl sulfate (SBS) and sodium dodecylbenzene sulfonate (SDBS), quaternary

ammonium halides (CTAB, cetyltrimethylammonium chloride (CTAC)]. However, the first and most frequent route to surfactant-stabilized copper nanoparticles is based on use of the di-(2-ethylhexyl)-sulfosuccinate anion, usually indicated by the acronym AOT (Figure 1.9) (for reviews dealing with NP soft-chemical syntheses using AOT, see Ref [7, 11–13, 115–122]).

AOT is a key species for the realization of thermodynamically stable reverse micelles in a ternary water/organic solvent/AOT salt system. Water-in-oil (w/o) microemulsions with a well-defined order and shape can be easily generated by correct selection of the operating conditions (emulsion composition, AOT counterion type, cosurfactant, temperature, pressure, etc.). Since 1991 [123–130], the outstanding studies published by the group of M.P. Pileni have shed light on the potentialities of this system for the controlled preparation of Cu NPs. As several interesting reviews have already been published by the same group on this topic [7, 11–13, 121, 122], we will limit our description here to a very brief survey of the existing literature.

In the case of surfactants consisting of a large polar head and a small lipophilic chain, a normal micelle is formed, in which the chains form the inner core and the polar groups are localized at the outer surface. In contrast, surfactant molecules with small polar moieties and bulky hydrocarbon chains tend to generate *reverse micelles* (see Ref. [121] and references therein), in which the mutual position of polar and nonpolar moieties is exchanged, as compared to the 'normal' case. As water becomes entrapped in the core of reverse micelles, there is a dynamic exchange of species within the micelle, and this is where the chemical reduction of the copper precursor occurs. Under selected experimental conditions, an increase in the water : surfactant molar ratio in the emulsion implies a proportional size increase of the template structure. In general, this provides a simple means of controlling the size of spherical Cu NPs generated in the polar core of the nanoreactors. Transmission electron microscopy (TEM) images of colloidal NPs obtained by varying the water content in a $Cu(AOT)_2$/water/isooctane system are shown in Figure 1.10 (top row), together with a sketch of the w/o droplet structure. Of note, such clear size control has been demonstrated in the case of relatively small w/o structures. Other self-assembled structures also become possible, as a

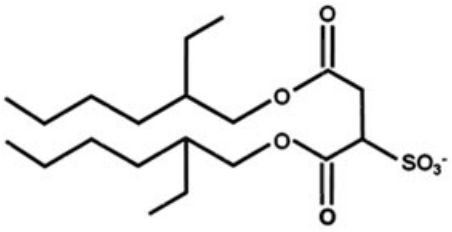

Figure 1.9 Chemical structure of the AOT anion. The branched chains afford for a surfactant shape frequently indicated as a 'champagne-cork', due to the bulky lipophilic moieties and a relatively small polar head.

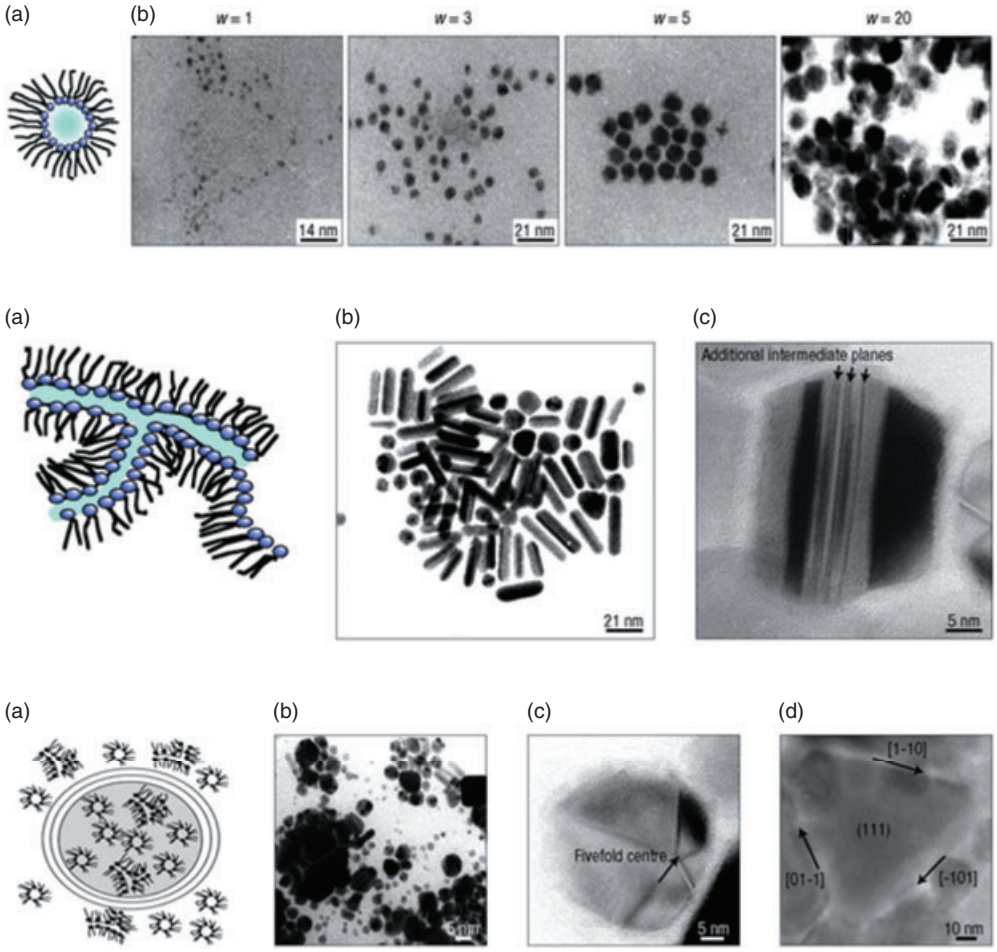

Figure 1.10 Different shapes of copper nanocrystals obtained in colloidal self-assemblies of a surfactant-H_2O-isooctane system. The surfactant, S, employed is either Na(AOT) or $Cu(AOT)_2$. The water amount $w = [H_2O]/[S]$ is related to the droplet radius by R (nm) = $0.15 \times w$. Top row: [AOT] = 0.1 *M*; $[Cu(AOT)_2] = 10^{-2}$ *M*; $[N_2H_4] = 2 \times 10^{-2}$ *M*. (a) Reverse micelles; (b) Control of nanocrystal size by means of the control of the size of water-in-oil droplets, *w*. Middle row: $[Cu(AOT)_2] = 5 \times 10^{-2}$ *M*, $[N_2H_4] = 1.5 \times 10^{-1}$ *M*, $w = 10$. (a) Interconnected cylinders; (b) formation of spherical and cylindrical nanocrystals; (c) cylindrical particle made of a set of deformed f.c.c. tetrahedra bounded by (111) faces parallel to the fivefold axis with additional lanes. Bottom row: $[Cu(AOT)_2] = 5 \times 10^{-2}$ *M*, $[N_2H_4] = 1.5 \times 10^{-1}$ *M*, $w = 20$. (a) Supra-aggregates; (b) nanocrystals; (c) particle composed of five deformed f.c.c. tetrahedra bounded by (111) planes; (d) large, flat nanocrystals [111]-oriented and limited by (111) faces at the top, bottom and edges. Reprinted with permission from Macmillan Publisher Ltd: *Nature Materials*, Pileni, M.P., **2003**, *2*, 145; © 2003.

function of the region of the phase-diagram in which the chemical reduction is operated. Insights into the phase composition of several surfactant/water/oil systems have already been reported [131–137], and a direct relationship between template morphology and the synthesis of Cu NPs has been demonstrated [11, 138–140]. For example, in the case of large amounts of both water and organic solvent, water channels/cylinders are generated in the system, thus allowing the growth of cylindrical Cu nanocrystals (Figure 1.10; middle row). Under other experimental conditions planar or onion-like lamellar phases are also possible, and their existence implies other Cu NP morphologies (see Figure 1.10; bottom row).

Whilst the micellar shape cannot afford for a tight size-control over NP shapes which differ from spherical, it has been shown that the presence of different salt ions in the aforementioned water cylinders may provide an independent and useful tool to prepare cubic NPs (in the presence of Br^- ions), elongated particles (in the presence of HSO_3^- ions), Cu nanorods (in the presence of relatively high Cl^- concentrations), or more elongated structures, namely Cu nanowires (in the presence of relatively low Cl^- concentrations, e.g. 1 m*M*) (see Figure 1.11) [141–143].

The use of alternative anionic surfactants such as SDS [144], or the use of AOT mixed with cationic surfactants [145] in more complex w/o microemulsions, has also been explored. Similar to the case of other metals, for the w/AOT/oil soft-synthesis of Cu NPs, a number of reducing agents has been investigated: hydrazine and $NaBH_4$ are definitively the most frequently employed, although alternative chemicals, including natural molecules such as quercetin [146] have also been proposed. More recently, the group of Pileni has shown that a large excess of hydrazine, when employed as reducing agent, can give access to other anisotropic morphologies such as Cu nanotriangles [147] and nanodisks [148] (Figure 1.12).

As interestingly outlined by Pileni [121], the changes in the Cu NPs shape are attributed to differences in the growth rate of crystallographic faces, and

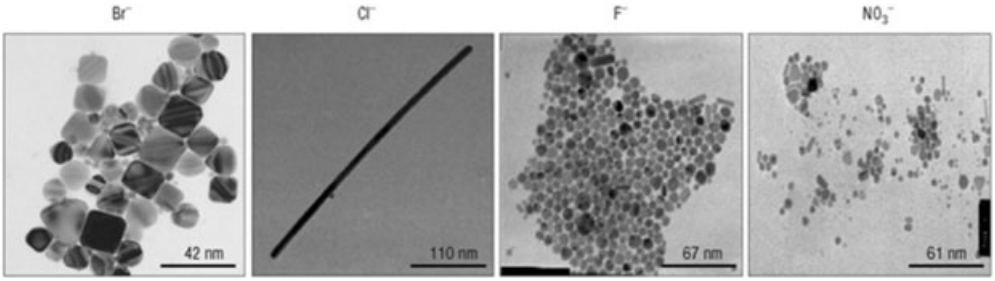

Figure 1.11 Different shapes of copper nanocrystals obtained in interconnected cylinders in the presence of various salt ions having the same concentration. 5×10^{-2} *M* $Cu(AOT)_2$ was dissolved in isooctane in the presence of various salts. Hydrazine was added to obtain $w = 10$ and a 10^{-1} *M* overall concentration $[N_2H_4]$, $[NaCl] = [NaBr] = [NaF] = [NaNO_3] = 10^{-3}$ *M*. Reprinted with permission from Macmillan Publisher Ltd. *Nature Materials*, Pileni, M.P., **2003**, *2*, 145; © 2003.

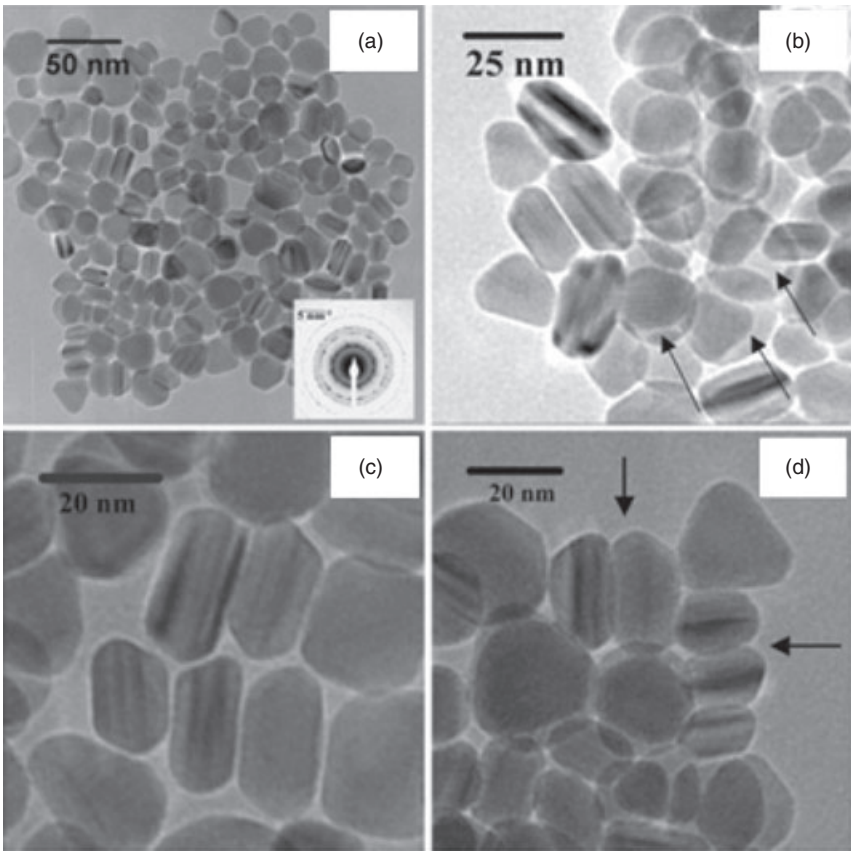

Figure 1.12 TEM images of copper nanocrystals. (a) Copper nanocrystals – the inset shows the SAED pattern of a collection of copper nanocrystals; (b) Thin nanocrystals; (c) Stacked elongated nanocrystals; (d) Overlapped nanocrystals. Reprinted with permission from *Advanced Functional Materials* **2005**, *15*, 1277–84; © 2005 Wiley-VCH Verlag GmbH &Co.

this is correlated to the selective adsorption of species/additives during crystal growth.

Other studies conducted by the group of C.R. Roberts have provided details about particle growth kinetics [149, 150]. Basically, as the ratio of the absorbance detected at about 560 nm (corresponding to the peak maximum) and 500 nm (off-peak) is correlated directly to the mean size of the Cu NPs core, these authors performed time-resolved *in situ* studies and followed the evolution of spherical Cu NPs, in turn proposing a theoretical model able to predict the NP size.

It is a fact that the chemical and physical properties of NPs can be tailored by controlling their size and/or their shape (see Ref. [151] and references therein; see also Refs [152, 153]). In Ref. [154], copper nanocrystals of different shapes were

shown to give rise to different UV-visible absorption features. In particular, the well-known plasmon resonance peak which falls at about 560 nm is attributed to spherical and cubo-octahedral NPs, whereas the peak falling at 650 nm can be shown to correlate to nanosized copper disks. Both, simulated and experimental UV-visible spectra obtained with Cu nanodisks prepared in reverse micelles are shown in Figure 1.13 [154, 155].

1.3.2.2 Alkyl-Phosphate-Capped Cu NPs

Bis(ethylhexyl)hydrogen phosphate (HDEHP) [156] and other phosphate derivatives, such as dialkyl-dithio-phosphates (DDP) [157, 158], have been recently proposed as capping agents, as alternatives to AOT, for the w/o synthesis of spherical Cu NPs. The chemical structure and ability to form micellar structures of these surfactants strongly resemble those of AOT; both HDEHP and DDP are characterized by a 'champagne-cork' aspect, and form reverse micelles in w/o mixed solvents. Consequently, Cu NPs could be easily generated using the approach already described for AOT. The NPs showed good film-forming properties, while the presence of DDP stabilizers afforded useful antiwear properties when used as additives in liquid paraffin [157, 158].

1.3.2.3 Alkyl-Sulfate-Capped Cu NPs

Another microemulsion route to Cu NPs is based on the use of sodium alkyl- or aryl-sulfates. Two anionic surfactants have been frequently employed, namely SDS [159–161] and SDBS [162], both of which generate micellar aggregates that are similar to those described in the above sections. For example, in 1999 Qiu *et al*. showed that the size of w/o droplets (in a microemulsion composed of SDS, isopentanol, cyclohexane and water) depended linearly on the water/SDS molar ratio, and that this parameter could be used to tune the size of spherical Cu NPs [159].

More recently, SDS has been used mixed with polysorbates (Tweens) in order to exploit the synergetic stabilizing effects [161] whilst, in a simplified approach, Lu and coworkers obtained Cu nanocubes (Figure 1.14) through the hydrazine-reduction of $CuCl_2$ in refluxing aqueous solutions containing millimolar concentrations of SDBS [162]. The latter route could also be successfully applied to other metals and bimetallic particles.

1.3.2.4 Alkyl-Thiol-Capped Cu NPs

The synthesis of thiol-capped nanocopper is basically a further development/modification of the Brust approach, that was originally applied to gold NPs [163]. In a typical reaction, a $Cu^{(II)}$ salt is dissolved in a polar solvent (usually water [164–166], although methanol has been also used [167]), and then mixed/shaken with a solution of a quaternary ammonium salt ['quat', frequently, a cetyltrimethylammonium (CTA) or tetra-octylammonium (TOA) bromide] dissolved in an apolar solvent such as toluene. A thiol capping agent is subsequently added, and in the last step $NaBH_4$ or an equivalent reducing agent is added dropwise. Due to ligand

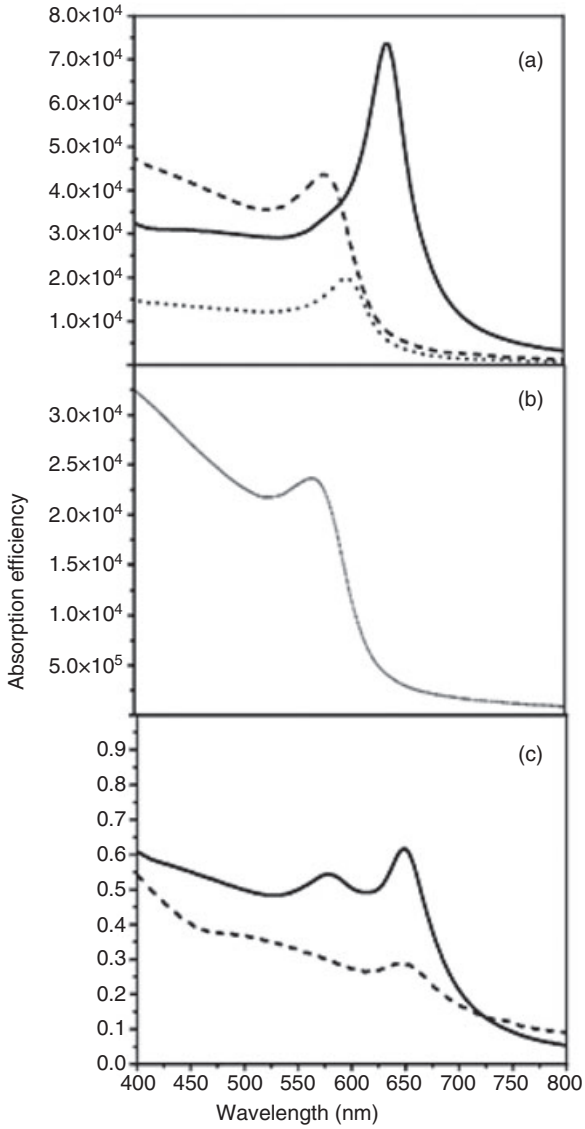

Figure 1.13 (a) Simulated absorption spectrum of copper particles having different shapes: nanodisks (size = 23 nm, aspect ratio = 1.8, truncature = 0), solid line; elongated particles (length = 22, width = 13, aspect ratio = 1.8), dotted line; cubo-octahedra (19 nm), dashed line; (b) Simulated absorption spectrum of 20 nm spherical copper particles; (c) Comparison between the experimental (dashed line) and simulated spectra (solid line). Reprinted with permission from *Journal of Physical Chemistry B* **2006**, *110*, 7208–12; © 2006 American Chemical Society.

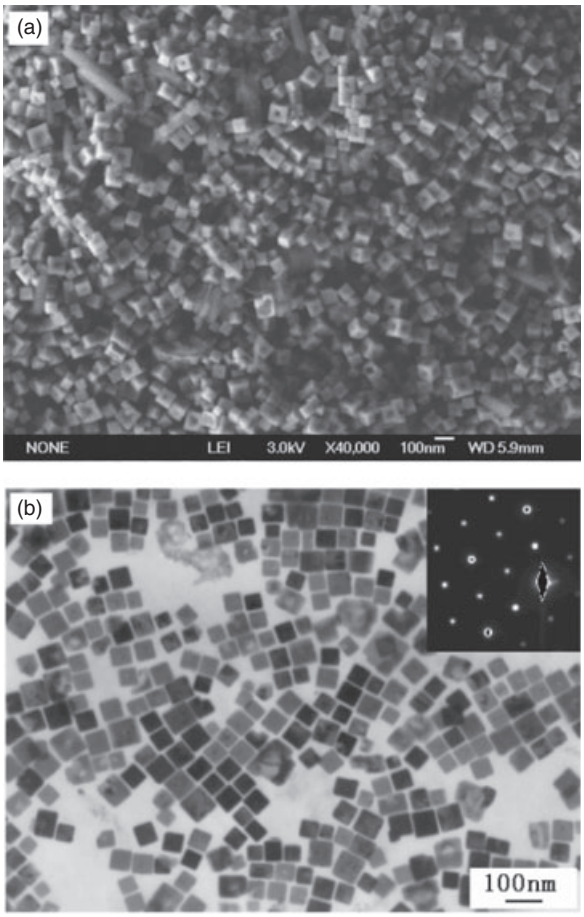

Figure 1.14 (a) SEM and (b) TEM images of copper nanocubes prepared under the final concentration C_{CuCl2} = 0.1 m*M* and C_{N2H4} = 3 m*M* and refluxed for 20 min at 100 °C in the presence of 1 m*M* SDBS. The inset in (b) shows the SAED pattern obtained by directing the electron beam parallel to the <111> direction. Reprinted with permission from *Langmuir* **2006**, *22*, 5900–3; © 2006 American Chemical Society.

exchange, the quat species are substituted by the thiol. Finally, alkyl-thiolate-Cu NPs can be collected/extracted in an appropriate organic phase such as toluene or benzene.

The effects of ligand structure on the stability of as-synthesized Cu NPs were assessed in several studies [164, 168–170]. Based on the appreciable stabilization provided by the thiol moieties, these core-shell NPs were subjected to several interesting investigations. For example, in differential pulse voltammetry experiments, Chen and Sommers observed that the as-produced Cu NPs showed quantized charging features [165]. Neckers and collaborators prepared Cu NPs capped by modified thiols bearing acrylic ending groups, allowing the copolymerization

of Cu NPs and acrylic monomers [167]. Finally, Dong *et al*. were able to prepare highly ordered Cu NP superlattices, by a controlled thermal annealing of octanethiolate-capped Cu NPs in molten TOA bromide [171].

1.3.2.5 Cu NPs Capped by Quaternary Ammonium Surfactants

Many examples have recently been reported of quaternary ammonium surfactants being employed directly as Cu NP capping agents, without making use of any ligand-exchange protocols. In two reports, TOA bromide or ethyl-hexadecyl-dimethyl-ammonium bromide were used to synthesize stabilized Cu NPs subjected to *in situ* spectroscopic investigations, such as XANES (X-ray absorption near-edge structure) [172] or EPR (electron paramagnetic resonance) [173]. The former study dates back to 1998, and provided interesting information about the existence of intermediate states during the formation of colloidal copper in toluene [172], whereas the latter was proposed as a general approach to the direct study of Cu NP oxidation kinetics [173]. Other papers have specifically investigated the potentialities of CTAB in the aqueous synthesis of Cu nanomaterials. In 2003, Cao *et al*. showed that it was possible to prepare nanotubes or nanorods composed of $Cu^{(0)}$ or its oxides, as a function of the experimental conditions [174]. The procedure was carried out in the presence of relatively high CTAB concentrations, but was quite simple as it could be considered a modified version of the simple reduction of an alkaline $Cu^{(II)}$ solution by means of hydrazine. In Ref. [174] evidence was provided that, upon increasing the $Cu^{(II)}$ initial concentration, the morphology of Cu nanostructures changed from nanotube to nanorod (see Figure 1.15 for examples of rod-like nanostructures). The authors hypothesized that electrostatic interactions induced the formation of ion pairs between CTA^+ and $Cu(OH)_4^{2-}$, and that modifying their relative abundances resulted in a change in the micellar aggregate shape.

By using the same chemical species, but different experimental conditions, Wu and Chen where able to prepare highly concentrated solutions of CTAB-capped Cu NPs (up to 0.2 *M*) at room temperature [175]. A slightly different approach was followed by Athawle *et al*., who employed isopropanol as both reducing agent and organic additive for the preparation of Cu NPs [176, 177]. Kumar and collaborators used a sulfobetaine stabilizer for the alkyl-borohydride conversion of $Cu^{(II)}$ ions into spherical Cu NPs; the use of the zwitterion aimed at improving the compatibility of Cu NPs with polar solvents [178]. These authors investigated two possible approaches, namely a batch and a microfluidic reactor process, and used reaction calorimetric investigations to study the intermediates involved in the NP synthesis.

1.3.2.6 Cu NPs Capped by Nonionic Surfactants or Stabilizers

During the late 1990s, the synthesis was reported of Cu NPs stabilized by nonionic commercially available surfactants such as Triton X-100 [179] and Genamin TO20 [180]. These surfactants were employed to generate reverse micelles and spherulite aggregates, respectively (Figure 1.16). The reduction of $Cu^{(II)}$ precursors encapsulated into spherulites was performed by conventional hydrazine treatment such

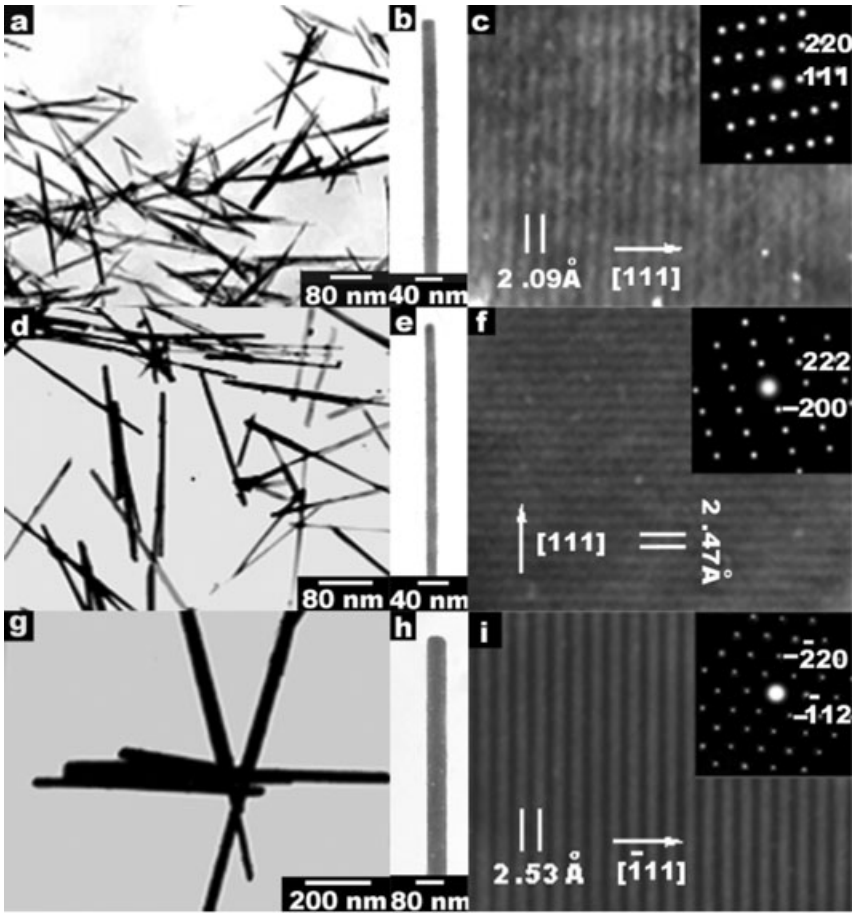

Figure 1.15 TEM images of Cu (a), Cu_2O (d) and CuO (g) nanorods. Single nanorod images of (b) Cu, Cu_2O (e) and CuO (h). High-resolution TEM micrographs of Cu (c), Cu_2O (f) and CuO (i) nanorods. The insets are SAED images of Cu, Cu_2O and CuO nanorods, respectively. Reproduced with kind permission from © Royal Society of Chemistry; DOI: 10.1039/b304505f.

that Cu NPs could be obtained. A phase diagram showing the typical experimental conditions used to prepare spherulites is shown in Figure 1.17. Interestingly, in the case of Genamin TO20, small Cu NPs were aggregated in spherical macroclusters which resembled the shape and size of the spherulite templates (Figure 1.18).

1.3.2.7 Cu NPs Capped by Cysteine, Oleic Acid and Other Small Molecules with Biological Relevance

Small biomolecules such as cysteine [181, 182], oleic acid [183–186] and/or oleamine [187, 188] have been intensely investigated during the past two years as

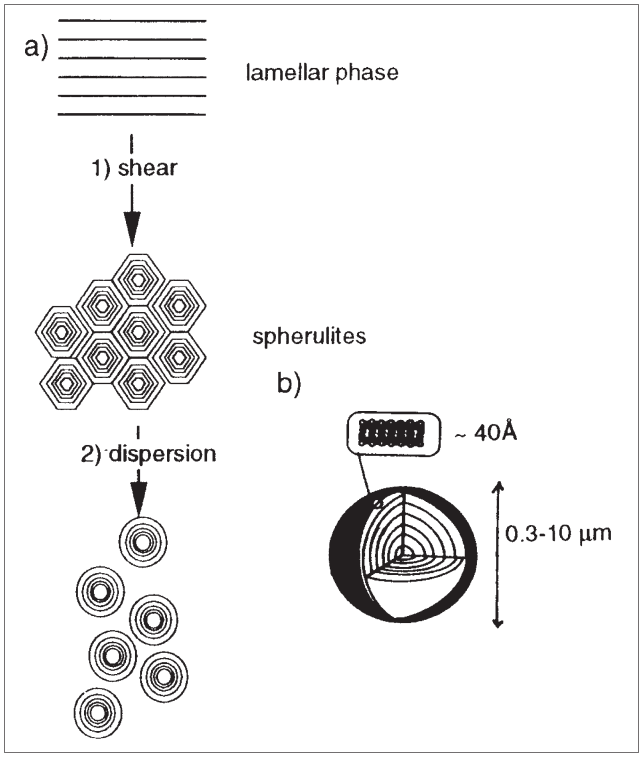

Figure 1.16 Stages in the preparation of a dispersion of spherulites (a) and their structure (b). (a) Route (1): the lamellar phase, under a controlled shear, organizes in a close-packed structure of multilamellar vesicles called spherulites; route (2): spherulites can be dispersed in an excess quantity of solvent; (b) Spherulites are composed of a regular stack of membranes separated by water layers. Reprinted with permission from *Langmuir* **1999**, *15*, 3738–47; © 1999 American Chemical Society.

innovative stabilizers for Cu NPs. Although at present they have been exclusively applied as catalysts [181, 182], amino acid-capped Cu NPs hold great promise in other fields, including the biofunctionalization of metal nanomaterials for biomedical applications, where they combine the properties of a biocompatible shell with those of a copper core capable of releasing antimicrobial ions under tightly controlled kinetics [189]. Using oleic acid as stabilizer and a mild multistep reduction based on glucose and ascorbic acid, Yang *et al.* obtained nanocrystalline copper with an hydrophobic shell, by means of the so-called AOIRT (Aqueous Organic Interface Reaction Technique) method [183–185]. In 2007, the group of Zhong reported a temperature-controlled route to Cu nanocrystals capped by oleic acid and oleamine [187]. The NP size was shown to depend linearly on the reaction temperature, in the 150–190 °C range, while higher values were found to induce the simultaneous formation of several shapes (cubic, tetrahedral, elongated, etc.). In the same year, Liu *et al.* applied a similar approach, in the presence of oleamine

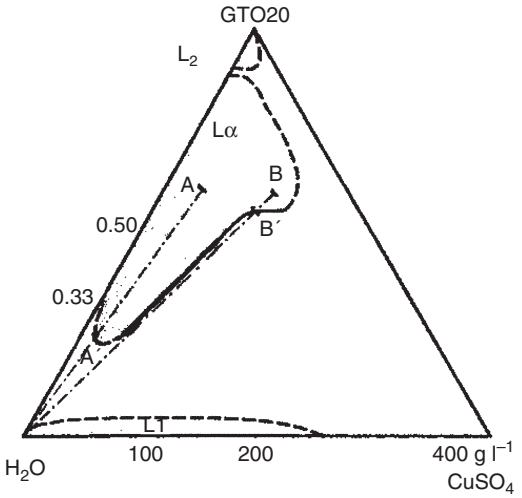

Figure 1.17 Experimental phase diagram of the Genamin TO20/H_2O/$CuSO_4$ system: Lα, lamellar; L_1, micellar; L_2, crystalline. The dashed lines are rough boundaries. Reprinted with permission from *Langmuir* **1999**, *15*, 3738–47; © 1999 American Chemical Society.

[188], to the preparation of Cu, Cu_2O and CuO NPs, while Su *et al*. obtained Cu cubic nanocages in the presence of sodium oleate [186]. Of note, in the latter case the formation of cubic-shaped and empty nanocages was shown to correlate with the structure of the Cu_2O intermediate particles.

1.3.3
Wet-Chemical Routes Based on Polymer and Dendrimer Capping Agents

Polymers represent one of the most frequently studied examples of NPs stabilizer showing steric effects. Physical hindrance of the space around the nanoclusters can prevent/minimize the direct contact between the NP metal cores, and thus afford an increased morphological stability. Polymer-capped Cu colloids have been investigated since the 1980s [190–193]; nano-Cu/polymer interface phenomena can be interpreted as cooperative noncovalent interactions of polymeric chains with surface metal atoms [193]. Moreover, the polymer action is due, at least partially, to the complexation of nanocluster surface atoms; polymer functional groups may in fact generate stronger interactions, leading to highly stabilized copper–polymer complexes.

The approaches to polymer-stabilized copper nanomaterials can be divided into three main classes: (i) the so-called ‘polyol process’; (ii) soft-template processes in which the polymer is employed (either as such or in combination with other capping agents), aiming exclusively at stabilization of the Cu phases; and (iii) dendrimer-encapsulation.

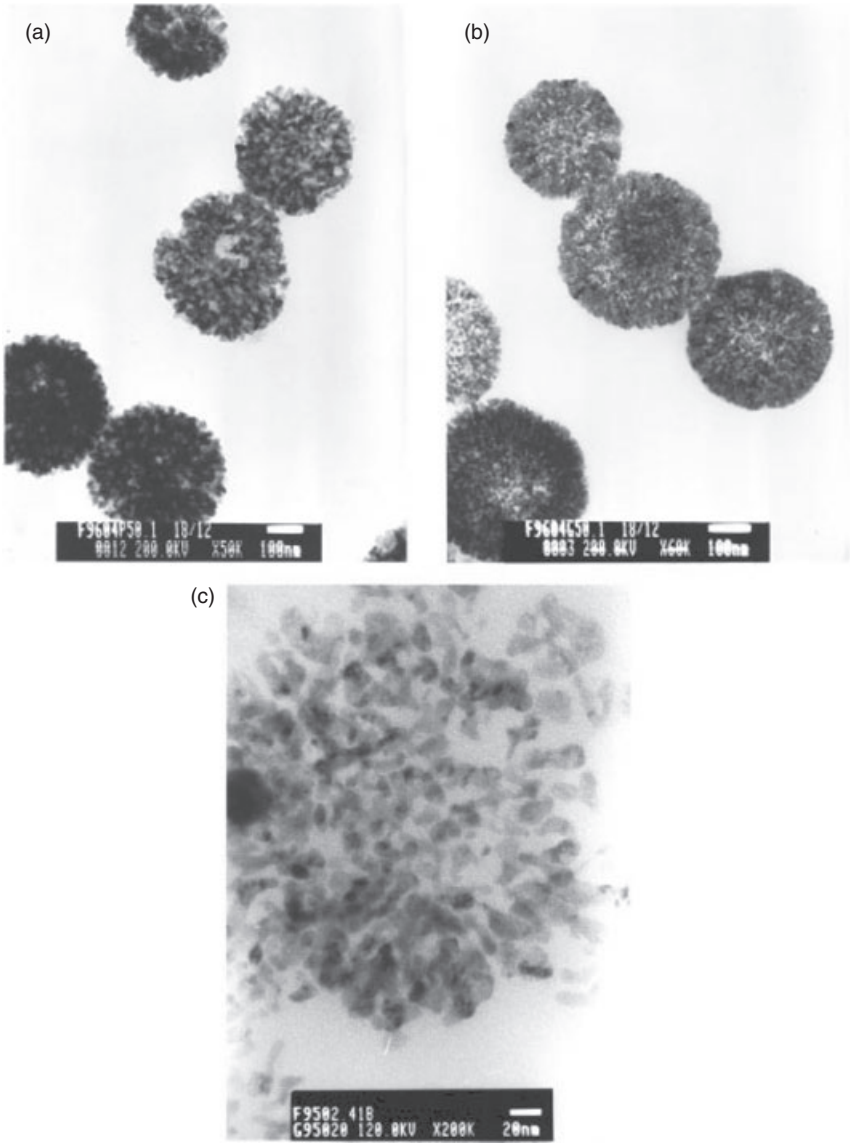

Figure 1.18 TEM images of spherulites after reduction of the encapsulated copper sulfate: (a) $C = 144\,g\,l^{-1}$, φ (volumic fraction in surfactant) = 0.54, manual shear; (b) $C = 85\,g\,l^{-1}$, $\varphi = 0.54$, shear rate = $107\,s^{-1}$; (c) Magnification of a single spherulite. Reprinted with permission from *Langmuir* **1999**, *15*, 3738–47; © 1999 American Chemical Society.

1.3.3.1 The Polyol Process

The polyol route to Cu NPs consists of the reduction of an appropriate precursor (copper salts, oxide, hydroxide, etc.) in a liquid alcohol medium, at relatively moderate temperatures. The solvent is typically glycerol or a glycol derivative (e.g. ethylene, diethylene), and has the dual role of a reducing and dispersing agent; to some extent it may also be useful as capping agent [194, 195], although more frequently additional stabilizers are employed [196–200]. Several parameters can be separately adjusted to tune the NP synthesis, including temperature, reaction time and the composition of the solution; the latter is expressed in terms of the nature of the precursors, the polyol type, the use of surfactants and additives, and the pH of the medium.

Multistep redox processes occur in the polyol process; for example, in case of ethylene glycol the first step implies that two solvent molecules are dehydrated, to form acetaldehyde. This latter species is then responsible for reduction of the metal precursor, generating Cu NPs and CO_2.

1.3.3.2 Polymer-Based Soft-Template Processes

Several polymers have been proposed as stabilizing agents for the Cu NPs synthesis. Used mixed with water and surfactants, polyethylene glycols (PEGs) have been successfully applied to the preparation of spherical Cu NPs by the group of Zhang [201], while Xie and collaborators obtained junctions of Cu nanorods [202] from a PEG/CTAB soft-template system. Unlike the polyol approach, the polymer species were barely used as modifiers in a soft-template micellar system, whilst the copper reduction was performed by a conventional reagent, such as ascorbic acid [201] or $NaBH_4$ [202].

A similar approach was also used in the case of poly(vinyl alcohol) (PVA). In 1999, Wang *et al.* used a soft-template method based on PVA/isopropanol/water micelles, and operated the $Cu^{(II)}$ reduction by means of borohydride [203]; more recently, Khanna *et al.* obtained Cu NPs in PVA/water emulsions, by employing hydrazine hydrate or sodium formaldehyde sulfoxylate as reducing agents [204].

It should be noted here that the use of polymer/surfactant complex mixtures such as those proposed in Ref. [202] seems particularly promising, due to some additional advantages. Surfactants associated with a polymeric additive may form micelles at concentrations considerably lower than those required by the surfactant alone. Moreover, in the case of polymer/surfactant mixtures, stabilization of the inorganic crystals may benefit from synergetic capping effects that improve both morphological stability and homogeneity [202].

Poly(vinylpyrrolidone) (PVP) is certainly one of the most investigated polymeric additives for the template Cu NP synthesis, having been employed in aqueous [205–208], amide [209], polyol [210–214] and alcohol solvents [215, 216].

In the first of these cases, spherical NPs were easily obtained by conventional reduction of a $Cu^{(II)}$ salt in the presence of alkaline borohydride [205, 207] or ascorbic acid [206] aqueous reducing solutions. Recently, a continuous and steady-flow reactor was proposed, in which a metal displacement reaction occurred. Basically, this involved a spontaneous redox reaction between $Cu^{(II)}$ ions and an

oxidizable metal foil, carried out in the presence of PVP and under hydrodynamic and mechanical assistance [208].

Interestingly, processes involving the use of polyol/alcohol solvents appear as a form of modified/improved version of the polyol method, in which the polyol/alcohol solvent is assisted by a specific (and generally stronger) reducing agent, such as hydrazine [215, 216], sodium phosphinate monohydrate [212] or ascorbic acid [210, 211]. The simultaneous presence of PVP and solvents with alcoholic moieties made it possible to obtain monodisperse copper nanocubes [211], nanoparticle arrays and aggregates [216] or nanorods [216], as a function of the experimental conditions.

The good morphological stability and size homogeneity of PVP-capped Cu NPs was exploited in several applications, including reusable catalysts [209] and nano-copper-based conductive ink-jet printing [212]. However, the use of PVP/Cu NPs in catalysis suffers severe limitations in terms of particle activity due to the strongly coordinating capping agent, and this often compromises the NP activity [1].

1.3.3.3 Encapsulation in Dendrimers

Dendritic molecules are repeatedly branched species with a symmetric and monodisperse structure and chemical composition [217–219]. Since the late 1990s, they have been shown to be useful template structures for the controlled synthesis of metal NPs [1, 220] and, particularly, of Cu NPs [221–224]. In one of his outstanding papers on this subject, R.M. Crooks defined the approach based on dendrimers as a "ship-in-a-bottle" route to obtain transition-metal NPs [221]. Interestingly, the dendrimer behaves as a monodisperse nanoreactor and allows the preorganization of the metal into its inner part. Basically, the process is based on a strong interaction between $Cu^{(II)}$ ions and the dendrimer core. It has been shown that the number of metal atoms adsorbed into the dendrimer inner part corresponds to the number of tertiary amines present therein [221], although nonspecific surface complexation may occur leading to undesired phenomena such as NP aggregation. Subsequently, the metal ions become entrapped in the template structure, while a conventional chemical reduction of the metal–dendrimer complex (e.g. by means of $NaBH_4$) induces the formation of a nanosized inorganic core inside the dendrimer shell (Figure 1.19).

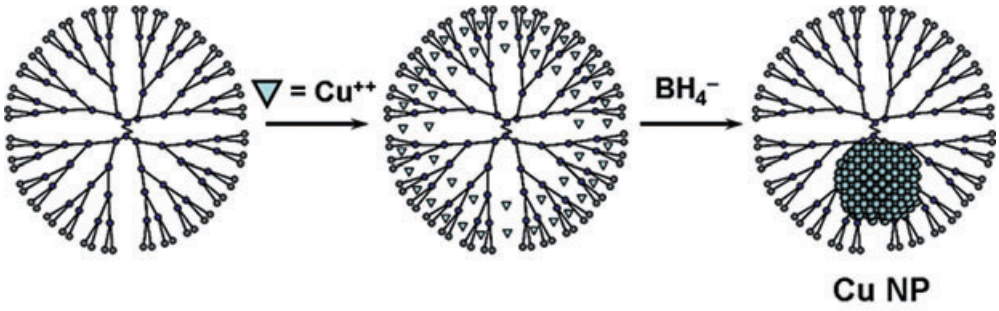

Figure 1.19 Schematic view of the processes occurring during the formation of Cu nanoparticles in a dendritic structure.

The main studies on dendrimer-stabilized Cu NPs relate to capping agents derived from just two structures, namely poly(propylene imine) [221, 222] and poly(amido amine) [223, 224].

1.3.4 Wet-Chemical Routes Based on Biotemplate Systems

Since the late 1990, templates consisting of biomolecules such as DNA have been investigated as a tool to produce elongated metal nanostructures, eventually aiming at the 'bottom-up' assembly of functional nanocircuits [225]. A few years later, in 2003/2004, DNA-templated copper nanowires were obtained by Wooley and colleagues [226, 227], the approach consisting of a time-controlled reduction of aqueous $Cu(NO_3)_2$ by ascorbic acid, in the absence of light, and in the presence of double-stranded DNA. Previously, the latter species had been bound electrostatically to a silicon substrate and mechanically aligned [228], as the authors had envisaged an ultimate application of Cu nanowires as interconnections in nanoscale integrated circuitry [226].

Methods to prepare elongated ensembles of copper NPs that had been generated on the surface of tubular templates were proposed by the groups of Matsui [229] and Wei [230]. Matsui's group, in 2003, studied the growth of Cu nanocrystals on the histidine-rich surface of peptide nanotubes. The Histidine moieties behaved as ligands for $Cu^{(II)}$ entrapment on the nanotube surface, after which a conventional borohydride reduction allowed Cu NPs growth (Figure 1.20). Similarly, in 2005, Wei and colleagues synthesized tubular glycolipid–copper nanotubular complexes which acted as a template for the subsequent thermal preparation of aligned Cu NP arrays (Figure 1.21).

Template methods based on microorganisms (or even plant roots) have also been proposed. In the former case, the 4 nm-wide inner channel of tobacco mosaic

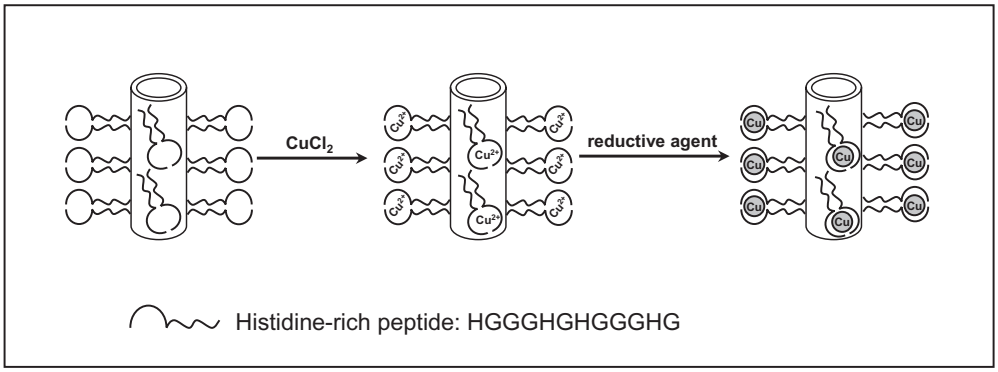

Figure 1.20 Scheme of copper nanotube preparation. From left to right: Cu ion–HG12 peptide complexation on the nanotube surfaces; Cu nanocrystal growth on the nanotubes nucleated at Cu ion-binding sites after reducing trapped Cu ions.

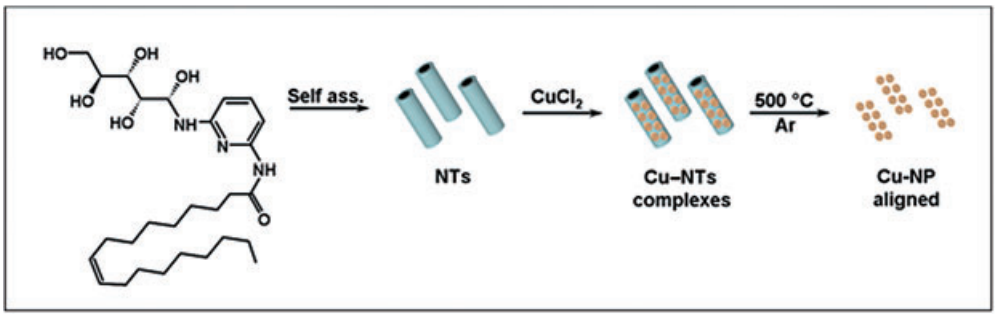

Figure 1.21 Glycolipid-template synthesis of aligned Cu NPs. NTs = nanotubes.

virus (TMV) allowed the preparation of copper nanowires [231]. A similar approach was followed by Demir *et al.* [232] in 2003, who photochemically reduced Cu species on the TMV surface such that ultimately the Cu NPs decorated the outer virus surface. Finally, in a recent study, Manceau *et al.* showed that Cu NPs could be generated at the root–soil interface [233].

1.3.5
Redox Routes in Compressed and Heated Fluids: Hydrothermal, Solvothermal and Supercritical Fluid Methods

The term 'hydrothermal', which is of geological origin, was first used by Sir Roderick Murchison during the nineteenth century to describe the action of water at high temperature and pressure, on the Earth's crust, leading to the formation of rocks and minerals. In a more modern definition, the same term is associated with any heterogeneous reaction occurring in the presence of aqueous solvents or mineralizers under high-pressure and -temperature conditions to dissolve and recrystallize (recover) materials that are relatively insoluble under ordinary conditions [234]. The term 'solvothermal' indicates an analogous process that is carried out in a generic nonaqueous solvent, including nonconventional media such as supercritical fluids (SCFs). Other, wider, definitions have also been proposed [234].

The various use of these terms is influenced by the customs of different research communities; for example, chemists and material scientists working in the supercritical region prefer explicitly to use the term 'supercritical fluid' to characterize their approach. As a consequence, in this section we have maintained a distinction among purely *hydrothermal* (e.g. water-based), *solvothermal* (e.g. based on other solvents) and *SCF* processes, although in some cases this classification might be found controversial, or based on terminological and/or usage rather than substantial differences.

1.3.5.1 Hydrothermal Routes

Because of the highly controlled diffusivity in a strong solvent medium and in a closed system, hydrothermal/solvothermal techniques offer interesting advantages in the processing or preparation of nanomaterials.

Knowledge of the fundamental aspects that drive hydrothermal/solvothermal processes has increased in recent years, and a solid understanding of changes in solvent parameters (e.g. structure at critical, supercritical and subcritical conditions, dielectric constant, pH, viscosity, density, etc.) under hydrothermal conditions, as well as on changing pressure and temperature, is considered a key aspect for programming experimental approaches, as they influence the solubility and transport behavior of the precursors involved in liquid–solid NP synthesis.

Of note, most of the studies which have dealt with the hydrothermal preparation of copper nanostructures have produced elongated or wire-like materials. One of the first applications of this approach was described by Liu *et al.*, who carried out the hydrothermal reduction of a $Cu^{(II)}$–glycerol complex in the presence of phosphite and SDS (used as capping agent). As a result, a wire length of several tens of microns was obtained [235]. A few years later, the group of Zheng [236, 237] used ascorbic acid as reducing agent and PVP as capping agent, for the one-step hydrothermal synthesis of Cu nanorods with rectangular cross-sections (a form of 'French fries' morphology), whereas the groups of Zhang and Huang both showed that ultralong Cu wires could be respectively obtained by using vitamin C [238] or octadecylamine [239]. In both studies, the additive had the dual role of reducing and capping agent. Carbon-coated Cu nanocables were obtained by Deng *et al.* using CTAB and hexamethylenetetramine [240].

Spherical [241] or platelet-shaped [242] Cu NPs could also be prepared. In the former case, glucose was used as reducing agent and CuO particles as precursor, whereas in the latter case hypophosphite and SDS were used to hydrothermally convert $Cu^{(II)}$ ions into elongated nanoplatelets.

1.3.5.2 **Solvothermal Routes**

Several solvents have been tested for the solvothermal preparation of Cu nanostructures. In particular, ethanol was employed as both solvent and reducing agent in the studies of Tang *et al.* [243] and Wei *et al.* [244]. In the former study, which was carried out in the presence of PVP, a shape control over spheres and cubes was possible. However, in both studies the experimental approach proved capable of producing $Cu^{(0)}$ or Cu_2O NPs, as a function of the experimental conditions. Higher temperatures and higher alkali concentrations generally lead to the elemental oxidation state, whereas the opposite conditions lead to cuprous oxides [243]. In a similar study, carried out in ethanol with the additional use of CTAB, Wang *et al.* obtained Cu nanowires [245]. When ethylene glycol [246], polysilane [247] and ethylenediamine [248] solvents were also investigated, the studies led prevalently to micron or submicron particles [246, 248] with crystalline structures.

1.3.5.3 **Routes Based on Supercritical Fluids**

During the late 1980s, Fulton and coworkers studied the generation of AOT reverse micelles in compressible fluids such as compressed propane or SCF propane [249, 250]. The group of C.R. Roberts extended Pileni's synthesis of Cu

NPs in AOT micelles (see Section 1.3.2) to the case of compressed propane and SCF solvents [251, 252]. The compressed solvent systems provide an alternative approach to thermodynamic control over NP synthesis; moreover, one of the main additional advantages over syntheses that employ conventional liquids is the ease of solvent removal, made possible simply by depressurizing the system [253, 254]. The same group proposed a total interaction energy model to predict the ultimate Cu NP size obtained in SCF solvents, and also provided evidence that, even in these media, AOT acts as a stabilizing agent sterically protecting Cu nanocrystals. From the interaction energy plot of Figure 1.22, it is possible to determine the dispersibility of the particles – that is, the separation distance corresponding to a minimum energy value. The effects on particle stability of NP size and SCF media pressure and temperature are shown in Figure 1.23.

Other authors investigated the synthesis of Cu NPs in different SCF media. When, in particular, Ziegler *et al.* employed supercritical water and alkyl thiols [255], the latter species were found to behave both as capping and reducing agent, assisting the conversion of $Cu^{(II)}$ precursor and intermediate species into capped $Cu^{(0)}$ NPs (see Figure 1.24).

Wai and collaborators explored also the potentialities of water-in-supercritical CO_2 microemulsions [256] and used sodium AOT and perfluoropolyetherphosphate as surfactants. More recently, Shervani *et al.* [257] proposed the use of a fluorinated analogue of AOT [sodium bis(1*H*,1*H*,7*H*-dodecafluoroheptyl)-2-sulfosuccinate] to create microemulsions in the same water/supercritical CO_2

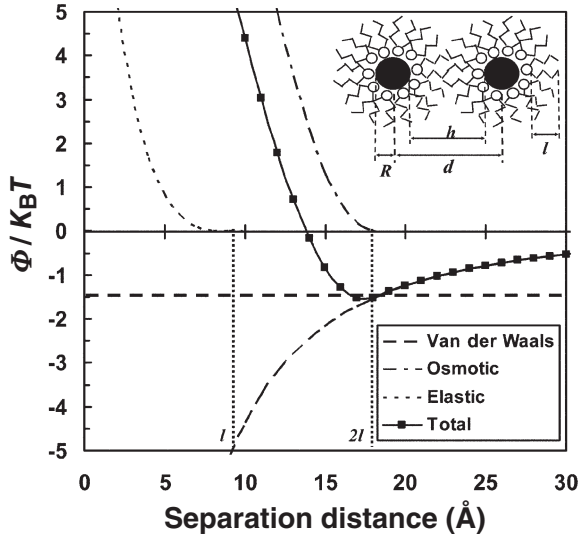

Figure 1.22 Contributions of each force to the total interaction energy model as a function of the separation distance of the particles. Reprinted with permission from *Industrial and Engineering Chemistry Research* **2004**, *43*, 6070–81; © 2004 American Chemical Society.

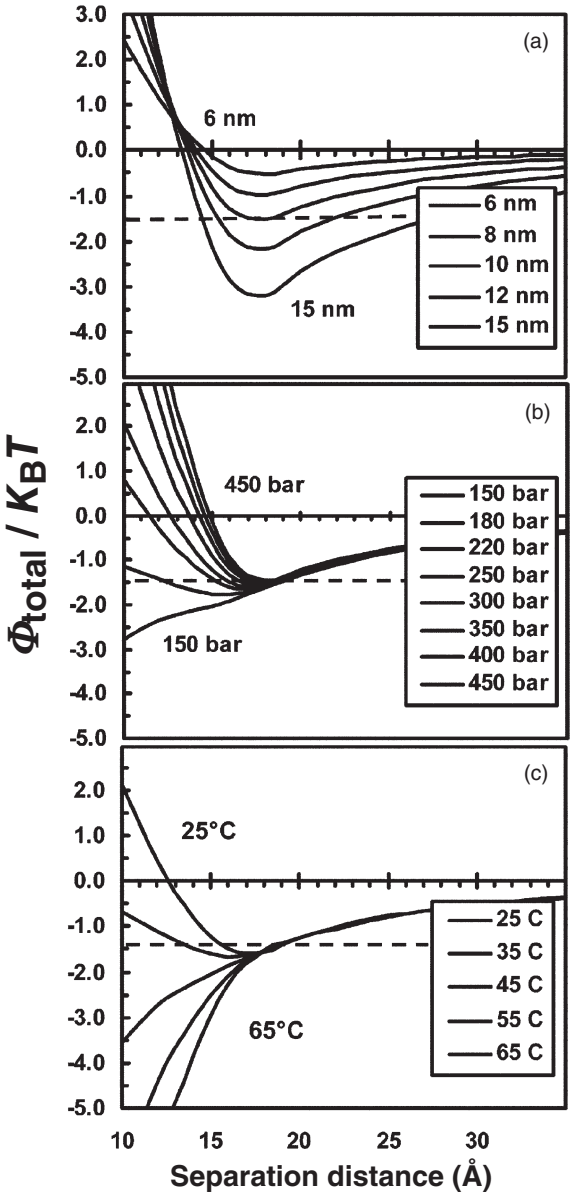

Figure 1.23 Plot of the Φ_{total}/k_BT curves for copper nanoparticles coated with AOT and dispersed in compressed propane. (a) Effect of particle diameter, *f*; (b) Effect of pressure; (c) Effect of temperature. Reprinted with permission from *Industrial and Engineering Chemistry Research* **2004**, *43*, 6070–81; © 2004 American Chemical Society.

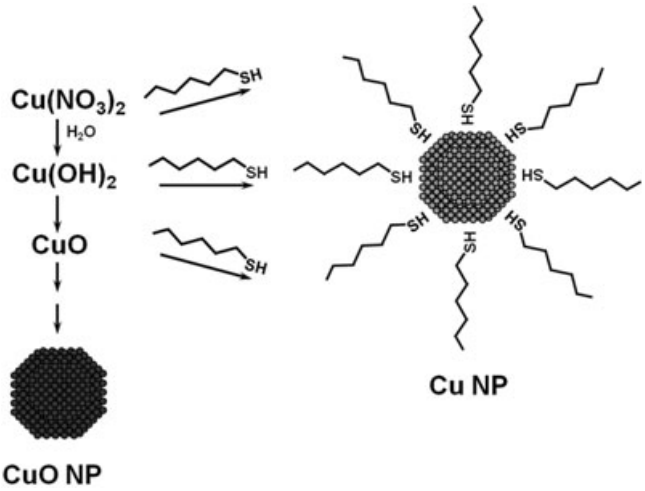

Figure 1.24 Processes occurring during the formation of Cu NPs in supercritical water, in the presence of alkane-thiols.

systems. Both groups used $NaBH_4$ derivatives as reducing agents and were able to obtain spherical Ag and Cu NPs.

Similarly, using alcohol/SCF CO_2/DBS mixed systems, Chen *et al.* converted copper$^{(II)}$ oxalate into Cu nanowires [258]. Cu nanotubes and nanowires were also obtained by Ziegler *et al.* by the SCF decomposition of copper precursors in the presence of mesoporous silica templates [259].

1.3.6
Redox Routes in Ionic Liquids

One valuable approach to NP synthesis and stabilization is via ionic liquids (ILs). Ionic liquids are low-vapor pressure, highly polar and viscous solvents, that have been recently investigated as suspension media for catalytically active nanoclusters [260] (see also Ref. [1] and references therein).The main advantages of synthesizing Cu NPs in ILs resides in the direct possibility of using them as highly recyclable catalysts in several processes, such that there is a low environmental impact (see Ref. [261] and references therein). The so-called 'green' character of such a synthetic approach is that it does not require conventional solvents; rather, separation of the reaction products can be easily achieved by physical treatments, such as distillation inducing solidification of the IL solvent, etc. Furthermore, the IL may itself afford the Cu NP stabilization, thus greatly facilitating catalyst recycling and improving the total turnover (TTO) number. Tetra-alkyl-ammonium halides [261], imidazolium derivatives [262] and other ILs with ammonium moieties [263, 264] have been employed as dispersing media where Cu NPs have been generated and successfully used as catalysts.

In these cases, reduction of the copper precursors was carried out by borohydride [263, 264], by microwave irradiation [262], or even by spontaneous dissolution of macroscopic copper powders (copper bronze) reacting with the counterions of the IL through an oxidation/reduction multistep process that occurs while using NPs in heterogeneous catalysis (as a part of the overall catalytic cycle) [261].

1.3.7
Ultrasonic-Chemical Processes

Ultrasounds often facilitate chemical reactions through an increase of the process kinetics, frequently due to the generation of radicals or other reactive species. Ultrasounds may also provide an unusual reaction medium due to the so-called *acoustic cavitation phenomenon*, which represents the formation, growth and implosive collapse of bubbles in a liquid medium. The discrimination among different effects related to ultrasounds (frequency, intensity and irradiation mode effects) is not easy, and useful insights can be found in a paper by Reisse *et al.* [265]. The first example of Cu nanocrystals synthesis by a sonochemical approach dates back to 1998, when Gedanken *et al.* achieved a sonochemical conversion of copper$^{(II)}$–hydrazine carboxylate into Cu NPs in aqueous medium [266]. Some two years later, the same group proposed a modified method in which the use of a zwitterionic surfactant (cetyltrimethylammonium *p*-toluene sulfonate) made possible the sonochemical preparation of elongated Cu nanostructures stabilized by a surfactant monolayer [267]. More recently, Cu NPs and nanorods were prepared sonochemically by the replacement reaction of copper 2-ethylhexoate with sodium in a paraffin solution [268]. More complex approaches to the sonochemical preparation of Cu NPs have also been proposed, based on a combination of sonochemistry and spray pyrolysis [269], the use of an electric plasma discharge in ultrasonic cavitation field [270], or with the use of sonoelectrochemistry [271].

1.4
Photochemical, Laser Ablation and Radiation- or Electron Beam-Assisted Processes

The wet-chemical synthesis of finely and homogeneously dispersed NPs of electropositive metals shows some challenging aspects. As strong reducing agents must be employed, when the metal precursor undergoes reduction it is possible that such agents are not distributed homogeneously through the solution. This implies local variations in the rates of nucleation and growth, and eventually results in the growth of polydisperse particles [272]. In order to address this problem, several strategies can be employed. Often, strong reducing agents with slow kinetics are used, to enable homogeneous nucleation and growth, but in these processes byproducts generated by the redox reactivity of the reducing

agent may contaminate the as-prepared NPs. An alternative approach is based on the photochemical conversion of appropriate copper precursors into Cu NPs, and indeed this may become an important and widespread route as it responds to the need to minimize the amount of byproducts/waste created in the NP synthesis [272]. It should be noted however, that some photochemical approaches are still based on the use of sensitizers, and this makes no substantial difference when compared to the aforementioned open issues related to wet-chemical approaches. In recent years, laser ablation and photofragmentation techniques have attracted great interest and, as they do not necessarily imply the use of additives, they can offer complementary advantages. In this section, the main photochemical routes to Cu NPs will be reviewed, together with other methods involving the use of either an external radiation source (e.g. γ-irradiation) or electron beams. Approaches based on microwave-irradiation are not described specifically at this point, due to the heterogeneity of the experimental conditions (reduction in ILs, polyol approach, etc.). However, a number of interesting reports dealing with this type of irradiation have been reviewed elsewhere in this chapter.

1.4.1 Photochemical Reduction in the Presence of Capping Agents and Sensitizers

In 2002, Kapoor and coworkers reported on the photochemical conversion of $CuSO_4$ into Cu NPs by using UV irradiation (Hg lamp, 254 nm) in the presence of a stabilizing agent such as gelatin [273] or PVP [274]. In both studies, benzophenone was employed as the sensitizer, and its photogenerated ketyl radical was hypothesized as being the species effectively responsible for $Cu^{(II)}$ reduction [274]. In 2002, Murakata *et al.* investigated the preparation of Cu NPs from mixed water/ethanol solutions in the presence of photocatalytically active TiO_2 NPs [275], whilst in 2003 Giuffrida *et al.* used UV irradiation to reduce bis(2,4-pentanedionate)copper$^{(II)}$ ($Cu(acac)_2$) [276, 277]. A spectrophotometric investigation of the process [277] showed that it proceeded through a multistep mechanism. First, it was observed that irradiation induced decomposition of the copper complex, releasing free ligand molecules (H-acac) and generating $Cu^{(I)}$ intermediates. In the overall conversion, H-acac behaved as a sensitizer and promoted the formation of Cu NPs. The NP plasmon resonance absorption was also monitored; some typical spectra are shown in Figure 1.25.

By using the same approach as Giuffrida, Darugar *et al.* prepared Cu NPs from the $Cu(acac)_2$ precursor and studied time-resolved transient absorption phenomena for nanoparticles of 12 and 30 nm. The conduction electron energy relaxation was found to be faster in the smaller particles, whereas fluorescence showed an opposite trend [151].

More recently, Warren *et al.* proposed a different photochemical route, based on the (long-term) ambient light irradiation of $Cu^{(II)}$–thiolate complexes; the result

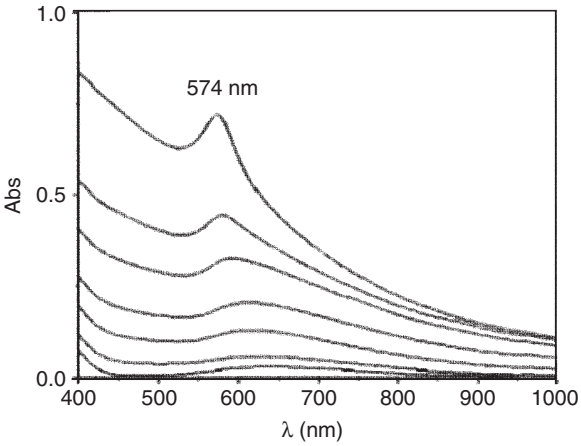

Figure 1.25 Spectral changes recorded upon irradiation of $Cu(acac)_2$ (5×10^{-4} mol l^{-1}) in ethanol solution (at 254 nm) at different times (0–270 min). The light intensity was 5×10^{-6} Einstein min^{-1}. Reproduced with kind permission from © Royal Society of Chemistry; DOI: 10.1039/b308418c.

$$Cu^{2+} + 2\ RSH \longrightarrow Cu(SR)_2 \xrightarrow{h\nu} Cu^0\ NP + \text{thiol degradation products}$$

Figure 1.26 Sketch of the route proposed by Warren *et al.* (see text for details) for the thiolate-assisted preparation of Cu nanoparticles.

was a complex degradation into metal nanocrystals and disulfide species (Figure 1.26).

1.4.2
Laser Ablation and Photo-Fragmentation Processes

The first examples of the laser ablation (LA) of metal films leading to the corresponding colloid date back to the early 1990s [278, 279]. Unfortunately, in the absence of stabilizers or any other precautions, the as-formed Cu NPs quickly turned into their oxide, leading to the type of olive green-colored solution [280] that those working on $Cu^{(0)}$ NPs (including the present authors!) have experienced disappointedly at least once during their studies.

In the late 1990, research into the LA synthesis of Cu nanostructures followed two roads: (i) depositions in vacuum or under an inert gas; and (ii) LA in the liquid phase.

A brief description of NP formation with LA in an inert gas atmosphere (route# i) is as follows. Initially, interaction between the laser and metal target generates a plume of evaporated atoms that collide with gas molecules at the front of the expanding plume. This causes the plume atoms to thermalize, and a shock wave

is initiated that confines the cooling plume; this in turn leads to atom condensation and NP formation. The primarily formed NPs may evolve into larger particles or aggregates, as a function not only of several parameters but also of the metal type [281].

Although, during recent years, several interesting studies on the fundamental aspects have been conducted [282], and papers providing evidence of Cu NPs formation [281, 283] from gas-phase processes have been prepared, during the past few years the technique has mainly evolved towards solution-based strategies.

The first examples of nonoxidized Cu NPs produced by LA in solution were provided by Yeh and collaborators, who converted an isopropanol suspension of CuO powder into Cu NPs by using a Nd:YAG laser [both fundamental (1064 nm) and second harmonic wavelengths were investigated] [284]. A few years later the same authors investigated the effect of thiols on the system [285], while Tsuji *et al.* studied the influence of laser wavelength on the efficiency of ablation of metallic copper targets immersed in an aqueous solution [286].

Subsequently, many studies have been conducted on the Nd:YAG laser ablation of bulk copper [287–289] or $Cu^{(0)}$ powder [290, 291], and on targets in solvents such as water [287, 291], isopropanol [289, 290], acetone [287] and polysiloxane [288]. In Ref. [289], PVP was investigated for the LA preparation of polymer-protected Cu NPs.

Very recently, an excimer laser was used to convert large Cu NPs into finer colloids by a controlled photofragmentation experiment. A TEM evaluation of the Cu NP core-size showed that it was approximately halved upon photofragmentation (10^4 laser pulses) by comparison with the pristine sample [292].

1.4.3
γ-Irradiation

The radiolytic reduction of copper ions in water or alcohols, which has been investigated since the 1970s [293–295], is usually performed by irradiating solutions which contain (besides the copper precursor) a suitable organic compound. The irradiation generates solvated electrons and organic radicals which are then responsible for the reduction of copper compounds to $Cu^{(0)}$ [296]. Several studies have detailed the stabilization of radiolytically prepared Cu clusters by means of polymers such as poly(ethyleneimine) [297], poly(vinyl acetate) [298], PVP [299], or even quaternary microemulsion systems [300]. One example of a mixed radiolytic/hydrothermal approach was proposed in 1994 [301]. Two recent studies have been carried out in the presence of alcohols (but without other stabilizers), and have assessed specific aspects of the synthesis mechanism, including the role of alcohol molecules in the scavenging of radical intermediates [296, 302]. Moreover, Henglein investigated a type of seeded-growth phenomenon in which γ-irradiation-generated Cu NPs were exposed to a fresh precursor solution, after which the mixed liquid was irradiated again, thus inducing an appreciable size increase in the pristine clusters [296].

1.4.4
Electron Beam Irradiation

Similarly to the situation in γ-irradiation, in aqueous solution the use of electron beams generates hydrated electrons and hydrogen atoms, both of which are highly active reducing agents [303–305]. These species have been successfully applied to the preparation of Cu nanocolloids, especially in the presence of stabilizers such as poly(vinyl alcohol) [304] and SDBS [305].

Another (quite exotic) route employing electron beams, which dates back to the 1980s [306, 307], consists of the small-scale preparation of Cu nanostructures by the controlled beam reduction of oxidized copper structures in a TEM instrument. In 2004, Chiu and collaborators used a convergent electron beam to induce the growth of $Cu^{(0)}$ structures from commercial CuCl crystals supported on TEM grids [308]. One year later, Schmittel *et al.* employed $Cu^{(I)}$-bisphenanthroline scaffolds to obtain pure crystalline Cu NPs [309]. Given these evidences, it might be considered straightforward – or even obvious – to turn oxidized copper materials into their elemental oxidation state while exposing them to a TEM electron beam.

In contrast, in 2003 Wang *et al.*, who previously had achieved the structural evolution of $Cu(OH)_2$ nanobelts to Cu nanowires in a TEM instrument, showed that the process was not induced by the electron beam but rather was a multistep process that involved hydroxide thermal dehydration and two subsequent one-electron conversions, in which carbon from the supporting grids acted as the reducing agent [310].

1.5
Electrochemical Approaches

Electrochemical procedures have not been used extensively for the synthesis of metal nanoparticles, despite possessing certain important advantages over other techniques. Yet, electrochemical procedures are of great interest as they not only afford high-purity products but also permit a strict control over the cluster morphology, that can be achieved by varying either the current density or the applied potential.

During the past two decades a variety of different electrochemical methods have been described for the preparation of metal nanostructures of different sizes and shapes. Among these, the most frequently used methods to prepare unsupported $Cu^{(0)}$ nanomaterials have included:

- Sacrificial anode electrolysis in the presence of surfactants
- Electrochemical milling
- Ultrasonic–electrochemical methods
- Electrolysis in ionic liquids
- Template-assisted electrosynthesis of Cu nanorods and nanowires.

Despite electrodeposition techniques, both pulsed and continuous, represent the most widespread and versatile methods for the preparation of nanostructured

metals [311–315], they have been intentionally left out of our list. Whilst, on the one hand, these electrochemical procedures enable a tight control on cluster morphology (grain size and shape), on the other hand they usually produce nanostructures that adhere to the electrode surface. Here, only procedures which lead to unsupported nanostructures, or supported nanostructures that are easily removable from the template, have been considered. The above-listed approaches will be reviewed in the following sections, with emphasis placed on the advantages of each method and the properties of the nanostructures.

1.5.1
Sacrificial Anode Electrolysis in the Presence of Surfactants

One valid alternative to the electrolytic deposition of metal clusters is the direct electroreduction of metal ions in the presence of an appropriate stabilizer capable of preventing particle adhesion to the electrode surface. Such stabilizers adsorb onto the growing particles, thus preventing their deposition and producing structures that usually are stable within the reaction environment. These molecules can be chosen from different types of surfactant; a good stabilizing agent should not interfere with the electroreduction of the metal ions, and neither should it passivate the electrode active surface.

This technique is performed using a sacrificial anode experimental set-up, and is referred to as *sacrificial anode electrolysis*. During the process, the stabilizing effect can occur either at the anode or at the cathode. In the former case, the anode is made from the metal to be electrodispersed as nanostructures; when the applied potential is sufficiently high, the anode dissolves into metal ions that subsequently are precipitated due to the presence of hydroxides or other anions [316].

More frequently, sacrificial anode electrolysis is combined with cathodic stabilization; the first report of the electrochemical production of Me-NPs using this technique can be traced back to M.T. Reetz in 1994 [317]. Such studies proved that size-selected nanostructured transition-metal particles could be electrosynthesized using tetra-alkyl-ammonium salts as surfactants, dissolved in organic solvents. This simple electrochemical approach was proposed by the same authors as a general and reliable route to nanosized transition metals, including copper [318, 319]. Following the Reetz studies, the authors of this chapter optimized sacrificial anode electrolysis to prepare copper nanoparticles for several technological applications, including biostatic/biocide nanocoatings [320, 321]. This synthesis was performed by using a three-electrode cell, equipped with an $Ag/AgNO_3$ reference electrode, a copper anode and a platinum cathode. Tetra-*n*-alkyl-ammonium chloride was dissolved (0.1 *M*) in tetrahydrofuran/acetonitrile mixed solvents; a sketch of the electrochemical cell used in the process is shown in Figure 1.27a.

The correct choice of experimental parameters causes the anode to become electrocorroded during electrolysis, leading to the production of metal ions. The halide–$Cu^{(II)}$ complexes are driven by the electric field to the cathode, where they are electrochemically reduced. The as-formed atoms undergo stages of nucleation and growth, although the presence in the double-layer region of an appropriate

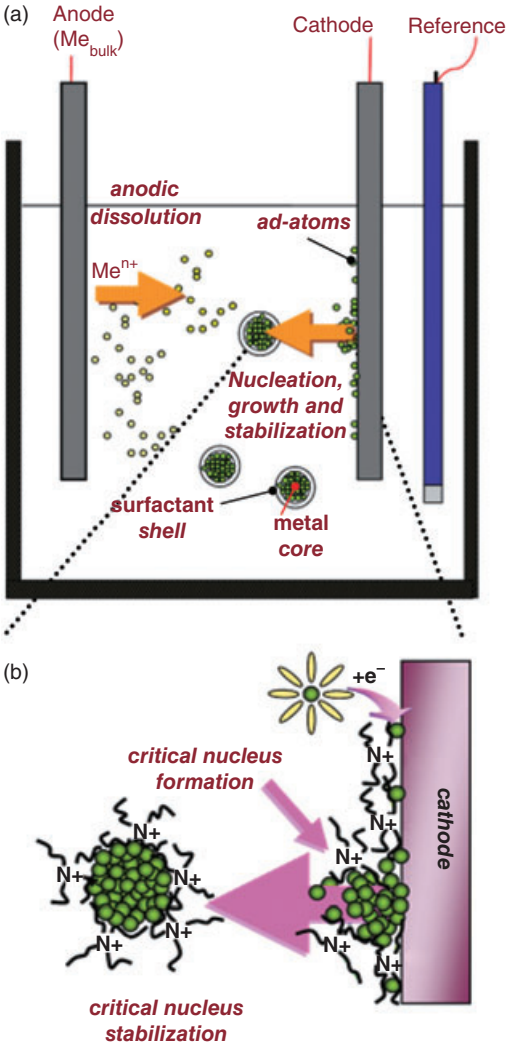

Figure 1.27 (a) Sketch of a sacrificial anode electrolysis; (b) Scheme of processes taking place at the cathode surface.

stabilizer will prevent undesired growth and aggregation. The stabilized core-shell particles are then obtained directly as colloidal NPs in solution (Figure 1.27b).

A variety of different stabilizer chain lengths was explored and potential values applied in order to understand how the experimental conditions can affect NPs size-modulation. The *shell thickness* can easily be tailored by changing the length of the alkyl chains of the surfactant [322], while modulation of the Cu-NPs *core-size* could be achieved only within a very limited size range (diameter <10 nm) by varying the electrochemical parameters. The morphology of the electropro-

duced nanoparticles was studied using TEM, and their chemical composition determined using X-ray photoelectron spectroscopy (XPS). TEM images of Cu-NPs electrosynthesized at +1.5 and +4.0 V are shown in the insets of Figures 1.28 and 1.29. With NP mean core sizes close to 6 and 3 nm, respectively, these results confirmed the inverse dependence of particle diameter on the applied potential.

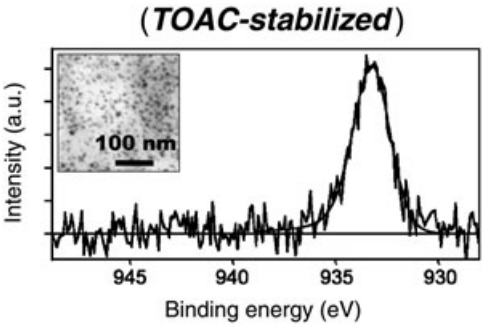

Figure 1.28 TOAC-stabilized Cu NPs electrosynthesized using a working electrode potential of +1.5 V. Main panel: $Cu2p_{3/2}$ XP high-resolution spectrum. Inset: TEM image of Cu-NPs. Reproduced with kind permission from Springer Science + Business Media: *Analytical and Bioanalytical Chemistry*, Synthesis, analytical characterization and bioactivity of Ag and Cu nanoparticles embedded in poly-vinyl-methyl-ketone films. Cioffi, N., Ditaranto, N., Torsi, L., Picca, R.A., De Giglio, E., Sabbatini, L., Novello, L., Tantillo, G., Bleve-Zacheo, T. and Zambonin, P.G., **2005**, *382*, 1912; © 2005 (inset from Figure 1.1; XPS from Figure 1.3).

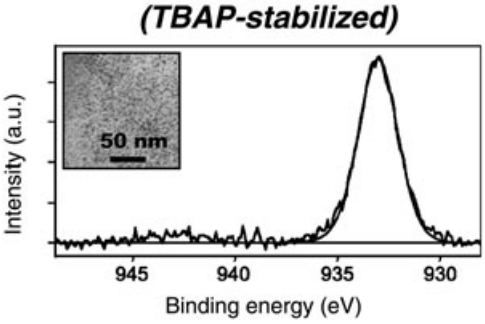

Figure 1.29 TBAP-stabilized Cu NPs electrosynthesized using a working electrode potential of +4.0 V. Main panel: $Cu2p_{3/2}$ XP high-resolution spectrum. Inset: TEM image of Cu-NPs (unpublished results). Reproduced with kind permission from Springer Science + Business Media: *Analytical and Bioanalytical Chemistry*, Synthesis, analytical characterization and bioactivity of Ag and Cu nanoparticles embedded in poly-vinyl-methyl-ketone films. Cioffi, N., Ditaranto, N., Torsi, L., Picca, R.A., De Giglio, E., Sabbatini, L., Novello, L., Tantillo, G., Bleve-Zacheo, T. and Zambonin, P.G., **2005**, *382*, 1912; © 2005 (Figure 1.3).

Typical $Cu2p_{3/2}$ X-ray photoelectron spectra of the same Cu NPs are shown in the main panels of Figures 1.28 and 1.29. It is worth noting that, in the case of the octyl-stabilized clusters (Figure 1.28), the spectrum shows a single peak falling at a binding energy (BE) of 933.1 ± 0.2 eV, this being ascribed to nanodispersed copper at zero oxidation state [323, 324]. In contrast, the signal related to the butyl-stabilized clusters (Figure 1.29) shows the presence of $Cu^{(II)}$ traces, along with nano-$Cu^{(0)}$. In fact, shorter alkyl chains demonstrate a worse ability to protect Cu nanophases against air-induced oxidation, especially upon prolonged exposure to the air [321].

A similar approach was followed by Chen and coworkers in 2003 [325] in the preparation of copper nanorods. These authors used a controlled-current electrochemical method and showed how the shape and yield of the nanorods depended on the current density applied during the electrosynthesis process.

Very recently, sacrificial anode electrolysis was employed by Singh and coworkers to prepare copper nanoparticles in the presence of deoxyribonucleic acid (DNA) as electrolyte [326]. Here, nanoparticles in the range 5–50 nm were synthesized by using a combination of electrolysis and electron-beam irradiation.

1.5.2
Electrochemical Milling

The origin of this approach can be traced back to a surprising byproduct obtained by Tarascon and coworkers [327, 328] during the discharge mechanism of a CuO electrode, when they observed the final product to be nanometer-sized copper grains. This encouraged Chen and coworkers to develop a novel 'top-down' method for the synthesis of metal nanoparticles, which became known as the electrochemical milling method (ECM). The process was carried out in an electrochemical cell equipped with a CuO electrode versus a Li counterelectrode; the size and morphology of the nanostructures was tailored by controlling the current density. In this way, copper nanofibers [329], nanospheres and pyramid-like Cu-particles [330] could be obtained (Figures 1.30 and 1.31). The morphology of the particles was shown to depend heavily on the electrode composition and on the number of charge–discharge cycles [330].

1.5.3
Ultrasonic–Electrochemical

Details relating to ultrasound effects were described briefly in Section 1.3.7, with regards to sonochemical approaches. Recently, the potential benefit derived from a combination of sonochemistry and electrochemistry was investigated more fully. Some of the advantages were seen to reside in the acceleration of mass transport and reaction rates, along with increases in the rates of electrode surface cleaning and degassing. Reisse and coworkers [265, 331, 332] have recently prepared copper nanopowders by means of a pulse sonoelectrochemical synthesis, starting from $copper^{(II)}$ sulfate and sulfuric acid. The experiment consisted of two successive

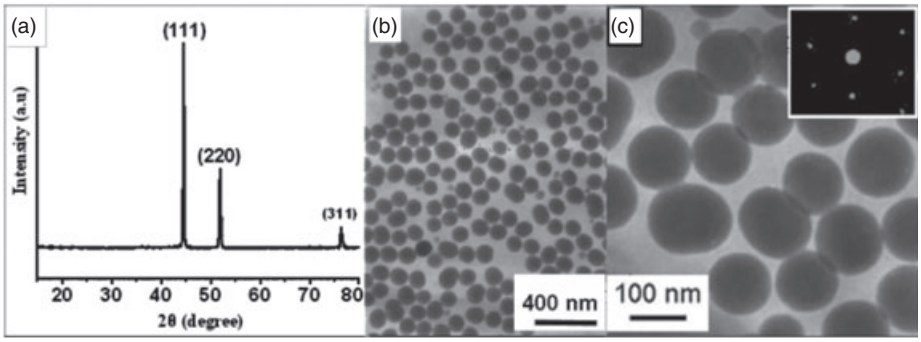

Figure 1.30 (a) XRD pattern; (b) TEM image; (c) High-magnification TEM image of copper nanospheres synthesized after charge–discharge for 50 cycles. The SAED pattern of Cu nanospheres is showed as the inset of panel (c). Reprinted with permission from *Journal of Physical Chemistry C* **2008**, *112*, 4176–9; © 2008 American Chemical Society.

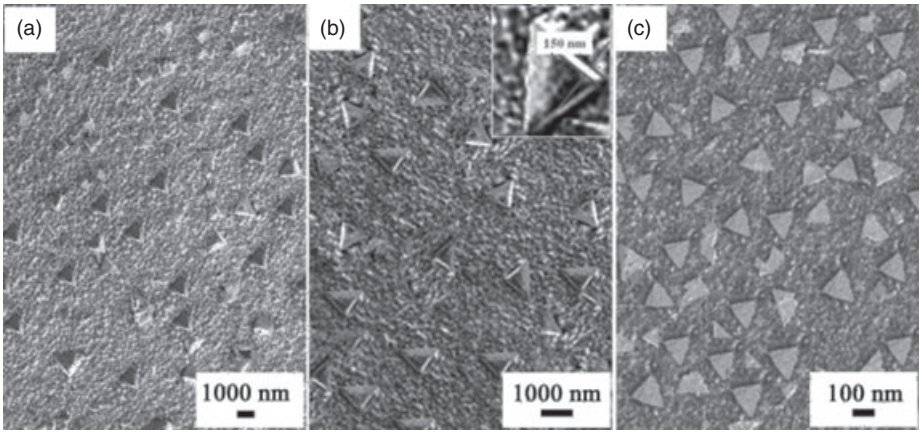

Figure 1.31 Field emission SEM images of the metal copper discharged by Li_2O Cu_2O thin-film electrodes on copper sheet. Panels (a), (b) and (c) refer to particles obtained with different charge–discharge cycles (1, 5 and 50, respectively). A current density of 0.1 mA cm^{-2} was used. The inset in (b) shows a side-view SEM image. Reprinted with permission from *Journal of Physical Chemistry C* **2008**, *112*, 4176–9; © 2008 American Chemical Society.

steps: first, an electric current pulse was applied to the electrode to allow cluster nucleation; second, a burst of ultrasonic energy removed the nanoparticles and micro-metal particles from the sonoelectrode. Later, Gedanken and coworkers developed a modified version of this synthesis by adding a surfactant or a polymer to the sonoelectrochemical cell [271, 333]. CTAB-capped nanosized products resulted in CuBr, while elemental copper nanoparticles were obtained using poly(*N*-vinyl-2-pyrrolidone) and poly(vinyl alcohol) [271].

1.5.4
Electrolysis in Ionic Liquids

This approach basically consists of an electrolytic reduction of copper salts, carried out in a nonconventional IL solvent. The technique exploits electrons as the 'green' reductant and the IL as the 'green' solvent. In contrast to the relatively narrow potential window of water or other solvents, ILs offer wider electrochemical windows, combined with a stabilizing effect capable of preventing the aggregation of kinetically unstable nanoparticles [334]. Wang and coworkers [335] have recently used this technique for the conversion of CuCl into copper nanoparticles.

1.5.5
Template-Assisted Electrochemical Growth of Cu Nanorods and Nanowires

Metal nanowires and nanorods are considered to be appealing nanomaterials, based on their interesting electronic and optical properties, and their possible application in nanodevices. As a result, the number of papers describing one-dimensional (1-D) metal nanostructures has grown exponentially during the past few years [2]. Today, 1-D nanocopper, in particular, is receiving a great deal of attention due to its high electrical conductance and consequently wide perspective of applications in fields such as microelectronics [336].

A search through *Chemical Abstracts* shows that the most widely used method to prepare metal nanowires and nanorods is based on template-directed electrochemical protocols. The reason for this resides in the advantages deriving from this technique – it is easy to perform, and it affords good control over the crystallinity of nanostructures and their composition. Moreover, key morphological parameters – the nanostructure length and aspect ratio – can be tuned by choosing the correct membrane geometry.

The first study to describe this approach can be traced back to a report by Penner and Martin, who studied the deposition of Pt-nanowires into the pores of alumina [337]. Subsequently, the method was investigated in great depth by several other groups, and recently employed specifically for the preparation of Cu nanorods, nanotubes and nanowires [338–343]. In fact, almost all template electrochemical depositions lead to supported or membrane-embedded nanostructures. As mentioned in Section 1.1, the aim of this chapter is to review only self-standing nanomaterials, and for this reason in the following sections particular attention will be paid to those approaches targeted at the production of unsupported nanomaterials, such as those which include an additional step to dissolve the membrane.

Investigations have been conducted with polycarbonate track-etched templates, aluminum oxide membranes and nonporous mica [344–352], and in all cases the nanomaterial preparation consists primarily of a controlled electrodeposition of copper from a precursor solution (usually $CuSO_4$) inside the nanochannels of the template. In a second step, the template is removed, thus releasing the elongated nanostructures. By following this approach, Gao and coworkers [353] prepared dense and continuous copper nanowires which were 30 μm long and had a uniform

diameter of 60 nm. Similar results were obtained by Zheng and coworkers [354], although in this case the nanowires presented a lower aspect ratio. Very recently, Haber and coworkers [343] investigated the effect of deposition parameters on the growth and uniformity of copper nanowires: in particular, they showed that the wave shape and pulse height could not only induce membrane damage but also affect the pore-filling and the resultant uniformity of the nanowires.

The same authors also investigated the possibility of developing voltage-controlled deposition sequences for the set-up of a bench-top electrochemical method capable of producing copper nanowires on the gram scale [355]. In the same report they also showed how the method of wire liberation significantly influenced their diameter and dispersion. Four scanning electron microscopy (SEM) images of Cu nanowires obtained by membrane dissolution under acidic or alkaline conditions are shown in the upper part of Figure 1.32. The simplified scheme shown in the lower part of the figure outlines the differences between the two treatments – that is, when aqueous H_3PO_4 is used the nanowires have a larger diameter and show a greater degree of aggregation.

A further means of gaining control over the diameter and diameter-dependent optical properties of Cu nanowires was proposed by Duan and coworkers [356], who identified a relationship between nanowire diameter and template etching time. By following this approach, they obtained Cu nanowires with a peculiar X-ray diffraction (XRD) pattern, which was suggestive of a preferential growth direction. They also observed a significant red-shift of the surface plasmon resonance peak as the wire diameter was increased.

Nanowires grown by the use of template-directed protocols usually possess a high degree of crystallinity. In particular, Gao and coworkers [353] demonstrated that a suitable choice of potential values during electrochemical deposition allowed the predictable synthesis of either single-crystal or polycrystalline copper nanowires.

1.6 Conclusions

In this chapter we have provided a 'bird's-eye view' of the main approaches for the synthesis of $Cu^{(0)}$ nanosized structures, together with characterization data regarding their morphology, structure and surface chemical composition.

As outlined in the Introduction, academic and industrial interest towards nanocopper is increasing exponentially and a vast number of papers and patents have been published during only the past two years. This represents part of a major trend that is evident in the case of many other transition metals. We believe that, in comparison with other nanosized metals, copper nanostructures may play a crucial role in the development of real-world applications, due to their relatively low cost (as compared to palladium, platinum, gold), and to the widespread use of copper (in other size ranges) in microelectronics and other technological applications. Unfortunately, such potential is counterbalanced by

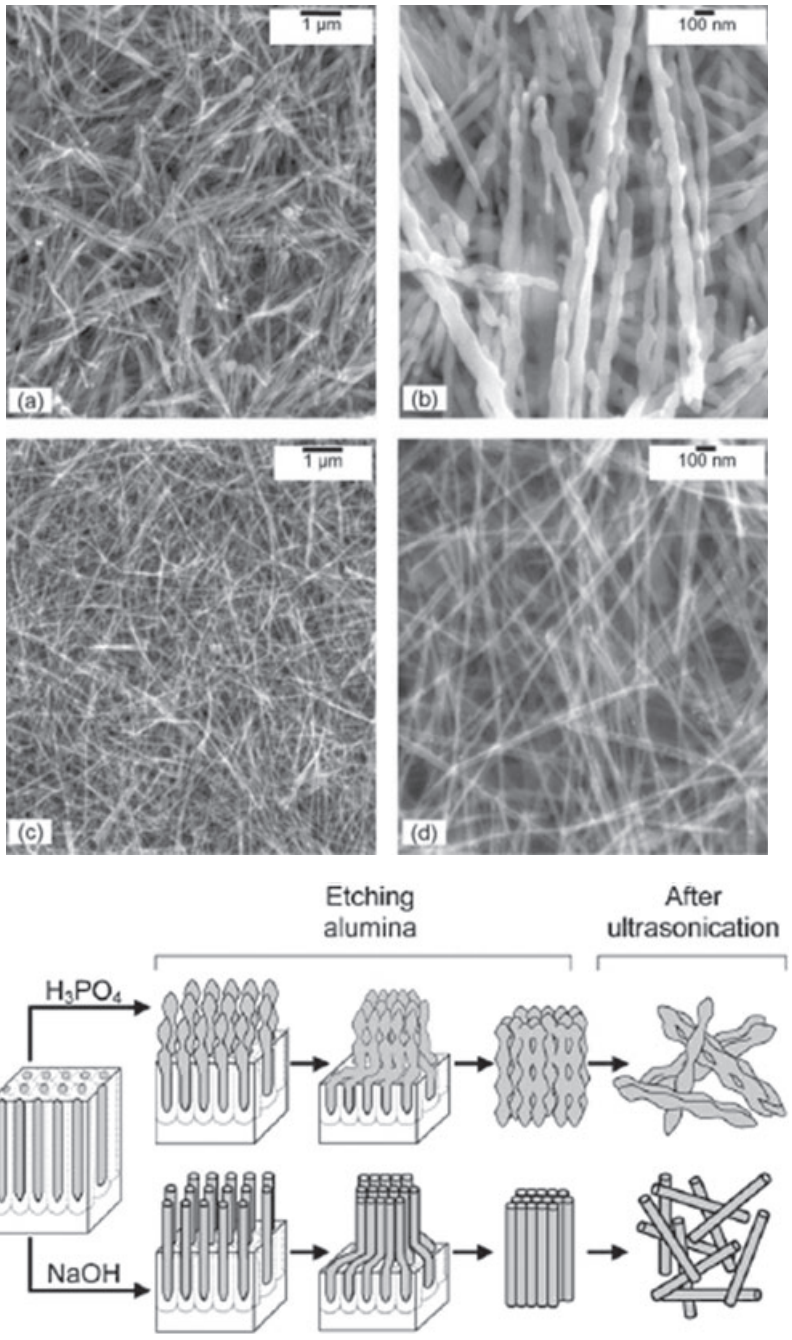

Figure 1.32 SEM images of (a) and (b) acid-liberated copper nanowires and (c) and (d) base-liberated copper nanowires. The lower part of the figure shows a scheme of the liberation process effect on the wire morphology. Reproduced with kind permission from © Royal Society of Chemistry; DOI: 10.1039/b603442j.

the pronounced instability of nanocopper towards degradation processes related to air-exposure.

Many present worldwide efforts in Cu nanomaterials synthesis have been shown to be directed towards the stabilization of nanostructures, aiming at morphologically, structurally and chemically homogeneous nanoparticle populations with an increased preservation of the elemental oxidation state. The interest towards *stability issues*–allowing the correct storage, handling and use of Cu nanomaterials, without having to use excessive precautions–will undoubtedly be intense over the next few years.

As the size of electronic devices continues to shrink with such rapidity, the number of investigations into elongated copper nanostructures such as nanorods (NRs) and nanowires (NWs) will surely increase, especially as both NRs and NWs are expected to play essential roles in future generations of electronic devices [357]. Indeed, NRs and NWs could become the new building blocks for the assembly of nanocircuitry; moreover, in the case of biocompatible or biologically derived capping agents (e.g. amino acids, peptides, DNA strains), aligned and self-assembling copper structures might even be used as a tool for the small-scale biointegration of microelectronic artificial components into living systems.

Today, copper nanoparticles are attracting much interest as low-cost heterogeneous catalysts for several chemical reactions, and have been also shown to provide excellent results when used in green-chemistry applications, such as those involving highly recyclable supported nanoparticles or ionic liquids. It is highly likely that this area of investigation will also undergo major development.

Finally, we would like to describe a potential real-world application of stabilized copper nanomaterials that, at present, we are studying in our laboratory. We have found that Cu NPs capped by quaternary ammonium salts can be used as nanoreservoirs for the controlled release of Cu^{2+} ions, and can be used in this manner as *tunable disinfecting agents*. The tight control of bioactive ion release is essential when maintaining concentrations that will be efficient in terms of antimicrobial activity, yet not show toxicity towards humans [320]. This key property will surely afford interesting applications in areas such as health care, antibacterial textiles, food-packaging, paints and space exploration.

Clearly, the number of methods available to create nanostructures–both at present and in the future–is vast, and will undoubtedly increase even further during years to come. In this respect, we hope that this chapter will serve as a valuable tool in the classification and understanding of these different methods, as well as provide a state-of-the-art review on advanced $Cu^{(0)}$ nanomaterials.

References

1 Ott, L.S. and Finke, R.G. (2007) Transition-metal nanocluster stabilization for catalysis: a critical review of ranking methods and putative stabilizers. *Coordination Chemistry Reviews*, **251**, 1075–100.

2 SCI Finder Scholar™ (2006) American Chemical Society.

3 Koponen, J. and Holappa, L. (2005) Nanocopper. Synthesis, properties and applications. Literature survey. *Helsinki University of Technology Publications in Materials Science and Metallurgy*, **I–IV**, 1–23.

4 Chen, C., Wang, L., Jiang, G. and Yu, H. (2006) Chemical preparation of special-shaped metal nanomaterials through encapsulation or inducement in soft solution. *Reviews on Advanced Materials Science*, **11**, 1–18.

5 Chmielewski, A.G., Michalik, J., Buczkowski, M. and Chmielewska, D.K. (2004) Ionizing radiation in nanotechnology. *Raporty Instyut Chemii I Techniki Jadrowej (ICHTJ) B*, 1–24.

6 Nasibulin, A.G., Shurygina, L.I. and Kauppinen, E.I. (2005) Synthesis of nanoparticles using vapour-phase decomposition of copper(II) acetylacetonate. *Colloid Journal*, **67**, 1–20.

7 Lisiecki, I. (2004) Size control of spherical metallic nanocrystals. *Colloids and Surfaces A – Physicochemical and Engineering Aspects*, **250**, 499–507.

8 Ensign, D., Young, M., Douglas, T., Panigrahi, S. and Pal, T. (2004) Ferritin-mediated photocatalytic synthesis of copper nanoparticles. *Chemtracts*, **17**, 218–24.

9 Stoltenberg, R.M. and Woolley, A.T. (2004) DNA-templated nanowire fabrication. *Biomedical Microdevices*, **6**, 105–11.

10 Esumi, K. (2004) Dendrimer-metal nanocomposites. *Encyclopedia of Nanoscience and Nanotechnology*, **2**, 317–26.

11 Pileni, M.P. (1998) Colloidal self-assemblies used as templates to control size, shape and self-organization of nanoparticles. *Supramolecular Science*, **5**, 321–9.

12 Pileni, M.P., Lisiecki, I., Motte, L., Petit, C., Tanori, J. and Moumen, N. (1998) Nanosized particles: self-assemblies, control of size and shape. *International Symposium on Micelles, Microemulsions and Monolayers, Gainesville, 1995*, pp. 289–304.

13 Pileni, M.P., Lisiecki, I., Motte, L., Petit, C., Cizeron, J., Moumen, N. and Lixon, P. (1993) Synthesis 'in situ' of nanoparticles in reverse micelles. *Progress of College of Polymer Science*, **93**, 1–9.

14 Koch, C.C. (2003) Top-down synthesis of nanostructured materials: mechanical and thermal processing methods. *Reviews on Advanced Materials Science*, **5**, 91–9.

15 Benjamin, J.S. (1976) Mechanical alloying. *Scientific American*, **234**, 40–8.

16 Fecht, H.J., Hellstern, E., Fu, Z. and Johnson, W.L. (1990) Nanocrystalline metals prepared by high-energy ball milling. *Materials Transactions A*, **21**A, 2333–7.

17 Suryanarayana, C. (2001) Mechanical alloying and milling. *Progress in Materials Science*, **46**, 1–184.

18 Koch, C.C. (1991) *Materials Science and Technology – A Comprehensive Treatment: Processing of Metals and Alloys*, Vol. **15** (eds Cahn, R.W., Haasen P. and Kramer, J.) Wiley-VCH Verlag GmbH, Weinheim, p. 193.

19 Murty, B.S. and Ranganathan, S. (1998) Novel materials synthesis via mechanical alloying. *International Materials Reviews*, **43**, 101–41.

20 Sanchez, F.H., Torres, C.E.R., Van Raap, M.B.F. and Zelis, L.M. (1998) Tool induced contamination of elemental powders during mechanical milling. *Hyperfine Interactions*, **113**, 269–77.

21 Huang, J.Y., Wu, Y.K. and Ye, H.Q. (1998) Microstructure investigations of ball-milled materials. *Microscopy Research and Technique*, **40**, 101–21.

22 Schilling, P.J., He, J.H. and Ma, E. (1997) EXAFS study of ball-milled elemental nanocrystalline powders. *Journal de Physique IV*, **7**, 1221–2.

23 Otsuki, A., Shingu, P.H. and Ishihara, K.N. (1997) Stored energy and electromotive force of mechanically milled copper. *Materials Science Forum*, **235–238**, 949–53.

24 Lee, G.G., Hashimoto, H. and Watanabe, R. (1995) Development of particle morphology during dry ball milling of Cu powder. *Material Transactions of The Japan Institute of Metals (JIM)*, **36**, 548–54.

25 Huang, J.Y., Wu, Y.K. and Ye, H.Q. (1996) Deformation structures in ball-milled copper. *Acta Materialia*, **44**, 1211–21.

26 Oleszak, D. and Shingu, P.H. (1996) Nanocrystalline metals prepared by low energy ball milling. *Journal of Applied Physics*, **79**, 2975–80.

27 Youssef, K.M., Scattergood, R.O., Linga Murty, K. and Koch, C.C. (2004) Ultrafine nanocrystalline copper with a narrow grain size distribution. *Applied Physics Letters*, **85**, 929–31.

28 Ding, J., Tsuzuki, T., McCormick, P.G. and Street, R. (1996) Ultrafine Cu particles prepared by mechanochemical process. *Journal of Alloys and Compounds*, **234**, L1–3.

29 Ding, J., Miao, W.F., Tsuzuki, T., McCormick, P.G. and Street, R. (1996) Mechanochemical synthesis of nano-powder. *Synthesis and Processing of Nanocrystalline Powder, Proceedings of a Symposium, Anaheim, California, February 4th–8th*, pp. 69–79.

30 Castricum, H.L., Bakker, H. and Poels, E.K. (1999) Mechanochemical reactions on copper-based compounds. *Materials Science Forum*, **312–314**, 209–14.

31 Bennet, F.D. (1958) Cylindrical shock waves from exploding wires. *Physics of Fluids*, **1**, 347–52.

32 Case, R.S., Jr and Guenther, A.H. (1968) Time-resolved spectroscopy of exploding wires. *Exploding Wires*, **4**, 195–209.

33 Weber, F.N. and Shear, D.D. (1969) Exploding wire particle size by light scattering measurement. *Journal of Applied Physics*, **40**, 3854–6.

34 Bhat, B.K. and Jordan, I.B. (1971) Explosion of bare and insulated copper wires. *Journal of Applied Physics*, **42**, 809–14.

35 Haendel, S.K. and Melzacki, K. (1983) Some aspects on the exploding wire current pause, in *16th International Conference on Phenomena in Ionized Gases*, Vol. **2** (eds Boetticher, W., Wenk, H., Schulz-Gulde, E.), University of Düsseldorf, Germany, pp. 254–5.

36 Tkachenko, S.I. and Kuskova, N.I. (1999) Dynamics of phase transitions at electrical explosion of wire. *Journal of Physics: Condensed Matter*, **11**, 2223–32.

37 Hu, M. and Kusse, B.R. (2004) Optical observations of plasma formation and wire core expansion of Au, Ag, and Cu wires with 0–1 kA per wire. *Physics of Plasmas*, **11**, 1145–50.

38 Grabatin, H., Weiss, H. and Kunze, H.D. (1986) Production of nanocrystalline metal powders using the wire explosion technique, in *Proceedings, International Powder Metallurgy Conference and Exhibition*, Vol. **1** (eds W.A. Kaysser, W.J. Huppmann and P.M. Horiz), Schmid, Freiburg/Br, Germany, pp. 109–12.

39 Pikuz, S.A., Shelkovenko, T.A., Sinars, D.B., Greenly, J.B., Dimant, Y.S. and Hammer, D.A. (1999) Multiphase foam-like structure of exploding wire cores. *Physical Review Letters*, **83**, 4313–16.

40 Sarathi, R., Murai, K., Kobayashi, R., Suematsu, H., Jiang, W. and Yatsui, K. (2006) Production and characterization of nano copper powder using pulsed power technique. *Synthesis and Reactivity in Inorganic, Metal-Organic, and Nano-Metal Chemistry*, **36**, 127–30.

41 Sedoi, V.S. and Valevich, V.V. (2001) Characterization of ultra-fine powders produced by the exploding wire method. *ICT's Annual International Conference*, **32**, 80/1–80/10.

42 Cho, C., Choi, Y.W. and Jiang, W. (2005) Time-resolved spectroscopic investigation of an exploding Cu wire process for nanosized powder synthesis. *Journal of the Korean Physical Society*, **47**, 987–90.

43 Kotov, Y.A., Rhee, C.K., Bagazeyev, A.V., Beketov, I.V., Demina, T.M., Murzakayev, A.M., Samatov, O.M., Timoshenkova, O.R., Medvedev, A.I. and Shtolts, A.K. (2003) Production of copper nanopowders by electrical explosion of wires: a study of their oxidation during storage and heating in air. *Journal of Metastable and Nanocrystalline Materials*, **15-16**, 343–8.

44 Li, D., Wang, Y. and Xia, Y. (2004) Electrospinning nanofibers as uniaxially aligned arrays and layer-by-layer stacked films. *Advanced Materials*, **16**, 361–6.

45 Kim, J.S. and Reneker, D.H. (1999) Polybenzimidazole nanofiber produced by electrospinning. *Polymer Engineering and Polymer Science*, **39**, 849–54.

46 Kameoka, J. and Craighead, H.G. (2003) Fabrication of oriented polymeric nanofibers on planar surfaces by electrospinning. *Applied Physics Letters*, **83**, 371–3.

47 Wang, C., Li, Z.Y., Dongmei, Y., Yang, Q.B. and Hong, Y. (2002) Preparation and stability of the nanochains consisting of copper nanoparticles and PVA nanofiber. *International Journal of Nanoscience*, **1**, 471–6.

48 Li, Z., Huang, H. and Wang, C. (2006) Electrostatic forces induce poly(vinyl alcohol)-protected copper nanoparticles to form copper/poly(vinyl alcohol) nanocables via electrospinning. *Macromolecular Rapid Communications*, **27**, 152–5.

49 Bognitzki, M., Becker, M., Graeser, M., Massa, W., Wendorff, J.H., Schaper, A., Weber, D., Beyer, A., Goelzhaeuser, A. and Greiner, A. (2006) Preparation of sub-micrometer copper fibers via electrospinning. *Advanced Materials*, **18**, 2384–6.

50 Gurav, A., Kodas, T., Pluym, T. and Xiong, Y. (1993) Aerosol processing of materials. *Aerosol Science and Technology*, **19**, 411–52.

51 Kim, J.H., Germer, T.A., Mulholland, G.W. and Ehrman, S.H. (2002) Size-monodispersed metal nanoparticles via hydrogen-free spray pyrolysis. *Advanced Materials*, **14**, 518–21.

52 Nagashima, K., Iwaida, T., Sasaki, H., Katatae, Y. and Kato, A. (1990) Preparation of fine, spherical copper particles by spray-pyrolysis technique. *Nippon Kagaku Zassihi*, **1**, 17–24.

53 Majumdar, D., Schiefelbein, T., Kodas, T. and Glicksman, H. (1996) Copper(I) oxide powder generation by spray pyrolysis. *Journal of Materials Research*, **11**, 2861–8.

54 Rosner, D.E. (2005) Flame synthesis of valuable nanoparticles: recent progress/current needs in areas of rate laws, population dynamics, and characterization. *Industrial and Engineering Chemistry Research*, **44**, 6045–55.

55 Stark, W.J. and Pratsinis, S.E. (2002) Aerosol flame reactors for manufacture of nanoparticles. *Powder Technology*, **126**, 103–8.

56 Makela, J.M., Keskinen, H., Forsblom, T. and Keskinen, J. (2004) Generation of metal and metal oxide nanoparticles by liquid flame spray process. *Journal of Materials Science*, **39**, 2783–8.

57 Lee, S.G., Choi, S.M. and Lee, D. (2007) The role of salt in nanoparticle generation by salt-assisted aerosol method: microstructural changes. *Thermochimica Acta*, **455**, 138–47.

58 Athanassiou, E.K., Grass, R.N. and Stark, W.J. (2006) Large-scale production of carbon-coated copper nanoparticles for sensor applications. *Nanotechnology*, **17**, 1668–73.

59 Wei, Z.Q., Xia, T.D., Ma, J., Dai, J.F., Feng, W.J., Wang, Q. and Yan, P.X. (2006) Growth mechanism of Cu nanopowders prepared by anodic arc plasma. *Transactions of Nonferrous Metals Society of China*, **16**, 168–72.

60 Wei, Z.Q., Xia, T.D., Ma, J., Feng, W.J., Dai, J.F., Wang, Q. and Yan, P.X. (2007) Processing parameters for Cu nanopowders prepared by anodic arc plasma. *Transactions of Nonferrous Metals Society of China*, **17**, 128–32.

61 Cui, Z., Zhang, Z., Hao, C., Dong, L., Meng, Z. and Yu, L. (1998) Structures and properties of nanoparticles prepared by hydrogen arc plasma method. *Thin Solid Films*, **318**, 76–82.

62 Jiao, J. and Seraphin, S. (1998) Carbon encapsulated nanoparticles of Ni, Co, Cu, and Ti. *Journal of Applied Physics*, **83**, 2442–8.

63 Xenoulis, A.C., Tsouris, P., Doukellis, G., Boukos, N., Valamontes, E., Chen, Y. and Tsakalakos, T. (1998) Size selection by cluster deflection in an electric field. *Nanostructured Materials*, **8**, 771–84.

64 Yadav, R.M., Singh, A.K. and Srivastava, O.N. (2003) Synthesis and characterization of Cu nanotubes and nanothreads by electrical arc evaporation. *Journal of Nanoscience and Nanotechnology*, **3**, 223–5.

65 Hao, C., Xiao, F. and Cui, Z. (2008) Preparation and structure of carbon encapsulated copper nanoparticles. *Journal of Nanoparticle Research*, **10**, 47–51.

66 Qin, C. and Coulombe, S., (2006) Synthesis of organic layer-coated copper nanoparticles in a dual-plasma process. *Materials Letters*, **60**, 1973–6.

67 Qin, C. and Coulombe, S. (2007) Organic layer-coated metal nanoparticles prepared by a combined arc evaporation/condensation and plasma polymerization process. *Plasma Sources Science and Technology*, **16**, 240–9.

68 Yao, W.T., Yu, S.H., Zhou, Y., Jiang, J., Wu, Q.S., Zhang, L. and Jiang, J. (2005) Formation of uniform CuO nanorods by spontaneous aggregation: selective synthesis of CuO, Cu2O, and Cu nanoparticles by a solid-liquid phase arc discharge process. *The Journal of Physical Chemistry B*, **109**, 14011–16.

69 Lo, C.H., Tsung, T.T. and Chen, L.C. (2005) Shape-controlled synthesis of Cu-based nanofluid using submerged arc nanoparticle synthesis system (SANSS). *Journal of Crystal Growth*, **277**, 636–42.

70 Xie, S.Y., Ma, Z.J., Wang, C.F., Lin, S.C., Jiang, Z.Y., Huang, R.B. and Zheng, L.S. (2004) Preparation and self-assembly of copper nanoparticles via discharge of copper rod electrodes in a surfactant solution: A combination of physical and chemical processes. *Journal of Solid State Chemistry*, **177**, 3743–7.

71 Kimoto, K. (1953) Study on the intensity anomaly of electron diffraction powder patterns from minute silver crystallites. *Journal of the Physical Society of Japan*, **8**, 762–8.

72 Olynick, D.L., Gibson, J.M. and Averback, R.S. (1995) In situ ultra-high vacuum transmission electron microscopy studies of nanocrystalline copper. *Materials Science and Engineering A*, A**204**, 54–8.

73 Nieman, G.W., Weertman, J.R. and Siegel, R.W. (1989) Microhardness of nanocrystalline palladium and copper produced by inert-gas condensation. *Scripta Metallurgica*, **23**, 2013–18.

74 Nieman, G.W., Weertman, J.R. and Siegel, R.W. (1991) Mechanical behavior of nanocrystalline copper and palladium. *Journal of Materials Research*, **6**, 1012–27.

75 Nieman, G.W., Weertman, J.R. and Siegel, R.W. (1991) Mechanical behavior of nanocrystalline copper, palladium and silver samples. *Microcomposite Nanophase Materials: Proceeding Symposium*, pp. 15–25.

76 Lin, H.M., Hsieh, S.H., Lee, P.Y., Lai, M.S. and Wu, J.S. (1993) Synthesis and characterization of nanocrystalline powders of pure nickel and copper. *Materials Chemistry and Physics*, **34**, 205–13.

77 Sanders, P.G., Fougere, G.E., Thompson, L.J., Eastman, J.A. and Weertman, J.R. (1997) Improvements in the synthesis and compaction of nanocrystalline materials. *Nanostructured Materials*, **8**, 243–52.

78 Sanders, P.G., Witney, A.B., Weertman, J.R., Valiev, R.Z. and Siegel, R.W. (1995) Residual stress, strain and faults in nanocrystalline palladium and copper. *Materials Science and Engineering A*, A**204**, 7–11.

79 Sanders, P.G., Eastman, J.A. and Weertman, J.R. (1997) Elastic and tensile behavior of nanocrystalline copper and palladium. *Acta Materialia*, **45**, 4019–25.

80 Reinhard, D., Hall, B.D., Berthoud, P., Valkealahti, S. and Monot, R. (1998) Unsupported nanometer-sized copper clusters studied by electron diffraction and molecular dynamics. *Physical Review B*, **58**, 4917–26.

81 Champion, Y. and Bigot, J. (1996) Characterization of nanocrystalline copper powders prepared by melting in a cryogenic liquid. *Materials Science and Engineering A*, A**217/218**, 58–63.

82 Champion, Y. and Bigot, J. (1996) Preparation and characterization of nanocrystalline copper powders. *Scripta Materialia*, **35**, 517–22.

83 Vitulli, G., Bernini, M., Bertozzi, S., Pitzalis, E., Salvadori, P., Coluccia, S. and Martra, G. (2002) Nanoscale copper particles derived from solvated Cu atoms in the activation of molecular oxygen. *Chemistry of Materials*, **14**, 1183–6.

84 Ponce, A.A. and Klabunde, K.J. (2005) Chemical and catalytic activity of copper nanoparticles prepared via metal vapor synthesis. *Journal of Molecular Catalysis A–Chemical*, **225**, 1–6.

85 Nasibulin, A.G., Ahonen, P.P., Richard, O., Kauppinen, E.I. and Altman, I.S. (2001) Copper and copper oxide nanoparticle formation by chemical vapor

nucleation from copper(II) acetylacetonate. *Journal of Nanoparticle Research*, **3**, 385–400.

86 Nasibulin, A.G., Kauppinen, E.I., Brown, D.P. and Jokiniemi, J.K. (2001) Nanoparticle formation via copper (II) acetylacetonate vapor decomposition in the presence of hydrogen and water. *Journal of Physical Chemistry B*, **105**, 11067–75.

87 Zhang, Y., Lam, F.L.Y., Hu, X. and Yan, Z. (2006) Fabrication of copper nanorods by low-temperature metal organic chemical vapor deposition. *Chinese Science Bulletin*, **51**, 2662–8.

88 Haase, D., Hampel, S., Leonhardt, A., Thomas, J., Mattern, N. and Buechner, B. (2007) Facile one-step-synthesis of carbon-wrapped copper nanowires by thermal decomposition of Copper(II)-acetylacetonate. *Surface and Coatings Technology*, **201**, 9184–8.

89 Wang, J.H., Su, P.Y., Lu, M.Y., Chen, L.J., Chen, C.H. and Chu, C.J. (2005) Synthesis of Cu nanotubes with silicon oxide nanowire templates by MOCVD. *Electrochemical and Solid-State Letters*, **8**, C9–11.

90 Wang, J.H., Yang, T.H., Wu, W.W., Chen, L.J., Chen, C.H. and Chu, C.J. (2006) Synthesis and growth mechanism of pentagonal Cu nanobats with field emission characteristics. *Nanotechnology*, **17**, 719–72.

91 Kim, Y.H., Lee, D.K., Jo, B.G., Jeong, J.H. and Kang, Y.S. (2006) Synthesis of oleate capped Cu nanoparticles by thermal decomposition. *Colloids and Surfaces A – Physicochemical and Engineering Aspects*, **284+285**, 364–8.

92 Kang, Y.S., Kim, Y.H., Jo, B.G. and Jeong, J.H. (2006) Synthesis and characterization of Cu nanoparticles prepared by thermal decomposition of Cu-oleate complex. *International Journal of Nanoscience*, **5**, 339–44.

93 Kim, Y.H., Kang, Y.S., Lee, W.J., Jo, B.G. and Jeong, J.H. (2006) Synthesis of Cu nanoparticles prepared by using thermal decomposition of Cu-oleate complex. *Molecular Crystals and Liquid Crystals*, **445**, 231–8.

94 Schaper, A.K., Hou, H., Greiner, A., Schneider, R. and Phillipp, F. (2004) Copper nanoparticles encapsulated in multi-shell carbon cages. *Applied Physics A*, **78**, 73–7.

95 Bunge, S.D., Boyle, T.J. and Headley, T.J. (2003) Synthesis of coinage-metal nanoparticles from mesityl precursors. *Nano Letters*, **3**, 901–5.

96 Hambrock, J., Becker, R., Birkner, A., Weiss, J. and Fischer, R.A. (2002) A non-aqueous organometallic route to highly monodispersed copper nanoparticles using [Cu(OCH(Me)CH2NMe2)2]. *Chemical Communications*, **1**, 68–9.

97 Schroter, M.K., Khodeir, L., Hambrock, J., Loffler, E., Muhler, M. and Fischer, R.A. (2004) Redox chemistry of Cu colloids probed by adsorbed CO: an in situ attenuated total reflection Fourier transform infrared study. *Langmuir*, **20**, 9453–5.

98 Meyer, E.M., Gambarotta, S., Floriani, C., Chiesivilla, A. and Guastini, C. (1989) Polynuclear aryl derivatives of Group 11 metals. Synthesis, solid state-solution structural relationship, and reactivity with phosphines. *Organometallics*, **8**, 1067–79.

99 Wang, X.L., Xu, B.S., Xu, Y., Yu, H.L., She, P.J. and Liu, Q. (2005) Preparation of nano-copper as lubricating oil additive. *Journal of Central South University of Technology*, **12**, 203–6.

100 Suryanarayanan, R., Frey, C.A., Sastry, S.M.L., Waller, B.E., Bates, S.E. and Buhro, W.E. (1996) Mechanical properties of nanocrystalline copper produced by solution-phase synthesis. *Journal of Materials Research*, **11**, 439.

101 Huang, C.-Y. and Sheen, S.R., (1997) Synthesis of nanocrystalline and monodispersed copper particles of uniform spherical shape. *Materials Letters*, **30**, 357–61.

102 Jiang, C., Zhang, W., Liu, Y. and Qian, Y. (2006) Self-assembled copper nanowalls intro microstructures with different shapes: a facile aqueous approach. *Crystal Growth Design*, **6**, 2603–6.

103 Jackelen, A.M.L., Jungbauer, M. and Glavee, G.N. (1999) Nanoscale materials synthesis. 1. Solvent effects on hydridoborate reduction of copper ions. *Langmuir*, **15**, 2322–6.

104 Ren, X., Chen, D. and Tang, F. (2005) Shape-controlled synthesis of copper

colloids with a simple chemical route. *The Journal of Physical Chemistry B*, **109**, 15803–7.

105 Chang, Y., Lye, M.L. and Zeng, H.C. (2005) Large-scale synthesis of high-quality ultralong copper nanowires. *Langmuir*, **21**, 3746–8.

106 Ding, L.P. and Fang, Y. (2007) The study of resonance Raman scattering spectrum on the surface of Cu nanoparticles with ultraviolet excitation and density functional theory. *Spectrochimica Acta, Part A: Molecular and Biomolecular Spectroscopy*, **67**A, 767–71.

107 Cong, H., Zhang, M. and Cao, W. (2005) Hollow Cu-NP spheres made from electroless Cu deposition with colloidal particles as templates. *Macromolecular Rapid Communications*, **26**, 734–7.

108 Kapoor, S., Joshi, R. and Murkherjee, T. (2002) Influence of I^- anions on the formation and stabilization of copper nanoparticles. *Chemical Physics Letters*, **354**, 443–8.

109 Sinha, A., Das, S.K., Kumar, T.V.V., Rao, V. and Ramachandrarao, P. (1999) Synthesis of nanosized copper powder by an aqueous route. *Journal of Materials Synthesis and Processing*, **7**, 373–7.

110 Panigrahi, S., Kundu, S., Ghosh, S.K., Nath, S., Praharaj, S., Basu, S. and Pal, T. (2006) Selective one-pot synthesis of copper nanorods under surfactantless condition. *Polyhedron*, **25**, 1263–9.

111 He, Y., Yu, X. and Yang, B. (2006) Novel Cu flower-like nanostructures synthesized from a solid-stabilized emulsion approach. *Materials Chemistry and Physics*, **99**, 295–9.

112 Buhro, W.E., Haber, J.A., Waller, B.E., Trentler, T.J., Suryanarayanan, R., Frey, C.A. and Sastry, S.M.L. (1995) Nanocrystalline metals, intermetallics, and a metal-matrix nanocomposite by solution-based chemical reductions. *Polymer Materials Science and Engineering*, **73**, 39–40.

113 Tsai, K.L. and Dye, J.L. (1991) Nanoscale metal nanoparticles by homogeneous reduction with alkalides or electrides. *Journal of the American Chemical Society*, **113**, 1650–2.

114 Tsai, K.L. and Dye, J.L. (1993) Synthesis, properties, and characterization of nanometer-size metal particles by homogeneous reduction with alkalides and electrides in aprotic solvents. *Chemistry of Materials*, **5**, 540–6.

115 Pileni, M.P. (2006) Self-organization of inorganic nanocrystals. *Journal of Physics: Condensed Matter*, **18**, S67–S84.

116 Andersson, M., Harelind, I.H., Palmqvist, A.E.C., Skoglundh, M. and Holmberg, K. (2003) Use of self-assembling surfactants as templates and reactants for the synthesis of noble metal particles. *Self Assembly*, 105–11.

117 Pileni, M.P. (2003) Nanocrystals. Size and shape control. *Self Assembly*, 25–31.

118 Blake, S., Limin, L., Vijay, J., Chad, T., Schwartz, D., McPherson, G., Bose, A. and Agarwal, V. (2003) Templating nanostructure through the self-assembly of surfactants, in *Synthesis, Functionalization and Surface Treatment of Nanoparticles*, American Scientific Publishers, Stevenson Ranch, California, pp. 51–65.

119 Ingert, D., Motte, L. and Pileni, M.P. (2000) Metal chalcogenides. CdS and CdTe nanoparticles made in reverse micelles: preparation modes and optical properties. *Surfactant Science Series*, **92**, 217–34.

120 Pileni, M.P. (1998) Optical properties of nanosized particles dispersed in colloidal solutions or arranged in 2D or 3D superlattices. *New Journal of Chemistry*, **22**, 693–702.

121 Pileni, M.P. (2003) The role of soft colloidal templates in controlling the size and shape of inorganic nanocrystals. *Nature Materials*, **2**, 145–50.

122 Pileni, M.P. (2002) Nanomaterials production by soft chemistry. *Nanostructured Materials*, 1–21.

123 Pileni, M.P., Lisiecki, I., Motte, L. and Petit, C. (1992) Nanometer particles synthesis in reverse micelles: influence of the size and the surface on the reactivity. *Research on Chemical Intermediates*, **17**, 101–13.

124 Lisiecki, I., Boulanger, L., Lixon, P. and Pileni, M.P. (1992) Synthesis of copper metallic particles using functionalized surfactants in w/o and o/w

microemulsions. *College of Polymer Science*, **89**, 103–5.

125 Lisiecki, I. and Pileni, M.P. (1993) Synthesis of copper metallic clusters using reverse micelles as microreactors. *Journal of the American Chemical Society*, **115**, 3887–96.

126 Pileni, M.P. and Lisiecki, I. (1993) Nanometer metallic copper particle synthesis in reverse micelles. *Colloids and Surfaces A – Physicochemical and Engineering Aspects*, **80**, 63–8.

127 Lisiecki, I., Pileni, M.P. and Metallic, C. (1995) Particles synthesized 'in situ' in reverse micelles: influence of various parameters on the size of the particles. *Journal of Physical Chemistry*, **99**, 5077–82.

128 Tanori, J., Duxin, N., Petit, C., Lisiecki, I., Veillet, P. and Pileni, M.P. (1995) Synthesis of nanosize metallic and alloyed particles in ordered phases. *College of Polymer Science*, **273**, 886–92.

129 Lisiecki, I., Billoudet, F. and Pileni, M.P. (1997) Syntheses of copper nanoparticles in gelified microemulsion and in reverse micelles. *Journal of Molecular Liquids*, **72**, 251–61.

130 Lisiecki, I., Lixon, P. and Pileni, M.P. (1991) Synthesis in situ in reverse micelle of copper metallic clusters. *Progress of College of Polymer Science*, **84**, 342–4.

131 Petit, C., Lixon, P. and Pileni, M.P. (1992) Structural change in AOT reverse micelles induced by changing the counterions. *Progress of College of Polymer Science*, **89**, 328–31.

132 Tanori, J., Gulik-Krzywicki, T. and Pileni, M.P. (1997) Phase diagram of copper(II) bis(2-ethylhexyl)sulfosuccinat e, $Cu(AOT)_2$-isooctane-water. *Langmuir*, **13**(4), 632–8.

133 Pileni, M.P., Tanori, J. and Filankembo, A. (1997) Biomimetic strategies for the control of size, shape and self-organization of nanoparticles. *Colloids and Surfaces A – Physicochemical and Engineering Aspects*, **123–124**, 561–73.

134 Lisiecki, I., Andre, P., Filankembo, A., Petit, C., Tanori, J., Gulik-Krzywicki, T. and Ninham, B.W. and Pileni, M.P. (1999) Mesostructured fluids. 1. $Cu(AOT)_2$-H_2O-isooctane in oil rich regions. *The Journal of Physical Chemistry B*, **103**, 9168–75.

135 Lisiecki, I., Andre, P., Filankembo, A., Petit, C., Tanori, J., Gulik-Krzywicki, T. and Ninham, B.W. and Pileni, M.P. (1999) Mesostructured fluids. 2. Microstructure and supra-aggregation. *The Journal of Physical Chemistry B*, **103**, 9176–89.

136 Filankembo, A., Andre, P., Lisiecki, I., Petit, C., Gulik-Krzywicki, T., Ninham, B.W. and Pileni, M.P. (2000) Mesostructured fluids: supra aggregates made of interdigitated reverse micelles. *Colloids and Surfaces A – Physicochemical and Engineering Aspects*, **174**, 221–32.

137 Pileni, M.P. (2001) Mesostructured fluids in oil-rich regions: structural and templating approaches. *Langmuir*, **17**, 7476–86.

138 Pileni, M.P., Ninham, B.W., Gulik-Krzywicki, T., Tanori, J., Lisiecki, I. and Filankembo, A. (1999) Direct relationship between shape and size of template and synthesis of copper metal particles. *Advanced Materials*, **11**, 1358–62.

139 Tanori, J. and Pileni, M.P. (1997) Control of the shape of copper metallic particles by using a colloidal system as template. *Langmuir*, **13**, 639–46.

140 Tanori, J. and Pileni, M.P. (1995) Change in the shape of copper nanoparticles in ordered phases. *Advanced Materials*, **7**, 862–4.

141 Pileni, M.P., Gulik-Krzywicki, T., Tanori, J., Filankembo, A. and Dedieu, J.C. (1998) Template design of microreactors with colloidal assemblies: control the growth of copper metal rods. *Langmuir*, **14**, 7359–63.

142 Filankembo, A. and Pileni, M.P. (2000) Shape control of copper nanocrystals. *Applied Surface Science*, **164**, 260–7.

143 Filankembo, A., Giorgio, S. and Lisiecki, I. and Pileni, M.P. (2003) Is the anion the major parameter in the shape control of nanocrystals? *The Journal of Physical Chemistry B*, **107**, 7492–500.

144 Lisiecki, I., Billoudet, F. and Pileni, M.P. (1996) Control of the shape and the size of copper metallic particles. *Journal of Physical Chemistry*, **100**, 4160–6.

145 Lisiecki, I., Bjoerling, M., Motte, L., Ninham, B. and Pileni, M.P. (1995) Synthesis of copper nanosize particles in anionic reverse micelles: effect of the addition of a cationic surfactant on the size of the crystallites. *Langmuir*, **11**, 2385–92.

146 Egorova, E.M. and Revina, A.A. (2000) Synthesis of metallic nanoparticles in reverse micelles in the presence of quercetin. *Colloids and Surfaces A – Physicochemical and Engineering Aspects*, **168**, 87–96.

147 Salzemann, C., Lisiecki, I., Urban, J. and Pileni, M.P. (2004) Anisotropic copper nanocrystals synthesized in a supersaturated medium: nanocrystal growth. *Langmuir*, **20**, 11772–7.

148 Salzemann, C., Urban, J., Lisiecki, I. and Pileni, M.P. (2005) Characterization and growth process of copper nanodisks. *Advanced Functional Materials*, **15**, 1277–84.

149 Kitchens, C.L., Chandler McLeod, M. and Roberts, C.B. (2003) Solvent effects on the growth and steric stabilization of copper metallic nanoparticles in AOT reverse micelle systems. *The Journal of Physical Chemistry B*, **107**, 11331–8.

150 Cason, J.P., Miller, M.E., Thompson, J.B. and Roberts, C.B. (2001) Solvent effects on copper nanoparticle growth behavior in AOT reverse micelle systems. *The Journal of Physical Chemistry B*, **105**, 2297–302.

151 Darugar, Q., Qian, W., El-Sayed, M.A. and Pileni, M.P. (2006) Size-dependent ultrafast electronic energy relaxation and enhanced fluorescence of copper nanoparticles. *The Journal of Physical Chemistry B*, **110**, 143–9.

152 Macalik, B. (2005) Optical properties of copper nanoparticles in soda-lime silicate glasses. *Physica Status Solidi C*, **2**, 608–11.

153 Hornyak, G.L., Patrissi, C.J. and Martin, C.R. (1997) Finite sized oblate and ortho-prolate metal nanoparticles: optical theory and potential as surface enhanced Raman spectroscopic substrates. *Nanostructured Materials*, **9**, 705–8.

154 Salzemann, C., Brioude, A. and Pileni, M.P. (2006) Tuning of copper nanocrystals optical properties with their shapes. *The Journal of Physical Chemistry B*, **110**, 7208–12.

155 Salzemann, C., Lisiecki, I., Brioude, A., Urban, J. and Pileni, M.P. (2004) Collections of copper nanocrystals characterized by different sizes and shapes: optical response of these nanoobjects. *The Journal of Physical Chemistry B*, **108**, 13242–8.

156 Song, X., Sun, S., Zhang, W. and Yin, Z., (2004) A method for the synthesis of spherical copper nanoparticles in the organic phase. *Journal of Colloid and Interface Science*, **273**, 463–9.

157 Xu, J., Dai, S., Cheng, G., Jiang, X., Tao, X., Zhang, P. and Du, Z. (2006) Structure and frictional properties of Langmuir–Blodgett films of Cu nanoparticles modified by dialkyldithiophosphate. *Applied Surface Science*, **253**, 1849–55.

158 Zhou, J., Yang, J., Zhang, Z., Liu, W. and Xue, Q. (1999) Study on the structure and tribological properties of surface-modified Cu nanoparticles. *Materials Research Bulletin*, **34**, 1361–7.

159 Qiu, S., Dong, J. and Chen, G. (1999) Preparation of Cu nanoparticles from water-in-oil microemulsion. *Journal of Colloid and Interface Science*, **216**, 230–4.

160 Male, K.B., Hrapovic, S., Liu, Y., Wang, D. and Loung, J.T.H. (2004) Electrochemical detection of carbohydrates using copper nanoparticles and carbon nanotubes. *Analytica Chimica Acta*, **516**, 35–41.

161 Zhang, X., Yin, H., Cheng, X., Hu, H., Yu, Q. and Wang, A. (2006) Effects of various polyoxyethylene sorbitan monooils (Tweens) and sodium dodecyl sulfate on reflux synthesis of copper nanoparticles. *Materials Research Bulletin*, **41**, 2041–8.

162 Zhou, G., Lu, M. and Yang, Z. (2006) Aqueous synthesis of copper nanocubes and bimetallic copper/palladium core-shell nanostructures. *Langmuir*, **22**, 5900–3.

163 Brust, M., Fink, J., Bethell, D., Schiffrin, D.J. and Kiely, C. (1995) Synthesis and reactions of functionalised gold nanoparticles. *Journal of the Chemical Society D – Chemical Communications*, **16**, 1655–6.

164 Aslam, M., Gopakumar, G., Shoba, T.L., Mulla, I.S., Vijayamohanan, K., Kulkarni, S.K., Urban, J. and Vogel, W. (2002) Formation of CuO and Cu_2O nanoparticles by variation of the surface ligand: preparation, structure, and insulating-to-metallic transition. *Journal of Colloid and Interface Science*, **255**, 79–90.

165 Chen, S. and Sommers, J.M. (2001) Alkanethiolate-protected copper nanoparticles: spectroscopy, electrochemistry, and solid-state morphological evolution. *The Journal of Physical Chemistry B*, **105**, 8816–20.

166 Garitaonandia, J.S., Insausti, M., Goikolea, E., Suzuki, M., Cashion, J.D., Kawamura, N., Ohsawa, H., De Muro, I.G., Suzuki, K., Plazaola, F. and Orjo, T. (2008) Chemically induced permanent magnetism in Au, Ag, and Cu nanoparticles: localization of the magnetism by element selective techniques. *Nano Letters*, **8**, 661–7.

167 Anyaogu, C.K., Fedorov, A.V. and Neckers, D.C. (2008) Synthesis, characterization, and antifouling potential of functionalized copper nanoparticles. *Langmuir*, **24**, 4340–6.

168 Kanninen, P., Johans, C., Merta, J. and Kontturi, K. (2008) Influence of ligand structure on the stability and oxidation of copper nanoparticles. *Journal of Colloid and Interface Science*, **318**, 88–95.

169 Chen, L., Zhang, D., Chen, J., Zhou, H. and Wan, H. (2005) The use of CTAB to control the size of copper nanoparticles and the concentration of alkylthiols on their surfaces. *Materials Science and Engineering A*, A**415**, 156–61.

170 Ang, T.P., Wee, T.S.A. and Chin, W.S. (2004) Three-dimensional self-assembled monolayer (3D SAM) of n-alkanethiols on copper nanoclusters. *The Journal of Physical Chemistry B*, **108**, 11001–10.

171 Dong, T.Y., Wu, H.H. and Lin, M.C. (2006) Superlattice of octanethiol-protected copper nanoparticles. *Langmuir*, **22**, 6754–6.

172 Rothe, J., Hormes, J., Boennemann, H., Brijoux, W., Siepen, K. and Situ, I. (1998) X-ray absorption spectroscopy investigation during the formation of colloidal copper. *Journal of the American Chemical Society*, **120**, 6019–23.

173 Tikhonov, A.P., Sorokina, O.N., Kovarskii, A.L., Solomatin, A.P., Afonin, A.V. and Sinitsa, P.P. (2006) EPR analysis of copper particles in aqueous systems. *Colloid Journal*, **68**, 93–7.

174 Cao, M., Hu, C., Wang, Y., Guo, Y., Guo, C. and Wang, E. (2003) A controllable synthetic route to Cu, Cu_2O, and CuO nanotubes and nanorods. *Chemical Communications*, **15**, 1884–5.

175 Wu, S.H. and Chen, D.H. (2004) Synthesis of high-concentration Cu nanoparticles in aqueous CTAB solutions. *Journal of Colloid and Interface Science*, **273**, 165–9.

176 Athawale, A.A., Katre, P.P. and Kumar, M. and Majumdar, M.B. (2005) Synthesis of CTAB-IPA reduced copper nanoparticles. *Materials Chemistry and Physics*, **91**, 507–12.

177 Athawale, A.A., Katre, P.P. and Majumdar, M.B. (2005) Nonaqueous phase synthesis of copper nanoparticles. *Journal of Nanoscience and Nanotechnology*, **5**, 991–3.

178 Song, Y., Doomes, E.E., Prindle, J., Tittsworth, R., Hormes, J. and Kumar, C.S.S. (2005) Investigations into sulfobetaine-stabilized Cu nanoparticle formation: toward development of a microfluidic synthesis. *The Journal of Physical Chemistry B*, **109**, 9330–8.

179 Qi, L., Ma, J. and Shen, J. (1997) Synthesis of copper nanoparticles in nonionic water-in-oil microemulsions. *Journal of Colloid and Interface Science*, **186**, 498–500.

180 Gauffre, F. and Roux, D. (1999) Studying a new type of surfactant aggregate ('Spherulites') as chemical microreactors. A first example: copper ion entrapping and particles synthesis. *Langmuir*, **15**, 3738–47.

181 Panigrahi, S., Kundu, S., Basu, S., Praharaj, S., Jana, S., Pande, S., Ghosh, S.K., Pal, A. and Pal, T. (2007) Nonaqueous route for the synthesis of copper organosol from copper stearate: an effective catalyst for the synthesis of octylphenyl ether. *Journal of Physical Chemistry C*, **111**, 1612–19.

182 Panigrahi, S., Kundu, S., Basu, S., Praharaj, S., Jana, S., Pande, S., Ghosh, S.K., Pal, A. and Pal, T. (2006) Cysteine functionalized copper organosol: synthesis, characterization and catalytic application. *Nanotechnology*, **17**, 5461–8.

183 Yang, J.G., Zhou, Y.L., Okamoto, T., Ichino, R. and Okido, M. (2007) A new method for preparing hydrophobic nano-copper powders. *Journal of Materials Science*, **42**, 7638–42.

184 Yang, J.G., Zhou, Y.-L., Okamoto, T., Bessho, T., Satake, S., Ichino, R. and Okido, M. (2006) Preparation of oleic acid-capped copper nanoparticles. *Chemistry Letters*, **35**, 1190–1.

185 Yang, J.G., Yang, S.H., Okamoto, T., Bessho, T., Satake, S., Ichino, R. and Okido, M. (2006) Synthesis of copper monolayer and particles at aqueous-organic interface. *Surface Science*, **600**, L318–20.

186 Su, X., Zhao, J., Bala, H., Zhu, Y., Gao, Y., Ma, S. and Wang, Z. (2007) Fast synthesis of stable cubic copper nanocages in the aqueous phase. *Journal of Physical Chemistry C*, **111**, 14689–93.

187 Mott, D., Galkowski, J., Wang, L., Luo, J. and Zhong, C.J. (2007) Synthesis of size-controlled and shaped copper nanoparticles. *Langmuir*, **23**, 5740–5.

188 Liu, X., Geng, B., Du, Q., Ma, J. and Liu, X. (2007) Temperature-controlled self-assembled synthesis of CuO, Cu_2O and Cu nanoparticles through a single-precursor route. *Materials Science and Engineering A*, A**448**, 7–14.

189 Cioffi, N., Torsi, L., Ditaranto, N., Tantillo, G., Ghibelli, L., Sabbatini, L., Bleve-Zacheo, T., D'Alessio, M., Zambonin, P.G. and Traversa, E. (2004) Antifungal activity of polymer based copper nanocomposite coatings. *Applied Physics Letters*, **85**, 2417–19.

190 Hirai, H., Wakabayashi, H. and Komiyama, I. (1983) *Chemistry Letters*, **12**, 1047–50.

191 Hirai, H., Wakabayashi, H. and Komiyama, M. (1986) Preparation of polymer-protected colloidal dispersion of copper. *Bulletin of the Chemical Society of Japan*, **59**, 367–72.

192 Huang, C. and Yang, C.Z. (1999) Fractal aggregation and optical absorption of copper nanoparticles prepared by in situ chemical reduction within a Cu^{2+}-polymer complex. *Applied Physics Letters*, **74**, 1692–4.

193 Papisov, I.M. (2003) The complexes of macromolecules and metal nanoparticles: Pseudo-template synthesis and behavior. *Macromolecular Symposia*, **204**, 237–50.

194 Larcher, D. and Patrice, R. (2000) Preparation of metallic powders and alloys in polyol media: a thermodynamic approach. *Journal of Solid-State Chemistry*, **154**, 405–11.

195 Sinha, A. and Sharma, B.P. (2002) Preparation of copper powder by glycerol process. *Materials Research Bulletin*, **37**, 407–16.

196 Park, B.K., Jeong, S., Kim, D., Moon, J., Lim, S. and Kim, J.S. (2007) Synthesis and size control of monodisperse copper nanoparticles by polyol method. *Journal of Colloid and Interface Science*, **311**, 417–24.

197 Xu, Q., Zhao, Y., Xu, J.Z. and Zhu, J.J. (2006) Preparation of functionalized copper nanoparticles and fabrication of a glucose sensor. *Sensors and Actuators B: Chemical*, B**114**, 379–86.

198 Yang, J.-G., Zhou, Y.-L., Okamoto, T., Ichino, R. and Okido, M. (2007) Surface modification of antioxidated nanocopper particles' preparation in polyol process. *Surface Engineering*, **23**, 448–52.

199 Cha, S.I., Mo, C.B., Kim, K.T., Jeong, Y.J. and Hong, S.H. (2006) Mechanism for controlling the shape of Cu nanocrystals prepared by the polyol process. *Journal of Materials Research*, **21**, 2371–8.

200 Nakamura, T., Tsukahara, Y., Sakata, T., Mori, H., Kanbe, Y., Bessho, H. and Wada, Y. (2007) Preparation of monodispersed Cu nanoparticles by microwave-assisted alcohol reduction. *Bulletin of the Chemical Society of Japan*, **80**, 224–32.

201 Cheng, X., Zhang, X., Yin, H., Wang, A. and Xu, Y. (2006) Modifier effects on chemical reduction synthesis of nanostructured copper. *Applied Surface Science*, **253**, 2727–32.

202 Cao, X., Yu, F., Li, L., Yao, Z. and Xie, Y. (2003) Copper nanorod junctions

templated by a novel polymer-surfactant aggregate. *Journal of Crystal Growth*, **254**, 164–8.

203 Wang, C.Y., Zhou, Y., Chen, Z.Y., Cheng, B., Liu, H.J. and Mo, X. (1999) Preparation of shell-core Cu_2O-Cu nanocomposite particles and Cu nanoparticles in a new microemulsion system. *Journal of Colloid and Interface Science*, **220**, 468–70.

204 Khanna, P.K., Gaikwad, S., Adhyapak, P.V., Singh, N. and Marimuthu, R., (2007) Synthesis and characterization of copper nanoparticles. *Materials Letters*, **61**, 4711–14.

205 Qin, Y., Zhang, P.Y. and Chen, J.F. (2006) Preparation of nanocrystalline copper powders by aqueous reduction. *Advanced Materials Research*, **11–12**, 575–8.

206 Wu, C., Mosher, B.P. and Zeng, T. (2006) One-step green route to narrowly dispersed copper nanocrystals. *Journal of Nanoparticle Research*, **8**, 965–9.

207 Harada, T. and Fujiwara, H. (2007) Formation of rod shape secondary aggregation of copper nanoparticles in aqueous solution of sodium borohydride with stabilizing polymer. *Journal of Physics: Conference Series*, **61**, 394–8.

208 Wu, C. and Zeng, T. (2007) Size-tunable synthesis of metallic nanoparticles in a continuous and steady-flow reactor. *Chemistry of Materials*, **19**, 123–5.

209 Sarkar, A., Mukherjee, T. and Kapoor, S. (2008) PVP-stabilized copper nanoparticles: a reusable catalyst for 'click' reaction between terminal alkynes and azides in nonaqueous solvents. *Journal of Physical Chemistry C*, **112**, 3334–40.

210 Yang, J.G., Okamoto, T., Ichino, R., Bessho, T., Satake, S. and Okido, M. (2006) A simple way for preparing antioxidation nano-copper powders. *Chemistry Letters*, **35**, 648–9.

211 Wang, Y., Chen, P. and Liu, M. (2006) Synthesis of well-defined copper nanocubes by a one-pot solution process. *Nanotechnology*, **17**, 6000–6.

212 Park, B.K., Kim, D., Jeong, S., Moon, J. and Kim, J.S. (2007) Direct writing of copper conductive patterns by ink-jet printing. *Thin Solid Films*, **515**, 7706–11.

213 Zhu, H.T., Zhang, C.Y. and Yin, Y.S. (2004) Rapid synthesis of copper nanoparticles by sodium hypophosphite reduction in ethylene glycol under microwave irradiation. *Journal of Crystal Growth*, **270**, 722–8.

214 Zhu, H., Zhang, C. and Yin, Y., (2005) Novel synthesis of copper nanoparticles: influence of the synthesis conditions on the particle size. *Nanotechnology*, **16**, 3079–83.

215 Huang, H.H., Yan, F.Q., Kek, Y.M., Chew, C.H., Xu, G.Q., Ji, W., Oh, P.S. and Tand, S.H. (1997) Synthesis, characterization, and nonlinear optical properties of copper nanoparticles. *Langmuir*, **13**, 172–5.

216 Liu, C.M., Guo, L., Xu, H.B., Wu, Z.Y. and Weber, J. (2003) Seed-mediated growth and properties of copper nanoparticles, nanoparticle 1D arrays and nanorods. *Microelectronic Engineering*, **66**, 107–14.

217 Emrick, T. and Fréchet, J.M. (1999) Self-assembly of dendritic structures. *Current Opinion in Colloid and Interface Science*, **4**, 15–23.

218 Fischer, M. and Vögtle, F. (1999) Dendrimers: from design to application – a progress report. *Angewandte Chemie – International Edition*, **38**, 885–905.

219 Bosman, A.W., Janssen, H.M., Meijer, E.W. and Dendrimers, A. (1999) Structure, physical properties, and applications. *Chemical Reviews*, **99**, 1665–88.

220 Crooks, R.M., Zhao, M., Sun, L., Chechik, V. and Yeung, L.K. (2001) Dendrimer-encapsulated metal nanoparticles: synthesis, characterization, and applications to catalysis. *Accounts of Chemical Research*, **34**, 181–90.

221 Niu, Y. and Crooks, R.M. (2003) Preparation of dendrimer-encapsulated metal nanoparticles using organic solvents. *Chemistry of Materials*, **15**, 3463–7.

222 Floriano, P.N., Noble, C.O., Schoonmaker, J.M., Poliakoff, E.D. and McCarley, R.L. (2001) Cu(0) nanoclusters derived from poly(propylene imine) dendrimer complexes of Cu(II). *Journal of*

the American Chemical Society, **123**, 10545–53.

223 Balogh, L. and Tomalia, D.A. (1998) Poly(amidoamine) dendrimer-templated nanocomposites. 1. synthesis of zerovalent copper nanoclusters. *Journal of the American Chemical Society*, **120**, 7355–6.

224 Zhao, M., Sun, L. and Crooks, R.M. (1998) Preparation of Cu nanoclusters within dendrimer templates. *Journal of the American Chemical Society*, **120**, 4877–8.

225 Braun, E., Eichen, Y., Sivan, U., Ben-Yoseph, G. and D.N. (1998) A-templated assembly and electrode attachment of a conducting silver wire. *Nature*, **391**, 775–8.

226 Monson, C.F. and Woolley, A.T. (2003) DNA-templated construction of copper nanowires. *Nano Letters*, **3**, 359–63.

227 Becerill, H.A., Stoltenberg, R.M., Monson, C.F. and Woolley, A.T. (2004) Ionic surface masking for low background in single- and double-stranded DNA-templated silver and copper nanorods. *Journal of Materials Chemistry*, **14**, 611–16.

228 Woolley, A.T. and Kelly, R.T. (2001) Deposition and characterization of extended single-stranded DNA molecules on surfaces. *Nano Letters*, **1**, 345–8.

229 Banerjee, I.A., Yu, L. and Matsui, H. (2003) Cu nanocrystal growth on peptide nanotubes by biomineralization: size control of Cu nanocrystals by tuning peptide conformation, *Proceedings of the National Academy of Sciences of the United States of America*, **100**, 14678–82.

230 Zhu, H., John, G. and Wei, B. (2005) Synthesis of assembled copper nanoparticles from copper-chelating glycolipid nanotubes. *Chemical Physics Letters*, **405**, 49–52.

231 Balci, S., Bittner, A.M., Hahn, K., Scheu, C., Knez, M., Kadri, A., Wege, C., Jeske, H. and Kern, K. (2006) Copper nanowires within the central channel of tobacco mosaic virus particles. *Electrochimica Acta*, **51**, 6251–7.

232 Demir, M. and Stowell, M.H.B. (2003) A chemoselective biomolecular template for assembling diverse nanotubular materials. *Nanotechnology*, **13**, 541–4.

233 Manceau, A., Nagy, K.L., Marcus, M.A., Lanson, M., Geoffroy, N., Jacquet, T. and Kirpichtchikova, T. (2008) Formation of metallic copper nanoparticles at the soil-root interface. *Environmental Science and Technology*, **42**, 1766–72.

234 Byrappa, K. and Adschiri, T. (2007) Hydrothermal technology for nanotechnology. *Progress in Crystal Growth and Characterization of Materials*, **53**, 117–66.

235 Liu, Z., Yang, Y., Liang, J., Hu, Z., Li, S., Peng, S. and Qian, Y. (2003) Synthesis of copper nanowires via a complex-surfactant-assisted hydrothermal reduction process. *Journal of Physical Chemistry B*, **107**, 12658–61.

236 Zhang, X., Zhang, D., Ni, X. and Zheng, H. (2006) One-step preparation of copper nanorods with. *Solid-State Communications*, **139**, 412–14.

237 Zhang, X., Zhang, D., Ni, X. and Zheng, H. (2006) Fabrication and characterization of porous copper nanorods with rectangular cross sections. *Chemistry Letters*, **35**, 1142–3.

238 Wang, W., Li, G. and Zhang, Z. (2007) A facile templateless, surfactantless hydrothermal route to ultralong copper submicron wires. *Journal of Crystal Growth*, **299**, 158–64.

239 Shi, Y., Li, H., Chen, L. and Huang, X. (2005) Obtaining ultra-long copper nanowires via a hydrothermal process. *Science and Technology of Advanced Materials*, **6**, 761–5.

240 Deng, B., Xu, A.W., Chen, G.Y., Song, R.Q. and Chen, L. (2006) Synthesis of copper-core/carbon-sheath nanocables by a surfactant-assisted hydrothermal reduction/carbonization process. *Journal of Physical Chemistry B*, **110**, 11711–16.

241 Zhang, Y.C., Xing, R. and Xiao, Y.H. (2004) A green hydrothermal route to copper nanocrystallites. *Journal of Crystal Growth*, **273**, 280–4.

242 Xu, R., Xie, T., Zhao, Y. and Li, Y. (2007) Single-crystal metal nanoplatelets: cobalt, nickel, copper, and silver. *Crystal Growth and Design*, **7**, 1904–11.

243 Tang, X.L., Ren, L., Sun, L.N., Tian, W.G., Cao, M.H. and Hu, C.W. (2006) A

solvothermal route to Cu_2O nanocubes and Cu nanoparticles, *Chemical Research in Chinese Universities*, **22**, 547–51.

244 Wei, M., Lun, N., Ma, X. and Wen, S. (2007) A simple solvothermal reduction route to copper and cuprous oxide. *Materials Letters*, **61**, 2147–50.

245 Wang, N., Lin, H., Li, J., Wang, N., Zhang, X., Yang, J., Li, J. and Yang, X. (2006) Facile synthesis of long, straight and uniform copper nanowires via a solvothermal method. *Xiyou Jinshu Cailiao Yu Gongcheng*, **35**, 644–5.

246 Liu, X.M., Miao, S.B. and Ji, B.M. (2007) Fabrication of novel Cu microspheres assembled with nanoparticles by a solvothermal reduction route. *Journal of Physics and Chemistry of Solids*, **68**, 1375–9.

247 Chang, Y.H., Wang, H.W., Chiu, C.W., Cheng, D.S., Yen, M.Y. and Chiu, H.T. (2002) Low-temperature synthesis of transition metal nanoparticles from metal complexes and organopolysilane oligomers. *Chemistry of Materials*, 4334–8.

248 Zhang, Y.C., Wang, G.Y., Hu, X.Y. and Xing, R. (2005) Preparation of submicrometer-sized copper and silver crystallites by a facile solvothermal complexation–reduction route. *Journal of Solid-State Chemistry*, **178**, 1609–13.

249 Fulton, J.L. and Smith, R.D. (1988) Reverse micelle and microemulsion phases in supercritical fluids. *Journal of Physical Chemistry*, **92**, 2903–7.

250 Gale, R.W., Fulton, J.L. and Smith, R.D. (1987) Organized molecular assemblies in the gas phase-reverse micelles and microemulsions in supercritical fluids. *Journal of the American Chemical Society*, **109**, 920–1.

251 Cason, J.P. and Roberts, C.B. (2000) Metallic copper nanoparticles synthesis in AOT reverse micelles in compressed propane and supercritical ethane solution. *Journal of Physical Chemistry B*, **104**, 1217–21.

252 Cason, J.P., Khambaswadkar, K. and Roberts, C.B. (2000) Supercritical fluid and compressed solvent effects on metallic nanoparticle synthesis in reverse micelles. *Industrial and Engineering Chemistry Research*, **39**, 4749–55.

253 Kitchens, C.L. and Roberts, C.B. (2004) Copper nanoparticle synthesis in compressed liquid and supercritical fluid reverse micelle system. *Industrial and Engineering Chemistry Research*, **43**, 6070–81.

254 Kitchens, C.L., Chandler McLeod, M. and Roberts, C.B. (2005) Chloride ion effects on synthesis and directed assembly of copper nanoparticles in liquid and compressed alkane microemulsion. *Langmuir*, **21**, 5166–73.

255 Ziegler, K.J., Doty, C.R., Johnston, K.P. and Korgel, B.A. (2001) Synthesis of organic monolayer-stabilized copper nanocrystals in supercritical water. *Journal of the American Chemical Society*, **123**, 7797–803.

256 Ohde, H., Hunt, F. and Wai, C.M. (2001) Synthesis of silver and copper nanoparticles in a water-in-supercritical-carbon dioxide microemulsion. *Chemistry of Materials*, **13**, 4130–5.

257 Shervani, Z., Ikushima, Y., Yokoyama, T., Sato, M., Hakuta, Y., Takako, N., Kunieda, H. and Aramaki, K. (2007) Size controlled synthesis of Ag and Cu nanocrystals in F-AOT/n-butanol/SC CO_2 microemulsions. *Colloids and Surfaces A – Physicochemical and Engineering Aspects*, **303**, 159–65.

258 Chen, C., Lou, Z. and Chen, Q. (2005) A novel way for preparing Cu nanowires. *Chemistry Letters*, **34**, 430–1.

259 Ziegler, K.J., Harrington, P.A., Ryan, K.M., Crowley, T., Holmes, J.D. and Morris, M.A. (2003) Supercritical fluid preparation of copper nanotubes and nanowires using mesoporous templates. *Journal of Physics: Condensed Matter*, **15**, 8303–14.

260 Caló, V., Nacci, A., Monopoli, A., Laera, S. and Cioffi, N. (2003) Pd-nanoparticles catalyzed stereospecific synthesis of β-aryl cinnamic esters in ionic liquids. *Journal of Organic Chemistry*, **68**, 2929–33.

261 Calò, V., Nacci, A., Monopoli, A., Ieva, E. and Cioffi, N. (2005) Copper bronze catalyzed Heck reaction in ionic liquids. *Organic Letters*, **7**, 617–20.

262 Jacob, D.S., Genish, I., Klein, L. and Gedanken, A. (2006) Carbon coated core shell structured copper and nickel nanoparticles synthesized in a ionic liquid. *Journal of Physical Chemistry B*, **110**, 17711–14.

263 Singh, P., Katyal, A., Kalra, R. and Chandra, R. (2008) Copper nanoparticles in an ionic liquid: an efficient catalyst for the synthesis of bis-(4-hydroxy-2-oxothiazolyl)methanes. *Tetrahedron Letters*, **49**, 727–30.

264 Singh, P., Katyal, A., Kalra, R. and Chandra, R. (2008) Copper nanoparticles in an ionic liquid: an easy and efficient catalyst for the coupling of thiazolidine-2,4-dione, aromatic aldehyde and ammonium acetate. *Catalysis Communications*, **9**, 1618–23.

265 Reisse, J., Caulier, T., Deckerkheer, C., Fabre, O., Vandercammen, J. and Delplancke, J.L. and Winand, R. (1996) Quantitative sonochemistry. *Ultrasonics Sonochemistry*, **3**, S147–51.

266 Dhas, N.A., Raj, C.P. and Gedanken, A. (1998) Synthesis, characterization, and properties of metallic copper nanoparticles. *Chemistry of Materials*, **10**, 1446–52.

267 Salkar, R.A., Jeevanandam, P., Kataby, G., Aruna, S.T., Koltypin, Y., Palchik, O. and Gedanken, A. (2000) Elongated copper nanoparticles coated with a zwitterionic surfactant. *Journal of Physical Chemistry B*, **104**, 893–7.

268 Tao, X.J., Li, Z.W., Zhou, C.H., Zhang, P.Y., Zhang, Z.J., Wu, Z.S. and Dang, H.X. (2005) A simple replacement reaction route for copper nanoparticles and nanorods preparation. *Wuji Huaxue Xuebao*, **21**, 763–6.

269 Stopic, S., Dvorak, P. and Friedrich, B. (2005) Synthesis of spherical nanosized copper powder by ultrasonic spray pyrolysis. *World of Metallurgy–Erzmetall*, **58**, 191–7.

270 Sergiienko, R., Shibata, E., Suwa, H., Nakamura, T., Akase, Z., Murakami, Y. and Shindo, D. (2006) Synthesis of amorphous carbon nanoparticles and carbon encapsulated metal nanoparticles in liquid benzene by an electric plasma discharge in ultrasonic cavitation field. *Ultrasonics Sonochemistry*, **13**, 6–12.

271 Haas, I. and Gedanken, A. (2006) Sonoelectrochemistry of Cu^{2+} in the presence of cetyltrimethylammonium bromide: obtaining CuBr instead of copper. *Chemistry of Materials*, **18**, 1184–9.

272 Warren, S.C., Jackson, A.C., Cater-Cyker, Z.D., DiSalvo, F.J. and Wiesner, U. (2007) Nanoparticle synthesis via the photochemical polythiol process. *Journal of the American Chemical Society*, **129**, 10072–3.

273 Kapoor, S., Palit, D.K. and Murkherjee, T. (2002) Preparation, characterization and surface modification of Cu metal nanoparticles. *Chemical Physics Letters*, **355**, 383–7.

274 Kapoor, S. and Murkherjee, T. (2003) Photochemical formation of copper nanoparticles in poly(*N*-vinylpyrrolidone). *Chemical Physics Letters*, **370**, 83–7.

275 Murakata, T., Higashi, Y., Yasui, N., Higuchi, T. and Sato, S. (2002) Photocatalytic preparation of noble metal nanoparticles with use of ultrafine TiO_2 particles. *Journal of Chemical Engineering of Japan*, **35**, 1270–6.

276 Condorelli, G.G., Costanzo, L.L., Fragalà, I.L., Giuffrida, S. and Ventimiglia, G. (2003) A single photochemical route for the formation of both copper nanoparticles and patterned nanostructured films. *Journal of Materials Chemistry*, **13**, 2409–11.

277 Giuffrida, S., Condorelli, G.G., Costanzo, L.L., Fragalà, I.L., Ventimiglia, G. and Vecchio, G. (2004) Photochemical mechanism of the formation of nanometer-sized copper by UV irradiation of ethanol bis(2,4-pentandionato)copper(II) solutions. *Chemistry of Materials*, **16**, 1260–6.

278 Fojtik, A. and Henglein, A. (1993) Laser ablation of films and suspended particles in a solvent: formation of cluster and colloid solutions. *Berichte der Bunsen-Gesellschaft fur Physikalische Chemie*, **97**, 252–4.

279 Neddersen, J., Chumanov, G. and Cotton, T.M. (1993) Laser ablation of metals: a new method for preparing SERS active

colloids. *Applied Spectroscopy*, **47**, 1959–64.

280 Yeh, Y.H., Yeh, M.S., Lee, Y.P. and Yeh, C.S. (1998) Formation of Cu nanoparticles from CuO powder by laser ablation in 2-propanol. *Chemistry Letters*, **11**, 1183–4.

281 Paszti, Z., Peto, G., Horvath, Z.E. and Karacs, A. (2000) Laser ablation induced formation of nanoparticles and nanocrystal networks. *Applied Surface Science*, **168**, 114–17.

282 Salle, B., Cheleard, C., Detalle, V., Lacour, J.L., Mauchien, P., Nouvellon, C. and Semerok, A. (1999) Laser ablation efficiency of metal samples with UV laser nanosecond pulses. *Applied Surface Science*, **138–139**, 302–5.

283 Paszti, Z., Horvath, Z.E., Peto, G., Karacs, A. and Guczi, L. (1997) Pressure-dependent formation of small Cu and Ag particles during laser ablation. *Applied Surface Science*, **109–110**, 67–73.

284 Yeh, M.S., Yang, Y.S., Lee, Y.P., Lee, H.F., Yeh, Y.H. and Yeh, C.S. (1999) Formation and characteristics of Cu colloids from CuO powder by laser irradiation in 2-propanol. *Journal of Physical Chemistry B*, **103**, 6851–7.

285 Chen, T.Y., Chen, S.F., Sheu, H.S. and Yeh, C.S. (2002) Reactivity of laser-prepared copper nanoparticles: oxidation of thiols to disulfides. *Journal of Physical Chemistry B*, **106**, 9717–22.

286 Tsuji, T., Iryo, K., Nishimura, Y. and Tsuji, M. (2001) Preparation of metal colloids by a laser ablation technique in solution: influence of laser wavelength on the ablation efficiency (II). *Journal of Photochemistry and Photobiology A: Chemistry*, **145**, 201–7.

287 Tilaki, R.M., Iraji-zad, A. and Mahdavi, S.M. (2007) Size, composition and optical properties of copper nanoparticles prepared by laser ablation in liquids. *Applied Physics A*, **88**, 415–19.

288 Saito, M., Yasukawa, K., Umeda, T. and Aoi, Y. (2008) Copper nanoparticles fabricated by laser ablation in polysiloxane. *Optical Materials*, **30**, 1201–4.

289 Chandra, M., Indi, S.S. and Das, P.K. (2006) First hyperpolarizabilities of unprotected and polymer protected copper nanoparticles prepared by laser ablation. *Chemical Physics Letters*, **422**, 262–6.

290 Lee, J., Kim, D.K. and Kang, W. (2006) Preparation of Cu nanoparticles from Cu powder dispersed in 2-propanol by laser ablation. *Bulletin of the Korean Chemical Society*, **27**, 1869–72.

291 Kim, D. and Jang, D. (2007) Synthesis of nanoparticles and suspensions by pulsed laser ablation of microparticles in liquid. *Applied Surface Science*, **253**, 8045–9.

292 Badr, Y. and Mahmoud, M.A. (2007) Excimer laser photofragmentation of metallic nanoparticles. *Physics Letters A*, **370**, 158–61.

293 Buxton, G.V. and Green, J.C. (1978) Reactions of some simple α- and β-hydroxyalkyl radicals with Cu^{2+} and Cu+ ions in aqueous solution. A radiation chemical study. *Journal of the Chemical Society–Faraday Transactions I*, **74**, 697–714.

294 Freiberg, M. and Meyerstein, D. (1980) Reactions of aliphatic free radicals with copper cations in aqueous solution. Part 2. Reactions with cupric ions: a pulse radiolysis study. *Journal of the Chemical Society–Faraday Transactions I*, **76**, 1825–37.

295 Freiberg, M., Mulac, W.A., Schmidt, K.H. and Meyerstein, D. (1980) Reactions of aliphatic free radicals with copper cations in aqueous solutions. Part 3. Reactions with cuprous ions: a pulse radiolysis study. *Journal of the Chemical Society–Faraday Transactions I*, **76**, 1838–48.

296 Henglein, A. (2000) Formation and absorption spectrum of copper nanoparticles from the radiolytic reduction of $Cu(CN)_2$. *Journal of Physical Chemistry B*, **104**, 1206–11.

297 Sosebee, T., Giersig, M., Holzwarth, A. and Mulvaney, P. (1995) The nucleation of colloidal copper in the presence of poly(ethyleneimine). *Berichte der Bunsen-Gesellschaft fur Physikalische Chemie*, **90**, 40–9.

298 Ni, Y., Ge, X., Liu, H., Zhang, Z., Ye, Q. and Wang, F. (2001) Fabrication of nano-rod copper-polymer composites by ?-irradiation route in a heterogeneous system. *Chemistry Letters*, **5**, 458–9.

299 Joshi, S.S., Patil, S.F., Iyer, V. and Mahumuni, S. (1999) Radiation induced synthesis and characterization of copper nanoparticles. *Nanostructured Materials*, **10**, 1135–44.

300 Kapoor, S., Adhikari, S., Gopinathan, C. and Mittal, J.P. (1999) Radiolytic production of metallic nanoclusters in a quaternary microemulsion system. *Materials Research Bulletin*, **34**, 1333–43.

301 Zhu, Y., Qian, Y., Zhang, M., Chen, Z., Lu, B. and Zhou, G. (1994) γ-radiation-hydrothermal synthesis and characterization of nanocrystalline copper powders. *Materials Science and Engineering B*, **B23**, 116–19.

302 Dey, G.R. (2005) Reduction of the copper ion to its metal and clusters in alcoholic media: a radiation chemical study. *Radiation Physics and Chemistry*, **74**, 172–84.

303 Ershov, B.G., Janata, E., Michaelis, M. and Henglein, A. (1991) Reduction of $Cu^{2+}_{(aq)}$ by CO_2^-: first steps and the formation of colloidal copper. *Journal of Physical Chemistry*, **95**, 8996–9.

304 Zhou, F., Zhou, R., Hao, X., Wu, X., Rao, W., Chen, Y. and Gao, D. (2008) Influences of surfactant (PVA) concentration and pH on the preparation of copper nanoparticles by electron beam irradiation. *Radiation Physics and Chemistry*, **77**, 169–73.

305 Zhou, R., Wu, X., Hao, X., Zhou, F., Li, H. and Rao, W. (2008) Influences of surfactants on the preparation of copper nanoparticles by electron beam irradiation. *Nuclear Instruments and Methods in Physics Research Section B*, **266**, 599–603.

306 Kratschmer, E., Whitehead, B., Isaacson, M. and Wolf, E. (1985) Nanometer scale metal wire fabrication. *Microelectronic Engineering*, **3**, 25–32.

307 Herley, P.J. and Jones, W. (1989) Metal hydrides as precursors for the generation of supported metal particles and alkali metal whiskers. *Zeitschrift fuer Physikalische Chemie*, **164**, 1151–6.

308 Yen, M.Y., Chiu, C.W., Chen, F.R., Kai, J.J., Lee, C.Y. and Chiu, H.T. (2004) Convergent electron beam induced growth of copper nanostructures: evidence of the importance of a soft template. *Langmuir*, **20**, 279–81.

309 Schmittel, M., Kalsani, V. and Kienle, L. (2004) Simple and supramolecular copper complexes as precursors in the HRTEM induced formation of crystalline copper nanoparticles. *Chemical Communications*, **13**, 1534–5.

310 Wang, Z.L., Kong, X.Y., Wen, X. and Yang, S. (2003) In situ structure evolution from Cu(OH)2 nanobelts to copper nanowires. *Journal of Physical Chemistry B*, **107**, 8275–80.

311 Zoval, J.V., Lee, J., Gorer, S. and Penner, R.M. (1998) Electrochemical preparation of platinum nanocrystallites with size selectivity on basal plane oriented graphite surfaces. *Journal of Physical Chemistry B*, **102**, 1166–75.

312 Zoval, J.V., Stiger, R.M., Biernacki, P.R. and Penner, R.M. (1996) Electrochemical Deposition of silver nanocrystallites on the atomically smooth graphite basal plane. *Journal of Physical Chemistry*, **100**, 837–44.

313 Penner, R.M. (ed.) (2007) Nanowires by electrochemical step edge decoration (ESED), in *Electrocrystallization in Nanotechnology* (ed. R.M., Penner), Wiley-VCH Verlag GmbH, pp. 1–24.

314 Natter, H. and Hempelmann, R. (1996) Nanocrystalline copper by pulsed electrodeposition: the effects of organic additives, bath temperature, and pH. *Journal of Physical Chemistry*, **100**, 19525–32.

315 Gorer, S., Hsiao, G.S., Anderson, M.G., Stiger, R.M., Lee, J. and Penner, R.M. (1998) A hybrid electrochemical/chemical synthesis of semiconductor nanocrystals on graphite: a new role for electrodeposition in materials synthesis. *Electrochimica Acta*, **43**, 2799–809.

316 Murray, B.J., Li, Q., Newberg, J.T., Menke, E.J., Hemminger, J.C. and Penner, R.M. (2005) Shape- and size-selective electrochemical synthesis of dispersed silver(I) oxide colloids. *Nano Letters*, **5**, 2319–24.

317 Reetz, M.T. and Helbig, W. (1994) Size-selective synthesis of nanostructured transition metal clusters. *Journal of the American Chemical Society*, **116**, 7401–2.

318 Reetz, M.T. and Quaiser, S.A. (1995) A new method for the preparation of nanostructured metal clusters. *Angewandte Chemie – International Edition in English*, **34**, 2240–1.

319 Reetz, M.T. and Quaiser, S.A. (1995) Eine neue methode zur herstellung nanostrukturierter metallcluster. *Angewandte Chemie*, **107**, 2461–3.

320 Cioffi, N., Torsi, L., Ditaranto, N., Tantillo, G., Ghibelli, L., Sabbatini, L., Bleve-Zacheo, T., D'Alessio, M., Zambonin, P.G. and Traversa, E. (2005) Copper nanoparticle/polymer composites with antifungal and bacteriostatic properties. *Chemistry of Materials*, **17**, 5255–62.

321 Cioffi, N., Ditaranto, N., Torsi, L., Picca, R.A., De Giglio, E., Sabbatini, L., Novello, L., Tantillo, G., Bleve-Zacheo, T. and Zambonin, P.G. (2005) Synthesis, analytical characterization and bioactivity of Ag and Cu nanoparticles embedded in poly-vinyl-methyl-ketone films. *Analytical and Bioanalytical Chemistry*, **382**, 1912–18.

322 Reetz, M.T., Helbig, W., Quaiser, S.A., Stimming, U., Breuer, N. and Vogel, R. (1995) Visualization of surfactants on nanostructured palladium clusters by a combination of STM and high-resolution TEM. *Science*, **267**, 367–9.

323 Jirka, I. (1990) An ESCA study of clusters on carbon. *Surface Science*, **232**, 307–15.

324 Wu, Y., Garfunkel, E. and Madey, T. (1996) Initial stages of Cu growth on ordered Al_2O_3 ultrathin films. *The Journal of Vacuum Science and Technology A*, **14**, 1662–7.

325 Yang, X., Chen, S., Zhao, S., Li, D. and Ma, H. (2003) Synthesis of copper nanorods using electrochemical methods. *Journal of The Electrochemical Society*, **68**, 843–7.

326 Singh, D.P. and Srivastava, O.N. (2007) Synthesis of copper nanoparticles by electrolysis of DNA utilizing copper as sacrificial anode. *Journal of Nanoscience and Nanotechnology*, **7**, 2105–9.

327 Grugeon, S., Laruelle, S., Herrera-Urbina, R., Dupont, L., Poizot, P., Tarascon, J.M. and Size, P. (2001) Effects on the electrochemical performance of copper oxides toward lithium. *Journal of The Electrochemical Society*, **148**, A285–92.

328 Debart, A., Dupont, L., Poizot, P., Leriche, J.B., Tarascon, J.M. and Transmission, A. (2001) Electron microscopy study of the reactivity mechanism of tailor-made CuO particles toward lithium. *Journal of The Electrochemical Society*, **148**, A1266–74.

329 Zhang, D.W., Chen, C.H., Zhang, J. and Ren, F. (2005) Novel electrochemical milling method to fabricate copper nanoparticles and nanofibers. *Chemistry of Materials*, **17**, 5242–5.

330 Yu, Y., Shi, Y., Chen, C.H. and Wang, C. (2008) Facile electrochemical synthesis of single-crystalline copper nanospheres, pyramids, and truncated pyramidal nanoparticles from lithia/cuprous oxide composite thin films. *Journal of Physical Chemistry C*, **112**, 4176–9.

331 Durant, A., Delplancke, J.L., Winand, R. and Reisse, J. (1995) A new procedure for the production of highly reactive metal powders by pulsed sonoelectrochemical reduction. *Tetrahedron Letters*, **36**, 4257–60.

332 Reisse, J., Francois, H., Vandercammen, J., Fabre, O., Kirsch-de mesmaeker, A., Maerschalk, C. and Delplancke, J.L. (1994) Sonoelectrochemistry in aqueous electrolyte: a new type of sonoelectroreactor. *Electrochimica Acta*, **39**, 37–9.

333 Haas, I., Shanmugam, S. and Gedanken, A. (2006) Pulsed sonoelectrochemical synthesis of size-controlled copper nanoparticles stabilized by poly(N-vinylpyrrolidone). *Journal of Physical Chemistry B*, **110**, 16947–52.

334 Silveira, E.T., Umpierre, A.P., Rossi, L.M., Machado, G., Morais, J., Soares, G.V., Baumvol, I.J.R., Teixeira, S.R., Fichtner, P.F.P. and Dupont, J. (2004) The partial hydrogenation of benzene to cyclohexene by nanoscale ruthenium catalysts in imidazolium ionic liquids. *Chemistry – A European Journal*, **10**, 3734–40.

335 Yu, L., Sun, H., He, J., Wang, D., Jin, X., Hu, X. and Chen, G.Z. (2007) Electro-reduction of cuprous chloride powder to copper nanoparticles in an ionic liquid.

Electrochemistry Communications, **9**, 1374–81.

336 Azarian, A., Iraji Zad, A., Dolati, A. and Ghorbani, M. (2007) Time dependence of the surface plasmon resonance of copper nanorods. *Journal of Physics: Condensed Matter*, **19**, 446007/1–446007/9.

337 Penner, R.M. and Martin, C.R. (1987) Preparation and electrochemical characterization of ultramicroelectrode ensemble. *Analytical Chemistry*, **59**, 2625–30.

338 Dobrev, D., Vetter, J., Angert, N. and Neumann, R. (1999) Electrochemical growth of copper single crystals in pores of polymer ion-track membranes. *Applied Physics A*, **69**, 233–7.

339 Gao, T., Meng, G.W., Zhang, J., Wang, Y.W., Liang, C.H., Fan, J.C. and Zhang, L.D. (2001) Template synthesis of single-crystal Cu nanowire arrays by electrodeposition. *Applied Physics A*, **73**, 251–4.

340 Toimil Molares, M.E., Brotz, J., Buschmann, V., Dobrev, D., Neumann, R., Scholz, R., Schuchert, I.U., Trautmann, C. and Vetter, J. (2001) Etched heavy ion tracks in polycarbonate as template for copper nanowires. *Nuclear Instruments and Methods in Physics Research Section B*, **185**, 192–7.

341 Wang, W., Li, N., Li, X., Geng, W. and Qiu, S. (2006) Synthesis of metallic nanotube arrays in porous anodic aluminum oxide template through electroless deposition. *Materials Research Bulletin*, **41**, 1417–23.

342 Tian, M., Wang, J., Kurtz, J., Mallouk, T.E. and Chan, M.H.W. (2003) Electrochemical growth of single-crystal metal nanowires via a two-dimensional nucleation and growth mechanism. *Nano Letters*, **3**, 919–23.

343 Gerein, N.J. and Haber, J.A. (2005) Effect of electrodeposition conditions on the growth oh high aspect ratio copper nanowires in porous alumina oxide templates. *Journal of Physical Chemistry B*, **109**, 17372–85.

344 Rivas, J., Kazadi Mukenga Bantu, A., Zaragoza, G., Blanco, M.C. and Lopez-Quintela, M.A. (2002) Preparation and magnetic behavior of arrays of electrodeposited Co nanowires. *Journal of Magnetism and Magnetic Materials*, **249**, 220–7.

345 Khan, H.R. and Petrikowski, K. (2002) Synthesis and properties of the arrays of magnetic nanowires of Co and CoFe. *Materials Science and Engineering C*, **19**, 345–8.

346 Williams, W.D. and Giordano, N. (1984) Fabrication of 80 Å metal wires. *Review of Scientific Instruments*, **55**, 410–12.

347 Riveros, G., Gomez, H., Schrebler, R., Marotti, R.E. and Dalchiele, E.A. (2008) An in situ EIS study during the electrochemical growth of copper nanowires into porous polycarbonate membranes. *Electrochemical and Solid-State Letters*, **11**, K19–23.

348 Enculescu, I., Siwy, Z., Dobrev, D., Trautmann, C., Toimil Molares, M.E., Neumann, R., Hjort, K., Westerberg, L. and Spohr, R. (2003) Copper nanowires electrodeposited in etched single-ion track templates. *Applied Physics A*, **77**, 751–5.

349 Toimil Molares, M.E., Buschmann, V., Dobrev, D., Newmann, R., Scholz, R., Schuchert, I.U. and Vetter, J. (2001) Single-crystalline copper nanowires produced by electrochemical deposition in polymeric ion track membranes. *Advanced Materials*, **13**, 62–5.

350 Peng, L., Xin, J., Wang, S., Xian, D., Chen, H. and He, Y. (1999) Fabrication and optical property of copper nanowires in nuclear track membranes. *Physics Letters*, **16**, 126–8.

351 Koshikawa, H., Maekawa, Y., Asano, M. and Yoshida, M. (2002) Preparation of copper nanowires using ion track membranes. *Japan Atomic Energy Research Institute (JAERI) – Review*, 113–14.

352 Xie, G., Li, X. and Jiao, H. (2008) Template-synthesized copper nanotubes via electroless plating. *Journal of Dispersion Science and Technology*, **29**, 120–3.

353 Gao, T., Meng, G., Wang, Y., Sun, S. and Zhang, L. (2002) Electrochemical synthesis of copper nanowires. *Journal of Physics: Condensed Matter*, **14**, 355–63.

354 Zheng, G.Q., Ni, S.Y., Zheng, H.J., Gan, X.H. and Zhang, J.Y. (2004) Preparation of copper nano-wires by template synthesis method. *Journal of Central South University of Technology*, **11**, 371–4.

355 Gelves, G.A., Murakami Zakari, T.M., Krantz, M.J. and Haber, J.A. (2006) Multigram synthesis of copper nanowires using ac electrodeposition into porous aluminium oxide templates. *Journal of Materials Chemistry*, **16**, 3075–83.

356 Duan, J.L., Liu, J., Yao, H.J., Mo, D., Hou, M.D., Sun, Y.M., Chen, Y.F. and Zhang, L., (2008) Controlled synthesis and diameter-dependent optical properties of Cu nanowire arrays. *Materials Science and Engineering B*, **147**, 57–62.

357 Liu, Z. and Bando, Y. (2003) A novel method for preparing copper nanorods and nanowires. *Advanced Materials*, **15**, 303–5.

2
Spherical and Anisotropic Copper Nanomaterials in Medical Diagnosis

Chi-Chung Chou, Jen-Lin Chang and Jyh-Myng Zen

2.1
Introduction

With the use of nanomaterials in medical diagnosis representing an important discipline in nanomedicine, the latter topic has become a major category among books and reviews related to the nanosciences. Today, the number of publications on nanomedicine has surpassed that of other nanorelated categories such as nanomaterials, electronics, fabrication technologies, sensors and imaging. Nanomedicine allows the transition to be made from molecular-based science to clinical medicine, thereby facilitating advances in the early detection, diagnosis and treatment of disease. According to information collected in the *NanoBiotech News 2006 Nanomedicine, Device & Diagnostic Report*, a total of 130 nanotech-based drugs and delivery systems and 125 devices or diagnostic tests have now entered preclinical, clinical or commercial development. Moreover, since 2005 the clinical pipeline has grown by some 68% (National Health Information, LLC), with $1.9 billion being invested in nanotechnology that year – an increase of 18% over 2004. The 2007 National Nanotechnology Initiative (NNI) budget request for nanotechnology R&D across the US Federal Government was $1.28 billion, thus highlighting the growing demand for nanoassociated knowledge. It is not surprising, therefore, that publications in nanosciences are not only rapidly increasing in number but also covering more ground than ever in terms of subject matter. Today, specific nanomaterials and their medical applications form the focal points of very many publications.

Among general publications, nanomedicine includes the areas of nanotools, materials and devices that are currently applied in medical research. According to the nanomedicine taxonomy provided by the Canadian Institutes of Health Research & Canadian NanoBusiness Alliance (2003), the major disciplines of nanomedicine comprise biopharmaceutics (e.g. drug delivery, encapsulation and discovery), implantable materials (e.g. tissue and bone repair, regeneration and replacement), implantable devices (e.g. sensors, sensory aids and other medical

Metallic Nanomaterials Vol. 1. Edited by Challa S. S. R. Kumar

ISBN: 978-3-527-32151-3

devices) and diagnostic tools such as ultrasensitive labeling, genetic detection technologies, high-throughput multiple analyses, and imaging using nanoparticle labels and contrast agents. Although many of the above are still in their experimental stages, the important components of nanomedicine – such as nanopharmaceuticals and nanodiagnostics – have already been described extensively. As many nanodiagnostic applications are involved with genetic testing and cancer imaging, there remains much to be explored and discussed regarding disease diagnosis and the detection of specific biomarkers with health implications. In attempting to fill any gaps in our knowledge relating to the biomedical application of nanoparticles and nanomaterials, this chapter outlines the development of sensitive and specific sensors to detect diseases in their early stages, of therapeutics and targeted on-particle drug delivery for treatments, and also of innovative contrast agents for localization and improved *in vivo* imaging.

Although copper (Cu) nanomaterial is readily available, exhibits exceptional properties and represents an exciting new class of nanomaterial for use in medical diagnosis, its medical applications are still in their infancy and consequently few reports have been made which relate directly to its use in medical diagnosis. Indeed, it is possible that this chapter may represent by far the most comprehensive review of copper nanomaterial prepared to date. Here, particular attention is paid not only to the ability of nanocopper to detect biological metabolic markers, but also to its relationship with disease processes. Because developments in nanomaterial applications depend on simple and efficient fabrication methods to produce pure and uniformly sized particles, we will first addresses the essential issues of nanoparticle production, at both theoretical and practical levels. The topic is approached systematically via the reduction phase, detailing processing methods and key components, after which a host of current and potential uses of copper nanomaterials in the biomedical sciences will de described. In this respect, in addition to providing an update on the recent developments of Cu-containing materials in medical imaging [e.g. magnetic resonance imaging (MRI) and positron emission tomography (PET)], special attention is also paid to the use of nanocopper-containing electrodes in the detection of glucose, amino acids, uric acid and other organic acids relevant to metabolic disorders. The final discussion centers on developing applications of nanocopper-complexes as drug carriers and antitumor agents, and suggests some potential uses of these complexes based on their antimicrobial activities.

It should be noted that the development of nanomedicine was not without challenge: nanobased products present a variety of safety issues, including their absorption, distribution, metabolism and elimination, which may differ from those of pharmaceuticals. In addition, biomedical nanoscale materials are at present neither well characterized nor standardized, and their interactions with traditional drugs/devices/metabolic pathways are largely unknown. The toxicological aspects of nanocopper materials should, therefore, always be borne in mind when developing new ideas or invasive devices.

2.2 Copper Nanoparticles

As copper is inexpensive and possesses superior catalytic activity, a large number of publications have focused on copper-based nanoparticles (e.g. Cu, CuO and Cu_2O) and modified electrodes. These nanoparticles have established widespread use in electronics, optics and sensors, and have also attracted attention from diverse disciplines such as chemists and materials scientists [1]. The catalytic activity relates undoubtedly to the copper particle size and is influenced by a variety of factors, including the increase in specific surface area with diminishing particle size, the variation of surface morphology (notably the contribution of different crystallographic lanes) and the shape of particle. Many approaches utilizing chemical, physical, photochemical and electrochemical methods have been applied in the preparation of copper nanoparticles (Cu-NPs). The application of Cu-NPs in medical analysis is especially attractive, with one of the main challenges for the analytical chemist being to satisfy the growing need to perform rapid '*in-situ*' analyses. To pursue such a goal, chemical modifications – especially dip-coating and electrodeposition – have been used to immobilize Cu-NPs on substrates, including metallic plate, carbon fibers and carbon nanotubes (CNTs), to produce electrodes with a diversified spectrum of biomedical analytes.

Since the 1990s, screen-printing technology has permitted the high-volume production of extremely inexpensive, yet highly reproducible and reliable, single-use sensors. Moreover, this technique also holds great promise for on-site monitoring. Currently, the use of screen printing technology to mass-produce disposable electrodes for the electrochemical determination of a wide range of substances is undergoing extensive growth [2]. In this chapter we review a variety of methods used for the creation of Cu-NPs, and emphasize the benefits of screen-printed electrodes (SPEs) in their application and production. The methods include chemical reduction in aqueous and organic media, photoreduction, sonochemical, radiolytic and machine–chemical reduction, in addition to deposition productions which employ metallic electrodes, carbon fibers, polymer film-modified electrodes and SPEs. In brief, the principle relies on 'the critical key factor', as shown in Figure 2.1, either to protect or clutch-generate Cu-NPs.

In the medical applications of copper, very little emphasis has been placed on the shape of the nanoparticles used. In general, for the chemical reduction of copper ions in mixed reverse micelles, a large excess of reducing agent was found to favor the production of a variety of copper nanocrystals. When using a low reducing agent concentration, the resultant nanocrystals are mostly spherical, whereas in the supersaturated regime they assume various shapes such as pentagons, squares, triangles and elongated forms. For the purpose of this chapter, spherical and anisopic copper nanomaterials will be referred to as 'copper nanomaterial'.

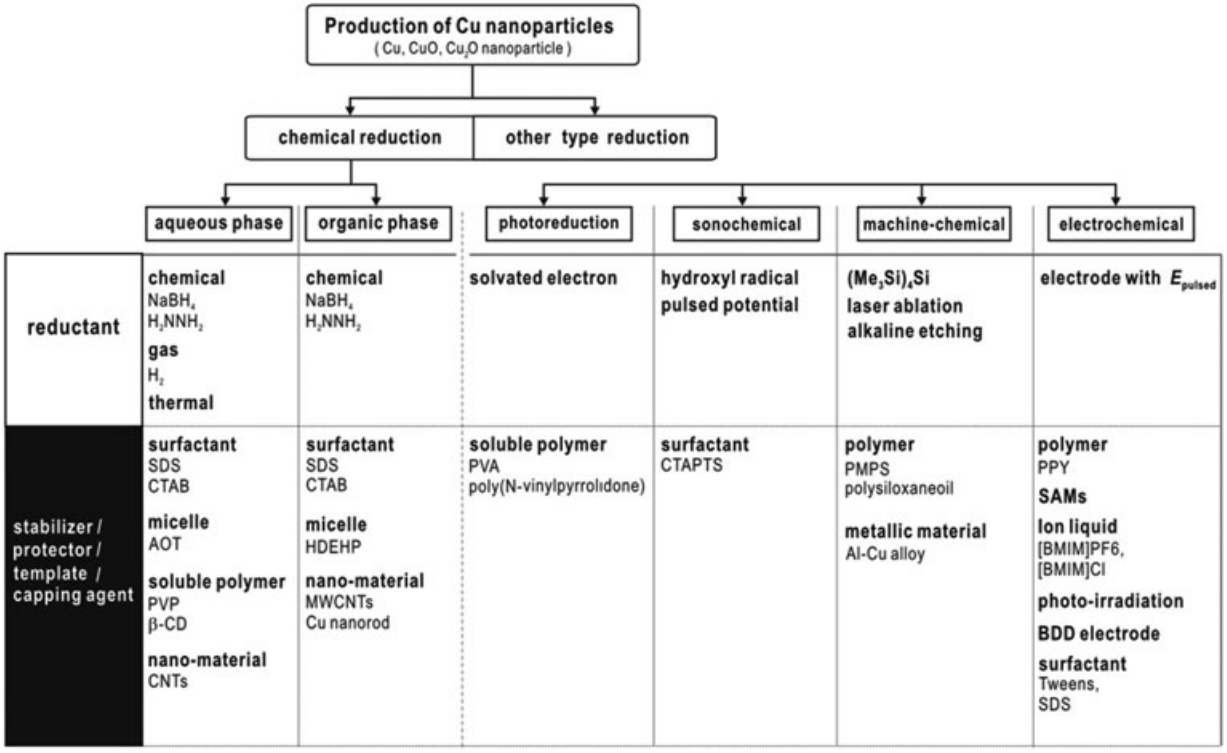

Figure 2.1 Schematic presentation of the production of copper nanoparticles according to the types of reduction.

2.3
Synthesis of Copper Nanoparticles

2.3.1
Chemical Reduction in Aqueous Media

A variety of reducing agents, such as hydrazine hydrate, sodium cyanoborohydride ($NaBH_3CN$), $NaBH(OAc)_3$, *N,N,N,N*-tetramethyl-*p*-phenylenediamine (TMPD), sodium borohydride and sodium hypophosphite [3, 4], have all been used to synthesize Cu-NPs. The main approach to the use of reducing agents to fabricate Cu-NPs is based on creating nanometer-sized particles, with a stable distribution. In recent years, a water-in-oil microemulsion (e.g. sodium bis(2-ethylhexyl)sulfos uccinate; AOT) was applied as a template to synthesize Cu-NPs with a narrow size distribution in supercritical carbon dioxide ($scCO_2$). The use of $scCO_2$ as a solvent for chemical synthesis [5, 6] is environmentally friendly, inexpensive, and allows rapid separation of the dissolved solute, providing a high diffusivity that is suited to the synthesis of Cu-NPs using microemulsions [7]. Pileni *et al.* [8] synthesized Cu-NPs of varied shapes by using microemulsions as microreactors and protecting shells, while others reported the synthesis of silver and copper nanoparticles, using $ScCO_2$ microemulsions [9]. Chen and Sommers [10] described the preparation of Cu-NPs protected by alkanethiolate monolayers in a one-phase system using superhydride as the reducing reagent, although the process required the use of a high-pressure cell (ca. 200 atm)—a drawback when using supercritical fluids. The use of a supercritical ethane solution [4] or $scCO_2$ also tends to cause problems when separating and removing the solvent from the products.

Soluble polymers or surfactants have also been used as capping agents to prepare Cu-NPs in aqueous solutions, although few studies have been reported due to the ease with which the Cu is oxidized. Lisiecki *et al.* [11] produced Cu-NPs in an aqueous solution of anionic surfactant of sodium dodecyl sulfate (SDS), while Chen [12] used cetyltrimethylammonium bromide (CTAB) in a glove box to prevent oxidation. When using poly(*N*-vinylpyrrolidone) (PVP) as surfactant, Cu-NPs were obtained by reduction in water or 2-ethoxyethanol [13]. Carbon nanotubes (CNTs) have, in particular, demonstrated some interesting results in the preparation of Cu-NPs. For example, Chen *et al.* [14] used CNTs as a template and H_2 as reducing agent to prepare Cu-NPs. In the absence of a reducing agent, the Cu-NPs were prepared using cupric acetate dispersed in CNT/ethanol, although the thermodynamic process formed CNT/Cu composites [15]. Khanna *et al.* [16] produced phase-pure Cu-NPs by using a mixture of sodium citrate and sodium formaldehyde sulfoxylate (SFS) in $CuCl_2$ solution; however, a similar reaction of hydrazine hydrate (HH) and SFS in polymer afforded only a mixture of Cu_2O and Cu. A further example of the thermodynamic process involved the production of monodispersed Cu-NPs by using the thermal decomposition of a Cu-oleate complex; here, various concentrations of sodium oleate were used to stabilize the Cu-NPs and protect against their oxidation [17]. Mallick *et al.* [18] used *o*-toluidine and cupric sulfate as precursors; during the reaction *o*-toluidine was oxidized and

formed poly(*o*-toluidine), while the cupric sulfate was reduced to form Cu-NPs. A 'green' approach to create CuO nanoparticles was also reported in which a physical mixture – copper acetate monohydrate encapsulated with β-cyclodestrin (β-CD) was subjected to calcinations in a furnace at 500 °C for 1 h [19].

The main advantages of chemical syntheses using reducing agents in the aqueous phase include the production of high concentrations of pure metallic Cu-NPs, and the need for only a regular atmosphere and room temperature. However, the main disadvantages are the broad size distribution of the metal particles produced, and their relatively poor stability. Although, the microemulsion technology has proven to be valuable for controlling the particle size, the amount of soluble copper salt deposited into the cores of a conventional microemulsion is relatively low, and this is not advantageous for bulk manufacture. Hence, a variety of methods involving the above-mentioned technology have been applied in the organic phase to produce Cu-NPs.

2.3.2
Chemical Reduction in Organic Media

When producing Cu-NPs in the organic phase, surfactants were generally used as modifiers not only to produce a stabilizing effect but also to control the particle sizes [20–22]. As an example, Athawale *et al.* [22] used the cationic surfactant CTAB, supposing that a bilayer assembly of CTAB would locate on the surface of the metallic nanorods [23], with the functional head groups of the inner layer bound to the metal surface. This bilayer formation might also serve as a possible source of 'zipping' which, once initiated, can assist in the growth of the nanorods. Song *et al.* [24] later described the use of bis(ethylhexy)hydrogen phosphate (HDEHP) as a phase-transfer agent, where the anion $DEHP^-$ bears a strong resemblance to AOT. The $Cu(DEHP)_2$ was directly reduced by an $NaBH_4$ solution composed of *n*-heptane and small aliquots of absolute alcohol, and the Cu-NPs were produced. As with a surfactant, the intention of which is to reduce the surface energy of metal nanoparticles for safer handling and control of agglomeration; precoated metal nanoparticles with an organic layer were used during the process of Cu-NPs synthesis, both to enhance their compatibility with host materials and to avoid oxidation of the copper. Subsequently, Qin and Coulombe [25] prepared organic layer-coated Cu-NPs which had been synthesized by a dual-plasma technology whereby a 6 mm-diameter Cu rod was used as the cathode, while a stainless steel tube (which was concentric with the cathode rod) acted as the grounded anode with an inert gas of argon (Ar) and ethane in the dual-plasma processing reactor. The copper vapor and cool Ar gas flowing upwards in the annular space between the cathode and anode caused a supersaturation of the copper vapor cloud, and this initiated the formation of Cu-NPs. The CNTs were also proven to be a versatile material for synthesizing the Cu-NPs; for example, when using multi-wall carbon nanotubes (MWCNTs) as template, and a copper(I) phenylacetylide/xylene solution as suspension, both Cu_2O and Cu-NPs were obtained on the MWCNTs [26].

In summary, there remains room for improvement when using either aqueous or organic phase chemical reduction for the synthesis of Cu-NPs, due mainly to the complicated procedure, the difficulty in separating Cu-NPs from the solvents, and higher laboratory requirements for reproduction. Consequently, a major effort has been made towards producing Cu-NPs by both physical and mechanical processes in order to simplify the procedure; examples of such modifications include extra-high-power light or constant-frequency ultrasonic vibration, the details of which are provided in the following section.

2.3.3 Photoreduction

Compared to chemical reduction, photoreduction generates more pure Cu^0-NPs. Using gamma radiation from ^{60}Co in the presence of surfactant or polymers and a scavenger, pure Cu-NPs at zero-valent state (Cu^0) could be produced [27]. The success of the reaction lies in the fact that the chief reducing agent is the solvated electron (e_{sol}^-), which has a very negative reducing potential, the reaction being carried out in the absence of oxygen. The e_{sol}^- was generated from 2-propanol $\left[(CH_3)_2CHOH \rightarrow e_{sol}^-, (CH_3)_2CHOH^+\right]$ through various routes [28], and the regeneration of alcohol was rapid, at a reaction rate of $1.5 \times 10^{10}\,dm^3\,mol^{-1}\,s^{-1}$) [29–31]. The Cu-NPs obtained were protected by poly(vinyl alcohol) (PVA) at atmospheric temperature. Among different routes, Cu-NPs have been produced in a N_2O-purged system [32]. Here, an oxygen radical was generated through the reaction of e_{sol}^- with N_2O before an organic radical (OR), such as $^{\bullet}CH_2OH$, $CH_3C^{\bullet}HOH$, and $(CH_3)_2C^{\bullet}OH$ could be generated by the produced oxygen radical reacted with alcohols, and then proceed to Cu reduction by the following representative reactions:

$$Cu^{2+} + OR \rightarrow Cu^{+\bullet} + OR^+, \text{ or, } Cu^{2+} + OR \rightarrow Cu(OR)^{2+} \rightarrow Cu^{+\bullet} + OR(-H) + H^+.$$

$$\text{Similarly, } Cu^{+\bullet} + OR \rightarrow Cu(OR)^+ \rightarrow Cu^o + OR(-H) + H^+.$$

Ultimately, copper nanoparticles are formed from the reaction of $Cu^{+\bullet}$ with Cu^o [$Cu(OR)^{2+}$ and $Cu(OR)^+$ are complex intermediates].

Despite pure Cu production, photoreduction is not free from either the formation of impurities (i.e. Cu and Cu_2O composites) or the agglomeration of Cu-NPs. Polymers or surfactants are required to act as protective agents. It is likely that this radiation-induced synthesis will attract further attention in the future.

2.3.4 Sonochemical Production

The sonochemical method has gained increasing attention as a useful technology for preparing nanoscale metals [33–35], metal oxides [36–38] and nanocomposites [39]. Excellent surface resonance can be obtained for nanoscale metallic copper

clusters during the reduction of copper(II) hydrazine carboxylate by hydroxyl radical formed from water radicals during ultrasonic irradiation; the process may yield a mixture of metallic copper and cupric oxide (Cu_2O) [40]. The presence of Ar and hydrogen atmospheres may trigger the formation of pure Cu-NPs and facilitate the reduction of Cu^{2+} ions [41]. Similar to the sonochemical approach, a zwitterionic surfactant, cetyltrimethylammonium *p*-toluene sulfonate (CTAPTS) has been used as an interconnected network of threadlike micelles and a template to produce elongated Cu-NPs [42]. Mancier and Leclercq [43, 44] integrated ultrasound with electrochemistry to prepare Cu_2O nanoparticles, using a pulsed sonoelectrochemical apparatus which electrochemically reduced the copper ions.

2.3.5
Machine–Chemical Reduction

In addition to chemical, ultrasonic and irradiative reduction, machine–chemical methods have also been used. The solid-state displacement reaction of $CuC1_2 + 2\,Na = Cu + 2\,NaCl$ could be induced by mechanical milling [45–47]. This approach can be used either in a steady-state manner or via unstable thermal combustion, depending on the enthalpy change and other reaction parameters. Combustion can lead to a significant rise in temperature, resulting in melting and vaporization that is undesirable for the production of ultrafine particles [48, 49]. Because the size of the milling ball is a function of the onset of combustion, insofar as a larger ball size results in an increased collision energy, which favors the occurrence of combustion. Therefore, the reduction in particle size and intimate mixing of the reactants can lower the ignition temperature of combustion and result in more uniformly sized NPs [47–49]. Non-uniformly sized Cu-NPs may be produced by irradiation with a convergent electron beam (CEB) that uses a vapor-phase permethylpolysilane (PMPS) oligomer as a soft template and $(Me_3Si)_4Si$ as the reducing agent to reduce $CuCl_2$ to CuCl particles [50]. This method has also been reported to reduce a solid-phase halide of Mo, W and Cu [51]; here, the soft template (PMPS) is the key factor controlling nanowire growth because it encapsulates a CuCl particle to restrict the outflow of CuCl molecules and guides the growth direction upon CEB irradiation. Although the procedure unavoidably generates Si, it also offers a route to tailor the shape, size and magnetization of metallic nanoparticles using a rich array of liquid crystalline and amphiphilic self-assembled systems. Electrochemical-scanning tunneling microscopy (EC-STM) [52], and laser electrodispersion [53], have also been used to allow fabrication of the stable monodispersive nanoparticles.

2.3.6
Electrochemical Reduction

Compared to physical vapor deposition, electrochemical deposition can be used to produce uniform and homogeneous distributions of Cu-NPs of similar size. Because electrochemical processes involve very few chemicals, they are known as

'green' reductants of electrode in that they are environmentally friendly. Cu-NPs have been prepared by the electroreduction of $CuCl_2$ powder in an ionic liquid of 1-butyl-3-methyl-imidizolium chloride ([BMIM]Cl) and hexafluorophosphate ([BMIM]PF_6) [54]. It was postulated that the electroreduction of a solid insulator compound in contact with a solid electronic conductor and a liquid electrolyte should take place at the conductor/insulator/electrolyte three-phase interlines (3PIs) [55]. The three phases consist of a solid metal phase (SMP), a solid compound phase (SCP), and a liquid electrolyte (LEP) [56–59]. The deposition of Cu onto a boron-doped diamond electrode has been reported, whereby the denser the deposit the larger nanoparticle composite generated [60].

A new photo-irradiation procedure has been reported by Zen *et al.* [61–64] demonstrating that the size of copper particles on screen-printed carbon electrodes can be controlled by the density of the xenon light during amperometric depositing process (Figure 2.2). Strong light-irradiation can attenuate the Cu-NPs (~100 nm)

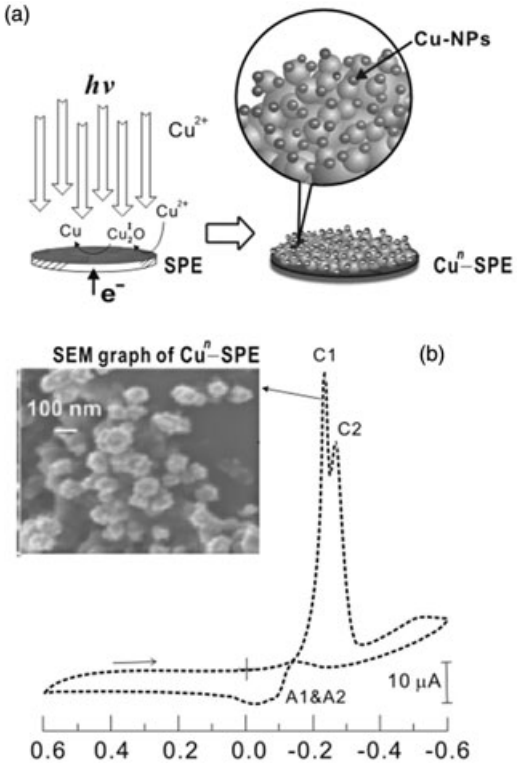

Figure 2.2 (a) Conceptual representation of the plating method for the Cu^n-SPE prepared with 49 klux light illumination; (b) Typical cyclic voltammogram (in pH 8 phosphate-buffered saline) of Cu^n-SPE. The inset shows a scanning electron microscopy (SEM) image of the Cu^n-SPE morphology. Reduction peaks at ~−0.2V(C1, $Cu_2O \rightarrow Cu_2{}^{I}O$) and ~−0.25V(C2, $Cu_2{}^{I}O \rightarrow Cu^0$) with an anodic shoulder at $E_{½} = -0.07$ V vs. Ag/AgCl (A1 & A2) were observed.

with smaller particles on the outer surface to further increase the surface area on electrode. The oxidation states of Cu can be controlled by the reductive potential such that a cupric copper oxide semiconductor could be easily formed to ameliorate the outgrowth of copper oxides during the synthesis of Cu-NPs [65]. This approach offers a new direction to Cu-NP development, without expensive apparatus and complicated procedures.

The modification and functionalization of metal electrodes with self-assembled thiol adlayers [66, 67] opens up many possibilities for electrochemical applications. At present, this very active field is centered on the studies of the electrochemical properties of self-assembled monolayers (SAMs) [68, 69]. In short, electrochemical deposition represents a promising technique for the preparation of Cu-NPs due to its ease of use, low cost, environmental friendliness and convenience of manufacture. In particular, the high sensitivity and low cost of the SPEs when using Cu-NPs should lead to their widespread use in a variety of scientific and medical fields, including medical diagnostics.

2.4 Applications of Cu-NPs in Medical Diagnosis

2.4.1 Medical Imaging

2.4.1.1 Magnetic Resonance Imaging

Nanocontrast agents have great potential in magnetic resonance imaging (MRI) for clinical diagnosis. Nanoparticle-based molecular imaging has set a unique platform for targeted diagnostic studies, cellular tracking and image-monitored therapy [70–73]. Previously, Au_3Cu_1 (gold and copper) nanoshells have been synthesized and demonstrated a promising enhancement of MR signals when used as contrast agents [74]. The anomalously high oxidation state of copper in Au_3Cu_1 hollow nanostructures highlights the first bimetallic MR contrast agents. The Au_3Cu_1 nanocontrast agent can enhance the contrast of blood vessels, and so holds great potential for use in MR angiography. The fabricated porous Au_3Cu_1 hollow nanostructures have an average diameter of 48.9 nm [75]; when the Cu-NPs had been synthesized in 2-propanol by laser ablation, $HAuCl_4$ (dehydrated) was added to the Cu colloidal solution to yield Au_3Cu_1 nanoshells at room temperature. Because of their higher surface area relative to their solid counterparticles, porous Au_3Cu_1 nanoshells with hollow interiors provide a greater number of inner-sphere water molecules that may be subject to high accessibility and interaction between the water molecules and the Au_3Cu_1. Currently, porous Au_3Cu_1 nanoshells may be used as nanocapsules to carry biomolecules for cell targeting and controlled drug release. Both the nanocapsules and nanoshells were biocompatible *in vitro* at dosages between 0.1 ng ml^{-1} and 10 μg ml^{-1}. In theory, an effective MR contrast agent must have a strong effect either to accelerate the spin–lattice relaxation (T_1), which produces bright or positive contrast images, or to shorten the spin–spin

relaxation (T_2), which produces dark or negative-contrast images. Au_3Cu_1 nanocapsules were shown to brightly illuminate the cardiac region and blood vessels of the liver, with the signal level being increased for a 2 h period after injection and persisting for a total of 4 h. The Au_3Cu_1 nanocapsules enhanced the signal contrast not only for T_1-weighted imaging but also for T_2- weighted imaging, at lower doses. The increased brightness of T_2-weighted MR images also contributed to the potential development of this agent for MR angiography. Moreover, Cu-NPs with a diameter of 23.5 nm proved to be only moderately toxic [76].

2.4.1.2 Positron Emission Tomography (*PET*)

Cu-containing NPs have also been developed as efficient imaging agents. For example, dextranated and diethylene triamine penta-acetic acid (DTPA)-modified magnetofluorescent 20 nm-diameter NPs, when labeled with the tracer ^{64}Cu (10 mCi mg^{-1} NPs), yielded an imaging agent that could be used for PET and magnetic resonance, and was also optically detectable. This novel agent accumulated predominantly in macrophages, thus highlighting the ability of this novel trimodal NP for the direct detection of such cells in atherosclerotic plaques. The advantages of these NPs include: an improved sensitivity; a direct correlation of the PET signal with an established biomarker (CD68); an ability to readily quantify the PET signal, to perform whole-body vascular surveys, and to spatially localize and follow the tri-reporter by using microscopy; and to allow 'clinical translatability' of the agent, given similarities to MRI probes in clinical trials [77]. In addition to macrophages, NPs targeting the intercellular adhesion molecule 1 (ICAM-1) also show promise for the delivery of therapeutics to the pulmonary endothelium in patients with acute and chronic respiratory diseases. The use of ^{64}Cu-labeled polymer NPs, coupled to PET, was successfully demonstrated as a noninvasive method for imaging the lung uptake and distribution of NPs coated with an anti-ICAM antibody. A potential was also demonstrated for the preclinical screening of new NP drug delivery agents targeted at the lung endothelium and other tissues [78].

2.4.2 Diagnosis of Metabolic Disorders

2.4.2.1 Glucose

The development of inexpensive and simple – yet sensitive – glucose biosensors is of ongoing interest. To date, the detection of H_2O_2 with oxygen as a mediator for the enzyme glucose oxidase (GOD) remains the most effective approach for glucose determination [79–81]. The H_2O_2 detection can be carried out on Pt, Pd, Rh and some alloy electrodes [82–85], or accompanied with horseradish peroxidase (HRP) and redox mediators [86–89]. Although these metal electrodes are relatively stable and easy to prepare as disposable SPEs, their main drawbacks are the high cost of the noble metal materials and significant interference at the relatively higher detection potential (i.e. 0.5 V versus Ag/AgCl). Recently, Zen's group demonstrated a simple and inexpensive H_2O_2 detection scheme based on a

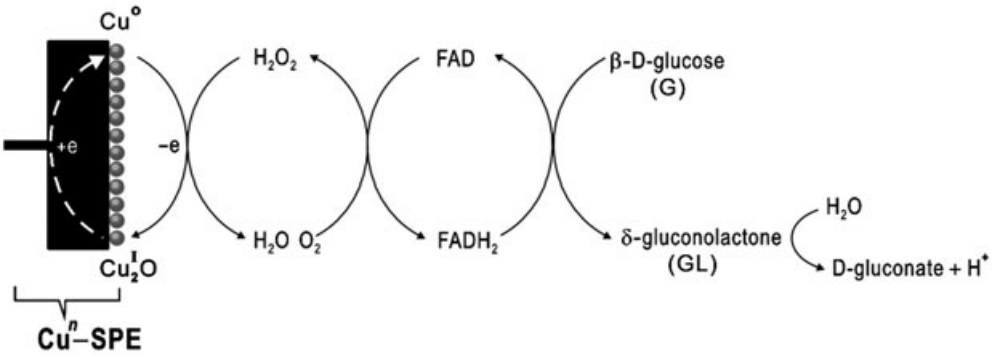

Figure 2.3 Schematic representation of the transducing biosensor signals on the Cu^{n}-SPE–glucose oxidase (GOD).

nanocopper-plated SPE ($Cu^{n}SPE$) [90]. As the electrocatalytic process proceeds at an electrode potential of −0.05 V, it is possible to eliminate the discharge of interfering species which cause erratic currents. The $Cu^{n}SPE$ provides a suitable catalytic surface for the amperometric detection of H_2O_2. In this process, GOD is immobilized on top of the $Cu^{n}SPE$ to form a 'glucose sensor'. Since the $Cu^{n}SPE$ with variable oxides such as $Cu^{II}O$ and $Cu^{I}_{2}O$ apparently has a strong interaction with GOD (Figure 2.3), nanocopper-based screen-printed biosensors for glucose determination have been shown to perform well against other metal-type glucose sensors. The system employed low potentials in order to avoid interferences, while the sensitivity was shown to be better than that of some Pt-based systems. The continuous and accurate monitoring of urinary and blood glucose levels represents by far the universal strategy for the early diagnosis of diabetes and related metabolic disorders; moreover, it is also a useful method for monitoring the prognosis of diabetic outpatients and evaluating their treatment.

2.4.2.2 **Organic Acids**

In recent years, electrochemical (EC) detection, which is typically operated in amperometric mode, has gained increasing popularity for the monitoring of underivatized sugars, sugar acids, alditols and uronic acids [91–96]. One major shortcoming of amperometric detection when using noble metal electrodes (i.e. Pt and Au) for a constant applied potential has been the loss of activity during the anodic detection of organic substances. Pulsed amperometric detection based on a multistep waveform could overcome the problem of lost activity on noble metals by alternating cathodic and anodic polarizations to clean and reactivate the electrode surface [96–98]. However, the slow dissolution of metal particles – and hence higher background noise levels – can occur during applications of the multistep waveforms. Cu-based working electrodes have shown that various electroactive organic molecules can be determined with good sensitivity and reproducibility at a constant applied potential in liquid chromatography (LC) detection schemes [92–95]. In particular, a copper oxide hydroxide film was anodically electrodepos-

ited onto a glassy carbon (GC) substrate from alkaline solutions containing cuprous cyanide ions [99]. The Cu–GC modified electrode showed a powerful catalytic activity towards the electro-oxidation of alditols, carbohydrates, amines and amino acids, and also served as an amperometric sensor in the detection of organic acids. In humans, the latter constitute one of the major families of urinary metabolites, and their clinical profiling can be very important because they are involved in many biochemical, physiological or pathological processes. The analysis of human urinary organic acids and metabolites is important in the diagnosis of 'inborn errors of metabolism' [100–105]. For example, an excess of uric acid (UA) in the urine is considered a key factor in the development of renal calculi (stones), while elevated levels of creatinine in the serum and urine are recognized as a sensitive and specific index for evaluating the glomerular filtration rate and, in general, for assessing renal, thyroid and muscular functions [104]. The presence of oxalic acid (OA) and citric acids in the urine are also indicators of various disorders, the most well-known being the formation of renal stones [101]. An abnormally high urinary level of cystine has been found in patients with urea cycle defects [103]. Difference in the profiles and concentrations of human urinary metabolites between unhealthy and healthy individuals may reveal possible clinical indications in the diagnosis of disorders associated with the metabolism of these materials. By using a disposable Cu^n-SPE, the presence of urinary organic acids and metabolites could be easily detected and quantitated, without any need for extensive clean-up and derivatization processes. The complexation mechanism at a copper electrode in a neutral medium has also been used to determine the presence of amino acids and amino alcohols [106, 107]. Because of the insoluble behavior of copper ions in phosphate, the Cu^n-SPE was found to be stable and free from electrode fouling and could thus be used in a simple, constant-potential amperometric detection form.

When developing a rational and effective approach to prevention and/or treat urolithiasis and its reoccurrence, it is important not only to recognize the types of urolith that might form, but also to create a favorable microenvironment to prevent such formation. In this respect, the disposable Cu^n-SPE proved to be valuable for determining the major urolithic organic acids. High concentrations of some organic acids (of which the major uroliths consist) represent an important predisposing factor for urolith formation [108] and, indeed, excessive urinary UA and OA are known to closely correlate with urolithiasis [109]. A comparison of urinary creatinine, cystine, UA, OA and citric acid levels in normal and urolithic humans revealed important differences that might be used in the early diagnosis of urolithiasis. Moreover, the simplicity and reproducibility of the Cu^nSPE allows routine urinalyses to be performed in order to diagnose urolithiasis and other clinical conditions related to the excess secretion of organic acids (unpublished data).

2.4.2.3 **Amino Acids**

Baldwin and coworkers reported strong complexing properties of certain amino acids such as tyrosine, tryptophan, methionine and cysteine with copper ions, due

to the chelating properties of the N-terminal group [110]. Based on these reported properties, a high-performance liquid chromatography (HPLC) method with electrochemical detection using Cu^n-SPE was developed to differentiate between food meat species of animal origin. Under appropriate chromatographic conditions, and with the simultaneous use of a Cu^n-SPE, reliable detection is feasible without sample pretreatment [111]. In this way 20 essential amino acids could each be detected and resolved in slightly modified similar mobile phases, and therefore HPLC-EC detection was seen to represent a very attractive analytical scheme to detect electroactive peptides/amino acids as a basis for species differentiation. This method also provides a suitable EC application to supplement current methods for the differentiation of meat species, and provides a possible basis for the monitoring of degradative changes in meat-derived proteins. A two-step electrochemical mechanism has been proposed for amino acid interactions with the Cu^n electrodes (Figure 2.4). Normally, amino acids possess a bidentate ligand, where the $–COO^–$ and -N termini function as the chelating site. The two-step process for the Cu^{II}(metal ion)–amino acid complexation could be represented as: $Cu^{II} + A^– = CuA^+$ (step 1) + $A^– = CuA_2$, where A denotes an α-amino acid. On the Cu^n-SPE surface, in step 1, the bidentate amino acid ligand is first chelated with Cu^n, followed by a reversible reduction of $Cu^{II}O \rightarrow Cu_2^{I}O$. As soon as the reduced $Cu_2^{I}O$ is regenerated back to $Cu^{II}O$, the same cycle can be repeated. The reaction mechanism implies a weak

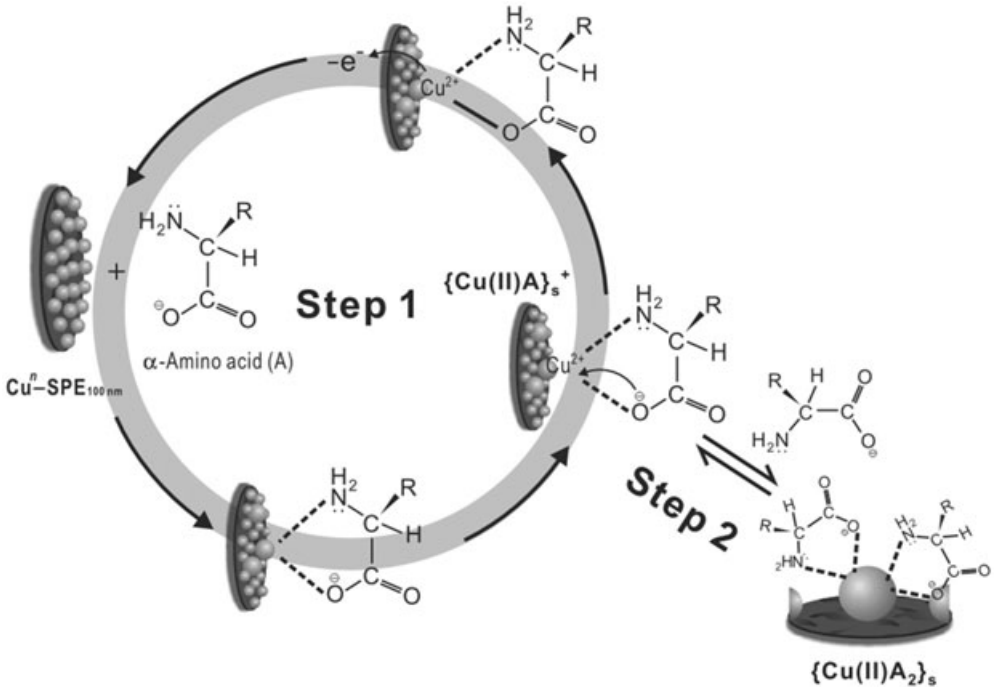

Figure 2.4 Reaction mechanism of copper(II)–amino acid complexation at the Cu^n-SPE.

adsorption of the amino acid onto the Cu^n during the complexation process, where the $Cu^{II}O$ is electrogenerated on the surface. The adsorbed amino acid can be easily desorbed as the $Cu^{II}O$ layer is reduced to $Cu_2^{I}O$. The rate of adsorption/desorption will significantly determine the reaction rate and resultant EC signal. The geometric structure of the chelation on Cu^n is also essential as $Cu^{II}O$ is less free on the electrode surface than the Cu^{II} metal ion in aqueous solution. Based on these mechanisms, the free amino acids would be more steadily accessible to the $Cu^{II}O$ reaction site than would peptides and proteins; and the density of functional $–COO^-$ and –N termini, size and geometric folding of which could sterically hinder the $Cu^{II}A_2$ structure at the Cu^nSPE surface. Although not related directly to any medical diagnosis, this application may prove to be valuable in the diagnosis of congenital amino acid-associated disorders of tyrosine and phenylalanine metabolism.

2.4.2.4 Urate and Uric Acid

Urate has a long history in clinical analysis, and has served as an important diagnostic marker in several contexts. Today's increasing interest in 'metabolic syndrome' has led to urate being used in combination with other biomarkers to assess cardiovascular risk. Although commonly regarded as an indicator of gout [112], urate has also been identified as a versatile 'handle' via which the progress of cardiovascular [113–117], kidney diseases [118–120] and various diabetic complications can be gauged [121–123]. It might be anticipated that an analysis of UA, when combined with other key biomarkers, would allow a more rounded evaluation of physiological well-being. A key example would be the combined analysis of glucose and urate, where the latter could provide an indication of the early onset of potential cardiovascular complications common to diabetes [121–123]. Uric acid arises within physiological fluids as a result of various biochemical processes that involve the production/consumption of nucleic acids. Substantially increased UA levels have been recognized as symptomatic of several diseases, the most prominent being cardiovascular [112–117], renal [118–120], arthritis [124, 125], stroke [123, 126, 127] and pre-eclamptic conditions [128–130]. Running simultaneous detections of UA along with other analytes (typically creatinine, glucose and cholesterol) enhances the diagnostic picture through which the clinician can view potential causes and treatments [131]. The Cu^n electrode is no doubt well positioned as one of the most economical and sensitive means of detecting UA, and may well be the best candidate for a system in the routine diagnosis of the above-mentioned disorders.

2.4.3 Other Medical Applications

2.4.3.1 Drug Delivery and Therapy

Nanotechnology provides a variety of nanoscale tools for medicine (nanomedicine), with one such revolutionary field being that of drug delivery. Nanocarriers for drugs have the potential to enhance therapeutic efficacy because they can be

engineered not only to modulate both the release and stability of a drug but also to prolong its circulation time and protect it against elimination by phagocytic cells or premature degradation. Nanoscale carriers can also be tailored to accumulate in tumor cells and tissues, due to an enhanced permeability and a retention effect, or by active targeting using ligands designed to recognize tumor-associated antigens. In future, synthetic materials that function as DNA-delivery systems for mammalian cells are expected to play critical roles in gene therapy. Several such new materials have been developed, including porous silica nanoparticles [132] and gold nanoparticles [133]. A new class of metal-mediated supramolecular materials using Cu can deliver large fragments of DNA into eukaryotic cells [134]. Here, the molecular design comprises the formation of amphiphilic Cu^{II} complexes that self-assemble into metalloliposomes in water and condense DNA plasmids into deliverable structures programmed to react with intracellular components via redox- and ligand-exchanged reactions. The metalloliposomes, which form bis-complexes with Cu^{II} ions, have the chemical formula $[Cu^{II}(Ldt)_2](OTf)_2$ and $[Cu^{II}(Lot)_2](OTf)_2$, where Ldt = 1-dodecyl-1,4,7-trazacyclononane, Lot = 1-ocatadecul-1,4,7-triazacuclononane, and OTf = trifluoromethanesulfonate [134]. In contrast, some copper complexes may bind covalently to DNA and thus act as therapeutic agents. Regardless of these successes, there remain areas for the development of new, metal-based anticancer drugs with curative potential and minimal side effects, with their design depending on the ligand framework, the choice of metal ion, and its oxidation state. Copper has long been used in metal-based therapies [135], and its complexes are the preferred molecules for cancer inhibition [136]. Copper has also been shown to accumulate in tumors due to the selective permeability of cancer cell membranes to copper compounds. Several copper complexes have been screened for anticancer activity, and some have been found to be active both *in vitro* and *in vivo* [137, 138]. A novel Cu^{II} complex containing L-tryptophan as chiral auxiliary shows *in vitro* antitumor activity in human neuroblastoma cells [139]. These trinuclear complexes, $C_{23}H_{31}N_6O_6CuSn_2Cl_5$ and $C_{23}H_{31}N_6O_6CuZr_2Cl_5$, both show strong binding with DNA and have proved to have good cancer therapeutic properties.

2.4.3.2 **Antibacterial Activity**

Today, there is a considerable interest in the pharmacology of heterocyclic ligands and their metal chelates [140, 141], mainly because these nitrogen- and sulfur-containing organic compounds and their metal complexes display a wide range of biological activities. For example, copper complexes have been used widely in metal-mediated DNA cleavage for the generation of activated oxygen species [142, 143], while tetra-aza macrocyclic copper complexes have shown anti-HIV activities. The antibacterial activity of Cu has long been recognized, notably because it is very effective and, most importantly, has a low toxicity. Although very few reports have been made of the antibacterial properties of Cu-NPs [75], Cu-SiO_2 showed activities against *Staphylococcus aureus, Enterobacter cloacae, Penicillium citrinum, Candida albicans* and *Escherichia coli*. It was also active against other fungi and yeasts, but notably less so than against Gram-negative bacteria. In the case of the Cu-SiO_2

nanocomposite the antibacterial activity against Gram-negative bacteria is superior to that against Gram-positive bacteria. The $[C_{20}H_{22}N_8S_2Cu]Cl_2$ ionic complexes were seen to possess a square–planar geometry, while the Cu^{II} complex in aqueous solution exhibited a quasi-reversible redox wave corresponding to a Cu^{II}/Cu^{I} redox couple; this was indicative of a DNA binding ability and corresponding antibacterial and antifungal effects [144]. Although the antimicrobial ability was reported as a biological phenomenon rather than a diagnostic application, the multiple antimicrobial effects of Cu-complexes are unique and worth further exploration. Clearly, the flexibility and versatility of newly designed Cu-complexes should result in more developments in medical science, and possibly also in diagnostic medicine.

2.5 Conclusions

Nanomaterials have unique physico-chemical properties such as an ultra small size, a large surface area-to-mass ratio, minimal diffusional limitations and high reactivity, all of which may differ widely from the properties of micro- or macro-sized materials with the same composition. Over the past decade, the ability to prepare well-defined nanomaterials has led to nanomedicine emerging as an area of great excitement, notably because the nanoscale-related properties can be used to overcome certain limitations associated with traditional therapeutic and medical applications. As a result, NP systems have become the promising new paradigm in pharmacotherapy and, indeed, are today being used in gene therapy, novel drug discovery, drug delivery, imaging technology and related clinical studies. Unlike conventional noble metals such as Au and Pt, Cu-NPs can be easily oxidized to form copper oxides (including CuO and Cu_2O; see Figure 2.5), a characteristic which in fact may have hindered the early development of Cu-NPs among certain scientific disciplines. Nevertheless, there has been increasing interest in Cu-NPs not only because of their optical, catalytic, mechanical and electrical properties, but also because of their low cost and excellent availability, and this has resulted in a wide range of applications in the fields of metallurgy, catalysis, optoelectronics and sensors. With regards to the medical sciences, and in comparison to other noble metals, the application of Cu-NPs is still in its infancy, especially in the area of diagnosis. To date, other than some success in preclinical medical imaging systems using Cu-NPs as contrast agents for MRI or PET scanning, the available information pertaining to the use of Cu nanomaterials in medical or disease diagnosis is very limited. Nevertheless, some exciting developments with Cu^n-SPEs have been reported, and have highlighted the potential use of Cu^n as biosensors for detecting early changes in biological metabolites/elements that carry significant implications in disease states. The active interactions between Cu-NP and various pathogens have extended the use of Cu nanomaterials as possible tools for the detection and diagnosis of infectious diseases. Some medical applications of Cu-nanomaterials are summarized in Table 2.1.

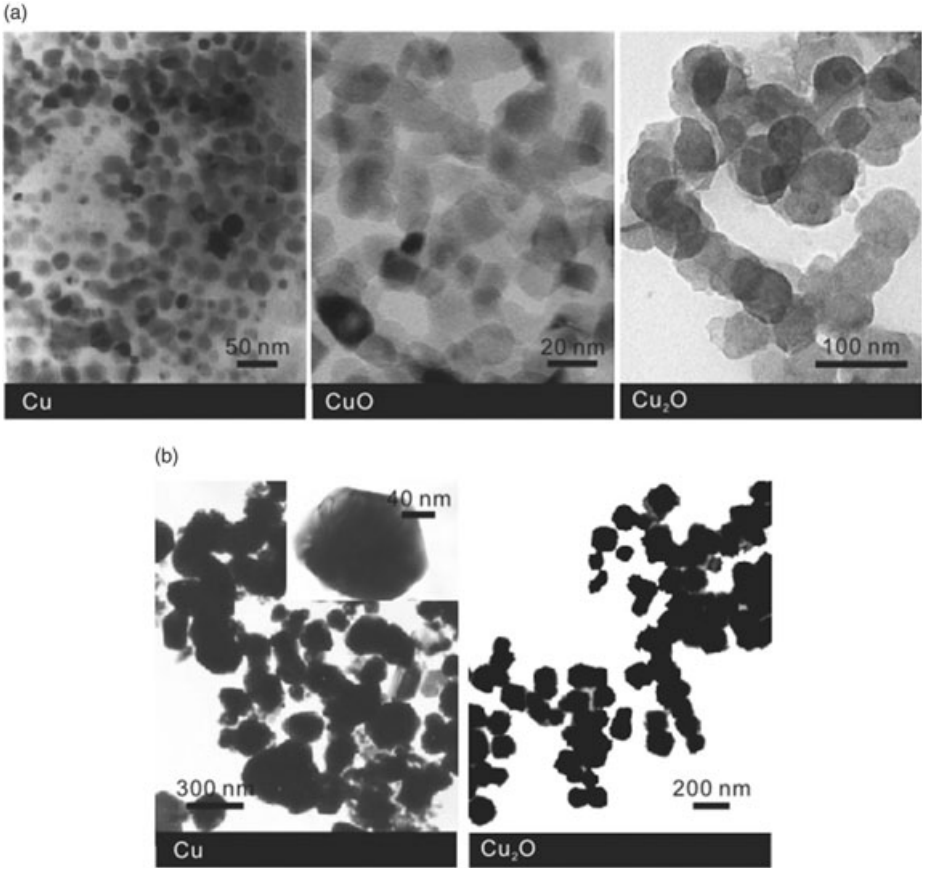

Figure 2.5 Transmission electron microscopy (TEM) images of Cu, CuO and Cu_2O nanoparticles. (a) Spherical copper nanoparticles; (b) Irregular, sharp copper nanoparticles. Reproduced with permission from corresponding publishers. (a) Left to right: (Cu): S. Kapoor, T. Mukherjee, Photochemical formation of copper nanoparticles in poly(*N*-vinylpyrrolidone). *Chemical Physics Letters* **2003**, *370*, 83–7. (CuO): T. Premkumar, Kurt E. Geckeler, A green approach to fabricate CuO nanoparticles, *Journal of Physics and Chemistry of Solids* **2006**, *67*, 1451–6. (Cu_2O): H. Yang, J. Ouyang, A. Tang, Y. Xiao, X. Li, X. Dong, Y. Yu, Electrochemical synthesis and photocatalytic property of cuprous oxide nanoparticles, *Materials Research Bulletin* **2006**, *41*, 1310–18. (b) Left to right: (Cu): N. A. Dhas, C. P. Raj, A. Gedanken, Synthesis, characterization, and properties of metallic copper nanoparticles, *Chemistry of Materials* **1998**, *10*, 1446–52. (Cu_2O): H. Zhang, Z. Cui, Solution-phase synthesis of smaller cuprous oxide nanocubes, *Materials Research Bulletin* **2008**, *43*, 1583–9.

Table 2.1 Summary of medical applications of Cu-nanomaterials.

Application		Type of Cu	Target analyte/tissue	Size (nm)	Reference(s)
Imaging	MRI	Au_3Cu_1	Angiography	49	[70–76]
	PET-CT	^{64}Cu	Macrophage, atherosclerosisICAM-1/pulmonary endothelium	20 NA	[77] [78]
Metabolic disorders	Glucose	Cu-GOD	H_2O_2	100–200	[90]
	Organic acid	Cu-SPE	Uric acid, oxalic acid, creatinine, citric acid/urine, urolith	100–200	[99, 106, 107]
	Amino acid	Cu-SPE	α-Amino acid/muscle	100	[110, 111]
	Uric acid	Cu-SPE	Urate/cardiovascular, kidney	100	[106, 107]
Drug delivery and therapy		Cu-complexes	DNA delivery/eukaryotic cell DNA/tumor cell	400	[134] [136, 139]
Antimicrobial activity		Cu-complexes	DNA/bacteria, fungus	NA	[75, 144]

GOD = glucose oxidase; NA = data not available; SPE = screen-printed electrode.

In conclusion, on the basis of the expanding spectrum of detectable biological elements outlined in this chapter, it is reasonable to expect that Cu-NPs will soon achieve more widespread success in their applications in medical diagnosis.

References

1 Alivisators, A.P. (1996) Perspectives on the physical chemistry of semiconductor nanocrystals. *Journal of Physical Chemistry*, **100**, 13226–39.

2 Zen, J.M., Senthil Kumar, A. and Tsai, D.M. (2003) Recent updates of chemically modified electrodes in analytical chemistry. *Electroanalysis*, **15**(13), 1073–87.

3 Lisiecki, I. and Pileni, M.P. (1993) Synthesis of copper metallic clusters using reverse micelles as microreactors. *Journal of the American Chemical Society*, **115**(10), 3887–96.

4 Carson, J.P., Khambaswadkar, K. and Robert, C.B. (2000) Supercritical fluid and compressed solvent effects on metallic nanoparticle synthesis in reverse

micelles. *Industrial and Engineering Chemistry Research*, **39**(12), 4749–55.
5 Wai, C.M., Hunt, F., Ji, M. and Chen, X. (1998) Chemical reactions in supercritical carbon dioxide. *Journal of Chemical Education*, **75**, 1641–5.
6 Savage, P.E., Gopalan, S., Mizan, T.I., Martino, C.J. and Brock, E.E. (1995) Reactions at supercritical conditions: applications and fundamentals. *AICHE Journal*, **41**, 1723–78.
7 Ohde, H., Hunt, F. and Wai, C.M. (2001) Synthesis of silver and copper nanoparticles in a water-in-supercritical-carbon dioxide microemulsion. *Chemistry of Materials*, **13**, 4130–5.
8 Pileni, M.P., Gulik-Lrzywicki Tanori, T., Filankembo, A. and Dedieu, J.C. (1998) Template design of microreactors with colloidal assemblies: control the growth of copper metal rods. *Langmuir*, **14**, 7359–63.
9 Welch, C.M., Simm, A.O. and Compton, R.G. (2006) Oxidation of electrodeposited copper on boron doped diamond in acidic solution: manipulating the size of copper nanoparticles using voltammetry. *Electroanalysis*, **18**, 965–80.
10 Chen, S. and Sommers, J.M. (2001) Alkanethiolate-protected copper nanoparticles: spectroscopy, electrochemistry, and solid-state morphological evolution. *Journal of Physical Chemistry B*, **105**, 8816–20.
11 Lisiecki, I., Billoudet, F. and Pileni, M.P. (1996) Control of the shape and the size of copper metallic particles. *Journal of Physical Chemistry*, **100**, 4160–6.
12 Chen, D.H. and Wu, S.H. (2004) Synthesis of high-concentration Cu nanoparticles in aqueous CTAB solutions. *Journal of Colloid and Interface Science*, **273**, 165–9.
13 Huang, H.H., Yan, F.Q., Kek, Y.M., Chew, C.H., Xu, G.Q., Ji, W., Oh, P.S. and Tang, S.H. (1997) Synthesis characterization, and nonlinear optical properties of copper nanoparticles. *Langmuir*, **13**, 172–5.
14 Chen, P., Wu, X., Lin, J. and Tan, J. (1999) Synthesis of Cu nanoparticles and microsized fibers by using carbon nanotubes as a template. *Journal of Physical Chemistry B*, **103**, 4559–61.
15 Wang, P., Huang, B., Wei, J., Qin, X., Yao, S. and Zhang, Q. (2007) Preparation of Cu nanoparticles on carbon nanotubes by solution infusion method and calcining in ambient atmosphere, Synthesis and characterization of copper nanoparticles. *Material Letters*, **61**, 5255–7.
16 Khanna, P.K., Gaikwad, S., Adhyapak, P.V., Singh, N. and Marimuthu, R. (2007) *Material Letters*, **61**, 4711–14.
17 Kima, Y.H., Lee, D.K., Jo, B.G., Jeong, J.H. and Kanga, Y.S. (2006) Synthesis of oleate capped Cu nanoparticles by thermal decomposition. *Colloids and Surfaces A – Physicochemical and Engineering Aspects*, **364**, 284–5.
18 Mallick, K., Witcomb, M.J. and Scurrell, M.S. (2006) In situ synthesis of copper nanoparticles and poly(*o*-toluidine): a metal–polymer composite material. *European Polymer Journal*, **42**, 670–5.
19 Premkumar, T. and Geckeler, K.E. (2006) A green approach to fabricate CuO nanoparticles. *Journal of Physical Chemistry – Solids*, **67**, 1451–6.
20 Zhang, X., Yin, H., Cheng, X., Hu, H., Yua, Q. and Wang, A. (2006) Effects of various polyoxyethylene sorbitan monooils (Tweens) and sodium dodecyl sulfate on reflux synthesis of copper nanoparticles. *Materials Research Bulletin*, **41**, 2041–8.
21 Chena, L., Zhang, D., Chena, J., Zhoua, H. and Wan, H. (2006) The use of CTAB to control the size of copper nanoparticles and the concentration of alkylthiols on their surfaces. *Materials Science and Engineering A*, **415**, 156–61.
22 Athawale, A.A., Katre, P.P., Kumar, M. and Majumdar, M.B. (2005) Synthesis of CTAB–IPA reduced copper nanoparticles. *Materials Chemistry and Physics*, **91**, 507–12.
23 Busbee, B.D., Obare, S.O. and Murphy, C.J. (2003) An improved synthesis of high-aspect-ratio gold nanorods. *Advanced Materials*, **15**, 414–16.
24 Song, X., Sun, S., Zhang, W. and Yin, Z. (2004) A method for the synthesis of spherical copper nanoparticles in the organic phase. *Journal of Colloid and Interface Science*, **273**, 463–79.

25 Qin, C. and Coulombe, S. (2006) Synthesis of organic layer-coated copper nanoparticles in a dual-plasma process. *Materials Letters*, **60**, 1973–6.

26 Martínez-Ruiz, A. and Alonso-Nuñez, G. (2008) New synthesis of Cu_2O and Cu nanoparticles on multi-wall carbon nanotubes. *Materials Research Bulletin*, **43**, 1492–6.

27 Jushi, S.S., Pat, S.F., Iyer, V. and Mahumuni, S. (1998) Radiation-induced synthesis and characterization of copper nanoparticles. *NanoStructured Materials*, **10**(7), 1135–44.

28 Day, G.R. (2005) Reduction of the copper ion to its metal and clusters in alcoholic media: a radiation chemical study. *Radiation Physics and Chemistry*, **74**, 172–6.

29 Fowles, P. (1971) Pulse radiolytic induced transient electrical conductance in liquid solutions. Part 4. The radiolysis of methanol, ethanol, 1-propanol and 2-propanol. *Transactions of the Faraday Society*, **67**, 428–39.

30 Tabata, Y., Ito, Y. and Tagawa, S. (1991) *Handbook of Radiation Chemistry*, CRC Press, Boca Raton, FL, p. 419.

31 Taub, I.A., Harter, D.A., Jr, Sauer, M.C. and Dorfman, L.M. (1964) Pulse radiolysis studies IV. The solvated electron in the aliphatic alcohols. *Journal of Physical Chemistry*, **41**, 979–85.

32 Buxton, G.V., Greenstock, C.L., Helman, W.P. and Ross, A.B. (1988) Critical review of rate constants for reactions of hydrated electrons, hydrogen atoms and hydroxyl radicals (OH/O^-) in aqueous solution. Chemical kinetic data base for combustion chemistry. Part 3: Propane. *Journal of Physical Chemistry Reference Data*, **17**, 513–882.

33 Suslick, K.S., Choe, S.B., Cichowlas, A.A. and Grinstaff, M.W. (1991) Sonochemical synthesis of amorphous iron. *Nature*, **353**, 414–17.

34 Koltypin, Y., Katabi, G., Prozorov, R. and Gedanken, A. (1996) Sonochemical preparation of amorphous nickel. *Journal of Non-Crystalline Solids*, **201**, 159–62.

35 Dhas, N.A., Cohen, H. and Gedanken, A. (1997) In situ preparation of amorphous carbon-activated palladium nanoparticles. *Journal of Physical Chemistry B*, **101**, 6834–8.

36 Mulvaney, P., Cooper, M., Grieser, F. and Meisel, D. (1990) Kinetics of reductive dissolution of colloidal manganese dioxide. *Journal of Physical Chemistry*, **94**, 8339–45.

37 Dhas, N.A. and Gedanken, A. (1997) Characterization of sonochemically prepared unsupported and silica-supported nanostructured pentavalent molybdenum oxide. *Journal of Physical Chemistry B*, **101**, 9495–503.

38 Dhas, N.A., Koltypin, Y. and Gedanken, A. (1997) Sonochemical preparation and characterization of ultrafine chromium oxide and manganese oxide powders. *Chemistry of Materials*, **9**, 3159–63.

39 Dhas, N.A. and Gedanken, A. (1997) Sonochemical synthesis of molybdenum oxide- and molybdenum carbide-silica nanocomposites. *Chemistry of Materials*, **9**, 3144–9.

40 Dhas, N.A., Raj, C.P. and Gedanken, A. (1998) Synthesis, characterization, and properties of metallic copper nanoparticles. *Chemistry of Materials*, **10**, 1446–52.

41 Suslick, K.S. (1988) *Ultrasounds: Its Chemical, Physical and Biological Effects*, Wiley-VCH Verlag GmbH, Weinheim.

42 Salkar, R.A., Jeevanandam, P., Kataby, G., Aruna, S.T., Yuri, K., Palchik, O. and Gedanken, A. (2000) Elongated copper nanoparticles coated with a zwitterionic surfactant. *Journal of Physical Chemistry B*, **104**, 893–7.

43 Mancier, V., Daltin, A.L. and Leclercq, D. (2008) Synthesis and characterization of copper oxide (I) nanoparticles produced by pulsed sonoelectrochemistry. *Ultrasonics Sonochemistry*, **15**, 157–63.

44 Delplancke, J.L., Dille, J., Reisse, J., Long, G.J., Mohan, A. and Grandjean, F. (2000) Magnetic nanopowders: ultrasound-assisted electrochemical preparation and properties. *Chemistry of Materials*, **12**, 946–55.

45 Mahalingam, T., Chitra, J.S.P., Rajendran, S. and Sebastian, P.J. (2002) Potentiostatic deposition and

characterization of Cu_2O thin films. *Semiconductor Science and Technology*, **17**, 565–9.
46 Ding, J., Tsuzuki, T., McCormick, E.G. and Street, R. (1996) Ultrafine Cu particles prepared by mechanochemical process. *Journal of Alloys and Compounds*, **234**, L1–3.
47 Schaffer, G.B. and McCormick, P.G. (1991) Anomalous combustion effects during mechanical alloying. *Metallurgical and Materials Transactions A*, **22**, 3019–24.
48 Yang, H. and McCormick, P.G. (1993) Reduction of tantalum chloride by magnesium during reaction milling. *Journal of Materials Sciences*, **12**, 1088–91.
49 Schaffer, G.B. and McCormick, P.G. (1990) Displacement reactions during mechanical alloying. *Metallurgical and Materials Transactions A*, **21**, 2789–94.
50 Yen, M.Y., Chiu, C.W., Chen, F.R., Kai, J.J., Lee, C.Y., Chiu, H.T. and Electron, C. (2004) Beam induced growth of copper nanostructures: evidence of the importance of a soft template. *Langmuir*, **20**(2), 279–81.
51 Chang, Y.H., Wang, H.W., Chiu, C.W., Cheng, D.S., Yen, M.Y. and Chiu, H.T. (2002) Low-temperature synthesis of transition metal nanoparticles from metal complexes and organopolysilane oligomers. *Chemistry of Materials*, **14**, 4334–8.
52 Wang, K., Niu, L., Zong, Z., Zhang, M., Wang, C. and Shi, X. (2008) Direct electrodeposition of copper ladder structures on a silicon substrate. *Crystallography Growth and Design*, **8**, 442–5.
53 An, S.H., Lim, T.H., Kim, Y.H., Bae, S.E., Yoon, J.H. and Lee, C.W.J. (2008) EC-STM studies on copper electrodeposition at n-Si(1 1 1):H electrodes. *Colloids and Surfaces A – Physicochemical and Engineering Aspects*, **313**, 339–42.
54 Yu, L., Sun, H., He, J., Wang, D., Jin, X., Hu, X. and Chen, G.Z. (2007) Electro-reduction of cuprous chloride powder to copper nanoparticles in an ionic liquid. *Electrochemical Communications*, **9**, 1374–81.
55 Deng, Y., Wang, D., Xiao, W., Jin, X., Hu, X. and Chen, G.Z. (2005) Electrochemistry at conductor/insulator/electrolyte three-phase interlines: a thin layer model. *Journal of Physical Chemistry B*, **109**, 14043–51.
56 Chen, X.J., Khor, K.A. and Chan, S.H. (2004) Electrochemical behavior of $La(Sr)MnO_3$ electrode under cathodic and anodic polarization. *Solid-State Ionics*, **167**, 379–87.
57 Wienecke, M., Bunescu, M.C., Pietrzak, M., Deistung, K. and Fedtke, P. (2003) PTFE membrane electrodes with increased sensitivity for gas sensor applications. *Synthetic Metals*, **138**, 165–71.
58 Wain, A.J., Wadhawan, J.D., France, R.R. and Compton, R.G. (2004) Biphasic redox chemistry of α-tocopherol: evidence for electrochemically induced hydrolysis and dimerization on the surface of and within femtolitre droplets immobilized onto graphite electrodes. *Physical Chemistry Chemical Physics*, **6**, 836.
59 Yamanaka, I., Funakawa, A. and Otsuka, K. (2004) Electrocatalytic synthesis of DMC over the Pd/VGCF membrane anode by gas–liquid–solid phase-boundary electrolysis. *Journal of Catalysis*, **221**, 110–18.
60 Rostovshchikova, T.N., Smirnov, V.V., Kozhevin, V.M., Yavsin, D.A., Zabelin, M.A., Yassievich, I.N. and Gurevich, S.A. (2005) New size effect in the catalysis by interacting copper nanoparticles. *Applied Catalysis A: General*, **296**, 70–9.
61 Zen, J.M., Chung, H.H. and Senthil Kumar, A. (2000) Flow injection analysis of hydrogen peroxide on copper-plated screen-printed carbon electrodes. *Analyst*, **125**(9), 1633–7.
62 Zen, J.M., Chung, H.H. and Senthil Kumar, A. (2001) Flow injection analysis of glucose based on an enzyme reactor coupled with a copper-plated screen-printed carbon electrode. *Analytical Sciences*, **17**, i287–90.
63 Zen, J.M., Chung, H.H. and Senthil Kumar, A. (2002) Selective detection of o-diphenols on copper-plated screen-printed electrodes. *Analytical Chemistry*, **74**(5), 1202–6.

64 Zen, J.M., Hsu, C.T., Senthil Kumar, A., Lyuu, H.J. and Lin, K.Y. (2004) Amino acid analysis using disposable copper nanoparticle plated. *Analyst*, **129**(9), 841–5.

65 Hsu, C.T., Chung, H.H., Senthil Kumar, A. and Zen, J.M. (2005) Novel preparation and photoelectrochemical properties of r-CuI semiconductor nanocrystallites on screen-printed carbon electrodes. *Electroanalysis*, **17**(20), 1822–7.

66 Nuzzo, R.G. and Allara, D.L. (1983) Adsorption of bifunctional organic disulfides on gold surfaces. *Journal of the American Chemical Society*, **105**, 4481–4.

67 Ulman, A. (1996) Formation and structure of self-assembled monolayers. *Chemical Reviews*, **96**, 1533–54.

68 Hayes, W.A. and Shannon, C. (1996) Electrochemistry of surface-confined mixed monolayers of 4-aminothiophenol and thiophenol on Au. *Langmuir*, **12**, 3688–94.

69 Bryant, M.A. and Crooks, R.M. (1993) Determination of surface pKa values of surface-confined molecules derivatized with pH-sensitive pendant groups. *Langmuir*, **9**, 385–7.

70 Winter, P.M., Morawski, A.M., Caruthers, S.D., Fuhrhop, R.W. and Wickline, S.A. (2003) Molecular imaging of angiogenesis in early-stage atherosclerosis with alpha(v)beta3-integrin-targeted nanoparticles. *Circulation*, **108**, 2270–4.

71 Krause, M.H., Kwong, K.K., Gragoudas, E.S. and Young, L.H. (2004) MRI of blood volume with superparamagnetic iron in choroidal melanoma treated with thermotherapy. *Magnetic Resonance Imaging*, **22**, 779–87.

72 Bulte, J.W., Zhang, S., van Gelderen, P., Herynek, V., Jordan, E.K., Duncan, I.D. and Frank, J. (1999) A neurotransplantation of magnetically labeled oligodendrocyte progenitors: magnetic resonance tracking of cell migration and myelination. *Proceedings of the National Academy of Sciences of the United States of America*, **96**, 15256–61.

73 Anderson, S.A., Glod, J., Arbab, A.S., Noel, M., Ashari, P., Fine, H.A. and Frank, J.A. (2005) Noninvasive MR imaging of magnetically labeled stem cells to directly identify neovasculature in a glioma model. *Blood*, **105**, 420–5.

74 Su, C.H., Sheu, H.S., Lin, C.Y., Huang, C.C., Lo, Y.W., Pu, Y.C., Weng, J.C., Shieh, D.B., Chen, J.H. and Yeh, C.S. (2007) Nanoshell magnetic resonance imaging contrast agents. *Journal of the American Chemical Society*, **129**, 2139–46.

75 Hsiao, M.T., Chen, S.F., Shieh, D.B. and Yeh, C.S. (2006) One-pot synthesis of hollow Au_3Cu_1 spherical-like and biomineral botallackite $Cu_2(OH)_3Cl$ flowerlike architectures exhibiting antimicrobial activity. *Journal of Physical Chemistry B*, **110**, 205–10.

76 Chen, Z., Meng, H., Xing, G., Chen, C., Zhao, Y., Jia, G., Wang, T., Yuan, H., Ye, C., Zhao, F., Chai, Z., Zhu, C., Fang, X., Ma, B. and Wan, L. (2006) Acute toxicological effects of copper nanoparticles in vivo. *Toxicology Letters*, **163**, 109–20.

77 Nahrendorf, M., Zhang, H., Hembrador, S., Panizzi, P., Sosnovik, D.E., Aikawa, E., Libby, P., Swirski, F.K. and Weissleder, R. (2008) Nanoparticle PET-CT imaging of macrophages in inflammatory atherosclerosis. *Circulation*, **117**, 379-87.

78 Rossin, R., Muro, S., Welch, M.J., Muzykantov, V.R. and Schuster, D.P. (2008) In vivo imaging of ^{64}Cu-labeled polymer nanoparticles targeted to the lung endothelium. *Journal of Nuclear Medicine*, **49**, 103–11.

79 Wang, J. (1999) Electroanalysis and biosensors. *Analytical Chemistry*, **71**, 328R–32R and references therein.

80 Zen, J.M. and Senthil Kumar, A. (2003) Electrochemical investigation of glucose sensor fabricated at copper-plated screen-printed carbon electrodes. *Electroanalysis*, **15**, 1073–87.

81 Chi, Q. and Dong, S. (1993) Flow-injection analysis of glucose at an amperometric glucose sensor based on electrochemical codeposition of palladium and glucose oxidase on a glassy carbon electrode. *Analytica Chimica Acta*, **278**, 17–23.

82 Xu, J.J. and Chen, H.-Y. (2000) Amperometric glucose sensor based on

coimmobilization of glucose oxidase and poly(p-phenylenediamine) at a platinum microdisk electrode. *Analytical Biochemistry*, **280**, 221–6.

83 Cere, S., Vazquez, M., de Sanchez, S.R. and Schiffrin, D.J. (1999) Surface redox catalysis and reduction kinetics of hydrogen peroxide on copper-nickel alloys. *Journal of Electroanalytical Chemistry*, **470**, 31–8.

84 Wang, J., Liu, J., Chen, L. and Lu, F. (1994) Highly selective membrane-free glucose membranes. *Analytical Chemistry*, **66**, 3600–3.

85 Somasundrum, M., Tanticharoen, M. and Kirtikara, K. (1996) H_2O_2 from an oxidase enzyme can be detected cathodically using metal microparticles dispersed in a polymeric film electrode. *Journal of Electroanalytical Chemistry*, **407**, 247–51.

86 Karyakin, A.A., Karyakina, E.E. and Gorton, L. (2000) Amperometric biosensor for glutamate using Prussian blue-based "artificial peroxidase" as a transducer for hydrogen peroxide. *Analytical Chemistry*, **72**, 1720–3.

87 Zen, J.M., Jeng, S.H. and Chen, H.-J. (1996) Catalysis of the electroreduction of hydrogen peroxide by nontronite clay coatings on glassy carbon electrodes. *Journal of Electroanalytical Chemistry*, **408**, 157–63.

88 Zen, J.M. and Lo, C.W. (1996) A glucose sensor made of an enzymatic clay-modified electrode and methyl viologen mediator. *Analytical Chemistry*, **68**, 2635–40.

89 Cai, L.T. and Chen, H.Y. (1999) Electrocatalytic reduction of hydrogen peroxide at platinum microparticles dispersed in a poly(*o*-phenylenediamine) film. *Sensors and Actuators. B, Chemical*, **55**, 14–18.

90 Zen, J.M., Chung, H.-H. and Senthil Kumar, A. (2000) Flow injection analysis of hydrogen peroxide on copper-plated screen-printed carbon electrodes. *Analyst*, **125**, 1633–7.

91 Sigvardson, K.W., Eliason, M.S. and Herbranson, D.E. (1996) Determination of raffinose and lactobionic acid in ViaSpan by anion exchange chromatography with pulsed amperometric detection. *Journal of Pharmaceutical and Biomedical Analysis*, **15**, 227–31.

92 Cataldi, T.R.I., Campa, C. and Casella, I.G. (1999) Study of sugar acids separation by high-performance anion-exchange chromatography–pulsed amperometric detection using alkaline eluents spiked with Ba^{2+}, Sr^{2+}, or Ca^{2+} as acetate or nitrate salts. *Journal of Chromatography A*, **848**, 71–81.

93 Lee, Y.C. (1996) Carbohydrate analyses with high-performance anion-exchange chromatography. *Journal of Chromatography A*, **720**, 137–49.

94 Kano, K., Takagi, K., Inoue, K. and Ikeda, T. (1996) Copper electrodes for stable subpicomole detection of carbohydrates in high-performance liquid chromatography. *Journal of Chromatography A*, **721**, 53–7.

95 Casella, I.G., Gatta, M. and Desimoni, E. (1998) Applications of a copper-modified gold electrode for amperometric detection of polar aliphatic compounds by anion-exchange chromatography. *Journal of Chromatography A*, **814**, 63–70.

96 LaCourse, W.R. (1997) *Pulsed Electrochemical Detection in High Performance Liquid Chromatography*, John Wiley & Sons, Inc., New York.

97 Johnson, D.C. and La Course, W.R. (1992) Pulsed electrochemical detection at noble metal electrodes in liquid chromatography. *Electroanalysis*, **4**, 367.

98 Wang, J., Naser, N., Agnes, L., Wu, H., and Chen, L. (1992) Metal-dispersed carbon paste electrodes. *Analytical Chemistry*, **64**, 1285–7.

99 Casella, I.G. and Gatta, M. (2001) Determination of electroactive organic acids by anion-exchange chromatography using a copper modified electrode. *Journal of Chromatography A*, **912**, 223–33.

100 Garcia, A., Barbas, C., Aguilar, R. and Castro, M. (1998) Capillary electrophoresis for rapid profiling of organic acidurias. *Clinical Chemistry*, **44**, 1905–11.

101 Williams, H.E. and Wandzilak, T.R. (1989) Oxalate synthesis, transport and the hyperoxaluric syndromes. *The Journal of Urology*, **141**, 742–9.

102 Tuchman, M., Knopman, D.S. and Shih, V.E. (1990) Episodic hyperammonemia in adult siblings with hyperornithinemia, hyperammonemia, and homocitrullinuria syndrome. *Archives of Neurology*, **47**, 1134–7.

103 Shin, J.H., Choi, Y.S., Lee, H.J., Choi, S.H., Ha, J., Yoon, I.J., Nam, H. and Cha, G.S. (2001) A planar amperometric creatinine biosensor employing an insoluble oxidizing agent for removing redox-active interferences. *Analytical Chemistry*, **73**, 5965–71.

104 Bakker, E., Diamond, D., Lewenstam, A. and Pretsch, E. (1999) Ion sensors: current limits and new trends. *Analytica Chimica Acta*, **393**, 11–18.

105 Spencer, K. (1986) Analytical reviews in clinical biochemistry: the estimation of creatinine. *Clinical Biochemistry*, **23**, 1–25.

106 Ye, J.N. and Baldwin, R.P. (1994) Determination of amino acids and peptides by capillary electrophoresis and electrochemical detection at a copper electrode. *Analytical Chemistry*, **66**, 2669–74.

107 Hsu, C.T., Lyuu, H.J., Yang, T.H., Conte, E.D. and Zen, J.M. (2006) Profiling clinically important metabolites in human urine by an electrochemical system containing disposable electrodes. *Sensors Actuators B*, **113**, 22–8.

108 Bartges, J.W., Kirk, C. and Lane, F. (2004) The natural activities of cells, the role of reactive oxygen species, and their relation to antioxidants, nutraceuticals, botanicals, and other biologic therapies. *Veterinary Clinics of North America: Small Animal Practice*, **34**, 969–75.

109 Jen, J.F., Hsiao, S.L. and Liu, K.H. (2002) Simultaneous determination of uric acid and creatinine in urine by an eco-friendly solvent-free high performance liquid chromatographic method. *Talanta*, **58**, 711–17.

110 Luo, P., Zhang, F., Baldwin, R.P. and Potential, C. (1991) Amperometric detection of underivatized amino acids and peptides at a copper electrode. *Analytical Chemistry*, **63**, 1702–7.

111 Chou, C.C., Lin, S.P., Lee, K.M., Hsu, C.T., Vickroy, T.W. and Zen, J.M. (2007) Fast differentiation of meats from fifteen animal species by liquid chromatography with electrochemical detection using copper nanoparticle plated electrodes. *Journal of Chromatography B*, **846**, 230–9.

112 Lee, S.J. and Terkeltaub, R.A. (2006) New developments in clinically relevant mechanisms and treatment of hyperuricemia. *Current Rheumatology Reports*, **8**, 224–30.

113 Deen, D. (2004) Metabolic syndrome: time for action. *American Family Physician*, **69**, 2875–82.

114 Kizer, J.R., Hoieggen, A., Alderman, M.H., Kjeldsen, S.E., Dahlof, B. and Devereux, R.B. (2004) Serum uric acid and ischemic stroke risk among hypertensive patients with left ventricular hypertrophy: the Losartan intervention for endpoint reduction in hypertension (LIFE) study. *Journal of the American College of Cardiology*, **43**, 475A.

115 Alderman, M. and Aiyer, K.J.V. (2004) Uric acid: role in cardiovascular disease and effects of losartan. *Current Medical Research and Opinion*, **20**, 369–79.

116 Alderman, M.H. (2002) Uric acid and cardiovascular risk. *Current Opinion in Pharmacology*, **2**, 126–30.

117 Conen, D., Wietlisbach, V., Bovet, P., Shamlaye, C., Riesen, W., Paccaud, F. and Burnier, M. (2004) Prevalence of hyperuricemia and relation of serum uric acid with cardiovascular risk factors in a developing country. *BMC Public Health*, **4**, 9.

118 Maalouf, N.M., Cameron, M.A., Moe, O.W. and Sakhaee, K. (2004) Novel insights into the pathogenesis of uric acid nephrolithiasis. *Current Opinion in Nephrology and Hypertension*, **13**, 181–9.

119 Hsu, S.P., Pai, M.F., Peng, Y.S., Chiang, C.K., Ho, T.I. and Hung, K.Y. (2004) Serum uric acid levels show a 'J-shaped' association with all-cause mortality in haemodialysis patients. *Nephrology, Dialysis, Transplantation*, **19**, 457–62.

120 Rafey, M.A., Lipkowitz, M.S., Leal-Pinto, E. and Abramson, R.G. (2003) Molecular cell biology and physiology of solute transport. *Current Opinion in Nephrology and Hypertension*, **12**, 511–16.

121 Hoeldtke, R.D., Bryner, K.D., McNeill, D.R., Hobbs, G.R., Riggs, J.E., Warehime, S.S., Christie, I., Ganser, G. and Van Dyke, K. (2002) Uric acid, and peripheral nerve function in early type 1 diabetes. *Diabetes*, **51**, 2817–25.

122 Nakanishi, N., Okamoto, M., Yoshida, H., Matsuo, Y., Suzuki, K. and Tatara, K. (2003) Serum uric acid and risk for development of hypertension and impaired fasting glucose or type II diabetes in Japanese male office workers. *European Journal of Epidemiology*, **18**, 523–30.

123 Seghieri, G., Moruzzo, D., Fascerti, S., Bambini, C., Anichini, R., De Bellis, A., Alviggi, L. and Franconi, F. (2002) Increase in serum uric acid is selectively associated with stroke in type 2 diabetes. *Diabetes Care*, **25**, 1095–6.

124 Yardim-Akaydin, S., Sepici, A., Ozkan, Y., Torun, M., Simsek, B. and Sepici, V. (2004) Oxidation of uric acid in rheumatoid arthritis: is allantoin a marker of oxidative stress? *Free Radical Research*, **38**, 623.

125 Urano, W., Yamanaka, H., Tsutani, H., Nakajima, H., Matsuda, Y., Taniguchi, A., Hara, M. and Kamatani, N. (2002) The inflammatory process in the mechanism of decreased serum uric acid concentrations during acute gouty arthritis. *The Journal of Rheumatology*, **29**, 1950–3.

126 Chamorro, A., Obach, V., Cervera, A., Revilla, M., Deulofeu, R. and Aponte, J. H. (2002) Prognostic significance of uric acid serum concentration in patients with acute ischemic stroke. *Stroke*, **33**, 1048–52.

127 Kanellis, J. and Johnson, R.J. (2003) Elevated uric acid and ischemic stroke: accumulating evidence that it is injurious and not neuroprotective. *Stroke*, **34**, 1956–7.

128 Yildirim, A., Altinkaynak, K., Aksoy, H., Sahin, Y.N. and Akcay, F. (2004) Plasma xanthine oxidase, superoxide dismutase and glutathione peroxidase activities and uric acid levels in severe and mild pre-eclampsia. *Cell Biochemistry and Function*, **22**, 213–17.

129 Kang, D.H., Finch, J., Nakagawa, T., Karumanchi, S.A., Kanellis, J., Granger, J. and Johnson, R.J. (2004) Uric acid, endothelial dysfunction and pre-eclampsia: searching for a pathogenetic link. *Journal of Hypertension*, **22**, 229–35.

130 Pasaoglu, H., Bulduk, G., Ogus, E., Pasaoglu, A. and Onalan, G. (2004) Nitric oxide, lipid peroxides, and uric acid levels in pre-eclampsia and eclampsia. *The Tohoku Journal of Experimental Medicine*, **202**, 87–92.

131 Jodi, S.N.D., Marco, F.C., Callum, L. and James, D. (2005) Diagnostic implications of uric Acid in electroanalytical measurements. *Electroanalysis*, **17**, 1233–43.

132 Luo, D., Han, E., Belcheva, N. and Saltzman, W.M. (2004) A self-assembled, modular DNA delivery system mediated by silica nanoparticles. *Journal of Controlled Release*, **95**, 333–41.

133 Sandhu, K.K., McIntosh, C.M., Simard, J.M., Smith, S.W. and Rotella, V.M. (2002) Gold nanoparticle-mediated transfection of mammalian cells. *Bioconjugate Chemistry*, **13**, 3–6.

134 Cruz-Campa, I., Arzola, A., Santiago, L., Parsons, J.G., Varela-Ramirez, A., Aguilera, R.J. and Noveron, J.C. (2007) A novel class of metal-directed supramolecular DNA-delivery. systems. *Chemical Communications*, 2944–6.

135 Dhar, S., Sennapati, D., Das, P.K., Chattopadhyay, P., Nethaji, M. and Chakravarty, A.R. (2003) Ternary copper complexes for photocleavage of DNA by red light: direct evidence for sulfur-to-copper charge transfer and d-d band involvement. *Journal of the American Chemical Society*, **125**, 12118–24.

136 Silvestri, A., Barone, G., Ruisi, G., Giudice, M.T. and Tumminello, S. (2004) The interaction of native DNA with iron(III)-*N,N′* -ethylene-bis (salicylideneiminato)-chloride. *Journal of Inorganic Biochemistry*, **98**, 589–94.

137 Fernandes, C., Parrilha, G.L., Lessa, J.A., Santiago, L.J.M., Kanashiro, M.M., Boniolo, F.S., Bortolauzzi, A.J., Vugman, N.V., Herbst, M.H. and Horn, A. (2006) Synthesis, crystal structure, nuclease and in vitro antitumor activities of a new mononuclear copper(II) complex containing a tripodal N_3O ligand. *Inorganica Chimica Acta*, **359**, 3167–76.

138 Bales, B.C., Kodama, T., Weledji, Y.N., Pitie, M., Meunier, B. and Greenberg, M.M. (2005) Mechanistic studies on DNA damage by minor groove binding copper-phenanthroline conjugates. *Nucleic Acids Research*, **33**, 5371–9.

139 Chauhan, M., Banerjee, K. and Arjmand, F. (2007) DNA binding studies of novel copper(II) complexes containing L-tryptophan as chiral auxiliary: in vitro antitumor activity of Cu-Sn_2 complex in human neuroblastoma cells. *Inorganic Chemistry*, **46**, 3072–82.

140 Mishra, L. and Yadaw, A.K. (2000) Exploring new bio-active Ru(II) polypyridyl complexes through their interaction with DNA. *Indian Journal of Chemistry, Section A*, **39**A, 660–3.

141 Naik, A.D., Annigeri, S.M., Gangadharmath, U.B., Revankar, V.K. and Mahale, V.B. (2002) Anchoring mercapto-triazoles on dicarbonyl backbone to assemble novel binucleating, acyclic SNONS compartmental ligands. *Indian Journal of Chemistry, Section B*, **41B**, 2046–53.

142 Liu, J., Zhang, H., Chen, C., Deng, H. Lu, T. and Ji, L. (2003) Interaction of macrocyclic copper(II) complexes with calf thymus DNA: effects of the side chains of the ligands on the DNA-binding behaviors. *Dalton Transactions*, **1**, 114–19.

143 Nagane, R., Chikira, M., Oumi, M., Shindo, H. and Antholine, W.E. (2000) How amino acids control the binding of Cu(II) ions to DNA Part III. A novel interaction of a histidine complex with DNA. *Journal of Inorganic Biochemistry*, **78**, 243–9.

144 Arjmand, F., Mohani, B. and Ahmad, S. (2005) Synthesis, antibacterial, antifungal activity and interaction of CT-DNA with a new benzimidazole derived Cu(II) complex. *European Journal of Medicinal Chemistry*, **40**, 1103–10.

3
Approaches to the Synthesis and Characterization of Spherical and Anisotropic Silver Nanomaterials

Deirdre M. Ledwith, Damian Aherne and John M. Kelly

3.1
Introduction

In recent years, the veritable explosion in interest towards silver nanoparticles has been reflected by the dramatic increase in the number of publications on this topic. Metal nanoparticles – and, in particular, silver nanoparticles – have proved to be good candidates for use in such areas as optoelectronics [1–3], surface-enhanced Raman scattering (SERS) [4–6] and, more recently, surface-enhanced fluorescence [7, 8]. Controlling the size, shape and surrounding media of metal nanoparticles is important because many of their intrinsic properties are determined by these factors. Particular emphasis has recently been placed on the control of shape, because in many cases this allows the properties to be fine-tuned with a greater versatility than can be achieved otherwise. It is only within the past decade that it has become possible to control the shape of silver nanoparticles synthesized in solution, and numerous methods have been developed subsequently. In this chapter we will discuss the approaches to the synthesis of both spherical and anisotropic silver nanoparticles. It is not within the scope of the chapter to provide an exhaustive review of the area; rather, we present different approaches that have been taken to prepare silver nanoparticles of various sizes and morphologies by solution-based chemical methods. The advantages of these methods over physical techniques such as lithography are that no specialized equipment is necessary, and scale-up of the procedure is relatively easy. This is important when the possibility is considered of incorporating such nanoparticles into devices.

3.2
Optical Properties of Metal Nanoparticles

Although the optical properties of metal nanoparticles have attracted much attention during recent years, this interest is not new and can in fact be dated back to the mid-1800s, when Michael Faraday made the first investigations into colloidal

Metallic Nanomaterials Vol. 1. Edited by Challa S. S. R. Kumar

ISBN: 978-3-527-32151-3

gold. However, it is only recently that the improvements to classical wet chemical techniques have been made that have enabled the production of noble nanoparticles of varying shape, size and dielectric environments.

The optical properties of nanosized metallic particles are significantly different to those of the bulk material. Absorption bands in the visible region are present in the UV-visible spectrum of gold, silver and copper nanoparticles, but these bands are absent when the spectrum of the bulk metal is recorded. These bands, which are known as surface plasmon resonance (SPR) bands, are the result of an interaction of the conduction electrons of the nanoparticles with an electromagnetic field. When a spherical nanoparticle is irradiated by light, the oscillating electric field induces the coherent oscillation of the conduction electrons, and this results in a displacement of the electron cloud relative to the nuclei. Because there is a coulombic force of attraction between the electrons and nuclei, the electron cloud oscillates relative to the nuclear framework. The frequency of this oscillation is determined by four factors: the density of electrons; the effective electron mass; and the size and shape of the charge distribution. The collective oscillation of the electrons is called the dipole plasmon resonance of the particle; this process is depicted schematically in Figure 3.1 [9].

In 1908, Mie presented a solution to the Maxwell equations that described the extinction spectra of spherical particles of arbitrary size [10]. This theory is the only simple exact solution to Maxwell's equations that is relevant to particles, and remains of great interest to this day. The extinction coefficient is taken as the 'sum over all electric and magnetic multipole oscillations contributing to the absorption and scattering of the interacting magnetic field'. This is the simplest theoretical model and is given by the equation

$$k = \frac{18\pi N V \varepsilon_m^{3/2}}{\lambda} \frac{\varepsilon_2}{[\varepsilon_1 + 2\varepsilon_m]^2 + \varepsilon_2^2} \tag{3.1}$$

where k is the extinction coefficient, N is the number of particles, V is the volume of the nanoparticle, λ is the wavelength of the absorbing radiation and ε_m is the dielectric constant of the surrounding medium (assumed to be frequency-

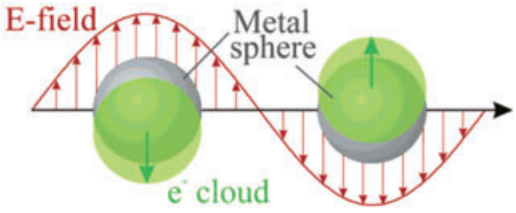

Figure 3.1 Schematic of plasmon oscillation for a sphere, showing displacement of the conduction electron cloud relative to the nuclei. Reprinted with permission from Ref. [9]; © 2003 The American Chemical Society.

independent). ε_1 and ε_2 represent the real and imaginary parts of the material dielectric function, respectively.

It must be noted that the Mie theory can only be directly applied to spherical particles of arbitrary size, so what happens when the optical properties of nonspherical particles are considered? El Sayed and coworkers [11] have shown that gold nanorods exhibit two distinct absorption bands, corresponding to oscillation of free electrons along and perpendicular to the long axis of the rods. The wavelength of the transverse mode is located at 525 nm, while the longitudinal mode is located at wavelengths in the far visible or near infrared, depending on the aspect ratio of the nanorods. Spectral studies carried out on particles of varying morphology have indicated that the number and position of SPR bands is strongly dependent on the symmetry of the particles concerned [12].

Some numerically exact methods have been developed in recent years to describe these nonspherical metal nanoparticles. The most commonly used method is the discrete dipole approximation (DDA), and DDA calculations have been performed for a range of shapes including cubes, discs and triangular plates. Recent advances in colloid chemistry and also of lithographic techniques have made it possible to synthesize triangular prisms of silver. However, the distribution of sizes and shapes generated so far is fairly broad (see Section 3.4), and many of the particles have missing tips. Schatz and colleagues have used the DDA method to model spectra for both perfectly triangular particles and truncated triangles [9], while Wiley *et al*. have carried out calculations which illustrate the effect of nanoparticle shape on the optical properties of various shapes of silver nanoparticles (Figure 3.2) [13]. Studies conducted by Noguez and coworkers also highlight the influence of shape and physical environment on the surface plasmons of metal nanoparticles [14–16].

3.3
Preparation of Spherical Nanoparticles

3.3.1
Stability of Electrostatically Stabilized Nanoparticles

The stability of a dispersion of particles depends upon the interplay of repulsive and attractive interactions between the particles. The attractive interaction, V_A, between particles arises from van der Waals interactions, while the repulsive interaction, V_R, can arise either from the electric double layer of charged particles or from the steric repulsion from an organic layer surrounding the particles. If there is an energy barrier between particles that is greater than ~$2\,kT$ then the dispersion is stable; otherwise, the dispersion is unstable and the particles flocculate out of solution.

Particles that are charged attract ions of the opposite polarity towards the particle's surface to maintain electrical neutrality. The concentration of these ions decays exponentially with distance away from the surface; this is known as the

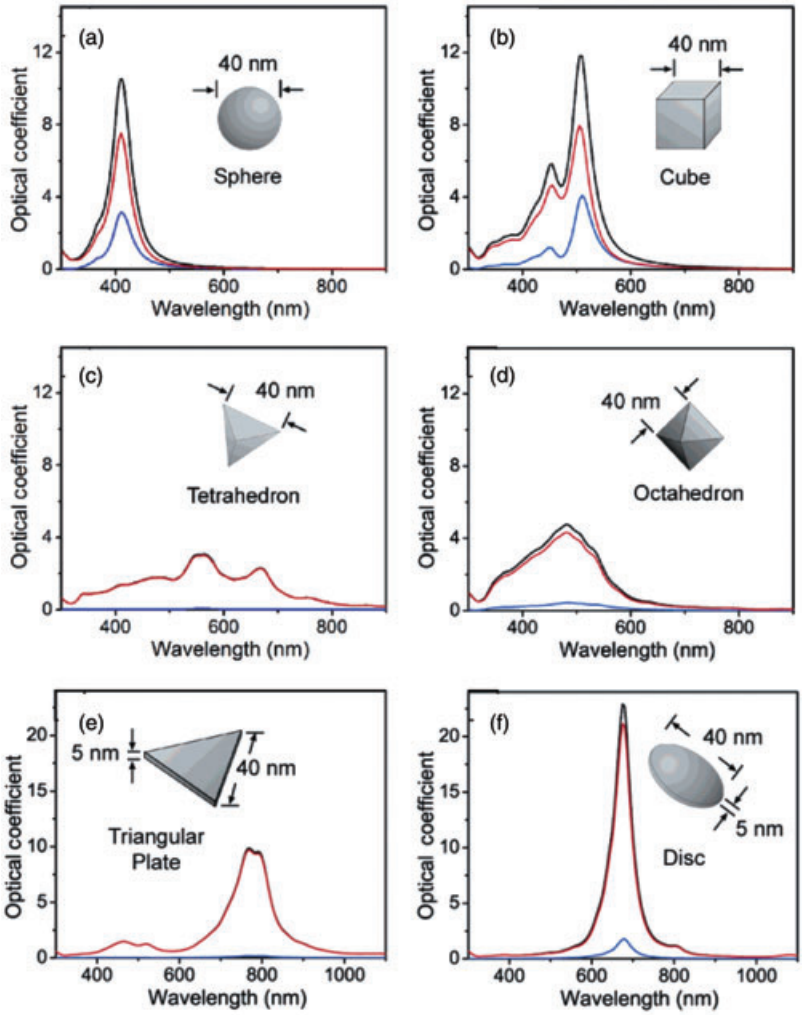

Figure 3.2 Calculated UV-visible extinction spectra (black), absorption spectra (red) and scattering spectra (blue), depicting the effect of nanoparticle shape on the spectral characteristics. Adapted with permission from Ref. [13]; © 2006 The American Chemical Society.

electric double layer. The repulsive interaction between two particles, V_R, arises from the interactions between these double layers, and includes the repulsion between the like charges on the particles; thus, $V_R = V_{ELEC}$. Subsequently, V_{ELEC} decays exponentially with interparticle separation, but it can also be decreased by increasing the electrolyte concentration and/or increasing the charge on the counterions.

$$V_{TOT} = V_A + V_{ELEC}$$

A common example of particles that are stabilized due to electrostatic repulsion is that of negatively charged citrate stabilized gold or sliver nanoparticles.

3.3.2 Aqueous Synthetic Methods

3.3.2.1 Chemical Reduction

This method was first introduced by Turkevich and coworkers during the early 1950s for the preparation of gold nanoparticles [17]. It basically involves the heating of a dilution solution of $HAuCl_4$ to its boiling point, followed by reduction with trisodium citrate; the resultant nanoparticles were very uniform, with a diameter of approximately 20 nm. This method was further studied by other groups [18–20] which, by varying the reaction conditions (e.g. the ratio of trisodium citrate to gold salt) were able to achieve a degree of control over the diameter of the resultant nanoparticles. The same procedure could be used to reduce silver salt, but the particles formed were larger, less uniform, and had a greater degree of polydispersity. This has been attributed to the fact that fewer seeds are formed initially and the growth of these seed particles is slow, leading to the formation of larger nanocrystals of varying shape and size. Despite this – or perhaps even because of it – this type of colloid is a popular substrate for SERS.

Another successful procedure is to use sodium borohydride; as this is a strong reducing agent, a larger number of nuclei are formed when it is used to reduce metal salts and therefore the resulting particles are typically small (<10 nm). Silver nitrate is reduced by sodium borohydride in the presence of trisodium citrate, where the citrate acts solely as the capping agent. These particles can then be used as seeds or nucleation centers for the preparation of nanoparticles with larger sizes and different shapes (this point is discussed further in Section 3.4). Briefly, the seed particles act as catalysts for the reduction of silver ion by weaker reducing agents such as ascorbic acid. The reaction conditions – especially the ratio of seed particles to metal ions – must be controlled carefully so as to avoid any secondary nucleation events. The advantage of using seeding to prepare larger spherical particles is that a greater control can be achieved over the size of the grown nanoparticles.

Other reducing agents such as hydrazine [21] and hydroxylamine [22, 23] have also been used to prepare spherical silver nanoparticles in aqueous solution. Again, similar to the case of the citrate reduction, particles larger than 20 nm with a high degree of polydispersity were formed. It was reported that poly(vinylpyrrolidone) (PVP) may serve as a reducing agent and that, by varying the ratio of metal salt to PVP, the size and shape of the nanoparticle could be tuned [24]. In addition to this, the reduction process is explained by two main reactions: (i) the direct abstraction of hydrogen atoms from the polymer by the metal ion; and (ii) subsequent reduction of the metal ion by the organic radical

formed by the former process. Another mechanism in which the end hydroxyl groups of PVP reduce silver ion has also been proposed by Washio *et al*. [25]; this same mechanism has been used to explain the anisotropic growth of silver nanoplates (see also Section 3.3).

Various sugars have also been used as reducing agents to prepare silver nanoparticles, with the controllable sizes ranging from 45 to 380 nm [26]. The nanoparticles were prepared by a reduction of the $[Ag(NH_3)_2]^+$ complex with four structurally different sugars: xylose, glucose, fructose and maltose. The size distribution of the resultant particles was found to depend heavily on the concentration of ammonia present, and also on the nature of the reducing sugar.

3.3.2.2 **Physical Methods**

The method of γ-radiolysis, which is used to prepare spherical metal nanoparticles, was pioneered by Henglein and coworkers. This technique is based on the formation of hydrated electrons and organic radicals in solutions through γ-radiolysis; these species then act as reducing agents for the metal ions in the presence of trisodium citrate, to yield metal atoms that then coalesce into larger nanoparticles [27]. This is shown schematically in Figure 3.3. The nanoparticles formed by this method are typically small, but these small nanoparticles can again be used as seeds to produce larger particles by the same technique [28]. The authors proposed two possible growth mechanisms: (i) the condensation of small silver clusters; and (ii) the reduction of silver ions onto silver particles via radical to particle electron transfer.

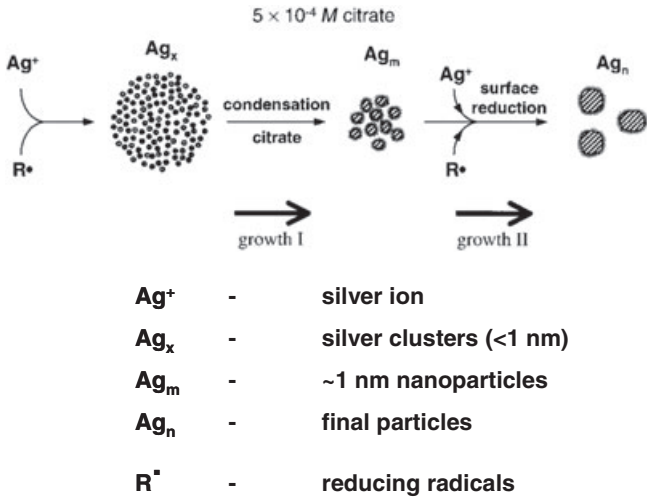

Figure 3.3 Proposed growth mechanism for silver nanoparticles at low citrate concentration via γ-radiolysis. Adapted with permission from Ref. [27]; © 2002 The American Chemical Society.

More recently, Liu *et al*. have demonstrated that the quantity and dimensions of the Ag nanoparticles can be controlled by varying the γ-radiation dose applied to the silver nitrate solution, with good batch-to-batch reproducibility [29]. These authors also highlighted the fact that the nanoparticles produced were 'clean' – that is, no polymer or surfactant is required to stabilize them.

In a similar method, the trisodium citrate can be replaced by PVP. In a study carried out by Shin *et al*. [30], transmission electron microscopy (TEM) findings showed that both the amount and the molecular weight of the PVP in the irradiated solution affected the average size of the nanoparticles produced. A three-step mechanism for the formation of these nanoparticles has been postulated. First, the silver ions interact with the PVP, after which nearby silver atoms that have been reduced by γ-radiation aggregate to form primary particles. Finally, nearby primary particles coalesce to form larger aggregates which are termed secondary particles.

Another report which involves the use of PVP describes the comparison of silver nanoparticles prepared by γ-radiation and by chemical reduction [31]. It was reported that the γ-radiation strategy produced silver nanoparticles with a narrower size distribution, with the final size also being tuned by varying the concentration of the silver nitrate precursor. In contrast, the chemical reduction method does not allow such ease in tuning the particle size.

Bogle *et al*. recently reported a method for the synthesis of silver nanoparticles of different sizes in the range 60–100 nm, using electron irradiation of silver nitrate in the presence of poly(vinyl alcohol) (PVA) [32]. The process of formation of the silver nanoparticles appeared to be initiated at an electron fluence of approximately 2×10^{13} e cm^{-2}, and by varying this electron fluence the size of the nanoparticle could be controlled. Larger nanoparticles (in the 100–200 nm range) could be produced by removing the PVA and thereby promoting coalescence of the particles.

Microwave irradiation has also been used to prepare silver nanoparticles, as described by Yin *et al*. In this method, the large-scale production of silver nanoparticles was achieved from a silver nitrate and trisodium citrate solution, in the presence of formaldehyde as the reducing agent [33].

A method for the size control of silver nanoparticles involving the UV-irradiation of argentine–tungstosilicic acid solution (Arg-TSA) was recently reported, with spherical nanoparticles between several nanometers and several hundred nanometers in diameter being produced [34]. This size control was achieved by varying the reaction conditions such as the molar ratio of silver nitrate to TSA, pH and reaction temperature. The authors proposed that the Arg-TSA colloidal particles were a new type of organic–inorganic template for the synthesis of silver nanoparticles, with the Arg–TSA complex acting as a UV-switchable reducing agent.

Tan *et al*. have recently reported the UV-assisted reduction of silver ion in polyamine solutions, namely branched poly(ethyleneimine) (BPEI), at low concentrations of HEPES, that resulted in the formation of positively charged Ag nanoparticles [35]. It was reported that the BPEI : silver nitrate : HEPES molar ratio

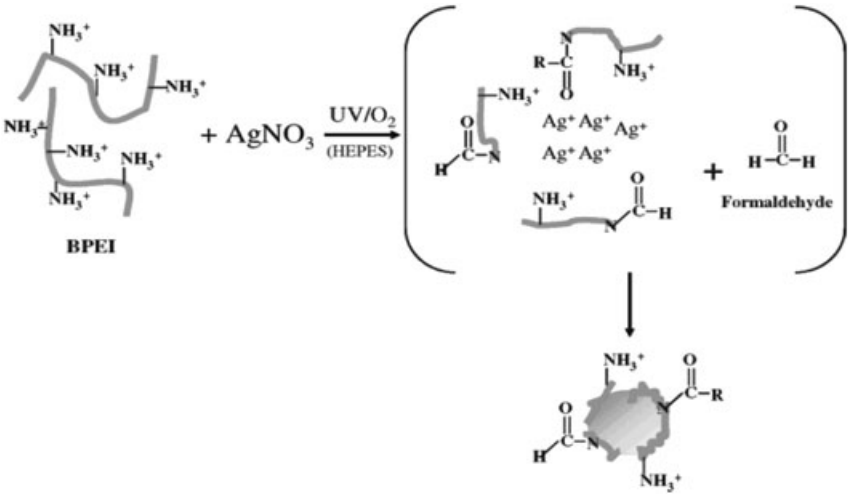

Figure 3.4 Suggested mechanism for the formation of positively charged silver nanoparticles. Reprinted with permission from Ref. [35]; © 2007 The American Chemical Society.

had a dramatic effect on nanoparticle size, with an increase in the BPEI : silver nitrate typically leading to a decrease in particle size. The size of the resultant nanoparticles could also be controlled by the BPEI molecular weight, there being an increase in particle diameter with increasing molecular weight of the polymer. The suggested reaction mechanism is shown in Figure 3.4. It is suggested that formation of the silver nanoparticles involves the oxidative cleavage of BPEI chains, which in turn results in the formation of fragments with both primary amine and amide groups. During this fragmentation process, formaldehyde is formed, and it is this species and not the polyamine (as has been suggested by others) that reduces the silver nitrate.

3.3.3 Organic Solvents

3.3.3.1 Stability of Sterically Stabilized Nanoparticles

An organic monolayer gives rise to a repulsive interaction between particles, called a steric repulsion. There are two contributions to the steric repulsion: first, an osmotic term, V_{OSM}, takes into account the thermodynamics associated with the exclusion of solvent molecules from interdigitating alkane chains on colliding particles (osmotic pressure); this depends greatly on the solvent. Second, an elastic term, V_{ELAS}, considers the thermodynamics associated with the loss of possible configurations of the interdigitating alkane chains due to reduced available volume (entropy). The attractive interaction, V_A, between particles arises form van der Waals interactions.

$$V_{TOT} = V_A + V_{OSM} + V_{ELAS}$$

A good example of particles stabilized by a monolayer of organic capping ligands is that of silver nanocrystals capped with dodecanethiol.

3.3.3.2 Reduction by the Solvent

Pastoriza-Santos and Liz-Marzán reported the ability of dimethylformamide (DMF) to behave as a reducing agent. In fact, in the absence of any additional reducing agent, and even at room temperature, DMF was shown capable of reducing silver nitrate in the presence of 3-aminopropyltrimethoxysilane (APS) to yield stable, silver nanoparticles [36]. It was also shown that the rate of reduction of silver ions by DMF is strongly temperature-dependent and that, if the reaction was carried out at reflux then the silver nanoparticles were found to be passivated by a thin layer of silica. In a later report the same group replaced APS with PVP, and this resulted in the formation of stable, PVP-protected silver nanoparticles [37]. This reaction was also carried out under microwave irradiation, when it was shown that greater control could be achieved compared to conventional refluxing. A one-pot procedure for the preparation of titania-coated silver nanoparticles has also been described [38]. Liu *et al.* have also reported the preparation of silver nanoparticles using DMF as the reducing agent; in this case the authors investigated the effectiveness of various macrocyclic compounds at capping the prepared nanoparticles [39]. It was shown that macrocyclic, multidentate thiol ligands were more effective at capping stable silver nanoparticles than monodentate ligands with similar structures, resulting in the production of smaller, more-stable nanoparticles.

Dimethylsulfoxide (DMSO) has also been used in the preparation of silver nanoparticles. Very stable capped nanoparticles of average diameters close to 4.4 nm and with a narrow size distribution were prepared by the addition of silver 2-ethylhexanoate to DMSO in the presence of trisodium citrate [40]. It was proposed that reduction took place through the formation of a silver–DMSO complex precursor, with both DMSO and trisodium citrate acting as reducing agents.

The polyol process, which has been used widely to prepare anisotropic silver nanoparticles (see Section 3.4.1.2), has also been used to prepare stable dispersions of spherical silver nanoparticles [41]. In general, silver nitrate is reduced by ethylene glycol in the presence of PVP. In a recent report by *Kim et al.*, the experimental set-up in the polyol process was found to be important. For example, the precursor injection rate and temperature ramping rate were found to be key factors in the production of monodisperse silver nanoparticles [42].

3.3.3.3 Microemulsion Methods

This type of approach, which is also known as the soft templating method, is typically carried out in aqueous surfactant systems such as cetyltrimethylammonium bromide (CTAB), sodium dodecylsulfate (SDS) or bis(2-ethylhexyl) sulfosuccinate

(AOT). The Pileni group, in particular, has carried out significant investigations in this area, with highly monodisperse silver nanoparticles being produced in the liquid phase, which starts from an initial synthesis in functionalized AOT micelles [43, 44]. A size-selective precipitation is then carried out using dodecanethiol to cap the particles, with ethanol being added to induce aggregation. Highly monodisperse samples could also be prepared in this way.

Initially it was postulated that, due to the very small size of the micelles, they could act as microreactors capable of controlling the size of the particles as well as preventing them from aggregating. In more recent years, however, the trend of thought has moved away from these micelles behaving as physical templates towards the possibility of them acting as growth-directing adsorbates. While this topic will be discussed again in Section 3.4.1, the exact nature of the growth mechanism remains a topic of debate.

The spherical nanoparticles prepared using the AOT reverse micelle method by Pileni's group have been shown to undergo a morphological evolution [45, 46]. The silver nanocrystals were deposited on a copper TEM grid which was covered by either an amorphous carbon or by highly oriented pyrolitic graphite (HOPG). When annealed at 50 °C under atmospheric pressure, triangular single crystal nanoparticles were produced. An example of this is shown in Figure 3.5. The size of the triangular nanocrystals depends on the initial order of the small spherical nanoparticles on the substrate. The single-crystal size is larger on HOPG than on amorphous carbon, as the ordering on the carbon substrate is local whereas it is more extended on the HOPG. In recent years, this microemulsion method has evolved into the use of supercritical fluids for the preparation of silver nanoparticles [47–49].

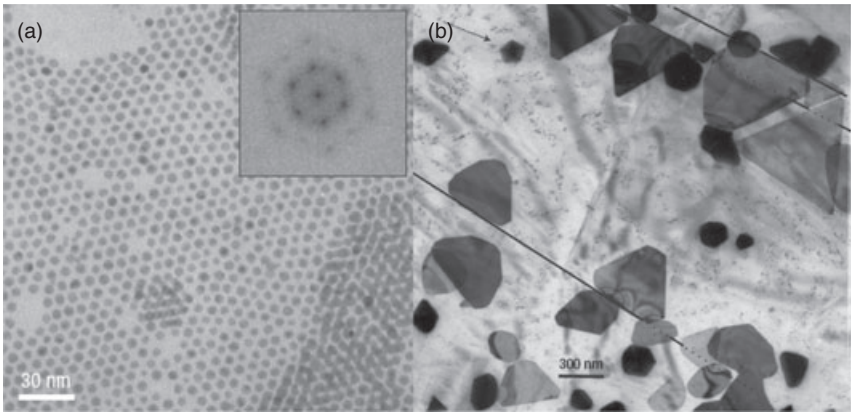

Figure 3.5 (a) Assembly of spherical silver nanoparticles prepared by the microemulsion method on HOPG; (b) Sample after annealing at 50 °C at atmospheric pressure for 8 days. Adapted with permission from Ref. [45]; © 2007 MacMillan Publishers Ltd.

3.3.3.4 Thiol-Stabilized Nanoparticles

This method for the synthesis of highly monodisperse gold nanoparticles was first developed by Brust *et al.* [50, 51], but has since been adapted to prepare silver nanoparticles. It involves the reduction of silver nitrate by sodium borohydride in a two-phase system, in the presence of an alkanethiol and a phase-transfer agent such as tetraoctylammonium bromide [52, 53]. Size-selective precipitation using a solvent/nonsolvent pair can then be carried out to narrow the particle size distribution. A polar solvent is added to the nanoparticle dispersion, and this results in the preferential precipitation of larger particles. This method has received considerable attention because it allowed, for the first time, the easy synthesis of small silver nanoparticles (<10 nm), which could be repeatedly isolated and resuspended in organic solvents, without aggregation or decomposition. The other advantage to particles prepared by this method is that the resultant nanoparticles can be treated and handled as common organic compounds. Ligand-exchange reactions have been utilized to introduce various different molecules such as thiol-functionalized oligonucleotides [54, 55], dithiols [56] and thioalkyated poly(ethylene glycol) compounds bearing amino or alcohol moieties [57].

A disadvantage of this method, however, is that the size of the nanoparticles produced is limited to below 25 nm. Also, in some cases the thiol ligands may be difficult to displace, making further surface functionalization difficult. Other groups have overcome these problems by preparing silver nanoparticles in a single-phase process in the presence of alkylamines [58], fatty acids [59] and carboxylates [60–63]. Hence, nanoparticles of up to 32 nm have been prepared but, because the ligands are weaker, they are easily displaced by thiols bearing whichever functional group may be required.

One important area of research involving nanoparticles prepared by the above-described methods is the assembly of two- and three-dimensional arrays, in which the nanoparticles are closely packed but uncontrollable aggregation is prevented. Thiol-stabilized silver nanoparticles, in particular, tend spontaneously to form highly ordered, hexagonal-packed superlattices when the solvent is slowly evaporated on a suitable substrate [53, 64–66]. It has been proposed that the hydrocarbon chains of the thiol ligands are necessary in the formation of superlattices through the interdigitation of chains on adjacent particles, as separation of the spheres is linearly dependent on the length of the alkyl chain [67]. Bimodal systems have also been produced in which thiol-stabilized silver nanoparticles of 8 and 3 nm formed a two-dimensional structure analogous to NaCl crystal structure (see Figure 3.6). Further to this, a superlattice containing both gold and silver thiol-stabilized nanoparticles has also been prepared [68].

3.4 Synthesis of Anisotropic Silver Nanoparticles

The synthesis of nonspherical silver nanoparticles has attracted much interest in recent years. As discussed in Section 3.2, the optical properties of silver

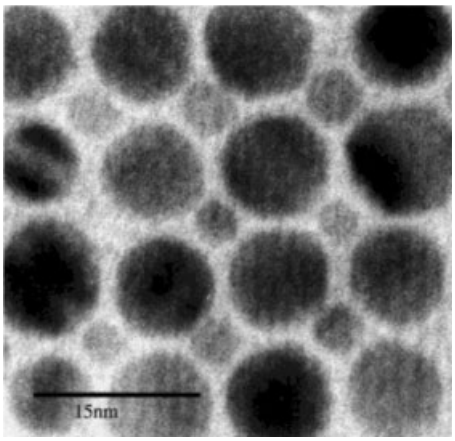

Figure 3.6 TEM image of bimodal superlattice consisting of 8 and 3 nm thiol-stabilized silver nanoparticles. Reprinted with permission from Ref. [68]; © 2000 Wiley-VCH Verlag GmbH & Co. KGaA.

nanoparticles depend heavily on their shape; hence, controlling the morphology of the nanoparticle provides an easy route for controlling the optical properties. Some general strategies for the synthesis of silver nanoparticles of various morphologies via solution-based methods are discussed in this section. For a general review on the shape-control of colloidal metal nanocrystals, the reader is directed to a recent article by Tao *et al.* [69].

3.4.1
Nanorods and Nanowires

Initially, it is necessary to differentiate between nanorods and nanowires. The aspect ratio of a shape is defined as the 'length of the major axis divided by the width of the minor axis'. Nanorods form a class of material that have a width of between 1 and 100 nm and an aspect ratio of greater than 1, but less than 20. Nanowires are similar materials but with an aspect ratio of greater than 20 [70]. Although this definition is by no means uniform in the literature, it is nevertheless a good guideline to use.

In the following sections, the main focus will be on the preparation of nanorods and nanowires via synthesis in solution. First, the surfactant-based aqueous method will be discussed, followed by the polyol, organic-based preparation. In both of these approaches the most important concept to understand is the preferential binding of an organic species or ion to a specific crystal face, usually a less-stable, higher-energy face. Calculations generally agree that the sequence of surface energies for low-index facets is $\gamma_{(111)} < \gamma_{(100)} < \gamma_{(110)}$ [71]; therefore the species interacts more strongly with crystal faces such as {100} (and in some cases the {110} if

present), promoting growth at the less-protected {111} faces and yielding one-dimensional (1-D) structures.

3.4.1.1 Aqueous Surfactant-Based Methods

A large number of studies in this area have been conducted by the group of Murphy [70, 72–75], with the majority of the investigations being carried out on the synthesis of gold nanowires and rods. Typically, a metal salt of gold or silver is initially reduced by a strong reducing agent such as sodium borohydride ($NaBH_4$) to form spherical nanoparticles. These seed particles are then used to grow the nanorods. In the presence of more metal salt, surfactant CTAB and an additional, milder reducing agent (e.g. ascorbic acid), the metal reduced on the seeds grows into nanowires or rods. Although the surfactant is critical to achieving non-spherical shapes, by changing various different synthetic parameters a degree of control can be achieved over the aspect ratio. For example, the lower the seed : metal ion ratio, the higher the aspect ratio of the resultant material. Silver nanorods of a different aspect ratio, prepared by this method are shown in Figure 3.7. The final state of the nanocrystals depends on a number of factors working both synergistically and dynamically [76]. Thus, the nature of the counterion, the size of the surfactant head group, the length of the

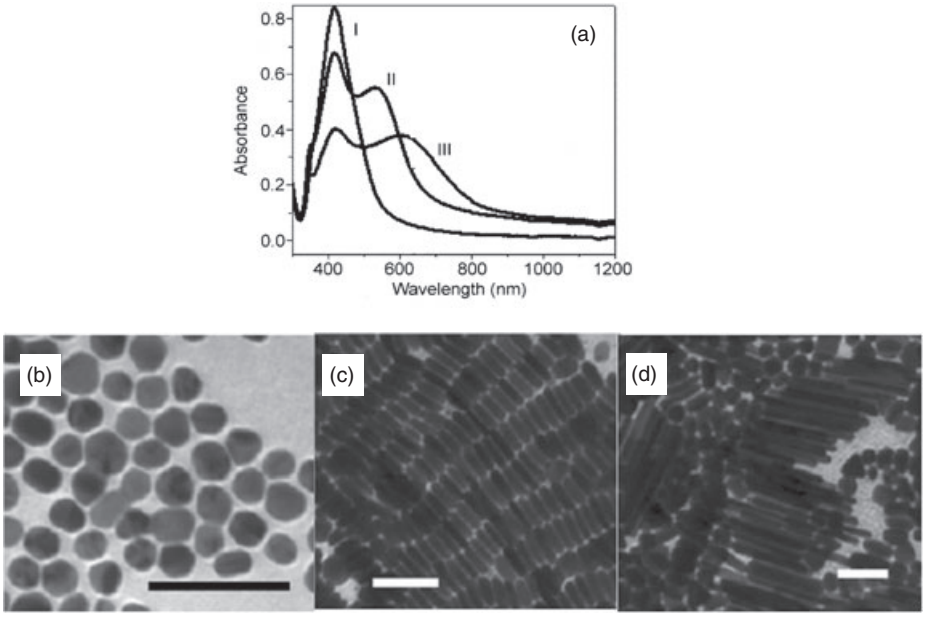

Figure 3.7 (a) UV-visible absorption spectra of silver nanorods of aspect ratio (b) 1, (c) 3.5 and (d) 10, with corresponding TEM images. The scale bar is 100 nm for each image. Adapted with permission from Ref. [75]; © 2006 PCCP Owner Societies.

surfactant tail group, the relative concentrations of all the reagents, pH, temperature, and the strength of the reducing agent, are all expected to play important roles, although a detail studied has yet to be carried out.

A number of different mechanisms have been proposed to explain the growth of 1-D structures from apparently spherical seed particles. Initially, it was suggested that the surfactant CTAB forms rod-like micelles in aqueous solution, creating dimensionally constrained waterpools that act as microreactors for a controlled synthesis [72, 77]. However, it has been proposed more recently that the surfactant molecules potentially bind to specific crystal faces and direct nanocrystal growth in one dimension [76, 78]. A schematic for this proposed mechanism is shown in Figure 3.8.

Based on the results of studies carried out with gold nanorods and wires, the following sequence has been postulated. The initial seed particles appear to be single crystals and, at an early stage in the growth process, the face-centered cubic symmetry of the gold or silver is broken by twinning events that occur to these seeds as the additional metal salt is reduced, to produce multiply twinned particles. At this stage, the preferential binding of the surfactant CTAB on the {100} side faces leads to a blocking of these faces and an elongation of the rods [72, 76, 78].

In a similar synthesis, cetyltrimethylammonium tosylate (CTAT) has been used to produce pentagonal silver nanorods [79]. It is worthy of mention here that only those seed particles with a multiple twinned decahedral structure could grow to

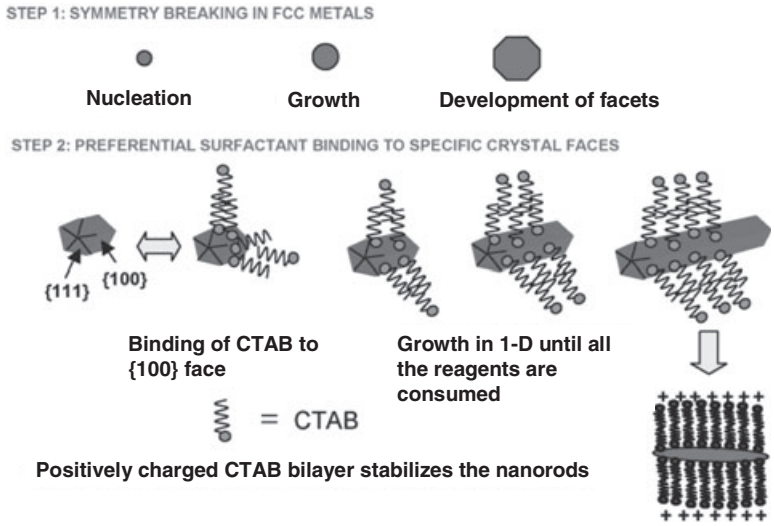

Figure 3.8 Mechanism proposed for the surfactant-directed growth of metallic nanorods. The single crystalline seeds develop facets to which there is differential adsorption of the surfactant. Addition of metal ions and a weak reducing agent leads to preferred growth on the exposed facets, resulting in growth in a one-dimensional fashion. Adapted with permission from Ref. [76]; © 2005 The American Chemical Society.

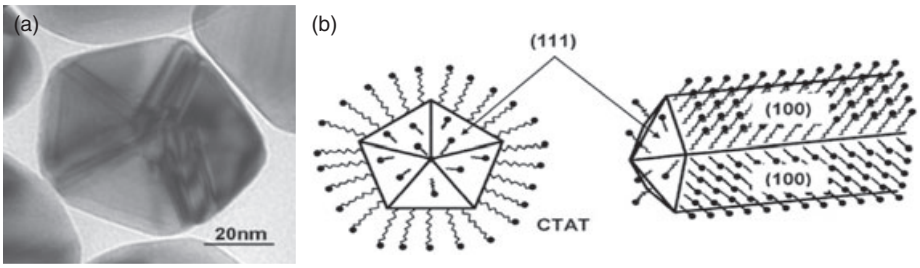

Figure 3.9 (a) Typical TEM image of a multiple twinned decahedral particle; (b) Preferential binding of the CTAT to the lateral {100} plane of the nanorod. Adapted with permission from Ref. [79]; © 2005 The American Chemical Society.

form rods. A TEM image of such a multiple twinned particle is shown in Figure 3.9. In the fcc lattice, the {111} planes have the highest atomic density, and are therefore less open to the binding of the hydrophobic ends of the CTAT molecule. The {100} planes have a lower atomic density, and the centers of octahedral interstitial sites offer more open sites to pin surfactant molecules. The {100} faces are passivated by the CTAT molecules leaving the {111} planes, which have the lowest surface energy, accessible to adatoms.

Another mechanism, which also derives from the growth of gold nanorods and wires, has been suggested by Pérez-Juste *et al*. [80] In this case, the gold(I) ions are bound to the CTAB micelles and transported to the growing seed particles; such transport is determined by the double-layer interaction, and is therefore dependent on the electric field surrounding the particles. The field at the tip of the nanorods is larger, which leads to a preferential binding of the ions on the tips, and causes elongation of the particles. This mechanism does not explain the initial change in morphology of the seeds, however, and it has been suggested that the presence of a stacking fault or twinning plane may also be necessary in the seed in order to create the initial electric field asymmetry. At this stage, it is important to highlight again that it is not only necessary to have a shape-directing organic species such as CTAB or CTAT present, but that the appropriate structure of the initial seed particles is also vital.

3.4.1.2 **Organic (Polyol-Based) Methods**

The majority of studies conducted in this area concern the polyol process, which involves heating a polyol with a precursor salt and a polymeric capping agent to generate a metal colloid. In the case of silver, this typically involves ethylene glycol (EG), silver nitrate ($AgNO_3$) and PVP, respectively. Here, the EG acts as both the solvent and the reducing agent. Although early studies involved the use of platinum seeds [81], further studies showed that such seeds were in fact dispensable. When the silver ions are reduced to atoms they come together to form nuclei; then when the nuclei are sufficiently small (<5 nm diameter) the available thermal

energy is sufficient to cause the structure to fluctuate, allowing defects to form [82]. Twinned crystals are readily formed in silver and gold as well as in silver halides, as the stacking fault energy is lower than in most metals, decreasing the energy required to form a twin plane [83]. The formation of twin defects is also thermodynamically favored for small sizes because they enable a greater surface coverage of the lowest energy {111} facets [84]. As the nuclei grow, they become stuck in a given morphology when changes to the defect structure become too costly relative to the thermal energy. This process results in a distribution of multiply twinned, singly twinned and single crystal seeds, with the five-fold twinned decahedron being the lowest in free energy. As a consequence, the five-fold twinned particles are the most abundant morphology. By manipulating the structure of the seed particles and the growth conditions, one shape of particle can be formed as the dominant product [85]. The possible seed structures are shown schematically in Figure 3.10.

Multiply twinned decahedra are the most chemically reactive of the seed structures listed above [86], and this can be taken advantage of when trying to produce a single dominant morphology (for further discussions, see Section 3.3.2). Silver atoms add preferentially to the twin defects of the decahedra, and this leads to an elongation of the seeds in one direction (Figure 3.11). As the seeds grow into pentagonal rods, the PVP interacts more strongly with the {100} side facets than with the {111} ends [87]; this in turn causes the sides of the nanorods to become tightly passivated by the PVP, while the ends remain accessible for the addition of atoms.

An additional reason for the 1-D growth of the decahedral seed particles is that they are strained. The twin boundaries represent areas of high energy because the preferred angle between them is 70.5°, yet 72° is available [83]. This means that there is 7.5° that needs to be filled, and this may promote growth at the unpassivated ends in order to reduce the overall surface energy of the crystal.

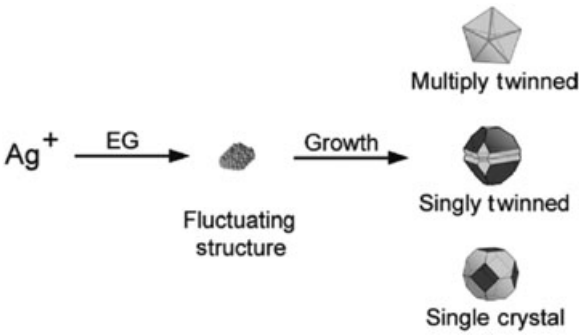

Figure 3.10 Reduction of Ag^+ by ethylene glycol produces small nuclei. The structure of these nuclei can fluctuate due to the thermal energy available. As the nuclei grow they become stuck in a given morphology (i.e. single crystal, single or multiply twinned) which then grow into nanostructures with different morphologies. Reprinted with permission from Ref. [85]; © 2005 The American Chemical Society.

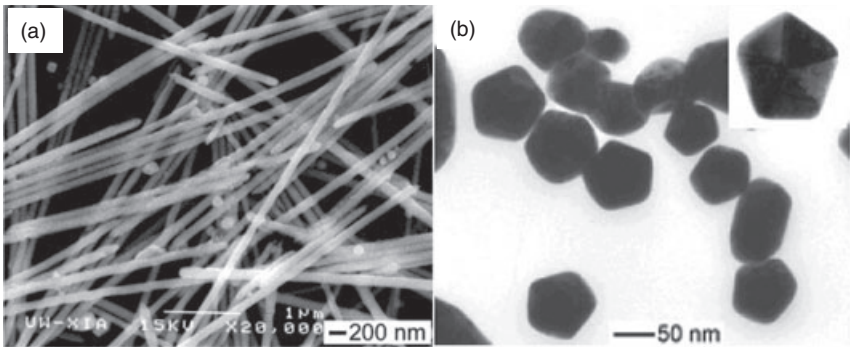

Figure 3.11 (a) SEM image of silver nanowires; (b) TEM image from microtomed sample. Adapted with permission from Ref. [87]; © 2003 The American Chemical Society.

As mentioned above, it was found that silver nanowires could be produced by the polyol process in the presence of platinum seeds. In a recent report by Tsuji *et al.*, using Pt seeds, the polyol method was carried out under microwave irradiation instead of reflux conditions [88]. Although the product of this reaction was a mixture of both 1-D nanorods and wires and 3-D spherical and triangular–bipyramidal particles, the reaction time was considerably shorter, taking just minutes, and the 1-D and 3-D structures could be easily separated by centrifugation. The final morphology of particles produced was found to depend on various parameters, including the concentrations of reactants and heating time. Interestingly, it was also found that 1-D structures were favored when PVP of molar mass ca. 360 000 Da was used.

The addition of trace amounts of salts to the polyol synthesis has also been shown to influence the morphology of the resultant particles. For example, when $Fe(acac)_3$ and $Fe(NO_3)_3$ were added to the synthesis, they were seen to facilitate the formation of silver nanowires [89]. It was deduced that the Fe(II)—either when added directly to the preparation or when resulting from the reduction of Fe(III) by EG—acted as an efficient oxygen scavenger, preventing the etching of the multiply twinned particles by atomic oxygen and thus favoring the production of silver nanowires (see Figure 3.12). It was proposed that the higher number of defects on the surface of twinned particles led to their greater activity for oxidative etching. In a similar manner, CuCl and $CuCl_2$ were found to facilitate the formation of nanowires [90]. However, in this case both the chloride anion and copper cation were found necessary for a successful formation of the wires, whereas the role of the counterion (be it nitrate or acac) in the Fe case discussed above was found to be negligible. The Cu(I) acts in a similar manner to the Fe(II), as an oxygen scavenger, while the chloride ion helps to reduce the initial concentration of Ag(I), effectively acting as a sink and controlling the rate of release of Ag(I), thereby promoting the formation of the more stable multiply twinned seed particles.

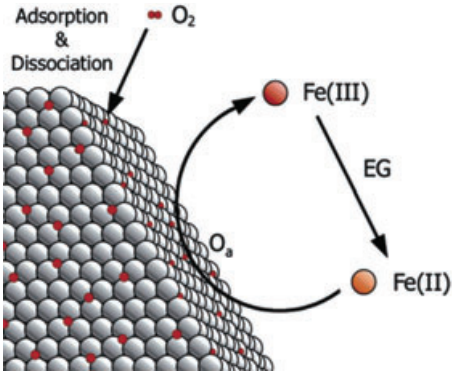

Figure 3.12 Schematic illustration depicting the role of Fe(II) salts in the growth of Ag nanowires. The Fe(II) scavenges the molecular oxygen that can adsorb on the silver seeds, thus preventing growth. Reduction by ethylene glycol competes with oxidation by atomic oxygen, setting up an equilibrium between Fe(III) and Fe(II). Reprinted with permission from Ref. [89]; © 2005 The American Chemical Society.

Studies performed by Chen *et al.* also highlighted the role of additives in the polyol process [91]. Here, silver nanowires with adjustable diameters were synthesized by introducing certain control agents into the conventional polyol process. The control agents were classified into three groups: inorganic anions, metal cations and molecules, and the authors presumed that these species influenced the size of the initial seed either by forming silver salt colloids, or by varying the rate of silver ion reduction.

In another variation on the polyol process, Zhang *et al.* recently described a steel-assisted method for the production of silver nanowires [92]. It was proposed that the *in situ* acidic etching of multiply twinned particles by nitric acid was one of the most harmful factors affecting the preparation of silver nanowires by the polyol process. As shown in Figure 3.13, by including the steel pieces in the synthesis, the nitric acid generated *in situ* is decomposed; consequently, the multiply twinned seed particles are not etched and the yield of nanowires is increased.

In order to investigate the nature of the interaction of PVP with nanowires and rods, the nanowires were incubated first in a dilute solution of 1,12-dodecanedithiol for 1 h, and then with gold nanoparticles (prepared by the Turkevich method) for 10 h [87]. The dithiol molecules allowed the gold nanoparticles to attach to the surface of the Ag nanowires, whereupon the latter were found to be decorated with the Au nanoparticles only on their ends, but not on their sides; this suggested that the PVP interacted more strongly with the {100} facets [93] than with the {111} facets. Further investigations were carried out by other groups using FT-Raman spectroscopy, X-ray photoelectron spectroscopy (XPS) and thermogravimetric analysis (TGA) to elucidate the spatial conformation of the PVP molecules on the surface of the nanowires [93, 94]. The results indicated that the one monolayer of PVP was probably adsorbed onto the surface of the nanowire

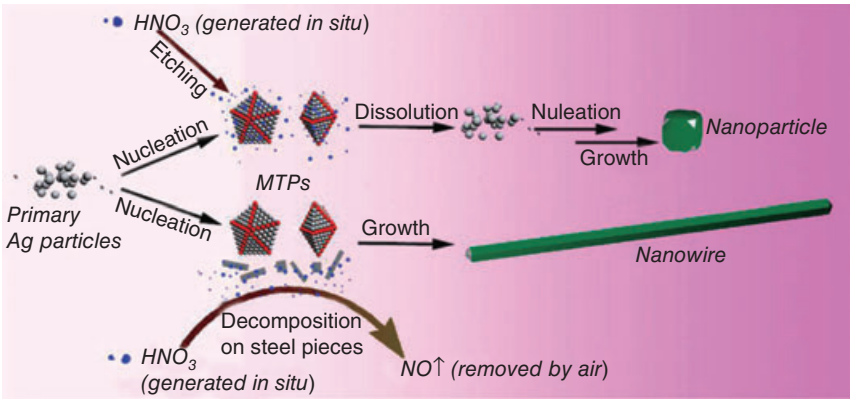

Figure 3.13 Schematic detailing the proposed steel-assisted polyol mechanism. MTPs = multiply twinned particles. Reprinted with permission from Ref. [92]; © 2008 The American Chemical Society.

through an Ag–O coordination. The results from SERS indicated that the skeletal chain of the PVP was lying on the surface of the nanowire, while the pyrrolidone ring might have been tilted on the surface of the Ag nanowire.

3.4.2 Cubes

3.4.2.1 Aqueous Surfactant-Based Methods

To the best of our knowledge, only one aqueous synthesis of silver nanocubes has been reported in the literature [95], and this involves the reduction of Ag^+ with glucose in the presence of CTAB. The reaction occurs in one pot, and there is no separate seeding step. CTAB is the key ingredient in this procedure, as the final morphology of the particles is heavily dependent on the CTAB : Ag^+ ratio. In this reaction it is proposed that first, the bromide ion (from the CTAB) combines with the silver ion to produce AgBr, and this then effectively acts as a reservoir for Ag^+, maintaining a low concentration in solution. Second, the CTAB stabilizes the higher-energy {100} faces (similar to the way that PVP does in the polyol synthesis of silver nanowires). Finally, the CTAB stabilizes the prepared nanocubes and prevents their agglomeration.

3.4.2.2 Organic Polyol-Based Methods

As in the synthesis of nanowires, the key to producing highly monodisperse nanocubes is to control the structure of the seed particles during the initial nucleation stage of growth. As mentioned in Section 3.4.1.2, the polyol process results in a distribution of multiply twinned, singly twinned and single crystal seeds being formed. When trace amounts of salts are added to this process, the structure of

the seeds can be controlled [13, 86, 89, 96–100]; as an example, silver nanocubes resulting from the addition of Na_2S to the polyol synthesis are shown in Figure 3.14. Twinned particles are more active towards oxidative etching due to the greater density of surface defects present [99]. These particles are dissolved and a situation develops where this oxidative etching competes with the reduction of Ag^+ by the EG; as a consequence this competing reaction slows the rate of nucleation, favoring the formation of single crystal seeds.

The single-crystal seeds have a cubo-octahedral geometry, which means they consist of a mixture of {111} and {100} faces. The higher-energy {100} faces are stabilized by the preferential binding of PVP to them, promoting growth on the {111} faces [101]. Again, the structure of the initial seed, as well as the presence of an organic species capable of specifically binding to one face, is of vital importance. The PVP here is acting in a similar manner to when it is used to prepare silver nanowires. The cubo-octahedral seeds will not grow to form 1-D structures under the same conditions, however, and herein lies the difference between the two polyol procedures.

The final morphology of the cubes produced – that is, whether they are truncated, or not – depends on the kinetics of the reduction process [13]. Sharp cubes are formed when the reduction rate is relatively fast, these cubes being bounded almost entirely by {100} facets and being the most kinetically favored shape. When the reduction rate is reduced, truncated cubes are the dominant product; these take longer to form because time is required for any surface reconstruction to occur. The driving force behind surface reconstruction is the need to reduce the surface coverage of the high-energy {100} faces by replacing them with the lowest-energy {111} facets on the corners. These truncated cubes are the most thermodynamically favored shape.

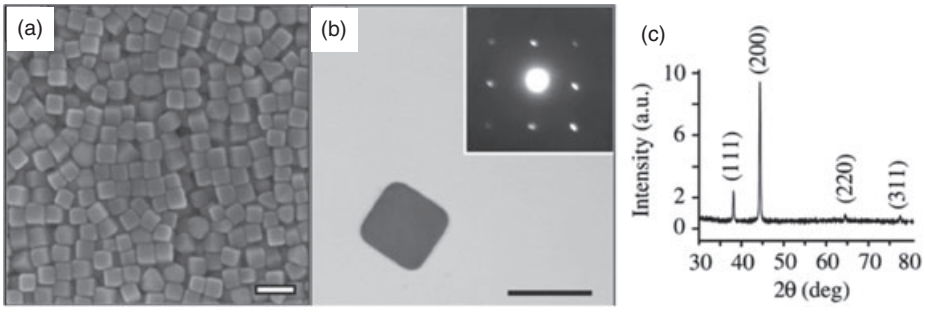

Figure 3.14 (a) SEM image of silver nanocubes resulting from the addition of Na_2S to the polyol synthesis (scale bar 100 nm); (b) TEM image of a single nanocube. Inset is the electron diffraction pattern indicating that the cube is a single crystal bounded by the {100} facet (scale bar 50 nm); (c) XRD pattern taken from the same batch of silver nanocubes. All peaks can be indexed to face-centered cubic (fcc) silver, and the abnormal ratio of (200) peak to (111) peak can be ascribed to the texturing effect of these nanocubes on a flat substrate. Adapted with permission from Ref. [96]; © 2006 Elsevier.

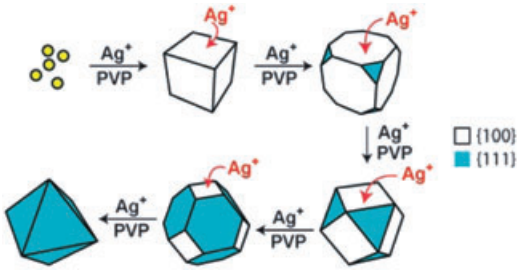

Figure 3.15 Schematic depicting the nucleation and growth process of polyhedral nanoparticles. Reprinted with permission from Ref. [102]; © 2000 Wiley-VCH Verlag GmbH & Co. KGaA.

In a modification of the synthetic procedure described above, Tao *et al.* reported a procedure in which nanocrystals with regular polyhedral shapes, bounded entirely by either the {100} or {111} facets, were produced [102]. In this case the metal salt was reduced by a diol solvent at near-reflux temperatures in the presence of PVP. By extending the polyol reaction for a given period of time, it was possible to obtain cubes, truncated cubes, cubo-octahedra, truncated octahedra and octahedra in high yield, as shown in Figure 3.15. It should be mentioned here that the authors stated that the stability of both {100} and {111} planes in the presence of PVP, especially for the cubo-octahedral and octahedral particles, indicated that shape control may not be explicitly dictated by the capping polymer. Rather, preferential growth would be favored by a kinetically limited equilibrium influenced by the reaction conditions.

3.4.3 Other Morphologies Prepared by the Polyol Process

3.4.3.1 Right Bipyramids

This novel type of nanostructure (see Figure 3.16) consists of two right tetrahedra placed base-to-base, and is formed from seeds with a single twin. In order to selectively produce seeds with a single twin plane, the extent of etching is controlled. In fact, the only difference between the synthesis of these right bipyramids and those that produce wires and cubes (as discussed above) is the incorporation of Br^- instead of Cl^- or Fe^{3+}. As Br^- is less corrosive than Cl^-, there is enough etching to remove the multiply twinned seeds, while those containing only a single twin remain intact; growth then continues as with the previous nanostructures. The PVP binds preferentially to the {100} surfaces, thus promoting growth on the {111} faces. The presence of the single twin plane is significant because it is the only factor that differentiates the bipyramid synthesis from that of the nanocube [103].

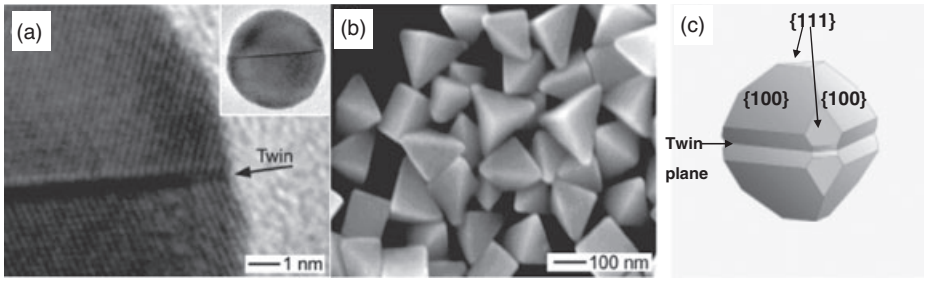

Figure 3.16 (a) High-resolution TEM image of twinned seeds, with the twin plane indicated by the arrow. Inset: TEM image of a twinned seed with the twin plane clearly visible; (b) SEM image of bipyramids; (c) Model of the seed shown in (a); truncation of the corners is clearly seen, as are the re-entrant {111} surfaces at the twin boundary and the re-entrant {100} surfaces at the twin boundary corners. Panels (a) and (b, c) adapted with permission from Refs [13] and [103], respectively; © 2006 The American Chemical Society.

3.4.3.2 **Nanobeams**

Single twinned crystals can also be grown into nanobeams. This type of silver nanostructure (see Figure 3.17) is so named because it has a cross-sectional aspect ratio similar to that of a beam of wood [104]. The synthesis of nanobeams is very similar to that of the right bipyramids described in Section 3.4.3.1; by decreasing the rate of addition of silver atoms to the single crystal seeds, nanobeams are produced. Although the growth mechanism of these nanostructures is not fully understood, it is proposed that defects at the twin boundary provide favorable sites for atomic addition. If there were to be a greater density of defects on one side of the seed particle, then beams could be produced.

3.4.3.3 **Nanobars and Nanorice**

The final type of nanostructure that can be prepared by the polyol synthesis to date is nanobars (see Figure 3.18). Unlike rods, nanobars are single crystals bounded by the {100} facets; in essence, they are elongated cubes displaying the sharp corners and edges of a cube. Nanobars are produced by increasing the concentration of Br^- added to the synthesis. The question as to how the single crystal seeds grow anisotropically has not been answered fully, though it has been suggested that all multiply twinned and single twinned crystals are etched away by the Br^- [105]. In addition to promoting production of the single-crystal seeds, oxidative etching could cause anisotropic growth if it were to remove material from one side of the seed more than from the other sides. It is also possible that AgBr is formed due to the increased concentration of Br^-, and that this has a critical effect on the growth, as has been suggested in the growth of silver nanoplates. In a post-synthesis step the corners and edges of the nanobars can be rounded to transform them into nanorice, by immersing them in a solution of PVP.

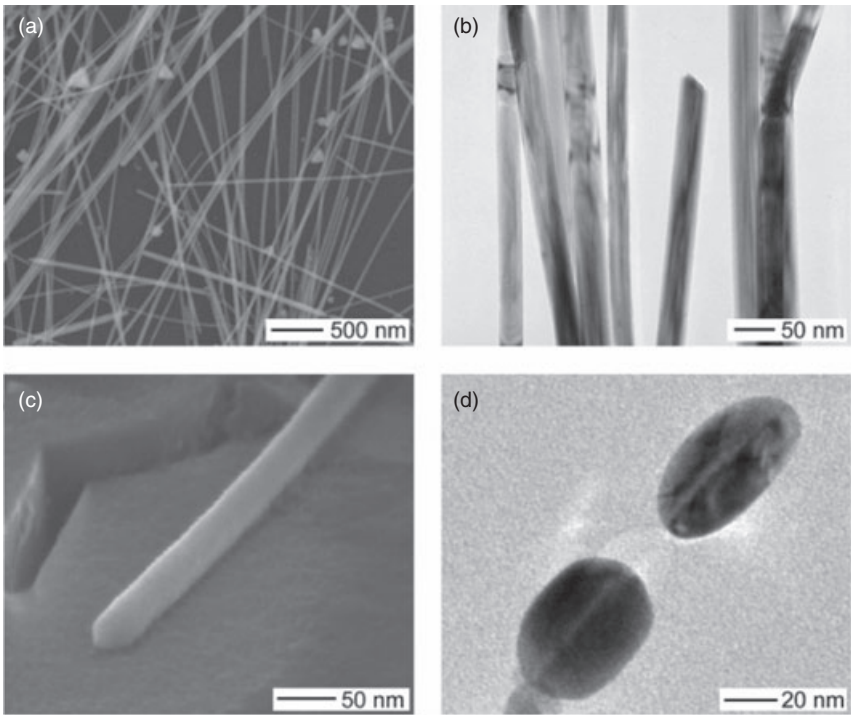

Figure 3.17 (a) SEM image and (b) TEM image of silver nanobeams; (c) SEM image of a nanobeam recorded at a 60° tilt, where the rounded tip can be clearly seen; (d) TEM image of a microtomed sample where the ellipsoidal cross-section bisected by a twin plane can be seen. Reprinted with permission from Ref. [104]; © 2006 The American Chemical Society.

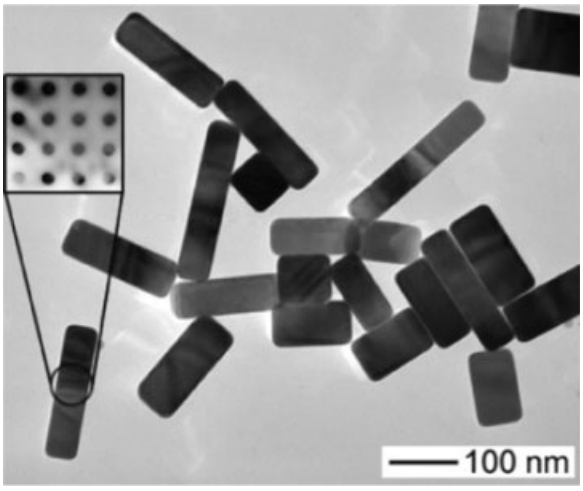

Figure 3.18 TEM image of silver nanobars. The inset includes the convergent beam electron diffraction pattern which indicates that the nanobars are single-crystal bounded by (100) facets. Reprinted with permission from Ref. [105]; © 2007 The American Chemical Society.

3.4.4 Nanoplates and Nanoprisms

Nanoplates, a term which includes nanodisks and nanoprisms, are a classification of material in which the lateral dimensions are larger than the height. Nanoprisms, which usually have an equilateral triangle shape, have in recent years received considerable attention due to the ability to tune the position of the in-plane dipole SPR across the entire visible spectrum and into the near-infrared region, by controlling the edge length and thickness.

In general, the synthetic approaches used to prepared silver nanoplates can be split into two categories – photochemical and thermal – with both procedures having associated advantages and disadvantages. Although the photochemical methods are used to prepare probably the most monodisperse, highest quality samples, the process usually requires days for completion. In contrast, thermal methods are rapid but often produce samples with a large range of shapes and sizes.

3.4.4.1 Photochemical Methods

The first report of the photochemical preparation of silver nanoprisms, which was published in 2001, consisted of a photoinduced method for converting large quantities of silver nanospheres into triangular nanoprisms on exposure to a white light source [106]. The method consists of photoconverting citrate-capped Ag spherical nanoparticles (<10 nm) into larger triangular particles (edge length ~100 nm) through irradiation of the small seeds with visible light in the presence of bis(p-sulfonatophenyl)phenylphosphine dihydrate dipotassium salt) (BSPP). The exact mechanism remains a subject of some controversy; initially, it was suggested that the BSPP played an important part in a two-step process, where the initial Ag seeds were converted into small clusters concurrent with the formation of small nanoprisms. The small nanoprisms then grew at the expense of the small clusters through a light-induced Ostwald ripening process. When all of the spherical particles and small nanoclusters had been consumed, the reaction was terminated. However, the presence of BSPP was found not to be vital since, when it was replaced by PVP, similar results were obtained. Further to this, Sun and Xia claimed that it is in fact the presence of citrate ions that promote this morphological evolution [107].

A deeper understanding of this process was gained through subsequent experiments carried out by Jin *et al.* using narrow band light sources [108]. Here, it was found that the excitation wavelength controlled the particle size so that, when longer wavelengths were used, particles with a larger edge length were produced. In these studies a dual-beam illumination was used since, when excitation with a single wavelength was carried out a bimodal distribution of nanoprism size was produced (types 1 and 2 nanoprisms). These two types of nanoprism are shown schematically in Figure 3.19. This situation also arises when an inappropriate secondary beam was chosen. The observed bimodal growth process was seen to occur through an edge-selective nanoprism fusion mechanism, with four type 1

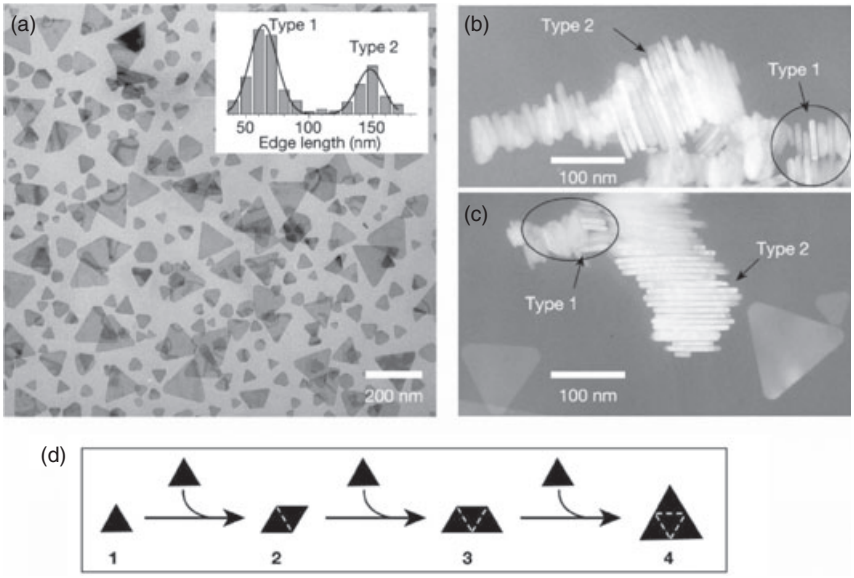

Figure 3.19 Bimodal growth. (a) TEM image of Ag nanoprisms formed by single-beam excitation; (b, c) SEM images of stacked type 1 and type 2 nanoprisms. Note that the thicknesses are almost identical; (d) Schematic illustrating the fusion process. Reprinted with permission from Ref. [108]; © 2003 MacMillan Publishers Ltd.

nanoprisms coming together in a step-wise fashion to form a type 2 nanoprism (see Figure 3.19d). When excitation of the samples with a secondary light source (corresponding to λ_{max} of the in-plane or out-of-plane quadrupole SPR) was carried out, nanoprism fusion was suppressed and only a unimodal growth process was observed. As shown in Figure 3.20, nanoprisms with a monodisperse size distribution are produced. Recently, the same group has reported that this process can be controlled by adjusting the pH [109].

The suggested growth mechanism for the photoconversion process is that the secondary beam excitation suppresses the fusion of preformed type 1 nanoprisms, by inducing charge redistribution on the particles surface caused by the excitation of the dipole plasmon. (It was also suggested that plasmon excitation could facilitate ligand dissociation at the particle edges where the local fields are the most intense, allowing type 1 prisms to grow.) It is therefore easy to see how this nanoprism fusion process might also be controlled by pH, in that electrostatic repulsive forces encountered by the nanoprisms may be tuned by varying the pH.

Another mechanism for the photoconversion of spherical seed particles into nanoprisms has been proposed by Callegari *et al.* [110]. In this case, a two-step irradiation process is involved whereby initially, the seed particles are irradiated by a conventional fluorescent tube for 1 h. Different illumination conditions are

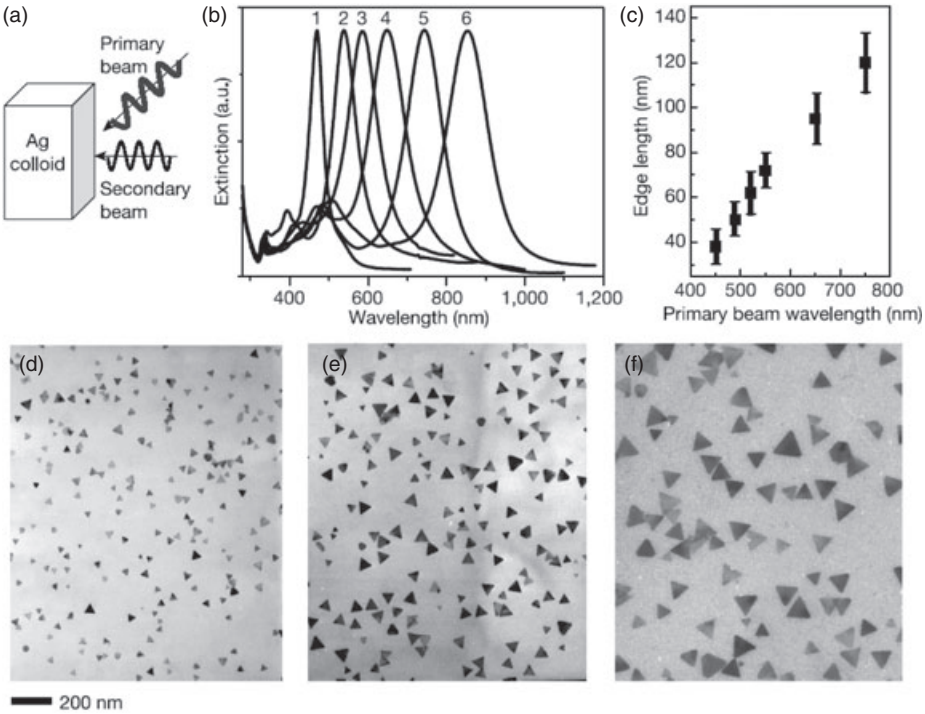

Figure 3.20 Unimodal growth. (a) A schematic of the experimental set-up; (b) Extinction spectra of nanoprisms with different edge lengths prepared by varying the primary excitation wavelength while keeping the secondary excitation wavelength constant; (c) Variation of edge length with primary beam excitation wavelength; (d–f) TEM images of different-sized nanoprisms prepared by varying the primary beam excitation wavelength. Reprinted with permission from Ref. [108]; © 2003 MacMillan Publishers Ltd.

then assigned by fitting colored glass filters in front of the fluorescent tube. According to this mechanism, in the initial irradiation period large spherical particles are formed by the aggregation of smaller seed particles, when the excess borohydride present is photo-oxidized, creating weak attractive forces around the Ag seeds. In the second irradiation period, light induces coalescence of these loose aggregates into solid particles, with subsequent growth. The transformation from aggregated to solid particles functions by excitation of the SPR, with the illumination conditions determining the final size of the nanoprisms.

Recently, Bastys *et al.* used light-emitting diode (LED) illumination to prepare silver nanoprisms with high absorption coefficients well within the near-infrared red region (see Figure 3.21) [111]. Similar to previous studies, the illumination wavelength was observed to determine the particle edge length. The mechanism proposed differed to those discussed above, in that although the Ag nanoprisms were formed via the consumption of seed particles, Ostwald ripening was not

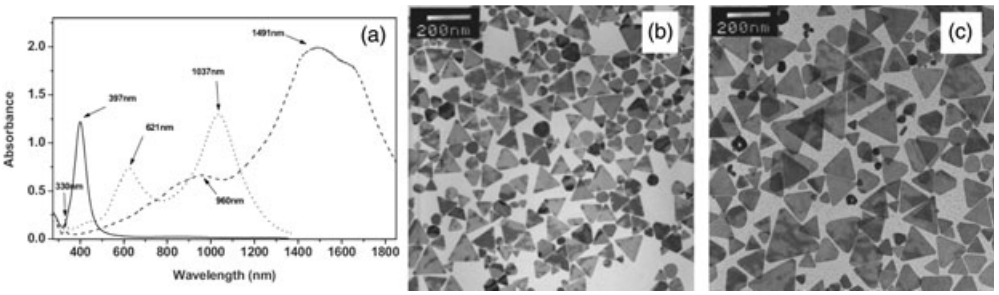

Figure 3.21 (a) UV-visible-NIR spectra of seeds; $\lambda_{max} = 397$ nm, nanoprisms grown with red ($\lambda_{max} = 1037$ nm) and green ($\lambda_{max} = 1491$ nm) LEDs in H_2O and D_2O, respectively. (b, c) TEM images of nanoprisms grown with red (b) and green (c) LED illumination. Reprinted with permission from Ref. [111]; © 2006 Wiley-VCH Verlag GmbH & Co. KGaA.

thought to play a role as no incomplete triangular plates were evident during the growth process. The type 1/type 2 nanoprism fusion mechanism was also ruled out, as a subsequent TEM analysis did not reveal the presence of any dimer or trimer intermediates.

In another plasmon-driven synthesis developed by Xue *et al.*, triangular core-shell nanoprisms were produced from gold seeds [112]. In a typical experiment, spherical gold and silver nanoparticles with diameters of 11 and 5 nm, respectively, were mixed together and irradiated with 550 nm light. A TEM analysis revealed that the resultant product consisted of nanostructures with a single gold particle core that had triangular sliver shells with average edge length ~70 nm (see Figure 3.22). During the initial irradiation period, the Au seeds were coated with silver shells of irregular shapes, but after an increased irradiation time the shells developed a triangular shape. As discussed above, the edge-length of the hybrid nanostructure is determined by the excitation wavelength, and growth stops when the dipole plasmon resonance becomes red-shifted with respect to the plasmon excitation.

A recent report by An *et al.* described the photoinduced shape evolution of triangular nanoplates to hexagonal nanoplates [113]. In this study, citrate-stabilized silver seeds were irradiated with a conventional 70 W sodium lamp; this caused the initial silver seeds to be first converted into triangular silver nanoplates (type 1) with an average edge length of 76 nm. Some small silver nanoparticles (~8 nm) were also present. On further irradiation, the type 1 particles evolved to a hexagonal shape, with a concurrent decrease in diameter and shape change of the small spherical particles to disks. The hexagonal plates then had an edge-length of 26 nm, while the disks had a diameter of 11 nm. The mechanism of formation of the triangular nanoplates suggested here is thought to be similar to that described in Refs [104] and [108], although a detailed understanding of the truncation process was not provided.

An alternative light-induced method for Ag nanoprism formation is that of photoinduced growth. The difference between this method and those described

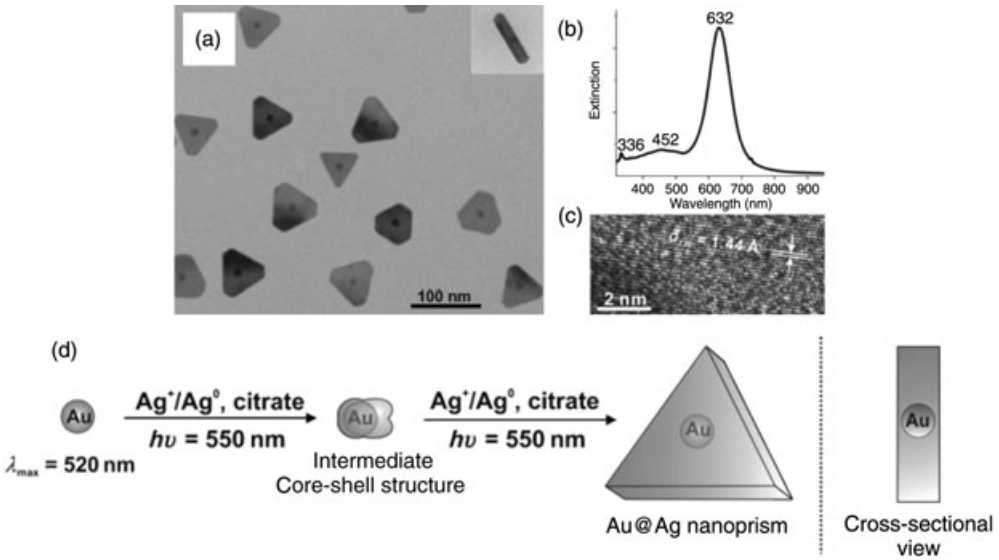

Figure 3.22 (a) TEM image of silver nanoprisms with gold cores prepared with 550 nm excitation. The inset includes a side view of the Au@Ag nanoprism; (b) Extinction spectrum of Au@Ag nanoprisms; (c) A high-resolution TEM image of the [111] face of the Au@Ag core-shell nanoprisms. The hexagonal lattice shows a spacing of 1.44 Å, indexed as {220} of fcc Ag; (d) Schematic illustrating the proposed growth mechanism. Reprinted with permission from Ref. [112]; © 2007 Wiley-VCH Verlag GmbH & Co. KGaA.

above is that the seeds are irradiated in the presence of additional Ag ions and trisodium citrate. In this method, which was devised by Maillard *et al.* [114], the proposed mechanism is as follows. At the start of the reaction the seeds absorb light isotropically and, as a degree of inhomogeneity occurs in the deposited silver layer, the particle begins to become ellipsoidal and the plasmon resonance splits in the longitudinal and transverse modes. It is assumed that reduced atoms are deposited in proportion to the near-field intensity enhancement at the surface position, while the longer axis grows preferentially. This process accelerates until the position of the longitudinal band shifts beyond the irradiation wavelength. A disk shape is produced because it is suggested that such a shape has a larger rotationally averaged absorption coefficient at the excitement wavelength than a rod. It is the concentration of silver ions that determines the final particle size, and not the excitation wavelength; however, the aspect ratio is determined by the irradiation wavelength. For a more in-depth analysis into this growth mechanism, the reader is directed to two recent reports by Rocha and coworkers [115, 116], in which the formation kinetics and the role of structural defects in the growth of silver nanoprisms are discussed. It is proposed here that, although SPR excitation plays an important role in determining the final edge-length of the nanoprisms, it is likely that a combination of suitable capping agents and the initial seed

nanoparticles' structure may be a crucial factor in determining the ultimate morphology of nanoparticles prepared by this method. This combination of capping agent and seed structure is further discussed in Section 3.4.4.2.

3.4.4.2 Thermal Methods

In a method similar to the polyol synthesis discussed earlier, one of the earliest approaches to successfully prepare silver nanoplates involved the reduction of silver nitrate by DMF in the presence of PVP under reflux [117]. The mechanism proposed by Liz-Marzan and coworkers involved the formation of small spheres which first aggregated and then, through a melting process, recrystallized into particles with well-defined edges. A similar approach was used by Jiang *et al.*, except that the reaction was exposed to high-intensity ultrasound irradiation instead of reflux conditions [118]. Seeds formed in the initial stage of the reaction quickly grew into larger crystals via Ostwald ripening. The presence of PVP is reported to be a key factor in the growth of silver nanoplates through a selective adsorption/desorption process. Such preparations usually result in a mixture of shapes being prepared, but these can be separated by careful centrifugation. More recently, Yang *et al.* reported that control of the molar ratio of silver ion to PVP can increase the percentage of one particular shape, and in the case of triangular plates a yield of 95% was reported [119]. The silver ions were first reduced into small Ag seeds, which then grew into circular, then hexagonal, and finally triangular plates, in the presence of PVP.

Xiong *et al.* have reported a method in which the polyol method described above was directly modified to prepare Ag nanoplates instead of nanowires [120]. In this procedure, silver ions are reduced by EG when the PVP is replaced by poly(acrylamide) (PAM). In this protocol, the PAM has a dual role as it can act as a steric stabilizer, protecting the particles from aggregation, while also complexing the silver ions through its amido group. This coordination effect serves to significantly reduce the rate of reaction, thereby dictating the end shape of the nanoparticles by kinetic means.

Although the first reported method for the preparation of silver nanoplates was made by Jin *et al.* and involved a photochemical route (as discussed above), the first published report of a thermal method was by Chen and Carroll [121, 122]. This solution-phase method is based on the reduction of silver ions with ascorbic acid on silver seeds in the presence of an alkaline solution of highly concentrated CTAB. The end product of the synthesis was truncated triangles, which could be converted to circular disks through aging at higher temperatures. These authors further showed that, by adjusting the CTAB concentrations and silver seed amounts, the lateral dimensions of these nanoplates could systematically be controlled from 40 to 300 nm (see Figure 3.23) [123]. The growth mechanism suggested by the authors involved the selective adsorption of CTAB on the (111) plane of the silver seeds, along with the formation of silver bromide on the seed particles. Although the exact mechanism was unclear, it had been suggested earlier (see Section 3.4.1.1) that, in the case of nanorods and wires, the CTAB would be selectively adsorbed onto the {100} crystal faces, thus promoting growth in the ⟨111⟩

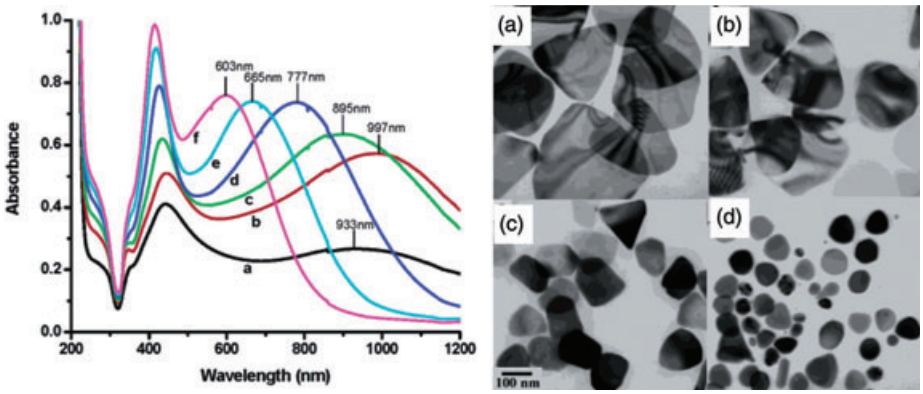

Figure 3.23 Left: UV-visible-NIR absorption spectra of nanoplates prepared by varying the concentration of seed added: (a) 0.1 ml, (b) 0.25 ml, (c) 0.5 ml, (d) 1 ml, (e) 2 ml, (f) 3 ml. Right: TEM images of sols (a) to (d). Reprinted with permission from Ref. [123]; © 2004 The American Chemical Society.

direction, and contradicting the growth mechanism suggested for the case of nanoprisms.

Another group employing surfactant-based methods was that of Pileni and colleagues [124]. In this case, truncated silver nanoplates were produced by the sonication of two reverse micellar solutions consisting of silver di(2-ethyl-hexyl)sulfosuccinate (Ag(AOT)) and sodium di(2-ethyl-hexyl)sulfosuccinate (Na(AOT)) isooctane with Na(AOT) and hydrazine. The nanoplate size could be tuned by the amount of reducing agent added during the synthesis.

In the above two syntheses, the particular products obtained were characterized as having a wide size and shape distribution, and also a low surface-to-volume ratio. Studies conducted by Jiang *et al.* [125], which involved a self-seeding coreduction method in the presence of NaAOT, witnessed an improvement in the quality of the triangular nanoplates – and hence of the circular nanodisks produced. Trace sodium borohydride was injected rapidly into a solution containing silver nitrate, ascorbic acid and citric acid, and this resulted in the formation of a short burst of nuclei. Subsequent particle growth was then achieved by a combined reduction by the citric and ascorbic acids, after which the silver nanocrystal then developed facets and grew into the desired shape, stabilized by the NaAOT through an Ostwald ripening process. It was predicted (by using molecular dynamic simulations) that the NaAOT molecules would be more apt to bind at the {111} plane, and this would lead to preferential growth of the other crystalline faces. The morphology of the particles was seen to change upon aging such that, after 100 h, the dominant product was circular nanodisks. This morphological evolution is shown in Figure 3.24. Although the exact mechanism of this transformation is not completely understood, the authors suggested that the small difference in interaction

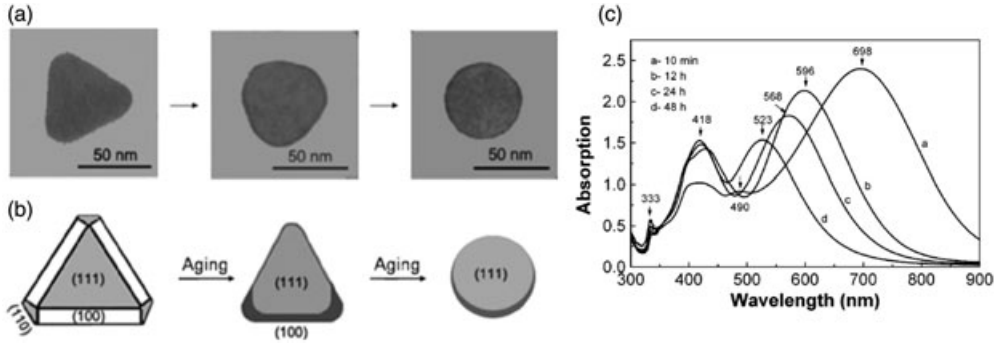

Figure 3.24 (a, b) TEM images and illustrations showing the truncation procedure with time; (c) UV-visible absorption spectra of sol with time, showing the blue-shift of the in-plane dipole, consistent with truncation of the sharp nanoprisms. Reprinted with permission from Ref. [126]; © 2007 Wiley-VCH Verlag GmbH & Co. KGaA.

energies between AOT-Ag{110} and AOT-Ag{100} might result in a possible atom migration with a reduction in the total surface free energy. In a later report, the same authors described a method for stopping this morphological change by using thiols [126]. Here, thiols such as 1-hexanethiol, 1-octanethiol, 1-dodecanthiol and 1-hexadecanethiol were shown (by molecular dynamic simulations) to exhibit larger interaction energies than AOT on the silver atomic surfaces and hence prevent the proposed atomic migration, thereby freezing the shape evolution.

The group of Xia have also prepared triangular nanoplates by using a thermal process [127]. Here, small-seed silver nanoparticles prepared by the reduction of silver nitrate by sodium borohydride in the presence of both trisodium citrate and PVP were refluxed in aqueous solution, under ambient conditions, instead of undergoing irradiation. After 10 h the predominant product was triangular nanoplates, with approximately 5% wire-like nanostructures present. Although the exact mechanism of this transformation process is not fully understood, it is thought that the thermal treatment provided a mild driving force to facilitate the transport of atoms from the spherical colloids to the anisotropic plates in a process similar to Ostwald ripening. A similar method involving photoconversion was also reported by the same group [107], but on this occasion the presence of citrate was found to be crucial to this transformation process, possibly by preferential binding to the {111} planes, while the PVP served only as a particle stabilizer.

The same group have also prepared silver nanoplates with PVP playing a dual role as both reductant and stabilizer [25, 128]. When silver nitrate and PVP were heated together in a capped vial to 60 °C, the hydroxyl end groups of commercially available PVP reduced the silver nitrate at a slow enough rate so as to promote the growth of triangular plates, which are the kinetically favored product. The edge length of the plates could be controlled by adjusting the reaction time. Unlike the

reflux method described above, light was found to have a negligible effect, and the presence of citrate was not vital for the production of nanoplates. This approach has been successfully adapted to prepare nanoplates of other noble metals such as gold, platinum and palladium.

In a recent report, the Xia group also suggested another mechanism for the formation of these triangular plates [129]. Trimeric silver clusters, which are a common species in silver nitrate solutions, act as nucleation sites for the addition of the newly reduced silver atoms. Mass spectrometry was used to identify the presence of silver clusters. It is worthy of mention at this point that the authors emphasized that the end morphology of a nanocrystal is determined by the interplay of many parameters, all of which must be considered before an appropriate growth mechanism can be proposed.

The Mirkin group have developed a procedure for the production of triangular nanoplates in excellent yield through a solely thermal process [130]. In a typical experiment, silver nitrate, trisodium citrate, PVP and H_2O_2 were combined with sodium borohydride. The small nanoparticles formed initially (indicated by the presence of a pale yellow color) were transformed into nanoprisms (indicated by a vivid blue color) over a 30-min period. The advantage of this procedure over other procedures is that it provides control (albeit limited) over the thickness of the nanoprism. This decrease in nanoprism thickness can be seen in the TEM images in Figure 3.25. The concentration of sodium borohydride used controls not only the edge length of the particles but also their thickness. Again, similar to other procedures discussed above, the presence of citrate was found to be crucial to this transformation process, while the PVP served only as a stabilizer.

Other aqueous procedures that produce nanoprisms with reasonable control over the size are discussed below. Zou and Dong's procedure involves the reduction of silver nitrate by hydrazine in the presence of seed particles and trisodium citrate [6]. The size of the nanoplates is simply controlled by adjusting the concentration of seed particles used – that is, larger nanoplates can be produced when a

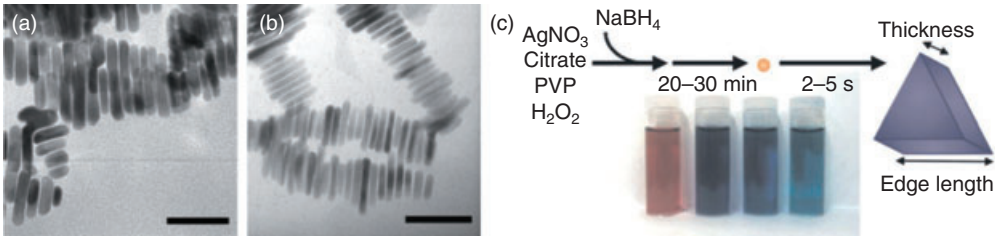

Figure 3.25 TEM images of nanoprisms prepared with (a) 0.3 m*M* and (b) 0.8 m*M* $NaBH_4$, showing decreasing nanoprism thickness with increasing $NaBH_4$ concentration; (c) Schematic detailing the preparation of silver nanoprisms. The inset shows solutions of nanoprisms prepared with (from left to right) 0.3 m*M*, 0.5 m*M*, 0.67 m*M* and 0.8 m*M* $NaBH_4$. Reprinted with permission from Ref. [130]; © 2005 Wiley-VCH Verlag GmbH & Co. KGaA.

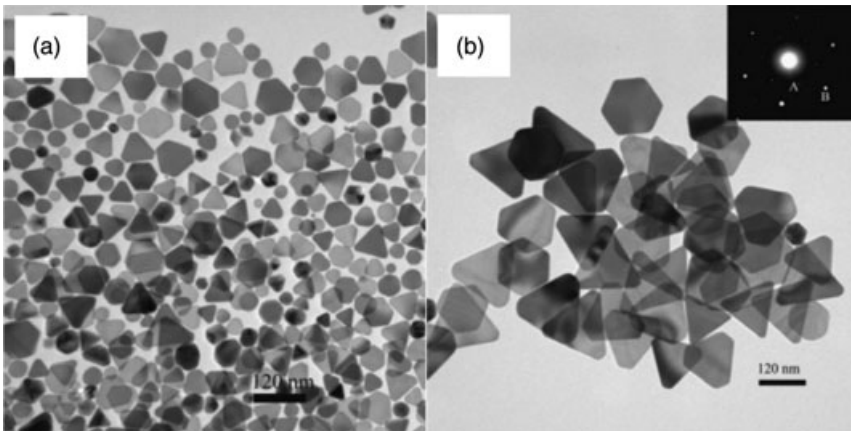

Figure 3.26 (a, b) TEM images of silver nanoplates prepared by Zou and Dong, where the nanoplates in (a) were prepared with a larger volume of seed particles; the resultant particles are therefore smaller. Reprinted with permission from Ref. [6]; © 2006 The American Chemical Society.

smaller number of seeds are used. As can be seen in Figure 3.26, the particles shown in image (b) were prepared with a smaller volume of seed particles and are therefore larger. The dominant morphologies present include truncated triangular, hexagonal and nanodisks.

Cao *et al*. have developed a method which involves reducing silver oxide with hydrazine in the presence of trisodium citrate and ethylenediaminetetra-acetic acid (EDTA) [131]. In this system, the citrate molecules serve only as colloid stabilizers, preventing aggregation, while the EDTA molecules complex with the silver ion and effectively act as a bank for the silver ions. The ratio of EDTA to silver ion, therefore significantly affects the rate of reaction, and the end particle morphology can be tuned as this chelation-mediated process offers kinetic control over the growth, with triangular particles being the favored product.

The Kelly group have developed a number of seed-mediated procedures for the growth of silver nanoplates. The first method involved the reduction of silver nitrate by ascorbic acid in the presence of seeds, followed by a seed-mediated reduction of silver nitrate by ascorbic acid in the presence of PVA [3]. The group's second method involved the reduction of silver nitrate by ascorbic acid in the presence of trisodium citrate and PVP [132]. In this case, the position of the in-plane dipole SPR could be tuned by varying the concentration of citrate present. The reaction was carried out at room temperature but interestingly, as the temperature was increased, the monodispersity and uniformity of the particles was also increased. Another procedure has also been developed within the group which involved the silver seed-catalyzed reduction of Ag^+ by ascorbic acid. Unlike the previous method, no additional citrate was required and the concentration of

spherical nanoparticles produced was minimal [133]. The nanoprisms were well-defined triangular plates, and the position of the in-plane dipole SPR could be tuned through the visible to the near-infrared simply by varying the concentration of seeds used (Figure 3.27). One important difference between the latter two reported procedures was the presence of a negatively charged polymer, poly(styrenesulfonate) sodium salt (PSSS), in the preparation of the seeds. Although the role that the PSSS played was not clear, its presence was crucial for the production of highly shaped, monodisperse triangular plates.

Recently, some procedures involving biomolecules have been reported to produce silver nanoplates. For example, Yang *et al.* used the small biomolecule glycylglycine to produce larger nanoplates (>100 nm) in a hydrothermal process [134]. For this, aqueous solutions of silver nitrate and glycylglycine were heated together to 160 °C for 24 h. The authors suggested that the biomolecule could adhere selectively to the {111} planes of the Ag crystal, thereby directing growth. Although the yield of nanoplates was lower (~80%) than in other reported procedures, the interest in this procedure lay in the ability of the biomolecule to direct growth. The authors also stated that other similar peptides such as alanylglycine could also be used to prepare such nanoplates.

Another recently published report described the synthesis of Ag nanoplates using proteins extracted from the unicellular green alga, *Chlorella vulgaris* [135]. Hydroxyl groups in tyrosine residues and carboxyl groups in aspartic acid and/or glutamic acid residues were further identified as the most active functional groups for the reduction of Ag ions, and for also directing the anisotropic growth of the nanoplates. A simple bifunctional peptide was designed which contained one tyrosine residue and two aspartic acid residues and which was able to produce

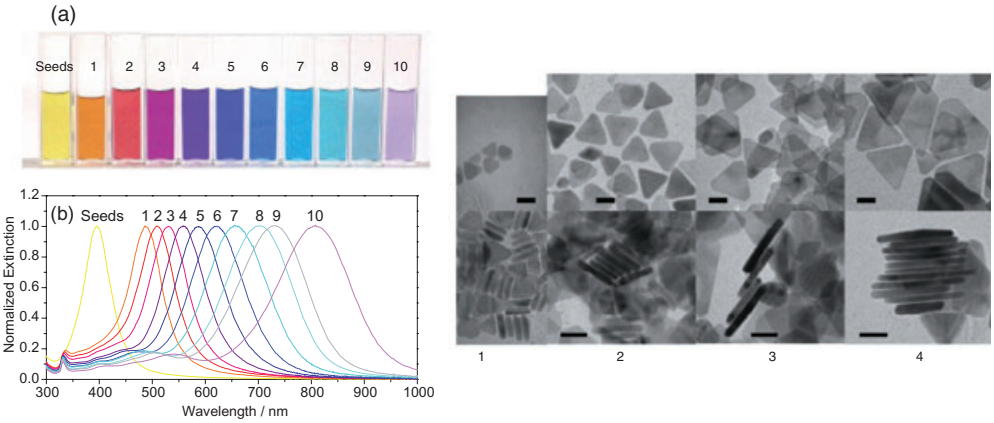

Figure 3.27 (a) Photograph of a series of nanoprisms obtained by varying the concentration of seeds used. (1) 650 µl, (2) 500 µl, (3) 400 µl, (4) 260 µl, (5) 200 µl, (6) 120 µl, (7) 90 µl, (8) 60 µl, (9) 40 µl, (10) 20 µl; (c) TEM images of flat-lying and stacked nanoprisms of increasing edge length but with a constant thickness (scale bar 20 nm). Reprinted with permission from Ref. [133]; © 2008 Wiley-VCH Verlag GmbH & Co. KGaA.

silver nanoplates in high yields. Similar to the case where the hydroxyl groups at the end of the PVP control the rate of reduction [25], the formation of nanoplates was found to be kinetically controlled. Again, the yield of nanoplates was lower than in other reported procedures; however, this was the first report of a biomolecule specifically designed to aid the production of silver nanoplates.

3.4.4.3 Physical Aspects

Based on the discussion of the previous section, it is clear that the theory of preferential adsorption of organic molecules such as polymers and surfactant onto specific crystal faces can result in a faster rate of addition of metal atoms to the more exposed faces, and therefore growth in a specific direction. This has recently been predicted computationally for the 1-D growth of gold nanorods [136]. However, it is also clear that the structure of the seed nanoparticles is of vital importance – that is, whether the seeds are single crystals or possess any twin planes. In the case of such structures as nanoplates and prisms, the growth mechanism cannot be adequately explained by the selective adsorption of molecules on certain crystallographic faces, and it is important to note that near-identical-shaped particles can be produced by very different methods. Also, if a specific molecule or surfactant were directing the growth of a given shape of nanoparticle, the presence of a sample containing a range of particle morphologies cannot be explained.

In order to propose any growth mechanism, it is of vital importance to understand the structure of the nanoparticles. Extensive characterization – some examples of which are shown in Figure 3.28 – has shown that the large flat faces of the silver nanoprisms consist of the {111} fcc planes. X-ray diffraction (XRD) patterns show a dominant sharp peak for {111}, indicating the presence of relatively large {111} planes in the sample. Electron diffraction patterns show spots corresponding to diffraction from the {220} and {422} planes of an fcc crystal. Also present are the signals arising from formally forbidden 1/3{422} reflections [82, 83, 106, 137, 138]. Lattice fringes associated with these forbidden reflections have also been seen in high-resolution (HR) TEM studies, as have lattice spacing from other crystallographic faces [111, 116, 119]. In summary, whilst the ⟨111⟩ orientation of silver nanoprisms is generally accepted, the identity of the crystal faces at the edge of the nanoplates has yet to be confirmed.

Since the growth of the nanoplates cannot be adequately explained by the surface binding model, recent reports have suggested that there might be an underlying defect structure in the seeds that is a direct factor influencing particle growth. Some theories associating this defect structure with the presence of the above-mentioned 'forbidden spots' have been proposed. Some authors state that the presence of these spots can be attributed to the presence of a local hexagonal-like structure, observed for silver structures that are atomically flat. Yet, others explain the presence of these diffraction spots by the presence of twin planes parallel to each other. In these two situations the presence of these defects or twin planes can also direct the growth of anisotropic plate-like nanoparticles.

In recent years, the silver halide model has been used to explain the growth of silver and gold nanoprisms in a manner analogous to the growth of silver halide

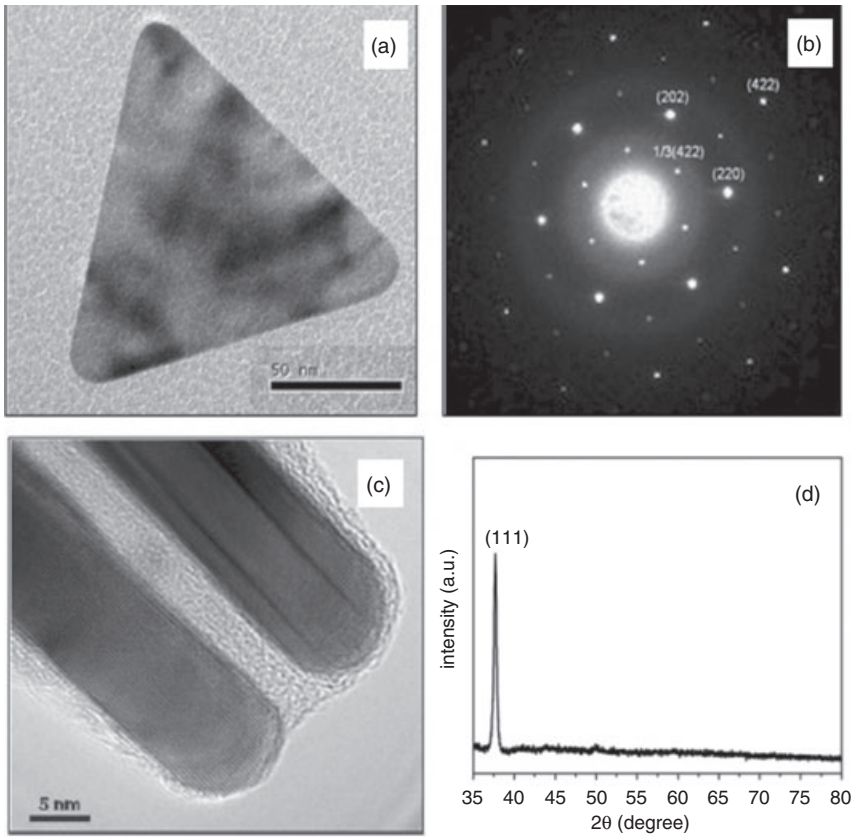

Figure 3.28 (a) TEM image of ⟨111⟩-oriented silver nanoprism; (b) Electron diffraction pattern of an individual silver nanoprism, showing the assigned reflection indices; (c) Edge-on view of silver nanoprisms; (d) Typical XRD pattern for a sample of nanoprisms. Panels (a–c) and panel (d) reprinted with permission from Refs [6] and [111], respectively; © 2006 The American Chemical Society. © 2006 Wiley-VCH Verlag GmbH & Co. KGaA.

plates [83]. In this model, the presence of twin planes parallel to the flat {111} face is used to explain the anisotropic growth of particles. These twin planes are formed readily in gold and silver systems, where the stacking fault energy is lower than in most metals, decreasing the energy required to form a twin plane. As shown in Figure 3.29, twin planes form re-entrant grooves which are favorable sites for the attachment of adatoms.

Stacking faults have also been used to explain the growth of silver nanoprisms [137]. The Pileni group have proposed that, when the ABCABCABC... stacking sequence of {111} layers, in an fcc structure, are disrupted by the removal of an A layer, there is a distortion in the stacking sequence. It is likely that the growth in parallel to the stacking fault plane is the fastest, and the existence

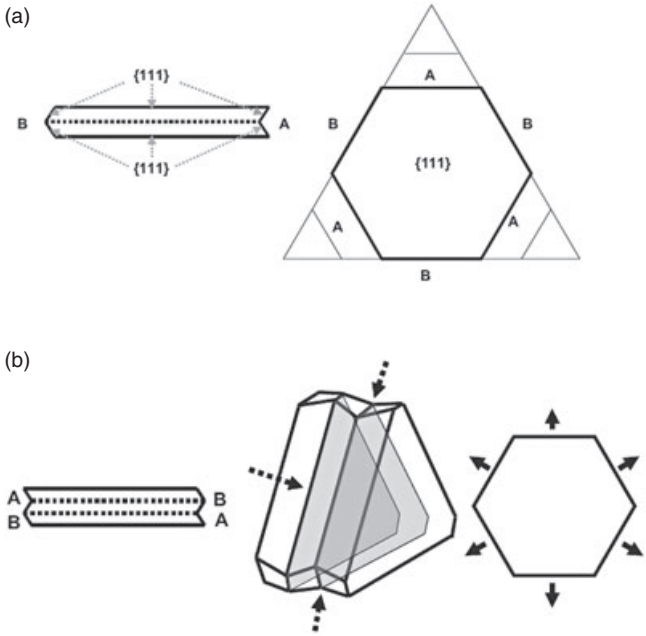

Figure 3.29 (a) Silver halide model of a single twin plane containing type A and type B faces. Type A faces contain re-entrant grooves which facilitate the rapid growth of these faces, while type B faces consist of a convex-like surface. Growth of the nanoprism is arrested when the fast-growing type A sides grow themselves out to meet the slow-growing type B faces; (b) Silver halide model of a particle with two parallel twin planes. The second twin plane causes all six sides to contain A-type faces with re-entrant grooves. This leads to rapid growth in two dimensions, as each A-type face regenerates another A-type face adjacent to it as it grows out. Adapted with permission from Ref. [83]; © 2005 Wiley-VCH Verlag GmbH & Co. KGaA.

of the stacking fault may be the key for the formation and growth of the diskette morphology.

Rocha and Zanchet [116] have studied the defect structure of silver nanoprisms in detail, and shown that the internal structure can be very complex, with many twins and stacking faults. It was shown that defects which are parallel to each other and to the {111} face of the nanoprism can give rise to local hexagonally close-packed regions. Recently, Aherne *et al.* [133] have investigated this defect structure further, whereby TEM analysis provided direct evidence of a defect-induced arrangement of silver atoms that resulted not only in a hcp structure in the vicinity of the defects but also in multiple defects combining to yield a continuous hcp lamellar region (see Figure 3.30). The presence of this hcp region was also confirmed by XRD when two additional peaks, corresponding to predicted positions from theoretical diffractograms for a defect-induced hcp arrangement of silver atoms, were observed (Figure 3.31). Due to this lamellar defect structure of the nanoprisms, it is at these edges that the hcp crystal structure is exposed to the

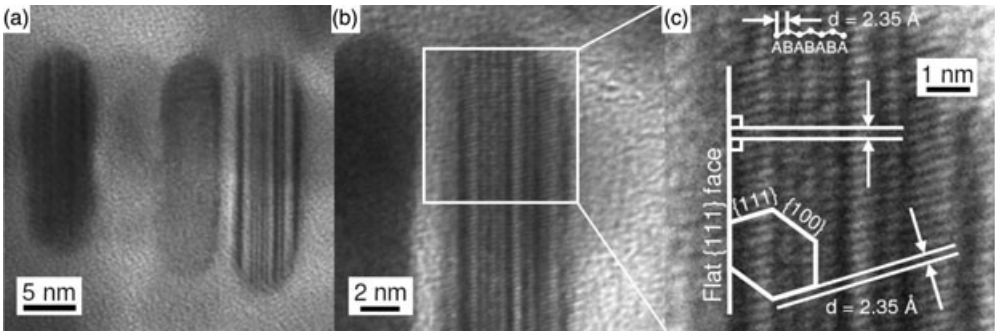

Figure 3.30 (a) TEM image of a stack of vertically oriented silver nanoprisms; (b) High-resolution TEM image of the nanoprism on the right-hand side of (a), showing the defect structure. This nanoprism is oriented such that the {110} plane is in the plane of the image—that is, the electron beam is along ⟨110⟩; (c) Analysis of the internal structure of the prism shown in (b). A series of intrinsic stacking faults has resulted in a hexagonally close-packed pattern emerging, and gives rise to an arrangement of atoms that is aligned perpendicular to the surface with a spacing of 2.5 Å. The correct spacing of 2.35 Å has been obtained for the {111} planes and also for the alternative ABAB.... layers of the hcp region. Reprinted with permission from Ref. [133]; © 2008 Wiley-VCH Verlag GmbH & Co. KGaA.

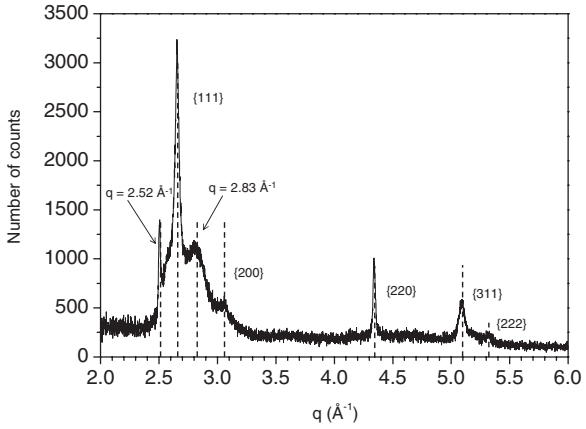

Figure 3.31 XRD data of silver nanoprisms. The peaks corresponding to fcc silver are labeled with the relevant Miller indices. Two additional peaks correspond to predicted positions from theoretical diffractograms for a defect induced hcp arrangement of silver atoms. Reprinted with permission from Ref. [133]; © 2008 Wiley-VCH Verlag GmbH & Co. KGaA.

growth solution, and it is clear that the flat morphology of the nanoprisms arises from much faster growth here than on any other crystal face.

At this stage it should be clear that the growth mechanism for silver nanoprism is not fully understood. However, it is also clear that growth of the nanoplates cannot be adequately explained by the surface binding model, and therefore a defect structure is a more likely model to explain the growth mechanism. In

particular, the above lamellar defect structure could produce a region on the surface of a seed nanoparticle in which the defects are exposed to the growth medium, thereby accelerating two-dimensional growth.

3.5 Applications

Improvements in the shape-controlled synthesis of silver nanomaterials have expanded the applications in which they can be used. Spherical nanoparticles, such as citrate-reduced particles, have long been used as substrates for SERS [4, 22, 23, 26]. Whilst this enhancement is mainly due to the intense electromagnetic field exhibited by silver nanoparticles, the intensity of enhancement is heavily dependent on the shape of the nanostructure [6, 119, 139, 140]. The Raman spectrum of adsorbed molecules can be enhanced several thousand-fold such that, in some cases, single-molecule detection is possible. Another area in which silver nanomaterials show great promise is that of metal-enhanced fluorescence (MEF). Many experiments have been carried out highlighting the importance of parameters such as nanoparticle shape and size, and the distance between the nanoparticle surface and the fluorophore that determine the degree of fluorescence quenching or enhancement that occurs [7, 8, 141–143]. The development of syntheses that provide control over the size and shape of the nanoparticles produced, combined with further investigations into the functionalization of such materials to control the distance and position of the fluorophore relative to the nanoparticle surface, will aid in the development of both technologies. Van Duyne [144–148] and Schatz [149] have pioneered the use of Ag nanoprisms as sensitive nanoscale affinity localized surface plasmon resonance (LSPR) nanobiosensors, the mode of operation of which is based on the shift in the SPR of a nanoparticle caused by a change in the refractive index of its surrounding medium. This change is induced by the specific binding of an analyte to the nanoparticles. Previously, the particles used in these biosensors have been prepared using lithographic techniques, but more recently the preparation of silver nanoparticles using solution-based techniques has improved and may prove to be a more cost-effective option.

In the past, silver has been used frequently to combat infections, and in this respect the antibacterial properties of silver, silver ions and other silver compounds have undergone extensive study. In recent years, silver nanoparticles have been shown to be good candidates for use in antimicrobial technologies, with some recent reports suggesting that their size, shape and surface chemistry are important factors in determining their efficacy as antibacterial agents [150–155].

3.6 Conclusions

Whilst the synthesis of silver nanoparticles of well-defined shape and size is not a trivial matter, recent developments in the production of metal nanoparticles via

solution-based methods have led to a remarkable range of morphologies and increasing control over the size of the particles produced.

A number of methods for the preparation of spherical silver nanoparticles have been developed. Organic-based procedures involving the steric stabilization of such nanomaterials with molecules such as alkanethiols have provided an excellent route for the preparation of highly monodisperse, well-ordered nanoparticles, although one weakness of this method lies in the difficulty in producing larger (>25 nm) particles. Aqueous methods, such as citrate reduction, can produce larger nanomaterials, but the control over the distribution of particle size is limited.

In the case of anisotropic nanomaterials, as discussed above, a wide range of morphologies, including cubes, right bipyramids and nanobeams, can be produced via one synthetic process, with only small variations in the procedure required to alter the final morphology of the product. However, while the growth mechanism from the seeds for most of these nanostructures can now be explained, the processes determining the initial seed formation are not yet fully understood. The achievement of a deeper understanding of this process would allow for greater control over the structure of the seed particles, and may open up the possibility of new shapes with higher yields being produced.

In addition to the structure of the seed particles, the coordination of organic species is usually required to maintain the stability of nanoparticles in solution. In many – but not all – cases, these molecules may selectively bind to higher-energy crystal faces, thus reducing the energy of the latter and directing crystal growth onto the more stable crystal faces. It is in this way that the anisotropic growth of nanostructures such as nanorods and nanowires may be explained. The defect structure – and in particular the lamellar defect structure of the seed nanoparticles – can be used to explain the growth of nanoprisms. In this case, growth occurs that cannot be explained by the selective binding model.

In this chapter, only a few of the current applications of silver nanoparticles of well-defined size and shape have been described. Clearly, future studies must include the surface functionalization of nanoparticles that will, in turn, allow for their easier incorporation into useful assemblies, and ultimately into nanoscale devices.

Abbreviations

APS = 3-aminopropyltrimethoxysilane
AOT = bis(2-ethylhexyl)sulfosuccinate or
AR = aspect ratio
BPEI = branched poly(ethyleneimine)
BSPP = bis(*p*-sulfonatophenyl)phenylphosphine dihydrate dipotassium salt)
CTAB = cetyltrimethylammonium bromide
CTAT = cetyltrimethylammonium tosylate
DDA = discrete dipole approximation

DMF = dimethylformamide
DMSO = dimethylsulfoxide
EDTA = ethylenediaminetetra-acetic acid
EG = ethylene glycol
FT-Raman = Fourier transform Raman
HEPES = 4-(2-hydroxyethyl)-1-piperazineethanesulfonic acid
HOPG = highly oriented pyrolitic graphite
HRTEM = high-resolution TEM
LED = light-emitting diode
LSPR = localized surface plasmon resonance
PAM = poly(acrylamide)
PSSS = poly(styrenesulfonate) sodium salt
PVA = poly(vinylalcohol)
PVP = poly(vinylpyrrolidone)
SDS = sodium dodecylsulfate
SEM = scanning electron microscopy
SERS = surface-enhanced Raman scattering
SPR = surface plasmon resonance
TEM = transmission electron microscopy
TSA = tungstosilicic acid
TGA = thermogravimetric analysis
UV-vis = ultraviolet-visible
XPS = X-ray photoelectron spectroscopy
XRD = X-ray diffraction

References

1 Kamat, P.V. (2002) Photophysical, photochemical and photocatalytic aspects of metal nanoparticles. *The Journal of Physical Chemistry B*, **106**, 7729–44.

2 Karpov, S.V., Gerasimov, V.S., Isaev, I.L. and Markel, V.A. (2005) Local anisotropy and giant enhancement of local electromagnetic fields in fractal aggregates of metal nanoparticles. *Physical Review B*, **72**, article no. 205425.

3 Whelan, A.M., Brennan, M.E., Blau, W.J. and Kelly, J.M. (2004) Enhanced third-order optical nonlinearity of silver nanoparticles with a tunable surface plasmon resonance. *Journal of Nanoscience and Nanotechnology*, **4**, 66–8.

4 Bell, S.E.J. and Sirimuthu, N.M.S. (2006) Surface-enhanced Raman spectroscopy (SERS) for sub-micromolar detection of DNA/RNA mononucleotides. *Journal of the American Chemical Society*, **128**, 15580–1.

5 Graham, D., Faulds, K. and Smith, W.E. (2006) Biosensing using silver nanoparticles and surface enhanced resonance Raman scattering. *Chemical Communications*, 4363–71.

6 Zou, X. and Dong, S. (2006) Surface-enhanced Raman scattering studies on aggregated silver nanoplates in aqueous solution. *The Journal of Physical Chemistry B*, **110**, 21545–50.

7 Stoermer, R.L. and Keating, C.D. (2006) Distance-dependent emission from dye-labeled oligonucleotides on striped Au/Ag nanowires: effect of secondary structure and hybridization efficiency. *Journal of the American Chemical Society*, **128**, 13243–54.

8 Aslan, K., Lakowicz, J.R. and Geddes, C.D. (2005) Rapid deposition of triangular silver nanoplates on planar surfaces: application to metal-enhanced fluorescence. *The Journal of Physical Chemistry B*, **109**, 6247–51.

9 Kelly, K.L., Coronado, E., Zhao, L.L. and Schatz, G.C. (2003) The optical properties of metal nanoparticles: the influence of size, shape, and dielectric environment. *The Journal of Physical Chemistry B*, **107**, 668–77.

10 Mie, G. (1908) Considerations on the optics of turbid media, especially colloidal metal sols. *Annals of Physics*, **25**, 377–442.

11 Link, S., Mohamed, M.B. and El-Sayed, M.A. (1999) Simulation of the optical absorption spectra of gold nanorods as a function of their aspect ratio and the effect of the medium dielectric constant. *The Journal of Physical Chemistry B*, **103**, 3073–7.

12 Sun, Y. and Xia, Y. (2003) Gold and silver nanoparticles: a class of chromophores with colors tunable in the range from 400 to 750 nm. *Analyst*, **128**, 686–91.

13 Wiley, B.J., Im, S.H., Li, Z.-Y., McLellan, J., Siekkinen, A. and Xia, Y. (2006) Maneuvering the surface plasmon resonance of silver nanostructures through shape-controlled synthesis. *The Journal of Physical Chemistry B*, **110**, 15666–75.

14 Gonzalez, A.L., Reyes-Esqueda, J.A. and Noguez, C. (2008) Optical properties of elongated noble metal nanoparticles. *The Journal of Physical Chemistry C*, **112**, 7356–62.

15 Noguez, C. (2007) Surface plasmons on metal nanoparticles: the influence of shape and physical environment. *The Journal of Physical Chemistry C*, **111**, 3806–19.

16 Sosa, I.O., Noguez, C. and Barrera, R.G. (2003) Optical properties of metal nanoparticles with arbitrary shapes. *The Journal of Physical Chemistry B*, **107**, 6269–75.

17 Turkevich, J., Stevenson, P.C. and Hillier, J. (1951) The nucleation and growth processes in the synthesis of colloidal gold. *Discussions of the Faraday Society*, **11**, 55–75.

18 Frens, G. (1973) Controlled nucleation for the regulation of the particle size in monodisperse gold suspensions. *Nature: Physical Science*, **241**, 20–2..

19 Biggs, S., Chow, M.K., Zukoski, C.F. and Grieser, F. (1993) The role of colloidal stability in the formation of gold sols. *Journal of Colloid and Interface Science*, **160**, 511–13.

20 Chow, M.K., Zukoski, C.F. and Sol, G. (1994) Formation mechanisms: role of colloidal stability. *Journal of Colloid and Interface Science*, **165**, 97–109.

21 Nickel, U., Mansyreff, K. and Schneider, S. (2004) Production of monodisperse silver colloids by reduction with hydrazine: the effect of chloride and aggregation on SER(R)S signal intensity. *Journal of Raman Spectroscopy*, **35**, 101–10.

22 Canamares, M.V., Garcia-Ramos, J.V., Gomez-Varga, J.D., Domingo, C. and Sanchez-Cortes, S. (2005) Comparative study of the morphology, aggregation, adherence to glass, and surface-enhanced Raman scattering activity of silver nanoparticles prepared by chemical reduction of Ag^+ using citrate and hydroxylamine. *Langmuir*, **21**, 8546–53.

23 Leopold, N., Lendl, B. and New, A. (2003) Method for fast preparation of highly surface-enhanced Raman scattering (SERS) active silver colloids at room temperature by reduction of silver nitrate with hydroxylamine hydrochloride. *The Journal of Physical Chemistry B*, **107**, 5723–7.

24 Hoppe, C.E., Lazzari, M., Pardinas-Blanco, I., Lopez-Quintela, M.A. (2006) One-step synthesis of gold and silver hydrosols using poly(N-vinyl-2-pyrrolidone) as a reducing agent. *Langmuir*, **22**, 7027–34.

25 Washio, I., Xiong, X., Yin, Y. and Xia, Y. (2006) Reduction by the end groups of poly(vinyl pyrrolidone): a new and versatile route to the kinetically controlled synthesis of Ag triangular nanoplates. *Advanced Materials*, **18**, 1745–9.

26 Kvitek, L., Prucek, R., Panacek, A., Novotny, R., Hrbac, J. and Zboril, R.

(2005) The influence of complexing agent concentration on particle size in the process of SERS active silver colloid synthesis. *Journal of Materials Chemistry*, **15**, 1099–105.

27 Henglein, A. and Giersig, M. (1999) Formation of colloidal silver nanoparticles: capping action of citrate. *The Journal of Physical Chemistry B*, **103**, 9533–9.

28 Henglein, A. (2001) Reduction of Ag $(CN)^{2-}$ on silver and platinum colloidal nanoparticles. *Langmuir*, **17**, 2329–33.

29 Liu, F.-K., Hsu, Y.-C., Tsai, M.-H. and Chu, T.-C. (2007) Using γ-irradiation to synthesize Ag nanoparticles. *Materials Letters*, **61**, 2402–5.

30 Shin, H.S., Yang, H.J., Kim, S.B. and Lee, M.S. (2004) Mechanism of growth of colloidal silver nanoparticles stabilized by polyvinyl pyrrolidone in [gamma]-irradiated silver nitrate solution. *Journal of Colloid and Interface Science*, **274**, 89–94.

31 Li, T., Park, H.G. and Choi, S. H. (2007) Gamma-irradiation-induced preparation of Ag and Au nanoparticles and their characterizations. *Materials Chemistry and Physics*, **105**, 325–30.

32 Bogle, K.A., Dhole, S.D. and Bhoraskar, V.N. (2006) Silver nanoparticles: synthesis and size control by electron irradiation. *Nanotechnology*, **17**, 3204–8.

33 Yin, H., Yamamoto, T., Wada, Y. and Yanagida, S. (2004) Large-scale and size-controlled synthesis of silver nanoparticles under microwave irradiation. *Materials Chemistry and Physics*, **83**, 66–70.

34 Yang, L.B., Shen, Y.H., Xie, A.J. and Zhang, B.C. (2007) Facile size-controlled synthesis of silver nanoparticles in UV-irradiated tungstosilicate acid solution. *Journal of Physical Chemistry C*, **111**, 5300–8.

35 Tan, S., Erol, M., Attygalle, A., Du, H. and Sukhishvili, S. (2007) Synthesis of positively charged silver nanoparticles via photoreduction of $AgNO_3$ in branched polyethyleneimine/HEPES solutions. *Langmuir*, **23**, 9836–43.

36 Pastoriza-Santos, I. and Liz-Marzán, L.M. (2000) Reduction of silver nanoparticles in DMF. Formation of monolayers and stable colloids. *Pure and Applied Chemistry*, **72**, 83–90.

37 Pastoriza-Santos, I. and Liz-Marzan, L.M. (2002) Formation of PVP-protected metal nanoparticles in DMF. *Langmuir*, **18**, 2888–94.

38 Pastoriza-Santos, I., Koktysh, D.S., Mamedov, A.A., Giersig, M., Kotov, N.A. and Liz-Marzan, L.M. (2000) One-pot synthesis of $Ag@TiO_2$ core-shell nanoparticles and their layer-by-layer assembly. *Langmuir*, **16**, 2731–5.

39 Liu, J., Ong, W., Kaifer, A.E. and Peinador, C. (2002) A macrocyclic effect on the formation of capped silver nanoparticles in DMF. *Langmuir*, **18**, 5981–3.

40 Rodriguez-Gattorno, G., Diaz, D., Rendon, L. and Hernandez-Segura, G.O. (2002) Metallic nanoparticles from spontaneous reduction of silver(I) in DMSO. Interaction between nitric oxide and silver nanoparticles. *The Journal of Physical Chemistry B*, **106**, 2482–7.

41 Silvert, P.-Y., Herrera-Urbina, R., Duvauchelle, N., Vijayakrishnan, V. and Elhsissen, K.T. (1996) Preparation of colloidal silver dispersions by the polyol process. Part 1. Synthesis and characterization. *Journal of Materials Chemistry*, **6**, 573–7.

42 Kim, D., Jeong, S. and Moon, J. (2006) Synthesis of silver nanoparticles using the polyol process and the influence of precursor injection. *Nanotechnology*, **17**, 4019–24.

43 Taleb, A., Petit, C. and Pileni, M.P. (1997) Synthesis of highly monodisperse silver nanoparticles from AOT reverse Micelles: a way to 2D and 3D self-organization. *Chemical Materials*, **9**, 950–9.

44 Petit, C., Lixon, P. and Pileni, M.P. (1993) In situ synthesis of silver nanocluster in AOT reverse micelles. *Journal of Physical Chemistry*, **97**, 12974–83.

45 Courty, A., Henry, A.I., Goubet, N. and Pileni, M.P. (2007) Large triangular single crystals formed by mild annealing of self-organized silver nanocrystals. *Nature Materials*, **6**, 900–7.

46 Henry, A.I., Courty, A., Goubet, N., Pileni, M.P. (2008) How do self-ordered

silver nanocrystals influence their growth into triangular single crystals? *The Journal of Physical Chemistry C*, **112**, 48–52.

47 Sun, Y.P., Atorngitjawat, P. and Meziani, M.J. (2001) Preparation of silver nanoparticles via rapid expansion of water in carbon dioxide microemulsion into reductant solution. *Langmuir*, **17**, 5707–10.

48 Ohde, H., Hunt, F. and Wai, C.M. (2001) Synthesis of silver and copper nanoparticles in a water-in-supercritical-carbon dioxide microemulsion. *Chemical Materials*, **13**, 4130–5.

49 Fernandez, C.A. and Wai, C.M. (2006) Continuous tuning of silver nanoparticle size in a water-in-supercritical carbon dioxide microemulsion. *Small*, **2**, 1266–9.

50 Brust, M., Walker, M., Bethell, D., Schiffrin, D.J. and Whyman, R. (1994) Synthesis of thiol-derivatised gold nanoparticles in a two-phase liquid–liquid system. *Chemical Communications*, **1994**, 801–2.

51 Brust, M., Fink, J., Bethell, D., Schiffrin, D.J. and Kiely, C. (1995) Synthesis and reactions of functionalised gold nanoparticles. *Chemical Communications*, **1995**, 1655–6.

52 Heath, J.R., Knobler, C.M. and Leff, D.V. (1997) Pressure/temperature phase diagrams and superlattices of organically functionalized metal nanocrystal monolayers: the influence of particle size, size distribution, and surface passivant. *The Journal of Physical Chemistry B*, **101**, 189–97.

53 Korgel, B.A., Fullam, S., Connolly, S. and Fitzmaurice, D. (1998) Assembly and self-organization of silver nanocrystal superlattices: ordered soft spheres. *The Journal of Physical Chemistry B*, **102**, 8379–88.

54 Zhang, J., Malicka, J., Gryczynski, I. and Lakowicz, J.R. (2005) Surface-enhanced fluorescence of fluorescein-labeled oligonucleotides capped on silver nanoparticles. *The Journal of Physical Chemistry B*, **109**, 7643–8.

55 Zhang, J. and Lakowicz, J.R. (2006) A model for DNA detection by metal-enhanced fluorescence from immobilized silver nanoparticles on solid substrate. *The Journal of Physical Chemistry B*, **110**, 2387–92.

56 Jiang, C., Cardin, D.J. and Tsang, S.C. (2008) Conductive three-dimensional material assembled from silver nanoparticles using a conjugated dithiol linker. *Chemical Materials*, **20**, 14–16.

57 Doty, R.C., Tshikhudo, T.R., Brust, M. and Fernig, D.G. (2005) Extremely stable water-soluble Ag nanoparticles. *Chemical Materials*, **17**, 4630–5.

58 Hiramatsu, H. and Osterloh, F.E. (2004) A simple large-scale synthesis of nearly monodisperse gold and silver nanoparticles with adjustable sizes and with exchangeable surfactants. *Chemical Materials*, **16**, 2509–11.

59 Jana, N.R. and Peng, X. (2003) Single-phase and gram-scale routes toward nearly monodisperse Au and other noble metal nanocrystals. *Journal of the American Chemical Society*, **125**, 14280–1.

60 Kashiwagi, Y., Yamamoto, M. and Nakamoto, M. (2006) Facile size-regulated synthesis of silver nanoparticles by controlled thermolysis of silver alkylcarboxylates in the presence of alkylamines with different chain lengths. *Journal of Colloid and Interface Science*, **300**, 169–75.

61 Lin, X.Z., Teng, X. and Yang, H. (2003) Direct synthesis of narrowly dispersed silver nanoparticles using a single-source precursor. *Langmuir*, **19**, 10081–5.

62 Charan, S., Singh, N., Khanna, P.K. and Patil, K.R. (2006) Direct synthesis of nanocrystalline silver from the reaction between silver carboxylates and n-trioctylphosphine. *Journal of Nanoscience and Nanotechnology*, **6**, 2095–102.

63 Lee, K.J., Jun, B.H., Choi, J., Lee, Y.I., Joung, J. and Oh, Y.S. (2007) Environmentally friendly synthesis of organic-soluble silver nanoparticles for printed electronics. *Nanotechnology*, **18**, article no. 335601.

64 Connolly, S., Fullam, S., Korgel, B. and Fitzmaurice, D. (1998) Time-resolved small-angle X-ray scattering studies of nanocrystal superlattice self-assembly. *Journal of the American Chemical Society*, **120**, 2969–70.

65 Brian, A. and Korgel, D.F. (1998) Self-assembly of silver nanocrystals into two-dimensional nanowire arrays. *Advanced Materials*, **10**, 661–5.

66 Harfenist, S.A., Wang, Z.L., Alvarez, M.M., Vezmar, I. and Whetten, R.L. (1996) Highly oriented molecular Ag nanocrystal arrays. *Journal of Physical Chemistry*, **100**, 13904–10.

67 Wang, Z.L., Harfenist, S.A., Whetten, R.L., Bentley, J. and Evans, N.D. (1998) Bundling and interdigitation of adsorbed thiolate groups in self-assembled nanocrystal superlattices. *The Journal of Physical Chemistry B*, **102**, 3068–72.

68 Kiely, C.J., Fink, J., Zheng, J.G., Brust, M., Bethell, D. and Schiffrin, D.J. (2000) Ordered colloidal nanoalloys. *Advanced Materials*, **12**, 640–3.

69 Tao, A.R., Habas, S. and Yang, P. (2008) Shape control of colloidal metal nanocrystals. *Small*, **4**, 310–25.

70 Jana, N.R., Gearheart, L. and Murphy, C.J. (2001) Wet chemical synthesis of silver nanorods and nanowires of controllable aspect ratio. *Chemical Communications*, 617–18.

71 Xia, Y. and Halas, N.J. (2005) Shape-controlled synthesis and surface plasmonic properties of metallic nanostructures. *Materials Research Bulletin*, **30**, 338–48.

72 Murphy, C.J., Sau, T.K., Gole, A. and Orendorff, C.J. (2005) Surfactant-directed synthesis and optical properties of one-dimensional plasmonic metallic nanostructures. *Materials Research Bulletin*, **30**, 349–55.

73 Caswell, K.K., Bender, C.M. and Murphy, C.J. (2003) Seedless, surfactantless wet chemical synthesis of silver nanowires. *Nano Letters*, **3**, 667–9.

74 Murphy, C.J. and Jana, N.R. (2002) Controlling the aspect ratio of inorganic nanorods and nanowires. *Advanced Materials*, **14**, 80–2.

75 Orendorff, C.J., Gearheart, L., Jana, N.R. and Murphy, C.J. (2006) Aspect ratio dependence on surface enhanced Raman scattering using silver and gold nanorod substrates. *Physical Chemistry Chemical Physics*, **8**, 165–70.

76 Murphy, C.J., Sau, T.K., Gole, A.M., Orendorff, C.J., Gao, J., Gou, L., Hunyadi, S.E. and Li, T. (2005) Anisotropic metal nanoparticles: synthesis, assembly, and optical applications. *The Journal of Physical Chemistry B*, **109**, 13857–70.

77 Jana, N.R. (2005) Gram-scale synthesis of soluble, near-monodisperse gold nanorods and other anisotropic nanoparticles. *Small*, **1**, 875–82.

78 Murphy, C.J., Gole, A.M., Hunyadi, S.E. and Orendorff, C.J. (2006) One-dimensional colloidal gold and silver nanostructures. *Inorganic Chemistry*, **45**, 7544–54.

79 Ni, C., Hassan, P.A. and Kaler, E.W. (2005) Structural characteristics and growth of pentagonal silver nanorods prepared by a surfactant method. *Langmuir*, **21**, 3334–7.

80 Pérez-Juste, J., Liz-Marzán, L.M., Carnie, S., Chan, D.Y.C. and Mulvaney, P. (2004) Electric-field-directed growth of gold nanorods in aqueous surfactant solutions. *Advanced Functional Materials*, **14**, 571–9.

81 Sun, Y., Yin, Y., Mayers, B.T., Herricks, T. and Xia, Y. (2002) Uniform silver nanowires synthesis by reducing $AgNO_3$ with ethylene glycol in the presence of seeds and poly(vinyl pyrrolidone). *Chemical Materials*, **14**, 4736–45.

82 Elechiguerra, J.L., Reyes-Gasga, J. and Yacaman, M.J. (2006) The role of twinning in shape evolution of anisotropic noble metal nanostructures. *Journal of Materials Chemistry*, **16**, 3906–19.

83 Lofton, C. and Sigmund, W. (2005) Mechanisms controlling crystal habits of gold and silver colloids. *Advanced Functional Materials*, **15**, 1197–208.

84 Ajayan, P.M. and Marks, L.D. (1988) Quasimelting and phases of small particles. *Physical Review Letters*, **60**, 585.

85 Wiley, B., Sun, Y. and Xia, Y. (2007) Synthesis of silver nanostructures with controlled shapes and properties. *Accounts of Chemical Research*, **40**, 1067–76.

86 Im Sang, H., Lee Yun, T., Wiley, B. and Xia, Y. (2005) Large-scale synthesis of silver nanocubes: the role of HCl in promoting cube perfection and

monodispersity. *Angewandte Chemie–International Edition*, **44**, 2154–7.
87 Sun, Y., Mayers, B., Herricks, T. and Xia, Y. (2003) Polyol synthesis of uniform silver nanowires: a plausible growth mechanism and the supporting evidence. *Nano Letters*, **3**, 955–60.
88 Tsuji, M., Matsumoto, K., Miyamae, N., Tsuji, T. and Zhang, X. (2007) Rapid preparation of Silver nanorods and nanowires by a microwave-polyol method in the presence of Pt catalyst and polyvinylpyrrolidone. *Crystal Growth and Design*, **7**, 311–20.
89 Wiley, B., Sun, Y. and Xia, Y. (2005) Polyol synthesis of silver nanostructures: control of product morphology with Fe(II) or Fe(III) species. *Langmuir*, **21**, 8077–80.
90 Korte, K.E., Skrabalak, S.E. and Xia, Y. (2008) Rapid synthesis of silver nanowires through a CuCl- or $CuCl_2$-mediated polyol process. *Journal of Materials Chemistry*, **18**, 437–41.
91 Chen, C., Wang, L., Jiang, G., Zhou, J., Chen, X., Yu, H. and Yang, Q. (2006) Study on the synthesis of silver nanowires with adjustable diameters through the polyol process. *Nanotechnology*, **17**, 3933–8.
92 Zhang, W., Chen, P., Gao, Q., Zhang, Y. and Tang, Y. (2008) High-concentration preparation of silver nanowires: restraining in situ nitric acidic etching by steel-assisted polyol method. *Chemical Materials*, **20**, 1699–704.
93 Jiang, P., Li, S.-Y., Xie, S.-S., Gao, Y. and Song, L. (2004) Machinable long PVP-stabilized silver nanowires. *Chemistry–A European Journal*, **10**, 4817–21.
94 Gao, Y., Jiang, P., Liu, D.F., Yuan, H.J., Yan, X.Q., Zhou, Z.P., Wang, J.X., Song, L., Liu, L.F., Zhou, W.Y., Wang, G., Wang, C.Y., Xie, S.S., Zhang, J.M. and Shen, D.Y. (2004) Evidence for the monolayer assembly of poly(vinylpyrrolidone) on the surfaces of silver nanowires. *The Journal of Physical Chemistry B*, **108**, 12877–81.
95 Yu, D. and Yam, V.W.-W. (2004) Controlled synthesis of monodisperse silver nanocubes in water. *Journal of the American Chemical Society*, **126**, 13200–1.
96 Siekkinen, A.R., McLellan, J.M., Chen, J. and Xia, Y. (2006) Rapid synthesis of small silver nanocubes by mediating polyol reduction with a trace amount of sodium sulfide or sodium hydrosulfide. *Chemical Physics Letters*, **432**, 491–6.
97 Lee, Y.T., Im, S.H., Wiley, B. and Xia, Y.N. (2005) Quick formation of single-crystal nanocubes of silver through dual functions of hydrogen gas in polyol synthesis. *Chemical Physics Letters*, **411**, 479–83.
98 Wiley, B., Sun, Y., Mayers, B. and Xia, Y. (2005) Shape-controlled synthesis of metal nanostructures: the case of silver. *Chemistry–A European Journal*, **11**, 454–63.
99 Wiley, B., Herricks, T., Sun, Y. and Xia, Y. (2004) Polyol synthesis of silver nanoparticles: use of chloride and oxygen to promote the formation of single-crystal, truncated cubes and tetrahedrons. *Nano Letters*, **4**, 1733–9.
100 Skrabalak, S.E., Au, L., Li, X. and Xia, Y. (2007) Facile synthesis of Ag nanocubes and Au nanocages. *Nature Protocols*, **2**, 2182–90.
101 Sun, Y. and Xia, Y. (2002) Shape-controlled synthesis of gold and silver nanoparticles. *Science*, **298**, 2176–9.
102 Tao, A., Sinsermsuksakul, P. and Yang, P. (2006) Polyhedral silver nanocrystals with distinct scattering signatures, *Angewandte Chemie–International Edition*, **45**, 4597–601.
103 Wiley, B.J., Xiong, Y., Li, Z.-Y., Yin, Y. and Xia, Y. (2006) Right bipyramids of silver: a new shape derived from single twinned seeds. *Nano Letters*, **6**, 765–8.
104 Wiley, B.J., Wang, Z.H., Wei, J., Yin, Y.D., Cobden, D.H. and Xia, Y.N. (2006) Synthesis and electrical characterization of silver nanobeams. *Nano Letters*, **6**, 2273–8.
105 Wiley, B.J., Chen, Y.C., McLellan, J.M., Xiong, Y.J., Li, Z.Y., Ginger, D. and Xia, Y.N. (2007) Synthesis and optical properties of silver nanobars and nanorice. *Nano Letters*, **7**, 1032–6.
106 Jin, R., Cao, Y., Mirkin, C.A., Kelly, K.L., Schatz, G.C. and Zheng, J.G. (2001) Photoinduced conversion of silver

nanospheres to nanoprisms. *Science*, **294**, 1901–3.

107 Sun, Y.A. and Xia, Y.N. (2003) Triangular nanoplates of silver. Synthesis, characterization, and use as sacrificial templates for generating triangular nanorings of gold. *Advanced Materials*, **15**, 695–9.

108 Jin, R.C., Cao, Y.C., Hao, E.C., Metraux, G.S., Schatz, G.C. and Mirkin, C.A. (2003) Controlling anisotropic nanoparticle growth through plasmon excitation. *Nature*, **425**, 487–90.

109 Xue, C. and Mirkin, C.A. (2007) pH-switchable silver nanoprism growth pathways. *Angewandte Chemie–International Edition*, **46**, 2036–8.

110 Callegari, A., Tonti, D. and Chergui, M. (2003) Photochemically grown silver nanoparticles with wavelength-controlled size and shape. *Nano Letters*, **3**, 1565–8.

111 Bastys, V., Pastoriza-Santos, I., Rodriguez-Gonzalez, B., Vaisnoras, R. and Liz-Marzan, L.M. (2006) Formation of silver nanoprisms with surface plasmons at communication wavelengths. *Advanced Functional Materials*, **16**, 766–73.

112 Xue, C., Millstone, J.E., Li, S. and Mirkin, C.A. (2007) Plasmon-driven synthesis of triangular core-shell nanoprisms from gold seeds. *Angewandte Chemie–International Edition*, **46**, 8436–9.

113 An, J., Tang, B., Ning, X., Zhou, J., Xu, S., Zhao, B., Xu, W., Corredor, C. and Lombardi, J.R. (2007) Photoinduced shape evolution: from triangular to hexagonal silver nanoplates. *The Journal of Physical Chemistry C*, **111**, 18055–9.

114 Maillard, M., Huang, P. and Brus, L. (2003) Silver nanodisk growth by surface plasmon enhanced photoreduction of adsorbed [Ag^{+}]. *Nano Letters*, **3**, 1611–15.

115 Rocha, T.C.R., Winnischofer, H., Westphal, E. and Zanchet, D. (2007) Formation kinetics of silver triangular nanoplates. *The Journal of Physical Chemistry C*, **111**, 2885–91.

116 Rocha, T.C.R. and Zanchet, D. (2007) Structural defects and their role in the growth of Ag triangular nanoplates. *The Journal of Physical Chemistry C*, **111**, 6989–93.

117 Pastoriza-Santos, I. and Liz-Marzan, L.M. (2002) Synthesis of silver nanoprisms in DMF. *Nano Letters*, **2**, 903–5.

118 Jiang, L.P., Xu, S., Zhu, J.M., Zhang, J.R., Zhu, J.J. and Chen, H.Y. (2004) Ultrasonic-assisted synthesis of monodisperse single-crystalline silver nanoplates and gold nanorings. *Inorganic Chemistry*, **43**, 5877–83.

119 Yang, Y., Matsubara, S., Xiong, L.M., Hayakawa, T. and Nogami, M. (2007) Solvothermal synthesis of multiple shapes of silver nanoparticles and their SERS properties. *The Journal of Physical Chemistry C*, **111**, 9095–104.

120 Xiong, Y., Siekkinen, A.R., Wang, J., Yin, Y., Kim, M.J. and Xia, Y. (2007) Synthesis of silver nanoplates at high yields by slowing down the polyol reduction of silver nitrate with polyacrylamide. *Journal of Materials Chemistry*, **17**, 2600–2.

121 Chen, S.H. and Carroll, D.L. (2002) Synthesis and characterization of truncated triangular silver nanoplates. *Nano Letters*, **2**, 1003–7.

122 Chen, S.H., Fan, Z.Y. and Carroll, D.L. (2002) Silver nanodisks: synthesis, characterization, and self-assembly. *The Journal of Physical Chemistry B*, **106**, 10777–81.

123 Chen, S., Carroll, D.L. and Nanoplates, S. (2004) Size control in two dimensions and formation mechanisms. *The Journal of Physical Chemistry B*, **108**, 5500–6.

124 Maillard, M., Giorgio, S. and Pileni, M.-P. (2002) Silver nanodisks. *Advanced Materials*, **14**, 1084–6.

125 Jiang, X., Zeng, Q. and Yu, A. (2006) A self-seeding coreduction method for shape control of silver nanoplates. *Nanotechnology*, **17**, 4929–35.

126 Jiang, X.C., Zeng, Q.H. and Yu, A.B. (2007) Thiol-frozen shape evolution of triangular silver nanoplates. *Langmuir*, **23**, 2218–23.

127 Sun, Y.G., Mayers, B. and Xia, Y.N. (2003) Transformation of silver nanospheres into nanobelts and triangular nanoplates through a thermal process. *Nano Letters*, **3**, 675–9.

128 Xiong, Y.J., Washio, I., Chen, J.Y., Cai, H.G., Li, Z.Y. and Xia, Y.N. (2006)

Poly(vinyl pyrrolidone): a dual functional reductant and stabilizer for the facile synthesis of noble metal nanoplates in aqueous solutions. *Langmuir*, **22**, 8563–70.

129 Xiong, Y., Washio, I., Chen, J., Sadilek, M. and Xia, Y. (2007) Trimeric clusters of silver in aqueous $AgNO_3$ solutions and their role as nuclei in forming triangular nanoplates of silver. *Angewandte Chemie–International Edition*, **46**, 4917–21.

130 Metraux, G.S. and Mirkin, C.A. (2005) Rapid thermal synthesis of silver nanoprisms with chemically tailorable thickness. *Advanced Materials*, **17**, 412–15.

131 Cao, Z., Fu, H., Kang, L., Huang, L., Zhai, T., Ma, Y. and Yao, J. (2008) Rapid room-temperature synthesis of silver nanoplates with tunable in-plane surface plasmon resonance from visible to near-IR. *Journal of Materials Chemistry*, **23**, 2673–8.

132 Ledwith, D.M., Whelan, A.M. and Kelly, J.M. (2007) A rapid, straight-forward method for controlling the morphology of stable silver nanoparticles. *Journal of Materials Chemistry*, **17**, 2459–64.

133 Aherne, D., Ledwith, D.M., Gara, M. and Kelly, J.M. (2008) Optical properties and growth aspects of silver nanoprisms produced by a highly reproducible and rapid synthesis at room temperature. *Advanced Functional Materials* (in press) DOI: 10.1002/adfm.200800233.

134 Yang, J.H., Lu, L.H., Wang, H.S., Shi, W.D. and Zhang, H.J. (2006) Glycyl glycine templating synthesis of single-crystal silver nanoplates. *Crystal Growth and Design*, **6**, 2155–8.

135 Xie, J., Lee, J.Y., Wang, D.I.C., Ting, Y.P. and Nanoplates, S. (2007) From biological to biomimetic synthesis. *ACS Nano*, **1**, 429–39.

136 Grochola, G., Snook, I.K. and Russo, S.P. (2007) Computational modeling of nanorod growth. *Journal of Chemical Physics*, **127**, 194707–13.

137 Germain, V., Li, J., Ingert, D., Wang, Z.L. and Pileni, M.P. (2003) Stacking faults in formation of silver nanodisks. *The Journal of Physical Chemistry B*, **107**, 8717–20.

138 Rodriguez-Gonzalez, B., Pastoriza-Santos, I. and Liz-Marzan, L.M. (2006) Bending contours in silver nanoprisms. *The Journal of Physical Chemistry B*, **110**, 11796–9.

139 Lu, L., Kobayashi, A., Tawa, K. and Ozaki, Y. (2006) Nanoplates silver with special shapes: controlled synthesis and their surface plasmon resonance and surface-enhanced Raman scattering properties. *Chemical Materials*, **18**, 4894–901.

140 McLellan, J.M., Li, Z.Y., Siekkinen, A.R. and Xia, Y.N. (2007) The SERS activity of a supported Ag nanocube strongly depends on its orientation relative to laser polarization. *Nano Letters*, **7**, 1013–17.

141 Aslan, K., Wu, M., Lakowicz, J.R., Geddes, C.D. and Core-Shell, F. (2007) $Ag@SiO_2$ nanocomposites for metal-enhanced fluorescence and single nanoparticle sensing platforms. *Journal of the American Chemical Society*, **129**, 1524–5.

142 Lakowicz, J.R. (2005) Radiative decay engineering 5: metal-enhanced fluorescence and plasmon emission. *Analytical Biochemistry*, **337**, 171–94.

143 Anger, P., Bharadwaj, P. and Novotny, L. (2006) Enhancement and quenching of single-molecule fluorescence. *Physical Review Letters*, **96**, 113002–4.

144 Haes, A.J., Van Duyne, R.P. and Nanoscale, A. (2002) Optical biosensor: sensitivity and selectivity of an approach based on the localized surface plasmon resonance spectroscopy of triangular silver nanoparticles. *Journal of the American Chemical Society*, **124**, 10596–604.

145 Riboh, J.C., Haes, A.J., McFarland, A.D., Yonzon, C., Van Duyne, R.P. and Nanoscale, A. (2003) Optical biosensor: real-time immunoassay in physiological buffer enabled by improved nanoparticle adhesion. *The Journal of Physical Chemistry B*, **107**, 1772–80.

146 Haes, A.J., Hall, W.P., Chang, L., Klein, W.L., VanDuyne, R.P. and Localized, A. (2004) Surface plasmon resonance biosensor: first steps toward an assay for Alzheimer's disease. *Nano Letters*, **4**, 1029–34.

147 McFarland, A.D. and VanDuyne, R.P. (2003) Single silver nanoparticles as real-time optical sensors with zeptomole sensitivity. *Nano Letters*, **3**, 1057–62.

148 Shafer-Peltier, K.E., Haynes, C.L., Glucksberg, M.R., Van Duyne, R.P. (2003) Toward a glucose biosensor based on surface-enhanced Raman scattering. *Journal of the American Chemical Society*, **125**, 588–93.

149 Malinsky, M.D., Kelly, K.L., Schatz, G.C., Van Duyne, R.P. and Length, C. (2001) Dependence and sensing capabilities of the localized surface plasmon resonance of silver nanoparticles chemically modified with alkanethiol self-assembled monolayers. *Journal of the American Chemical Society*, **123**, 1471–82.

150 Jung, W.K., Koo, H.C., Kim, K.W., Shin, S., Kim, S.H. and Park, Y.H. (2008) Antibacterial activity and mechanism of action of the silver ion in *Staphylococcus aureus* and *Escherichia coli*. *Applied and Environmental Microbiology*, **74**, 2171–8.

151 Pal, S., Tak, Y.K. and Song, J.M. (2007) Does the antibacterial activity of silver nanoparticles depend on the shape of the nanoparticle? A study of the gram-negative bacterium *Escherichia coli*. *Applied and Environmental Microbiology*, **73**, 1712–20.

152 Gogoi, S.K., Gopinath, P., Paul, A., Ramesh, A., Ghosh, S.S. and Chattopadhyay, A. (2006) Green fluorescent protein-expressing *Escherichia coli* as a model system for investigating the antimicrobial activities of silver nanoparticles. *Langmuir*, **22**, 9322–8.

153 Kim, J.S., Kuk, E., Yu, K.N., Kim, J.H., Park, S.J., Lee, H.J., Kim, S.H., Park, Y. K., Park, Y.H., Hwang, C.Y., Kim, Y.K., Lee, Y.S., Jeong, D.H. and Cho, M.H. (2007) Antimicrobial effects of silver nanoparticles. *Nanomedicine: Nanotechnology, Biology and Medicine*, **3**, 95–101.

154 Panacek, A., Kvitek, L., Prucek, R., Kolar, M., Vecerova, R., Pizurova, N., Sharma, V.K., Nevecna, T. and Zboril, R. (2006) Silver colloid nanoparticles: synthesis, characterization, and their antibacterial activity. *The Journal of Physical Chemistry B*, **110**, 16248–53.

155 Shrivastava, S., Bera, T., Roy, A., Singh, G., Ramachandrarao, P. and Dash, D. (2007) Characterization of enhanced antibacterial effects of novel silver nanoparticles. *Nanotechnology*, **18**, 225103.

4
Spherical and Anisotropic Silver Nanomaterials in Medical Therapy

Kenneth K. Y. Wong

4.1
Introduction

Although throughout human history, silver has been very widely used, its main applications have lain mainly in nonmedical fields. Nonetheless, silver's extremely potent disinfectant properties – in solution, a concentration of only one part per 100 million of elemental silver shows effective antimicrobial activity – have been well documented. As with other heavy metals, the efficacy of silver depends on the aqueous concentration of its ions. Silver ions are effective against a wide range of microbes, and conduct their antibacterial efficacy in several ways. Whereas, in ancient times, metallic silver vessels were used to preserve water and wine, in medical practice it is mainly silver compounds that have been utilized; an example is the use, during the 19th century, of a 1% silver nitrate solution to prevent gonococcal eye infections [1]. One of the major problems associated with the use of silver compounds is an irreversible pigmentation of the tissues after their prolonged exposure to silver or silver compounds [2, 3]. Indeed, it is due to this problem, coupled with the advent of powerful antibiotics, that the role of silver as an antimicrobial agent has gradually diminished. Currently, the use of silver nitrate is limited to that of an effective cauterizing agent and as an inflammation-inducing agent in pleurodesis [4–6]. One other commonly used silver compound is that of silver sulfadiazine, the cream formulation of which has long been a standard antibacterial treatment for serious burn wounds worldwide. Unfortunately, although inherently nontoxic in its pure form, the use of silver compounds encounters problems due to side effects caused by the nonsilver components [7–9].

As science has advanced, the emergence of nanotechnology has provided new ways of producing silver in its pure form as silver nanoparticles, the sizes of which – as the name suggests – are measured in nanometers. Upon reaching nanoscale, silver particles – like other nanomaterials and primarily by virtue of their extremely small size – exhibit remarkably unusual physico-chemical properties and biological activities, and in recent years major research efforts in this area

Metallic Nanomaterials Vol. 1. Edited by Challa S. S. R. Kumar

ISBN: 978-3-527-32151-3

have provided exciting and encouraging results [10–13]. The ability to nanocrystallize silver has led to the development of an extremely effective pure silver particles delivery system. A major advantage here is that, as the particles become smaller, their surface area-to-volume ratio increases. This means that, the larger the surface area, the more reactions can take place in a shorter time between molecules on the surface [14–18]. Under conventional vapor deposition conditions, silver crystals produced by sputtering result in tightly adherent masses of 100–900 nm diameter. In contrast, by applying nanotechnology the particle size can be reduced to about 10–22 nm (average 15 nm), and as a consequence the exposed surface area of the crystal is markedly increased. The result of this is that the application of silver nanoparticles within the healthcare sector has 'exploded', and current estimations are that, ultimately, silver nanoparticles will have the highest degree of commercialization among all of the nanomaterials. Today, in the medical arena, wound dressings, contraceptive devices, surgical instruments and bone prostheses all coated or embedded with silver nanoparticles. In this chapter, we will first discuss the current understanding of the actions of silver nanoparticles, after which their various uses in clinical medicine will be described.

4.2 Actions of Silver Nanoparticles

4.2.1 Antimicrobial Effects

It has been observed that, when silver nanoparticles come into contact with microorganisms, the speed of killing is almost instantaneous. Indeed, ionic silver begins to inhibit bacterial growth at a concentration equivalent to approximately 35 ppb. The efficacy of microbe killing is not only based on the amount of silver ions present; it also depends on a sustained release of silver onto the microbe. Although the exact mechanism of action of killing by silver nanoparticles is not fully understood, some insights have been derived from preliminary studies with silver ions. To date, three possible mechanisms may be considered:

- Silver ions are small enough to be ingested by the microbe and, once inside the cell, the silver nanoparticles bind to the cell wall, blocking its energy transfer system.
- Silver interrupts the RNA replication process of the microbe, thereby preventing cell multiplication.
- Through an oxidation process, silver ions block respiration, effectively choking the microbe, but having no toxic effect on human cells *in vivo* [19–21].

Indeed, by using a proteomic approach, Lok *et al.* found that treatment with silver nanoparticles destabilized the outer membrane of *Escherichia coli* by disrupting the outer membrane barrier components such as lipopolysaccharides or porins,

and this culminated in a perturbation of the cytoplasmic membrane. Silver nanoparticles further elicited a rapid collapse of the proton motive force by inducing a loss of intracellular potassium and thus decreasing the cellular adenosine triphosphate (ATP) levels. [22, 23]. Silver is effective against a broad range of aerobic, anaerobic, Gram-negative and Gram-positive bacteria, yeast, filamentous fungi and viruses. It has also been shown to be effective against both methicillin- and vancomycin-resistant strains, whereas no strains resistant to silver have ever been encountered [24, 25]. In the case of silver nanoparticles, the research investigations performed thus far have proved that the antibacterial activity is dependent not only on particle size but also on shape [26–28]. As this is the case, the intrinsic problem of the aggregation of silver nanoparticles would lead to a loss of antibacterial activity. As a result, the stabilization of nanosilver, not only with various polymers but also with nonionic and anionic surfactants can enhance antibacterial activity, and this was indeed demonstrated in a recent study [29].

4.2.2
Anti-Inflammatory Effects

In addition to its recognized antimicrobial properties, the question remains as to whether there are other cellular actions of silver. Indeed, further information on silver's pro-healing and anti-inflammatory effects have been suggested [30, 31]. In several studies which compared silver released from the pure silver delivery system with other topical antibiotics, an increase in the rate of re-epithelialization of partial-thickness wounds and meshed skin grafts was demonstrated [32, 33]. As bacterial growth was negligible in both wound groups, the faster re-epithelialization rate in the silver nanoparticles group strongly suggested a direct wound-healing effect of pure silver, but which was unrelated to its underlying antimicrobial properties. Preliminary findings indicated that this acceleration in wound healing induced by the silver nanoparticles was associated with a reduction of local matrix metalloproteinase (MMP) activity, as well as with an increased incidence of neutrophil apoptosis within the wound. As an excess in MMP levels is known to increase inflammation by increasing inflammatory cell exudates, leading to a nonhealing chronic wound [31, 34], an anti-inflammatory action of silver is thus suspected. Indeed, based on the results of our own experiments using a burn injury model in mice, the previous findings were confirmed of a faster healing when using silver nanoparticles. A reduction in the levels of pro-inflammatory cytokines was also demonstrated both at the wound sites and in the systemic circulation [35]. In support of these findings, a recent report examining the effects of silver nanoparticles on peripheral blood mononuclear cells also showed that such nanoparticles strongly inhibited – in concentration-dependent manner – the activities of interferon-gamma (IFN-γ) and tumor necrosis factor-alpha (TNF-α), both of which are cytokines associated with inflammation [36]. Taken together, these findings suggest an anti-inflammatory action of silver nanoparticles, and this may provide a novel pharmacological rationale for the treatment of inflammatory and immunologic diseases. Nonetheless, the underlying molecular-level

mechanism of action of the anti-inflammatory effects of nanosilver remains to be determined.

4.3 Applications of Silver Nanoparticles in Medicine

Traditionally, as crystalline silver is relatively insoluble in both water and dilute acids, the concentration of silver ions normally available on a wound surface would be inadequate for use as an antimicrobial agent. In order to exert a bactericidal effect, silver ions must be available in solution at the bacterial surface and, indeed, their efficacy depends on their aqueous concentration. To achieve this, silver compounds have been used in solution form as an antimicrobial for wound management for almost a century. In the past, silver has been used to treat a variety of conditions, including epilepsy, venereal infections, acne and leg ulcers. Silver foil was also applied to surgical wounds to improve healing and to reduce postoperative infections, while silver and 'lunar caustic' (a pencil containing a mixture of silver nitrate and potassium nitrate) were used for wart removal and ulcer debridement [37]. During the early 1920s, the method used was to pass a small electrical charge through a mixture of water and silver crystals in order to obtain an effective silver (electrocolloidal) ion solution that could be used topically on wounds and, indeed, some wound centers still use this approach today. However, due to the instability of the solution the method has been shown to be highly impractical for use on large wounds or for extended time periods. Today, with the advent of nanotechnology, the availability of silver in nanoparticle form has allowed the use of pure silver to become widely used in medical practice. As the size, shape and composition of the silver nanoparticles can have significant effects on their antibacterial efficacy, many extensive investigations have been conducted aimed at their synthesis and characterization. The application of nanosilver can, therefore, be broadly divided into diagnostic and therapeutic uses.

4.3.1 Nanosilver in Diagnosis, Imaging and Targeting

The early diagnosis of any disease condition is vital to ensure that treatment is prescribed early, thus ensuring a better chance for cure. For example, the risk of developing pulmonary complications is greater in patients undergoing surgery and requiring general anesthesia if they have upper respiratory tract viral infections. Yet, the patients' risk would be minimized if the viral infections could be detected before the presentation of any symptoms. As current antibody-based detection methods generally lack the sensitivity required for low-level virus detection, surface-enhanced Raman spectroscopy (SERS) has emerged as a powerful analytical tool which extends the possibilities of vibrational spectroscopy. SERS differs from standard Raman scattering in that the incoming laser beam interacts with the oscillations of plasmonic electrons in metallic nanostructures to enhance

the vibrational spectra of molecules adsorbed to the surface. In a recent study, SERS was used to obtain the Raman spectra of respiratory syncytial virus (RSV), using substrates composed of silver nanorods (anisotropic silver). Here, the four virus strains tested were readily detected at low detection limits and classified using the multivariate statistical methods [38]. The power of SERS was further demonstrated in its use in immunoassays, where the detection level of immunoglobulins was as low as $4\,ng\,ml^{-1}$ [39].

In terms of detecting cancer, whilst many molecular probes can recognize the unique cell surface molecules on cancer cells, some of these probes have only relatively weak binding affinities. In a recent study, Au-Ag nanorods (NRs) were used as a nanoplatform for multivalent binding by multiple aptamers to increase both the signal and binding strengths of the aptamers in cancer cell recognition. The molecular assembly of aptamers on the NR was shown to lead to a 26-fold higher affinity than the original aptamer probes [40]. Thus, these NR–aptamer conjugates show great promise for use in specific cell targeting, as well as having the detection and targeting ability required for cell studies, disease diagnosis and therapy.

The use of silver nanoparticles has also been described in matrix-assisted laser desorption/ionization (MALDI), a powerful laser-based soft ionization technique for mass spectrometric analysis and the investigation of peptides, proteins, nucleic acids, pharmaceuticals, bacterial characterization and imaging studies. Here, liquid–liquid microextraction base-modified silver nanoparticles were employed for the extraction of a hydrophobic peptide (gramicidin) from biological samples through hydrophobic interactions, prior to MALDI analysis (Figure 4.1) [41]. The application of silver nanoparticles was shown to provide an excellent sample clean-up procedure, and also assisted in the enhancement of signal of peptides and proteins.

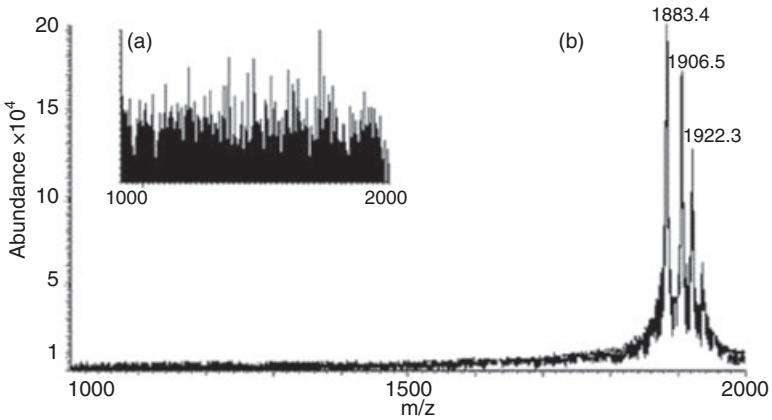

Figure 4.1 Atmospheric pressure (AP)-MALDI-MS spectra of gramicidin obtained from a spiked urine sample with (a) conventional AP-MALDI-MS and (b) by using octadecanethiol-modified silver nanoparticles. (Reproduced with permission from Ref. [41]).; © 2008 ACS Publishing)

Recently, third-harmonic-generation (THG) microscopy has emerged as an important noninvasive intravital imaging modality of *in vivo* biological research. The advantages of the technique include an intrinsic optical sectioning capability and no energy release, thus allowing a much improved cell viability. For this imaging modality, a recent study demonstrated the use of silver nanoparticles as exogenous contrast agents in cultured mouse bladder carcinoma cells [42]. Here, by successfully conjugating anti-her2 antibodies with the citrated silver nanoparticles, Her2/neu in the cancerous cell membranes was successfully imaged with THG microscopy.

4.3.2 Nanosilver in Therapeutics

4.3.2.1 Wound Dressings

The ability to incorporate silver nanoparticles into fabrics has been well demonstrated [43], with perhaps the most well-documented and commonly used application of nanosilver being that of wound dressings [44, 45]. In this regard, Acticoat®, which is the first commercial dressing made from two layers of polyamide ester membranes covered with nanocrystalline silver ions and a core absorption layer in the middle, has been studied extensively. In *in vitro* studies, the antimicrobial barrier properties of Acticoat® were compared to that of silver nitrate and silver sulfadiazine (Silvazine®; the traditional hydrophilic cream treatment for burn wounds in clinical settings), with the minimum inhibitory concentration (MIC) and minimum bactericidal concentration (MBC) being determined using five clinically significant bacteria: *Staphylococcus aureus, Staphylococcus epidermidis, Escherichia coli, Klebsiella pneumoniae* and *Pseudomonas aeruginosa*. In these studies, Acticoat® was shown to have the lowest MIC and MBC values of the three silver-containing agents. Moreover, when the kill kinetics were studied, Acticoat® demonstrated the fastest kill times for all five bacteria with, in most instances, bacterial viability being lost in less than 30 min after inoculation with silver nanoparticles, whereas at least 2–4 h elapsed before loss of viability with either silver nitrate or silver sulfadiazine [46, 47]. Although the silver particles are very quickly inactivated in the wound, the rapid bactericidal effect and sustained release of silver particles achieved with the nanosilver delivery system should minimize the likelihood of bacteria developing resistance to silver. Therefore, although the concentrations of aqueous silver ions released from the dressings were about 30-fold lower than those found with silver nitrate and silver sulfadiazine, a more rapid killing rate was produced by the nanosilver-coated dressing [48].

In a randomized prospective clinical study involving 30 patients, with each group of patients having comparable burn wound size, depth and location, the wounds were treated with either a nanosilver dressing or a gauze soaked in 0.5% silver nitrate solution. The frequency of burn wound sepsis was shown to be less in wounds treated with nanosilver than in those treated with silver nitrate. Furthermore, secondary bacteremia arising from infected wounds was also less frequent [49]. As well as burn wounds, there is now increasing evidence for the use

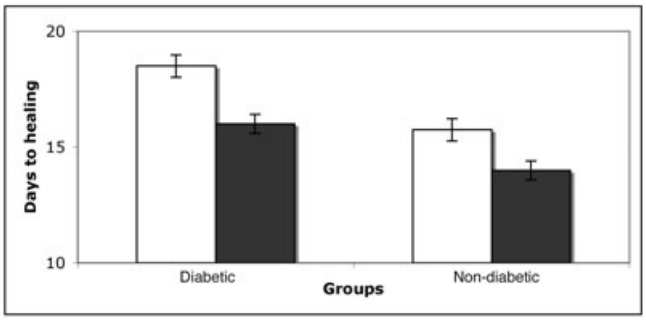

Figure 4.2 Times of wound closure (group mean ± SE) in diabetic and nondiabetic mice treated with nanosilver (shaded) and conventional dressing (nonshaded). A $1 \times 1\,cm^2$ full-thickness wound was excised in genetically diabetic (C57BLKs/J-m+/db, db/db) and non-diabetic control C57BLKs/J-m mice, and coated dressings were applied daily to each wound (n = 5). The wounds were assessed daily to check for healing.

of nanosilver in the treatment of chronic wounds such as leg ulcers, diabetic foot ulcers and pressure ulcers. Indeed, when using a contaminated wound model in diabetic mice, a faster healing was found in animals treated with nanosilver compared to controls (Figure 4.2). In concurring with our findings, Sibbald *et al.* conducted a prospective study to evaluate the use of a nanosilver dressing on a variety of chronic, nonhealing wounds. These authors concluded that nanosilver dressing had a beneficial effect of protecting the wound site from bacterial contamination [50]. A further clinical study conducted in a burns unit in Australia showed that patients treated with Acticoat® had a decrease in wound cellulitis (55% versus 10.5%), antibiotic use (57% versus 5.2%), length of stay (17.3 days versus 12.5 days) and overall treatment costs compared to those treated with Silvazine® [51]. Taken together, the use of nanosilver in wound dressings appears to hold the greatest promise.

4.3.2.2 **Silver-Impregnated Catheters**

4.3.2.2.1 **Central Venous Catheters** Central venous catheters (CVCs) are widely used in hospital practice; indeed it has been estimated that, in the United States alone, about 5 million of these units are inserted annually [52]. The widespread use of CVCs is associated with potential infective complications, with the annual incidence of catheter-related bloodstream infection estimated at around 80 000 cases in the US [53, 54].

Previous studies have suggested that, although the impregnation of catheters with antiseptics or antibiotics might reduce the rates of catheter colonization [55–57], there would be a risk that the increasing use of such catheters could lead to greater antimicrobial resistance. Recently, a new generation of silver-impregnated catheters, based on the use of an inorganic silver powder in which silver ions are bonded with an inert ceramic zeolite (Agion), has become available for clinical

use. This combination releases silver ions from both the inner and outer surfaces, in continuous fashion. A recent study was performed comparing these silver-impregnated catheters with standard catheters, with the rate of colonization as the primary end point and catheter-related bloodstream infections as the secondary end point. The results showed the overall colonization rate to be significantly lower for the silver-impregnated CVC tips than for control tips (58% versus 73%; $p < 0.025$). In addition, there was a lower rate of tip colonization by coagulase-negative staphylococci in the silver zeolite-impregnated CVC tips as compared to control tips (34% versus 47%; $p < 0.05$) [58]. As the concern of bacterial resistance is minimal with silver, it would appear that silver-impregnated catheters are destined for increased use in the future.

4.3.2.2.2 **Vascular Prostheses** On a larger scale, vascular prosthetic grafts are used to repair diseased blood vessels, such as the aorta. Extensive research in vascular surgery hence has focused on the development of infection-resistant prosthetic grafts. In a recent multicenter study evaluating the use of the InterGard Silver bifurcated polyester graft coated with collagen and silver, the silver-impregnated vascular grafts achieved excellent patency over a long-term period, with a low rate of graft infection [59]. A randomized trial with this graft is awaited.

4.3.2.2.3 **Urinary Catheters** The urinary tract is the most common site of nocosomial infections in hospital patients. Indeed, it has been estimated that, in the United States, 25% of hospitalized patients undergo indwelling urinary catheterization, and each procedure is associated with a risk of bacteriuria of approximately 5% per day of catheterization [60, 61]. Catheter-associated infections result from an ascending bacterial colonization within the glycocalyx-enclosed biofilm on the inner and outer surfaces of the catheter [62]. With time, organisms may also move up from the bladder to the ureters, and then to the kidneys, as well as invading the bloodstream and causing sepsis. With each urinary tract infection (UTI) resulting in 1 to 3.8 extra hospital days, a potential annual saving of US$ 500 million could be made in hospital costs if UTIs were to be avoided [63, 64]. Although systemic antibiotic therapy is effective for eliminating the bacterial population adherent to the bladder mucosa and in the urine, any bacterial biofilm on a Foley catheter could be eradicated only by a very high dose of antibiotics [65]. Previously, an antibiotic-bonded nephrostomy catheter for use in percutaneous nephrostomies, as well as a catheter with a nitrofurazone matrix, have been designed; however, comparative studies showed no significant differences in clinical outcome compared to the conventional catheter system [66–68].

The use of silver may prove to be a valuable alternative in the treatment of UTIs, as it is known to be highly active against a broad spectrum of bacteria commonly found in these conditions. Recently, when a new technology where the entire catheter was impregnated with silver nanoparticles (3–8 nm) was described, the

safety of these catheters was determined and showed excellent results [69, 70]. The antimicrobial activity of silver in a polyurethane matrix may also extend to preventing bacterial adherence on the surface of the catheter, thus preventing biofilm formation. When the duration of silver release was investigated by continuous rinsing of the material with physiological saline, a steady state release of 35 ng cm^{-2} was revealed at day 10. Such a concentration would provide the antimicrobial activity observed in samples obtained between days 10 and 30. Indeed, a meta-analysis of data from prospective trials highlighted not only the efficacy of these silver alloy/hydrogel-coated catheters but also their excellent cost-effectiveness [71].

4.3.2.2.4 **Ventricular Drainage Catheters** The insertion of temporary external ventricular drainage (EVD) is common in intensive care patients for the management of acute occlusive hydrocephalus. One very important complication of external cerebrospinal fluid (CSF) drainage is bacterial colonization of the catheter, as this results in ventriculomeningitis and encephalitis. As with CVCs, the use of antimicrobial-impregnated catheters, although useful, can induce the emergence of bacterial multiresistance. Since 2004, silver-impregnated EVD catheters have been available commercially in the European Union and, indeed, a recent pilot study addressed their efficacy in neurological and neurosurgical patients requiring external CSF drainage to treat acute occlusive hydrocephalus. It was found that CSF cultures, performed at least three times weekly, yielded 25% more positive cultures in control subjects compared to 0% in patients where silver catheters were used. Furthermore, reactive pleocytosis in CSF, which is an indicator of aseptic meningitis due to inflammation, was not seen in patients where the silver-impregnated biomedical material was used [72].

4.3.2.3 Orthopedic Applications

4.3.2.3.1 **Bone Cement** In recent years, artificial joint replacements have become the 'gold standard' treatment for many arthritic diseases. Today, bone cement based on polymethylmethacrylate (PMMA) is commonly used for the anchoring of artificial joints. Like all biomaterials, PMMA has an elevated risk of infection when implanted into the human body when compared to autogenous tissue [73]. Whilst the loading of PMMA with antibiotics has been postulated to reduce the risk of joint infections [74, 75], an increasing number of joint infections with multiresistant bacteria means that an adequate prophylaxis against these organisms becomes essential. For the same reasons as described above, silver nanoparticles seem here to be the obvious choice. In recent studies conducted to evaluate bone cement loaded with nanosilver [76], an absence of *in vitro* cytotoxicity of nanosilver-loaded bone cement was shown, as was a high antibacterial activity against all tested strains, including methicillin-resistant *Staphylococcus aureus* (MRSA). In addition, no cytotoxicity towards osteoblasts grown *in vitro* was observed. Taking these results together, silver-loaded bone cement would

appear to be a potential candidate for the next generation of biomaterials in orthopedics.

4.3.2.3.2 **Artificial Joints** The use of silver nanoparticles has also been studied in artificial joints where, for many years, ultra-high-molecular-weight polyethylene (UHMWPE) has been the material of choice for fabricating the bearing inserts for total joint replacement components. Despite being resistant to corrosion and abrasion, a major problem with the longevity of UHMWPE is that of wear and concomitant debris generation, which can lead to macrophage activation with subsequent inflammation, and eventual failure of the artificial joint. In one study, the supercritical fluids processing of UHMWPE and formation in silver nanoparticles was shown to lead to both physical and chemical stabilization of the polymer surface layer towards friction oxidation and degradation (Figure 4.3) [77]. This procedure was shown to significantly decrease the process of polymer/metal tribochemical debris formation, and at the same time enhance UHMWPE biocompatibility and antimicrobial activity.

4.3.2.4 **Surgical Mesh**

Currently, the standard measures for protection against surgical infection include perioperative antibiotics, antiseptic skin preparations and sterile surgical technique. Nonetheless, in many instances surgical implants are unavoidable and carry a risk of infection due to the presence of foreign material. At present, one million nocosomial infections are seen each year in patients with implanted pros-

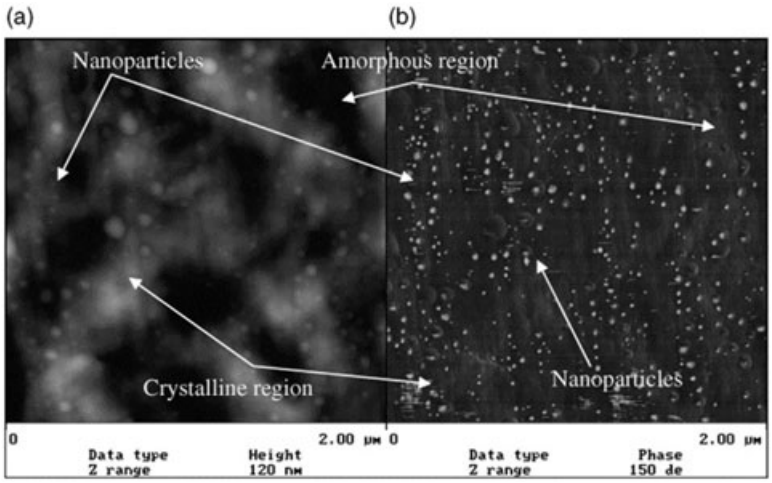

Figure 4.3 Tapping mode atomic force microscopy height (a) and phase (b) images of UHMWPE with silver nanoparticles deposited. The images were collected from a cryomicrotomed surface; the crystalline regions of the polymer and nanoparticles can be clearly identified in both images. (Reproduced with permission from Ref. [77]; © 2007 Elsevier.)

thetic materials [78]. Surgical meshes are used commonly for bridging large wounds, as well as acting as reinforcements in tissue repair, of which the most common purpose is in the repair of inguinal hernias. With the goal of creating a successful antibacterial coating for a prosthetic material, an analysis was carried out to examine the *in vitro* properties of a silver nanoparticle-coated polypropylene mesh. Similar to other studies using silver nanoparticles, the results here showed the nanosilver polypropylene mesh to have significant bactericidal efficacy against *S. aureus*. It was further shown that the silver particles could diffuse from the mesh and had antibacterial activity that increased with increasing doses [79]. These *in vitro* results clearly warranted further *in vivo* studies to determine whether nanosilver-coated polypropylene mesh could reduce the prosthetic infection rate and the host inflammatory response within the clinical setting. It also remains to be seen if nanosilver particles might serve as an ideal coating for all surgically implanted devices.

4.3.2.5 Disinfectants

A more recent application of nanosilver is its addition to disinfecting agents. Contaminated surfaces can act as a reservoir for pathogenic microorganisms, and potentially exacerbate the risk of infection. Although surface disinfection provides bacterial killing, disinfected surfaces soon become recontaminated; hence, in order to improve on the current state an ideal disinfectant should also provide persistent antimicrobial action. Brady *et al.* described the use of a silver-based disinfectant technology designed to provide longlasting sanitization and disinfection [80].

These authors demonstrated silver to be active against household pathogens (*E. coli, S. aureus, Klebsiella pneumoniae, Enterobacter aerogenes, Enterococcus faecium* and *Salmonella choleraesuis*). The silver-based disinfectant also showed significant and equivalent efficacy against antibiotic-resistant bacteria. In addition, significant residual activity was seen after 10 min against all organisms tested after five cycles of water rinsing, abrasion and microbial contamination. A silver nanowire/mesoporous silica composite was also shown to be highly effective antiseptic in another report [81]. Taken together, these findings highlighted the ability of a silver-based disinfectant to reduce the risk of infection within the home and healthcare settings.

4.4 Are Silver Nanoparticles Toxic?

As the widespread use of silver nanoparticles in medical appliances continues to expand, the exposure of the body to silver will clearly increase. Although, traditionally, silver is believed to be relatively nontoxic to mammalian cells, in 2005 a review was conducted of the occupational risks of workers in the silver industry, when metallic silver was considered to represent a minimal health risk [82]. It is not known, however, whether this holds true for silver nanoparticles. This is of

particular concern because, due to its small particle size, nanosilver may gain an increasing access to tissues, cells and biological molecules within the human body. Once achieving nanoscale, some materials do exhibit significant toxicity to mammalian cells, an example being carbon nanotubes [83, 84]. The underlying concern with nanoparticles is that their small size leads to an ultra-large surface area per mass, such that a large proportion of the atoms are in immediate contact and readily available for reaction. Already, some unique interactions with microorganisms have been demonstrated with silver nanoparticles of certain size ranges and shapes [13, 22, 85]. A small size also confers a greater particle mobility and various electric charges within the body. These modifications of the intrinsic physico-chemical properties of silver thus give rise to various cellular uptakes, and interactions with other biological molecules within the human body. Silver nanoparticles can gain access to different body surfaces through both clinical and environmental routes and, at the sites of contact, can bind to and react with proteins. It follows, therefore, that uptake through phagocytosis can also take place. Furthermore, nanoparticles may elicit a spectrum of tissue responses including cell activation, the generation of reactive oxygen species (ROS), inflammation and cell death [86, 87].

4.4.1 Access via the Skin

As the most popular nanosilver products in clinical use today are wound dressings, there will inevitably be an increase in interest in the potential adverse side effects of nanosilver due to its close contact with human skin. One of skin's major roles is to provide protection to the underlying organs. The skin comprises an outer epidermis and dermis; the stratum corneum layer of the epidermis acts as a strict barrier, allowing only a limited penetration of particulate materials. However, the transdermal penetration of fine particles has been documented [88]. Until now, the available data on nanosilver are few to none; nonetheless, as nanosilver wound dressings are applied to wounded skin – where the epidermal barrier is broken – it is to be expected that entry of the nanoparticles into the body would be easier. This, along with the observation that particles in the skin can be phagocytosed by macrophages and Langerhans cells, might lead to perturbations of the immune system. A case of activation of mast cells by silver nanoparticles in a patient with localized argyria has been reported [89], while one other clinical report described an abnormal elevation in the blood levels of silver and argyria-like symptoms following the use of nanosilver-coated dressings for burns. The absorption of nanosilver into the circulation has thus been indicated [90].

When cultured keratinocytes were exposed to extracts of silver-containing dressings, their proliferation was significantly inhibited and cell morphology affected [91]. In another study, nanosilver released from a commercially available dressing was found to be toxic to both keratinocytes and fibroblasts [92]. Nonetheless, there was no increase in cell death in these experiments using

keratinocytes. In contrast, when using an *in vitro* wounding model, nanosilver was found to increase the growth rate of these cells (K.K.Y. Wong, unpublished data). The obvious discrepancies between these data and those reported by others might be attributable to differences in laboratory conditions and the techniques employed, while the concentration of silver used in these experiments might also be an important factor. Clearly, the establishment of a set of integrated and standardized evaluation protocols is necessary for these investigations. It should also be noted that most experiments were carried out using *in vitro* models, the findings of which might differ from those performed *in vivo*. Indeed, in a clinical situation wound exudation might also contribute towards the effect of nanosilver on wound healing, with the high protein content perhaps neutralizing the tissue toxicity.

4.4.2 Pulmonary Entry

Access via the respiratory system serves as a major route for ambient particulate materials. The deposition of inhaled particles <100 nm in size mainly occurs in the alveolar region. As healthcare and hygiene spray products containing silver nanoparticles continue to enter daily use, concern is increasing with regards to the fate of these nanoparticles in the respiratory system, as they may in time be channeled into the lungs. At the alveolar level, the particles are first submersed into the surfactant lining of the alveoli before coming into contact with any cell. Results from studies using different types of particle have suggested that the surfactant di-palmitoyl-phosphatidyl-choline (DPPC) and surfactant protein are adsorbed to the particle surface, and that this may be a mediation mechanism for the toxicity of particulate matter [93]. Based on the results of studies using silica, the surface structures were found to interact with the lining fluid layer and to produce surface radicals and ROS, which were associated with silica particle's specific toxicity, while a particle–surfactant lining interaction influenced any subsequent particle–cell interaction [94]. Toxicological data on silver nanoparticles in this respect are limited, nonetheless. Furthermore, as silver has an oxidation state it can act as a catalyst; indeed, a high catalytic activity for oxidation has been demonstrated in silver nanoparticle-based catalysts [95]. It is thus sound to assume, that the huge surface area of silver nanoparticles may serve as an efficient facilitator for the generation of radicals and ROS. Further, the phagocytosis of nanoparticles can lead to the activation of macrophages and the release of chemokines, cytokines and other mediators, which may result in a sustained inflammation [96–98]. In inhalation experiments in rats, silver nanoparticles were shown to be taken up by alveolar macrophages and to persist for up to 7 days. Nonetheless, the silver content in the lung decreased rapidly with time after the inhalation of a relatively low concentration of ultrafine silver [99]. Two recent articles addressed the effects of prolonged inhalation of silver nanoparticles on the lungs in rats [100, 101]. At high doses of silver, there were detectable lung function changes as well as an abnor-

mality of liver enzymes, which suggested that silver might indeed have adverse effects on the tissues. Clearly, additional studies aimed at examining these points are required.

4.4.3 Gastrointestinal Tract

As the gastrointestinal tract provides a large surface area for efficient nutrient exchange, gastrointestinal ingestion may represent a common route for exposure to nanosilver in the way of health supplements. For example, colloidal silver has been marketed by many commercial companies to have immune-boosting effects. Silver nanoparticles are also used in products for water disinfection and food stabilization. Despite such extensive (potential) exposure, reports on local or systemic adverse effects of orally ingested nanosilver are few in number. The mechanism of nanosilver translocation has been postulated as occurring either via the intestinal lymphatic tissues or transcellularly via normal enterocytes [102]. Those nanoparticles which enter the capillaries become circulatory and very soon encounter the liver (via an hepatic first-pass), perhaps causing the liver to be exposed to a high dose of silver nanoparticles. Although toxic effects of silver nanoparticles to liver cells have been reported *in vitro* [103], the systemic toxicity of ingested nanosilver has scarcely been seen. In support of these data, when nanosilver particles were injected intravenously into experimental mice, no overt systemic effects were observed, despite the nanosilver solution being used at a relatively high concentration of 100 μM (K.K.Y. Wong, unpublished data).

4.4.4 Other Tissues

By taking into account the existence of silver nanoparticle-impregnated catheters for clinical use, hemocompatibility becomes a top safety concern. Previous reports have suggested that nanoparticles present in the blood were associated with thrombosis and the activation of immunological reactions. Various studies have provided evidence that exposure to ambient ultrafine particles elicits an inflammatory response in vascular endothelial cells and blood cells [104, 105]. In the case of silver, a recent study revealed that silver nanoparticles could greatly enhance the electron-transfer reactivity of myoglobin [106].

The recent identification of the cytotoxicity of silver nanoparticles towards a spermatogonial stem cell line has aroused great concern over the biosafety of nanomaterials [107]. As discussed previously, the liver appears to be an eventual accumulation site for circulatory silver nanoparticles, and similar patterns of cytotoxicity for silver nanoparticles (decreased mitochondrial function, lactate dehydrogenase (LDH) leakage and abnormal cell morphologies) were observed *in vitro*. Nonetheless, during other experiments using nanosilver, a variety of

organs (e.g. liver, spleen, lung, heart, kidney) were routinely harvested and, after trypsin digestion, analyzed for their silver content using inductively coupled plasma mass spectroscopy (ICP-MS). Thus far, in experiments with mice, and using therapeutic doses of nanosilver, only very low levels of silver ($<0.5\,\mu g\,g^{-1}$) were detected in the tissues, which suggested that nanosilver was safe at these concentrations.

4.5 Possible New Therapeutic Options

4.5.1 Anti-Inflammatory Agents

The potential anti-inflammatory action of nanosilver has been suggested in various studies. Initially, the anti-inflammatory effects of nanocrystalline silver were examined in a rat model of ulcerative colitis induced by the intracolonic administration of dinitrobenzenesulfonic acid [108]. Quantitative macroscopic and microscopic observations in this study revealed that intracolonic treatment with nanosilver at concentrations of 40 and $4\,mg\,kg^{-1}$ significantly reduced the colonic inflammation. Here, nanosilver was seen to significantly suppress the protein expression of TNF-α, interleukin (IL)-12 and IL-1β, while a reduction in MMP-9 was also seen. These cytokines and MMP-9 were up-regulated in the colonic tissues of rats after the induction of colitis. The results suggested that nanosilver, when administered either intracolonically or orally, may have therapeutic potential for the treatment of inflammatory bowel disease (Figure 4.4).

In contrast, inflammation has been noted to play a significant part in the formation of postoperative adhesions. In a mouse model, it was shown that an intraperitoneal injection of nanosilver significantly reduced the degree of postoperative fibrous adhesions (Figure 4.5; also K.K.Y. Wong, unpublished data). Taken together, these results suggest that nanosilver can indeed reduce inflammation, and its use in other inflammatory conditions is eagerly anticipated.

4.5.2 Anti-Viral Drugs

The anti-viral properties of metal nanoparticles remain an undeveloped area which, potentially, is of major medical interest. With finding a cure for human immunodeficiency virus (HIV) in mind, the postinfected anti-HIV-1 activities of silver nanoparticles towards Hut/CCR5 cells were evaluated in a study conducted by our group [109] (Figure 4.6). Here, the silver nanoparticles were shown to possess a dose-dependent anti-retroviral activity and to exhibit a high potency at $50\,\mu M$ (98%) in inhibiting HIV-1 replication. Moreover, the nanoparticles did not show any acute cytotoxicity to either the Hut/CCR5 cells or to normal

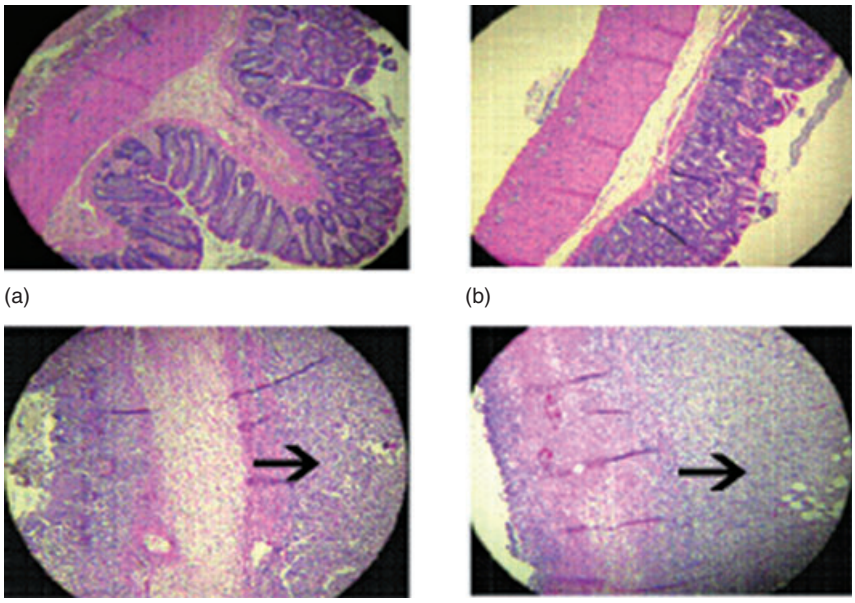

Figure 4.4 Histological sections of the colon showing the effects of oral nanocrystalline silver (NP) on a rat colitis model, where colitis was produced using a single intracolonic injection of dinitrobenzenesulfonic acid (DNBS). Treatment groups consisted of oral administration of nanosilver particles (40, 4 or 0.4 mg kg^{-1}) or sulfasalazine suspension. Placebo and untreated groups served as controls. Colonic sections were stained with hematoxylin and eosin and examined microscopically. (a) Treated with NP; (b) Treated with sulfasalazine; (c) Treated with placebo; (d) Untreated. Generally, colonic damage consisted of transmural ulceration extending through the serosal surface, with the presence of edematous muscularis mucosa and submucosa, infiltration of neutrophils, and lymphocytes (arrows). Note the healed mucosa and few residual inflammatory infiltrates in the sections of rats treated with NP and sulfasalazine (a, b), and the extensive ulceration and inflammatory infiltrates in the sections of placebo-treated and untreated rats (c, d). (Reproduced with permission from Ref. [108]; © 2007 Springer.)

peripheral blood mononuclear cells (PBMC). It remains to be seen whether silver nanoparticles have activities against other types of virus, and further experimental studies are clearly required before any clinical trial could be contemplated.

4.6 Conclusions

The recent advances in nanotechnology that have enabled us to utilize particles on a nanoscale basis have also created new therapeutic horizons. In the case of

Figure 4.5 Photograph showing the absence of peritoneal adhesions in a mouse 2 weeks after receiving an intraperitoneal injection of nanosilver in a postoperative adhesion model.

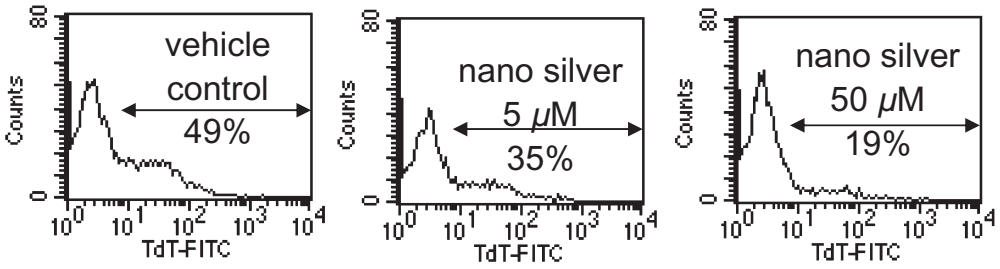

Figure 4.6 The TUNEL assay was performed with flow cytometry to assess the degree of cell death of Hut/CCR5 cells following the introduction of human immunodeficiency virus 1 (HIV-1) *in vitro*. A comparison was made between cells pretreated with nanosilver particles (5 μ*M* and 50 μ*M*) and untreated controls. The silver nanoparticles were shown to have cytoprotective activity towards HIV-1 infection, reflected by a much lower degree of cell death. (Reproduced with permission from Ref. [109]; © RSC Publishing.)

silver, the currently available data have merely 'scratched the surface' of the potential benefits and wide range of applications of these materials. Although we have yet to elucidate the exact cellular pathway of nanosilver, it remains to be seen whether any potential complications for silver nanoparticles might surface after their prolonged clinical use. Nonetheless, a bright future holds for this precious metal.

References

1 Russell, A.D. and Hugo, W.B. (1994) Antimicrobial activity and action of silver. *Progress in Medicinal Chemistry*, **31**, 351–70.

2 Van de Voorde, K., Nijsten, T., Schelfhout, K., Moorkens, G. and Lambert, J. (2005) Long-term use of silver containing nose-drops resulting in systemic argyria. *Acta Clinica Belgica*, **60**(1), 33–5.

3 Spencer, W.H., Garron, L.K., Contreras, F., Hayes, T.L. and Lai, C. (1980) Endogenous and exogenous ocular and systemic silver deposition. *Transactions of the Ophthalmological Societies of the United Kingdom*, **100**(Pt 1), 171–8.

4 Wied, U., Andersen, K., Schultz, A., Rasmussen, E. and Watt-Boolsen, S. (1981) Silver nitrate pleurodesis in spontaneous pneumothorax. *Scandinavian Journal of Thoracic and Cardiovascular Surgery*, **15**(3), 305–7.

5 Wied, U., Halkier, E., Hoeier-Madsen, K., Plucnar, B., Rasmussen, E. and Sparup, J. (1983) Tetracycline versus silver nitrate pleurodesis in spontaneous pneumothorax. *The Journal of Thoracic and Cardiovascular Surgery*, **86**(4), 591–3.

6 Quitkin, H.M., Rosenwasser, M.P. and Strauch, R.J. (2003) The efficacy of silver nitrate cauterization for pyogenic granuloma of the hand. *The Journal of Hand Surgery*, **28**(3), 435–8.

7 Fox, C.L., Jr (1975) Silver sulfadiazine for control of burn wound infections. *International Surgery*, **60**(5), 275–7.

8 Fraser, G.L. and Beaulieu, J.T. (1979) Leukopenia secondary to sulfadiazine silver. *The Journal of the American Medical Association*, **241**(18), 1928–9.

9 Caffee, H.H. and Bingham, H.G. (1982) Leukopenia and silver sulfadiazine. *The Journal of Trauma*, **22**(7), 586–7.

10 Lee, K.S. and El-Sayed, M.A. (2006) Gold and silver nanoparticles in sensing and imaging: sensitivity of plasmon response to size, shape, and metal composition. *The Journal of Physical Chemistry B*, **110**(39), 19220–5.

11 Evanoff, D.D. Jr and Chumanov, G. (2005) Synthesis and optical properties of silver nanoparticles and arrays. *Chemphyschem*, **6**(7), 1221–31.

12 Makarava, N., Parfenov, A. and Baskakov, I.V. (2005) Water-soluble hybrid nanoclusters with extra bright and photostable emissions: a new tool for biological imaging. *Biophysical Journal*, **89**(1), 572–80.

13 Elechiguerra, J.L., Burt, J.L., Morones, J.R., Camacho-Bragado, A., Gao, X., Lara, H.H. *et al.* (2005) Interaction of silver nanoparticles with HIV-1. *Journal of Nanobiotechnology*, **3**, 6.

14 Birringer, R. (1989) Nanocrystalline materials. *Materials Science and Engineering A*, **117**, 33–43.

15 Sant, S., Gill, K. and Burrell, R. (2000) Novel duplex antimicrobial silver films deposited by magnetic sputtering. *Philosophical Magazine Letters*, **148**, 249–56.

16 Djokic, S., Burrell, R. and Field, P. (2001) An electrochemical analysis of thin silver films produced by reactive sputtering. *Journal of the Electrochemistry Society*, **148**, 791–6.

17 Ovington, L. (2001) Nanocrystalline silver: where the old and familiar meets a new frontier. *Wounds*, **13**, 5–10.

18 Fu-Ren, F. and Bard, A. (2002) Chemical, electrochemical gravimetric and microscopic studies on antimicrobial silver films. *Journal of Physical Chemistry*, **106**, 279–87.

19 Modak, S.M. and Fox, C.L., Jr (1973) Binding of silver sulfadiazine to the cellular components of *Pseudomonas aeruginosa*. *Biochemical Pharmacology*, **22**(19), 2391–404.

20 Cervantes, C. and Silver, S. (1996) Metal resistance systems in *Pseudomonas*. *Revista Latinoamericana de Microbiologia*, **38**(1), 45–64.

21 Nikawa, H., Yamamoto, T., Hamada, T., Rahardjo, M.B., Murata, H. and Nakanoda, S. (1997) Antifungal effect of zeolite-incorporated tissue conditioner against *Candida albicans* growth and/or acid production. *Journal of Oral Rehabilitation*, **24**(5), 350–7.

22 Lok, C.N., Ho, C.M., Chen, R., He, Q.Y., Yu, W.Y., Sun, H. *et al.* (2006) Proteomic

analysis of the mode of antibacterial action of silver nanoparticles. *Journal of Proteome Research*, **5**(4), 916–24.

23 Lok, C.N., Ho, C.M., Chen, R., He, Q.Y., Yu, W.Y., Sun, H. *et al.* (2007) Silver nanoparticles: partial oxidation and antibacterial activities. *Journal of Biological Inorganic Chemistry*, **12**(4), 527–34.

24 Lansdown, A.B. (2002) Silver. I: its antibacterial properties and mechanism of action. *Journal of Wound Care*, **11**(4), 125–30.

25 Lansdown, A.B. (2002) Silver. 2: toxicity in mammals and how its products aid wound repair. *Journal of Wound Care*, **11**(5), 173–7.

26 Baker, C., Pradhan, A., Pakstis, L., Pochan, D.J. and Shah, S.I. (2005) *Journal of Nanoscience and Nanotechnology*, **5**, 244.

27 Panacek, A., Kvitek, L., Prucek, R., Kolar, M., Vecerova, R., Pizurova, N., Sharma, V.K., Nevecna, T. and Zboril, R. (2006) *Journal of Physical Chemistry B*, **110**, 16248.

28 Pal, S., Tak, Y.K. and Song, J.M. (2007) *Applied and Environmental Microbiology*, **73**, 1712.

29 Kvitek, L., Panacek, A., Soukupova, J., Kolar, M., Vecerova, R., Prucek, R., Holecova, M. and Zboril, R. (2008) Effect of surfactants and polymers on stability and antibacterial activity of silver nanoparticles (NPs). *Journal of Physical Chemistry*, **112**(15), 5825–34.

30 Demling, R.H. and Leslie DeSanti, M.D. (2002) The rate of re-epithelialization across meshed skin grafts is increased with exposure to silver. *Burns*, **28**(3), 264–6.

31 Wright, J.B., Lam, K., Buret, A.G., Olson, M.E. and Burrell, R.E. (2002) Early healing events in a porcine model of contaminated wounds: effects of nanocrystalline silver on matrix metalloproteinases, cell apoptosis, and healing. *Wound Repair and Regeneration*, **10**(3), 141–51.

32 Guerrero, R., Menezes, J., Reilly, D.A. *et al.* (2000) Wound care with Acticoat® in patients with non-burn skin loss. *Journal of Investigative Medicine*, **48**(1S), 322.

33 Olson, M.E., Wright, J.B., Lam, K. *et al.* (2000) Healing of porcine donor sites covered with silver-coated dressings. *European Journal of Surgery*, **166**(6), 486–9.

34 Kirsner, R., Orsted, H. and Wright, B. (2001) Matrix, metalloproteases in normal and impaired wound healing: a potential role of nanocrystalline silver. *Wounds*, **13**(5C), 5–10.

35 Tian, J., Wong, K.K., Ho, C.M., Lok, C.N., Yu, W.Y., Che, C.M. *et al.* (2007) Topical delivery of silver nanoparticles promotes wound healing. *ChemMedChem*, **2**(1), 129–36.

36 Shin, S.H., Ye, M.K., Kim, H.S. and Kang, H.S. (2007) The effects of nano-silver on the proliferation and cytokine expression by peripheral blood mononuclear cells. *International Immunopharmacology*, **7**(13), 1813–18.

37 Klasen, H.J. (2000) A historical review of the use of silver in the treatment of burns. II. Renewed interest for silver. *Burns*, **26**(2), 131–8.

38 Shanmukh, S., Jones, L., Zhao, Y.P., Driskell, J.D., Tripp, R.A. and Dluhy, R.A. (2008) Identification and classification of respiratory syncytial virus (RSV) strains by surface-enhanced Raman spectroscopy and multivariate statistical techniques. *Analytical and Bioanalytical Chemistry*, **390**(6), 1551–5.

39 Zhang, M.L., Yi, C.Q., Fan, X., Peng, K.Q., Wong, N.B., Yang, M.S., Zhang, R.Q. and Lee, S.T. (2008) A surface-enhanced Raman spectroscopy substrate for highly sensitive label-free immunoassay. *Applied Physics Letters*, **92**(4), 04136/1–04136/3.

40 Huang, Y.F., Chang, H.T. and Tan, W.H. (2008) Cancer cell targeting using multiple aptamers conjugated on nanorods. *Analytical Chemistry*, **80**(3), 567–72.

41 Shrivas, K. and Wu, H.F. (2008) Modified silver nanoparticle as a hydrophobic affinity probe for analysis of peptides and proteins in biological samples by using liquid-liquid microextraction coupled to AP-MALDI-Ion trap and MALDI-TOF mass spectrometry. *Analytical Chemistry*, **80**(7), 2583–9.

42 Tai, S.P., Wu, Y., Shieh, D.B., Chen, L.J., Lin, K.J., Yu, C.H., Chu, S.W., Chang, C.H., Shi, X.Y., Wen, Y.C., Lin, K.H., Liu, T.M. and Sun, C.K. (2007) Molecular imaging of cancer cells using plasmon-resonant-enhanced third-harmonic-generation in silver nanoparticles. *Advanced Materials*, **19**(24), 4520–3.

43 Kong, H. and Jang, J. (2008) Antibacterial properties of novel poly(methyl methacrylate) nanofiber containing silver nanoparticles. *Langmuir*, **24**(5), 2051–6.

44 Fong, J. and Wood, F. (2006) Nanocrystalline silver dressings in wound management: a review. *International Journal of Nanomedicine*, **1**(4), 441–9.

45 Leaper, D.J. (2006) Silver dressings: their role in wound management. *International Wound Journal*, **3**(4), 282–94.

46 Wright, J.B., Lam, K. and Burrell, R.E. (1998) Wound management in an era of increasing bacterial antibiotic resistance: a role for topical silver treatment. *American Journal of Infection Control*, **26**(6), 572–7.

47 Yin, H.Q., Langford, R. and Burrell, R.E. (1999) Comparative evaluation of the antimicrobial activity of ACTICOAT antimicrobial barrier dressing. *The Journal of Burn Care and Rehabilitation*, **20**(3), 195–200.

48 Coombs, C.J., Wan, A.T., Masterton, J.P. *et al.* (1992) Do burn patients have a silver lining? *Burns*, **18**(3), 179–84.

49 Tredget, E.E., Shankowsky, H.A., Groeneveld, A. *et al.* (1998) A matched-pair, randomized study evaluating the efficacy and safety of Acticoat® silver-coated dressing for the treatment of burn wounds. *The Journal of Burn Care and Rehabilitation*, **19**(6), 531–7.

50 Sibbald, R.G., Contreras-Ruiz, J., Coutts, P., Fierheller, M., Rothman, A. and Woo, K. (2007) Bacteriology, inflammation, and healing: a study of nanocrystalline silver dressings in chronic venous leg ulcers. *Advances in Skin and Wound Care*, **20**(10), 549–58.

51 Cuttle, L., Naidu, S., Mill, J., Hoskins, W., Das, K. and Kimble, R.M. (2007) A retrospective cohort study of Acticoat® versus Silvazine® in a paediatric population. *Burns*, **33**(6), 701–7.

52 Raad, I. (1998) Intravascular-catheter-related infections. *Lancet*, **351**(9106), 893–8.

53 Pittet, D., Tarara, D. and Wenzel, R.P. (1994) Nosocomial bloodstream infection in critically ill patients. Excess length of stay, extra costs, and attributable mortality. *The Journal of the American Medical Association*, **271**(20), 1598–601.

54 Mermel, L.A. (2000) Prevention of intravascular catheter-related infections. *Annals of Internal Medicine*, **132**(5), 391–402.

55 George, S.J., Vuddamalay, P. and Boscoe, M.J. (1997) Antiseptic-impregnated central venous catheters reduce the incidence of bacterial colonization and associated infection in immunocompromised transplant patients. *European Journal of Anaesthesiology*, **14**, 428–31.

56 Tennenberg, S., Lieser, M., McCurdy, B. *et al.* (1997) A prospective randomized trial of an antibiotic- and antiseptic-coated central venous catheter in the prevention of catheter-related infections. *Archives of Surgery*, **132**, 1348–51.

57 Sheng, W.H., Ko, W.J., Wang, J.T. *et al.* (2000) Evaluation of antiseptic-impregnated central venous catheters for prevention of catheter-related infection in intensive care unit patients. *Diagnostic Microbiology and Infectious Disease*, **38**, 1–5.

58 Khare, M.D., Bukhari, S.S., Swann, A., Spiers, P., McLaren, I. and Myers, J. (2007) Reduction of catheter-related colonisation by the use of a silver zeolite-impregnated central vascular catheter in adult critical care. *The Journal of Infection*, **54**(2), 146–50.

59 Ricco, J.B. (2006) InterGard silver bifurcated graft: features and results of a multicenter clinical study. *Journal of Vascular Surgery*, **44**(2), 339–46.

60 Haley, R.W., Hooten, T.M., Culver, D.H., Stanley, R.C., Emori, T.G. and Hardison, C.D. *et al.* (1981) Nosocomial infections in U.S. hospitals, 1975–1976: estimated frequency by selected characteristics of patients, *The American Journal of Medicine*, **70**, 947–59.

61 Garibaldi, R.A., Mooney, B.R., Epstein, B.J. and Britt, M.R. (1982) An evaluation of daily bacteriologic monitoring to identify preventable episodes of catheter-associated urinary tract infection. *Infection Control*, **6**, 466–70.

62 Haley, R.W., Culver, D.H., White, J.W., Morgan, W.M. and Emory, T.G. (1985) The nationwide nosocomial infection rate: a new need for vital statistics. *American Journal of Epidemiology*, **121**, 159–67.

63 Saint, S., Veenstra, D.L., Sullivan, S.D., Chenoweth, C. and Fendrick, A.M. (2000) The potential clinical and economic benefits of silver alloy urinary catheters in preventing urinary tract infection. *Archives of Internal Medicine*, **160**, 2670–5.

64 Plowman, R., Graves, N., Esquivel, J. and Roberts, J.A. (2001) An economic model to assess the cost and benefits of the routine use of silver alloy coated urinary catheters to reduce the risk of urinary tract infection sin catheterized patients. *The Journal of Hospital Infection*, **48**, 33–42.

65 Olson, M.E., Nickel, J.C., Khoury, A.E., Morck, D.W., Cleeland, R. and Costerton, J.W. (1989) Amdinocillin treatment of catheter associated bacteriuria in rabbits. *The Journal of Infectious Diseases*, **159**, 1056–72.

66 Huajijin, C. (1988) Manufacture and clinical employment of an antibiotic silicone rubber catheter. *European Urology*, **14**, 72–4.

67 Sakamoto, I., Umemura, Y. and Kitano, T. (1988) Efficacy of an antibiotic coated indwelling catheter: a preliminary report. *Journal of Biomedical Materials Research*, **19**, 1031–41.

68 Johnson, J.R., Berggren, T. and Conway, A.J. (1993) Activity of nitrofurazone matrix urinary catheter against catheter-associated uropathogens. *Antimicrobial Agents and Chemotherapy*, **37**, 2033–66.

69 Böswald, M., Mende, K., Bernschneider, W., Bonakdar, S., Ruder, H., Kissler, H. *et al.* (1999) Biocompatibility testing of a new silver impregnated catheter in vivo. *Infection*, **27**, 38–42.

70 Lundeberg, T. (1986) Prevention of catheter-associated urinary tract infections by use of silver impregnated catheters. *Lancet*, **2**, 1031.

71 Saint, S., Elmore, J.G., Sullivan, S.D., Emerson, S.S. and Koepsell, T.D. (1998) The efficacy of silver alloy-coated urinary catheters in preventing urinary tract infection: a meta-analysis. *The American Journal of Medicine*, **105**(3), 236–41.

72 Galiano, K., Pleifer, C., Engelhardt, K., Brossner, G., Lackner, P., Huck, C. *et al.* (2008) Silver segregation and bacterial growth of intraventricular catheters impregnated with silver nanoparticles in cerebrospinal fluid drainages. *Neurological Research*, **30**(3), 285–7.

73 Gristina, A.G. (1987) Biomaterial-centered infection; microbial adhesion versus tissue integration. *Science*, **237**, 1588–95.

74 Josefsson, G., Gudmundsson, G., Kolmert, L. and Wijkstrom, S. (1990) Prophylaxis with systemic antibiotics versus gentamicin bone cement in total hip arthroplasty. A five-year survey of 1688 hips. *Clinical Orthopaedics*, **253**, 173–8.

75 Josefsson, G. and Kolmert, L. (1993) Prophylaxis with systemic antibiotics versus gentamicin bone cement in total hip arthroplasty. A 10-year survey of 1688 hips. *Clinical Orthopaedics*, **292**, 210–14.

76 Alt, V., Bechert, T., Steinrücke, P., Wagener, M., Seidel, P., Dingeldein, E., Domann, E. and Schnettler, R. (2004) An in vitro assessment of the antibacterial properties and cytotoxicity of nanoparticulate silver bone cement. *Biomaterials*, **25**(18), 4383–91.

77 Morley, K.S., Webb, P.B., Tokareva, N.V., Krasnov, A.P., Popov, V.K., Zhang, J., Roberts, C.J. and Howdle, S.M. (2007) Synthesis and characterization of advanced UHMWPE/silver nanocomposites for biomedical applications. *European Polymer Journal*, **43**(2), 307–14.

78 Darouiche, R.O. (2004) Current concepts: treatment of infections associated with surgical implants. *The New England Journal of Medicine*, **350**, 1422–9.

79 Cohen, M.S., Stern, J.M., Vanni, A.J., Kelley, R.S., Baumgart, E., Field, D. *et al.*

(2007) In vitro analysis of a nanocrystalline silver-coated surgical mesh. *Surgical Infections*, **8**(3), 397–403.

80 Brady, M.J., Lisay, C.M., Yurkovetskiy, A.V. and Sawan, S.P. (2003) Persistent silver disinfectant for the environmental control of pathogenic bacteria. *American Journal of Infection Control*, **31**(4), 208–14.

81 Zhang, D.Q., Wan, Y., Li, G.S., Zhang, J. and Li, H.X. (2007) Synthesis of silver nanowire/mesoporous silica composite as a highly active antiseptic. *Studies in Surface Science and Catalysis*, **165**, 841–6.

82 Drake, P.L. and Hazelwood, K.J. (2005) Exposure-related health effects of silver and silver compounds: a review. *The Annals of Occupational Hygiene*, **49**, 575–85.

83 Shvedova, A.A., Kisin, E.R., Mercer, R., Murray, A.R., Johnson, V.J., Potapovich, A.I., Tyurina, Y.Y., Gorelik, O., Arepalli, S., Schwegler-Berry, D., Hubbs, A.F., Antonini, J., Evans, D.E., Ku, B.K., Ramsey, D., Maynard, A., Kagan, V.E., Castranova, V. and Baron, P. (2005) Unusual inflammatory and fibrogenic pulmonary responses to single-walled carbon nanotubes in mice. *American Journal of Physiology. Lung Cellular and Molecular Physiology*, **289**, L698–708.

84 Magrez, A., Kasas, S., Salicio, V., Pasquier, N., Seo, J.W., Celio, M., Catsicas, S., Schwaller, B. and Forro, L. (2006) Cellular toxicity of carbon-based nanomaterials. *Nano Letters*, **6**, 1121–5.

85 Jose, R.M., Jose, L.E., Alejandra, C., Katherine, H., Juan, B.K., Jose, T.R. and Miguel, J.Y. (2005) The bactericidal effect of silver nanoparticles. *Nanotechnology*, **16**, 2346–53.

86 Ahn, M.H., Kang, C.M., Park, C.S., Park, S.J., Rhim, T., Yoon, P.O., Chang, H.S., Kim, S.H., Kyono, H. and Kim, K.C. (2005) Titanium dioxide particle-induced goblet cell hyperplasia: association with mast cells and IL-13. *Respiratory Research*, **13**(6), 34.

87 Xia, T., Kovochich, M., Brant, J., Hotze, M., Sempf, J., Oberley, T., Sioutas, C., Yeh, J.I., Wiesner, M.R. and Nel, A.E. (2006) Comparison of the abilities of ambient and manufactured nanoparticles to induce cellular toxicity according to an oxidative stress paradigm. *Nano Letters*, **6**, 1794–807.

88 Lademann, J., Weigmann, H., Rickmeyer, C., Barthelmes, H., Schaefer, H., Mueller, G. and Sterry, W. (1999) Penetration of titanium dioxide microparticles in a sunscreen formulation into the horny layer and the follicular orifice. *Skin Pharmacology and Applied Skin Physiology*, **12**, 247–56.

89 Kakurai, M., Demitsu, T., Umemoto, N., Ohtsuki, M. and Nakagawa, H. (2003) Activation of mast cells by silver particles in a patient with localized argyria due to implantation of acupuncture needles. *The British Journal of Dermatology*, **148**, 822.

90 Trop, M., Novak, M., Rodl, S., Hellbom, B., Kroell, W. and Goessler, W. (2006) Silver-coated dressing Acticoat® caused raised liver enzymes and argyria-like symptoms in burn patient. *Journal of Traumatology*, **60**, 648–52.

91 Paddle-Ledinek, J.E., Nasa, Z. and Cleland, H.J. (2006) Effect of different wound dressings on cell viability and proliferation. *Plastic and Reconstructive Surgery*, **117**, 110S–18S.

92 Poon, V.K. and Burd, A. (2004) In vitro cytotoxicity of silver: implication for clinical wound care. *Burns*, **30**, 140–7.

93 Kendall, M., Brown, L. and Trought, K. (2004) Molecular adsorption at particle surfaces: a PM toxicity mediation mechanism. *Inhalation Toxicology*, **16** (Suppl.), 99–105.

94 Fubini, B. (1997) Surface reactivity in the pathogenic response to particulates. *Environmental Health Perspectives*, **5** (Suppl.), 1013–20.

95 Zhai, H.J., Sun, D.W. and Wang, H.S. (2006) Catalytic properties of silica/silver nanocomposites. *Journal of Nanoscience and Nanotechnology*, **6**, 1968–72.

96 Hubbard, A.K., Timblin, C.R., Shukla, A., Rincon, M. and Mossman, B.T. (2002) Activation of NF-kappa B-dependent gene expression by silica in lungs of luciferase reporter mice. *American Journal of Physiology. Lung Cellular and Molecular Physiology*, **282**, L968–75.

97 Brown, D.M., Donaldson, K., Borm, P.J., Schins, R.P., Dehnhardt, M., Gilmour, P., Jimenez, L.A. and Stone, V. (2004)

Calcium and ROS-mediated activation of transcription factors and TNF-alpha cytokine gene expression in macrophages exposed to ultrafine particles. *American Journal of Physiology. Lung Cellular and Molecular Physiology*, **286**, L344–53.

98 Kang, C.M., Jang, A.S., Ahn, M.H., Shin, J.A., Kim, J.H., Choi, Y.S., Rhim, T.Y. and Park, C.S. (2005) Interleukin-25 and interleukin-13 production by alveolar macrophages in response to particles. *American Journal of Respiratory Cell and Molecular Biology*, **33**, 290–6.

99 Takenaka, S., Karg, E., Roth, C., Schulz, H., Ziesenis, A., Heinzmann, U., Schramel, P. and Heyder, J. (2001) Pulmonary and systemic distribution of inhaled ultrafine silver particles in rats. *Environmental Health Perspectives*, **4** (Suppl.), 547–51.

100 Sung, J.H., Ji, J.H., Yoon, J.U., Kim, D.S., Song, M.Y., Jeong, J., Han, B.S., Han, J.H., Chung, Y.H., Kim, J., Kim, T.S., Chang, H.K., Lee, E.J., Lee, J.H. and Yu, I.J. (2008) Lung function changes in Sprague-Dawley rats after prolonged inhalation exposure to silver nanoparticles. *Inhalation Toxicology*, **20**(6), 567–74.

101 Kim, Y.S., Kim, J.S., Cho, H.S., Rha, D.S., Kim, J.M., Park, J.D., Choi, B.S., Lim, R., Chang, H.K., Chung, Y.H., Kwon, I.H., Jeong, J., Han, B.S. and Yu, I.J. (2008) Twenty-eight-day oral toxicity, genotoxicity, and gender-related tissue distribution of silver nanoparticles in Sprague-Dawley rats. *Inhalation Toxicology*, **20**(6), 575–83.

102 Jani, P., Halbert, G.W., Langridge, J. and Florence, A.T. (1990) Nanoparticle uptake by the rat gastrointestinal mucosa: quantitation and particle size dependency. *The Journal of Pharmacy and Pharmacology*, **42**, 821–6.

103 Hussain, S.M., Hess, K.L., Gearhart, J.M., Geiss, K.T. and Schlager, J.J. (2005) In vitro toxicity of nanoparticles in BRL 3A rat liver cells. *Toxicology In Vitro*, **19**, 975–83.

104 Andrea, G., Bing, G., Rama, S.K., John, C.R., Ian, M.K. and Abdul, I.B. (2007) Induction of inflammation in vascular endothelial cells by metal oxide nanoparticles: effect of particle composition. *Environmental Health Perspectives*, **115**, 403–9.

105 Regina, R., Richard, P.P., Alexandra, S., Mark, F., Josef, C., Günther, O., Erich, W. and Annette, P. (2007) Ultrafine particles and platelet activation in patients with coronary heart disease–results from a prospective panel study. *Particle and Fibre Toxicology*, **4**, 1.

106 Gan, X., Liu, T., Zhong, J., Liu, X. and Li, G. (2004) Effect of silver nanoparticles on the electron transfer reactivity and the catalytic activity of myoglobin. *Chembiochem*, **5**, 1686–91.

107 Braydich-Stolle, L., Hussain, S., Schlager, J.J. and Hofmann, M.C. (2005) In vitro cytotoxicity of nanoparticles in mammalian germline stem cells. *Toxicological Sciences*, **88**, 412–19.

108 Bhol, K.C. and Schechter, P.J. (2007) Effects of nanocrystalline silver (NPI 32101) in a rat model of ulcerative colitis. *Digestive Diseases and Sciences*, **52**(10), 2732–42.

109 Sun, R.W., Chen, R., Chung, N.P., Ho, C.M., Lin, C.L. and Che, C.M. (2005) Silver nanoparticles fabricated in Hepes buffer exhibit cytoprotective activities toward HIV-1 infected cells. *Chemical Communications*, **28**(40), 5059–61.

5
Spherical and Anisotropic Silver Nanomaterials in Medical Diagnosis

Yiping Zhao and Ralph A. Tripp

5.1
Introduction

The convergence of scales for which diagnostic applications are becoming available has produced a paradigm shift in biological diagnostics. Recent advances in the development of diagnostic devices based on nanometer-scale systems and novel nanoparticles with unique chemical and physical properties have been used as biosensing systems and helped to improve older or existing technology in the development of new and novel diagnostic methods. A range of nanomaterial-based diagnostic applications range from optical imaging tags to help identify pathogens and diseases to the development of nanomaterials being utilized to develop more sensitive and specific point-of-care diagnostics. In addition, nanotechnology has realized the potential to revolutionize cancer diagnosis and therapy by allowing for the rapid and sensitive detection of cancerous cells and tissues, as well as in prognosis by determining the relationship between biomarkers of disease.

There are several major areas where nanomaterials have advanced or improved medical diagnosis. One area is the development of biochips [1–4]. The use of various nanomaterials in a lab-on-a-chip format has refined the detection of biologics, and is becoming an indispensable tool for molecular diagnostics. However, there are limitations to this technology as it is a format which often relies on species-specific reagents for detection that restrict the breadth of detection capability and often require labeling of the analytes for detection. Further, species-specific reagents as a means of detection can lead to the detection of false-positives or failure to detect analytes – that is, false-negatives. Newer nanotechnologies can provide label-free detection and are being applied to overcome some of these limitations.

By using new nanomaterials for molecular diagnostics that embody new optical instrumentation and methods, a broader diagnostic lab-on-chip platform has been developed [5–7]. These new devices place molecules at defined locations on a surface with nanometer spatial resolution and use customized atomic force microscopy (AFM) for reading the chips. The use of AFM as a readout method

Metallic Nanomaterials Vol. 1. Edited by Challa S. S. R. Kumar

ISBN: 978-3-527-32151-3

not only optimizes the analysis with the advantages of not needing a secondary reporter system (e.g. a fluorophore), but also reduces the materials used (several thousand molecules can be covered with one test) and increases the sensitivity with single-molecule detection potential. Other optical detection methods also include a sensitive technique using nanogold particle-labeled molecules on protein microarrays that apply surface plasmon resonance (SPR)-based detection [8]. The particles can be analyzed using mass spectrometry, where knowledge of the masses of the bound proteins provides an indication of their identity. Unfortunately, this is a cumbersome and equipment-intense method of detection and has multiple limitations in broad applications for medical diagnosis.

Other extrinsic diagnostic approaches employ nanogold particles attached to DNA or antibodies that require Raman-active dyes for detection [9–12]. These gold nanoparticles are particularly good labels for sensors because a variety of analytical techniques can be used to detect them, including optical absorption, fluorescence, Raman scattering and atomic and magnetic forces. An advantage of this nanomaterial is that, when it is exposed to a light, scanner detection is facilitated because the Raman band is narrower than other bands (e.g. fluorescence bands), and therefore it allows for a more sensitive detection. The narrow emission spectra of certain nanomaterials, such as quantum dots (QDs) have also been used to aid medical diagnosis [13–16]. QDs are nanoscale crystals of semiconductor material that fluoresce when excited by a laser light source. They have significant advantages over conventionally used fluorescent markers as they have broad excitation spectra that can be tuned, depending on their size and composition. This provides the QDs with narrow emission spectra, making it possible to resolve the emissions of different nanoparticles simultaneously and with minimal overlap. In addition, QDs can be attached to other reagents that aid the specificity of detection; examples are antibodies or oligomers that provide a process which allows for a wide range of applications in medical diagnostics. A more versatile diagnostic tool, particularly for *in vivo* diagnostic applications, may be nanoparticles, as these can be used in magnetic imaging techniques to detect pathogenesis. These nanoparticles, when conjugated similarly to QDs, target molecules or disease-causing organisms and produce magnetic signals on exposure to a magnetic field. In this way, those antibodies bound to targets can be identified, while any unbound antibodies remain dispersed. However, as the functionality of the QDs or magnetic nanoparticles in detection relies on their coupling to species-specific detection reagents, their utility and sensitivity is limited by the availability and sensitivity of the detection moieties.

Nanomaterials capable of identifying individual DNA elements with single-base resolution have been described [17–19]. These types of biosensor consist of an individual oligonucleotide attached within the inside of an alpha-hemolysin pore to form a 'DNA-nanopore'. The binding of single-stranded DNA (ssDNA) to the DNA nanopore strand causes changes in the ionic current flowing through a nanopore, and these changes can be detected. Although this technology is relatively new, its indicated speed and apparent simplicity might facilitate the development of molecular diagnoses. An issue that remains to be resolved is whether the

nanopore technology is actually useful for molecular diagnosis, as single-strand nucleic acids are readily degraded *in vivo* by exogenous and endogenous nucleases; hence, the technology may have a very narrow window of application. Routine DNA analysis will also require a robust nanopore to accommodate different conformational states possible with ssDNA.

One area in nanomaterial development that may lead to a potentially useful diagnostic tool is the development of cantilevers [20, 21]. Cantilevers are similar to those used in AFM to screen biological samples for the presence of genetic sequences. The cantilever surface is coated with an oligomer that can bind to one particular target sequence, and upon exposure of the sample to beams, the surface stress bends the beams to indicate target detection in the sample. The current cantilever technology is similar to DNA microarray methods, and potentially superior to other diagnostic methods noted above, as it involves nanomechanical detection without the need for extrinsic labels; moreover, it is rapid, specific and sensitive. There are, however, some limitations in sensitivity that are related to the nanofabrication methods and application of the analyte to the sensor. Given that cantilevers can be manufactured in microarrays [22, 23] to monitor up to a 1000 integrated events, and individual cantilevers may (potentially) be coated with different detection agents such as antibodies to oligomers, this technology offers the potential for high-throughput molecular diagnostics. However, the caveat of the need for species-specific detection reagents may ultimately limit its applicability in medical diagnosis.

The advent of biobarcode technology [24–26] may help to improve medical diagnostics. Nanobarcodes are metallic barcodes with unique patterns prepared by the sequential electrochemical deposition of metal ions. The different reflectivity of the individual metallic barcodes enables identification of analyte. This method has shown promise for detecting protein analytes where the technology relies on magnetic nanoprobes with antibodies that specifically bind a target of interest [27].

The use of surface-enhanced resonant Raman spectroscopy (SERRS) beads has been validated for some aspects of diagnostics [28, 29]. The SERRS technology focuses on the use of nanoparticles with fluorescent dyes having excitation peaks that overlap with a metal plasmon frequency to amplify the signal intensity of detection. At the center of the detection method is a Raman-active substrate that provides surface-enhancement of the signal with that of the dye specific to the detection bead. In order to protect the SERRS-active complex from degradation, the aggregate is encapsulated in a polymer coating containing the dye. The polymer coating is then surrounded by a polymer shell for conjugation to a variety of biologically relevant probes that include antibodies and oligomers. This highly sensitive and specific method extrinsic detection offers great potential but, like all extrinsic methods of medical diagnosis, suffers from a need for species-specific detection reagents.

Raman spectroscopy has also been applied for the extrinsic diagnostic detection of medically relevant pathogens. The use of surface-enhanced Raman spectroscopy (SERS) has been shown to be a powerful tool for the rapid, near-real-time detection

of potentially subattomolar concentrations of an analyte in limiting volumes, without the need for amplification of the analyte [30, 31]. The method relies on the analysis of a molecule in close proximity to a roughened silver surface, which has been shown to enhance the intensity of the Raman signal by as much as six orders of magnitude [32, 33]. In SERS, the incident laser photons couple to free conducting electrons within the metal, and this causes the electron cloud to resonate. The resultant surface plasmon field provides a pathway for the transfer of energy to the molecular vibrational modes of a molecule within the field, thereby generating Raman spectra that can be collected and analyzed. The result is a 'molecular fingerprint' of the analyte. Although the metal employed may be any 'coin' metal, silver nanorods of approximately 100 nm appear optimal for generating a surface plasmon field [32, 33]. SERS has been shown capable of both rapidly and sensitively detecting RNA and DNA viruses in media and their biological matrix, and does so without utilizing intrinsic methods that involve dyes or related detection agents. The extreme sensitivity of SERS using silver nanorods has been demonstrated by its ability to detect differences between virus types, virus strains, viruses with gene deletions, as well as differences between bacteria. Perhaps, more than any other method, this technique has great potential for use as an enabling platform technology to detect a range of viral and bacterial pathogens, as well as specific proteins and nucleic acids.

Today, other nanobased materials and systems are under development but, given their breadth and often overlapping nature with the methods discussed here, they will not be discussed at this point. However, it is clear that nanotechnology offers not only refinements and improvements in conventional diagnostic techniques but also new platform technologies. Currently, advances in nanotechnology are continuing to provide new fabricated devices that are small and sensitive, and may one day be used commonly in the field and at point-of-care facilities. The rapid development of new nanomaterials provides new opportunities and tools in all fields of biology, including virology, bacteriology, cell biology, genomics, proteomics, molecular diagnostics and high-throughput screening (HTS).

5.2 Silver Nanostructure-Based Diagnostic Techniques

Most metallic nanostructure-based diagnostic techniques, especially for silver or gold, are based on the physical phenomenon of SPR. Surface plasmons are coherent oscillations of electrons that occur at the interface between conductors and dielectrics. When such a thin film is excited by different wavelengths of light, there will be an absorbance maximum that occurs at a specific measurement configuration. The resonant wavelength for a nanostructured thin film depends on the dielectric constant of the material, the film thickness, the morphological or topological structure, and the dielectric constant of the environment surrounding the thin film. Any changes in these parameters could induce a shift in the SPR resonant wavelength, thus give a sensing response. For most chemical and biological

sensing, such a change usually occurs in the surrounding environment of the thin film (e.g. the binding of antibody or proteins on the surface), and this causes an alteration in the dielectric constant of the environment. This is the well-known principle for the SPR sensor, a commercially available version of which is available from Biocore. For nanoparticles, the surface plasmon oscillations are confined by the dimensions of the particle, and cannot propagate along the extended surface, as can those in a metallic thin film. Thus, the charge oscillations become localized – a situation referred to as localized surface plasmon resonance (LSPR). The optical absorbance spectroscopy also shows a maximum strength at the so-called localized surface plasmon resonance wavelength (LSPRW). For LSPR, the LSPRW depends on the dielectric constant of the material, the size, shape and topological structure of the particle, as well as the dielectric constant of the environment surrounding the particle. When compared to SPR, LSPR has two additional unique features:

- When the nanoparticle is excited by its LSPRW, the local electric field near the surface of the particle can be greatly enhanced, which provides a way of enhancing the vibration of the molecules attached to that surface.
- When two or more nanoparticles are in close approximation, the coupling of the electric field during external light excitation might also shift the LSPRW and change the strength of the local electric field.

These two unique features have been used to develop advanced nanostructured biosensors for diagnostics.

5.2.1 Surface Plasmon Resonance (SPR)

One popular SPR sensor configuration is shown in Figure 5.1. This comprises a laser, a prism, a thin metal coating (<100 nm thickness, usually Au or Ag) on one side of the prism, and the analyte. The laser light is *p*-polarized in order to excite the SPR, and the reflectivity of the laser as a function of the incident angle is measured. Under the SPR condition, the reflectivity versus incident angle curve will show a dip, as shown in Figure 5.2. When the targeted molecule is immobilized on the metal surface, the location of the reflectivity minimum will shift to a higher incident angle, as shown in Figure 5.2, and this produces the detection signal. When the metal surface is immobilized with different recognition molecules, the SPR sensor can be used to selectively detect desired analyte molecules. The system's sensitivity is less than 100 degree RIU^{-1}, and depends on the dielectric constant of the detecting molecules: the larger the dielectric constant, the better the sensitivity. In order to further enhance the sensitivity of SPR, metal nanoparticles (especially Au or Ag) have been used [34–39]. By inserting a metal nanoparticle layer (particularly Au or Ag) in between the recognition molecule layer and the analyte molecules (Figure 5.3), due to the large dielectric constant of metal, the detection signal can be amplified by the presence of metal nanoparticles. Figure 5.4 shows the Au-nanoparticle-enhanced SPR and conventional SPR

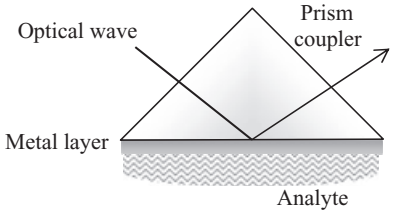

Figure 5.1 A typical surface plasmon resonance (SPR) set-up. The laser is incident near the critical angle of a prism, to the bottom of which is attached a thin metal (Ag or Au) layer. The surface of the metal interacts with the analyte, which causes an angular shift in the reflection peak.

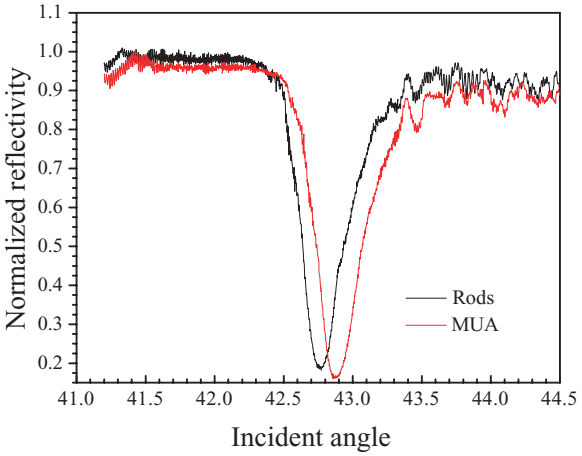

Figure 5.2 A typical SPR profile from Ag thin film before (black) and after (red) interaction with the analyte. Note that the reflection dip in the red curve shifts to a higher angle compared to the black curve.

detections of DNA molecules [38]. The Au nanoparticle can greatly enhance the angular shift for the same DNA concentrations. These SPR-based biosensors have been used widely in medical diagnostics, and further information can be found in some recent review articles [40–52].

5.2.2 Localized Surface Plasmon Resonance (LSPR)

The shift of the LSPR absorbance peak from metallic nanoparticles can also be used to detect the dielectric constant change of the environment, in very similar manner to the SPR detection technique [53]. However, the set-up for LSPR sensor is fairly simple. There are two basic measurement configurations: nanoparticle

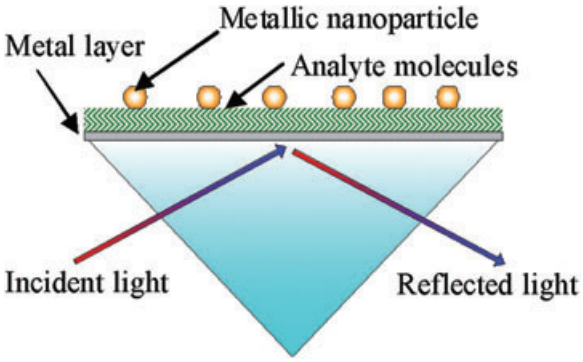

Figure 5.3 A typical configuration for nanoparticle-enhanced SPR detection. First, the metal film captures the analyte molecules, which in turn capture metallic nanoparticles immobilized with complementary molecules or functional groups to the analyte molecules.

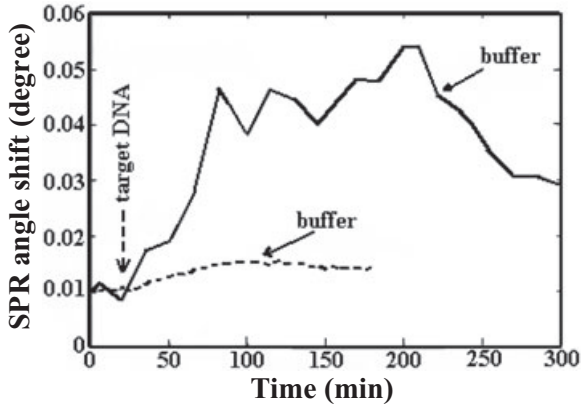

Figure 5.4 Enhanced SPR detection of the DNA hybridization process. The solid curve indicates the nanoparticle-enhanced SPR results; the dashed curve indicates conventional SPR results [38].

assay and nanoparticle substrates, as shown in Figure 5.5 [54]. The surfaces of uniform nanoparticles of various shapes, either in solution or on the substrate surface, can be coated with identification agents. For example, Figure 5.6a shows a substrate uniformly coated with Ag nanoparticles. The optical absorbance spectroscopy before the analyte is present is first measured and the LSPRW λ_{LSPR} identified (Figure 5.6b). After addition of the analyte to the solution, and due to an interaction of the analyte and identification agents on nanoparticle surfaces, the local dielectric constant of some nanoparticles is changed; this mediates a red-shift LSPRW, $\Delta\lambda_{LSPR}$ (Figure 5.6b). The magnitude of the LSPRW shift, $\Delta\lambda_{LSPR}$,

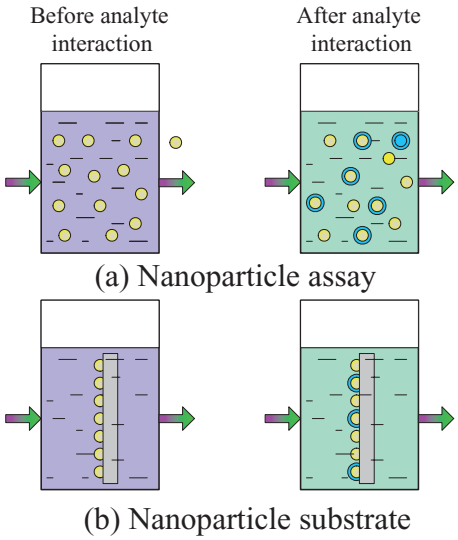

Figure 5.5 LSPR detection schemes. (a) nanoparticle assay and (b) nanoparticle substrate. Usually, the incident light is a white light; the optical absorbance spectra through the particles before and after analyte interaction are measured.

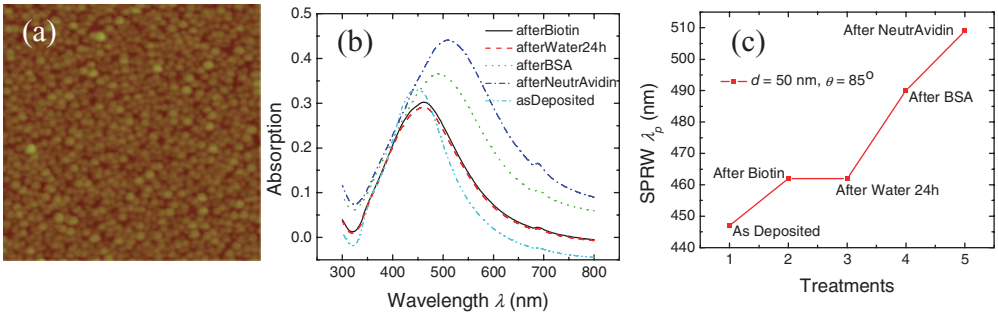

Figure 5.6 Changes in the LSPR curves of Ag nanoparticle arrays on a glass substrate after treatment with different biological agents. (a) A representative atomic force microscopy image of the Ag nanoparticle array; (b) LSPR absorbance curves of an Ag nanoparticle array treated with different agents; (c) Shift of the LSPR peaks after such treatments [54].

changes monotonically with the concentration of the analyte (Figure 5.6c); hence, by varying the recognition agents on the nanoparticle surfaces one can selectively detect different bioagents. The sensor set-up can be as simple as a hand-held spectrometer, and the current detection limit for this sensor platform is typically 100–200 nm RIU^{-1}, which is better than SPR. The key requirement for the LSPR-based sensor is to tune the LSPRW into a desired wavelength range and to syn-

thesize the nanoparticles as uniformly as possible so as to make the absorbance peak sharp. A large number of investigations have been conducted, concentrating on the particle fabrication and shape engineering. Applications for biodiagnostics have been demonstrated recently, such as DNA hybridization [55–59] and Alzheimer's disease [60–62].

Both, SPR- and LSPR-based sensors utilize the property that nanostructured thin film or particles are very sensitive to the dielectric constant change of their local environment, and the enhanced detection sensitivity really depends on how the nanostructures respond to such change. Although some of these techniques (especially SPR) are already available commercially, their sensitivity and specificity are relatively poor, especially for trace amounts of biomolecules or complicated systems such as viruses and bacteria. As stated above, metallic nanostructures – especially particles – may also enhance the local electric field when the incident wavelength is close to the LSPRW, and this provides yet another means of designing enhanced spectroscopic sensors, especially the so-called surface-enhanced vibrational spectroscopy (SEVS) sensors.

5.2.3
Metal-Enhanced Florescence

In the past, fluorescent dyes have been used extensively for biodetection, imaging and diagnostics. When an organic dye molecule is placed on top of a metal surface, its florescence signal would be quenched due to charge transfer between the dye molecule and the metal surface. However it has been discovered that, when placing the dye molecule a small distance (a few tens of nanometers) away from the metal surface, the florescence signal can be greatly enhanced (Figure 5.7). Depending upon the distance and geometry, metal surfaces or particles can cause either a quenching or an enhancement of the fluorescence by factors of up to 1000 [63–75]. The effects of this so-called metal-enhanced florescence (MEF) on fluorophores are due to at least three mechanisms [65]:

- The energy transfer is quenched by these metals with a d^{-3} dependence; such quenching is due to a damping of the dipole oscillation by the nearby metal.

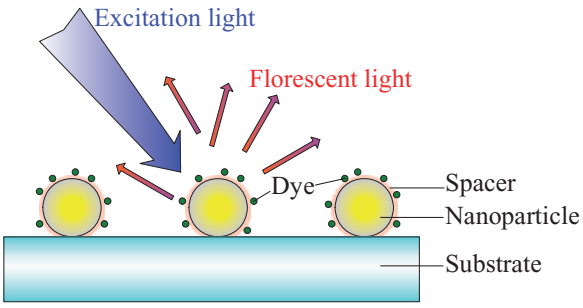

Figure 5.7 The experimental set-up for metal-enhanced fluorescence.

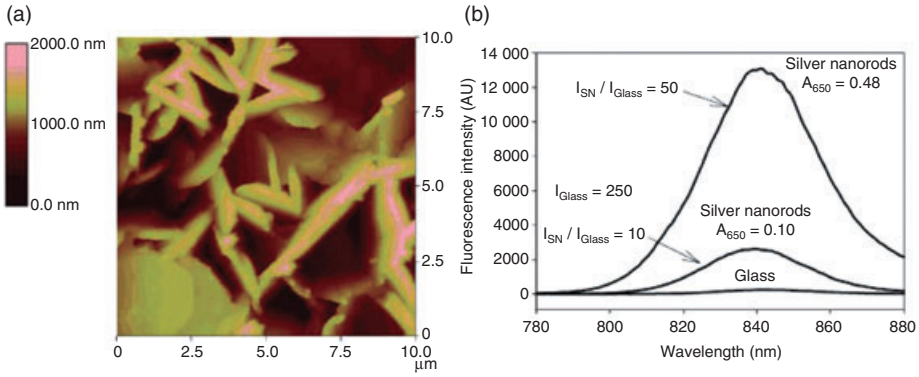

Figure 5.8 (a) Atomic force microscopy image of the surface with a high Ag nanorod load; (b) Fluorescence emission intensity of ICG-HSA on silver nanorods with low (0.10) and high (0.48) loading densities [75].

- There is an increase in intensity due to the metal concentrating the incident field.
- There is a fluorophore–metal interaction, which results in an increase in the intrinsic radiative decay rate of the fluorophore.

The MEF is usually observed by separating the fluorophore molecules from the metal surface by a distance of 10 nm, or more. Many of the reported MEF studies have used Ag islands, colloids, Ag surfaces or films, or mirrors, with the more dramatic effects having been found for islands and colloids rather than for continuous metallic surfaces. Recently, a 50-fold enhancement in florescence was reported on a fractal-like Ag nanorod structure by Lakowicz's group [75]. A comparison of fluorescence intensity of ICG-HSA on a glass surface and on Ag nanostructure surfaces is shown in Figure 5.8 [75]. This technique has been widely used to study DNA hybridization and imaging-related diagnostics [63–75].

5.2.4
Surface-Enhanced Infrared Absorbance Spectroscopy

When the frequency (wavelength) of incident light is the same as the vibration frequencies of a molecule, the light will be strongly absorbed. As most of the molecular vibration occurs in the infrared wavelength region, this is referred to as infrared absorbance spectroscopy (IRAS). The different vibrational frequencies of the molecule are caused by different chemical bonds (or a group of chemical bonds) in the molecule, and are considered as characteristic absorbance peaks for that particular molecule (or the fingerprint peaks of that molecule). Based on this unique characteristic, IRAS has become one of the most popular techniques for identifying molecules. Unfortunately, it is very difficult to utilize IRAS as a practical sensor as it requires either a significant amount of sample or a special detection

configuration. However, it has been found that when the molecules are attached to particular nanostructured Ag or Au surfaces, the IRAS can be enhanced. This so-called surface-enhanced IRA (SEIRA) involves an enhancement of the infrared band intensities for molecules adsorbed onto metal surfaces and composed ideally of shaped nanoparticles. The enhancement predicted for SEIRA by the local enhanced electric field mechanism may be as large as 10^3, although in practice most enhancements are in the range of 10–100 [76–78]. The improved sensitivity provided by SEIRA compared to traditional infrared analysis allows for the quantitative and qualitative determination of chemical species in the picogram to microgram range [79]. Recently, Ag nanorod arrays were used in the infrared external reflection mode in order to evaluate their SEIRA characteristics (Figure 5.9). The SEIRA enhancement factor was calculated for chemisorbed organic films of *para*-nitrobenzoic acid (PNBA), and found to be 30.6 ± 8.9 compared to a standard infrared reflection–absorption spectrum of PNBA obtained using a 500 nm Ag film substrate. The estimated SEIRA detection limit for PNBA for the Ag nanorod arrays was ~1 ng [80]. As yet, this technique has not been widely applied for medical diagnostics.

5.2.5
Surface-Enhanced Raman Spectroscopy

When monochromatic light passes through a group of molecules, a very small portion of that light will shift its wavelength due to an interaction with different vibrational modes of the molecules. This type of light–molecule interaction phenomenon is known as Raman scattering. Like IRAS, the locations of the Raman

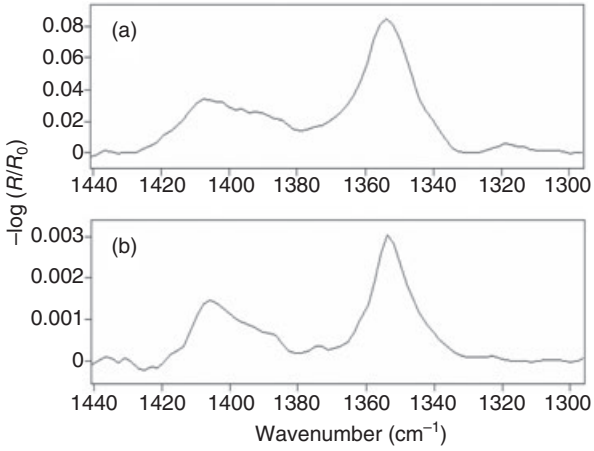

Figure 5.9 (a) External reflection SEIRA of a rinsed monolayer of PNBA on Ag nanorod array (32 scans); (b) IRAS of rinsed monolayer of PNBA on planar isotropic Ag surface (500 scans) [80].

peaks reflect certain vibration bonds in the molecules, and these can be used as fingerprint to identify or differentiate different molecules. The Raman scattering technique is also one of the most useful methods in materials research. Usually, the Raman scattering cross-section is extremely small compared to florescence spectroscopy, and is not suitable for low-concentration analyte detection. However, during the 1970s it was found that the Raman scattering intensity could be enhanced 10^6-fold when molecules were placed near roughened Ag surfaces [81–83]. Since then, SERS has emerged as a powerful analytical tool that extends the possibilities of vibrational spectroscopy to solve a vast array of chemical and biochemical problems. SERS is another SEVS technique that provides detailed information about the materials under investigation, often at the molecular level [84, 85]. As has been reviewed in detail elsewhere [86–94], two primary mechanisms are believed to be responsible for the SERS enhancement: (i) a long-range classical electromagnetic (EM) effect [94]; and (ii) a short-range chemical (CHEM) effect [95]. These two mechanisms contribute simultaneously to the overall enhancement; the EM mechanism is proposed to contribute the most ($\sim 10^4$–10^7) to the observed intensity enhancement, while the CHEM mechanism is thought to contribute a lesser amount ($\sim$10–10^2). A detailed discussion of the applications of SERS in biosensing, bioimaging and medical diagnostics is presented later in this chapter.

A summary of the different nanodiagnostics techniques is presented in Table 5.1.

Table 5.1 Comparison of different metallic nanostructure-based detection techniques.

	Incident light	Detection signal	Enhancing nanostructures	Specificity
SPR	White light	Reflection wavelength	Nanoparticles	Recognition agent required
	Laser	Reflection angle		
LSPR	White light	Absorbance	Nanoparticles Nanoparticle surfaces	Recognition agent required
MEF	Laser	Fluorescence	Nanoparticle surfaces Fractal structures Nanostructure arrays	Recognition agent required
SEIRA	IR light	Absorbance	Particles Nanostructure array	Intrinsic fingerprints
SERS	Laser	Scattering	Nanoparticles Nanoparticle aggregates Nanostructure arrays	Intrinsic fingerprints; Recognition agent required

5.3
Overview of Ag Nanostructure Synthesis and Fabrication

In the case of the above-mentioned diagnostic techniques, metallic nanostructures (especially Ag nanoparticles or nanostructures) play an essential role in determining sensitivity, specificity and application. In order to obtain the best sensitivity, some detection techniques (e.g. SERS and SEIRA) require stringent Ag nanostructures, and it is for this reason that most such methods have not yet been commercialized. As many of the detection or enhancement phenomena are associated with the LSPR of the metallic nanostructures, the quest for the 'ideal' nanostructured substrate to provide the best response has been central to the situation. In general, however, the following three configurations of metallic nanostructures have undergone extensive exploration.

5.3.1
Individual Metallic Nanoparticles

The optical absorbance of individual nanoparticles has been studied extensively [96–114]. The LSPR depends heavily on the shape and structure of the nanoparticles, including the diameter [115], aspect ratio [116], shape [99, 117], construction (e.g. core-shell, or hollow) [114], and the dielectric constant of the host medium [118–120]. The tunability of the optical properties of metallic nanoparticles has enabled the development of several important applications, such as environmental sensors [121, 122], Raman sensors [122, 123], optical triggers for drug delivery implants [124–126] and resonant photo-oxidation inhibitors [127]. The most popular means of fabricating metallic nanoparticles is through chemical synthesis [128–130], although other methods [131] such as laser ablation, combustion and electrochemistry have also been used. A variety shapes of Ag nanostructures can be fabricated through different techniques; the example of wet chemical synthesis is shown in Figure 5.10 [129].

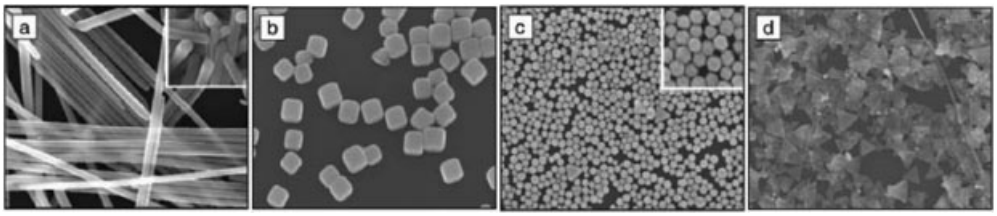

Figure 5.10 Ag nanostructures with different shapes.
(a) Wires; (b) Cubes; (c) Truncated cubes and tetrahedral;
(d) Triangular plates [129].

5.3.2
Aggregates of Metallic Nanoparticles

Aggregates of metallic nanoparticles are normally seen to demonstrate a large field-enhancement effect. For example, a SERS enhancement factor of 10^{14} has been reported for aggregates of Ag nanoparticles, and single-molecule detection has been achieved [132–134]. Several studies have demonstrated an enhanced electric field due to a coupling effect between metal nanoparticles placed in close proximity to one another [97, 135–137]. Thus, nanostructures have been intensely investigated as substrates for SEVS, such as SERS [138–140], SEIRA [79] and MEF [64, 73, 74].

5.3.3
Arrays of Metallic Nanoparticles

Regular arrays of metallic particles have shown some extraordinary optical properties. For example, a linear chain of Au or Ag nanoparticles can channel the flow of electromagnetic energy over distances of hundreds of nanometers, without significant loss [55], a property which has become the foundation for a new concept of integrated nanoscale photonic devices [56]. It has also been found that a double periodic array of pairs of parallel Au nanorods may show a negative refractive index in the optical range [57]. In addition, the regular array of metallic nanoparticles has a significant effect on SERS. The variation of shape, size and lattice spacing of regular arrays of Au nanodiscs significantly affects the Raman enhancement factor [58–60]. Usually, nanoparticle arrays are fabricated by using techniques such as electron-beam lithography, focused ion beam lithography or scanning probe microscope lithography.

From a practical sensing point of view, regardless of the specific detection technique, the Ag nanostructures that best fit the diagnostic purpose should meet the following requirements:

- Produce extremely high sensitivity
- Provide good specificity
- False alarms caused by the sensors should be within limits of tolerance
- Be produced routinely with uniform response, in large quantity, and relatively cheaply
- Sustain different biological environments and have a relatively long shelf-life.

In the case of SERS, for example, practical application of the remarkable analytical sensitivity of SERS has not been widely accepted as a viable diagnostic technique due to problems in preparing robust substrates of the correct surface morphology to provide maximum SERS enhancements [94]. Some of the most important requirements for an ideal SERS substrate in practical diagnostic applications are that the substrate: (i) produces a high enhancement; (ii) generates a

reproducible response; (iii) provides a uniform response; (iv) has a stable shelf-life; and (v) is simple to fabricate.

Many substrate preparation techniques exist that can form the roughened metal surfaces required for ideal SERS enhancement. These include roughening of the surface by oxidation–reduction cycles (ORC) [81], metal colloid hydrosols [141], laser ablation of the metals by high-power laser pulses [142], chemical etching [143], roughened films prepared by Tollen's reagent [144], photodeposited Ag films on TiO_2 [144], and vapor-deposited Ag metal films [145–148]. While the majority of substrate preparation techniques reported in the literature have focused on the problem of achieving a large SERS enhancement, the other requirements listed above for the production of a practical SERS sensing substrate are seldom addressed. Currently, there are five fabrication techniques that could potentially produce desired SERS substrates meeting these requirements, namely electron-beam lithography (EBL), nanosphere lithography, template method, hybrid methods and an oblique angle vapor-deposition method.

The EBL method is ideal for producing uniform and reproducible SERS substrates (Figure 5.11) [149–153]. However, it is very expensive to produce large-area substrates using EBL, unless it is combined with a nanoimprint lithography method [154]. The nanosphere lithography method pioneered by Van Duyne and

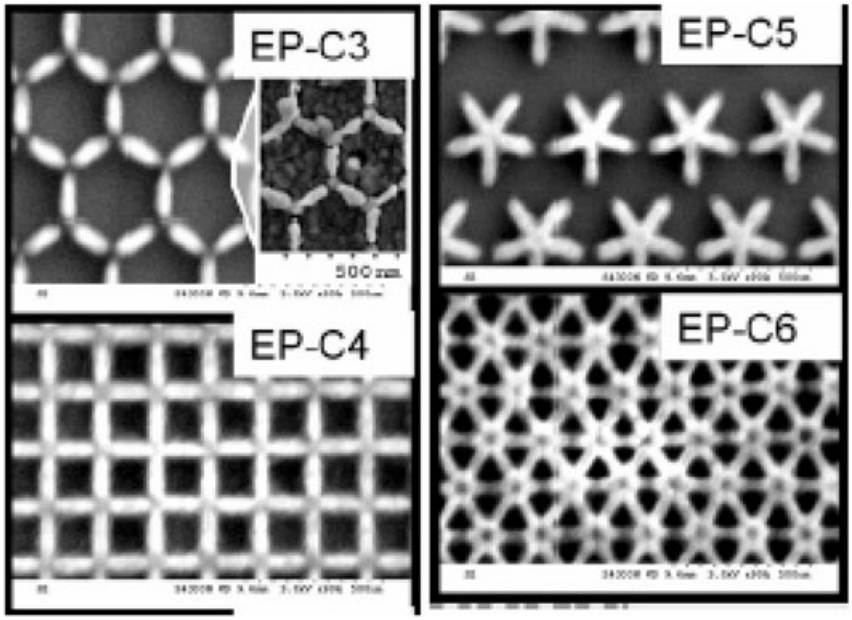

Figure 5.11 Regular Ag nanopatterns generated through electron-beam lithography. (Reproduced with permission from Ref. [150]; ©2005, Society of Applied Spectroscopy.)

coworkers involves evaporating Ag on preformed arrays of nanopore masks by colloid particles; the masks are subsequently removed, leaving behind the Ag metal deposited in the interstices to form a regular Ag nanoparticle array (Figure 5.12) [155–162]. The template method utilizes a nanotube-like array such as anodized aluminum oxide as a template to directly deposit Ag or Au nanorods into the channels via an electrochemical plating method (Figure 5.13) [163–169]. Hybrid methods fabricate SERS substrates by depositing metal particles onto nanoporous scaffolds such as porous silicon, nanorod arrays, and so on [170–177].

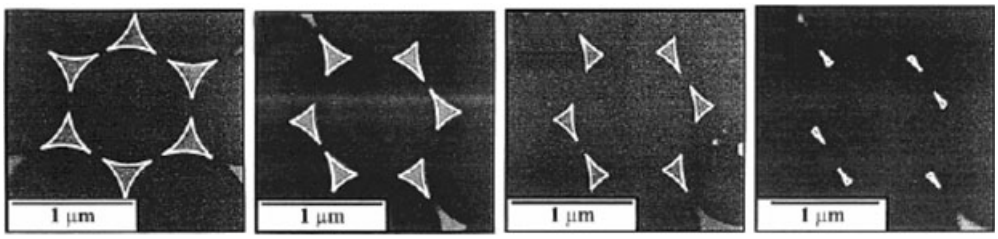

Figure 5.12 Different shapes of Ag nanoparticle arrays generated using the nanosphere lithography method [162].

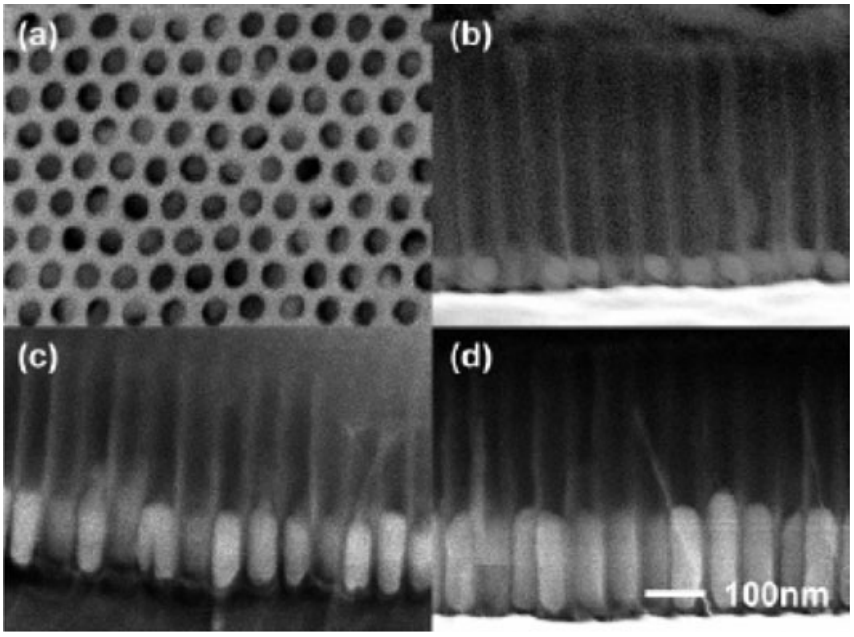

Figure 5.13 Ag nanorod arrays synthesized through template growth. Here, the template was anodized alumina [168]. (a) Top view of the template; (b–d) Cross-sectional views of templates with Ag nanorods grown at different heights.

Recently, we have found that an Ag nanorod array substrate fabricated by a so-called oblique angle deposition (OAD) method can serve as an excellent SERS substrate [178–180]. This particular Ag nanorod structure is shown in Figure 5.14. Our group has demonstrated that the SERS enhancement factor closely depended on the nanorod length. The SERS surface enhancement factor (SEF) of *trans*-1,2-bis(4-pyridyl)ethene (BPE) calculated from the 1200 cm^{-1} band increased from 10^5 to ~10^9 when the Ag nanorod length was increased from 190 to 1000 nm. The intense SERS enhancement factors observed were orders of magnitude larger than those obtained from previously published methods of forming nanoparticle arrays by vapor deposition (~10^4) [181, 182], and compared favorably with the best SEFs that have been reported using very elaborate nanolithography procedures (10^8) [183]. Only near-field SERS measurements (10^{13}) [184] or substrates with specifically engineered nanometer-scale 'hot spots' (10^{14}) [132, 133] have demonstrated larger SEFs.

This extremely high SERS response can be used to detect very low levels of chemical molecules, down to the subfemtomole (0.1 f*M* BPE) regime [180]. The spectra were recorded using a laser power of 15 mW and an integration time of 1 s, yet the signal-to-noise ratio (SNR) was very large at the characteristic Raman peaks of BPE (1200 cm^{-1}, 1610 cm^{-1} and 1640 cm^{-1}, respectively). For the 0.1 f*M* spectrum, it is estimated that there were only about 120 BPE molecules inside the microscope focus. With these Ag nanorod array substrates, it was also shown that SERS could distinguish between trace amount of viruses, including respiratory syncytial virus (RSV), rhinovirus, adenovirus, human immunodeficiency virus (HIV) and influenza virus [185]. The system could also be used to detect minor

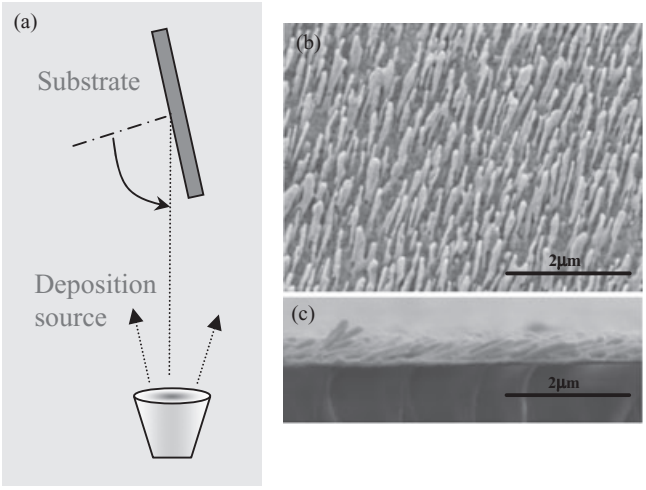

Figure 5.14 (a) A schematic illustration of oblique angle deposition; (b) Top and (c) cross-sectional scanning electron microscopy images of the Ag nanorod array SERS substrates.

Table 5.2 Comparison of different SERS substrate fabrication techniques that could potentially generate uniform and large area SERS substrates.

	Fabrication method				
	EBL	**NSL [161]**	**Template method**	**Hybrid method**	**OAD**
Enhancement factor	NA	10^7–10^9	10^6–10^7 [165, 168, 169]	10^6–10^8 [175]	>10^8 [180]
Substrate area	Typically < 0.1 × 0.1 mm2	~1 × 1 cm^2	>2.5 × 2.5 cm^2	>2.5 × 5.0 cm^2	>2.5 × 7.5 cm^2
Uniformity	NA	NA	<15% [166]	NA	<10% [180]
Reproducibility	<20% [150]	NA	NA	NA	<15% [180]
Shelf life	NA	NA	NA	>40 days (for Au) [176, 177]	~7 days (for Ag)
Fabrication steps	≥3 steps	3 steps	3 steps	>2 steps	1–2 steps
Cost	Expensive	Inexpensive	Inexpensive	Inexpensive	Moderate

NA = no data available in the literature; NSL = nanosphere lithography; OAD = oblique angle deposition.

spectral differences within strains of single virus types such as influenza virus strains A/HKx31, A/WSN/33 and A/PR/8/34. This suggests that such technology could be applied to detect genetically modified viruses that may be used as agents of bioterrorism. It has also been shown that similar substrates can be used for MEF and SEIRA [80].

The benefits and limitations of the different methods used to prepare SERS-active substrates are summarized in Table 5.2.

5.4 Applications

Although the above-described diagnostics techniques have been widely used in medical diagnostic-related studies, each of the different methods has not only unique advantages but also certain limitations. Among the detection techniques discussed here, SERS is considered to show the most promise and, in comparison to other methods, has the following advantages:

1. Because many molecules have their own Raman spectroscopic fingerprints, for most SERS detections no chemical modification is required, either to the substrate or to the analyte.

2. The excitation wavelength can vary from near-UV to IR, especially when excited at IR or near-IR wavelengths; for most biological systems this eliminates the fluorescence from the biological background, which gives a better SNR.
3. When using SERS, it is very easy obtain molecular specificity due to the specific Raman fingerprints of the different molecules.
4. SERS can provide a very high detection sensitivity in a very short time (30–60 s).

Since SERS is useful for determining molecular structural information, and also provides ultrasensitive detection limits (including single-molecule sensitivity [186, 187]), it has been widely used for biosensing, imaging and diagnostics [188–192]. Two principal SERS configurations have been used in biosensing, namely 'intrinsic' or 'extrinsic' (see Figure 5.15).

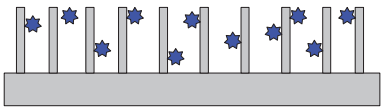

(a) Direct intrinsic detection

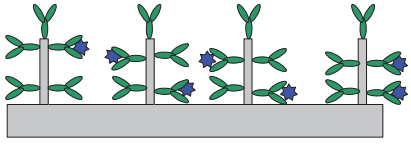

(b) Indirect intrinsic detection

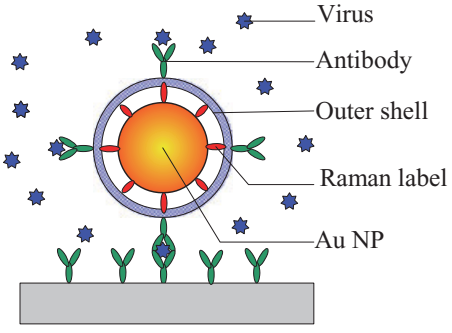

(c) Extrinsic detection

Figure 5.15 Different SERS detection configurations.
(a) Direct intrinsic detection; (b) Indirect intrinsic detection;
(c) Extrinsic detection.

In the case of intrinsic detection, the analyte can be directly applied to the nanostructured surfaces and the inherent Raman spectrum of the biomolecule directly measured to identify the specimen. In order to allow for capture and to aid the specificity of detection, antibodies, aptamers or related molecules can be immobilized onto nanostructured surfaces, as shown in Figure 5.15b; the Raman spectral differences before and after capture of the specimen can then be used to identify the species.

In extrinsic detection, a Raman reporter molecule is used to generate a signal for detection. For example, as shown in Figure 5.15c, either an Au or Ag nanoparticle may be used as the SERS-active substrate to which a Raman reporter molecule is immobilized. By coating this structure with another layer of dielectric (e.g. SiO_2, TiO_2 or polymer), a core-shell complex is formed in which the outer-shell may be decorated with captured molecules, such as antibodies. In this way the specimens may be captured and detected via a sandwich structure, as shown in Figure 5.15c. This extrinsic SERS detection method has been used successfully for the *in vivo* SERS imaging of unique or rare cancer cells [193–195]. Some specific applications of SERS based on different Ag nanostructures are outlined in the following section.

5.4.1
Small Biomolecule Detection

Raman scattering technique is a well-known and sophisticated chemical analysis technique which enables the detection and identification of different types of biomolecule, and especially of small biomolecules such as metabolite or drug molecules, or certain biomarkers. The method has been widely used in the analysis of drug mixtures and active ingredients, the identification of contaminants, and the exploration of drug–excipient interactions [196]. Likewise, SERS has been used to identify different vitamins [197–211], alkaloids [203, 212–216], antimicrobial agents [217–219] and antitumor agents [220–227], under different environments and conditions such as pH-dependence, solvent-dependence and surface interaction. Most of those studies have been based on Ag nanoparticle substrates, or Ag sol. A recent review on drug application can be found in Ref. [196]. The application of biomolecule detection to disease research has helped enhance the understanding and treatment of many human diseases through the identification of molecular profiles associated with each condition. These biomarkers of disease offer the utility of prognoses or detection of disease states. A sensitive and rapid detection of disease biomarkers also provides insight into the cellular processes involved in pathogenesis, disease progression and resolution; consequently, small biomolecules detection is also relevant to the direction of clinical management. In most cases, biomarkers are relatively small molecules, and thus serve as excellent analytes for SERS detection. In fact, the SERS detection of biomarkers has recently focused on cancer biomarkers, such as lysophosphatidic acid (LPA) for ovarian cancer [228], the phospholipase Cγ1 (PLCγ1) biomarker protein [229], and interleukin (IL-10) and osteopontin (OPN) [230]. In particular, Seballos *et al*. have used

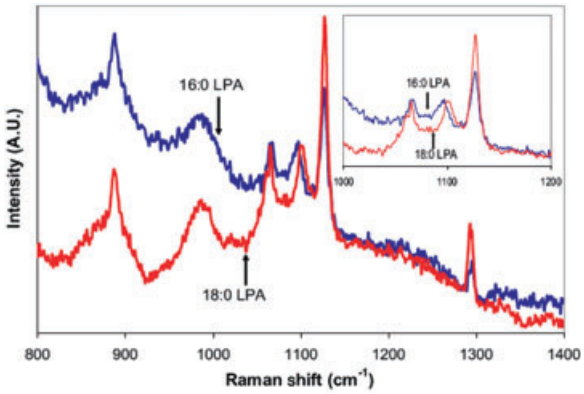

Figure 5.16 SERS spectra of dried samples from solutions of 100 μ*M* 16:0 LPA and 18:0 LPA on silver nanoparticles. The inset shows the SERS region between 1000–1200 cm^{-1} for the same samples, showing the distinguishable mode at 1097 cm^{-1} and 1101 cm^{-1}. (Reproduced with permission from Ref. [228]; © 2005, ■■■■■■■■.)

Ag nanoparticles as a SERS substrate for the selective, reproducible and sensitive detection of 16:0 LPA versus 18:0 LPA [228]. The SERS spectra of 16:0 LPA versus 18:0 LPA are shown in Figure 5.16; here, very strong similarities between the spectra of the two LPA molecules are noted, in particular the 889 cm^{-1}, 1294 cm^{-1}, 1060 cm^{-1} and 1128 cm^{-1} bands. However, the 16:0 LPA is distinguishable from the 18:0 LPA by the shift of the C–C vibration of the gauche-bonded chain, from 1097 cm^{-1} for 16:0 LPA to 1101 cm^{-1} for 18:0 LPA. In addition to biomarkers for diseases, SERS has also been used to detect other biomarkers, such as calcium dipicolinate (CaDPA) for *Bacillus anthracis* [231, 232], and glucose for diabetes [122, 189, 232]. Although the use of SERS to detect biomarkers has not been widely studied, the method holds great potential for future diagnostics.

5.4.2
Detection of MicroRNAs as Biomarkers of Disease

MicroRNAs (miRNAs) are 19–25 nucleotide noncoding RNAs that regulate gene expression through mRNA degradation or translation inhibition [233–235]. Recent studies have shown that some miRNAs have key roles in regulatory pathways, including development, apoptosis, cell proliferation and differentiation, organ development and cancer [234, 236–239]. The recognized roles of miRNAs suggest that the patterns of miRNAs expressed may serve as biomarkers for disease, particularly in the development of some cancers. For example, miR-15 and miR-16 are frequently deleted and/or downregulated in B-cell chronic lymphocytic leukemia [240, 241], while levels of miR-143 and miR-145 are reduced in colorectal cancer [242]. The findings that miRNAs are associated with aspects of cancer suggest that miRNA expression profiles may be useful to classify and diagnose human cancers [243]. Thus, the development of rapid and sensitive miRNA

profiling methods is essential for evaluating normal and diseased states. Our group has recently applied SERS Ag nanorod array substrate analysis to show that SERS can be used to detect the spectra of related and unrelated miRNAs in near-real time, and that miRNA detection is sequence-dependent, and can be used to classify miRNA patterns with great accuracy. In these studies, two sets of miRNA samples are prepared: five unrelated human miRNAs (Table 5.3) and eight members of the let-7 family with different sequences (Table 5.4). The SERS spectra for each of the five unrelated miRNAs were taken from three different substrates, each with a collection time of 10 s, and their unique molecular signatures were used to classify each sample. Figure 5.17 shows the average raw spectra (n = 27) for each of the miRNA sequences. The spectra reveal several features between 400 and 1800 cm^{-1} that are characteristic of nucleic acid bands [244–248]; for example, the band at 731 cm^{-1} is assigned to a ring-breathing mode of adenine, while the band at 656 cm^{-1} is assigned to a ring-breathing mode for guanine. Classification of the SERS spectra was accomplished using a partial least squares discriminate analysis (PLS-DA), which determines the best fit between the descriptor and classes by minimizing the within class variance and maximizing the between class variance. The PLS-DA model generated was used to classify the 135 spectra examined (five miRNAs by 27 replicates). Class predictions calculated by the PLS-DA model for the unrelated miRNA data are shown in Figure 5.18. The plots reveal that each sample is only assigned membership to its correct class. The perfor-

Table 5.3 Sequences for five unrelated miRNAs examined via SERS.

let-7a	5′-U.G.A.G.G.U.A.G.U.A.G.G.U.U.G.U.A.U.A.G.U.U
miR-16	5′-U.A.G.C.A.G.C.A.C.G.U.A.A.A.U.A.U.U.G.G.C.G
miR-21	5′-U.A.G.C.U.U.A.U.C.A.G.A.C.U.G.A.U.G.U.U.G.A
miR-24a	5′-U.G.G.C.U.C.A.G.U.U.C.A.G.C.A.G.G.A.A.C.A.G
miR-133a	5′-U.U.G.G.U.C.C.C.C.U.U.C.A.A.C.C.A.G.C.U.G.U

Table 5.4 Sequence for the let-7 family miRNAs where differences from let-7a are highlighted in red.

let-7a	U.G.A.G.G.U.A.G.U.A.G.G.U.U.G.U.A.U.A.G.U.U
let-7b	U.G.A.G.G.U.A.G.U.A.G.G.U.U.G.U.G.U.G.G.U.U
let-7c	U.G.A.G.G.U.A.G.U.A.G.G.U.U.G.U.A.U.G.G.U.U
let-7d	A.G.A.G.G.U.A.G.U.A.G.G.U.U.G.C.A.U.A.G.U.—
let-7e	U.G.A.G.G.U.A.G.G.A.G.G.U.U.G.U.A.U.A.G.U.—
let-7f	U.G.A.G.G.U.A.G.U.A.G.A.U.U.G.U.A.U.A.G.U.U
let-7g	U.G.A.G.G.U.A.G.U.A.G.U.U.U.G.U.A.C.A.G.U.—
let-7i	U.G.A.G.G.U.A.G.U.A.G.U.U.U.G.U.G.C.U.G.U.—

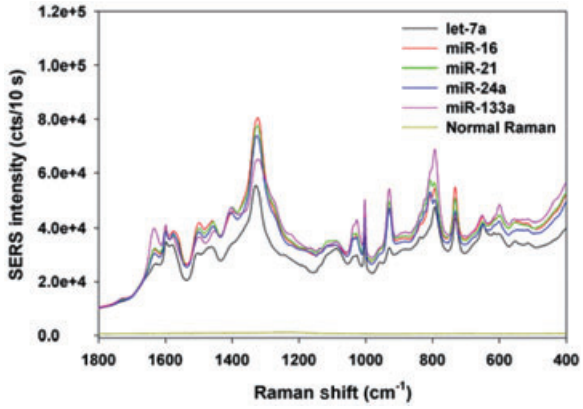

Figure 5.17 Raw SERS spectra for each unrelated miRNA and a normal Raman spectrum for let-7a adsorbed onto a smooth silver surface. Each plot shown is an average of 27 spectra.

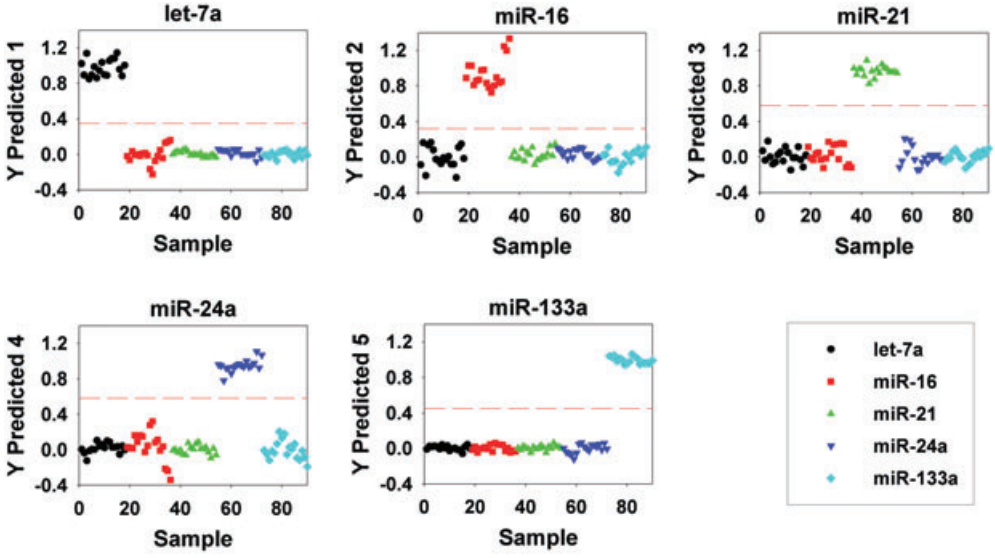

Figure 5.18 PLS-DA predicted plots. Each plot predicts a sample as either belonging to, or not belonging to, the specified miRNA class. let-7a (▼); miR-16(*); miR-21 (■); miR-24a(+); miR-133a (◇).

mance of the classification model was evaluated by measuring sensitivity and specificity, where sensitivity is defined as the number of samples assigned to the class divided by the actual number of samples belonging to the class, and specificity is defined as the number of samples not classified as member of the class divided by the actual number of samples not belonging to the class. A summary

Table 5.5 Summary of PLS-DA results [training (Cal) data and cross-validated (CV) data] for the unrelated miRNA samples.

Sample	let-7a	miR-16	miR-21	miR-24a	miR-133a
Sensitivity (Cal)	1	1	1	1	1
Specificity (Cal)	1	1	1	1	1
Sensitivity (CV)	1	1	1	1	1
Specificity (CV)	1	1	1	1	1

of the sensitivity and specificity of the PLS-DA classification results is provided in Table 5.5. SERS-based profiling classified the samples with 100% sensitivity and specificity. Similar results have been observed for the eight members of the let-7 family with different sequence. This result clearly demonstrates that, as long as a reproducible SERS substrate can be produced, the ability of SERS to distinguish small changes in large biomolecules will be greatly enhanced, which in turn provides an excellent route to disease diagnostics.

5.4.3 Nucleic Acids (DNA and RNA) Detection

A complete viral particle, or virion, consists of nucleic acid surrounded by a protective coat of protein called a capsid; some viruses may also possess a lipid envelope derived from the host cell membrane. A virus may employ either DNA or RNA as its nucleic acid, but only rarely do they contain both (cytomegalovirus is an exception as it possesses a DNA core with several mRNA segments). Nonetheless, by far the largest majority of viruses have RNA, the majority being respiratory viruses. While SERS has been used for DNA and RNA detection in biological systems, until now most studies on DNA or RNA detection have been based on the extrinsic detection scheme (as illustrated in Figure 5.15). Two general detection configurations are used: the first is based on Ag nanoparticle substrates [249–253], and the second on Ag or Au nanoparticle assays [254–257]. The SERS signals from florescence dyes are used to label either the detecting DNA/RNA or the immunoassays. In other words, the SERS is used as a labeling signal to discriminate different hybridization interaction due to the specificity of DNAs or RNAs. Vo-Dinh's group has developed gene probes based on the Ag nanoparticle substrates [249–253]. Here, the SERS substrates are Ag islands surface, Ag-coated nanobeads surface, roughened Ag surface or Ag nanoparticle-embedded polymer films [250]. The detection involves the following steps:

- Preparing the SERS active substrates
- Immobilizing complementary DNA strands or segments on the SERS active substrates

- Attaching SERS active dyes onto the target DNA molecules
- Applying the dye labeled DNA to the SERS active surface.

Due to the hybridization interaction between the target DNAs and its complements, it is possible to detect the SERS signal from the dyes attached to the target DNA strand. This method, which has been used successfully to detect both the HIV gene [249] and cancer genes [251–253, 258], requires that the DNA strands – both on the SERS active surface and to be detected – have no (or only very weak) SERS signals compared to the dye molecules. The results of breast cancer gene detection using this method are shown in Figure 5.19 [251]. Recently, a self-assembly monolayer was applied for this type of detection [259, 260], wherein the nanoparticle assay-based method used Ag or Au nanoparticles as cores, while both the dye molecules and complementary DNA segments or strands were immobilized onto the nanoparticle core surface to serve as signaling and recognition units [254–257]. The complex core-shell nanoparticle assays were then mixed together with the target DNA solution for detection. The reported DNA detection limit was in the order of $10^{-12}\,M$ [254] or $10^{-14}\,M$ [255]. In this way, genes related to hepatitis A, hepatitis B, HIV, Ebola virus, smallpox and *Bacillus anthracis* have been detected and distinguished [255]. This strategy is very similar to that of florescence-labeled detection, although as SERS can be excited by NIR laser, and the SERS label produces narrow spectral lines, the SERS labeling technique could suppress the noise present in florescence detection, and so be used for multiplexing detection. In fact, by changing the dyes on the nanoparticle core, and altering the hybridization segments, SERS multiplexing for gene detection has been achieved [261–264]. A similar strategy has also been used for cell imaging [229, 265–267] or *in vivo* cancer detection [268, 269].

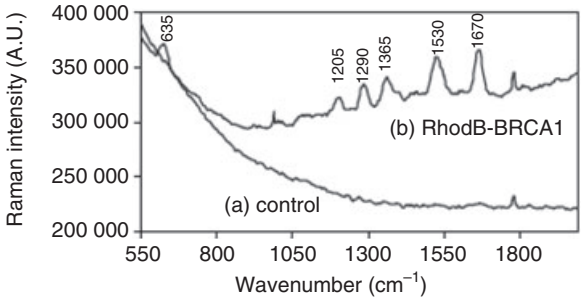

Figure 5.19 Hybridization results for the breast cancer *BRCA1* gene. SERS spectrum on a silver island substrate of (a) the hybridization control and (b) the hybridized *BRCA1* oligonucleotide labeled with Rhodamine B [251].

5.4.4 Virus Detection

A number of studies have used Ag nanoparticle-based SERS substrates to detect different viruses. To date, three different methods have been used employing using SERS: biomarker detection, DNA detection, and whole-viral particle detection. Whilst the former two methods were discussed in Sections 5.4.2 and 5.4.3, and represent the major research effort in this field, fewer studies have been conducted with whole-viral particle SERS detection. In the latter case, both intrinsic and extrinsic detection methods have been applied. Driskell *et al*. used Au nanoparticle as a carrier and immobilized a Raman reporter inner layer and an antibody outer layer to form a bioassay for feline calicivirus detection [195]. Using a similar method, but with an Ag-stained Au core, Xu *et al*. successfully demonstrated the detection of hepatitis B viruses [270]. Similarly, Bao *et al*. have used Ag hydrosols to directly measure the SERS spectra of insect nuclear polyhydrosis virus [271]. The SERS spectral differences in the polydrin of *Trabala vishnou* nuclear polyhedrosis virus and polydrin of *Dendrolimus punctatus* nuclear polyhedrosis virus enable these authors to differentiate between these two types of virus [271]. Recently, based on the Ag nanorod array SERS substrates, the ability of SERS as a virus diagnostic tool has been extensively demonstrated by our group (see Section 5.4.4.1).

5.4.4.1 Using SERS to Distinguish between Different Virus Types

By using the direct intrinsic SERS configuration (as shown in Figure 5.15a), it has been shown possible to rapidly and sensitively distinguish different viruses by their SERS spectra. For example, the baseline-corrected SERS spectra of wild-type strains of RSV (strain A2), HIV, *Mycoplasma* and influenza were collected from several locations from at least three different substrates, and representative spectra (smoothed, baseline-corrected and normalized) plotted (see Figure 5.20) [272]. Here, unique spectra, each with distinct SERS signatures, can be easily visualized for each infectious agent. By using the well-known statistical classification technique of principal component analysis (PCA), a resultant score plot is produced (see Figure 5.21). The spectrum for each pathogen are clearly separated into individual clusters, while the narrow distribution of the spectra within a single cluster provides evidence that the different types of virus are well classified. Clearly, the unique nature of the SERS spectrum provides a molecular fingerprint for the detection of specific viruses, as well as providing the foundation for SERS-based biosensing.

5.4.4.2 Using SERS to Detect Viruses in Biological Media

The ability of SERS to distinguish viruses in the presence of a complicated background was demonstrated by comparing the SERS spectra of uninfected Vero cell lysate, RSV-infected cell lysate and purified RSV (Figure 5.22) [273]. This figure shows that, although there are common SERS peaks for the three samples, the

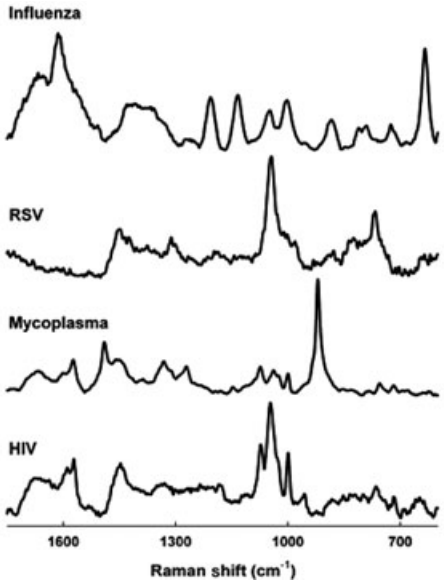

Figure 5.20 Representative SERS spectra for influenza virus, RSV, *M. pneumoniae* and HIV adsorbed onto a Ag nanorod substrate. The spectra have been baseline-corrected, normalized and offset for visualization [272].

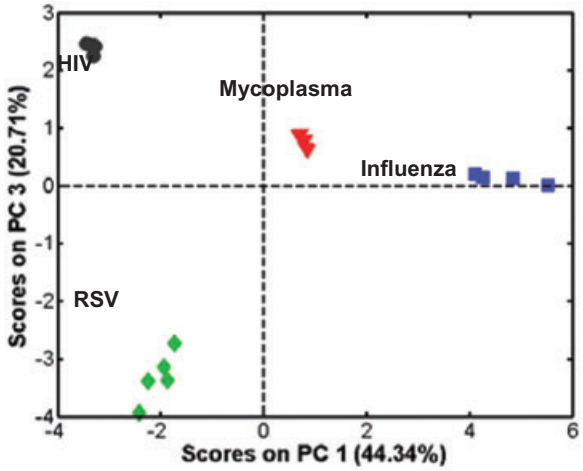

Figure 5.21 PCA scores plot of PC3 versus PC1 computed from the SERS spectra of the infectious agent samples. HIV (●), influenza (■), RSV (◆), *M. pneumoniae* (▼) [272].

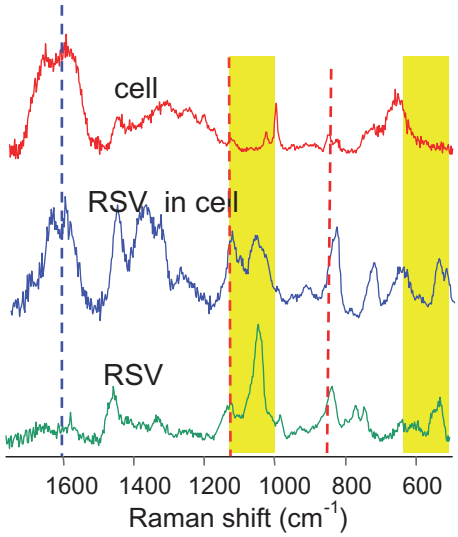

Figure 5.22 SERS spectra of Vero cell lysate before (top) and after (middle) infection with RSV. The SERS spectrum of purified RSV (bottom) is shown for comparison. Reprinted with permission from Ref. [273]; © 2006, American Chemical Society.

SERS spectra of RSV-infected cell lysate and purified RSV both have SERS bands at 1000–1100 cm^{-1} and 500–600 cm^{-1}, whereas the SERS spectrum of the Vero cell lysate does not show these two signature peaks.

5.4.4.3 Using SERS to Detect Very Low Levels of Virus

The sensitivity and dynamic range of the SERS technique for virus detection was investigated by analyzing dilutions of a RSV mutant lacking the G (attachment) gene (ΔG). The SERS peak areas of the main band at 1045 cm^{-1} (C N stretching mode) are plotted against the ΔG RSV concentration in Figure 5.23 [273]. The concentrations of the diluted solutions were calculated from the volume of water used for the dilutions. The SERS intensity was seen to increase with the concentration of the viral solution, reaching a plateau at concentrations above 10^3 PFU ml^{-1}. Although, at this stage, minimal effort was placed on determining the lowest detectable titer, values as low as 100 PFU ml^{-1} were readily detectable. Hence, in this assay format these data suggest a limit of virus detection ranging between 1–10 PFU.

5.4.4.4 Using SERS to Differentiate between Strains of a Single Virus Type

In addition to the capacity of SERS to differentiate between different virus types, it can also be used to distinguish virus strains of a single virus type [273]. One such example is the detection of RSV strains (Figure 5.24) [273]. By using SERS,

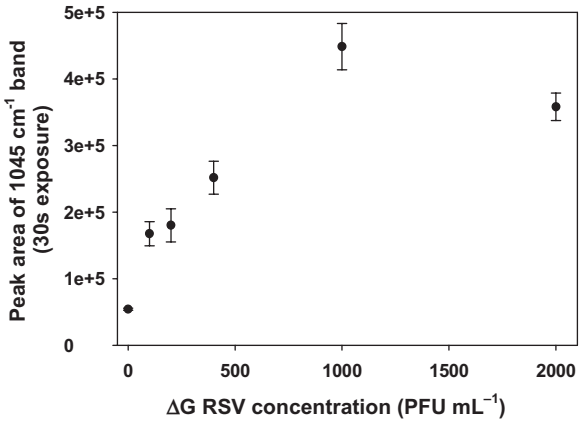

Figure 5.23 The SERS calibration curve for ΔG RSV constructed with the peak area for the C–N stretching band at 1045 cm^{-1}. Reprinted with permission from Ref. [273]; © 2006, American Chemical Society.

RSV viruses A/Long, A2 and ΔG (belonging to the RSV A strain), as well as RSV strain B1, were analyzed and their corresponding baseline corrected spectra (1400–600 cm^{-1}) recorded (see Figure 5.24). Distinct spectral differences were observed among the A/Long, A2 and B1 strains, as predicted. The spectra in Figure 5.24 were analyzed using PCA, and a scores plot derived (see Figure 5.25) [274]. Although all three RSV strains were clearly separated into individual clusters (i.e. A/Long, A2 and B1 viral strains), a significant overlap in the ΔG and A2 virus clusters was observed in the two-dimensional scores plot, reflecting the extremely close biochemical similarity between these two strains.

5.4.5
Bacteria Detection

Many foodborne diseases are caused by bacteria. In fact, in the United States the Centers for Disease Control (CDC) has estimated that foodborne diseases cause approximately 76 million illnesses, 325 000 hospitalizations and 5000 deaths each year. Known pathogens account for an estimated 14 million illnesses, 60 000 hospitalizations and 1800 deaths [275]. The most recent foodborne outbreaks have included the *E. coli* O157:H7-contaminated spinach and *Salmonella* outbreak linked to Peter Pan Peanut butter in 2006. There is, therefore, a natural requirement to apply SERS techniques for bacteria detection. When compared to viral or SERS nanostructures, bacteria cells are relatively large; Figure 5.26 shows a top view scanning electron microscopy (SEM) image of *E. coli* O157:H7 cells on top of an Ag nanorod SERS substrate [276]. The bacterial cell is significantly larger than a single Ag nanorod, with each cell covering 10–30 nanorods. As the cells are

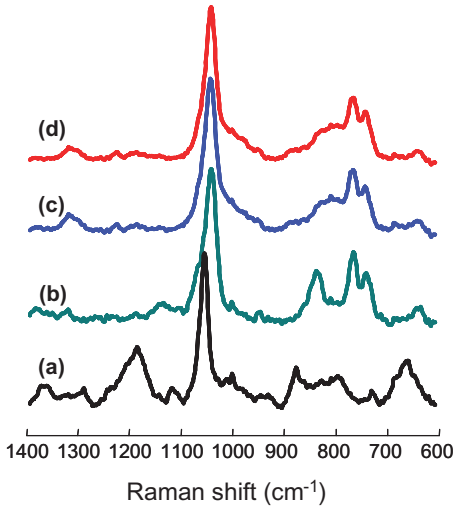

Figure 5.24 Summed SERS spectra of the individual RSV strains. (a) Strain A/Long; (b) Strain B1; (c) Strain A2 with a G gene deletion (ΔG); (d) Strain A2. Reprinted with permission from Ref. [273]; © 2006, American Chemical Society.

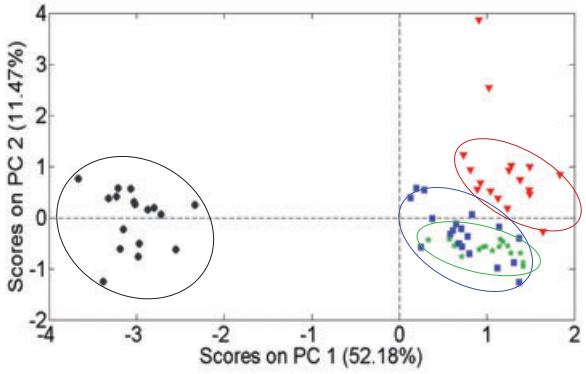

Figure 5.25 PCA scores plot of PC2 versus PC1 computed from the SERS spectra of the RSV strains A/Long (●), B1 (▼), A2 (■), and the recombinant strain A2 G gene deletion mutant (ΔG) (*) [274].

not broken apart but merely lie on top of the Ag nanorods, the SERS spectrum is very sensitive to the outermost layer of bacterial cells, which are very different from viruses. Those molecules and functional groups in the immediate proximity of the metal surface should predominate in a SERS measurement, and this in turn makes the SERS identification of bacteria more difficult. In order to obtain the SERS spectra of bacteria, two general methods are used: (i) to coat the surface of

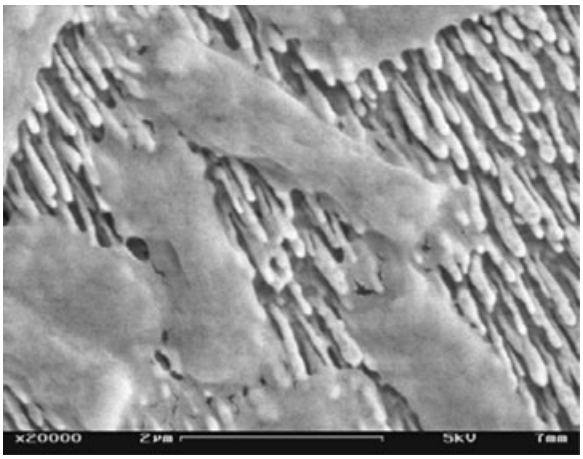

Figure 5.26 A SEM image of *E. coli* bacteria on a silver nanorod array substrate. Scale bar = 2 µm. As the cells did not appear to be lysed, the shifts observed in the SERS spectra were a product of cell wall biochemistry or other chemical components external to the cell [276].

the microorganisms with Ag or Au nanoparticles; or (ii) to spread the cells on the roughened Ag surfaces. For example, Zeiri *et al.* suspended bacteria in sodium borohydride and used the reduction of Ag ions to generate a layer of Ag coating on the bacterial surface [277, 278]. In this way, they have studied different types of bacteria such as *E. coli, Acinetobacter calcoaceticus* RAG-1, *Pseudomonas aeruginosa* YS-7 and *Bacillus megaterium* [277, 278]. In a similar study, Alexander *et al.* used an optical trapping technique to study the SERS response of a single *Bacillus* spore [279], while Grow *et al.* used the roughened metal surfaces to investigate Gram-positive and Gram-negative bacteria, as well as their viability [280]. For nanoparticle-based bacteria detection, a key issue is the reproducibility of the SERS spectra, since different experimental conditions can alter the SERS spectra [281]. The discrimination and reproducibility of the SERS spectra of bacteria have been addressed, when a statistical classification method was employed to distinguish different bacteria [281–286]. These studies demonstrated spectral differences among bacteria and bacterial strains. Recently, by using an Ag nanorod array substrate, we have demonstrated a series of advantages for SERS in the detection of bacteria (for details, see Section 5.4.5.1).

5.4.5.1 Using SERS to Differentiate between Types of Bacteria

In order to determine the ability of SERS to distinguish between different bacterial species, the SERS spectra of Gram-negative *E. coli* O157:H7 and *S. typhimurium*, and Gram-positive *S. aureus* and *S. epidermidis* were obtained. All four species were intact and had viable cells before being deposited on the silver nanorod array sub-

strates. The average SERS spectra of the four species, plotted in the 400–1800 cm^{-1} region, are shown in Figure 5.27 [276]. In order to remove any spectral discrepancies caused by the substrates, each SERS spectrum was normalized with respect to its most intense peak; all spectra were acquired with ~24 mW of incident laser power and a 10 s collection time. The results showed that SERS spectra of bacteria can be readily obtained (with a good SNR) when the cells were absorbed onto silver nanorod array substrates and excited with low laser power at 785 nm. The SERS spectra in Figure 5.27 are arranged from top to bottom according to their Gram-staining classification, with bacteria of the same Gram type adjacent to each other. The spectral differences ascribed to different Gram types (e.g. *E. coli* O157:H7, *S. typhimurium* and *S. aureus*) could be discerned by the naked eye, whereas spectral differences attributed to closely related species were not immediately striking. However, by applying the PCA method it became a straightforward process to classify the different bacteria. Figure 5.28 shows the PCA analysis performed using the SERS spectral data from the four pure bacterial samples, *E. coli* O157:H7, *S. typhimurium, S. aureus* and *S. epidermidis* in the 400–1800 cm^{-1} range. Four different clusters were apparent in the PCA plot, with each cluster corresponding to an individual bacterial species. The *E. coli* O157:H7 had positive PC1 and PC2 scores, while *S. typhimurium* had a positive PC1 score but a negative PC2 score. *S. aureus* had negative PC1 and PC2 scores (except for one datum point), while *S. epidermidis* had a negative PC1 score and a positive PC2 score. These results indicated that a clear distinction could be made between different bacteria species when using the PCA process, despite some of the spectra having very similar visual appearances.

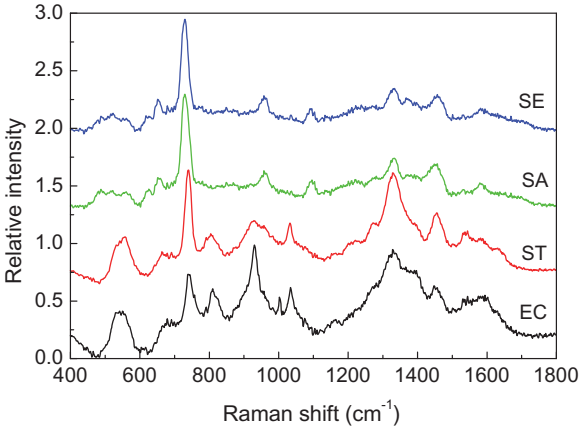

Figure 5.27 Average SERS spectra of four bacterial species obtained on silver nanorod array substrates. EC, *E. coli* O157:H7; ST, *Salmonella. typhimurium*; SA, *Staphylococcus aureus*; SE, *Staphylococcus epidermidis*. The spectra were offset vertically for display clarity [276].

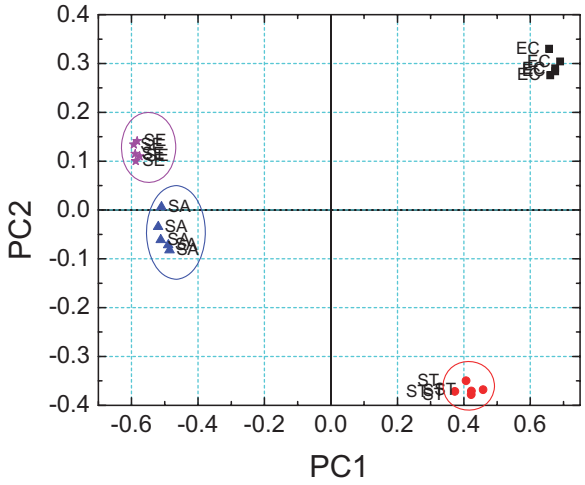

Figure 5.28 PCA scores plot of *E. coli* O157:H7 (EC), *Salmonella typhimurium* (ST), *Staphylococcus aureus* (SA) and *Staphylococcus epidermidis* (SE) pure cell samples. The PCA model was constructed using the spectral range from 400–1800 cm^{-1} [276].

5.4.5.2 Using SERS to Differentiate between Different Bacterial Strains

Having shown that SERS can be used to detect and differentiate among different species, it was important to determine if different strains of the same species could be distinguished in the same way. Three different *E. coli* strains – *E. coli* O157:H7, generic *E. coli* and *E. coli* DH 5α – were analyzed, and their SERS spectra recorded (see Figure 5.29) [276]. Although, the closely related chemical composition and structure of the *E. coli* strains would give rise to very similar SERS spectra, minor – but noticeable – differences were expected in the spectra for the different *E. coli* strains. Whilst all of these *E. coli* samples shared some similar characteristic peaks, the relative bandwidths and intensities of the peaks in the spectra were somewhat different. This effect could be observed in the spectral region of 400–800 cm^{-1}, and again in the 800–1100 cm^{-1} region, which highlighted intensity differences as well as frequency shifts among the different strains. A PCA analysis was carried out for all three sets of SERS spectra for the different *E. coli* strains; Figure 5.30 shows the PCA score plot using spectral data from *E. coli* O157:H7, generic *E. coli* and *E. coli* DH 5α, in the 400–1800 cm^{-1} range. Clearly, the three different strains of *E. coli* could be separated into three clusters: based on the PC scores, the cluster for the generic *E. coli* had positive PC1 and PC2 scores, while that for *E. coli* O157:H7 had a negative PC1 score. Although, the cluster for *E. coli* DH had a positive PC1 score (except for one datum point), the negative PC2 score separated the cluster from that of generic *E. coli* and *E. coli* O157:H7, both of which had positive PC2 scores.

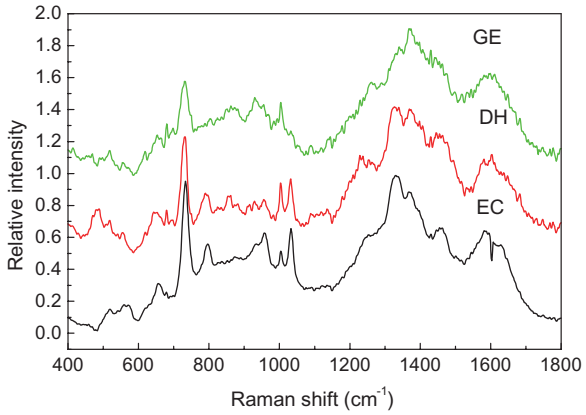

Figure 5.29 Average SERS spectra of the *E. coli* strains. EC, *E. coli* O157:H7; DH, *E. coli* DH 5α; GE, generic *E. coli* [276].

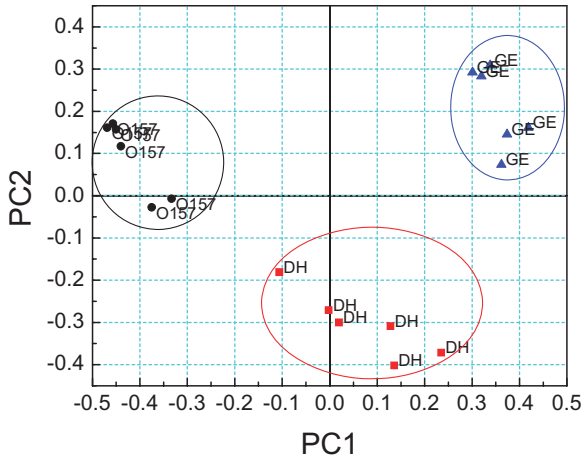

Figure 5.30 PCA scores plot of *E. coli* O157:H7 (O157), *E. coli* DH 5α (DH) and generic *E. coli* (GE). The PCA model was constructed using the spectral range from 400–1800 cm^{-1} [276].

5.4.5.3 Using SERS to Distinguish between Live and Dead Bacteria

Another important aspect for identifying pathogens is the ability to distinguish between viable and nonviable cells. The spectra of viable and nonviable cells of *E. coli* O157:H7 are shown in Figure 5.31 [276]. Here, the nonviable cells were prepared by boiling the bacteria in a hot-water bath for 10 min at 100 °C.

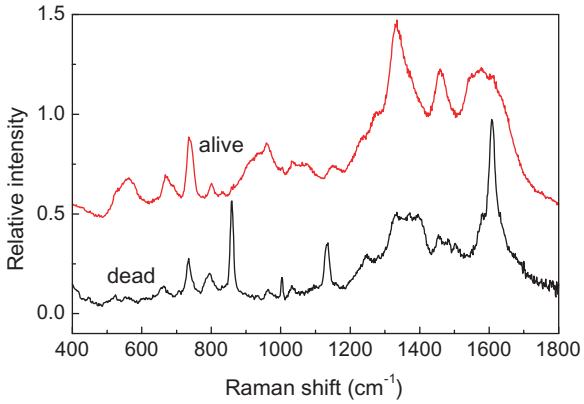

Figure 5.31 SERS spectra of viable (alive) and nonviable (dead) *E. coli* O157:H7 [276].

Subsequently, the dead cells showed a significantly reduced SERS response at the characteristic bands of ~550 cm^{-1}, 735 cm^{-1}, 1330 cm^{-1} and 1450 cm^{-1} that were present in viable cells. Such a result provides encouragement when considering possible applications of SERS in pathogen detection, where differentiation between viable and nonviable cells is imperative.

5.4.5.4 SERS has Single-Bacterium Detection Sensitivity

The sensitivity of SERS – that is, the SERS spectra of bacteria at the single-cell level – has been observed on the silver nanorod array substrate. A Renishaw Raman microscope, with an approximately 1 micro;m laser spot, was used to observe the scattering excited by a 785 nm diode laser and 12 μW laser power. Some images of bacterial cells (*E. coli* O157:H7) obtained under a ×50 microscope objective are shown in Figure 5.32 [276], where the area under the focal laser region is highlighted by a circle. In Figure 5.32a can be seen an isolated cell chain, consisting of two to three cells, where the laser beam was focused. A cluster with congested multiple cells is shown in Figure 5.32b, while the associated Raman spectra, after exposing the areas to the 1 micro;m laser beam for 10 s, are shown in Figure 5.32c. The SERS spectrum of the isolated cell chain appeared quite similar to that of the more congested cells. All of the major bands (~735, 1330 and 1450 cm^{-1}) matched what was observed from the more concentrated samples (Figure 5.31; estimated ~500 cells excited under the 100 micro;m laser spot). Most bands corresponded to functional groups in the main constituents of a microbial cell, such as proteins, carbohydrates, lipids and nucleic acids. These results highlighted the ability to observe Raman signatures of bacteria on a single-cell level when using a silver nanorod substrate.

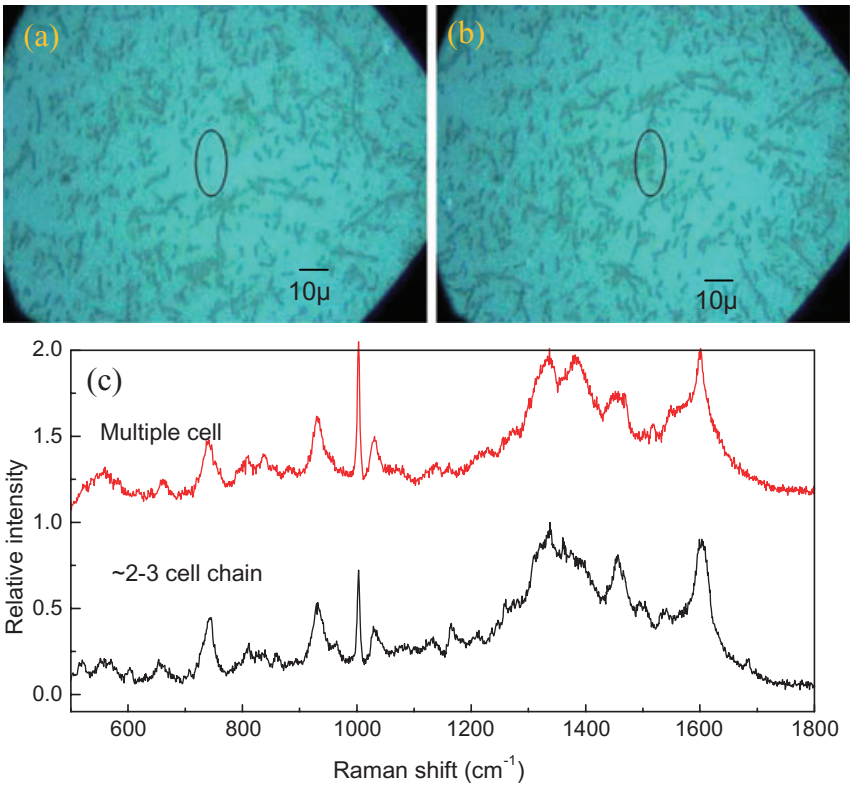

Figure 5.32 Raman microscopy measurements; bacterial imaging under a ×50 microscope objective. (a) Single *E. coli* O157:H7 2- to 3-cell chain contributing to the SERS spectrum; (b) A multiple cell cluster contributing to the SERS spectrum. The spectra are offset vertically for display clarity [276].

5.5 Conclusions

Nanostructure–especially Ag nanostructure based optical sensing techniques–has been shown to be an effective and highly sensitive diagnostic technique for biomedical applications. Some of the techniques developed have relatively simple requirements for equipment, and are also economical–features which offer great potential for use as practical diagnostics tools in conventional medical clinics. For most nanostructure-based detection techniques, several common problems must be resolved, including: (i) nanostructure fabrication; (ii) the cost of the fabrication and detection; and (iii) the need for any further enhancement of detection. For practical applications, the sensors must be reproducible and capable of being produced on a large scale. These features may require that the nanostructures be fabricated using different methods, so as to achieve reproducibility and production in large quantities. Today, with the advance of new nanofabrication techniques,

metal-based structures – either simple component or mixtures of multiple components – with better enhanced detection capabilities are emerging. Yet, even if these goals are achieved, the nanostructure-based diagnostic techniques may often still be impractical, generally because the environment in which the detection is carried out can also cause problems. For example, in the detection of viruses and/or bacteria, systems were tested using only purified viruses or bacteria, whereas in a practical diagnostic test the detection of a specimen or analyte must overcome often-complex biological matrices that affect the thresholds of both sensitivity and specificity. There is also often a need for a multiplex detection of more than one analyte; hence, in order to produce more practical nanostructure-based detection techniques, the following three issues will require extensive study:

- The collection and pretreatment of 'real' samples; that is, whether any background interference must be eliminated or reduced before the samples reach the detection stage.
- The development of a multiplexing scheme to identify different analytes and interference effects.
- The improvement of the intrinsic classification ability of detection techniques; this includes further improvement of the diagnostics techniques, and advancement of any associated data analysis techniques.

Clearly, even when these nanostructure fabrication techniques become more sophisticated, and the detection techniques more robust, there will still be practical barriers to overcome, potentially through advanced nanostructure design.

Acknowledgments

The authors would like to thank all the contributions from their collaborators and students over the past three years, with special thanks to Prof. R.A. Dluhy, Prof. D.C. Krause, Dr J.D. Driskell, Dr S. Shanmukh, Dr L. Jones, Dr S.J. Jokela, Dr J.-G. Fan, Mr Y.-J. Liu, Ms. J.-X. Fu, Ms S. Hennigan, Mr Z.-Y. Zhang and Mr S. Chaney. Financial support for these studies was provided by National Science Foundation, National Institute of Health, US Army Research Laboratory and Georgia Research Alliance.

References

1 Richter, L., Stepper, C., Mak, A., Reinthaler, A., Heer, R., Kast, M., Bruckl, H. and Ertl, P. (2007) Development of a microfluidic biochip for online monitoring of fungal biofilm dynamics. *Lab on a Chip*, **7**, 1723–31.

2 Ito, Y. (2006) Photoimmobilization for microarrays. *Biotechnology Progress*, **22**, 924–32.

3 Popovtzer, R., Neufeld, T., Biran, D., Ron, E.Z., Rishpon, J. and Shacham-Diamand, Y. (2005) Novel integrated electrochemical nano-biochip for toxicity

detection in water. *Nano Letters*, **5**, 1023–7.
4 Haglmuller, J., Rauter, H., Bauer, G., Pittner, F. and Schalkhammer, T. (2005) Resonant nano-cluster devices. *IEE Proceedings, Nanobiotechnology*, **152**, 53–63.
5 Song, J.M., Culha, M., Kasili, P.M., Griffin, G.D. and Vo-Dinh, T. (2005) A compact CMOS biochip immunosensor towards the detection of a single bacteria. *Biosensors & Bioelectronics*, **20**, 2203–9.
6 Sharma, S., Johnson, R.W. and Desai, T.A. (2004) XPS and AFM analysis of antifouling PEG interfaces for microfabricated silicon biosensors. *Biosensors and Bioelectronics*, **20**, 227–39.
7 Jung, A., Berlin, P. and Wolters, B. (2004) Biomolecule-compatible support structures for biomolecule coupling to physical measuring principle surfaces. *IEE Proceedings, Nanobiotechnology*, **151**, 87–94.
8 Hsu, H.Y. and Huang, Y.Y. (2004) RCA combined nanoparticle-based optical detection technique for protein microarray: a novel approach. *Biosensors and Bioelectronics*, **20**, 123–6.
9 Hering, K.K., Moller, R., Fritzsche, W. and Popp, J. (2008) Microarray-based detection of dye-labeled DNA by SERRS using particles formed by enzymatic silver deposition. *Chemphyschem*, **9**, 867–72.
10 Basu, S., Jana, S., Pande, S. and Pal, T. (2008) Interaction of DNA bases with silver nanoparticles: assembly quantified through SPRS and SERS. *Journal of Colloid and Interface Science*, **321**, 288–93.
11 Shang, L., Wang, Y., Huang, L. and Dong, S. (2007) Preparation of DNA-silver nanohybrids in multilayer nanoreactors by in situ electrochemical reduction, characterization, and application. *Langmuir*, **23**, 7738–44.
12 Schwartzberg, A.M., Oshiro, T.Y., Zhang, J.Z., Huser, T. and Talley, C.E. (2006) Improving nanoprobes using surface-enhanced Raman scattering from 30-nm hollow gold particles. *Analytical Chemistry*, **78**, 4732–6.
13 Zhang, H., Yee, D. and Wang, C. (2008) Quantum dots for cancer diagnosis and therapy: biological and clinical perspectives. *Nanomedicine*, **3**, 83–91.
14 Johnson, C.J., Zhukovsky, N., Cass, A.E. and Nagy, J.M. (2008) Proteomics, nanotechnology and molecular diagnostics. *Proteomics*, **8**, 715–30.
15 Iga, A.M., Robertson, J.H., Winslet, M.C. and Seifalian, A.M. (2007) Clinical potential of quantum dots. *Journal of Biomedicine and Biotechnology*, article no. 76087.
16 DaCosta, R.S., Wilson, B.C. and Marcon, N.E. (2007) Fluorescence and spectral imaging. *The Scientific World Journal [Electronic Resource]*, **7**, 2046–71.
17 Chansin, G.A., Mulero, R., Hong, J., Kim, M.J., DeMello, A.J. and Edel, J.B. (2007) Single-molecule spectroscopy using nanoporous membranes. *Nano Letters*, **7**, 2901–6.
18 Gerland, U., Bundschuh, R. and Hwa, T. (2004) Translocation of structured polynucleotides through nanopores. *Physical Biology*, **1**, 19–26.
19 Howorka, S., Cheley, S. and Bayley, H. (2001) Sequence-specific detection of individual DNA strands using engineered nanopores. *Nature Biotechnology*, **19**, 636–9.
20 Frederix, P.L., Akiyama, T., Staufer, U., Gerber, C., Fotiadis, D., Muller, D.J. and Engel, A. (2003) Atomic force bio-analytics. *Current Opinion in Chemical Biology*, **7**, 641–7.
21 Allison, D.P., Hinterdorfer, P. and Han, W. (2002) Biomolecular force measurements and the atomic force microscope. *Current Opinion in Biotechnology*, **13**, 47–51.
22 Braun, T., Backmann, N., Vogtli, M., Bietsch, A., Engel, A., Lang, H.P., Gerber, C. and Hegner, M. (2006) Conformational change of bacteriorhodopsin quantitatively monitored by microcantilever sensors. *Biophysical Journal*, **90**, 2970–7.
23 McKendry, R., Zhang, J., Arntz, Y., Strunz, T., Hegner, M., Lang, H.P., Baller, M.K., Certa, U., Meyer, E., Guntherodt, H.J. and Gerber, C. (2002) Multiple label-free biodetection and quantitative DNA-binding assays on a

nanomechanical cantilever array. *Proceedings of the National Academy of Sciences of the United States of America*, **99**, 9783–8.

24 Um, S.H., Lee, J.B., Kwon, S.Y., Li, Y. and Luo, D. (2006) Dendrimer-like DNA-based fluorescence nanobarcodes. *Nature Protocols*, **1**, 995–1000.

25 Sha, M.Y., Walton, I.D., Norton, S.M., Taylor, M., Yamanaka, M., Natan, M.J., Drmanac, C.X.S., Huang, S., Borcherding, A., Drmanac, R. and Penn, S.G. (2006) Multiplexed SNP genotyping using nanobarcode particle technology. *Analytical and Bioanalytical Chemistry*, **384**, 658–66.

26 Eastman, P.S., Ruan, W., Doctolero, M., Nuttall, R., de Feo, G., Park, J.S., Chu, J.S., Cooke, P., Gray, J.W., Li, S. and Chen, F.F. (2006) Qdot nanobarcodes for multiplexed gene expression analysis. *Nano Letters*, **6**, 1059–64.

27 Nam, J.M., Stoeva, S.I. and Mirkin, C.A. (2004) Bio-bar-code-based DNA detection with PCR-like sensitivity. *Journal of the American Chemical Society*, **126**, 5932–3.

28 McCabe, A.F., Eliasson, C., Prasath, R.A., Hernandez-Santana, A., Stevenson, L., Apple, I., Cormack, P.A., Graham, D., Smith, W.E., Corish, P., Lipscomb, S.J., Holland, E.R. and Prince, P.D. (2006) SERRS labelled beads for multiplex detection. *Faraday Discussions*, **132**, 303–8; discussion 309–19.

29 Rohr, T.E., Cotton, T., Fan, N. and Tarcha, P.J. (1989) Immunoassay employing surface-enhanced Raman spectroscopy. *Analytical Biochemistry*, **182**, 388–98.

30 Shanmukh, S., Jones, L., Zhao, Y.P., Driskell, J.D., Tripp, R.A. and Dluhy, R.A. (2008) Identification and classification of respiratory syncytial virus (RSV) strains by surface-enhanced Raman spectroscopy and multivariate statistical techniques. *Analytical and Bioanalytical Chemistry*, **390**, 1551–5.

31 Shanmukh, S., Jones, L., Driskell, J., Zhao, Y., Dluhy, R. and Tripp, R.A. (2006) Rapid and sensitive detection of respiratory virus molecular signatures using a silver nanorod array SERS substrate. *Nano Letters*, **6**, 2630–6.

32 Zhao, Y.P., Chaney, S.B., Shanmukh, S. and Dluhy, R.A. (2006) Polarized surface enhanced Raman and absorbance spectra of aligned silver nanorod arrays. *Journal of Physical Chemistry B*, **110**, 3153–7.

33 Zhao, Y., Jiang, Y. and Fang, Y. (2006) Spectroscopy property of Ag nanoparticles. *Spectrochimica Acta. Part A, Molecular and Biomolecular Spectroscopy*, **65**, 1003–6.

34 He, L., Musick, M.D., Nicewarner, S.R., Salinas, F.G., Benkovic, S.J., Natan, M.J. and Keating, C.D. (2000) Colloidal Au-enhanced surface plasmon resonance for ultrasensitive detection of DNA hybridization. *Journal of the American Chemical Society*, **122**, 9071–7.

35 Hutter, E., Cha, S., Liu, J.F., Park, J., Yi, J., Fendler, J.H. and Roy, D. (2001) Role of substrate metal in gold nanoparticle enhanced surface plasmon resonance imaging. *Journal of Physical Chemistry B*, **105**, 8–12.

36 Soh, N., Tokuda, T., Watanabe, T., Mishima, K., Imato, T., Masadome, T., Asano, Y., Okutani, S., Niwa, O. and Brown, S. (2003) A surface plasmon resonance immunosensor for detecting a dioxin precursor using a gold binding polypeptide. *Talanta*, **60**, 733–45.

37 Zayats, M., Pogorelova, S.P., Kharitonov, A.B., Lioubashevski, O., Katz, E. and Willner, I. (2003) An nanoparticle-enhanced surface plasmon resonance sensing of biocatalytic transformations. *Chemistry–A European Journal*, **9**, 6108–14.

38 Chen, S.J., Chien, F.C., Lin, G.Y. and Lee, K.C. (2004) Enhancement of the resolution of surface plasmon resonance biosensors by control of the size and distribution of nanoparticles. *Optics Letters*, **29**, 1390–2.

39 He, L., Smith, E.A., Natan, M.J. and Keating, C.D. (2004) The distance-dependence of colloidal Au-amplified surface plasmon resonance. *Journal of Physical Chemistry B*, **108**, 10973–80.

40 Homola, J., Yee, S.S. and Gauglitz, G. (1999) Surface plasmon resonance sensors: review. *Sensors and Actuators B–Chemical*, **54**, 3–15.

41 Nelson, R.W. and Krone, J.R. (1999) Advances in surface plasmon resonance biomolecular interaction analysis mass spectrometry (BIA/MS). *Journal of Molecular Recognition*, **12**, 77–93.

42 Mullett, W.M., Lai, E.P.C. and Yeung, J.M. (2000) Surface plasmon resonance-based immunoassays. *Methods*, **22**, 77–91.

43 Rich, R.L. and Myszka, D.G. (2000) Advances in surface plasmon resonance biosensor analysis. *Current Opinion in Biotechnology*, **11**, 54–61.

44 Homola, J. (2003) Present and future of surface plasmon resonance biosensors. *Analytical and Bioanalytical Chemistry*, **377**, 528–39.

45 Leonard, P., Hearty, S., Brennan, J., Dunne, L., Quinn, J., Chakraborty, T. and O'Kennedy, R. (2003) Advances in biosensors for detection of pathogens in food and water. *Enzyme and Microbial Technology*, **32**, 3–13.

46 Rich, R.L. and Myszka, D.G. (2003) Spying on HIV with SPR. *Trends in Microbiology*, **11**, 124–33.

47 Pattnaik, P. (2005) Surface plasmon resonance–applications in understanding receptor-ligand interaction. *Applied Biochemistry and Biotechnology*, **126**, 79–92.

48 Hoa, X.D., Kirk, A.G. and Tabrizian, M. (2007) Towards integrated and sensitive surface plasmon resonance biosensors: a review of recent progress. *Biosensors and Bioelectronics*, **23**, 151–60.

49 Shankaran, D.R., Gobi, K.V.A. and Miura, N. (2007) Recent advancements in surface plasmon resonance immunosensors for detection of small molecules of biomedical, food and environmental interest. *Sensors and Actuators B–Chemical*, **121**, 158–77.

50 Shankaran, D.R. and Miura, N. (2007) Trends in interfacial design for surface plasmon resonance based immunoassays. *Journal of Physics D–Applied Physics*, **40**, 7187–200.

51 Sharma, A.K., Jha, R. and Gupta, B.D. (2007) Fiber-optic sensors based on surface plasmon resonance: a comprehensive review. *IEEE Sensors Journal*, **7**, 1118–29.

52 Tanious, F.A., Nguyen, B. and Wilson, W.D. (2008) Biosensor-surface plasmon resonance methods for quantitative analysis of biomolecular interactions. *Biophysical Tools for Biologists: Volume 1 – In Vitro Techniques*, **84**, 53–77.

53 Willets, K.A. and Van Duyne, R.P. (2007) Localized surface plasmon resonance spectroscopy and sensing. *Annual Review of Physical Chemistry*, **58**, 267–97.

54 Fu, J.-X., Collins, A. and Zhao, Y.-P. (2008) The optical properties and biosensor application of ultra thin silver films. *Journal of Physical Chemistry C* (submitted).

55 Endo, T., Kerman, K., Nagatani, N., Takamura, Y. and Tamiya, E. (2005) Label-free detection of peptide nucleic acid-DNA hybridization using localized surface plasmon resonance based optical biosensor. *Analytical Chemistry*, **77**, 6976–84.

56 Kim, D.K., Kerman, K., Saito, M., Sathuluri, R.R., Endo, T., Yamamura, S., Kwon, Y.S. and Tamiya, E. (2007) Label-free DNA biosensor based on localized surface plasmon resonance coupled with interferometry. *Analytical Chemistry*, **79**, 1855–64.

57 Shin, Y.B., Lee, J.M., Park, M.R., Kim, M.G., Chung, B.H., Pyo, H.B. and Maeng, S. (2007) Analysis of recombinant protein expression using localized surface plasmon resonance (LSPR). *Biosensors and Bioelectronics*, **22**, 2301–7.

58 Stadler, B., Solak, H.H., Frerker, S., Bonroy, K., Frederix, F., Voros, J. and Grandin, H.M. (2007) Nanopatterning of gold colloids for label-free biosensing. *Nanotechnology*, **18**, article no. 155306.

59 Wark, A.W., Lee, H.J., Qavi, A.J. and Corn, R.M. (2007) Nanoparticle-enhanced diffraction gratings for ultrasensitive surface plasmon biosensing. *Analytical Chemistry*, **79**, 6697–701.

60 Haes, A.J., Hall, W.P., Chang, L., Klein, W.L. and Van Duyne, R.P. (2004) A localized surface plasmon resonance biosensor: first steps toward an assay for Alzheimer's disease. *Nano Letters*, **4**, 1029–34.

61 Haes, A.J., Chang, L., Klein, W.L. and Van Duyne, R.P. (2005) Detection of a

biomarker for Alzheimer's disease from synthetic and clinical samples using a nanoscale optical biosensor. *Journal of the American Chemical Society*, **127**, 2264–71.

62 Georganopoulou, D.G., Chang, L., Nam, J.M., Thaxton, C.S., Mufson, E.J., Klein, W.L. and Mirkin, C.A. (2005) Nanoparticle-based detection in cerebral spinal fluid of a soluble pathogenic biomarker for Alzheimer's disease. *Proceedings of the National Academy of Sciences of the United States of America*, **102**, 2273–6.

63 Liebermann, T. and Knoll, W. (2000) Surface-plasmon field-enhanced fluorescence spectroscopy. *Colloids and Surfaces A – Physicochemical and Engineering Aspects*, **171**, 115–30.

64 Geddes, C.D. and Lakowicz, J.R. (2002) Metal-enhanced fluorescence. *Journal of Fluorescence*, **12**, 121–9.

65 Lakowicz, J.R., Gryczynski, I., Shen, Y., Malicka, J., D'Auria, S. and Gryczynski, Z. (2002) Fluorescence spectra engineering – biophysical and biomedical applications, in *Fluorescence Spectroscopy, Imaging and Probes: New Tools in Chemical, Physical and Life Sciences* (eds R. Kraayenhof, A.J.W.G. Visser and H.C. Gerritsen), Springer-Verlag, Berlin, pp. 43–68.

66 Geddes, C.D., Roll, D., Parfenov, A. and Lakowicz, J.R. (2003) Noble-metal surfaces for use in metal-enhanced fluorescence. *Biophysical Journal*, **84**, 477A.

67 Geddes, C.D., Cao, H., Gryczynski, I., Gryczynski, Z., Fang, J.Y. and Lakowicz, J.R. (2003) Metal-enhanced fluorescence (MEF) due to silver colloids on a planar surface: potential applications of indocyanine green to in vivo imaging. *Journal of Physical Chemistry A*, **107**, 3443–9.

68 Geddes, C.D., Parfenov, A., Gryczynski, I., Malicka, J., Roll, D. and Lakowicz, J.R. (2003) Fractal silver structures for metal-enhanced fluorescence: applications for ultra-bright surface assays and lab-on-a-chip-based nanotechnologies. *Journal of Fluorescence*, **13**, 119–22.

69 Geddes, C.D., Parfenov, A., Roll, D., Gryezynski, I., Malicka, J. and Lakowicz, J.R. (2004) Roughened silver electrodes for use in metal-enhanced fluorescence. *Spectrochimica Acta Part A – Molecular and Biomolecular Spectroscopy*, **60**, 1977–83.

70 Aslan, K., Lakowicz, J.R., Szmacinski, H. and Geddes, C.D. (2004) Metal-enhanced fluorescence solution-based sensing platform. *Journal of Fluorescence*, **14**, 677–9.

71 Aslan, K., Leonenko, Z., Lakowicz, J. and Geddes, C. (2005) Annealed silver-island films for applications in metal-enhanced fluorescence: interpretation in terms of radiating plasmons. *Journal of Fluorescence*, **15**, 643–54.

72 Aslan, K., Lakowicz, J.R. and Geddes, C.D. (2005) Metal-enhanced fluorescence using anisotropic silver nanostructures: critical progress to date. *Analytical and Bioanalytical Chemistry*, **382**, 926–33.

73 Aslan, K., Lakowicz, J.R. and Geddes, C.D. (2005) Advanced surfaces for metal-enhanced fluorescence. *Biophysical Journal*, **88**, 374A.

74 Aslan, K., Gryczynski, I., Malicka, J., Matveeva, E., Lakowicz, J.R. and Geddes, C.D. (2005) Metal-enhanced fluorescence: an emerging tool in biotechnology. *Current Opinion in Biotechnology*, **16**, 55–62.

75 Aslan, K., Leonenko, Z., Lakowicz, J.R. and Geddes, C.D. (2005) Fast and slow deposition of silver nanorods on planar surfaces: application to metal-enhanced fluorescence. *Journal of Physical Chemistry B*, **109**, 3157–62.

76 Osawa, M. (2002) Surface-enhanced infrared absorption spectroscopy, in *Handbook of Vibrational Spectroscopy* (eds J.M. Chalmers and P.R. Griffiths), John Wiley & Sons, Ltd, Chichester, pp. 785–99.

77 Gussoni, M., Castiglioni, C. and Zerbi, G. (2002) Vibrational intensities: interpretation and use for diagnostic purposes, in *Handbook of Vibrational Spectroscopy* (eds J.M. Chalmers and P.R. Griffiths), John Wiley & Sons, Ltd, Chichester, pp. 2040–77.

78 McCreery, R.L. (2000) *Raman Spectroscopy for Chemical Analysis*, John Wiley & Sons, Inc., New York.

79 Aroca, R.F., Ross, D.J. and Domingo, C. (2004) Surface-enhanced infrared spectroscopy. *Applied Spectroscopy*, **58**, 324A–38A.

80 Leverette, C.L., Jacobs, S.A., Shanmukh, S., Chaney, S.B., Dluhy, R.A. and Zhao, Y.-P. (2006) Aligned silver nanorod arrays as substrates for surface-enhanced infrared absorption spectroscopy (SEIRA). *Applied Spectroscopy*, **60**, 906–13.

81 Fleischmann, M., Hendra, P.J. and McQuillan, A.J. (1974) Raman spectra of pyridine adsorbed at a silver electrode. *Chemical Physics Letters*, **26**, 163–6.

82 Albrecht, M.G. and Creighton, J.A. (1977) Anomalously intense Raman spectra of pyridine at a silver electrode. *Journal of the American Chemical Society*, **99**, 5215–17.

83 Jeanmaire, D.L. and Van Duyne, R.P. (1977) Surface Raman spectroelectrochemistry. Part I. Heterocyclic, aromatic, and aliphatic amines adsorbed on the anodized silver electrode. *Journal of Electroanalytical Chemistry*, **84**, 1–20.

84 Long, D.A. (1977) *Raman Spectroscopy*, McGraw-Hill, New York.

85 Carey, P.R. (1982) *Biochemical Applications of Raman and Resonance Raman Spectroscopies*, Academic Press, New York.

86 Campion, A. and Kambhampati, P. (1998) Surface-enhanced Raman scattering. *Chemical Society Review*, **27**, 241–50.

87 Otto, A., Mrozek, I., Grabhorn, H. and Akermann, W. (1992) Surface enhanced Raman scattering. *Journal of Physics: Condensed Matter*, **4**, 1143–212.

88 Cotton, T.M. and Brandt, E.S. (1993) Surface-enhanced Raman scattering, in *Physical Methods of Chemistry*, Vol. **9**, Part B, Investigations of Surfaces and Interfaces (eds B.W. Rossiter and R.C. Baetzold), 2nd edn, John Wiley & Sons, Inc., New York, pp. 633–718.

89 Moskovits, M. (1985) Surface-enhanced spectroscopy. *Reviews of Modern Physics*, **57**, 783–826.

90 Pemberton, J.E. (1991) Surface enhanced Raman scattering, in *Electrochemical Interfaces. Modern Techniques for In-Situ Characterization* (ed. H.D. Abruna), VCH Verlag Chemie, Berlin, pp. 195–263.

91 Weaver, M.J. and Zou, S. (1998) Vibrational spectroscopy of electrochemical interfaces. Some walls and bridges to surface science understanding, in *Spectroscopy for Surface Science*, Vol. 26 (eds R.J.H. Clark and R.E. Hester), John Wiley & Sons, Ltd, Chichester, UK, pp. 219–72.

92 Chang, R.K. and Furtak, T.E. (1982) *Surface-Enhanced Raman Scattering*, Plenum, New York.

93 Ruperez, A. and Laserna, J.J. (1996) Surface enhanced Raman spectroscopy, in *Modern Techniques in Raman Spectroscopy* (ed. J.J. Laserna), John Wiley & Sons, Ltd, Chichester, UK, pp. 227–61.

94 Moskovits, M. (2005) Surface-enhanced Raman spectroscopy: a brief retrospective. *Journal of Raman Spectroscopy*, **36**, 485–96.

95 Liang, E.J. and Kiefer, W. (1996) Chemical effect of SERS with near-infrared excitation. *Journal of Raman Spectroscopy*, **27**, 879–85.

96 Klar, T., Perner, M., Grosse, S., von Plessen, G., Spirkl, W. and Feldmann, J. (1998) Surface-plasmon resonances in single metallic nanoparticles. *Physical Review Letters*, **80**, 4249–52.

97 Krenn, J.R., Dereux, A., Weeber, J.C., Bourillot, E., Lacroute, Y., Goudonnet, J.P., Schider, G., Gotschy, W., Leitner, A., Aussenegg, F.R. and Girard, C. (1999) Squeezing the optical near-field zone by plasmon coupling of metallic nanoparticles. *Physical Review Letters*, **82**, 2590–3.

98 Markel, V.A., Shalaev, V.M., Zhang, P., Huynh, W., Tay, L., Haslett, T.L. and Moskovits, M. (1999) Near-field optical spectroscopy of individual surface-plasmon modes in colloid clusters. *Physical Review B*, **59**, 10903–9.

99 Mock, J.J., Barbic, M., Smith, D.R., Schultz, D.A. and Schultz, S. (2002) Shape effects in plasmon resonance of individual colloidal silver nanoparticles. *Journal of Chemical Physics*, **116**, 6755–9.

100 Prodan, E., Nordlander, P. and Halas, N.J. (2003) Electronic structure and optical properties of gold nanoshells. *Nano Letters*, **3**, 1411–15.

101 Teperik, T.V., Popov, V.V. and de Abajo, F.J.G. (2004) Radiative decay of plasmons in a metallic nanoshell. *Physical Review B*, 69.

102 Imura, K., Nagahara, T. and Okamoto, H. (2004) Characteristic near-field spectra of single gold nanoparticles. *Chemical Physics Letters*, **400**, 500–5.

103 Arbouet, A., Christofilos, D., Fatti, N. Del, Vallee, F., Huntzinger, J.R., Arnaud, L., Billaud, P. and Broyer, M. (2004) Direct measurement of the single-metal-cluster optical absorption. *Physical Review Letters*, 93.

104 Kalkbrenner, T., Hakanson, U. and Sandoghdar, V. (2004) Tomographic plasmon spectroscopy of a single gold nanoparticle. *Nano Letters*, **4**, 2309–14.

105 Radloff, C. and Halas, N.J. (2004) Plasmonic properties of concentric nanoshells. *Nano Letters*, **4**, 1323–7.

106 Nehl, C.L., Grady, N.K., Goodrich, G.P., Tam, F., Halas, N.J. and Hafner, J.H. (2004) Scattering spectra of single gold nanoshells. *Nano Letters*, **4**, 2355–-9.

107 Talley, C.E., Jackson, J.B., Oubre, C., Grady, N.K., Hollars, C.W., Lane, S.M., Huser, T.R., Nordlander, P. and Halas, N.J. (2005) Surface-enhanced Raman scattering from individual Au nanoparticles and nanoparticle dimer substrates. *Nano Letters*, **5**, 1569–74.

108 Sherry, L.J., Chang, S.H., Schatz, G.C., Van Duyne, R.P., Wiley, B.J. and Xia, Y.N. (2005) Localized surface plasmon resonance spectroscopy of single silver nanocubes. *Nano Letters*, **5**, 2034–8.

109 Van Dijk, M.A., Lippitz, M. and Orrit, M. (2005) Far-field optical microscopy of single metal nanoparticles. *Accounts of Chemical Research*, **38**, 594–601.

110 Xu, G., Chen, Y., Tazawa, M. and Jin, P. (2006) Influence of dielectric properties of a substrate upon plasmon resonance spectrum of supported Ag nanoparticles. *Applied Physics Letters*, **88**, article no. 043114.

111 Muskens, O., Christofilos, D., Del Fatti, N. and Vallee, F. (2006) Optical response of a single noble metal nanoparticle. *Journal of Optics A – Pure and Applied Optics*, **8**, S264–72.

112 Nehl, C.L., Liao, H.W. and Hafner, J.H. (2006) Optical properties of star-shaped gold nanoparticles. *Nano Letters*, **6**, 683–8.

113 Moreno, F., Gonzalez, E. and Saiz, J.M. (2006) Plasmon spectroscopy of metallic nanoparticles above flat dielectric substrates. *Optics Letters*, **31**, 1902–4.

114 Hirsch, L.R., Gobin, A.M., Lowery, A.R., Tam, F., Drezek, R.A., Halas, N.J. and West, J.L. (2006) Metal nanoshells. *Annals of Biomedical Engineering*, **34**, 15–22.

115 Alivisatos, A.P. (1996) Semiconductor clusters, nanocrystals, and quantum dots. *Science*, **271**, 933–7.

116 Link, S., Mohamed, M.B. and El-Sayed, M.A. (1999) Simulation of the optical absorption spectra of gold nanorods as a function of their aspect ratio and the effect of the medium dielectric constant. *Journal of Physical Chemistry B*, **103**, 3073–7.

117 Chen, S.H., Webster, S., Czerw, R., Xu, J.F. and Carroll, D.L. (2004) Morphology effects on the optical properties of silver nanoparticles. *Journal of Nanoscience and Nanotechnology*, **4**, 254–9.

118 Orfanides, P., Buckner, T.F., Buncick, M.C., Meriaudeau, F. and Ferrell, T.L. (2000) Demonstration of surface plasmons in metal island films and the effect of the surrounding medium – an undergraduate experiment. *American Journal of Physics*, **68**, 936–42.

119 Xu, G., Tazawa, M., Jin, P., Nakao, S. and Yoshimura, K. (2003) Wavelength tuning of surface plasmon resonance using dielectric layers on silver island films. *Applied Physics Letters*, **82**, 3811–13.

120 Mock, J.J., Smith, D.R. and Schultz, S. (2003) Local refractive index dependence of plasmon resonance spectra from individual nanoparticles. *Nano Letters*, **3**, 485–91.

121 Sun, Y.G. and Xia, Y.N. (2002) Increased sensitivity of surface plasmon resonance of gold nanoshells compared to that of gold solid colloids in response to environmental changes. *Analytical Chemistry*, **74**, 5297–305.

122 Yonzon, C.R., Stuart, D.A., Zhang, X.Y., McFarland, A.D., Haynes, C.L. and Van Duyne, R.P. (2005) Towards advanced

chemical and biological nanosensors – an overview. *Talanta*, **67**, 438–48.

123 Jackson, J.B., Westcott, S.L., Hirsch, L.R., West, J.L. and Halas, N.J. (2003) Controlling the surface enhanced Raman effect via the nanoshell geometry. *Applied Physics Letters*, **82**, 257–9.

124 Sershen, S.R., Westcott, S.L., Halas, N.J. and West, J.L. (2000) Temperature-sensitive polymer-nanoshell composites for photothermally modulated drug delivery. *Journal of Biomedical Materials Research*, **51**, 293–8.

125 Lin, A.W.H., Lewinski, N.A., West, J.L., Halas, N.J. and Drezek, R.A. (2005) Optically tunable nanoparticle contrast agents for early cancer detection: model-based analysis of gold nanoshells. *Journal of Biomedical Optics*, **10**, article no. 064035.

126 Gobin, A.M., Lee, M.H., Drezek, R.A., Halas, N.J. and West, J.L. (2005) Nanoshells for combined cancer therapy and imaging in vivo. *Clinical Cancer Research*, **11**, 9095S.

127 Hale, G.D., Jackson, J.B., Shmakova, O.E., Lee, T.R. and Halas, N.J. (2001) Enhancing the active lifetime of luminescent semiconducting polymers via doping with metal nanoshells. *Applied Physics Letters*, **78**, 1502–4.

128 Murphy, C.J., Sau, T.K., Gole, A. and Orendorff, C.J. (2005) Surfactant-directed synthesis and optical properties of one-dimensional plasmonic metallic nanostructures. *MRS Bulletin*, **30**, 349–55.

129 Wiley, B., Sun, Y.G., Chen, J.Y., Cang, H., Li, Z.Y., Li, X.D. and Xia, Y.N. (2005) Shape-controlled synthesis of silver and gold nanostructures. *MRS Bulletin*, **30**, 356–61.

130 Halas, N. (2005) Playing with plasmons. Tuning the optical resonant properties of metallic nanoshells. *MRS Bulletin*, **30**, 362–7.

131 Hutter, E. and Fendler, J.H. (2004) Exploitation of localized surface plasmon resonance. *Advanced Materials*, **16**, 1685–706.

132 Nie, S.M. and Emery, S.R. (1997) Probing single molecules and single nanoparticles by surface-enhanced Raman scattering. *Science*, **275**, 1102–6.

133 Kneipp, K., Kneipp, H., Manoharan, R., Hanlon, E.B., Itzkan, I., Dasari, R.R. and Feld, M.S. (1998) Extremely large enhancement factors in surface-enhanced Raman scattering for molecules on colloidal gold clusters. *Applied Spectroscopy*, **52**, 1493–7.

134 Moskovits, M. (2005) Surface-enhanced Raman spectroscopy: a brief retrospective. *Journal of Raman Spectroscopy*, **36**, 485–96.

135 Wei, Q.H., Su, K.H., Durant, S. and Zhang, X. (2004) Plasmon resonance of finite one-dimensional Au nanoparticle chains. *Nano Letters*, **4**, 1067–71.

136 Su, K.H., Wei, Q.H., Zhang, X., Mock, J.J., Smith, D.R. and Schultz, S. (2003) Interparticle coupling effects on plasmon resonances of nanogold particles. *Nano Letters*, **3**, 1087–90.

137 Atay, T., Song, J.H. and Nurmikko, A.V. (2004) Strongly interacting plasmon nanoparticle pairs: From dipole-dipole interaction to conductively coupled regime. *Nano Letters*, **4**, 1627–31.

138 Vo-Dinh, T. (1998) Surface-enhanced Raman spectroscopy using metallic nanostructures *TRAC Trends in Analytical Chemistry*, **17**, 557–82.

139 Tian, Z.Q., Ren, B. and Wu, D.Y. (2002) Surface-enhanced Raman scattering: from noble to transition metals and from rough surfaces to ordered nanostructures. *Journal of Physical Chemistry B*, **106**, 9463–83.

140 Campion, A. and Kambhampati, P. (1998) Surface-enhanced Raman scattering. *Chemical Society Reviews*, **27**, 241.

141 Ahern, A.M. and Garrell, R.L. (1987) In-situ photoreduced silver nitrate as a substrate for surface-enhanced Raman spectroscopy. *Analytical Chemistry*, **59**, 2813–16.

142 Neddersen, J., Chumanov, G. and Cotton, T.M. (1993) Laser ablation of metals – a new method for preparing SERS active colloids. *Applied Spectroscopy*, **47**, 1959–64.

143 Xue, G., Dong, J. and Zhang, M.S. (1991) Surface-enhanced Raman scattering

(SERS) and surface-enhanced resonance Raman scattering (SERRS) on HNO_3-roughened copper foil. *Applied Spectroscopy*, **45**, 756–9.

144 Norrod, K.L., Sudnik, L.M., Rousell, D. and Rowlen, K.L. (1997) Quantitative comparison of five SERS substrates: sensitivity and limit of detection. *Applied Spectroscopy*, **51**, 994–1001.

145 Schlegel, V.L. and Cotton, T.M. (1991) Silver island films as substrates for enhanced Raman scattering: effect of deposition rate on intensity. *Analytical Chemistry*, **63**, 241–7.

146 Van Duyne, R.P., Hulteen, J.C. and Treichel, D.A. (1993) Atomic force microscopy and surface-enhanced Raman spectroscopy. I. Ag island films and Ag film over polymer nanosphere surfaces supported on glass. *Journal of Chemical Physics*, **99**, 2101–15.

147 Semin, D.J. and Rowlen, K.L. (1994) Influence of vapor deposition parameters on SERS active Ag film morphology and optical properties. *Analytical Chemistry*, **66**, 4324–31.

148 Roark, S.E. and Rowlen, K.L. (1994) Thin silver films: influence of substrate and postdeposition treatment on morphology and optical properties. *Analytical Chemistry*, **66**, 261–70.

149 Kahl, M., Voges, E., Kostrewa, S., Viets, C. and Hill, W. (1998) Periodically structured metallic substrates for SERS. *Sensors and Actuators B–Chemical*, **51**, 285–91.

150 De Jesus, M.A., Giesfeldt, K.S., Oran, J.M., Abu-Hatab, N.A., Lavrik, N.V. and Sepaniak, M.J. (2005) Nanofabrication of densely packed metal-polymer arrays for surface-enhanced Raman spectrometry. *Applied Spectroscopy*, **59**, 1501–8.

151 Sackmann, M., Bom, S., Balster, T. and Materny, A. (2007) Nanostructured gold surfaces as reproducible substrates for surface-enhanced Raman spectroscopy. *Journal of Raman Spectroscopy*, **38**, 277–82.

152 Billot, L., Grimault, M.L. de la Chapelle, A.S., Vial, A., Barchiesi, D., Bijeon, J.L., Adam, P.M. and Royer, P. (2006) Surface enhanced Raman scattering on gold nanowire arrays: evidence of strong multipolar surface plasmon resonance enhancement. *Chemical Physics Letters*, **422**, 303–7.

153 Reilly, T.H., Corbman, J.D. and Rowlen, K.L. (2007) Vapor deposition method for sensitivity studies on engineered surface-enhanced Raman scattering-active substrates. *Analytical Chemistry*, **79**, 5078–81.

154 Alvarez-Puebla, R., Cui, B., Bravo-Vasquez, J.-P., Verse, T. and Fenniri, H. (2007) Nanoimprinted SERS-active substrates with tunable surface plasmon resonances. *Journal of Physical Chemistry C*, **111**, 6720.

155 Jensen, T.R., Schatz, G.C. and Van Duyne, R.P. (1999) Nanosphere lithography: Surface plasmon resonance spectrum of a periodic array of silver nanoparticles by ultraviolet-visible extinction spectroscopy and electrodynamic modeling. *Journal of Physical Chemistry B*, **103**, 2394–401.

156 Hulteen, J.C., Treichel, D.A., Smith, M.T., Duval, M.L., Jensen, T.R. and Van Duyne, R.P. (1999) Nanosphere lithography: size-tunable silver nanoparticle and surface cluster arrays. *Journal of Physical Chemistry B*, **103**, 3854–63.

157 Jensen, T.R., Duval, M.L., Kelly, K.L., Lazarides, A.A., Schatz, G.C. and Van Duyne, R.P. (1999) Nanosphere lithography: effect of the external dielectric medium on the surface plasmon resonance spectrum of a periodic array of sliver nanoparticles. *Journal of Physical Chemistry B*, **103**, 9846–53.

158 Jensen, T.R., Malinsky, M.D., Haynes, C.L. and Van Duyne, R.P. (2000) Nanosphere lithography: tunable localized surface plasmon resonance spectra of silver nanoparticles. *Journal of Physical Chemistry B*, **104**, 10549–56.

159 Haynes, C.L. and Van Duyne, R.P. (2001) Nanosphere lithography: a versatile nanofabrication tool for studies of size-dependent nanoparticle optics. *Journal of Physical Chemistry B*, **105**, 5599–611.

160 Ormonde, A.D., Hicks, E.C.M., Castillo, J. and Van Duyne, R.P. (2004)

Nanosphere lithography: fabrication of large-area Ag nanoparticle arrays by convective self-assembly and their characterization by scanning UV-visible extinction spectroscopy. *Langmuir*, **20**, 6927–31.

161 Zhang, X., Yonzon, C.R., Young, M.A., Stuart, D.A. and Van Duyne, R.P. (2005) Surface-enhanced Raman spectroscopy biosensors: excitation spectroscopy for optimisation of substrates fabricated by nanosphere lithography. *IEE Proceedings, Nanobiotechnology*, **152**, 195.

162 Haynes, C.L., McFarland, A.D., Smith, M.T., Hulteen, J.C. and Van Duyne, R.P. (2002) Angle-resolved nanosphere lithography: manipulation of nanoparticle size, shape, and interparticle spacing. *Journal of Physical Chemistry B*, **106**, 1898–902.

163 Yao, J.L., Pan, G.P., Xue, K.H., Wu, D.Y., Ren, B., Sun, D.M., Tang, J., Xu, X. and Tian, Z.Q. (2000) A complementary study of surface-enhanced Raman scattering and metal nanorod arrays. *Pure and Applied Chemistry*, **72**, 221–8.

164 Kartopu, G., Es-Souni, M., Sapelkin, A.V. and Dunstan, D. (2006) A novel SERS-active substrate system: template-grown nanodot-film structures. *Physica Status Solidi A–Applications and Materials Science*, **203**, R82–4.

165 Zhang, L.S., Zhang, P.X. and Fang, Y. (2007) An investigation of the surface-enhanced Raman scattering effect from new substrates of several kinds of nanowire arrays. *Journal of Colloid and Interface Science*, **311**, 502–6.

166 Ruan, C.M., Eres, G., Wang, W., Zhang, Z.Y. and Gu, B.H. (2007) Controlled fabrication of nanopillar arrays as active substrates for surface-enhanced Raman spectroscopy. *Langmuir*, **23**, 5757–60.

167 Broglin, B.L., Andreu, A., Dhussa, N., Heath, J.A., Gerst, J., Dudley, B., Holland, D. and El-Kouedi, M. (2007) Investigation of the effects of the local environment on the surface-enhanced Raman spectra of striped gold/silver nanorod arrays. *Langmuir*, **23**, 4563–8.

168 Gu, G.H., Kim, J., Kim, L. and Suh, J.S. (2007) Optimum length of silver nanorods for fabrication of hot spots. *Journal of Physical Chemistry C*, **111**, 7906–9.

169 Lombardi, I., Cavallotti, P.L., Carraro, C. and Maboudian, R. (2007) Template assisted deposition of Ag nanoparticle arrays for surface-enhanced Raman scattering applications. *Sensors and Actuators B–Chemical*, **125**, 353–6.

170 Jung, D.S., Lee, Y.M., Lee, Y., Kim, N.H., Kim, K. and Lee, J.K. (2006) Facile fabrication of large area nanostructures for efficient surface-enhanced Raman scattering. *Journal of Materials Chemistry*, **16**, 3145–9.

171 Walsh, R.J. and Chumanov, G. (2001) Silver coated porous alumina as a new substrate for surface-enhanced Raman scattering. *Applied Spectroscopy*, **55**, 1695–700.

172 Chan, S., Kwon, S., Koo, T.W., Lee, L.P. and Berlin, A.A. (2003) Surface-enhanced Raman scattering of small molecules from silver-coated silicon nanopores. *Advanced Materials*, **15**, 1595–8.

173 Lin, H.H., Mock, J., Smith, D., Gao, T. and Sailor, M.J. (2004) Surface-enhanced Raman scattering from silver-plated porous silicon. *Journal of Physical Chemistry B*, **108**, 11654–9.

174 Henley, S.J., Carey, J.D. and Silva, S.R.P. (2006) Silver-nanoparticle-decorated carbon nanoscaffolds: application as a sensing platform. *Applied Physics Letters*, **89**, article no. 183120.

175 Chattopadhyay, S., Lo, H.C., Hsu, C.H., Chen, L.C. and Chen, K.H. (2005) Surface-enhanced Raman spectroscopy using self-assembled silver nanoparticles on silicon nanotips. *Chemistry of Materials*, **17**, 553–9.

176 Suzuki, M., Maekita, W., Wada, Y., Nakajima, K., Kimura, K., Fukuoka, T. and Mori, Y. (2006) In-line aligned and bottom-up Ag nanorods for surface-enhanced Raman spectroscopy. *Applied Physics Letters*, **88**, 203121.

177 Suzuki, M., Nakajima, K., Kimura, K., Fukuoka, T. and Mori, Y. (2007) Au nanorod arrays tailored for surface – enhanced Raman spectroscopy. *Analytical Sciences*, **23**, 829–33.

178 Chaney, S.B., Shanmukh, S., Dluhy, R.A. and Zhao, Y.-P. (2005) Aligned silver nanorod arrays produce high sensitivity surface-enhanced Raman spectroscopy substrates. *Applied Physics Letters*, **87**, article no. 031908.

179 Zhao, Y.-P., Chaney, S.B., Shanmukh, S. and Dluhy, R.A. (2006) Polarized surface enhanced Raman and absorbance spectra of aligned silver nanorod arrays. *Journal of Physical Chemistry B*, **110**, 3153–7.

180 Driskell, J., Shanmukh, S., Liu, Y., Chaney, S., Tang, X.-J., Zhao, Y.-P. and Dluhy, R.A. (2008) The use of aligned silver nanorod arrays prepared by oblique angle vapor deposition. *Journal of Physical Chemistry C*, **112**, 895–901.

181 Nikoobakht, B., Wang, J.P. and El-Sayed, M.A. (2002) Surface-enhanced Raman scattering of molecules adsorbed on gold nanorods: off-surface plasmon resonance condition. *Chemical Physics Letters*, **366**, 17–23.

182 Mulvaney, S.P., He, L., Natan, M.J. and Keating, C.D. (2003) Three-layer substrates for surface-enhanced Raman scattering: preparation and preliminary evaluation. *Journal of Raman Spectroscopy*, **34**, 163–71.

183 Green, M. and Liu, F.M. (2003) SERS substrates fabricated by island lithography: the silver/pyridine system. *Journal of Physical Chemistry B*, **107**, 13015–21.

184 Stockle, R.M., Deckert, V., Fokas, C., Zeisel, D. and Zenobi, R. (2000) Sub-wavelength Raman spectroscopy on isolated silver islands. *Vibrational Spectroscopy*, **22**, 39–48.

185 Shanmukh, S., Jones, L., Zhao, Y.-P., Dluhy, R.A. and Tripp, R.A. (2006) Rapid and sensitive detection of respiratory virus molecular signatures using surface enhanced Raman. *Nano Letters*, **6**, 2630–6.

186 Xu, H., Bjerneld, J., Käll, M. and Börjesson, L. (1999) Spectroscopy of single hemoglobin molecules by surface enhanced Raman spectroscopy. *Physical Review Letters*, **83**, 4357–60.

187 Kneipp, K., Wang, Y., Kneipp, H., Perelman, L.T., Itzkan, I., Dasari, R. and Feld, M.S. (1997) Single molecule detection using surface-enhanced Raman scattering (SERS). *Physical Review Letters*, **78**, 1667–70.

188 Baker, G.A. and Moore, D.S. (2005) Progress in plasmonic engineering of surface-enhanced Raman-scattering substrates toward ultra-trace analysis. *Analytical and Bioanalytical Chemistry*, **382**, 1751–70.

189 Haynes, C.L., Yonzon, C.R., Zhang, X.Y. and Van Duyne, R.P. (2005) Surface-enhanced Raman sensors: early history and the development of sensors for quantitative biowarfare agent and glucose detection. *Journal of Raman Spectroscopy*, **36**, 471–84.

190 Vo-Dinh, T., Yan, F. and Wabuyele, M.B. (2005) Surface-enhanced Raman scattering for medical diagnostics and biological imaging. *Journal of Raman Spectroscopy*, **36**, 640–7.

191 Doering, W.E., Piotti, M.E., Natan, M.J. and Freeman, R.G. (2007) SERS as a foundation for nanoscale, optically detected biological labels. *Advanced Materials*, **19**, 3100–8.

192 Hering, K., Cialla, D., Ackermann, K., Dorfer, T., Moller, R., Schneidewind, H., Mattheis, R., Fritzsche, W., Rosch, P. and Popp, J. (2008) SERS: a versatile tool in chemical and biochemical diagnostics. *Analytical and Bioanalytical Chemistry*, **390**, 113–24.

193 Qian, X., Peng, X.-H., Ansari, D.O., Yin-Goen, Q., Chen, G.Z., Shin, D.M., Yang, L., Young, A.N., Wang, M.D. and Nie, S. (2007) In vivo tumor targeting and spectroscopic detection with surface-enhanced Raman nanoparticle tags. *Nature Biotechnology*, **26**, 83.

194 Kneipp, K., Haka, A.S., Kneipp, H., Badizadegan, K., Yoshizawa, N., Boone, C., Shafer-Peltier, K.E., Motz, J.T., Dasari, R.R. and Feld, M.S. (2002) Surface-enhanced Raman spectroscopy in single living cells using gold nanoparticles. *Applied Spectroscopy*, **56**, 150.

195 Driskell, J.D., Kwarta, K.M., Lipert, R.J., Porter, M.D., Neill, J.D. and Ridpath, J.F. (2005) Low-level detection of viral pathogens by a surface-enhanced Raman scattering based immunoassay. *Analytical Chemistry*, **77**, 6147–54.

196 Pinzaru, S.C., Pavel, I., Leopold, N. and Kiefer, W. (2004) Identification and characterization of pharmaceuticals using Raman and surface-enhanced Raman scattering. *Journal of Raman Spectroscopy*, **35**, 338–46.

197 Tsai, C.W. and Morris, M.D. (1975) Application of resonance Raman spectrometry to determination of Vitamin-b12. *Analytica Chimica Acta*, **76**, 193–8.

198 Taniguchi, I., Umekita, K. and Yasukouchi, K. (1986) Surface-enhanced Raman-scattering of nicotinamide adenine-dinucleotide (NAD+) adsorbed on silver and gold electrodes. *Journal of Electroanalytical Chemistry*, **202**, 315–22.

199 Suh, J.S. and Moskovits, M. (1986) Surface-enhanced Raman-spectroscopy of amino-acids and nucleotide bases adsorbed on silver. *Journal of the American Chemical Society*, **108**, 4711–18.

200 Barthelmes, J., Pofahl, G. and Plieth, W. (1992) pH-dependent Raman spectra of nicotinic acid–spectra of aqueous solutions and surface enhanced Raman spectra on silver electrodes. *Berichte der Bunsen-Gesellschaft–Physical Chemistry Chemical Physics*, **96**, 1055–60.

201 Quaroni, L., Reglinski, J. and Smith, W.E. (1995) Surface enhanced resonance Raman scattering from cyanocobalamin and 5′-deoxyadenosylcobalamin. *Journal of Raman Spectroscopy*, **26**, 1075–6.

202 Iliescu, T., Cinta, S., Astilean, S. and Bratu, I. (1997) pH influence on the Raman spectra of PP vitamin in silver sol. *Journal of Molecular Structure*, **410**, 193–6.

203 Pal, T., Narayanan, V.A., Stokes, D.L. and Vo-Dinh, T. (1998) Surface-enhanced Raman detection of nicotinamide in vitamin tablets. *Analytica Chimica Acta*, **368**, 21–8.

204 Dong, S.L., Padmakumar, R., Maiti, N., Banerjee, R. and Spiro, T.G. (1998) Resonance Raman spectra show that coenzyme B-12 binding to methylmalonyl-coenzyme A mutase changes the corrin ring conformation but leaves the Co-C bond essentially unaffected. *Journal of the American Chemical Society*, **120**, 9947–8.

205 Balakrishnan, G., Babaei, A., McQuillan, A.J. and Umapathy, S. (1998) Resonance Raman and infrared spectral studies on radical anions of model photosynthetic reaction center quinones (naphthoquinone derivatives). *Journal of Biomolecular Structure and Dynamics*, **16**, 123–31.

206 Cinta, S., Morari, C., Vogel, E., Maniu, D., Aluas, M., Iliescu, T., Cozar, O. and Kiefer, W. (1999) Vibrational studies of B-6 vitamin. *Vibrational Spectroscopy*, **19**, 329–34.

207 Lin, S., Quaroni, L., White, W.S., Cotton, T. and Chumanov, G. (2000) Localization of carotenoids in plasma low-density lipoproteins studied by surface-enhanced resonance Raman spectroscopy. *Biopolymers*, **57**, 249–56.

208 Yang, H. and Irudayaraj, J. (2002) Rapid determination of vitamin c by NIR, MIR and FT-Raman techniques. *Journal of Pharmacy and Pharmacology*, **54**, 1247–55.

209 Failloux, N., Bonnet, I., Baron, M.H. and Perrier, E. (2003) Quantitative analysis of vitamin A degradation by Raman spectroscopy. *Applied Spectroscopy*, **57**, 1117–22.

210 Wang, Y., Li, Y.S., Zhang, Z.X. and An, D.Q. (2003) Surface-enhanced Raman scattering of some water insoluble drugs in silver hydrosols. *Spectrochimica Acta Part A–Molecular and Biomolecular Spectroscopy*, **59**, 589–94.

211 Wang, Y., Li, Y.S., Zhang, Z.X. and An, D.Q. (2004) SERS spectra of vitamin A acid in silver solution. *Spectroscopy and Spectral Analysis*, **24**, 1376–8.

212 Chowdhury, J., Ghosh, M. and Misra, T.N. (2000) Surface enhanced Raman scattering of 2,2′ biquinoline adsorbed on colloidal silver particles. *Spectrochimica Acta Part A–Molecular and Biomolecular Spectroscopy*, **56**, 2107–15.

213 Pavel, I., Szeghalmi, A., Moigno, D., Cinta, S. and Kiefer, W. (2003) Theoretical and pH dependent surface enhanced Raman spectroscopy study on caffeine. *Biopolymers*, **72**, 25–37.

214 Horvath, E., Mink, J. and Kristof, J. (1997) Surface-enhanced Raman

spectroscopy as a technique for drug analysis. *Mikrochimica Acta*, 745–6.

215 Carter, J.C., Brewer, W.E. and Angel, S.M. (2000) Raman spectroscopy for the in situ identification of cocaine and selected adulterants. *Applied Spectroscopy*, **54**, 1876–81.

216 Sagmuller, B., Schwarze, B., Brehm, G., Trachta, G. and Schneider, S. (2003) Identification of illicit drugs by a combination of liquid chromatography and surface-enhanced Raman scattering spectroscopy. *Journal of Molecular Structure*, **661**, 279–90.

217 Lecomte, S., Moreau, N.J., Manfait, M., Aubard, J. and Baron, M.H. (1995) Surface-enhanced Raman spectroscopy investigation of fluoroquinolone DNA/DNA gyrase Mg^{2+} interactions. 1. Adsorption of pefloxacin on colloidal silver–effect of drug concentration, electrolytes, and pH. *Biospectroscopy*, **1**, 423–36.

218 Lecomte, S. and Baron, M.H. (1997) Surface-enhanced Raman spectroscopy investigation of fluoroquinolones-DNA-DNA gyrase-Mg^{2+} interactions. 2. Interaction of pefloxacin with Mg^{2+} and DNA. *Biospectroscopy*, **3**, 31–45.

219 Iliescu, T., Cinta, S. and Kiefer, W. (2000) FT-Raman and SERS spectra of rivanol in silver sol. *Talanta*, **53**, 121–4.

220 Iliescu, T., Marian, I., Misca, R. and Smarandache, V. (1994) Surface-enhanced Raman-spectroscopy of 9-phenylacridine on silver sol. *Analyst*, **119**, 567–70.

221 Nabiev, I., Baranov, A., Chourpa, I., Beljebbar, A., Sockalingum, G.D. and Manfait, M. (1995) Does adsorption on the surface of a silver colloid perturb drug-DNA interactions–comparative SERS, FT-SERS, and resonance Raman-study of mitoxantrone and its derivatives. *Journal of Physical Chemistry*, **99**, 1608–13.

222 Beljebbar, A., Sockalingum, G.D., Angiboust, J.F. and Manfait, M. (1995) Comparative FT SERS, resonance Raman and SERRS studies of doxorubicin and its complex with DNA. *Spectrochimica Acta Part A–Molecular and Biomolecular Spectroscopy*, **51**, 2083–90.

223 Beljebbar, A., Morjani, H., Angiboust, J.F., Sockalingum, G.D., Polissiou, M. and Manfait, M. (1997) Molecular and cellular interaction of the differentiating antitumour agent dimethylcrocetin with nuclear retinoic acid receptor as studied by near-infrared and visible SERS spectroscopy. *Journal of Raman Spectroscopy*, **28**, 159–63.

224 Chourpa, I., Beljebbar, A., Sockalingum, G.D., Riou, J.F. and Manfait, M. (1997) Structure-activity relation in camptothecin antitumor drugs: Why a detailed molecular characterisation of their lactone and carboxylate forms by Raman and SERS spectroscopies? *Biochimica et Biophysica Acta–General Subjects*, **1334**, 349–60.

225 Murza, A., Sanchez-Cortes, S., Garcia-Ramos, J.V., Guisan, J.M., Alfonso, C. and Rivas, G. (2000) Interaction of the antitumor drug 9-aminoacridine with guanidinobenzoatase studied by spectroscopic methods: a possible tumor marker probe based on the fluorescence exciplex emission. *Biochemistry*, **39**, 10557–65.

226 Vivoni, A., Chen, S.P., Ejeh, D. and Hosten, C.M. (2001) Normal-mode analysis of the Raman-active modes of the anti-tumor agent 6-mercaptopurine. *Journal of Raman Spectroscopy*, **32**, 1–8.

227 Streltsov, S., Oleinikov, V., Ermishov, M., Mochalov, K., Sukhanova, A., Nechipurenko, Y., Grokhovsky, S., Zhuze, A., Pluot, M. and Nabiev, I. (2003) Interaction of clinically important human DNA topoisomerase I poison, topotecan, with double-stranded DNA. *Biopolymers*, **72**, 442–54.

228 Seballos, L., Zhang, J.Z. and Sutphen, R. (2005) Surface-enhanced Raman scattering detection of lysophosphatidic acid. *Analytical and Bioanalytical Chemistry*, **383**, 763–7.

229 Lee, S., Kim, S., Choo, J., Shin, S.Y., Lee, Y.H., Choi, H.Y., Ha, S.H., Kang, K.H. and Oh, C.H. (2007) Biological imaging of HEK293 cells expressing PLC gamma 1 using surface-enhanced Raman microscopy. *Analytical Chemistry*, **79**, 916–22.

230 Sekhar, P.K., Ramgir, N.S. and Bhansali, S. (2008) Metal-decorated silica nanowires: An active surface-enhanced Raman substrate for cancer biomarker detection. *Journal of Physical Chemistry C*, **112**, 1729–34.

231 Zhang, X.Y., Young, M.A., Lyandres, O. and Van Duyne, R.P. (2005) Rapid detection of an anthrax biomarker by surface-enhanced Raman spectroscopy. *Journal of the American Chemical Society*, **127**, 4484–9.

232 Zhang, X.Y., Shah, N.C. and Van Duyne, R.P. (2006) Sensitive and selective chem/biosensing based on surface-enhanced Raman spectroscopy (SERS). *Vibrational Spectroscopy*, **42**, 2–8.

233 Scherr, M. and Eder, M. (2004) RNAi in functional genomics. *Current Opinion in Molecular Therapeutics*, **6**, 129–35.

234 Bartel, D.P. (2004) MicroRNAs: genomics, biogenesis, mechanism, and function. *Cell*, **116**, 281–97.

235 Zhang, B., Wang, Q. and Pan, X. (2007) MicroRNAs and their regulatory roles in animals and plants. *Journal of Cellular Physiology*, **210**, 279–89.

236 Bartel, B. (2005) MicroRNAs directing siRNA biogenesis. *Nature Structural and Molecular Biology*, **12**, 569–71.

237 Yeung, M.L., Bennasser, Y. and Jeang, K.T. (2007) miRNAs in the biology of cancers and viral infections. *Current Medicinal Chemistry*, **14**, 191–7.

238 Pfeffer, S. and Voinnet, O. (2006) Viruses, microRNAs and cancer. *Oncogene*, **25**, 6211–19.

239 Nair, V. and Zavolan, M. (2006) Virus-encoded microRNAs: novel regulators of gene expression. *Trends in Microbiology*, **14**, 169–75.

240 Calin, G.A. and Croce, C.M. (2006) Genomics of chronic lymphocytic leukemia microRNAs as new players with clinical significance. *Seminars in Oncology*, **33**, 167–73.

241 Cimmino, A., Calin, G.A., Fabbri, M., Iorio, M.V., Ferracin, M., Shimizu, M., Wojcik, S.E., Aqeilan, R.I., Zupo, S., Dono, M., Rassenti, L., Alder, H., Volinia, S., Liu, C.G., Kipps, T.J., Negrini, M. and Croce, C.M. (2005) miR-15 and miR-16 induce apoptosis by targeting BCL2. *Proceedings of the National Academy of Sciences of the United States of America*, **102**, 13944–9.

242 Michael, M.Z., SM, O.C., Pellekaan, N.G. van H., Young, G.P. and James, R.J. (2003) Reduced accumulation of specific microRNAs in colorectal neoplasia. *Molecular Cancer Research*, **1**, 882–91.

243 Calin, G.A. and Croce, C.M. (2006) MicroRNA-cancer connection: the beginning of a new tale. *Cancer Research*, **66**, 7390–4.

244 Kneipp, K. and Flemming, J. (1986) Surface enhanced Raman scattering (SERS) of nucleic Acids adsorbed on colloidal silver particles. *Journal of Molecular Structure*, **145**, 173–9.

245 Nabiev, I.R., Sokolov, K.V. and Voloshin, O.N. (1990) Surface-enhanced Raman spectroscopy of biomolecules. *Journal of Raman Spectroscopy*, **21**, 333–6.

246 Otto, C., Tweel, T.J.J.v., deMul, F.F.M. and Greve, J. (1986) Surface-enhanced Raman spectroscopy of DNA bases. *Journal of Raman Spectroscopy*, **17**, 289–98.

247 Suh, J.S. and Moskovits, M. (1986) Surface-enhanced Raman spectroscopy of amino acids and nucleotide bases adsorbed on silver. *Journal of the American Chemical Society*, **108**, 4711–18.

248 Thornton, J. and Force, R.K. (1991) Surface-enhanced Raman spectroscopy of nucleic acid compounds and their mixtures. *Applied Spectroscopy*, **45**, 1522–6.

249 Isola, N.R., Stokes, D.L. and Vo-Dinh, T. (1998) Surface enhanced Raman gene probe for HIV detection. *Analytical Chemistry*, **70**, 1352–6.

250 Vo-Dinh, T., Stokes, D.L., Griffin, G.D., Volkan, M., Kim, U.J. and Simon, M.I. (1999) Surface-enhanced Raman scattering (SERS) method and instrumentation for genomics and biomedical analysis. *Journal of Raman Spectroscopy*, **30**, 785–93.

251 Vo-Dinh, T., Allain, L.R. and Stokes, D.L. (2002) Cancer gene detection using surface-enhanced Raman scattering (SERS). *Journal of Raman Spectroscopy*, **33**, 511–16.

252 Allain, L.R. and Vo-Dinh, T. (2002) Surface-enhanced Raman scattering

detection of the breast cancer susceptibility gene BRCA1 using a silver-coated microarray platform. *Analytica Chimica Acta*, **469**, 149–54.

253 Pal, A., Isola, N.R., Alarie, J.P., Stokes, D. and Vo-Dinh, T. (2006) Synthesis and characterization of SERS gene probe for BRCA-1 (breast cancer). *Faraday Discussions*, **132**, 293.

254 Graham, D., Mallinder, B.J. and Smith, W.E. (2000) Detection and identification of labeled DNA by surface enhanced resonance Raman scattering. *Biopolymers*, **57**, 85–91.

255 Charles, Y.W., Jin, R.C. and Mirkin, C.A. (2002) Nanoparticle with Raman spectroscopic fingerprints for DNA and RNA detection. *Science in China Series B–Chemistry*, **297**, 1536.

256 Faulds, K., Smith, W.E. and Graham, D. (2005) DNA detection by surface enhanced resonance Raman scattering (SERRS). *Analyst*, **130**, 1125–31.

257 Macaskill, A., Chernonosov, A.A., Koval, V.V., Lukyanets, E.A., Fedorova, O.S., Smith, W.E., Faulds, K. and Graham, D. (2007) Quantitative surface-enhanced resonance Raman scattering of phthalocyanine-labelled oligonucleotides. *Nucleic Acids Research*, **35**, e42.

258 Culha, M., Stokes, D. and Vo-Dinh, T. (2003) Surface-enhanced Raman scattering for cancer diagnostics: detection of the BClL2 gene. *Expert Reviews of Molecular Diagnostics*, **3**, 669–75.

259 Culha, M., Stokes, D., Allain, L.R. and Vo-Dinh, T. (2003) Surface-enhanced Raman scattering substrate based on a self-assembled monolayer for use in gene diagnostics. *Analytical Chemistry*, **75**, 6196–201.

260 Green, M., Liu, F.M., Cohen, L., Kollensperger, P. and Cass, T. (2006) SERS platforms for high density DNA arrays. *Faraday Discussions*, **132**, 269–80.

261 Graham, D., Mallinder, B.J., Whitcombe, D. and Smith, W.E. (2001) Surface enhanced resonance Raman scattering (SERRS)–a first example of its use in multiplex genotyping. *Chem Phys Chem*, 746.

262 Graham, D., Mallinder, B.J., Whitcombe, D., Watson, N.D. and Smith, W.E. (2002) Simple multiplex genotyping by surface-enhanced resonance Raman scattering. *Analytical Chemistry*, **74**, 1069–74.

263 Faulds, K., Smith, W.E. and Graham, D. (2004) Evaluation of surface-enhanced resonance Raman scattering for quantitative DNA analysis. *Analytical Chemistry*, **76**, 412.

264 Jun, B.H., Kim, J.H., Park, H., Kim, J.S., Yu, K.N., Lee, S.M., Choi, H.J., Kwak, S.Y., Kim, Y.K., Jeong, D.H., Cho, M.H. and Lee, Y.S. (2007) Surface-enhanced Raman spectroscopic-encoded beads for multiplex immunoassay. *Journal of Combinatorial Chemistry*, **9**, 237.

265 Kneipp, K., Kneipp, H. and Kneipp, J. (2006) Surface-enhanced Raman scattering in local optical fields of silver and gold nanoaggregates–from single-molecule Raman spectroscopy to ultrasensitive probing in live cells. *Accounts of Chemical Research*, **39**, 443–50.

266 Tang, H.W., Yang, X.B., Kirkham, J. and Smith, D.A. (2007) Probing intrinsic and extrinsic components in single osteosarcoma cells by near-infrared surface-enhanced Raman scattering. *Analytical Chemistry*, **79**, 3646–53.

267 Kneipp, J., Kneipp, H., Wittig, B. and Kneipp, K. (2007) One- and two-photon excited optical pH probing for cells using surface-enhanced Raman and hyper-Raman nanosensors. *Nano Letters*, **7**, 2819–23.

268 Qian, X.M., Peng, X.H., Ansari, D.O., Yin-Goen, Q., Chen, G.Z., Shin, D.M., Yang, L., Young, A.N., Wang, M.D. and Nie, S.M. (2008) In vivo tumor targeting and spectroscopic detection with surface-enhanced Raman nanoparticle tags. *Nature Biotechnology*, **26**, 83–90.

269 Sha, M.Y., Xu, H., Penn, S.G. and Cromer, R. (2007) SERS nanoparticles: a new optical detection modality for cancer diagnosis. *Nanomedicine*, **2**, 725–34.

270 Xu, S.P., Ji, X.H., Xu, W.Q., Li, X.L., Wang, L.Y., Bai, Y.B., Zhao, B. and Ozaki, Y. (2004) Immunoassay using probe-labelling immunogold nanoparticles with silver staining enhancement via surface-enhanced Raman scattering. *Analyst*, **129**, 63–8.

271 Bao, P.D., Huang, T.Q., Liu, X.M. and Wu, T.Q. (2001) Surface-enhanced Raman spectroscopy of insect nuclear polyhedrosis virus. *Journal of Raman Spectroscopy*, **32**, 227–30.

272 Driskell, J.D., Shanmukh, S., Liu, Y.-J., Hennigan, S., Jones, L., Zhao, Y.-P., Dluhy, R.A., Krause, D.C. and Tripp, R.A. (2008) Infectious agent detection with SERS-active silver nanorod arrays prepared by oblique angle deposition. *IEEE Sensors*, **8**, 863–70.

273 Shanmukh, S., Jones, L., Driskell, J., Zhao, Y.-P., Dluhy, R.A. and Tripp, R.A. (2006) Rapid and sensitive detection of respiratory virus molecular signatures using surface enhanced Raman. *Nano Letters*, **6**, 2630–6.

274 Shanmukh, S., Jones, L., Zhao, Y.-P., Driskell, J.D., Tripp, R.A. and Dluhy, R.A. (2008) Identification and classification of respiratory syncytial virus (RSV) strains by surface enhanced Raman spectroscopy and multivariate statistical techniques. *Analytical and Bioanalytical Chemistry*, **390**, 1551–5.

275 Mead, P.S., Slutsker, L., Dietz, V., McCaig, L.F., Bresee, J.S., Shapiro, C., Griffin, P.M. and Tauxe, R.V. (1999) Food-related illness and death in the United States. *Emerging Infectious Diseases*, **5**, 607.

276 Chu, H.-Y., Huang, Y.-W. and Zhao, Y.-P. (2008) Silver nanorod array as a SERS substrate for foodborne pathogenic bacteria detection. *Applied Spectroscopy*, ••, ••–••.

277 Zeiri, L., Bronk, B.V., Shabtai, Y., Czege, J. and Efrima, S. (2002) Silver metal induced surface enhanced Raman of bacteria. *Colloids and Surfaces a-Physicochemical and Engineering Aspects*, **208**, 357–62.

278 Zeiri, L., Bronk, B.V., Shabtai, Y., Eichler, J. and Efrima, S. (2004) Surface-enhanced Raman spectroscopy as a tool for probing specific biochemical components in bacteria. *Applied Spectroscopy*, **58**, 33–40.

279 Alexander, T.A., Pellegrino, P.M. and Gillespie, J.B. (2003) Near-infrared surface-enhanced-Raman-scattering-mediated detection of single optically trapped bacterial spores. *Applied Spectroscopy*, **57**, 1340–5.

280 Grow, A.E., Wood, L.L., Claycomb, J.L. and Thompson, P.A. (2003) New biochip technology for label-free detection of pathogens and their toxins. *Journal of Microbiological Methods*, **53**, 221–33.

281 Kahraman, M., Yazici, M.M., Sahin, F., Bayrak, O.F. and Culha, M. (2007) Reproducible surface-enhanced Raman scattering spectra of bacteria on aggregated silver nanoparticles. *Applied Spectroscopy*, **61**, 479–85.

282 Jarvis, R.M. and Goodacre, R. (2004) Discrimination of bacteria using surface-enhanced Raman spectroscopy. *Analytical Chemistry*, **76**, 40–7.

283 Premasiri, W.R., Moir, D.T., Klempner, M.S., Krieger, N., Jones, G. and Ziegler, L.D. (2005) Characterization of the Surface Enhanced Raman Scattering (SERS) of bacteria. *Journal of Physical Chemistry B*, **109**, 312–20.

284 Harz, M., Rosch, P., Peschke, K.D., Ronneberger, O., Burkhardt, H. and Popp, J. (2005) Micro-Raman spectroscopic identification of bacterial cells of the genus *Staphylococcus* and dependence on their cultivation conditions. *Analyst*, **130**, 1543–50.

285 Jarvis, R., Clarke, S. and Goodacre, R. (2006) Rapid analysis of microbiological systems using SERS, in *Topics in Applied Physics*, Vol. **103**, Surface-Enhanced Raman Scattering: Physics and Applications, Springer, Berlin, pp. 397–408.

286 Pearman, W.F. and Fountain, A.W. (2006) Classification of chemical and biological warfare agent simulants by surface-enhanced Raman spectroscopy and multivariate statistical techniques. *Applied Spectroscopy*, **60**, 356–65.

6
Health and Environmental Impact of Silver Nanomaterials

Il Je Yu and Bruce Kelman

6.1
Introduction

The antimicrobial activity of silver nanoparticles (NPs) has resulted in their widespread use in consumer products such as bedding, washers, water purification, toothpaste, shampoo and rinse, nipples and nursing bottles, fabrics, deodorant, filters, kitchen utensils, toys and humidifiers [1, 2]. Among 580 consumer nanotechnology-based products, the most common material mentioned in the product descriptions is now silver (139), followed by carbon (including fullerenes) (44), zinc (including zinc oxide) (28), titanium (including titanium dioxide) (28), silica (27) and gold (13) [3]. The biocidal properties of silver NPs have led to the regulation of silver particles in washing machines as pesticides [4], when the manufacturer claimed, incorrectly, that their washing machines did not release silver NPs to waste water. The United States Environmental Protection Agency has taken the position that these washing machines are to be regulated as pesticides [5]. Today, the public is exposed to increasing amounts of silver NPs of anthropomorphic origin, with ever-new applications. Moreover, the toxicity of silver NPs remains a controversial area of research.

6.2
Antimicrobial Activity

Sondi and Salopek-Sondi [6] have shown that silver NPs (12 nm diameter) were an effective bactericide. Both, scanning and transmission electron microscopy (TEM) revealed that silver NPs damaged *Escherichia coli* cells by disrupting the cell wall, and subsequently accumulated in the bacterial membrane. The antimicrobial effects of silver NPs (13.5 nm) on microorganisms such as yeast, *E. coli* and *Staphylococcus aureus* were investigated by Kim *et al.* [7].

For the antimicrobial tests, these organisms were grown on Muller–Hinton agar (MHA) plates treated with different concentrations of silver NPs, from 0.2 to

Metallic Nanomaterials Vol. 1. Edited by Challa S. S. R. Kumar

ISBN: 978-3-527-32151-3

33 n*M*. The silver NPs (33 n*M*) caused an inhibition of growth similar to that caused by the positive control, itraconazole, on yeast isolated from bovine mastitis, while a significant inhibition of growth was observed at 13.2 n*M*. For these organisms the minimal inhibitory concentration (MIC) for silver NPs was estimated to be between 6.6 and 13.2 n*M*. For *E. coli* O157:H7 (a pathogen causing hemorrhagic enteritis), the MIC of silver nanoparticles was estimated at between 3.3 and 6.6 n*M*, while for *S. aureus* a mild growth-inhibitory effect was detected with high concentrations (the MIC was estimated as >33 n*M*).

An investigation was conducted to determine whether the antimicrobial effect was due to the silver NPs releasing free radicals that would in turn would cause a breakdown of the bacterial membrane function. And, indeed, by monitoring the silver-specific electron spin resonance (ESR) spectra of the NPs, this was confirmed to be the case (Figure 6.1) [7]. Whereas, partially oxidized silver NPs have antibacterial activity, zero-valent NPs do not. In fact, the antibacterial activity of silver NPs was seen to be related to the particle size, with small particles having higher activities than larger particles on the basis of equivalent silver mass content. The silver NPs also aggregated in media with a high electrolyte content, and this resulted in a loss of antibacterial activity. However, the complexing of silver NPs with albumin caused them to be stabilized such that they failed to aggregate, and this in turn led to a retention of their antibacterial activity [8].

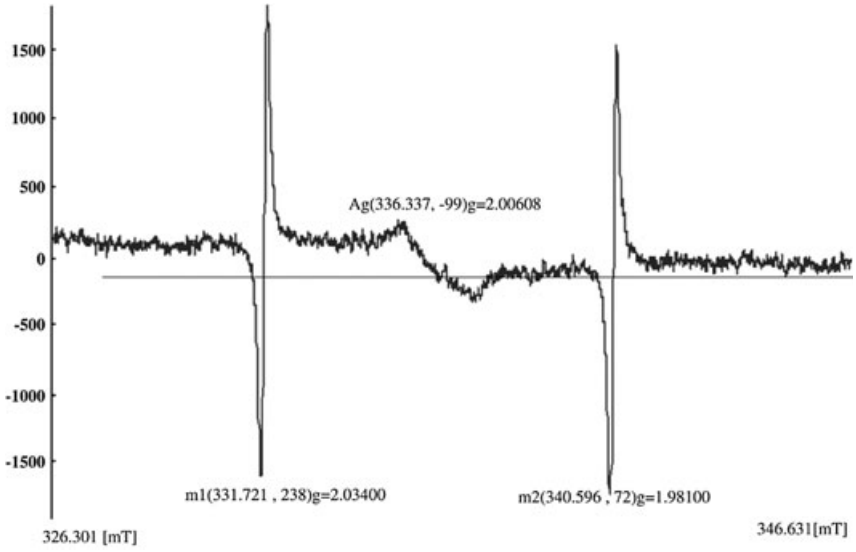

Figure 6.1 The electron spin resonance spectrum of Ag nanoparticles recorded at room temperature. m1 and m2 indicate the control peaks of Mn; the peak (mT: 336.337) indicates the released free radical from Ag nanoparticles. The spectrum was obtained at room temperature. Instrument and settings: JEOL JES-TE 200 spectrometer; microwave power, 8.0 mW; modulation (MOD); 100 kHz; time constant: 0.3 s. (Reproduced with permission from Ref. [7]; © 2007 Elsevier).

The effect of the shape of silver NPs on antibacterial activity was studied in *E. coli* [9]. For this, NPs of different shapes were synthesized via solution-phase routes and their interactions with *E. coli* then studied. As a result, truncated triangular silver NPs with a {1,1,1} lattice plane as the basal plane displayed the strongest biocidal action, compared to spherical and rod-shaped NPs and Ag^+. Based on these findings, Pal *et al.* [9] suggested that the nanoscale size and the presence of a {1,1,1} plane would combine to promote the biocidal property.

6.3 *In Vitro* Toxicity

6.3.1 Liver Cells

Silver NPs (15 and 100 nm) were evaluated for their potential toxicity *in vitro* in BRL 3A rat liver cells [10]. In order to evaluate such toxicity, the cellular morphology, mitochondrial function {MTT [3-(4,5-dimethylthiazol-2-yl)-2,5-diphenyltetrazolium bromide] assay}, membrane leakage of lactate dehydrogenase (LDH), reduced glutathione (GSH) levels, reactive oxygen species (ROS) and mitochondrial membrane potential (MMP) were assessed during a 24-h exposure period.

The leakage of LDH was shown to be significantly increased in cells exposed to silver NPs (10–50 $\mu g\,ml^{-1}$) in a concentration-dependent manner. A statistically significant difference was also seen between silver NP sizes of 100 and 15 nm, with the 100 nm particles showing greater toxicity. Significant cytotoxicity, as measured with the MTT assay, also occurred over a silver NP range from 5 to 50 $\mu g\,ml^{-1}$. Treatment with silver NPs at 2 and 50 $\mu g\,ml^{-1}$ each resulted in a 10-fold increase in the generation of ROS over control levels, and also induced a significant decrease (80%) in MMP at silver NP concentrations of 25 and 50 $\mu g\,ml^{-1}$ (using 15 and 100 nm-diameter NPs). The level of GSH (a ubiquitous, intracellular sulfhydryl-containing molecule which is responsible for maintaining cellular oxidation–reduction homeostasis) was significantly depleted following treatment with silver NPs [10].

6.3.2 Neuronal Cells

Peripheral neuronal PC12 cells were treated with silver NPs (15 nm, 5 $\mu g\,ml^{-1}$ culture media) for 24 h. After treatment, on examination at low magnification the cells appeared shrunken, with irregular cell borders; moreover, the cells showed more reductive activity following exposure to silver NPs than to other nanoparticles, such as Mn particles of 40 nm diameter. The addition of silver NPs (50 $\mu g\,ml^{-1}$) also led to a depletion of dopamine and its metabolites dihydroxyphenylacetic acid (DOPAC) and homovanilic acid (HVA). In addition, the treatment of PC12 cells

with silver NPs caused an almost threefold increase in ROS relative to basal control levels [11].

6.3.3 Germ Cells

C18-4 cells (established from type A spermatogonia isolated from 6-day-old mouse testes; [12]) were maintained in DMEM medium with 10% fetal bovine serum and treated with silver NPs (15 nm) at concentrations of 2, 10, 25, 50 and 100 $\mu g\,ml^{-1}$ for 48 h [13]. The effects of the NPs were evaluated using light microscopy, and cell proliferation and standard cytotoxicity assays. Cells treated with silver NPs at 10 $\mu g\,ml^{-1}$ showed drastic changes in morphologically and a reduced mitochondrial function, as measured by the MTS assay and cell viability, between 5 and 10 $\mu g\,ml^{-1}$ (Figure 6.2). The EC_{50} of the cells was calculated as 8.75 $\mu g\,ml^{-1}$. Silver carbonate, which is generally considered to be nonhazardous, had no significant cytotoxic effect on mitochondrial function and cell viability up to concentrations of 100 $\mu g\,ml^{-1}$ [13]. In addition, LDH leakage was observed at 5 $\mu g\,ml^{-1}$, but not at 10 $\mu g\,ml^{-1}$, which suggested that such effect was caused by an interference with cell metabolism rather than by disruption of the plasma membrane. Taken

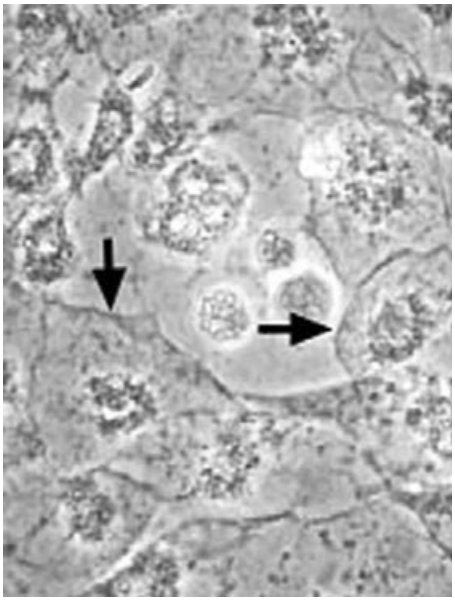

Figure 6.2 Morphology of C18-4 spermatogonial stem cells after incubation with silver nanoparticles (diameter 15 nm; concentration 10 $\mu g\,ml^{-1}$) for 48 h. The arrows indicate the intact plasma membrane. (Reproduced with permission from Ref. [13]; © 2005 Oxford University Press).

together, these findings suggested that C18-4 cells were more sensitive than BRL 3A liver cells (which are widely used in toxicity studies), at least on the basis of the MTT EC_{50} and LDH EC_{50}. For example, the MTT EC_{50} values for 15 nm silver NPs in C18-4 cells and BRL 3A cells were 8.75 and 24.0 $\mu g\,ml^{-1}$, respectively, while the LDH EC_{50} values were 2.5 and 50 $\mu g\,ml^{-1}$, respectively.

6.3.4 Peripheral Mononuclear Cells

Peripheral blood mononuclear cells (PBMCs) obtained from healthy human volunteers were used to investigate the effects of silver NPs (1.3 nm) on the production of cytokines and cell proliferation [14]. The PBMCs were first stimulated with 5 $\mu g\,ml^{-1}$ phytohemagglutin (PHA) in the presence of silver NPs (from 1 to 30 ppm). Then, after incubation with silver NPs for 72 h, assays were performed to monitor levels of interleukin-5 (IL-5), interferon-γ (INF-γ) and tumor necrosis factor-α (TNF-α). Cell proliferation was shown to be significantly decreased when the silver NP concentration exceeded 15 ppm. The PHA-induced proliferation was not inhibited by silver NP concentrations of 1 and 5 ppm, but cell proliferation was significantly inhibited by 10 ppm of silver NPs under the same conditions. At silver NP levels over 15 ppm, there was a significant decrease in the proliferation of PBMCs, and PHA-induced cytokine production was also significantly inhibited (IL-5 at 10 ppm, and INF-γ and TNF-α at 3 ppm). The reason for such inhibition of the inflammation associated with infections was suggested to be an effect on the production of Th1 cytokines [14].

6.4 *In Vivo* Toxicity

6.4.1 *In Vivo* Toxicity in Birds

The influence of hydrocolloidal silver NPs (2–7 nm) on the gastrointestinal microflora and morphology of enterocytes of 10-day-old quail was investigated by adding 5–25 $mg\,kg^{-1}$ of silver NPs to the birds' drinking water for 12 days [15]. No adverse symptoms or changes in either food or water consumption were observed, and there was no effect on body weight. The administration of silver NPs did not influence the number of *E. coli* and other enterobacteria; neither did a histological examination of the duodenum wall reveal any adverse effects.

6.4.2 *In Vivo* Genotoxicity in Rodents

The *in vivo* genotoxic effect of the silver NPs was examined using a micronucleus test [16]. For this, silver NPs (60 nm) were administered orally for 28 days at doses

of 0, 30, 300 and 1000 mg kg^{-1} per day to male and female Sprague-Dawley rats. All animals appeared normal and remained healthy until the bone marrow was harvested, at which time there was no statistically significant difference in the body weights of the test animals. Although a dose-dependent deposition of silver NPs was found in the blood, stomach, brain, liver, kidneys, lungs and testes (which indicated that the silver NPs had been distributed systemically among the rat tissues), no genotoxicity was detected.

6.4.3
Acute Toxicity in Rodents

The National Institute of Environment Research (NIER) [17] studied the acute inhalation toxicity of silver NPs in Sprague-Dawley rats. The animals were exposed to silver NPs (20 nm) for 4 h in an inhalation chamber at doses of 0, 0.9×10^6 particles cm^{-3} (76 μg m^{-3}), 1.6×10^6 particles cm^{-3} (135 μg m^{-3}) and 3.1×10^6 particles cm^{-3} (750 μg m^{-3}), and then observed over a 14-day period to monitor morbidity, behavioral changes and clinical changes. In lung function tests performed during the observation period the rats showed no adverse changes in either tidal volume or minute volume; neither were any changes seen in the body weight or other exposure-related parameters. It was concluded that the silver NPs, at concentrations up to 3.1×10^6 particles cm^{-3} (750 μg m^{-3}), did not induce any acute toxicological effects.

6.4.4
28-Day Repeated Oral Dose Studies in Rodents

Kim *et al.* [16] investigated the oral toxicity of silver NPs (60 nm) over a period of 28 days in 8-week-old Sprague-Dawley rats (mean body weight ca. 283 g for males and 192 g for females). The rats were allocated to four groups (10 rats per group): vehicle control; a low-dose group (30 mg NP kg^{-1}); a middle-dose group (300 mg NP kg^{-1}); and a high-dose group (1000 mg NP kg^{-1}). After the 28-day exposure period, the blood biochemistry and hematology were measured, in addition to a histopathological examination and tissue distribution study. Compared to controls, no significant changes were seen in body weight at any of the dose levels. However, significant dose-dependent changes were found in alkaline phosphatase and cholesterol suggesting that exposure to over 300 mg kg^{-1} of silver NPs may result in slight liver damage. Histopathological examination of the liver revealed dose-dependent increases in bile duct hyperplasia, with infiltration of inflammatory cells, including eosinophils, in the hepatic lobule and portal tract. The tissue distribution of silver NPs showed a dose-dependent accumulation of silver content in all tissues examined, including the testes, kidneys, liver, brain, lung, stomach and blood (Table 6.1). A gender-related difference in silver accumulation was noted in kidneys, with a twofold increase in females compared to males.

Table 6.1 Tissue distribution of silver (μg g^{-1} tissue, wet weight; values are mean ± SD).

Dose level	Gender	Tissue						
		Testis	Kidney	Liver	Brain	Lung	Stomach	Blood
Control	M	0.1 ± 0.1	0.02 ± 0.01	0.02 ± 0.0	0.03 ± 0.0	0.04 ± 0.0	0.2 ± 0.1	0.01 ± 0.01
	F		0.02 ± 0.00	0.01 ± 0.0	0.02 ± 0.0	0.02 ± 0.0	0.2 ± 0.1	0.00 ± 0.00
Low	M	1.2 ± 0.4*	1.3 ± 0.6*	0.5 ± 0.3	0.3 ± 0.0**	0.2 ± 0.1	10.7 ± 8.8	0.18 ± 0.0**
	F		2.8 ± 0.9**	0.5 ± 0.3	0.2 ± 0.1**	0.1 ± 0.0*	6.9 ± 3.6	0.16 ± 0.0**
Middle	M	3.6 ± 0.6**	6.0 ± 2.4*	8.7 ± 3.7*	0.8 ± 0.1**	4.3 ± 0.9**	56 ± 25*	0.43 ± 0.1**
	F		16.8 ± 2.8**	9.6 ± 3.6*	0.6 ± 0.1**	6.1 ± 2.5*	37 ± 19	0.44 ± 0.1**
High	M	7.4 ± 1.7**	24 ± 11*	71 ± 56	2.0 ± 0.3**	17 ± 4*	228 ± 79*	0.80 ± 0.2**
	F		69 ± 22**	65 ± 32*	1.8 ± 0.3**	27 ± 8**	176 ± 44**	0.70 ± 0.3**

*, $P < 0.05$; **, $P < 0.01$ versus control.
(Reproduced with permission from Ref. [16]; © 2008 Taylor & Francis).

6.4.5
28-Day Inhalation Studies in Rodents

Ji *et al.* [18] used a device that generates silver NPs by evaporation/condensation to evaluate the effect of dispersed, ambient nanosized particles on the respiratory system. The concentration and distribution of NPs (15 nm diameter) were measured directly using a differential mobility analyzer and ultrafine condensation particle counter. Eight-week-old rats (body weight ca. 283 g for males and 192 g for females) were allocated to four groups (10 rats per group): a fresh-air control; a low-dose group (1.73×10^4 NP cm^{-3}, 0.5 μg m^{-3}); a middle-dose group (1.27×10^5 NP cm^{-3}, 3.5 μg m^{-3}); and a high-dose group (1.32×10^6 NP cm^{-3}, 61 μg m^{-3}). The animals were exposed to the silver NPs for 6 h per day, five days per week, for a total of four weeks. No significant changes were seen in the body weight of males or females; neither were any significant changes noted in the hematology or blood biochemistry. It was concluded from these initial results that exposure to silver NPs at a concentration close to the current American Conference of Governmental Industrial Hygienists (ACGIH) silver dust threshold limit (100 μg m^{-3}) did not appear to have any significant adverse effects on health.

6.4.6
90-Day Inhalation Toxicity Study in Rodents

Sung *et al.* [19] recently completed a study investigating inflammatory responses and pulmonary function changes in rats during a 90-day period of inhalational

exposure to silver NPs. The rats were exposed to silver NPs (18 nm diameter) at concentrations of 0.7×10^6 NP cm^{-3} (495 $\mu g\, m^{-3}$), 1.4×10^6 NP cm^{-3} (135 $\mu g\, m^{-3}$) and 2.9×10^6 NP cm^{-3} (515 $\mu g\, m^{-3}$) for 6 h per day for 90 days, in an inhalation chamber. Lung function was measured at weekly intervals, immediately after the daily exposure, and the animals were sacrificed after the 90-day exposure period. Cellular differential counts and albumin, LDH and total protein were monitored in acellular bronchoalveolar lavage (BAL) fluid. The tidal volume and minute volume each showed statistically significant decreases during the 90 days of silver-NP exposure. Although no statistically significant differences were found in the cellular differential counts, the levels of inflammatory markers were increased in high-dose female rats. A preliminary histopathological examination indicated dose-dependent increases in lesions related to silver NP exposure, such as infiltrate mixed cell and chronic alveolar inflammation, including thickened alveolar walls and small granulomatous lesions. Decreases in the tidal volume, minute volume and other inflammatory responses after prolonged exposure to silver NPs seemed to indicate that inhalational exposure to nanosized particles may induce lung function changes, along with inflammation, at much lower mass dose concentrations when compared to submicron particles.

6.5 Environmental Exposure and Risk from Silver Nanoparticles

Following an exhaustive search of the peer-reviewed literature, we were able to find only one publication on environmental risk from silver NPs. Here, Blaser *et al.* [20] conducted an analysis of risk to freshwater ecosystems from silver released from NPs incorporated into textiles and plastics. The study only addressed silver released from textiles and plastics containing NPs rather than the particles themselves. Unfortunately, Blaser and colleagues [20] were unable to find sufficient data to characterize the risk to the environment from silver released from textiles and plastics; hence, they were unable to rule out that predicted environmental concentrations would not exceed predicted 'no-effect' concentrations. Thus, they concluded that there was no risk of adversely affecting the microbial communities in sewage treatment plants.

6.6 Conclusions

At present, insufficient data exist for the adequate evaluation of the potential effects of silver NPs on the health of environmental communities or individuals. However, a considerable body of *in vitro* data indicates there is at least a potential for adverse effects. The genotoxicity data provided by Kim *et al.* [16] suggest that silver NPs may not cause genotoxicity *in vivo*, as they caused no micronucleus formation, despite being distributed through many parts of the body, including

the bone marrow. Oral 28-day repeated dose studies in rats showed significant dose-dependent changes in liver damage markers at 300 mg of silver NPs per kg body weight, with supportive evidence provided by the presence of dose-dependent increases in bile duct hyperplasia [16]. Inhalational studies of silver NPs currently show conflicting results that are difficult to interpret. For example, whilst acute [18] and 28-day inhalational studies in rats failed to show adverse effects, a 90-day inhalation study showed significant decreases in lung function and increases in inflammatory markers in the lung, together with some supporting histopathological changes (I.J. Yu, unpublished data). It also appears that inhalational exposure to silver NPs at levels below the current threshold limit values are unlikely to cause adverse effects in factory workers.

However, it is clear that additional investigations must be conducted before the safety of silver NPs can be fully assessed.

References

1 Maynard, A.D. (2006) *Nanotechnology: A Research Strategy for Addressing Risk*, Woodrow Wilson International Center for Scholars, Washington DC.

2 KISTI (Korea Institute of Science and Technology Information) (2006) The present status of Korean nanotechnology industrialization. *Nano Weekly*, no. 210, Seoul, Korea.

3 Woodrow Wilson International Center for Scholars (2007) A nanotechnology consumer products inventory, http://www.nanotechproject.org/consumerproducts.

4 Weiss, R. (2006) EPA to Regulate Nanoproducts Sold As Germ-Killing. *Washington Post*, 23 November 2006, Washington, DC.

5 EPA (Environment Protection Agency) (2007) Pesticide registration; clarification for ion-generating equipment. *Federal Register*, **72**(183), 54039–41.

6 Sondi, I. and Salopek-Sondi, B. (2004) Silver nanoparticles as antimicrobial agent: a case study on *E. coli* as a model for Gram-negative bacteria. *Journal of Colloid and Interface Science*, **275**(1), 177–82.

7 Kim, J.S., Kuk, E., Yu, K.N., Kim, J.H., Park, S.J., Lee, H.J., Kim, S.H., Park, Y.K., Park, Y.H., Hwang, C.Y., Kim, Y. K., Lee, Y.S., Jeong, D.H. and Cho, M.H. (2007) Antimicrobial effects of silver nanoparticles. *Nanomedicine*, **3**(1), 95–101.

8 Lok, C.N., Ho, C.M., Chen, R., He, Q.Y., Yu, W.Y., Sun, H., Tam, P.K., Chiu, J.F. and Che, C.M. (2007) Silver nanoparticles: partial oxidation and antibacterial activities. *Journal of Biological Inorganic Chemistry*, **12**(4), 527–34.

9 Pal, S., Tak, Y.K. and Song, J.M. (2007) Does the antibacterial activity of silver nanoparticles depend on the shape of the nanoparticle? A study of the Gram-negative bacterium *Escherichia coli*. *Applied and Environmental Microbiology*, **73**(6), 1712–20.

10 Hussain, S.M., Hess, K.L., Gearhart, J.M., Geiss, K.T. and Schlager, J.J. (2005) In vitro toxicity of nanoparticles in BRL 3A rat liver cells. *Toxicology in vitro*, **19**(7), 975–83.

11 Hussain, S.M., Javorina, A.K., Schrand, A.M., Duhart, H.M., Ali, S.F. and Schlager, J.J. (2006) The interaction of manganese nanoparticles with PC-12 cells induces dopamine depletion. *Toxicological Sciences*, **92**(2), 456–63.

12 Hofmann, M.C., Braydich-Stolle, L., Dettin, L., Johnson, E. and Dym, M. (2005) Immortalization of mouse germ line stem cells. *Stem Cells*, **23**, 200–10.

13 Braydich-Stolle, L., Hussain, S., Schlager, J.J. and Hofmann, M.C. (2005) In vitro cytotoxicity of nanoparticles in mammalian

germline stem cells. *Toxicological Sciences*, **88**(2), 412–19.

14 Shin, S.H., Ye, M.K., Kim, H.S. and Kang, H.S. (2007) The effects of nano-silver on the proliferation and cytokine expression by peripheral blood mononuclear cells. *International Immunopharmacology*, **7**(13), 1813–18.

15 Sawosz, E., Binek, M., Grodzik, M., Zielinska, M., Sysa, P., Szmidt, M., Niemiec, T. and Chwalibog, A. (2007) Influence of hydrocolloidal silver nanoparticles on gastrointestinal microflora and morphology of enterocytes of quails. *Archives of Animal Nutrition*, **61**(6), 444–51.

16 Kim, Y.S., Kim, J.S., Cho, H.S., Rha, D.S., Kim, J.M., Park, J.D., Choi, B.S., Lim, R., Chang, H.K., Chung, Y.H., Kwon, I.H., Jeong, J., Han, B.S. and Yu, I.J. (2008) Twenty-eight-day oral toxicity, genotoxicity, and gender-related tissue distribution of silver nanoparticles in Sprague-Dawley rats. *Inhalation Toxicology*, **20**(6), 575–83.

17 N.I.E.R. (National Institute of Environment Research) (2007) Final report of acute toxicity of silver nanoparticles, N. I.E.R., Incheon, Korea.

18 Ji, J.H., Jung, J.H., Kim, S.S., Yoon, J.U., Park, J.D., Choi, B.S., Chung, Y.H., Kwon, I.H., Jeong, J., Han, B.S., Shin, J.H., Sung, J.H., Song, K.S. and Yu, I.J. (2007) Twenty-eight day inhalation toxicity study of silver nanoparticles in Sprague-Dawley rats. *Inhalation Toxicology*, **19**(10), 857–71.

19 Sung, J.H., Ji, J.H., Yun, J.U., Kim, D.S., Song, M.Y., Jeong, J., Han, B.S., Han, J.H., Chung, Y.H., Kim, J., Kim, T.S., Chang, H.K., Lee, E.J., Lee, J.H. and Yu, I.J. (2008) Lung function changes in Sprague-Dawley rats after prolonged inhalation exposure to silver nanoparticles. *Inhalation Toxicology*, **20**(6), 567–74.

20 Blaser, S., Scheringer, M., MacLeod, M. and Hungerbühler, K. (2008) Estimation of cumulative aquatic exposure and risk due to silver: contribution of nano-functionalized plastics and textiles. *The Science of the Total Environment*, **390**, 396–409.

7
Approaches to Synthesis and Characterization of Spherical and Anisotropic Gold Nanomaterials

Tai Hwan Ha

7.1
Introduction

The diverse optoelectronic properties of metallic nanomaterials are largely attributed to their controllable sizes and shapes, in addition to their inherent electronic properties. The shape-controlled manufacture of the metallic nanomaterials, therefore, will permit the development of innovative biosensors [1–4], bioimaging contrast agent [5–13] and biochip applications [14] of the next generation. Until now, metallic nanomaterials have experienced relatively limited applications in the life sciences compared to other fields such as nano-optics and nanoelectronics, fueled by surface plasmon activation and the electrical conductivity of tiny dimensions [15, 16]. Before the 'blossom of nanotechnology' was ignited by the advent of carbon nanotubes, a tracking agent for monitoring biological interactions at the microscopic level was a major application. The advantages of metallic nanomaterials are attributed mainly to the typical optical properties (strong Mie scattering in the visible range) that are prominent at dimensions of nanometer scale [17]. Among the various metallic nanomaterials, gold and silver (which also are known as 'noble' metals) have attracted much attention from research groups aiming to exploit such novel materials for the bioimaging systems and therapeutics of the 'new era'. Moreover, the properties of these materials – their chemical inertness, the tunability of their optical properties through size control, and their biologically mild side effects after either oral or intravenous intake – enable them to be used for applications considered impossible with conventional materials chemistry.

Whilst most gold and silver nanomaterials with dimensions >2 nm have metallic characteristics, much smaller gold nanomaterials lose their metallic characteristics and behave as a dielectric or semiconductor. Indeed, the discrete nature of the conduction/valence bands of gold clusters has been reported as creating a fluorescence signal [18–20]. Although gold and silver have very similar lattice parameters, bearing face-centered cubic symmetry with lattice parameters of 0.129 and 0.145 nm, respectively, gold has a better chemical inertness than silver, and therefore is favored for applications in the life sciences. As a contrast-enhancing agent in bioimaging, gold nanocrystals are generally preferred to silver with regards to

Metallic Nanomaterials Vol. 1. Edited by Challa S. S. R. Kumar

ISBN: 978-3-527-32151-3

their long-term storage and/or structural robustness, and also as selective passivating agents (containing thiol or amine functional groups) for the oriented immobilization of biomolecules.

Hitherto, the existence of a variety of gold nanomaterials with diverse shapes – including rods (or wires) [21–24], cubes [25, 26], bipyramids [24], octahedrals [25, 27, 28], tetrahedrals [28, 29], triangular (and often hexagonal) plates [30–33], icosahedrals [34] and branched multipods of irregular shapes [35, 36] – has been reported. Yet, a rational explanation covering the many observed morphologies of gold nanocrystals and their reaction conditions has not been derived. On the contrary, the rationale presented in each experiment for the evolution of a specific morphology appears to depend on – or at best be adjusted to – the individual reaction conditions, rather than present a concrete physico-chemical logic underlying the observations. In other words, the experiments with various shapes were not properly integrated into a solid hierarchy on which a *de novo* design of a reaction condition for a selective crystal growth of a particular shape might be realized. As such, although a number of valuable reviews have been presented for anisotropic gold nanostructures, each coverage has been either limited to the structural features of the nanocrystals [37] or confined to limited reaction environments [38–41].

In this chapter we will attempt to rationalize the current science for the syntheses of gold nanomaterials of various shapes, aiming to provide a solid basis for a 'design on demand' growth scheme for gold nanocrystals of desired morphology. To accomplish this rather major challenge, the current state of the art of crystal formation will be summarized. First, the optical properties of gold nanocrystals will be summarized, after which the basic empirical constituents for the growth of gold nanocrystals, extracted from a variety of growth schemes, will be categorized to provide a systematic approach towards the growth protocols. These protocols – most of which are centered on thermal reductions and seed-mediated schemes – will be revisited and classified on the basis of the reducing agents. The observed morphologies in various protocols will be examined according to the presence of twinning planes, which in turn should provide a multilateral insight for the growth mechanisms. The influences of passivating agents and surface-active chemicals on crystal growth will also be reviewed and, accordingly, a plausible picture of crystal growth presented. Finally, the two major biological applications of gold nanomaterials, namely contrast-enhancing agents and photothermal therapeutics, as well as cytotoxic aspects, will be introduced. Despite the obvious similarities between gold and silver with regards to their chemical and electronic properties, the discussions here will be limited to gold nanomaterials.

7.2
Optical Properties of Gold Nanocrystals

The characteristic optical property of a noble metal originates from collective excitation of conduction electrons confined in a nanometer scale; these are termed

localized surface plasmons. The observed optical extinction spectra are consistent with theoretical values based on Mie theory and solving the Maxwell equation with a spherical assumption [42–44]. For more complex shapes, a few approximations including discrete dipole approximation (DDA) [45, 46], the boundary element method [47], and the finite difference time domain (FDTD) [48, 49] may be successfully applied to describe the experimentally observed extinction spectra. The peak wavelength in an extinction spectrum of a form of gold nanocrystal can be easily tuned by judicious control over its size and shape. A peak Rayleigh scattering of gold nanocrystals is blue for the 50 nm or smaller nanocrystals, but red for the 100 nm nanocrystals; in contrast, apparent colors seen in the far field shift from red to blue as the nanocrystals grow; this is because the complementary color of the scattered wavelength survives to be seen [17]. For anisotropic nanomaterials, more than one plasmon excitation bands (longitudinal or transverse waves) may be simultaneously observable according to the symmetric axes of excitation [46, 50, 51]; quadrupole excitations may often be recorded in the synthesis of triangular nanoplates [30]. The typical plasmon bands associated with characteristic dimensions are summarized in Figure 7.1, and also match well with the theoretical values calculated from the above-mentioned numerical methods. For spherical gold nanoparticles, the major dipole excitation peaks at about 510 nm, while the excitation band at 400 nm is prominent in spherical silver nanoparticles; therefore, silver nanocrystals of small size are necessary in order to develop truly multicolored tag systems that cover the entire color sets in the visible range. As a spherical gold particle grows over 20 nm, light scattering begins to contribute to the extinction coefficient, predominantly over the absorption process [46].

The apparently absorbed light exists as a build-up of electric fields near the surface of nanocrystals, and is eventually dissipated as heat. It has been reported that the intensity of the electric field confined to a metal surface is greater than that of incident light by two to six orders of magnitude, and could be verified with the theoretical frames mentioned above [52]. The enhanced near field is

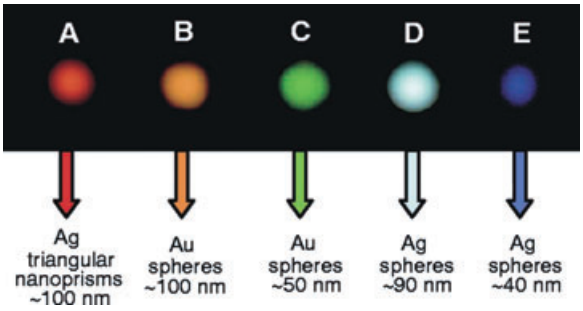

Figure 7.1 Rayleigh light-scattering of nanoparticles deposited on a microscope glass slide. The slide is used as a planar waveguide, which is illuminated with a tungsten source. (Adapted from Ref. [17].)

crucial to understand surface-enhanced Raman scattering (SERS) [53] and surface-enhanced fluorescence [54]. As Raman scattering has an additional enhancement mechanism – that is, a chemical enhancement closely related to the molecular electronic structure – SERS spectra require the chromophore to be tightly bound on the surface. It has also been reported that a single molecule in between apexes of these noble metal sometimes experiences an enhancement factor of ~10^{12}, which enables detection of the SERS signal of a single molecule directly [55–57]. It is generally accepted that, although silver is a better field enhancer than gold, gold seems better with respect to long-term stability. On the other hand, fluorophores which float on the surface by about 10 nm demonstrate a 100-fold brighter luminescence, whereas the same dye would quench in the vicinity (closer than 5 nm) of the metal surface. The enhanced local field can be also harnessed to amplify the weak signal from a second harmonic generation [19, 45].

7.3 Chemical Constituents for the Growth of Gold Nanocrystal

In a routine synthesis of gold nanocrystals, the gold precursors are chemically reduced from the reaction medium, if necessary in the presence of passivating organic compounds; a typical set-up for the seed-mediated growth of gold nanocrystals is shown in Figure 7.2. Here, the crucial experimental components – extracted from a wealth of articles on the growth of nanocrystals hitherto investigated – can be categorized into gold precursors, reducing agents, the reaction medium and capping agents, the roles of which can be performed in overlapping fashion by one of the other reagents [38, 39, 52].

7.3.1 Gold Precursors

The key element of crystal growth appears to be gold precursors, the most prevalent precursor being the tetrachloroaurate ion, $AuCl_4^-$. This has a square-planar structure, and the ion is very stable at room temperature in various solvent systems, including boiling aqueous solutions. In electrochemical crystal growth, the bulk gold plate would be a source of gold ions, which subsequently recrystallize at the platinum cathode into nanocrystals of various shapes [23, 26]. Whichever condition is applied for the reduction, a nucleus formation and subsequent surface reactions on the as-formed nucleation center are generally assumed. However, the corresponding mechanistic or molecular picture seems to depend on an individual reaction that is largely unknown but is assumed to depend on the reducing agent and the gold precursor used. It has been reported that the bromide ion is a more efficient bridging ligand than the chloride ion for electron transfer from nucleophiles, as well as sulfite ions [59].

When a nucleation has a substantially higher free energy barrier than the corresponding surface reaction, then larger nanocrystals will be obtained; in contrast,

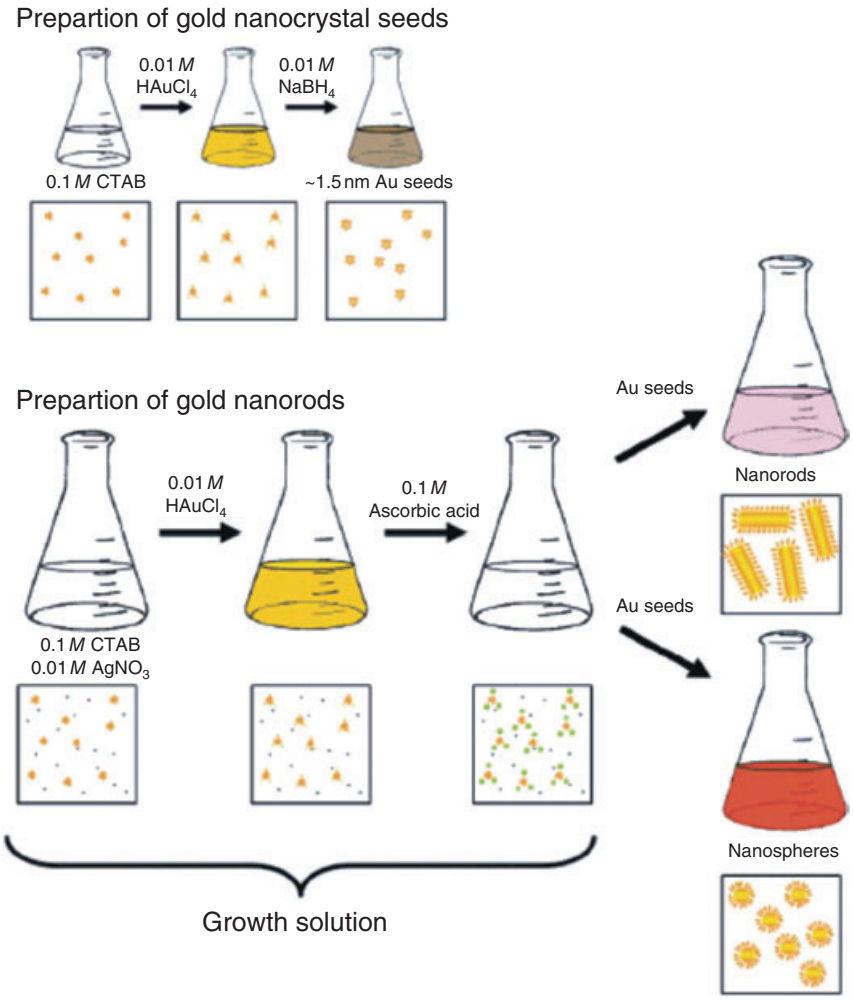

Figure 7.2 Schematic illustration of a typical seed-mediated growth of gold nanorod. The black dots represent Ag^+ ion, the orange zigzags are CTAB in the form of micelle, and the yellow circles and green squares are $AuCl_4^-$, and $AuCl_2^-$, respectively, complexed with CTAB micelles. The gold nanocrystals seeds are injected into the growth solution in the final step of the nanorod synthesis. (Adapted from Ref. [58].)

smaller nanocrystals will be dominated with a lower barrier. For instance, crystal growth using $NaBH_4$ in aqueous solution produced mostly isotropic nanocrystals of 1~2 nm size distribution [24], whereas on average 50 nm or larger particles were formed in a reaction where ethylene glycol was employed as the reducing agent [25, 28]. In the latter case, it is possible that the formation of a nucleation center is a much rarer event than the counterpart, the growth of an as-formed nucleus [39]. It is also possible that, although the nuclei form easily, most of them are not

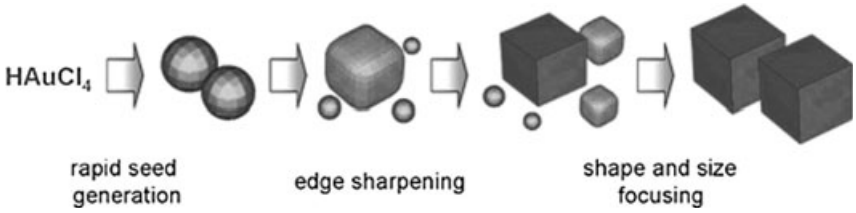

Figure 7.3 Proposed scheme of gold nanocubes through Ostwald ripening in the modified polyol process. (Adapted from Ref. [25].)

stable enough to survive in the medium. In fact, it is assumed that once a reduced gold adatom is able to redissolve in the solution phase, the initially formed gold nanocrystals can evolve further into various morphologies that are thermodynamically more favorable upon longer incubation; this process is often referred to as 'Ostwald ripening' (Figure 7.3) [25, 60]. Nevertheless, at the molecular level the exact reaction routes between two reductions – solution-phase reduction and surface reduction – remain a matter of conjecture, at best. Furthermore, the two mechanisms may – or may not – be different, depending upon which reducing agent and reaction medium are used, and whether other cofactors such as shape-directing organic compounds exist, or not.

7.3.2 Influences of Reducing Agents

Chemical reducing agent can be either single, or a combination of sodium borohydride [24], citrate ion [61], alcohols including ethylene glycol [28], pentanediol [25] and sugars [62, 63], and amine groups [32, 33, 64–66]; dimethylformamide (DMF) [67–70] can reduce tetrachloroaurate ions by acting simultaneously as both a reductant and a solvent. In the electrochemical synthesis of gold nanorods (as shown in Figure 7.4) [23, 26], the electrons for the reduction are provided directly from electrodes, and the protocol demonstrated a relatively high yield and a good monodispersity in the presence of silver ions. In addition, a high flux of photons could represent another exotic route for the reduction of gold precursors through a disproportionate cleavage process, thus providing a versatile arm for the control of shape and size evolution [17, 21, 71, 72]. Moreover, these reaction conditions can be further complicated by cooperatively applying such methods, yielding a number of useful ramifications for the tune of the crystal shapes and sizes [73]. Among those protocols, ascorbic acid reduces Au(III) in solution only to its single oxidation state, Au(I), but not to a neutral atom (or to the eventual formation of nanoparticles) [22, 30, 34, 36, 38, 58, 74–78]. Further reduction can only occur on the surface of appropriate seed crystals, which can be prepared heterogeneously; the same partial reduction was recently observed in the mild heating of a DMF solution containing $HAuCl_4$ [67, 70]. As the reaction coordinate at a molecular level

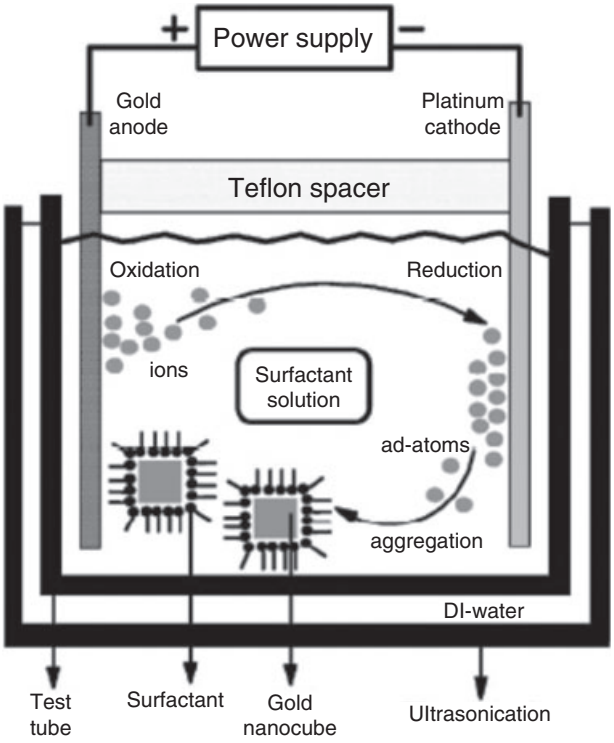

Figure 7.4 Schematic diagram of the electrochemical apparatus for the synthesis of gold nanocubes. (Adapted from Ref. [26].)

appears to be determined by the choice of the 'pair' of gold precursor and reducing agent, and by the dependence on other parameters such as solvent, temperature and other chemicals present in the reaction container, the choice of a major reducing agent appears to be a critical stage in the synthesis of nanocrystals with desired morphology. Indeed, such a choice becomes extremely important for anisotropic growth, since preferential growth on a facet to others would be accomplished by inherent differences in the growth rates of the chosen reductant.

7.3.3
Influences of the Reaction Medium

The reaction medium represents another important factor for anisotropic nanocrystal growth, as the viscosity and boiling temperature can influence chemical reduction at a specific crystal facet, leading to different growth rates for different facets [25, 28, 29, 39]. In fact, hexagonal nanoplates that were produced almost quantitatively in an aqueous solution totally disappeared in THF solution. Rather, faceted isotropic particles were dominant under the same reductant,

polyethylenimine (PEI) [32]. As mentioned above, small compounds containing amine and alcohol groups can act, at higher temperature, both as a solvent and as a reducing agent. These molecules can reduce gold precursors as the temperature of reaction vessel is elevated, such that nucleation occurs quite homogeneously all over the vessel, thus enhancing the resultant monodispersity of the nanocrystals. This contrasts with a mechanical mixing of the reductant and gold precursors, which is diffusively controlled and thus inherently inhomogeneous to some degree. Whilst such homogeneity appears advantageous for mass production, it is also valuable for applications targeted at the life sciences; in the latter case, reproducibility is an important issue when evaluating the adverse side effects or potential toxicity of the materials, especially when they are administered to humans [79–82]. As will be discussed later, in a polyol synthesis the boiling point of the solvent drastically affects the crystal shapes; changing the solvent from ethylene glycol to pentanediol increases the boiling temperature at which the polyol reduction occurs [25, 29].

7.3.4 Roles of Passivation Components

Passivating chemicals that encapsulate as-formed nanocrystals physically regulate the access of reactants during growth, and ultimately prevent as-grown nanocrystals from aggregating until the growth stages are completed. For example, ligands bearing thiol groups can contribute to enhance the monodispersity and size distribution by chemically stabilizing the as-synthesized nanocrystals. In addition, the capping agents – which may be a polymer or a small molecule bearing surface-active functional group(s) – may alter the resultant crystal shapes, as shown in Figure 7.5. It has been shown that the shapes of gold nanocrystals can be changed simply by modulating the content of poly(vinylpyrrolidone) (PVP), which may in turn control the growth and/or etching rates at the surface (Figure 7.5). The other important role of the passivating layer is to provide nanocrystals with specialized functionalities after the synthesis, such as inertness to the nonspecific adsorption of biomolecules [9], stress responsiveness as an intelligent carrier [4, 83], and/or a homing agent for targeting specific tissues [8, 12, 13]. These two roles can be combined into one process by soaking a sophisticatedly designed ligand with a gold precursor during the crystal growth [84–86]. Alternatively, the scheme can be separated into multiple processes, perhaps first passivating with simple thiols and then changing the ligand to a more functional version by using a process of ligand exchange [87, 88]. Changing the working medium can also be facilitated through ligand exchange; thus, monodisperse gold nanocrystals capped with hydrophobic aliphatic thiols can be transferred to the aqueous phase by soaking with an excessive amount of an alternative ligand bearing hydrophilic end groups such as poly(ethylene glycol) (PEG) [89]. For the anisotropic synthesis, cetyltrimethylammonium bromide (CTAB), PVP, PEI, citrate ion and small amine molecules have been used as passivating agents. Thiol compounds have proved unpopular in this situation, presumably due to their strong binding affinity to the gold surface.

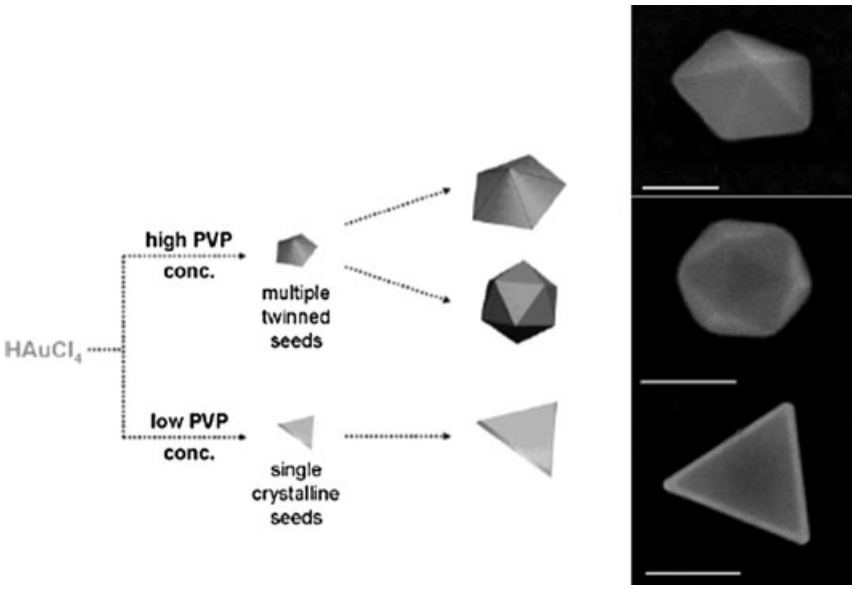

Figure 7.5 Reaction mechanism of gold polyhedrals in the modified polyol synthesis, and SEM images of as-formed gold nanocrystals showing the dependence on the content of passivating agent, polyvinylpyrrolidone (PVP). (Adapted from Ref. [29].)

7.3.5
Hard Templates for the Fabrication of Anisotropic Nanomaterials

Nanostructures fabricated on a solid substrate can be adopted as an exotic source of gold nanomaterials. In this scheme, the nanostructures act as a 'hard template' for the syntheses of gold structures, whereupon gold is deposited physico-chemically onto the template. After fabrication, the gold structures can be liberated into solution phase by dissolving the template. These hard templates include nanoporous structures obtained by anodizing aluminum oxide (AAO) [90], bead lithography [91], silver crystal for transmetallation [92] and the self-assembly of block copolymers [93–95]. In a simple application, the vacancy on a hard template can be structured with gold that is then liberated by a subsequent lift-off process; alternatively, it may be further decorated by the next stage of process. Although, at first glance, these protocols appear to be handy processes for the syntheses of anisotropic gold nanomaterials, the fabrication and manipulation of the templates is a 'hidden cost' for synthesis of nanocrystals of various shapes, with a number of size variances. As yet, this protocol has been helpful only for the formation of nanorods with limited dimensions; the many drawbacks involved mean that it should be considered only for very specialized purposes, such as in life sciences applications.

7.4
Representative Reactions Categorized by Reducing Agents

7.4.1
Fast Reduction by Sodium Borohydride

Sodium borohydride ($NaBH_4$) has long been the most popular reducing agent for the synthesis of isotropic nanoparticles [84–86, 88, 96], mainly because its reducing power is so huge that the inherent nucleation process seems simple compared to the use of any other reducing agent. The harsh conditions appear to show no preference for any specific shape of gold crystal. In general, the crystal size is determined as 1~2 nm, but this sometimes is overestimated during transmission electron microscopy (TEM) analysis due to coagulation of the nanoparticles on the copper grid under electron bombardment [24]. Citrate ions in hot aqueous solution also reduce chloroaurate ions quickly into isotropic nanocrystals, of size 10~20 nm [61]. Apparently, isotropic gold nanocrystals with diameters of several tens of nanometers can be further classified into decahedrons, icosahedrals or more highly twinned particles under a more stringent investigation. For the isotropic nanocrystals, the control of size and monodispersity has been a dominant issue in terms of practical applications [85, 96, 97]. Monolayer-protected nanoparticles, which employ phase-transfer agents or other stabilizing organic chemicals, are especially stable. Their sizes range from 1.0 to 3.5 nm, and their monodispersity can be improved by partial crystallization, extraction and annealing, as well as chromatography. Under other reaction conditions the crystal surface can be modified with dendrimers [85], block copolymers [83, 98], aliphatic thiols [84], aliphatic amines [97] and micellar compounds [99, 100].

In the meantime, as these small nanocrystals may serve as a seed for the production of much larger nanocrystals (often with anisotropic shapes), their crystallinity has become another issue not only for applications in the life sciences but also in terms of their growth mechanisms. Whilst small nanocrystals which were reduced by $NaBH_4$ and capped with CTAB demonstrated single crystalline features, those nanocrystals in the presence of citrate ion included a substantial content of multiple twinning planes (Figure 7.6) [24]. This multiple twinning was reported to reduce surface energy by exposing most stable facets and {111} planes, such that twinned morphologies were favorable in small nanocrystals [29, 101]. It seems that single crystalline seeds can be converted to their twinned counterparts on further growth; however, the reverse process, where twinned particles convert into single crystalline ones, have not yet been observed; however, this conversion does appear to occur at a higher temperature [101, 102]. It has been reported that selective etching on these twinning planes appeared to accelerate the disappearance of twinned particles, while other single crystalline nanocrystals survived the same condition [29, 60]. After this annealing process, the twinned particles apparently 'convert' into less twinned particles, although the conversion of an individual crystal seems barely observable at that temperature.

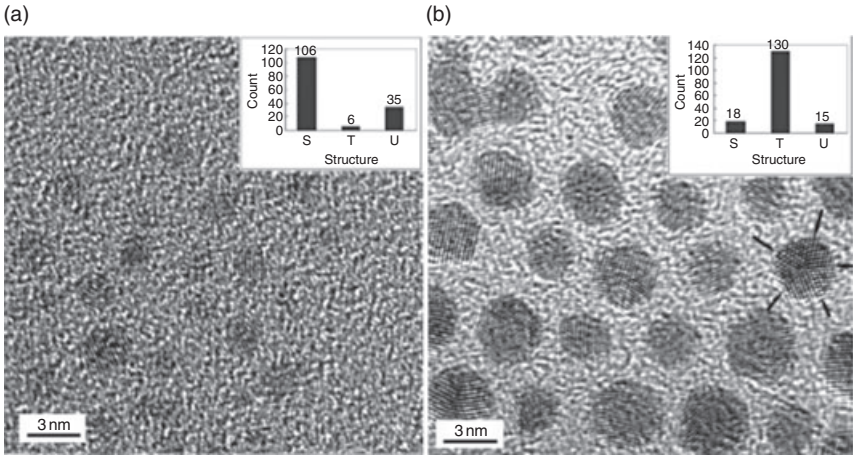

Figure 7.6 (a) High-Resolution TEM images of CTAB-capped gold seeds; (b) High-resolution TEM image of citrate-capped gold seeds. One of the seeds shows a very clear penta-fold twinning. The twinning planes are indicated by the arrows. The histograms are plotted by counting about 150 nanoparticles from different areas on the TEM grid for each sample. S, T and U represent for single crystalline, twinned and unidentified nanoparticles, respectively. (Adapted from Ref. [24].)

7.4.2 Polyol Synthesis in the Presence of PVP

In the polyol process for the synthesis of gold nanocrystals, small molecules containing several alcohol groups play a dual and simultaneous role, both as an active reductant and as a reaction medium. This protocol was first devised by Xia's group and extensively investigated for the formation of silver nanocrystals [40, 41, 60]. Studies on gold nanocrystals have been relatively rare, however [25, 28, 103]. Nevertheless, it is generally accepted that the theoretical frame for the growth of gold nanocrystals is quite similar to that of silver, based on the physico-chemical similarities between both crystals.

7.4.2.1 Influences of Reaction Medium

In a typical synthetic scheme where ethylene glycol (b.p. 195 °C) was employed as a reaction medium, icosahedrals, truncated tetrahedral and cubes were the major products; a miniscule amount of silver ion was added for the synthesis of cubes (Figure 7.7) [28]. In this reaction scheme, PVP was also added as a passivating agent – partly in order to prevent the as-synthesized nanocrystals from precipitating into agglomerates, and partly as a coparticipating reducing agent along with the polyols [104]. Unfortunately, PVP appears to be more of a passivating agent than a reducing agent since, as the content of PVP increased, smaller nanocrystals were obtained in the synthesis of octahedrons and cubes [25]; here, the major

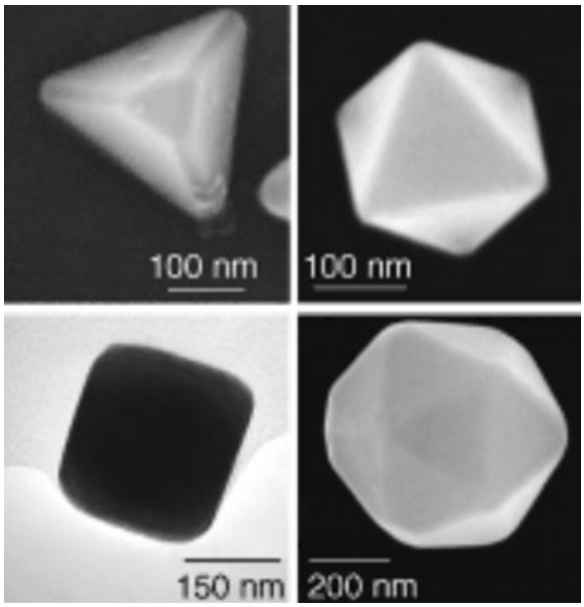

Figure 7.7 SEM and TEM images of platonic gold nanocrystals grown in the modified polyol synthesis. For cubes and octahedrons, a small amount of silver nitrate was added. Ethylene glycol was employed both as reaction medium and as a reducing agent. (Adapted from Ref. [28].)

reductant appeared to be ethylene glycol, while PVP prevented coagulation between the as-grown crystals. Although PVP was known to be a surface-regulating agent, promoting the directional growth of planes other than {100} planes yielding {100}-bound silver nanocubes [60], the polymer appears not to function (as it did with silver) in the reduction of the gold precursor; rather, the main role seems to be more one of passivation [25].

Cubes and tetrahedrons are single-crystalline polygons, whereas icosahedrons bear 20 twinning planes and belong to the group of multiply twinned particles (MTPs) [37]; in the case of cubes, a small amount of silver ion was added to the ethylene glycol solution. In similar reaction conditions, but using pentanediol (b.p. 242 °C) together with silver ions, an almost quantitative formation of cubes and octahedrons resulted [25], without twinned particles (Figure 7.8). The 'frustrated formation' of twinned particles was attributed to a vulnerability of the twinned nucleus at the higher reaction temperature (b.p. of pentanediol ~242 °C) compared to reduction under $NaBH_4$ (at room temperature) or to the polyol process in ethylene glycol (b.p. ~195) [25]. Presumably, as-formed MTP seeds in the polyol process are more liable to a possible etching process (e.g. Cl/O_2) than are single-crystalline seed particles [29].

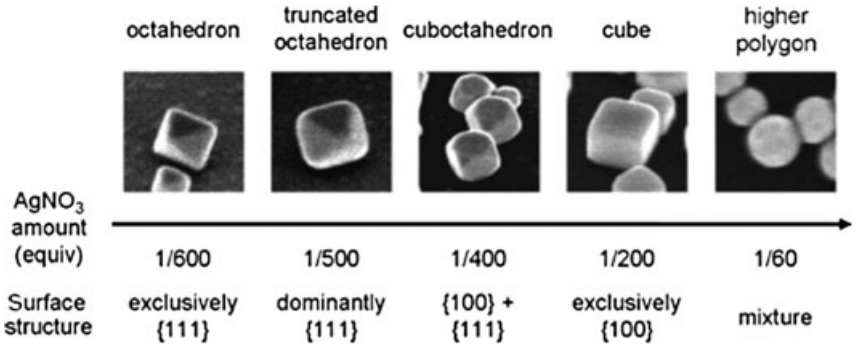

Figure 7.8 Evolution of polyhedral structures of gold nanocrystals with respect to the $AgNO_3$ amount added in the reaction mixture in which pentanediol was employed as a major reaction medium. (Adapted from Ref. [25].)

In contrast, the twinned nuclei formed at room temperature (as often observed in seed-mediated growth) seem to be kinetically trapped in a local 'energy well', due to there being a high energy barrier for the dissolution (or Ostwald ripening) that is often observed with polyol synthesis. Although, the formation of twinning planes affected the accumulation of fault energy, the simultaneous build-up of most stable {111} planes might compensate for the strains to some degree [37]. Taken together, it has been calculated that MTPs bounded with {111} planes are the most stable species in the world of small gold particles.

7.4.2.2 **Influences of Silver Ions and PVP**

Besides using a solvent with a higher boiling point, silver ions also seem to be the major shape-directing additive to avoid twinned crystals. The growth rate was substantially retarded as silver ion was added, thus hindering the formation of twinned crystals that might be kinetically favored in nucleus growth [24]. On the other hand, a high content of PVP in the absence of silver ions appears only to reduce the size of the decahedrons formed in diethylene glycol (DEG) (b.p. ~250 °C). Overall, PVP appears to be more conspicuous in terms of its size control and protection of MTPs, at least in the gold reduction, whereas silver ions exert a major and surface-directing control over the development of specific crystal habits [29]. Under similar reaction conditions employing PVP, but in the presence of citrate ion and in aqueous solution, triangular or hexagonal nanoplates were the major products bearing single or dual twinning planes, respectively [31]. When considering crystallinity in the polyol syntheses, either without (tetrahedrons, decahedrons, triangular nanoplates) [28, 29] or with silver ions (octahedrons, cubes, and their derivatives) [25, 103], additives such as silver ions, distinct solvents (water versus diol), and/or distinct reducing agents (citrate ion versus diol) appear to be more dominant reaction parameters compared to the common factor of PVP.

Intriguingly it is also noticeable that, in the polyol process, gold nanorod (either penta-twinned or single crystalline) has been seen not as a major but rather only a minor product, whereas silver nanowire has been identified as a major product in a similar polyol process under relatively diverse reaction conditions [60]. Closely related penta-twinned decahedrons were observed in the growth of gold crystals, however [29]. These observations reflect another subtle difference in the growth mechanisms and chemical properties of these two noble metals.

Furthermore, silver ion is able not only to control the overall shape but also to provide an exotic route for the precise modulation of each crystal habits in the polyol process. As the silver ion content increases monotonically in the modified polyol synthesis employing pentanediol, the shape evolves from cube to octahedral, through an intermediate cubo-octahedral [25]. As the content of silver ion was increased from 1/600 equivalent with respect to the gold precursors to 1/60, the crystal shape evolved almost quantitatively from a {111}-bound octahedron to a {100}-bound cube, and eventually to a higher polygon. In this experimental scheme, it was proposed that silver ion was reduced on the surface of the growing nanocrystals and differentiated the growth rate on different facets. Apparently, as shown by X-ray photoelectron spectroscopy (XPS) analyses, the silver residing on {100} planes seems to hinder surface growth more selectively compared to other facets, such as {111} planes; thus, at higher concentrations of silver ions {100}-bound cubes were the major product. This hypothesis was partly supported by the underpotential deposition (UPD) experiment using silver ions on the gold surface [24, 105]. Here, silver is grown preferentially on {100} plane, but not on {111} planes at mild deposition rates. It is then assumed that the underpotentially deposited silver species, combined with the presence of chloride ions, appear to exert a cooperative control on crystal growth; this is in contrast to the initial assumption that PVP plays a major role in the shape development of silver during the polyol process [25]. Silver ions appear not only to be responsible for the drastic shape deviations, but also to be advantageous for fine-tuning of the crystal shape, again emphasizing the unique position of silver ions in the polyol process of gold crystals.

7.4.3 Other Thermal Reductions of Gold Precursors

7.4.3.1 Citrate Reduction in the Presence of PVP

As mentioned briefly in Section 7.3.2, a spin-off application of the diol reduction has been the citrate or DMF reductions in the presence of PVP at an elevated temperature [31, 68, 70]. When citrate ion in aqueous solution is used in the reduction of gold precursors, a mass production of triangular nanoplates was realized. It was also shown that the nanoplate could be further fabricated, by using fast ion bombardment (FIB), into a future component of a possible nanomachine, such as a nanometer-sized gear element [31]. As more PVP was added the width and thickness of the nanoplates increased monotonically; this contrasted with the polyol process, where smaller crystals were formed as the molar ratio of PVP increased

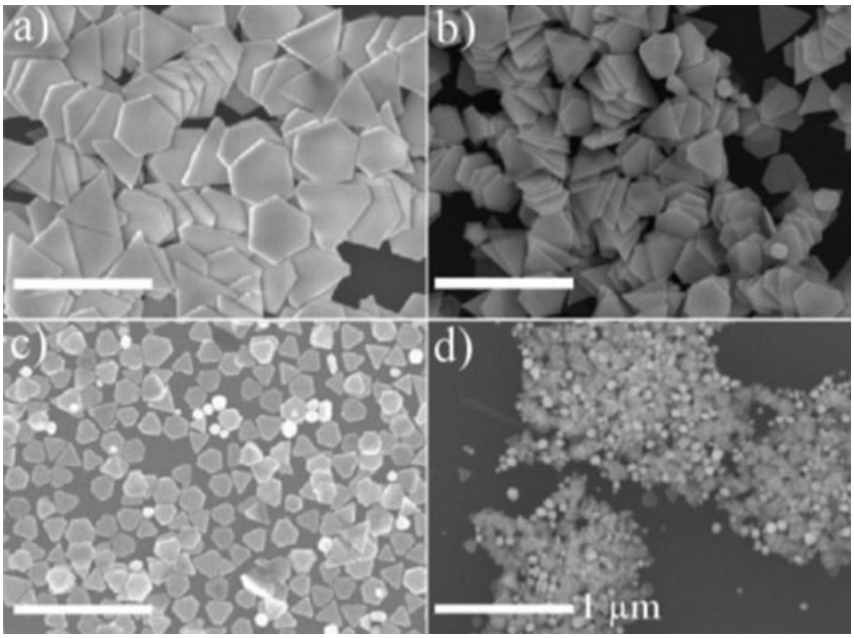

Figure 7.9 (a–d) Field effect SEM images of gold nanoplates obtained under the thermal reduction employing citrate ions and PVP in aqueous solution. Average width and thickness of the acquired nanoplates was (a) 450 nm and 39 nm; (b) 310 nm and 28 nm; (c) 158 nm and 18 nm; and (d) 96 nm and 14 nm with the molar ratio of the repeating unit of PVP (MW ~ 55 000, n ~500) to $HAuCl_4$ (a) 8 : 1; (b) 5 : 1; (c) 2 : 1; and (d) 0.1 : 1; respectively. (Adapted from Ref. [31].)

(see Figure 7.9). The larger nanoplates were attributed to a lesser nuclei formation in the higher content of PVP and, in similar vein, the larger dimension on the decrease in citrate ions was attributed to the more rare or retarded nucleus formation. On the other hand, the opposing result in the polyol process was also attributed to a greater protection from further crystal growth. These apparent contradictions might be attributed to the different growth conditions (boiling water versus boiling ethylene glycol) for the nucleus formation, or to hidden variables which until now had not been identified.

7.4.3.2 DMF Reduction in the Presence of PVP

In another branch of thermal reduction, DMF can be used both as a reductant and as a solvent, while PVP acts as a major passivating agent. In the silver crystal growth employing refluxing DMF as reaction medium, a variety of shapes such as spheres, nanoplates and wires was successfully produced; however, a similar thermal reduction of gold precursors resulted not only in only lower yields of defined morphologies but also in a higher polydispersity [70]. It was reported that an additional power source, namely ultrasonication, was crucial for the successful fabrication of gold nanocrystals and, aided by this power source, decahedrons were

seen to be a major product, with their sizes being controlled by controlling the seed content. In another separate modification, similar conditions facilitated the production of nanocubes and octahedrons by the addition of NaOH or NaCl, in conjunction with temperature control (Figure 7.10) [68]. Likewise, by adding a small amount of salts, the morphology of major product changed dramatically from penta-twinned decahedrons to {100}-bound cubes, indicating that the corresponding adsorbate (OH^- or Cl^-) had stabilized the {100} planes. This observation might represent another example emphasizing the importance of specific adsorption in shape-controlled synthesis. Furthermore, a slight increase in the reaction temperature, from 140 °C to 147 °C (in the presence of OH^-), drastically changed the major product from {100}-bound cubes to {111}-bound octahedrons (see Figure 7.11d). A fivefold increase in the concentration of gold precursors, again with OH^- ions, resulted in the formation of hexagonal plates bound with {111} planes. In this reaction scheme it was notable that the morphology of the resultant crystals responded sensitively to variations in the reaction parameters, and that single crystalline or less-twinned nanoparticles were obtained by the addition of OH^- or Cl^- ions, albeit without the aid of silver ions.

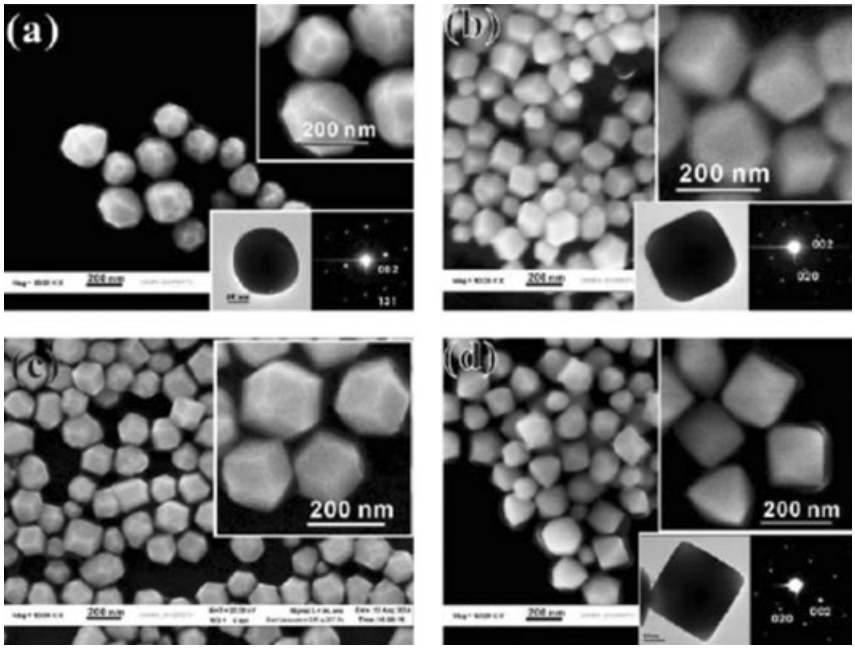

Figure 7.10 SEM images of the as-prepared truncated tetrahedral (a); cube (b); cubic (c); octahedral; and (d) gold nanoparticles in refluxing DMF solution aided by addition of salts. The insets in the figures show the enlarged SEM image (top-right), the TEM image of an individual typical nanoparticle (left) and its corresponding selected area electron diffraction (SAED) pattern (right). (Adapted from Ref. [68].)

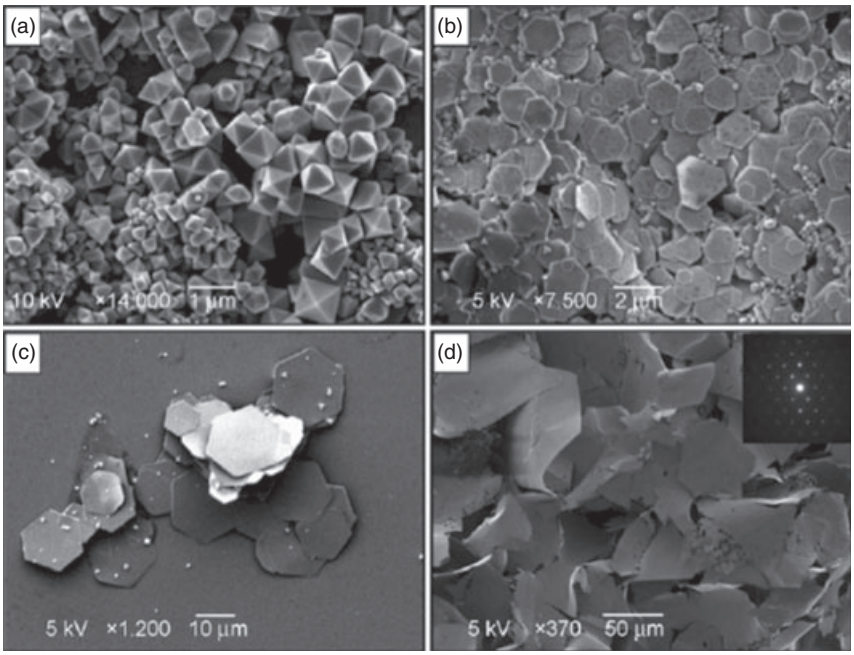

Figure 7.11 SEM images of gold crystals synthesized via mildly refluxing toluene solution (81 °C) containing combinations of amine molecules: (a) TDAC/DA-coated octahedral (1 : 1 molar ratio); (b) TDAC/DA-coated gold plates (1.2 : 1 molar ratio); (c) DDAB/DA-coated plates (4 : 1 molar ratio); (d) DDAB/dibutylamine-coated thin plates (1 : 1 molar ratio). Inset: representative electron diffraction pattern of the thin plates. (Adapted from Ref. [64].)

7.4.3.3 **Amine Reduction**

Instead of DMF or citrate ions, amine compounds may also be employed as a reductant and, at the same time, as a capping agent in mildly refluxing (~81 °C) toluene solution [64]. This growth environment enables the formation of MTPs and some platonic single crystals. In this reaction, MTPs such as decahedrons and icosahedrons, penta-twinned nanowire, hexagonal nanoplates, and single crystalline particles such as octahedrons may be formed. In this protocol, the morphology of gold nanocrystals was controlled by modulation of the molar ratio of quaternary ammonium ions to primary amines. As the molar ratio (γ) of quaternary amine to primary amine (didodecyldimethylammonium bromide, DDAB, versus dodecylamine, DA) increased, the morphology evolved from decahedrons with some octahedrons to hexagonal nanoplates. When tridodecylmethylammonium chloride (TDAC) was used instead of DDAB, though without changing other parameters, octahedrons were produced in almost quantitative yield. However, the morphology was changed dramatically, to a mixture of various shapes when the counterion was

exchanged into bromide ions; this appeared to be another example of the halide effect. In addition, as shown in Figure 7.11, the dimension of the hexagonal plates could be controlled by varying either the composition of the amines (via the primary : quaternary molar ratio) or the identities of the primary amine and counteranion. On the other hand, the combination of a tertiary amine, trioctylamine (TOA), with DDAB (1 : 1 molar ratio) yielded uniform penta-twinned nanowires of micrometer length. Overall, this amine reduction scheme is unique because almost whole morphologies of possible gold crystals were seen simply by varying the amine contents, without any addition of surface-active species such as halide and silver ions.

It was also noteworthy that, as the content of quaternary ammonium ions increased, the formation of hexagonal nanoplates was facilitated. This inclination bore some similarity to the formation of nanoplates performed in aqueous solution, where linear PEI was employed simultaneously as both a passivating agent and a reducing agent [32]. The PEI was partially modified with a long alkyl chain through reaction with 1-epoxydodecane; however, only spherical nanocrystals were formed without the alkylation. As the PEI became positively charged by the addition of HCl, hexagonal nanoplates were generated in good yields, this being indicative of the importance of positive charges in shape development [32].

Other amine compounds such as triethylamine or diamines may form spherical nanoparticles at room temperature [65, 66]. Among several amine compounds utilized for gold reduction, aniline compounds demonstrated some intriguing aspects; for example, aniline is oxidatively polymerized in conjunction with the reduction of gold precursors to give unique, polyaniline-coated nanoparticles [106] or polymer nanoblets [33]. In other words, an oxidative reaction coupled with nanocrystal growth may lead to the creation of additional intriguing nanostructures with defined chemical structures. When *ortho*-phenylenediamine was adopted for the reduction of $HAuCl_4$, uniform hexagonal plates were prepared in near-quantitative yield along with poly(*o*-phenylenediamine), but spherical nanoparticles were predominantly observed as the amount of the diamine was increased [33]. Intriguingly, hexagonal nanoplates were the most frequent products in the diverse amine reduction; in general, either decreasing the reducing power by lowering the amines concentration, or increasing the passivating power (by increasing the charges) tended to yield hexagonal nanoplates almost exclusively.

7.4.4
Seed-Mediated Growth by Ascorbic Acid

Ascorbic acid is a weak, albeit unique, reductant for the syntheses of gold crystals because it cannot reduce gold precursors in solution phase into gold atoms at room temperature, suggesting that formation of the nucleus is substantially hindered by ascorbic acid [38]. The reduction stops intriguingly at Au(I), as indicated by the disappearance of the characteristic color of $AuCl_4^-$, with no further color change.

Nonetheless, as ascorbic acid is able to reduce the Au(I) further into the elemental metal when an appropriate seed is present in the reaction medium, it can be used as a main reductant exclusively in the presence of seed particles that may be prepared in other reaction conditions.

7.4.4.1 Overview of Seed-Mediated Growth

The so-called seed-mediated growth procedure in which CTAB is assumed to play a central role to create gold nanocrystals of various shapes (but mostly nanorods) has been extensively studied by Murphy and coworkers (Figure 7.12). The dependence upon surfactant chain length [107], seed preparation [77] and effect of additives [36, 78, 108] rendered the production of nanorod (and/or nanowire) with a variety of aspect ratios, with a higher yield, or with deviations in their morphologies. As the aliphatic chain length of CTAB was increased, the resultant aspect ratio of the rod also increased [107]. It is indicated that the counterion of CTAB – the bromide ion – appears also to be crucial for the formation of nanorod [38]. With the exchange of counterion into chloride ion, only spherical (or faceted isotropic) nanocrystals were observed, while the nanorod structure totally disappeared and triangular nanoplate (and decahedrons) was a major product with the addition of iodide ion in the presence of bromide ion (Figure 7.13) [74]. The silver ion appears to have an additionally critical role in the synthesis of nanorods, the yield of which was dramatically improved although only shorter and single crystalline nanorods were observed [75, 108]. Furthermore, by adding a minute amount of silver ion and concomitant control of stoichiometry of ascorbic acid with respect to gold precursors, nanocubes, icosahedrons, tetrahedrons and highly branched tetrapods could be synthesized at room temperature. However,

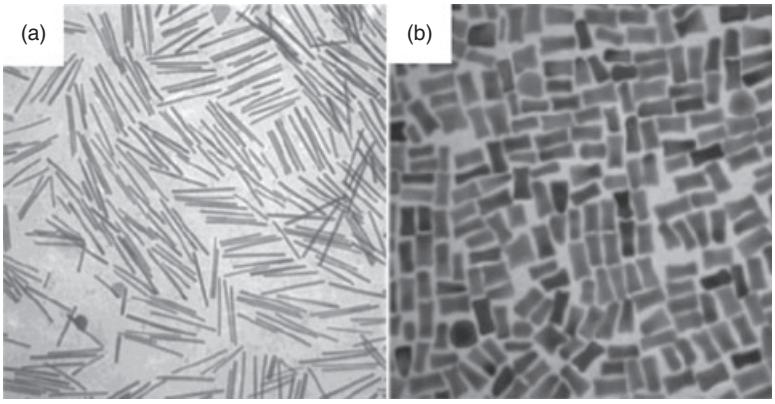

Figure 7.12 Typical TEM images of gold nanorods produced in the absence (a) and presence (b) of Ag^+ ions. The average length of the rods is ~500 nm in (a) and ~100 nm in (b). (Adapted from Ref. [38].)

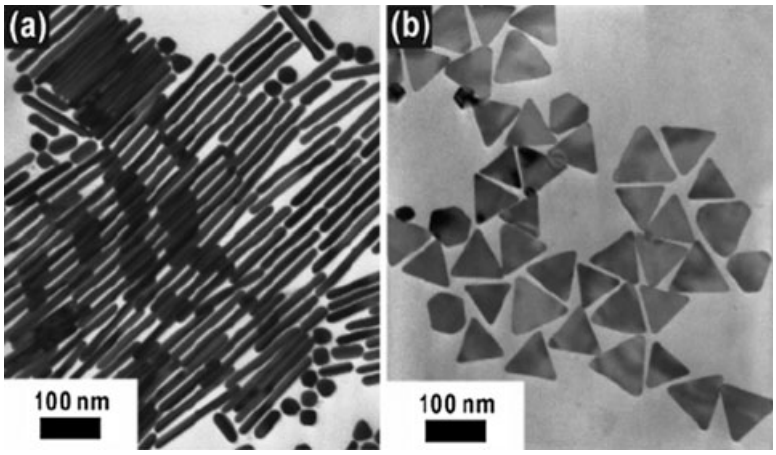

Figure 7.13 TEM images of manufactured gold nanostructures in the absence (a) and presence (b) of a trace amount of iodide ions (~10 μM). The as-prepared gold nanocrystals were mildly centrifuged at ~1000 rpm for 5 min to separate isotropic small nanoparticles before being loaded onto the TEM grids. (Adapted from Ref. [74].)

these diverse shapes were only observed in the presence of excessive bromide ion [36].

7.4.4.2 Controversial Issues with the Seed-Mediated Growth

The experimental results obtained during the past decade have barely been integrated into a 'concrete' logic; rather, only scattered observations have been gleaned from diversified reaction conditions. The lack of consistency can be ascribed to controversial observations identified whilst attempting to reproduce a seed-mediated growth protocol proposed by one research group. For instance, only triangular nanoplates in conjunction with isotropic faceted nanoparticles were observed in one study aimed at producing nanorods [30]. In another report, low-grade CTAB was shown to be effective in the synthesis of nanorods, whereas the use of 99% CTAB gave only isotropic nanoparticles [11]. Bipyramidal nanocrystals grown from faceted seed that has been protected with citrate ion were not observed under similar growth conditions by another group [24]. Even in the extreme case, variation among CTAB reagents produced by different manufacturers could guarantee the manufacture of nanorods with other parameters fixed [58]. These discrepancies in the manufacture of nanorods suggest that a variety of impurities exert major influences on crystal formation during the early stages of growth. In other words, the reaction scheme using ascorbic acid is vulnerable to subtle, but unknown, changes in the environment. Recently, it was shown that minute quantities of iodide ion (~μ*M*) could provoke a drastic deviation in morphology in the presence of excessive bromide or chloride ions, thus verifying the importance of the specific adsorption of halide ions [74]. It seems, however, that the halide effect

cannot account for all discrepancies ever reported, and further intensive investigation is clearly required.

7.4.4.3 Influences of Silver and Halide Ions

Although, as mentioned above, the quaternary ammonium ion of CTAB was considered to direct the morphologies of nanocrystals at their growth stage, the attachment of CTA^+ to the gold crystals does not necessarily dominate the growth of a specific facet or otherwise hinder crystal growth. Several groups, including Pileni and colleagues, have argued that anions might represent a real and crucial control factor in the crystal growth of various metals [109]. Likewise, silver ions appear to affect crystal growth by reductive adsorption onto the crystal surface, via a mechanism similar to UPD, in conjunction with the adsorption of halide ions [24, 25, 105]. Another mechanism has also been proposed where silver halide is grown epitaxially, as a precipitation, on the growing gold surface [38]. Nonetheless, since other polymers such as PEI or poly(acrylic acid) failed to produce the expected nanorod, it seems certain that CTAB plays a further important role in seed-mediated crystal growth (see Section 7.5.2.6).

7.4.5 Electrochemical and Photochemical Growth of Gold Nanocrystals

For the electrochemical synthesis of gold nanocrystals, bulk gold and platinum electrodes are used as the anode and counter-cathode, respectively, in the simple two-electrode system [23, 26, 110]. It is postulated that oxidized gold ions from the anode are recrystallized at the cathode under the influence of a surfactant such as CTAB. The major product was nanorods of single crystalline lattice with a dimension of ~100 nm, that differed from the penta-twinned nanorods formed in seed-mediated growth [76]. The morphology may be further tuned to nanocubes by the systematic addition of acetone and the concomitant application of ultrasound. The cubes were mostly bounded with {100} planes, as observed in the polyol synthesis [26].

The UV-irradiation of the aqueous precursor solution also resulted in the formation of gold nanorod in the presence of a cationic surfactant (CTAB) and $AgNO_3$, both of which are popular additives for the growth of gold crystals (Figure 7.14) [21]. As observed in the electrochemical synthesis, the gold nanorod was single crystalline and [100]-directing, with the side facets covered with {110} and {100} planes. Intriguingly, the photochemical generation of anisotropic silver nanocrystals, converting isotropic silver particles into triangular nanoplates, has not been observed for isotropic gold crystals [17]. This process appears to be related to the excitation of surface plasmon and subsequent physico-chemical changes (e.g. heat generation) on silver crystals. Although, by using dual-beam illumination, the Mirkin group was able to modulate the resultant dimensions of triangular silver nanoplates [72], a similar process appears impossible for gold, presumably due to the inherent hardness of gold metal and differences in electric field intensities excited by surface plasmons.

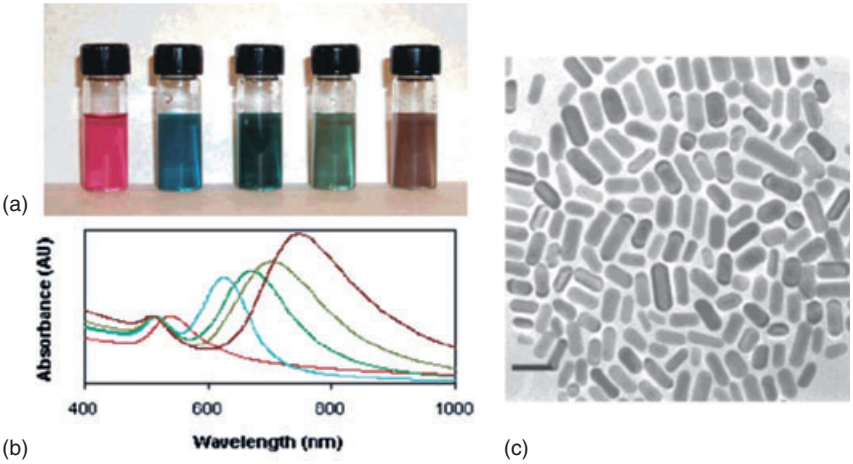

Figure 7.14 (a) Image of photochemically prepared gold nanorods solution; (b) Corresponding UV-visible spectrum. The leftmost solution was prepared with no silver ions added. The other solutions were prepared with the addition of 15.8, 31.5, 23.7 and 31.5 µl of silver nitrate solution, respectively. The middle solution was prepared with a longer irradiation time (54 h) compared to that for all other solutions (30 h), and the transformation into shorter rods can be seen; (c) A typical TEM image of gold nanorod prepared by the addition of 15. 8 µl of silver nitrate solution. (Adapted from Ref. [21].)

7.5 Morphologies of Representative Gold Nanocrystals and Possible Growth Mechanisms

7.5.1 Frequently Observed Morphologies of Gold Nanocrystals

7.5.1.1 Twinned Gold Nanorods and Related Decahedrons

Gold nanorod grown under diverse environments, for example by seed-mediated growth using ascorbic acid and at the DMF reduction in the presence of PVP, showed pentagonal symmetry with five twinning planes [76]. Similar and closely related isomorphs are decahedrons, which seems to have the same origin as the nanorod [29, 70]. A possible scenario might be presented that seeds for the two structures are indiscriminate at the early stages of crystal development but soon differentiate as the growth proceeds. It is noteworthy that the penta-twinned structures are favorable for small nanocrystals due to the fact that the crystal is bounded with most stable Au (111) faces [29, 37, 111]. However, the ideal penta-twinned decahedrons have an inherent strain energy caused by mismatches in the way that five tetrahedrons are assembled to a single apex (Figure 7.15). As the dimension grows, the strain energy accumulates to destabilize the crystals over a certain size. The internal gap of 7° 20′ is often released either by forming two parallel twin

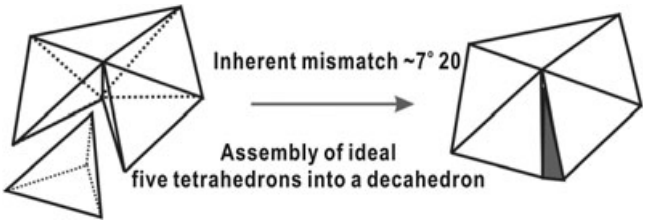

Figure 7.15 Schematic illustration demonstrating inherent angular mismatch when creating a decahedron from five ideal single crystalline *fcc* tetrahedrons. In the real crystal world, the strains is usually compensated with off-centered multiple axes or substantially rounded shapes.

axes or by forming truncated or round decahedrons [29, 74]. By this inherent constriction, the slow growth rate along the short axis of nanorods is explained in part, but the growth mechanism along the long axis remains elusive. According to a growth model developed in silver halide crystals, additional re-entrant grooves (or additional twin planes) formed at the very initial stage of a penta-twinned seed particle can provide the elongation site, or the ridge structure itself of the penta-twinning can provide highly active catalytic sites for the gold reductions [112]. The exact mechanism, however, remains a matter of conjecture. Nevertheless, fully developed decahedrons are barely observed to transform into nanowires, indicating that the two nuclei differentiate irreversibly into each shape over a critical dimension; recently, it was shown that silver nanorod was capable of growing from decahedron gold seeds [113]. The other minor crystal bearing pentagonal twinning is bipyramidal, and was observed in the seed-mediated growth scheme similar to that of the synthesis of nanorods in the presence of silver ions; however, acidification of the solution with HCl was required to lower the pH to 3~4 [24]. Similar structures were also observed in the seed-mediated growth that adopted cetyltrimethylammonium chloride (CTAC) as a major surfactant in the absence of silver ions, but adding KBr to control the halide effect [74].

7.5.1.2 Gold Icosahedrons and Nanoplates

Icosahedrons bear 20 twinning planes, and are recognized as belonging to the family of MTPs [34]; ideally, 20 smaller tetrahedrons are assembled to meet at a single apex to form an icosahedron, although the same strains as are observed in decahedrons exist as ideal tetrahedrons barely pack into ideal icosahedrons, for geometric reasons [37, 111]. Another popular morphology is the triangular nanoplate, which bears single twin planes, while hexagonal nanoplates are assumed to bear two parallelized twinned planes according to the silver halide model. The detailed growth model is described precisely on grounds that the *fcc* gold crystals mimic the growth of the same *fcc* silver halide crystals [112]. Occasionally, truncated tetrahedrons can be seen to be a triangular nanoplates, but these can be resolved by using high-resolution scanning electron microscopy (SEM). Addition-

ally, since 1/3{422} spots in the diffraction pattern are forbidden in the single crystalline nanoplate, the truncated tetrahedral or single crystalline triangular nanoplate can be discriminated from the twinned counterparts [28, 29, 31, 112, 114].

7.5.1.3 Single Crystalline Gold Nanocrystals

Cubes and octahedrons are single crystalline gold nanoparticles belonging to O_h symmetry, and represent a major product of modified polyol synthesis.[25, 28, 37]. Whichever morphology is preferred in the *fcc* metal crystals is known to be dominated by distinct growth rates between the [111] and [100] facets. If the ratio of the growth rate, *R*, along the <100> to that of <111> is 0.58, then perfect cubes surrounded by {100} planes are formed. However, as the ratio increases to 1.73, perfect octahedrons bound by most stable {111} planes are formed through an intermediate state of cubo-octahedrals [25, 37]. The tetrahedron is another single crystal morphology (Figure 7.16) in which tetrahedrons bounded by three {100} facets and a (111) base evolve to another tetrahedron bounded by all {111} facets as the growth rate on {111} planes surpass that on {100}, while truncated tetrahedrons exist in between [28, 37]. Under the electrochemical production and seed-mediated growth of nanorod, single crystalline (not twinned) particles can be observed in the presence of silver ion [108, 110]. As the growth rate of gold nanocrystals is substantially retarded in the presence of silver ions [24], the formation of penta-twinned seed particles appears to be strongly hindered under these conditions. The axial growth direction is [001] and the side surface was covered with {110} and {100} planes.

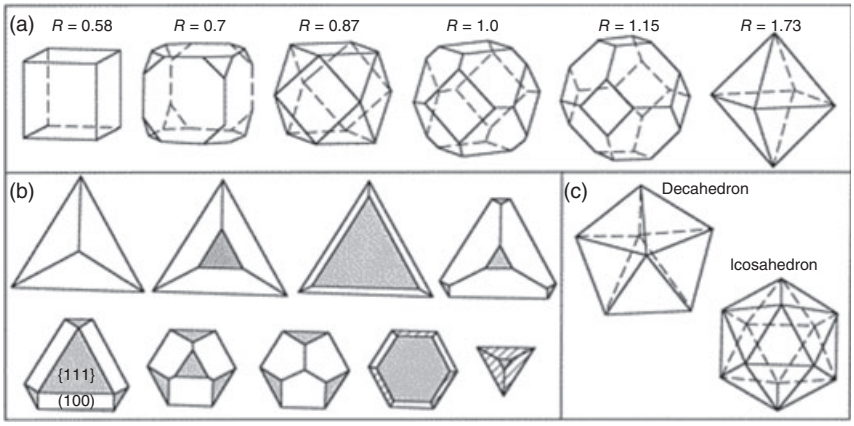

Figure 7.16 Geometric shapes of cubo-octahedral nanocrystals as a function of the ratio, *R*, of the growth rate along the <100> to that of the <111>; (b) Evolution in shapes of a series of (111)-based nanoparticles as the ratio of {111} to {100} increases. The beginning particle is bounded by three {100} facets and a (111) base, while the final one is a {111} bounded tetrahedron; (c) Geometric shapes of multiply twinned decahedral and icosahedral particles. (Adapted from Ref. [37].)

7.5.1.4 Irregular Multipods

The other minor morphologies that gold crystals can take are irregular multipodes or branched nanoparticles. These are generated by heterogeneous growth stages such as seeded growth by the addition of excessive ascorbic acid in seed-mediated crystal growth [36, 78], or the periodic addition of gold precursors with sodium dodecylsulfate (SDS) as a surfactant at the end of the previous growth stage [35]. It was also reported that the yield of branched nanoparticles, reduced by ascorbic acid, was substantially improved by the addition of NaOH; this implies that increasing the chemical potential accelerated the reduction to provide a variety of multipodes, as shown in Figure 7.17 [115].

7.5.1.5 Post-Treatment of As-Grown Nanocrystals

Intriguingly, as-formed gold nanocrystals can be post-annealed with an etching process which is heavily dependent on crystal habits. It was reported that chloride ion and gaseous O_2 cooperatively etch MTPs of silver, palladium and gold at greater rates, apparently yielding single crystals which survive in the reaction vessel [60, 116]. Indeed, penta-twinned decahedrons could be substantially

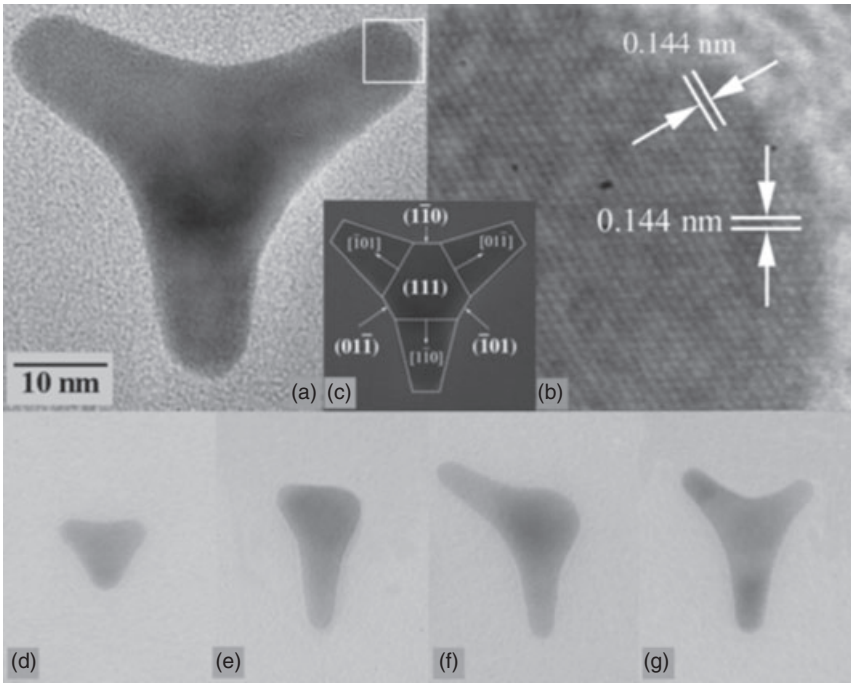

Figure 7.17 TEM image of a regular tripod nanocrystal and (b) high-resolution image of the pod end as marked by a white frame in panel (a); (c) Diagram showing the crystal planes and pod directions. The lower row of panels exhibits the particles developed at various stages: (d) Embryo of triangular shape; (e) Monopod; (f) V-shaped bipod; (g) Y-shaped tripod. (Adapted from Ref. [115].)

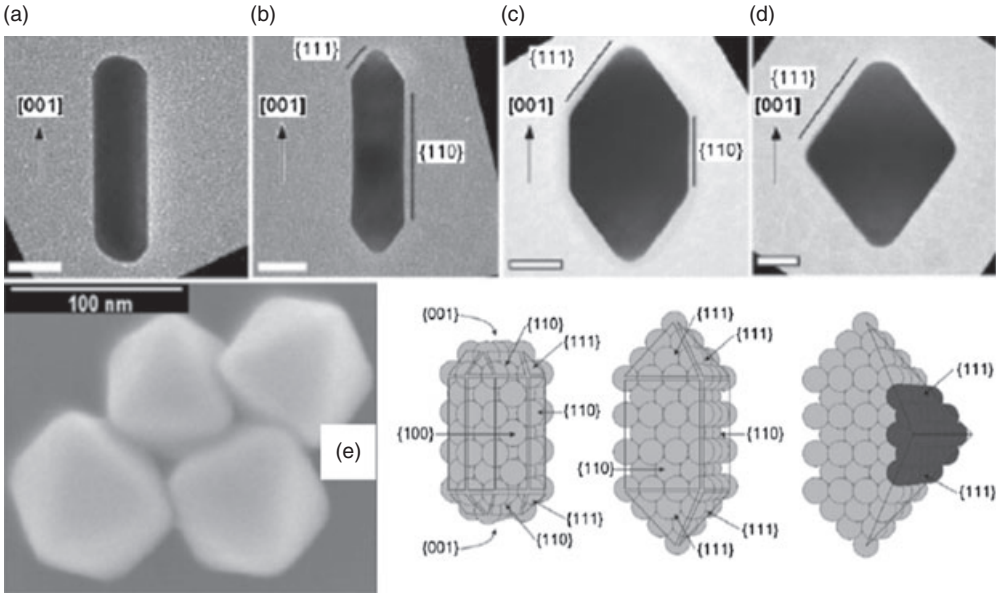

Figure 7.18 (a) Representative TEM images of the original nanorods and (b) particles obtained with $R = 2.7$ (ratio of the concentration of $HAuCl_4$ to that of Au seeds), (c) with $R = 8.2$, and (d) with $R = 13.7$. All particles are oriented along the [001] direction, as indicated by the arrows. (e) SEM image of octahedral particles formed by the chemical sharpening and corresponding structure model of an original nanorod and an octahedral particle. Growth of a sharpened rod into an octahedral particle accomplished by deposition of Au atoms (dark spheres) along the {110} facets. (Adapted from Ref. [27].)

suppressed by the addition of HCl in the diol synthesis of gold crystals, which otherwise would be produced quantitatively [29]. Similarly, as-prepared single crystalline gold nanorods could be transformed octahedrons by an additional growth condition using $HAuCl_4$; in this scheme, the passivating agent (CTAB) for as-formed crystals was exchanged for PVP, so that further growth steps were possible in DMF solution (Figure 7.18) [27]. Although the initial experimental design appeared to elongate the 'seed' nanorod, the growth solution – unexpectedly – resulted in shorter and thicker nanorods, and eventually in octahedrons.

7.5.1.6 Noticeable Features in the Observed Morphologies

It is notable that gold nanorod was not formed under the modified polyol synthesis, whereas pentagonal silver nanowire was a major product under similar conditions. Instead, closely related decahedrons were observed under a high content of PVP and in the absence of silver ions [29]. This dependence on PVP was attributed to a protective effect of the polymer against a higher chemical etching rate on the MTPs compared to single crystals [60]. On the other hand, single crystals were

barely observable under seed-mediated growth, but could be produced by the addition of a small amount of silver ion [36].

The unique growth environment that enables MTPs and single crystalline nanoparticles to be formed together is the thermal reduction of $HAuCl_4$ in toluene solution, employing amine surfactant simultaneously as both a reductant and a passivating agent [64]. The combination of primary amines with other secondary, tertiary and quaternary amines diversified the crystal morphologies and sizes. Under these conditions, MTPs (decahedrons and icosahedrons), penta-twinned nanowires, single-twinned triangular nanoplates and single crystalline particles (e.g. octahedrons) could be formed. It was also notable that no halide or silver ions were added externally in this scheme; rather, the chloride ions were inherently present in the form of $HAuCl_4$.

7.5.2 Growth Mechanism of Gold Nanocrystals

Although a myriad of reaction combinations has been applied for the growth of gold nanocrystals hitherto, the observed morphologies are largely categorized into approximately 10 crystals, including cubes, octahedrons, tetrahedrons, triangular nanoplates, hexagonal nanoplates, decahedrons, penta-twinned nanorods, single crystalline nanorods, penta-twinned bipyramids and icosahedrons; these limited morphologies indicate that the development of each morphology is less affected by the individual reaction mechanism of the reducing agents adopted. Aside from tetrahedrons, octahedrons, cubes and related derivatives, the observed nanocrystals contain one or more twin planes, which are energetically favored at the early stage of crystal growth [37, 111]. The observed crystal shapes and possible seed structures are shown schematically in Figure 7.19. Although, at the very early stages the seed structures are assumed to be interchangeable, they soon determine to grow into a given structure.

7.5.2.1 Seed Structures at the Early Stage of Growth

In order to understand the shape evolution of gold nanocrystals, it seems especially fruitful to investigate the crystal structure of small seed particles. The small nanocrystals reduced by $NaBH_4$ in the presence of CTAB appear to be mostly single crystalline with a 1~2 nm size distribution, while citrate-capped nanoparticles allowed some twinning planes [24]. To further complicate matters, it can be seen directly that an initially formed single crystal can transform into twinned crystal during its growth [112]; this transformation is observed indirectly, albeit routinely, in an experiment where several twinned nanocrystals are developed from single crystalline seeds in the seed-mediated growth [38]; however, it is not clear which parameter determines the extent of twinning. The reverse transformation – from a twinned particle to a single crystalline version – is unlikely at room temperature as twinned particles are more stable species at the onset of growth, while additional high energy seems to be required to relocate whole atoms in a twinned particle.

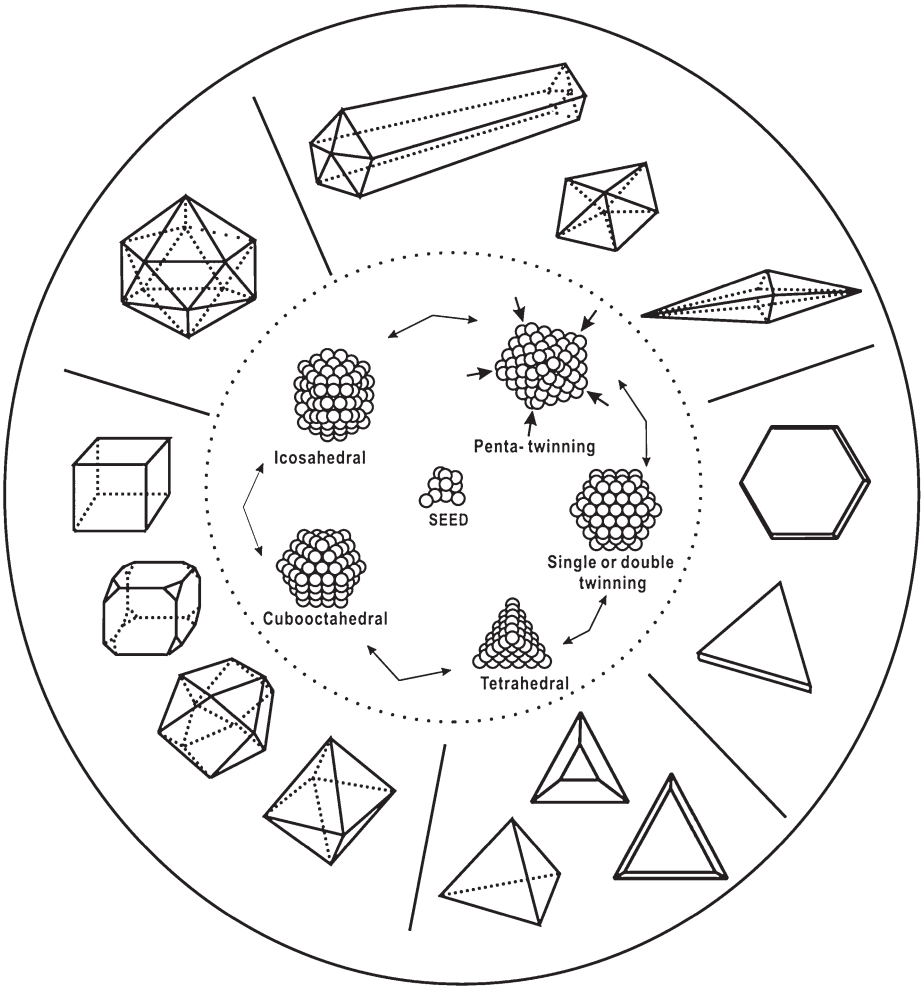

Figure 7.19 Schematic illustration showing diverse morphologies of gold nanocrystals grown from several seed structures. It is assumed that the initially formed seed crystals are structurally interchangeable one with another, but are soon confined to a certain growth track leading to corresponding morphologies.

Indeed, a relatively higher temperature (over 400 °C) was necessary for the process in a high-vacuum system [101].

7.5.2.2 **Twinning and Reaction Temperature**

In summarizing the observations obtained hitherto, twinned nanocrystals were dominant in the synthesis at room temperature, a rapid reduction seemed to afford highly twinned particles such as penta-twinned decahedrons or icosahedrals, and

nanoplates were the main products in a slow reduction [112]. In contrast, in the polyol process the formation of twinned seed seems to be strongly hindered and/or to be rapidly redissolved during continuous incubation, compared to the growth of single crystalline seeds [29, 60]. The prepared seed particles (either twinned or single crystalline) over a critical size will begin to increase their dimension under the empirical constraints imposed on polyol synthesis; single and double-twinned particles can grow into triangular and hexagonal nanoplates, respectively, as depicted in Figure 7.20. Penta-twinned seeds grow into decahedrons, rods and bipyramids, although the individual conditions for the differentiation continue to be elusive (see Figure 7.19). Single crystalline seeds grow into octahedrons, cubes, cubo-octahedrons and tetrahedrons depending on the growth rates on {111} and {100} planes (see Figure 7.16) [37]. Without any restraint in the relative growth rates of individual facets, isotropic nanocrystals would be produced, no matter how many twinning planes existed in the seeds. In the prolonged incubation, the

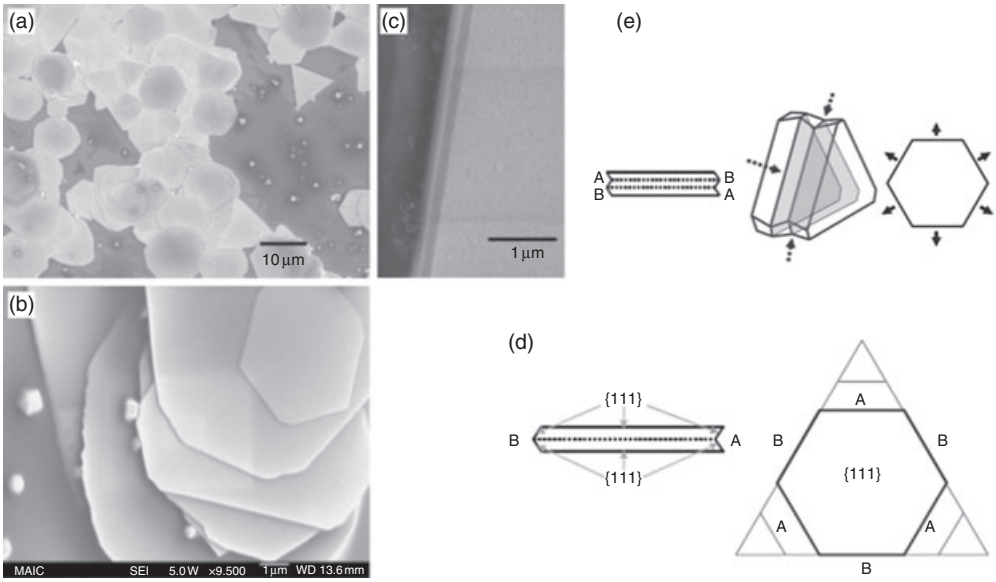

Figure 7.20 (a, b) SEM images of gold nanoplates synthesized using a competitive-growth stage to remove untwinned particles in the modified DMF reduction; (c) SEM image of triangular nanoplate obtained at a tilted angle (45°) showing an edge containing a single re-entrant groove; Corresponding silver halide models for the growth of (d) triangular and (e) hexagonal nanoplate bearing one and two parallel twin planes, respectively; (d) The re-entrant grooves of A-type faces cause rapid growth that is arrested when the face grows itself out, leaving a triangular prism with slow-growing B-type faces; (e) On the other hand, all faces in a plate containing two parallel twin planes contain A-type faces (dashed arrows), which leads to each A-type face regenerating those adjacent to it, allowing rapid growth in two dimensions (solid arrows). (Adapted from Ref. [112].)

selective etching on twinned seeds resulted in mainly single crystals of gold in the presence of silver, or some twinned particles in its absence [25, 29].

In a striking contrast, the as-grown nanocrystals at room temperature might be kinetically arrested due to a lower rate of Ostwald ripening; in other words, once a seed structure is determined, then the etching or redissolving of seed particles is barely seen, even upon prolonged incubation (or annealing). This process seems to depend largely on the temperature where a major reduction reaction occurs (boiling EG versus aqueous solution at room temperature). The Ostwald ripening appears to explain why twinned crystals prevail in the seed-mediated growth at room temperature, while twinning is less observed in the modified polyol synthesis. Twinning planes may provide more defect sites or reaction centers for the etching process, similar to that observed in the rapid elongation of penta-twinned nanowires at the tips. The various additives mentioned to date (halide ions, silver ions, hydroxide ions and polymer) may either affect seed development from an early stage, or affect further preferential growth on a specific facet of a seed, causing the ramification of decahedrons, rods or bipyramids from penta-twinned seeds.

7.5.2.3 Thermodynamic Stability of Twinned Particles

The thermodynamic stability of an individual crystal facet is generally determined in terms of lowering the surface energy; {111} planes are the most stable due to the higher surface density of gold atoms or greater coordination number with neighbors compared to other, low-indexed surfaces [25]; however, such preference might be changed under the influences of adlayers by halide or silver ions adsorbed onto the as-grown surface. As such, the crystal growth of diverse shapes is most easily explained kinetically – in other words, by distinct growth rates at different facets at given reaction environments, and not by the universal stability of a specific facet. As described in Section 7.5.1.3, the apparent surface morphologies such as cubes and octahedrons can be rationalized by distinct growth rates on different two facets, typically on {100} and {111} facets. Indeed, in the modified polyol process the initially formed gold cubes were transformed to octahedrals through cubo-octahedrals as the content of silver ions increased to suppress the growth of {100} planes [25].

7.5.2.4 Roles of Passivating Chemicals in Shape Development

During early investigations of the seed-mediated growth of gold nanorods, it was postulated that CTA^+ molecules were adsorbed preferentially to the side faces of the rod, thereby hindering growth along the transverse axis and selectively elongating the dimension along the long axis; a similar proposal was presented for the role of PVP in the polyol synthesis of silver nanocrystals [38, 60]. However, several research groups have expressed a degree of skepticism for this model [74, 109, 112], which has been contradicted by several instances of experimental evidence and scientific intuition. First, although typical surface-directing agents such as PVP and CTAB are known to form rod-like micelles, this does not explain the generation of nanocrystals of varying morphologies, as seen in the simultaneous

synthesis of micrometer-long nanowires along with triangular nanoplates, icosahedrons and shorter nanorods. Furthermore, as the proposed superstructures were not rigid, they are able to merge into larger structures, or vice versa. Ultimately, the formation of gold nanorods can be perfectly hindered by the addition of a miniscule amount of iodide ion (~μM) in seed-mediated growth under a CTAB template, which would not interfere with the micellar structures [74]. Second, the head groups of these polymer or superstructures of surfactants generally lack a corresponding atomic-scale periodicity, which explains the facet discrimination, for instance, on the two facets of Au(111) and Au(100) planes. While the lattice parameters of a low-indexed gold surface corresponds to 2~3 Å, the polar head of the quaternary ammonium group facing the gold surface appears to rotate freely so that its hypothetical radius expands to over ~4 Å, or more if including the hydration layer. Finally, the major products are drastically influenced by certain additives such as silver or halide ions, even in the presence of an excess of CTAB; this suggests that the surface adsorptions and the heterogeneous interface structures basically determine the final morphologies of gold in the growth, the concept of which is manifest in the seeded growth of metal heterostructures. For example, the presence of a platinum seed dramatically changed the resultant crystal morphologies of gold from isotropic particles to nanorods [117], while a similar seed led to the manufacture of palladium cubes or octahedrons of well-defined dimensions that otherwise seemed impossible [118].

7.5.2.5 **Influences of Surface-Active Chemicals**

As noted above, when considering drastic changes in shape development the most powerful shape-directing constituents appear to be chemical species capable of specifically (and tightly) adsorbing to the surface of growing nanocrystals. For example, by adding a miniscule quantity of iodide ion, the penta-twinned seeds seem not to develop nanowire but only to be arrested in decahedrons; hence, the adsorbed iodide ion might hinder a defect site necessary for the elongation [74]. The addition of chloride and hydroxide ions to the DMF reduction in the presence of PVP can differentiate the growth rates on facets into the formation of cubes, octahedrons and tetrahedrons, in addition to decahedron and hexagonal nanoplates [68]. Exogenous chloride ions may be used as a selective etchant for twinned crystals in the polyol synthesis [29], or for reducing the size of single crystalline nanorod in the presence of O_2 [116]. Silver ion has been a versatile, but exotic, additive for shape evolution in the growth of gold nanocrystals, due largely to the chemical similarity of metallic silver or related compounds such as silver chloride with metallic gold. The presence of silver ions allowed the growth of single crystalline nanorod in the seed-mediated growth, where otherwise penta-twinned nanorods and other twinned particles would be the dominant products [24]. A systematic evolution of morphology from cubes to octahedrons during polyol synthesis was also facilitated by the presence of silver ions [25]. In the seed-mediated synthesis, single crystalline nanocrystals such as cubes, tetrahedrons and octahedrons were successfully produced by the addition of silver ions (along with modulating molar ratios of reactants), which otherwise could be barely realized [36].

7.5.2.6 Overall Picture for the Growth of Gold Nanocrystals

In spite of the impressive roles of halide and silver ions, it is also clear that nanocrystals without any preferential shape developed in the absence of passivating agents such as CTAB or PVP. Additionally, the results of experiments conducted with varying aliphatic chain lengths of CTAB in seed-mediated growth suggest an important role for the surfactant [107]. In general, selecting the appropriate passivating agent for crystal growth seems to be equally as important as modulating the relative growth rates on crystal facets with halide or silver ions. In an attempt to build a theoretical architectonic, it can be hypothesized that the surfactants in a crystal growth largely retard the reduction rate, irrespective of specific facets, thereby enabling distinct growth rates to be distinguished by adsorbed adlayers (see Figure 7.21). In other words, without retarding the overall reduction rate by the surfactant layer, differences in growth rates with respect to crystal facets are so negligible that isotropic or uncontrolled growth over all facets seems dominant.

Circumstantially, this unprecedented hypothesis may be supported in part by the observation that nanoplates were exclusively produced as the pH was lowered by adding HCl in a linear PEI solution. The indication here was that the tight binding of amine groups to the negatively charged gold surface enabled a morphology change from isotropic particles to hexagonal nanoplates, in quantitative fashion [32]. It has also been shown that by separating the crystal growing procedure from seed preparations, without changing the chemical environment, it is possible to

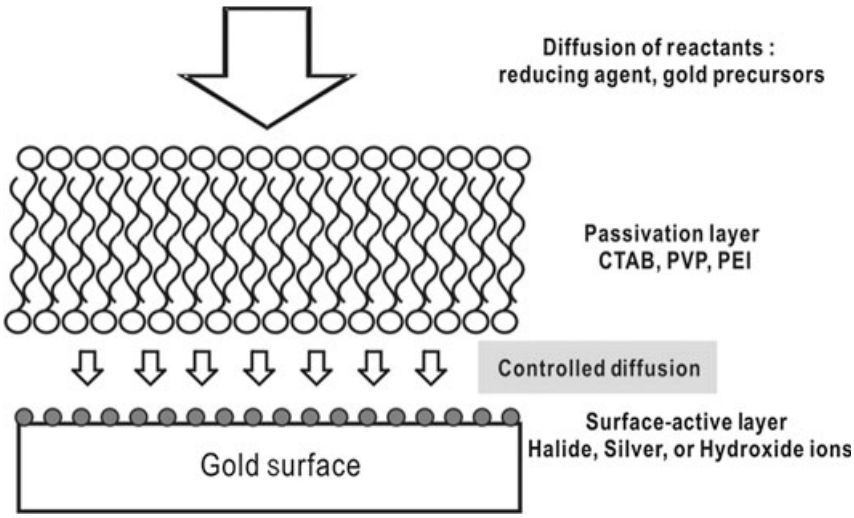

Figure 7.21 Schematic illustration showing the cooperative roles of passivation layer and surface-active layer during the growth at a specific facet of gold crystal.

produce quite different nanocrystals, ranging from penta-twinned decahedrons to hexagonal nanoplates; however, the growth rate was slowed drastically by the dropwise addition of gold precursors [112]. This observation might also suggest that the twinning of nanocrystals could be controlled simply by adjusting the reaction rates by using appropriate passivation agents. Taken together, these findings suggest that modulating the growth rate can be used to control the faceted growth of seed particles cooperatively with other parameters such as halide and silver ions. However, in order to verify this hypothesis, intensive efforts will be required with carefully designed experimental schemes.

When investigating growth mechanisms, atomic force microscopy (AFM) has much potential in that it allows the growth stage to be monitored continuously, seed by seed. In fact, by using AFM it was observed that small seed particles resulted in small-diameter nanorod, while larger seeds yielded 'plump' nanorods [119]. In a separate experiment, gold seeded onto an amine-modified Si(100) surface was observed to grow nanorods with a local preferential direction of growth, although the reason for this remains elusive [120].

7.6
Applications of Gold Nanocrystals in the Life Sciences

7.6.1
Contrast-Enhancing Agents

Traditionally, isotropic gold nanostructures have been used as contrast agents for bioimaging in dark (or bright) -field imaging systems [121]. As an extended application, gold nanorod [11, 13], silica-supported gold shell [12] and hollow nanoshells generated by the galvanic exchange reaction (transmetallation) [7, 8, 10] have been intensively investigated, and have provided a 'proof of concept' for the use of such nanomaterials as contrast agents for bioimaging [6]. When comparing the absorption and scattering powers of the materials one with another, there were no fundamental differences other than a higher scattering efficiency for silica-supported gold nanoshells; this effect was attributed to the interaction between the gold shell and the supporting materials [46]. Due to the higher atomic number of gold, enhanced contrast agents using gold nanostructures have found application in computer-aided tomography (CT), with outstanding efficacy compared to a conventional contrast agent based on iodinated small molecules [9]. Small-molecule contrast agents provide only a limited imaging time due to their rapid renal clearance, and consequently tend to cause renal toxicity. The arrested electromagnetic fields on the surface also facilitated the acquisition of two-photon luminescence of cancer cells in shallow tissues [11]. Although quantum dots have the highest two-photon cross-section, gold nanocrystals are better applicable in terms of minimal cytotoxic effects and higher cross-section compared to organic fluorophores.

7.6.2 Photothermal Therapeutics

Recently, it has been reported that gold nanostructures may be used not only as contrast agents but also as nanomedicines to destroy malignant cells, through photothermal heating using a focused laser beam. In this way, breast cancer cells may be selectively ablated by targeting them through a specifically designed coating layer [5, 12, 115]. The efficacy of the treatment is based on the intense electromagnetic fields arrested in the vicinity of the metal surface, and which eventually is converted to heat that destroys the malignant cells. Photothermal therapy, especially for cancer, is generally less harmful to the normal tissues than are conventional chemotherapies. As the wavelength of the surface plasmon band with which a gold nanostructure resonates can be finely tuned according to its characteristic dimensions [46], gold nanocrystals can provide great versatility, especially when used in conjunction with a selective homing agent immobilized on the surface. For photothermal treatment, it is beneficial to use gold nanostructures of near-infrared (NIR) radiation due to their greater transparency for human tissues [5, 8, 12]. A gold nanocage of 45 nm size [8], gold nanoshells supported on 120 nm silica particles [12] and gold nanorods of 50 nm length (prepared via seed-mediated growth) have all been used in the experimental photothermal treatment of cancer cells [11].

7.6.3 Renal Barrier and Cytotoxicity of Gold Nanomaterials

For applications of both bioimaging contrast agents and optothermal nanomedicines, gold nanostructures appear to have inherent advantages in terms of size control, the ability to tune their characteristic wavelengths on demand, and an inherent biocompatibility due to their chemical inertness and robust nature of the structure. As gold nanocrystals neither decompose nor are reoxidized to leak gold ions within the physiological environment (this is a problem with quantum dots), when passivated with targeting and passivating ligands they can be treated with conventional macromolecules such as polymer nanoparticles or proteins in the short term [80]. It is important to appreciate the ultimate fate of gold nanocrystals administered intravenously to humans in order to evaluate the toxicity of these nanomaterials when used as therapeutics or contrast agents. Charged gold nanocrystals may cause complement activation; for example, cationic nanocrystals (i.e. encapsulated with cationic polymer PEI) may cause a severe complement response, leading to cytotoxicity. The binding of gold nanocrystals with opsonins or other immunoproteins can also expedite a rapid clearance from the bloodstream to the reticuloendothelial system (RES), eventually causing a toxic response [81, 122]. Based on studies using molecular sieves within the glomerular capillaries, the minimum threshold to avoid rapid renal clearance is about ~10 nm [81]. In contrast, when gold nanoparticles exceed 100 nm in size, they are not cleared from the body but rather accumulate in the RES (liver, spleen, or lymph nodes), causing

inflammation or apoptosis of the tissue cells. Without an active homing agent, gold nanocrystals would be targeted to cancer cells or inflammatory tissues via a process called enhanced permeation and retention in those tissues [81, 82]. The particle size relevant to this effect ranges from 50 to 100 nm, and is heavily dependent on the coating layers (notably also to a hydration layer). Consequently, gold nanostructures used for imaging and photothermal therapeutics must meet size criteria so as not to compromise the efficacy of the treatment and cause adverse side effects.

7.7 Summary and Perspectives

In this chapter we have briefly described the representative morphologies of gold nanocrystals observed under diverse growth conditions, and provided details of their experimental conditions and theoretical backgrounds. When growing gold nanocrystals, twinning is a key issue in shape evolution, as more than half of the nanocrystals have at least one twinning plane. Therefore, an understanding of the mechanism and an ability to control twinning during crystal growth is important in the shape-controlled synthesis of gold nanomaterials.

Overall, thermal reduction schemes such as modified polyol synthesis appear to facilitate Ostwald ripening, and the consequent preferential formation of single crystals rather than the growth of twinned crystals at room temperature. With regards to reaction conditions, a higher temperature favors the growth of single crystals, which are more stable than their twinned counterparts towards the etching process. Twinned structures formed rapidly during the early stages of growth seem too vulnerable to survive these harsh conditions. In contrast, seed-mediated growth conducted at room temperature, without the aid of silver ions, produced mostly twinned nanoparticles. The initially formed twinned crystals are kinetically trapped in local energy minima where they may then grow into corresponding twinned crystals.

In seed-mediated growth, the controversial observations often reported were tentatively ascribed to unknown impurities in CTAB reagents, or to other sources. Although impurities of unknown source may interfere with the synthetic procedure, this provides a glimpse of the growth mechanism of gold nanocrystals. Nonetheless, reproducibility problems associated with seed-mediated growth by ascorbic acid remain an issue for further strides.

In addition to providing control over the reaction conditions, chemical additives such as silver and halide ions dramatically change the crystal shapes, or improve yields. Adding silver ions retards the growth rate such that single crystals are favored over twinned, whilst a silver adlayer favors growth on {111} planes or suppresses {100} planes. The addition of halide or hydroxide ions resulted in the formation of gold nanocrystals of diverse shape. Concomitantly, polymer or surfactant molecules acting as passivating agents may play a crucial role in much the same way as halide and silver ions. It is hypothesized that, while these tightly

adsorbing chemicals can directly differentiate growth rates on distinct crystal facets, passivating agents such as PVP and CTAB control overall growth rates by physically regulating the access of reagents to the crystal surface.

In the past, gold nanocrystals have most often been used as contrast-enhancing agents for bioimaging tools and in the selective destruction of malignant cells via photothermal therapy with a focused laser beam. In these applications, gold nanocrystals have inherent advantages of superior biocompatibility that originates from their chemical inertness and robust nature. With regards to cytotoxicity, the control of particle size distribution is important when these nanomaterials are used in humans, as nanocrystals administered intravenously experience different fates according to their size. Surface treatment is also important for applications in the life sciences, as the opsonization process induces phagocytosis or complement activation, which in turn reduces the effectiveness of the treatment. The long-term physical and chemical stability during storage represents another practical and important issue when using gold nanomaterials in a clinical setting.

Acknowledgment

These studies were supported financially by KRIBB initiative programs.

References

1 Orendorff, C.J., Gole, A., Sau, T.K. and Murphy, C.J. (2005) Surface-enhanced Raman spectroscopy of self-assembled monolayers: sandwich architecture and nanoparticle shape dependence. *Analytical Chemistry*, **77**, 3261–6.

2 Raschke, G., Brogl, S., Susha, A.S., Rogach, A.L., Klar, T.A., Feldmann, J., Fieres, B., Petkov, N., Bein, T., Nichtl, A. and Kurzinger, K. (2004) Gold nanoshells improve single nanoparticle molecular sensors. *Nano Letters*, **4**, 1853–7.

3 Sun, Y. and Xia, Y. (2002) Increased sensitivity of surface plasmon resonance of gold nanoshells compared to that of gold solid colloids in response to environmental changes. *Analytical Chemistry*, **74**, 5297–305.

4 Slocik, J.M., Tam, F., Halas, N.J. and Naik, R.R. (2007) Peptide-assembled optically responsive nanoparticle complexes. *Nano Letters*, **7**, 1054–8.

5 Huang, X., El-Sayed, I.H., Qian, W. and El-Sayed, M.A. (2006) Cancer cell imaging and photothermal therapy in the near-infrared region by using gold nanorods. *Journal of the American Chemical Society*, **128**, 2115–20.

6 El-Sayed, I.H., Huang, X. and El-Sayed, M.A. (2005) Surface plasmon resonance scattering and absorption of anti-EGFR antibody conjugated gold nanoparticles in cancer diagnostics: applications in oral cancer. *Nano Letters*, **5**, 829–34.

7 Chen, J., Saeki, F., Wiley, B., Cang, H., Cobb, M.J., Li, Z.-Y., Au, L., Zhang, H., Kimmey, M.B., Li, X. and Xia, Y. (2005) Gold nanocages: bioconjugation and their potential use as optical imaging contrast agents. *Nano Letters*, **5**, 473–7.

8 Chen, J., Wang, D., Xi, J.. Au, L., Siekkinen, A., Warson, A., Li, Z.-Y., Zhang, H., Xia, Y. and Li, X. (2007) Immuno gold nanocages with tailored optical properties for targeted photothermal destruction of cancer cells. *Nano Letters*, **7**, 1318–22.

9 Kim, D., Park, S., Lee, J.H., Jeong, Y.Y. and Jon, S. (2007) Antibiofouling

polymer-coated gold nanoparticles as a contrast agent for in vivo X-ray computed tomography imaging. *Journal of the American Chemical Society*, **129**, 7661–5.

10 Shukla, S., Priscilla, A., Banerjee, M., Bhonde, R.R., Ghatak, J., Satyam, P.V. and Sastry, M. (2005) Porous gold nanospheres by controlled transmetallation reaction: a novel material for application in cell imaging, *Chemistry of Materials*, **17**, 5000–5.

11 Durr, N.J., Larson, T., Smith, D.K., Korgel, B.A., Sokolov, K. and Ben-Yakar, A. (2007) Two-photon luminescence imaging of cancer cells using molecularly targeted gold nanorods. *Nano Letters*, **7**, 941–5.

12 Loo, C., Lowery, A., Halas, N.J., West, J. and Drezek, R. (2005) Immunotargeted nanoshells for integrated cancer imaging and therapy. *Nano Letters*, **5**, 709–11.

13 Oyelere, A., Chen, P.C., Huang, X., El-Sayed, I.H. and El-Sayed, M.A. (2007) Peptide-conjugated gold nanorods for nuclear targeting. *Bioconjugate Chemistry*, **18**, 1490–7.

14 Huang, W., Qian, W. and El-Sayed, M.A. (2005) The optically detected coherent lattice oscillations in silver and gold monolayer periodic nanoprism arrays: the effect of interparticle coupling. *Journal of Physical Chemistry B*, **109**, 18881–8.

15 Maier, S.A., Brongersma, M.L., Kik, P.G., Meltzer, S., Requicha, A.A.G. and Atwater, H.A. (2001) Plasmonics – a route to nanoscale optical devices. *Advanced Materials*, **13**, 1501–5.

16 Maier, S.A., Kik, P.G., Atwater, H.A., Meltzer, S., Harel, E., Koel, B.E. and Requicha, A.A.G. (2003) Local detection of electromagnetic energy transport below the diffraction limit in metal nanoparticle plasmon waveguides. *Nature Materials*, **2**, 229–32.

17 Jin, R., Cao, Y., Mirkin, C.A., Kelly, K.L., Schatz, G.C. and Zheng, J.G. (2001) Photoinduced conversion of silver nanospheres to nanoprisms. *Science*, **294**, 1901–3.

18 Duan, H. and Nie, S. (2007) Etching colloidal gold nanocrystals with hyperbranched and multivalent polymers: a new route to fluorescent and water-soluble atomic clusters. *Journal of the American Chemical Society*, **129**, 2412–13.

19 Clark, H.A., Campagnola, P.J., Wuskell, J.P., Lewis, A. and Loew, L.M. (2000) Second harmonic generation properties of fluorescent polymer-encapsulated gold nanoparticles. *Journal of the American Chemical Society*, **122**, 10234–5.

20 Bao, Y., Zhong, C., Vu, D.M., Temirov, J.P. and Dyer, R.B. and Martinez, J.S. (2007) Nanoparticle-free synthesis of fluorescent gold nanoclusters at physiological temperature. *Journal of Physical Chemistry C*, **111**, 12194–8.

21 Kim, F., Song, J.H. and Yang, P. (2002) Photochemical synthesis of gold nanorods. *Journal of the American Chemical Society*, **124**, 14316–17.

22 Wu, H.-Y., Huang, W.-L. and Huang, M.H. (2007) Direct high-yield synthesis of high aspect ratio gold nanorods. *Crystal Growth and Design*, **7**, 831–5.

23 Chang, Y.-Y., Yu, S.-S., Lee, C.-L. and Wang, C.R.C. (1997) Gold nanorods: electrochemical synthesis and optical properties. *Journal of Physical Chemistry B*, **101**, 6661–4.

24 Liu, M. and Guyot-Sionnest, P. (2005) Mechanism of silver(I)-assisted growth of gold nanorods and bipyramids. *Journal of Physical Chemistry B*, **109**, 22192–200.

25 Seo, D., Park, J.C. and Song, H. (2006) Polyhedral gold nanocrystals with O_h symmetry: from octahedra to cubes. *Journal of the American Chemical Society*, **123**, 14863–70.

26 Huang, C.-J., Wang, Y.-H., Chiu, P.-H., Shih, M.-C. and Meen, T.-H. (2006) Electrochemical synthesis of gold nanocubes. *Materials Letters*, **60**, 1896–900.

27 Carbó-Argibay, E., Rodríguez-González, B., Pacifico, J., Pastoriza-Santos, I.J. and Pérez Juste, J. and Liz-Marzan, L.M. (2007) Chemical sharpening of gold nanorods: the rod-to-octahedron transition. *Angewandte Chemie - International Edition*, **46**, 8983–7.

28 Kim, F., Connor, S., Song, H., Kuykendall, T. and Yang, P. (2004) Platonic gold nanocrystals. *Angewandte Chemie - International Edition*, **43**, 3673–7.

29 Seo, D., Yoo, C.I., Chung, I.S., Park, S.M., Ryu, S. and Song, H. (2008) Shape adjustment between multiply twinned and single-crystalline polyhedral gold nanocrystals: decahedra, icosahedra, and truncated tetrahedra. *Journal of Physical Chemistry C*, **112**, 2469–75.

30 Millstone, J.E., Park, S., Shufor, K.L., Qin, L., Schatz, G.C. and Mirkin, C.A. (2005) Observation of a quadrupole plasmon mode for a colloidal solution of gold nanoprisms. *Journal of the American Chemical Society*, **127**, 5312–13.

31 Ah, C.S., Yun, Y.J., Park, H.J., Kim, W.-J., Ha, D.H. and Yun, W.S. (2005) Size-controlled synthesis of machinable single crystalline gold nanoplates. *Chemistry of Materials*, **17**, 5558–61.

32 Chen, C.-C., Hsu, C.-H. and Kuo, P.-L. (2007) Effects of alkylated polyethylenimines on the formation of gold nanoplates. *Langmuir*, **23**, 6801–6.

33 Sun, X., Dong, S. and Wang, E. (2004) Large-scale synthesis of micrometer-scale single-crystalline Au plates of nanometer thickness by a wet-chemical route. *Angewandte Chemie – International Edition*, **43**, 6360–3.

34 Kwon, K., Lee, K.Y., Lee, Y.W., Kim, M., Heo, J., Ahn, S.J. and Han, S.W. (2007) Controlled synthesis of icosahedral gold nanoparticles and their surface-enhanced Raman scattering property. *Journal of Physical Chemistry C*, **111**, 1161–5.

35 Kuo, C.-H. and Huang, M.H. (2005) Synthesis of branched gold nanocrystals by a seeding growth approach. *Langmuir* **21**, 2012–16.

36 Sau, T.K. and Murphy, C.J. (2004) Room temperature, high-yield synthesis of multiple shapes of gold nanoparticles in aqueous solution. *Journal of the American Chemical Society*, **126**, 8648–9.

37 Wang, Z.L. and Electron, T. (2000) Microscopy of shape-controlled nanocrystals and their assemblies. *Journal of Physical Chemistry B*, **104**, 1153–75.

38 Murphy, C.J., Sau, T.K., Gole, A.M., Orendorff, C.J., Gao, J., Gou, L., Hunyadi, S.E. and Li, T. (2005) Anisotropic metal nanoparticles: synthesis. assembly, and optical applications. *Journal of Physical Chemistry B*, **109**, 13857–70.

39 Tao, A.R., Habas, S. and Yang, P. (2008) Shape control of colloidal metal nanocrystals. *Small*, **4**, 310–25.

40 Wiley, B., Sun, Y., Mayers, B. and Xia, Y. (2005) Shape-controlled synthesis of metal nanostructures: the case of silver. *Chemistry - A European Journal*, **11**, 454-63.

41 Wiley, B., Sun, Y. and Xia, Y. (2007) Synthesis of silver nanostructures with controlled shapes and properties. *Accounts of Chemical Research*, **40**, 1067–76.

42 Mie, G. (1908) Beiträge zur Optik trüber Medien, speziell kolloidaler. *Metallösungen Annalen der Physik*, **330**, 377–445.

43 Bohren, C.F., Huffman, D.R. (1983) *Absorption and Scattering of Light by Small Particles*, John Wiley & Sons, Inc., New York, pp. 477–82.

44 Kelly, K.L., Coronado, E., Zhao, L.L. and Schatz, G.C. (2003) The optical properties of metal nanoparticles: the influence of size, shape, and dielectric environment. *Journal of Physical Chemistry B*, **107**, 668–77.

45 Yang, W.-H., Schatz, G.C. and van Duyne, R.P. (1995) Discrete dipole approximation for calculating extinction and Raman intensities for small particles with arbitrary shapes. *Journal of Chemical Physics*, **103**, 869–75.

46 Jain, P.K., Lee, K.S., El-Sayed, I.H. and El-Sayed, M.A. (2006) Calculated absorption and scattering properties of gold nanoparticles of different size, shape, and composition: applications in biological imaging and biomedicine. *Journal of Physical Chemistry B*, **110**, 7238–48.

47 García de Abajo, F.J. and Howie, A. (1998) Relativistic electron energy loss and electron-induced photon emission in inhomogeneous dielectrics. *Physical Review Letters*, **80**, 5180–3.

48 Novotny, L., Bian, R.X. and Xie, X.S. (1997) Theory of nanometric optical tweezers. *Physical Review Letters*, **79**, 645.

49 Bian, R.X., Dunn, R.C., Xie, X.S. and Leung, P.T. (1995) Single molecule

emission characteristics in near-field microscopy. *Physical Review Letters*, **75**, 4772–5.
50 Kooij, E.S. and Poelsema, B. (2006) Shape and size effects in the optical properties of metallic nanorods. *Physical Chemistry Chemical Physics*, **8**, 3349–57.
51 Hutter, E. and Fendler, J.H. (2004) Exploitation of localized surface Plasmon resonance. *Advanced Materials*, **16**, 1685–706.
52 Xia, Y. and Halas, N.J. (2005) Shape-controlled synthesis and surface plasmonic properties of metallic nanostructures. *MRS Bulletin*, **30**, 338–348.
53 Kneipp, K., Kneipp, H., Itzkan, I., Dasari, R.R. and Feld, M.S. (1999) Ultrasensitive chemical analysis by Raman spectroscopy. *Chemical Reviews*, **99**, 2957–76.
54 Fort, E. and Grésillon, S. (2008) Surface enhanced fluorescence. *Journal of Physics D: Applied Physics*, **41**, 013001.1–013001.31.
55 Doering, W.E. and Nie, S. (2002) Single-molecule and single-nanoparticle SERS: examining the roles of surface active sites and chemical enhancement. *Journal of Physical Chemistry B*, **106**, 311–17.
56 Le Ru, E.C., Meyer, M. and Etchegoin, P.G. (2006) Proof of single-molecule sensitivity in surface enhanced Raman scattering (SERS) by means of a two-analyte technique. *Journal of Physical Chemistry B*, **110**, 1944–8.
57 Etchegoin, P.G., Meyer, M., Blackie, E. and LeRu, E.C. (2007) Statistics of single-molecule surface enhanced Raman scattering signals: fluctuation analysis with multiple analyte techniques. *Analytical Chemistry*, **79**, 8411–15.
58 Smith, D.K. and Korgel, B.A. (2008) The importance of the CTAB surfactant on the colloidal seed-mediated synthesis of gold nanorods. *Langmuir*, **24**, 644–9.
59 Berglund, J. and Elding, L.I. (1995) Kinetics and mechanism for reduction of tetrachloroaurate(III), *trans*-dicyanodi chloroaurate(III), and trans-dicyanodibr omoaurate(III) by sulfite and hydrogen sulfite. *Inorganic Chemistry*, **34**, 513–19.
60 Wiley, B., Herricks, T., Sun, Y. and Xia, Y. (2004) Polyol synthesis of silver nanoparticles: use of chloride and oxygen to promote the formation of single-crystal, truncated cubes and tetrahedrons. *Nano Letters*, **4**, 1733–9.
61 Lee, P.C. and Meisel, D. (1982) Adsorption and surface-enhanced Raman of dyes on silver and gold sols. *Journal of Physical Chemistry*, **86**, 3391–5.
62 Mallikarjuna, N.N. and Varma, R.S. (2007) Microwave-assisted shape-controlled bulk synthesis of noble nanocrystals and their catalytic properties. *Crystal Growth and Design*, **7**, 686–90.
63 Qi, Z., Zhou, H., Matsuda, N., Honma, I., Shimada, K., Takatsu, A. and Kato, K. (2004) Characterization of gold nanoparticles synthesized using sucrose by seeding formation in the solid phase and seeding growth in aqueous solution. *Journal of Physical Chemistry B*, **108**, 7006-11.
64 Liu, X., Wu, N., Wunsch, B.H., Barsotti, R.J.J. and Stellacci, F. (2006) Shape-controlled growth of micrometer-sized gold crystals by a slow reduction method. *Small*, **2**, 1046–50.
65 Kuo, P.-L. and Chen, C.-C. (2006) Generation of gold thread from Au(III) and triethylamine. *Langmuir*, **22**, 7902–6.
66 Selvakannan, P., Kumar, P.S., More, A.S., Shingte, R.D., Wadgaonkar, P.P., Sastry, M., (2004) One-pot, spontaneous and simultaneous synthesis of gold nanoparticles in aqueous and nonpolar organic solvents using a diamine-containing oxyethylene linkage. *Langmuir*, **20**, 295–8.
67 Pastoriza-Santos, I., Sánchez-Iglesias, A., García de Abajo, J. and Liz-Marzan, L.M. (2007) Environmental optical sensitivity of gold nanodecahedra. *Advanced Functional Materials*, **17**, 1443–50.
68 Chen, Y., Gu, X., Nie, C.-G., Jiang, Z.-Y., Xie, Z.-X. and Lin, C.-J. (2005) Shape controlled growth of gold nanoparticles by a solution synthesis. *Chemical Communications*, 4181–3.
69 Pastoriza-Santos, I. and Liz-Marzán, L.M. (2002) Formation of PVP-protected metal nanoparticles in DMF. *Langmuir*, **18**, 2888–94.

70 Sánchez-Iglesias, A., Pastoriza-Santos, I., Pérez-Juste, J., Rodríguez-González, B., García de Abajo, J. and Liz-Marzan, L.M. (2006) Synthesis and optical properties of gold nanodecahedra with size control. *Advanced Materials*, **18**, 2529–34.

71 Bastys, V., Pastoriza-Santos, I., Rodríguez-González, B., Vaisnoras, R. and Liz-Marzan, L.M. (2006) Formation of silver nanoprisms with surface plasmon at communication wavelengths. *Advanced Functional Materials*, **16**, 766–73.

72 Jin, R., Cao, Y.C., Hao, E., Métraux, G.S., Schatz, G.C. and Mirkin, C.A. (2003) Controlling anisotropic nanoparticle growth through plasmon excitation. *Nature*, **425**, 487–90.

73 Kundu, S., Panigrahi, S., Praharaj, S., Basu, S., Kumar Sujit, G., Pal, A. and Pal, T. (2007) Anisotropic growth of gold clusters to gold nanocubes under UV irradiation. *Nanotechnology*, **18**, 075712.1–075712.7.

74 Ha, T.H., Koo, H.-J. and Chung, B.H. (2007) Shape-controlled syntheses of gold nanoprisms and nanorods influenced by specific adsorption of halide ions. *Journal of Physical Chemistry C*, **111**, 1123–30.

75 Nikoobakht, B. and El-Sayed, M.A. (2003) Preparation and growth mechanism of gold nanorods (NRs) using seed-mediated growth method. *Chemistry of Materials*, **15**, 1957–62.

76 Johnson, C.J., Dujardin, E., Davis, S.A., Murphy, C.J. and Mann, S. (2002) Growth and form of gold nanorods prepared by seed-mediated surfactant-directed synthesis. *Journal of Materials Chemistry*, **12**, 1765–70.

77 Gole, A.M. and Murphy, C.J. (2004) Seed-mediated synthesis of gold nanorods: role of the size and nature of the seed. *Chemistry of Materials*, **16**, 3633–40.

78 Gou, L. and Murphy, C.J. (2005) Fine-tuning the shape of gold nanorods. *Chemistry of Materials*, **17**, 3668–72.

79 Chithrani, B.D., Ghazani, A.A. and Chan, W.C.W. (2006) Determining the size and shape dependence of gold nanoparticle uptake into mammalian cells. *Nano Letters*, **6**, 662–8.

80 Choi, H.S., Liu, W., Misra, P., Tanaka, E., Zimmer, J.P., Ipe, B.I., Bawendi, M.G. and Frangioni, J.V. (2007) Renal clearance of quantum dots. *Nature Biotechnology*, **25**, 1165–70.

81 Bartlett, D.W. and Davis, M.E. (2007) Physicochemical and biological characterization of targeted, nucleic acid-containing nanoparticles. *Bioconjugate Chemistry*, **18**, 456–68.

82 Duncan, R. (2003) The dawning era of polymer therapeutics. *Nature Reviews Drug Discovery*, **2**, 347–60.

83 Nuopponen, M. and Tenhu, H. (2007) Gold nanoparticles protected with pH and temperature-sensitive diblock copolymers. *Langmuir*, **23**, 5352–7.

84 Wang, Z., Tan, B., Hussain, I., Schaeffer, N., Wyatt, M.F., Brust, M. and Cooper, A.I. (2007) Design of polymeric stabilizers for size-controlled synthesis of monodisperse gold nanoparticles in water. *Langmuir*, **23**, 885–95.

85 Kim, Y.-G., Oh, S.-K. and Crooks, R.M. (2004) Preparation and characterization of 1–2 nm dendrimer-encapsulated gold nanoparticles having very narrow size distributions. *Chemistry of Materials*, **16**, 167–72.

86 Ohno, K., Koh, K.-m., Tsujii, Y. and Fukuda, T. (2002) Synthesis of gold nanoparticles coated with well-defined, high-density polymer brushes by surface-initiated radical polymerization. *Macromolecules*, **35**, 8989–93.

87 Rucareanu, S., Gandubert, V.J. and Lennox, R.B. (2006) 4-(N,N-Dimethylamino)pyridine-protected Au nanoparticles: versatile precursors for water- and organic-soluble gold nanoparticles. *Chemistry of Materials*, **18**, 4674-80.

88 Zubarev, E.R., Xu, J., Sayyad, A. and Gibson, J.D. (2006) Amphiphilic gold nanoparticles with V-shaped arms. *Journal of the American Chemical Society*, **128**, 4958-9.

89 Foos, E.E., Snow, A.W., Twigg, M.E. and Ancona, M.G. (2002) Thiol-terminated di-, tri-, and tetraethylene oxide functionalized gold nanoparticles: a water-soluble, charge-neutral cluster. *Chemistry of Materials*, **14**, 2401–8.

90 Hurst, S.J., Payne, E.K., Qin, L. and Mirkin, C.A. (2006) Multisegmented one-dimensional nanorods prepared by hard-template synthetic methods. *Angewandte Chemie - International Edition*, **45**, 2672–92.

91 McLellan, J.M., Geissler, M. and Xia, Y. (2004) Edge spreading lithography and its application to the fabrication of mesoscopic gold and silver rings. *Journal of the American Chemical Society*, **126**, 10830–1.

92 Sun, Y. and Xia, Y. (2002) Shape-controlled synthesis of gold and silver nanoparticles. *Science*, **298**, 2176–9.

93 Zehner, R.W., Lopes, W.A., Morkved, T.L., Jaeger, H. and Sita, L.R. (1998) Selective decoration of a phase-separated diblock copolymer with thiol-passivated gold nanocrystals. *Langmuir*, **14**, 241–4.

94 Zschech, D., Kim, D.H., Milenin, A.P., Scholz, R., Hillebrand, R., Hawker, C.J., Russell, T.P., Steinhart, M. and Gosele, U. (2007) Ordered arrays of <111>-oriented silicon nanorods by CMOS-compatible block copolymer lithography. *Nano Letters*, **7**, 1516–20.

95 Minelli, C., Hinderling, C., Heinzelmann, H., Pugin, R. and Liley, M. (2005) Micrometer-long gold nanowires fabricated using block copolymer templates. *Langmuir*, **21**, 7080–2.

96 Wilcoxon, J.P. and Provencio, P.P. (2004) Heterogeneous growth of metal clusters from solutions of seed nanoparticles. *Journal of the American Chemical Society*, **126**, 6402–8.

97 Hiramatsu, H. and Osterloh, F.E. (2004) A simple large-scale synthesis of nearly monodisperse gold and silver nanoparticles with adjustable sizes and with exchangeable surfactants. *Chemistry of Materials*, **16**, 2509–11.

98 Youk, J.H., Park, M.K., Locklin, J., Advincula, R., Yang, J. and Mays, J. (2002) Preparation of aggregation stable gold nanoparticles using star-block copolymers. *Langmuir*, **18**, 2455–8.

99 Smetana, A.B., Wang, J.S., Boeckl, J., Brown, G.J. and Wai, C.M. (2007) Fine-tuning size of gold nanoparticles by cooling during reverse micelle synthesis. *Langmuir*, **23**, 10429–32.

100 Hou, G., Zhu, L., Chen, D. and Jiang, M. (2007) Core-shell reversion of hybrid polymeric micelles containing gold nanoparticles in the core. *Macromolecules*, **40**, 2134–40.

101 Vogel, W., Bradley, J., Vollmer, O. and Abraham, I. (1998) Transition from fivefold symmetric to twinned FCC gold particles by thermally induced growth. *Journal of physical Chemistry B*, **102**, 10853–9.

102 Wang, Y., Teitel, S. and Dellago, C. (2004) Melting and equilibrium shape of icosahedral gold nanoparticles. *Chemical Physics Letters*, **394**, 257–61.

103 Seo, D., Yoo, C.I., Park, J.C., Park, S.M., Ryu, S. and Song, H. (2008) Directed surface overgrowth and morphology control of polyhedral gold nanocrystals. *Angewandte Chemie - International Edition*, **47**, 763–7.

104 Kan, C., Cai, W., Li, C. and Zhang, L. (2005) Optical studies of polyvinylpyrrolidone reduction effect on free and complex metal ions. *Journal of Materials Research*, **20**, 320–4.

105 Garcia, S., Salinas, D., Mayer, C., Schmidt, E., Staikov, G. and Lorenz, W.J. (1998) Ag UPD on Au(100) and Au(111). *Electrochimica Acta*, **43**, 3007–19.

106 Selvakannan, P.R., Mandal, S., Pasricha, R., Adyanthaya, S.D. and Sastry, M. (2002) One-step synthesis of hydrophobized gold nanoparticles of controllable size by the reduction of aqueous chloroaurate ions by hexadecylaniline at the liquid-liquid interface. *Chemical Communications*, 1334–5.

107 Gao, J., Bender, C.M. and Murphy, C.J. (2003) Dependence of the gold nanorod aspect ratio on the nature of the directing surfactant in aqueous solution. *Langmuir*, **19**, 9065–70.

108 Sau, T.K. and Murphy, C.J. (2004) Seeded high yield synthesis of short Au nanorods in aqueous solution. *Langmuir*, **20**, 6414–20.

109 Filankembo, A., Giorgio, S., Lisiecki, I. and Pileni, M.P. (2003) Is the anion the major parameter in the shape control of nanocrystals? *Journal of Physical Chemistry B*, **107**, 7492–500.

110 Wang, Z.L., Mohamed, M.B., Link, S. and El-Sayed, M.A. (1999) Crystallographic facets and shapes of gold nanorods of different aspect ratios. *Surface Science*, **440**, L809–14.

111 Gryaznov, V.G., Heydenreich, J., Kaprelov, A.M., Nepijko, S.A., Romanov, A.E. and Urban, J. (1999) Pentagonal symmetry and disclination in small particles. *Crystal Research and Technology*, **34**, 1091–119.

112 Lofton, C. and Sigmund, W. (2005) Mechanisms controlling crystal habits of gold and silver colloids. *Advanced Functional Materials*, **15**, 1197–208.

113 Seo, D., Yoo, C.I., Jung, J. and Song, H. (2008) Ag-Au-Ag heterometallic nanorods formed through directed anisotropic growth. *Journal of the American Chemical Society*, **130**, 2940–1.

114 Jiang, P., Zhou, J.-J., Li, R., Gao, Y., Sun, T.-L., Zhao, X.-W., Xiang, Y.-J. and Xie, S.-S. (2006) PVP-capped twinned gold plates from nanometer to micrometer, *Journal of Nanoparticle Research*, **8**, 927–34.

115 Chen, S., Wang, Z.L., Ballato, J., Foulger, S.H. and Carroll, D.L. (2003) Monopod, bipod, tripod, and tetrapod gold nanocrystals. *Journal of the American Chemical Society*, **125**, 16186–7.

116 Tsung, C.-K., Kou, X., Shi, Q., Zhang, J., Yeoung, M.H., Wang, J. and Stucky, G.D. (2006) Selective shortening of single-crystalline gold nanorods by mild oxidation. *Journal of the American Chemical Society*, **128**, 5352–3.

117 Ducamp-Sanguesa, C., Herrera-Urbina, R. and Figlarz, M. (1992) Synthesis and characterization of fine and monodisperse silver particles of uniform shape. *Journal of Solid State Chemistry*, **100**, 272–80.

118 Habas, S.E., Lee, H., Radmilovic, V., Somorjai, G.A. and Yang, P. (2007) Shaping binary metal nanocrystals through epitaxial seeded growth. *Nature Materials*, **6**, 692–7.

119 Wei, Z. and Zamborini, F.P. (2004) Directly monitoring the growth of gold nanoparticle seeds into gold nanorods. *Langmuir*, **20**, 11301–4.

120 Mieszawska, A., Slawinski, G.W. and Zamborini, F.P. (2006) Directing the growth of highly aligned gold nanorods through a surface chemical amidation reaction. *Journal of the American Chemical Society*, **128**, 5622–3.

121 Brabander, M.D., Nuydens, R., Geuens, G., Moeremans, M. and Mey, J.D. (1986) The use of submicroscopic gold particles combined with video contrast enhancement as a simple molecular probe for the living cell. *Cell Motility and the Cytoskeleton*, **6**, 105–13.

122 Owens, D.E.I. and Peppas, N.A. (2006) Opsonization, biodistribution, and pharmacokinetics of polymeric nanoparticles. *International Journal of Pharmaceutics*, **307**, 93–102.

8
Spherical and Anisotropic Gold Nanomaterials in Medical Therapy

Takuro Niidome, Atsushi Shiotani, Yoshiki Katayama and Yasuro Niidome

8.1
Introduction

The medical use of gold nanoparticles can be traced back to ancient China and India, where red colloidal gold was used as a drug for longevity and revitalization [1–3]. In Europe, gold has long been used as a nerve tonic for nervous disorders, and as a drug to treat epilepsy and syphilis [4, 5].

Gold nanoparticles display unique optical properties such as distinctive extinction bands in the visible region, these being due to the surface plasmon (SP) oscillation of free electrons [6]. As a result, colored gold nanoparticles are currently used as a marker for immunoelectron microscopy in cellular biology, and as a dye for immunochromatography to detect not only human chorionic gonadotrophin secreted into the urine during pregnancy but also the antigens of influenza viruses. Reddish-colored, antigen-modified gold nanoparticles allow diagnoses to be carried out rapidly and in straightforward manner both at home and in hospital, without the need for expensive equipment. When gold is employed for medical purposes as a drug, it is gold compounds rather than metallic gold nanoparticles that are used. Among common ailments, rheumatic diseases are the major group associated with the clinical use of gold compounds, and in this respect several types of compound, including sodium aurothiomalate, aurothioglucose and auranofin, have been developed and approved for clinical use [7, 8]. Several gold compounds have also been designed and tested as drugs to treat cancer, AIDS, bronchial asthma and malaria [9]. Gold compounds also affect DNA replication, the immune system and the functions of various enzymes in cells.

Today, the use of metallic gold nanoparticles in medical research is centered on employing the optical character of gold nanoparticles, as well as their application as photosensitizers for photothermal therapy and as contrast agents in optical imaging. In this chapter, we describe details of current research trends in the use of gold nanoparticles, especially gold nanospheres and gold nanorods, in diagnosis and therapeutic technology, and also discuss their prospective medical applications. This chapter also presents state-of-the-art information regarding novel nanomedicinal technologies. The groundbreaking results presented here provide

Metallic Nanomaterials Vol. 1. Edited by Challa S. S. R. Kumar

ISBN: 978-3-527-32151-3

an invaluable resource for researchers and engineers in the fields of nanotechnology, molecular medicine, biochemical engineering and biotechnology.

8.2
Gold Nanospheres

Among the various types of gold nanoparticle described here, the spherical form is the most widely used. As gold nanospheres can be easily prepared by reducing the gold ion and controlling the particle size, it is possible to carry out the production of gold nanoparticles with relative ease and subsequently to use them not only in a variety of medical diagnoses but also as therapeutic and drug delivery systems [10].

8.2.1
Cellular Imaging using Light Scattering from Gold Nanospheres

When gold nanoparticles are observed under a dark-field microscope, the typical view is of bright particles undergoing Brownian motion. This brilliant light scattering, which is caused by the nanoparticle movements, was used by El-Sayed and coworkers to perform cellular imaging [11, 12]. For this, the group modified gold nanospheres with anti-epidermal growth factor receptor (EGFR) antibodies, and then added these to three types of cell, namely HaCaT cells (human keratinocyte cell line) as a nonmalignant cell line, and to HOC and HSC cells (human oral squamous carcinoma cell lines) as malignant cell lines. Specific binding of the antibody-modified gold nanospheres to the HOC and HSC cells was detected by observing the surface plasmon resonance absorption of the nanospheres onto the cells, and light scattering from the nanospheres under dark-field microscopy. The specific binding of the gold nanospheres to target cells allowed their use as a contrast agent in the diagnosis of diseases, with biomaging of the disease site achieved by combining absorption spectroscopy and light-scattering imaging techniques.

8.2.2
Gold Nanospheres as a Contrast Agent for Computed Tomography

Kattumuri *et al*. developed nontoxic gum arabic-modified gold nanospheres and tested their ability as a contrast agent for computed tomography (CT) [13]. The modified nanospheres were prepared from Au ions with nontoxic phosphino amino acids in the presence of gum arabic. When for biodistribution studies, these modified nanospheres were injected intravenously into pigs, the majority was found to have accumulated in the liver and lungs at between 30 min and 24 h after injection. After 72 h, 43–69% and 46–66% of the dose was retained in the liver of pigs treated with nanospheres at doses of 2 and 4 mg Au per kg body weight, respectively. Delivery of the nanospheres to these organs appeared to be effected by the polysaccharide–protein network. Although the extent of clearance of the

nanospheres from the kidneys was low (1–2% of the total dose), no toxicity due to the nanospheres was observed even at 72 h after injection. Modification with poly(ethylene glycol) (PEG) further stabilized the nanospheres, while an additional functional peptide [receptor-mediated endocytosis (RME) peptide], which is derived from the adenovirus fiber protein and induces receptor-mediated endocytosis, significantly enhanced their uptake into cells [14]. Taken together, the results of these studies demonstrated the future prospects for the use of gold nanoparticles in medical diagnosis and therapy.

8.2.3
Photothermal Cellular Damage

The photothermal effect, whereby absorbed light energy is efficiently converted to heat, represents a unique optical property of metal nanoparticles. When gold nanospheres are irradiated with visible light that corresponds to the absorbance band of the nanospheres, the temperature of both the nanoparticles and their surrounding media is increased. Thus, if the nanospheres are bound to the cells, and the cells then irradiated with visible laser light, it follows that any specific cellular damage would be limited to those cells bound with nanospheres (Figure 8.1). To demonstrate this, El-Sayed and coworkers added anti-EGFR-modified gold nanospheres (as described in Section 8.2.1) to HaCaT, HOC and HSC cells, and then irradiated them with a continuous-wave (CW) argon laser light at 514 nm. As a result, the malignant cells – the HOC and HSC cells – required a lower laser energy (~20 W cm^{-2}) in order to be killed, whereas a higher energy (>57 W cm^{-2}) was required to kill the nonmalignant, HaCaT, cells [12]. It was clear that the heat produced by the photothermal effect as the gold nanospheres became bound to the cells had destroyed the cellular function and eventually caused cell death. It was these initial findings that ignited interest in the use of gold nanoparticles as a medical nanodevice for diagnosis and therapy.

8.2.4
Radiofrequency Thermal Damage of Cells

An external radiofrequency (RF) field is known to induce heat in gold nanoparticles, and this heat can be used to thermally damage cells – in similar fashion to the photothermal effect described above. Gannon *et al.* added gold nanoparticles to human cancer cell lines, and then exposed the cells to a 13.56 MHz RF field for several minutes. Although the nanoparticles alone did not show any cytotoxicity towards the cells, those cells treated with both nanoparticles and RF were significantly damaged [15]. These findings suggested that RF-induced heat release in nanoparticles might be utilized in cancer therapies.

Induced heat can also be used control protein folding. For example, Kogan *et al.* modified gold nanospheres with a peptide, H-Cys-Leu-Pro-Phe-Phe-Asp-NH_2, that binds to the amyloid β (Aβ) protein and interferes with the growth of Aβ aggregates. The peptide-modified gold nanospheres bound to free $A\beta_{1-42}$ protein,

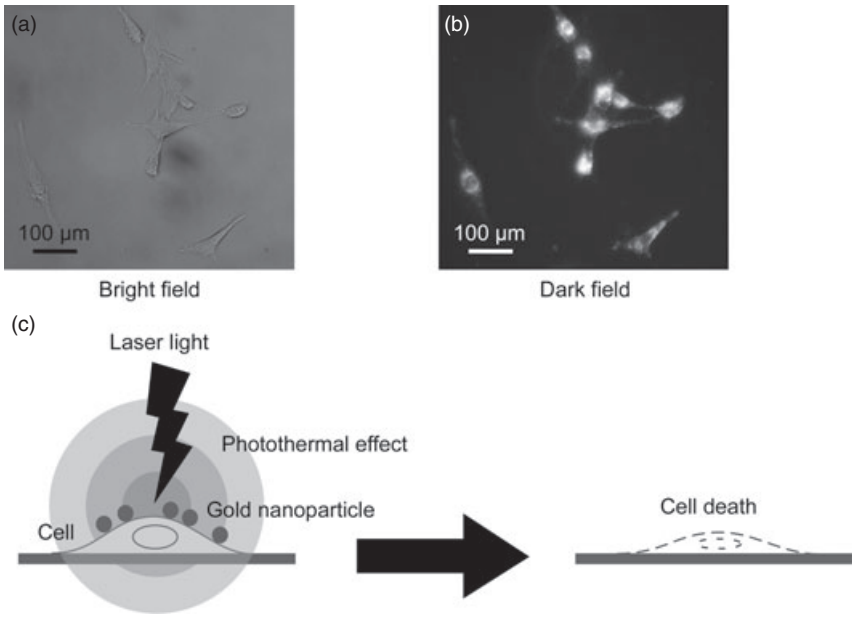

Figure 8.1 Light scattering cellular imaging using gold nanoparticles and the scheme of photothermal cellular damage. Gold nanoparticles were added to Chinese hamster ovary (CHO) cells, after which bright (a) and dark-field (b) images were acquired under microscopy. Strong light scattering from the bound gold nanoparticles on the cells was observed. If cells are irradiated with laser light, the wavelength of which corresponds to the absorbance of the nanoparticles, they may be damaged as a result of the photothermal effect of the gold nanoparticles (c).

and were then incorporated into insoluble aggregates of the $A\beta_{1-42}$ protein. When the aggregates were irradiated with a 12 GHz RF field (microwave) they dissolved as the induced heat enhanced the activity of the peptide [16]. Such controlled conformational change of the $A\beta_{1-42}$ protein provides not only provides an important clue for the development of therapeutic strategies for amyloidosis, such as Alzheimer's disease, but also heralds a powerful tool for altering protein structures in order to better understand the dynamics of protein conformation.

Recently, Mukherjee *et al*. reported that gold nanospheres had shown antitumor activity [17]. In this study, the process of binding the nanospheres with cancerous B-chronic lymphocytic leukemia (BCLL) cells was initiated by attaching the vascular endothelial growth factor (VEGF) antibody to the surface of the nanospheres. After mixing these modified nanospheres with BCLL cells, a significant apoptosis of the cells was observed, with transmission electron microscopy examination revealing that the nanospheres had been internalized into the cells via an endocytosis pathway. This anticancer effect of gold nanospheres was seen as an integration of nanotechnology with cancer therapy and that, by harnessing the RF thermal and photothermal effects of nanospheres, an effective therapeutic strategy might be constructed for future application.

8.2.5
DNA Carrier for Gene Therapy

Previously, the gene delivery system in cells has been studied using a cationic dendritic polymer [18–20]. The dendritic molecule has a spherical shape of ~6 nm diameter, and forms a DNA complex which is several hundreds of nanometers in diameter. The complex was internalized into cells via an endocytosis pathway, after which an efficient gene expression from the DNA was observed. Based on this experience, it was proposed that gold nanospheres might indeed be utilized as a gene carrier system, and that gene expression could be controlled by an external stimulation such as light irradiation and electric pulses. Initially, cationic gold nanospheres were prepared modified with 2-aminoethanethiol by reducing $HAuCl_4$ with $NaBH_4$ in the presence of 2-aminoethanethiol [21]. Although the binding ability with plasmid DNA and significant transfection efficiency was observed when the DNA complex was added to HeLa cells, the stability of the nanospheres was poor, and large aggregates were formed. Subsequently, a PEG chain was added to the cationic nanospheres to provide stability and biocompatibility in biological conditions [22]. The PEG- and amine-modified gold nanospheres were prepared by $NaBH_4$ reduction of $HAuCl_4$ in the presence of 2-aminoethanethiol and methoxypoly(ethylene glycol) containing thiol groups at the terminus (mPEG-SH). After PEG-modification, the zeta-potential of the nanospheres was almost neutral. The PEG- and amine-modified gold nanospheres were bound to plasmid DNA (Figure 8.2), and extended the half-life of the DNA in the blood of mice due to a

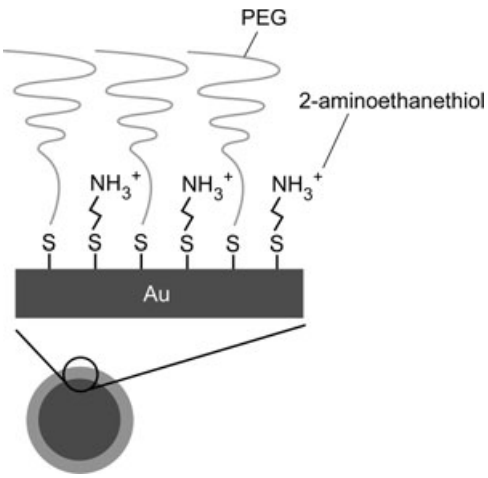

Figure 8.2 Structure of PEG- and amine-modified gold nanoparticles. The gold nanoparticles were prepared by $NaBH_4$ reduction of $HAuCl_4$ in the presence of 2-aminoethanethiol and mPEG-SH.

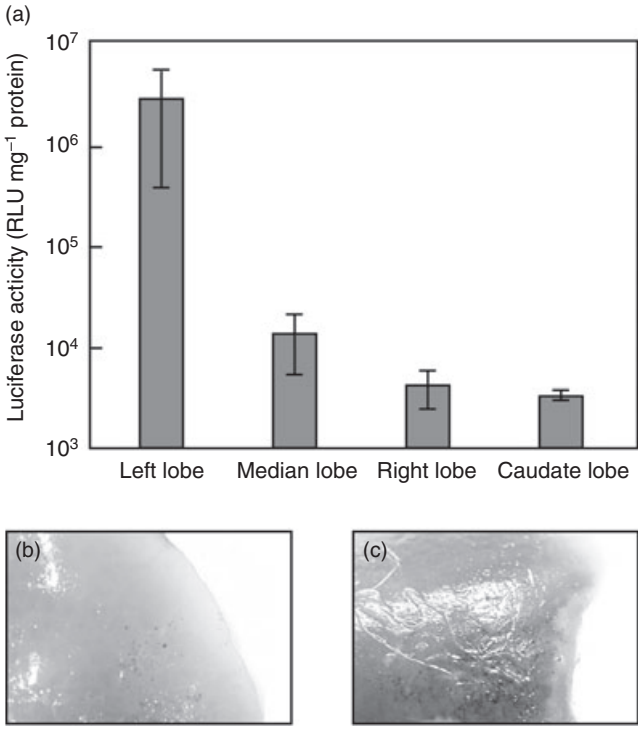

Figure 8.3 Gene expression of systemically injected DNA complexed with the PEG- and amine-modified gold nanoparticles, and gene expression triggered by electric pulses. (a) Plasmid DNA complexed with nanoparticles was injected intravenously into mice. Electric pulses (250 V cm^{-1}, 20 ms per pulse, 8 pulses, 1 Hz) were applied to the left lobe of the liver at 1 min after injection, and luciferase activity in each lobe was evaluated after 6 h. (b, c) X-gal staining of livers of mice receiving β-galactosidase-expression plasmid DNA. Naked DNA (b) and DNA complexes with the nanoparticles (c) were injected into the mice, and electric pulses applied to the left lobe of the liver at 5 min after injection. Gene expression was evaluated at 24 h after injection; the stained areas (black) in panel (c) correspond to the gene-expressing cells. RLU = relative light unit.

'stealth effect' of the PEG chains on the surface of the gold nanospheres. Although no gene expression was observed in any of the organs, when electric pulses were applied to the left liver lobe after an intravenous injection of the DNA complex of the nanospheres, a significant gene expression was observed specifically in the pulsed lobe (Figure 8.3). Whilst electric pulse-dependent gene expression is a unique phenomenon, its application was limited to use with conductive gold nanospheres.

8.3
Gold Nanoshells

Gold nanoshells are optically tunable nanoparticles composed of a dielectric core (silica) coated with a metallic gold layer [23]. The optical resonance of nanoshells can be continuously tuned for wavelengths ranging between the UV and infrared (IR) regions by changing the relative core and shell thickness (Figure 8.4). In particular, the near-IR region (650–900 nm) is ideally suited for *in vivo* imaging and therapy due to a minimum light absorption by the intrinsic chromophores, hemoglobin (<650 nm) and water (>900 nm), which allows a maximal penetration of light into the tissues [24]. Hence, gold nanoshells are expected to be useful as imaging and therapeutic agents.

When using nanoshells tuned to an absorbance at 820 nm, Hirsch *et al.* achieved the photothermal ablation of cultivated tumor cells by irradiation using near-IR laser light at 820 nm *in vitro* [25]. When this system was applied to *in vivo* tumor therapy, the laser light irradiation of solid tumors inoculated in mice treated with the nanoshells caused an increase in the temperature of the irradiation site, although a minimal increase was detected in the absence of nanoshell treatment. In addition, irreversible tissue damage was observed at the site treated with the nanoshells and laser-irradiated [25]. The same group also reported a photothermal therapeutic effect on solid tumors in mice when they injected PEG-modified gold

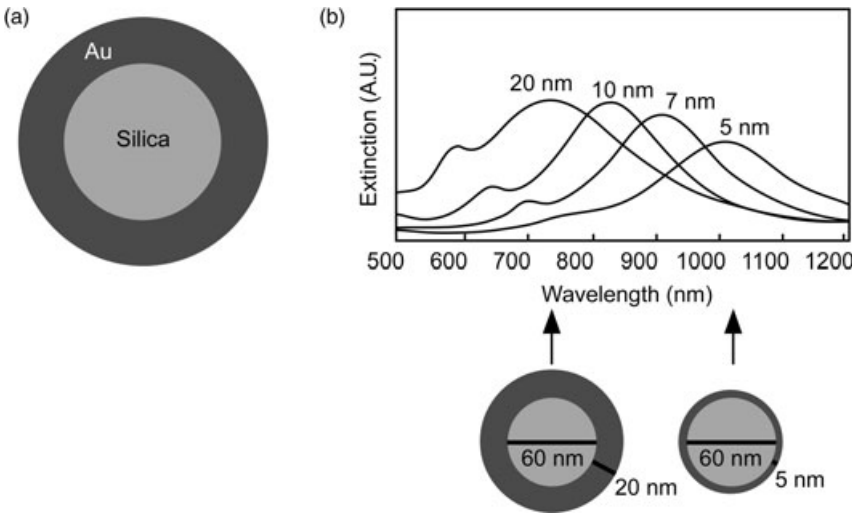

Figure 8.4 (a) Structure of gold nanoshells and (b) demonstration of optical tunability with a 60 nm silica core radius and gold shells of 5, 7, 10 and 20 nm thickness. The plasmon resonance of the gold nanoshells red shifts with decreasing thickness of the gold shell or an increasing core/shell ratio.

nanoshells intravenously and then irradiated with near-IR laser light at 808 nm at 6 h after the injection. The result was a significant suppression of tumor growth in mice treated with the nanoshell injection plus laser irradiation; subsequently, all of the treated mice survived for at least 60 days, whereas the control mice all died within 20 days [26]. Such a simple system – namely, intravenous injection of nanoshells followed by laser irradiation of the tumor – showed great promise as a strategy for photothermal tumor therapy.

In a later study, Loo *et al.* prepared immunotargeted nanoshells modified with an anti-HER2 antibody, and then succeeded in inducing photothermal damage specifically to cancer cells expressing HER2 on the cell surface [27]. The targeted delivery of nanoshells may further increase the accuracy and efficiency of photothermal therapy by combining nanoshell treatment with laser irradiation.

8.4 Gold Nanorods

Gold nanorods, which are rod-shaped anisotropic gold nanoparticles, have unique optical properties [28, 29]. Typically, they show two surface plasmon bands corresponding to the transverse and longitudinal surface plasmon bands in the visible (~520 nm) and near-IR regions, respectively (Figure 8.5). The longitudinal band has a substantially larger extinction coefficient than the transverse band, while the optical resonances of the gold nanorods can be continuously tuned by changing the length and aspect ratio of the rod shape. Thus, the gold nanorods are unusual materials with an intense surface plasmon band that affords near-IR absorption, fluorescence [30, 31] and light scattering [32, 33], and two-photon luminescence [34, 35]. Clearly, these unique optical characteristics of gold nanorods may lead to many medical applications in the future.

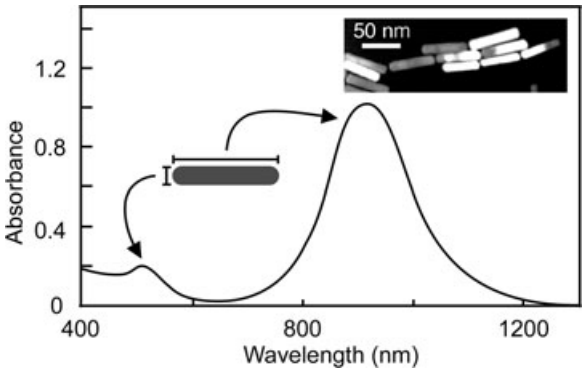

Figure 8.5 Extinction (absorption) spectrum and transmission electron microscopy (TEM) image (inset) of gold nanorods. Nanorods of 11 nm diameter and 65 nm length showed absorbances at 520 and 900 nm corresponding to the transverse (diameter) and longitudinal (length) surface plasmon bands, respectively.

8.4.1
Preparation of Biocompatible Gold Nanorods

Despite their unique characteristics, the use of gold nanorods in the life sciences is very much limited by the presence of the highly cytotoxic material cetyltrimethylammonium bromide (CTAB). This cationic detergent, which is used as a stabilizing agent during the preparation of gold nanorods [28], must be removed first by washing the gold nanoparticles with water and redepositing them by centrifugation [36]. Unfortunately, the CTAB bilayers normally remain on the surface of the gold nanorods, where they adsorb noncovalently such that any further removal will result in the nanorods becoming aggregated. In order to reduce the cytotoxicity of gold nanorods and to stabilize them under biological conditions, we have developed a technique for the removal of CTAB. This involved modifying the nanorods with phosphatidylcholine (PC) – that is, the CTAB was extracted from the nanorod solution into a chloroform phase containing PC (Figure 8.6) [37]. After modification, the PC on the gold surface was identified using transmission electron microscopy (TEM) and energy-dispersive X-ray analysis. It became clear that this PC-modification of the gold nanorods had reduced the zeta-potential of the nanorods from +67 mV to +21 mV; this meant not only that the cationic CTAB had been removed from the surface, but also that the cytotoxicity had been markedly reduced (Figure 8.7).

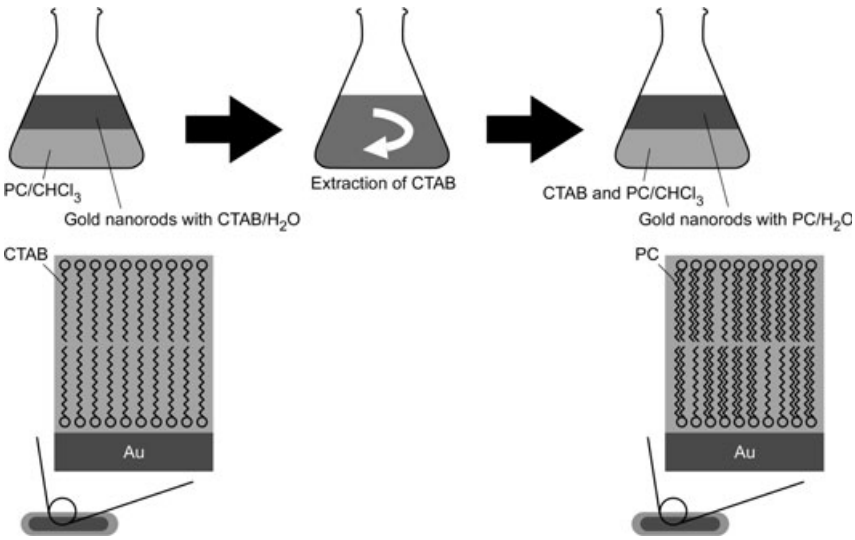

Figure 8.6 Preparation scheme of phosphatidylcholine (PC)-modified gold nanorods. CTAB in the original gold nanorods solution was extracted into a chloroform solution of PC. After three extractions of the aqueous solutions, the PC-modified gold nanorods were isolated by centrifugation and then redispersed in water.

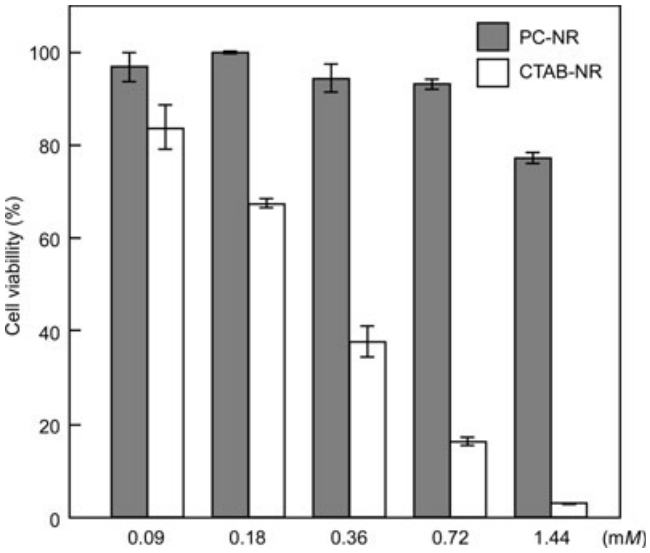

Figure 8.7 Viability of HeLa cells after contacting with PC-modified gold nanorods (PC-NR) and original CTAB-stabilized gold nanorods (CTAB-NR). Gold nanorod solutions (0.09, 0.18, 0.36, 0.72 and 1.44 m*M* as Au atom at final concentrations) were added to the cells, which were incubated for 24 h; cell viability was then evaluated using the MTT assay.

When applying gold nanorods to the medical field – including tumor imaging, photothermal therapy, gene delivery and drug delivery – their targeted delivery following systemic injection is a key objective. For targeted delivery *in vivo*, a 'stealth character' is required in the blood circulation that will allow the efficient delivery of nanorods to a specific target site. This approach can also provide images of a higher contrast, and more effective photothermal therapy compared to current techniques. In order to test whether the PC-modified nanorods may be useful for *in vivo* applications, a primary study was conducted to evaluate the biodistribution of gold nanorods in mice after intravenous injection (Figure 8.8). The fact that about 25% of the injected gold was detected in the liver indicated that, although the PC-modified gold nanorods had been cleared from the blood within 30 min, it had then become trapped in the liver, most likely in Kupffer cells (which are able to retain such cationic particles). In order to overcome the instability of the gold nanorods in the blood, they were modified with a PEG chain and their cytotoxicity *in vitro* and biodistribution then evaluated in mice after intravenous injection [38]. PEG-modification was achieved by adding $mPEG_{5000}$-SH to the CTAB solution, with any excess CTAB being removed by dialysis. The PEG-modified gold nanoparticles showed a near-neutral surface (–0.5 mV) and minimal cytotoxicity *in vitro*. Following intravenous injection into mice, 54% of the PEG-modified gold nanoparticles were found in the blood at

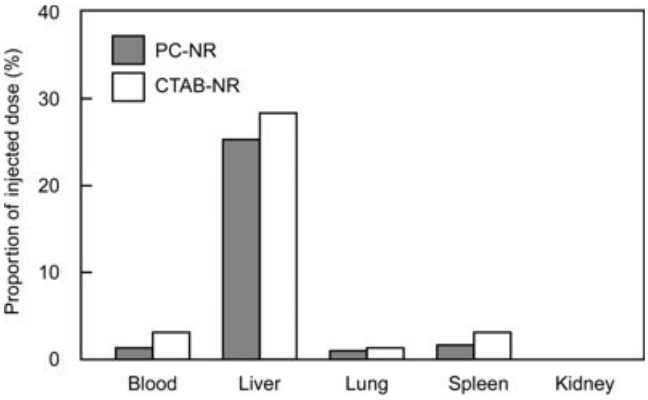

Figure 8.8 Biodistribution of PC-modified (PC-NR) and CTAB-stabilized (CTAB-NR) gold nanorods in mice after intravenous injection. The tissues were collected at 30 min after injection and lysed in aqua regia; quantities of gold ion in the lysates were quantified using inductively coupled plasma (ICP) mass spectrometry.

30 min, whereas most of the gold was detected in the liver, as in the case of the original gold nanorods stabilized with CTAB (Figure 8.9). Based on the formation of a stealth character, the modification of ligands such as RGD peptides and antibodies with gold nanorods will allow the development of targeted delivery systems [39–45].

8.4.2 *In Vitro* Bioimaging and Photothermal Ablation of Cells

In order to demonstrate the value of gold nanorods as medical nanodevices for both bioimaging and photothermal therapy, El-Sayed and colleagues investigated tumor imaging and photothermal therapy by combining near-IR light and gold nanorods as light scattering and photothermal agents in the *in vitro* system using the HaCaT, HOC and HSC cells (as described in Section 8.2.2) [46]. To do this, they prepared anti-EGFR antibody-modified gold nanorods and then observed specific binding in those malignant cell lines expressing EGFR, which showed strong light scattering from adsorbed nanorods on the cells. Irradiation with a CW laser at 800 nm led to damage of those cells bound with nanorods, which in turn indicated that gold nanorods were a candidate functional agent for dual imaging and the therapy of tumor cells. Cellular ablation specific to cells irradiated with a near-IR laser were also observed after binding of the PC-modified gold nanorods to the cell surface. By using focused laser light, it was found that the cells could be damaged one by one in a culture dish (Figure 8.10) [47]. Interestingly, the pulsed-laser irradiation induced a reshaping of the gold nanorods into spherical

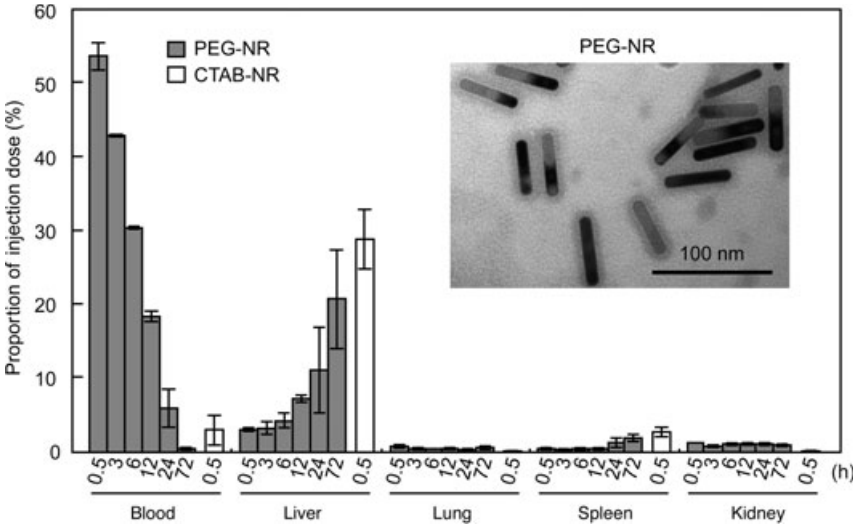

Figure 8.9 Biodistribution of PEG-modified gold nanorods (PG-NR) in mice after intravenous injection. Quantities of gold in the tissue samples were evaluated with ICP mass spectrometry at several time points after injection. The graph shows the biodistribution of PEG-modified gold nanorods at 0.5, 3, 6, 12, 24 and 72 h after injection, and of CTAB-stabilized gold nanorods (CTAB-NR) at 0.5 h after injection. The inset shows an electron micrograph of the PEG_{5000}-modified gold nanorods.

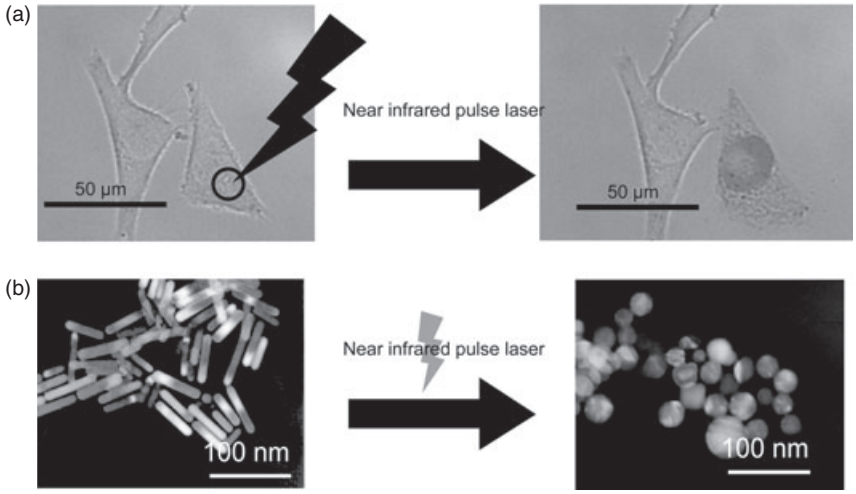

Figure 8.10 Photothermal damage of a cell mediated by focused laser irradiation and photothermal reshaping of gold nanorods. (a) PC-modified gold nanorods were added to HeLa cells, which were then irradiated with pulsed laser light (1064 nm, 10 Hz, 2 mJ per pulse, 2 min). Cellular damage was detected using Trypan blue dye to stain dead cells (dark region); (b) The shape of the gold nanorods was changed to spherical by irradiating with near-IR laser light.

nanoparticles, but as the reshaped particles showed no absorption in the near-IR region the successive laser irradiation did not affect the cells [48]. The photo-reshaping of gold nanorods would be expected to prove advantageous in preventing any unwanted cell damage following the destruction of target cells.

8.4.3 *In Vivo* Bioimaging

The gold nanorods excited at 830 nm in a laser scanning microscope produced strong two-photon luminescence (TPL) intensities [49, 50]. Wang *et al.* observed TPL of the gold nanorods inside cultivated cells [35], and in cells circulating in mouse ear blood vessels using a femtosecond Ti : Sapphire laser [34]. However, in order to detect TPL from the nanorods, it is necessary to use femtosecond laser light focused by the objective lens of the microscope. Consequently, this technique is not suitable for bioimaging of the whole human body, nor of a wide area of the body. In order to establish a convenient and speedy bioimaging system using gold nanorods, an attempt was made to use the absorption of near-IR light by the nanorods. Initially, an anesthetized mouse was placed backwards on a path of monochromatic light (900 nm) and the PEG-modified gold nanorods were injected intravenously. At the same time, near-IR images of the mouse were obtained using a CCD camera. Soon after the injection, brightness in the abdomen decreased drastically (Figure 8.11), indicating that the injected gold nanorods had spread to

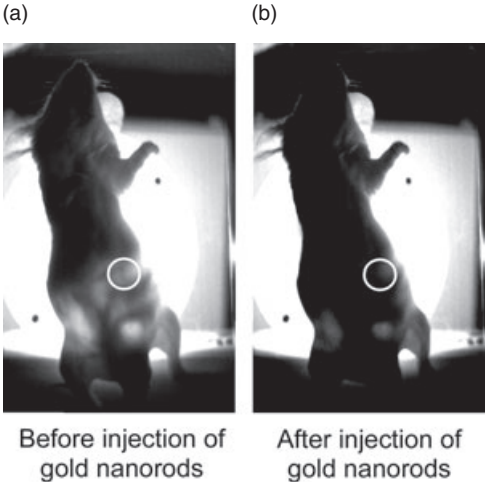

Figure 8.11 Transmitted near-IR light images of a mouse. The anesthetized mouse (ddY, 30–35 g, male) was placed in the path of near-IR light at 900 nm, and PEG-modified gold nanorods (300 µl of 3 m*M* Au atoms) were injected intravenously. The images of the mouse before injection (a) and at 3.6 s after injection (b) were captured using a CCD camera. The white circles indicate typical points at which changes could be clearly observed.

the entire body via the blood vessels, and that those nanorods present in the abdomen had obstructed transmittance of the near-IR light. The absorption of intravenously injected PEG-modified gold nanorods was directly monitored in the mouse abdomen using a spectrophotometer equipped with an integrating sphere. Absorbance at 900 nm from the gold nanorods was increased immediately after injection, and reached a plateau (Figure 8.12). The injection of PC-modified gold nanorods also caused a sharp increase in absorbance at 900 nm, but this then decreased single-exponentially with a half-life of 1.3 min. Changes in the SP bands were seen to depend on the surface character of the gold nanorods. It is possible that this monitoring system could be constructed using a cheaper light-emitting diode (LED) light source and CCD camera. Then, by combining this technique with tomography it would be possible to construct a simple and easy-to-use diagnostic system, using gold nanorods as a contrast agent.

Photoacoustic imaging is a new bioimaging technique which is based on the use of laser-generated ultrasound, and combines the high contrast of optical methods with the high special resolution of ultrasound [51, 52]. Gold nanorods were applied as a contrast agent for photoacoustic imaging by Eghtedari *et al.*, who injected the gold nanorods into nude mice and then succeeded in detecting the injected nanorods using a single-channel acoustic transducer (Figure 8.13) [53]. These results suggested that photoacoustic imaging could be used for the *in vivo* detection of gold nanorods at low concentrations, and that the nanoparticles could be engineered to enhance the diagnostic power of photoacoustic imaging.

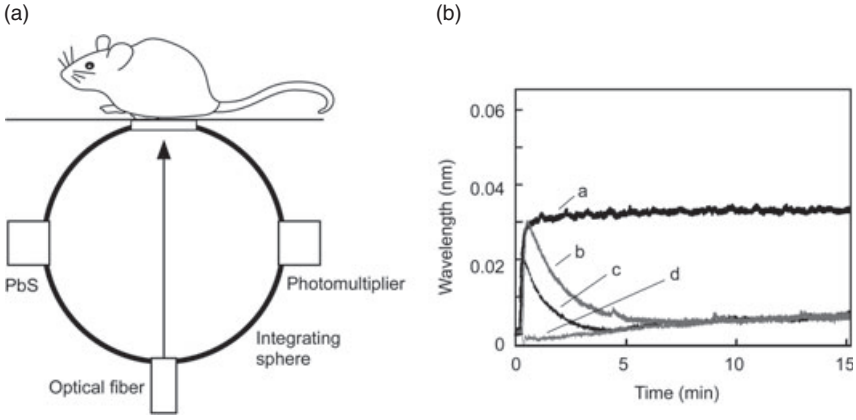

Figure 8.12 (a) Schematic representation of the spectroscopic analysis of gold nanorods in a mouse. The anesthetized mouse was placed on a port of an integrating sphere; monochromatic light from a spectrophotometer was then introduced into the mouse abdomen through optical fibers. Scattered light from the mouse abdomen was detected using a photomultiplier and PbS detector, and processed via the spectrophotometer; (b) Real-time observation of absorption at 900 nm in mice. The curves are indicated as: a, PEG-modified gold nanorods; b, PC-modified gold nanorods; c, original gold nanorods stabilized with CTAB; d, 5% glucose solution as control.

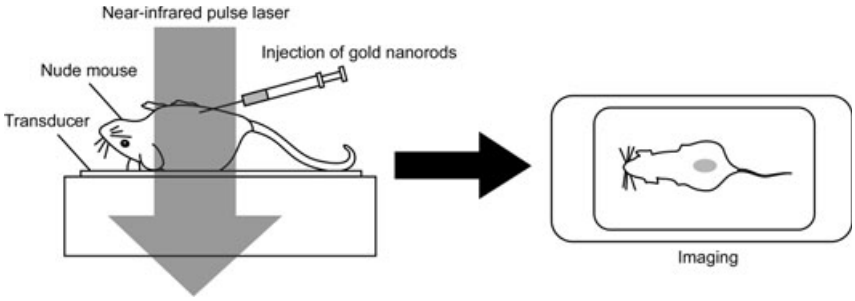

Figure 8.13 Schematic representation of the *in vivo* detection of subcutaneously injected gold nanorods, using optoacoustic imaging.

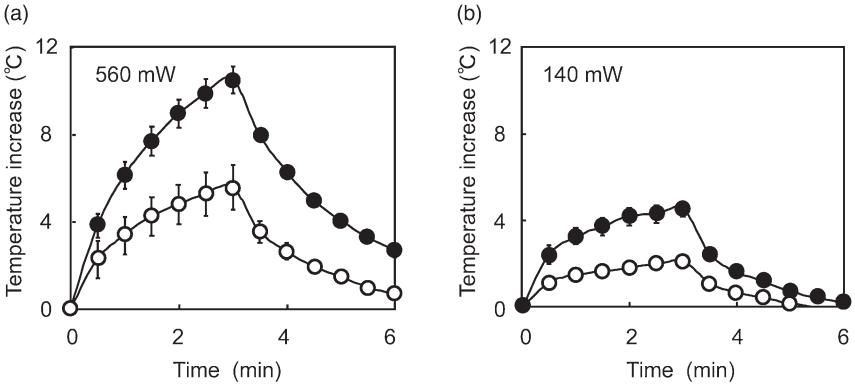

Figure 8.14 Temperature increases in muscle due to the photothermal effect of gold nanorods. The muscle was irradiated for 3 min with (a) 560 mW and (b) 140 mW of near-IR light after intramuscular injection of the gold nanorods. Temperatures increases at the irradiation site were monitored using an IR thermometer. ●, PEG_{5000}-modified gold nanorod injection; ○, 5% glucose injection as a control.

8.4.4
Photothermal Therapy

After having delivered the gold nanorods to targeted tissues, near-IR laser irradiation can cause damage to the tissues as a result of the photothermally produced heat. Since a photothermal therapeutic system using gold nanoshells has been reported previously [25, 26], the original protocol in mice was followed whereby, after injecting the PEG-modified gold nanorods, the injection site was irradiated using near-IR laser light and tissue damage at the irradiation sites then evaluated. The gold nanorods were injected into a hind-limb muscle of a mouse, after which – during near-IR pulsed-laser irradiation (Nd:YAG 1064 nm, 560 mW, 20 Hz, 3 min, ~3 mm beam diameter) – an 11 °C increase in temperature was detected at the irradiation site, while an increase of 5 °C was observed after 5% glucose injection into the muscle (Figure 8.14). The temperature increase in

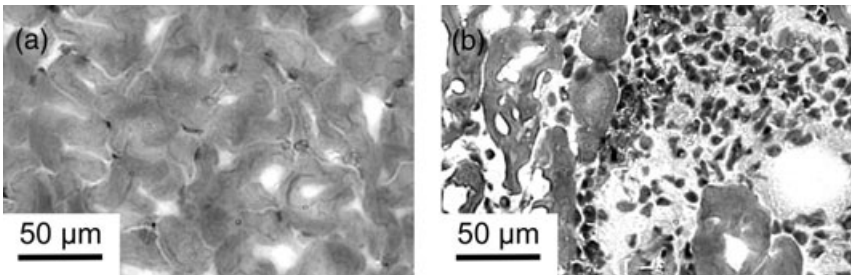

Figure 8.15 Hematoxylin and eosin staining of muscle tissues. (a) After injection with PEG-modified gold nanorods; (b) After injection with PEG-modified gold nanorods followed by continuous-wave laser irradiation (Nd:YAG 1064 nm, 280 mW, 20 Hz, 3 min).

control mice originated from the water in the tissue, which was heated by the irradiation (water has a moderate absorbance at 1064 nm) [24]. The contrast due to the heating effect could be improved if laser light of wavelength 700–900 nm were to be used, as this region corresponds to a band between the absorptions of hemoglobin and water. For the evaluation of tissue damage at the irradiation site, the muscle at the injection site was removed, sectioned, and stained with hematoxylin and eosin (H&E). Only the case of a combination of injected gold nanorods and laser irradiation (280 mW for 3 min) showed any significant tissue damage (Figure 8.15).

The next step was to perform photothermal cancer therapy in tumor-bearing mice. Initially, the gold nanorods were injected directly into a tumor of 6–8 mm diameter, after which the tumor was irradiated with near-IR pulsed laser light (280 mW for 3 min). In order to confirm the therapeutic effect of the photothermal system, tumor growth was measured after the treatment (Figure 8.16). Only in the case where there was both injection of gold nanorods and irradiation with laser light, was any significant suppression of tumor growth observed, whereas tumor growth in the control mice (i.e. mice injected with gold nanorods or treated with laser irradiation) showed no difference from nontreated mice. These results indicated that the tumor damage was due to a photothermal effect of the gold nanorods. Intravenous injection of the gold nanorods and irradiation with laser light showed a moderate effect that was weaker than in the case of direct injection of the gold nanorods. The quantity of gold nanorods in the tumor after intravenous injection may not be adequate to show a stronger antitumor effect than would the direct injection of gold nanorods into the tumor.

8.4.5
Drug Release System Responding to Laser Irradiation

The combination of a thermoresponsive polymer and photothermal device allows the development of a photoresponsive polymer composite that is able to release

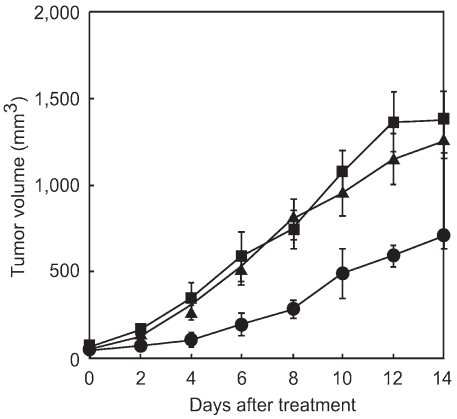

Figure 8.16 Tumor growth after photothermal treatment. BALB/c mice with a subcutaneous homograft of B16 melanoma cells were injected with PEG-modified gold nanorods and continuous-wave laser irradiation (750 mW, 3 min). ●, direct injection of gold nanorods followed by laser irradiation; ■, direct injection of 5% glucose followed by laser irradiation; ▲, nontreated mice.

drugs on demand under the control of irradiating light from outside the body. Previously, West and coworkers prepared millimeter-sized *N*-isopropylacrylamide (NIPAM)-*co*-acrylamide gels containing gold nanoshells, which could convert the energy of the near-IR light to heat, successfully causing the gel to shrink [54, 55]. Gorelikov *et al.* also succeeded in the near-IR-driven shrinking of hydrogels [56] by incorporating CTAB-stabilized gold nanorods into submicron-sized spheres of a NIPAM-*co*-acrylic acid hydrogel by electrostatic interaction, and then using near-IR irradiation to successfully shrink the gel. Recently, we succeeded in dispersing PEG-modified gold nanorods in NIPAM gel [57]; after preparing a microcapillary gel to analyze the phase-transition manner of the gel in detail, shrinkage of the gel was monitored microscopically. Near-IR CW laser irradiation (Nd : YVO4, 1064 nm, 490 mW) then resulted in shrinkage of the gel that began with the formation of a 'waist' around the irradiation spot, followed by growth of the waist along the axial direction of the gel (Figure 8.17). Furthermore, a composite gel was prepared containing the model drug (rhodamine-labeled dextran) to demonstrate the light-controlled drug release system using this gel. When the gel containing the drug was irradiated with a near-IR laser light, a rapid release of the drug was observed under fluorescence microscopy (Figure 8.18).

As the gel composite prepared in the microcapillary mold could not be directly used *in vivo*, the next step was to prepare NIPAM-coated gold nanorods (Figure 8.19). A dispersed light-responsive and nanosized gel composite of this type is injectable not only site-directly but also systemically. In order to coat the surface of the gold nanorods with NIPAM gel, PEG-modified gold nanorods were first coated with silica gel using tetraethoxysilane. After modifying with a metacryl group on the surface using 3-metacryloxypropyltrimethoxysilane, NIPAM gel

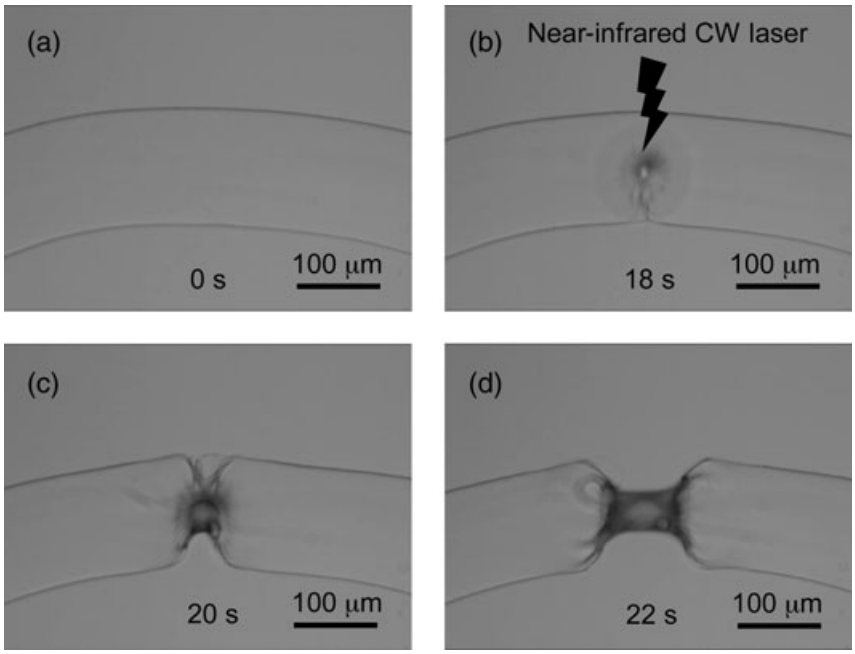

Figure 8.17 The shrinking process of a thermosensitive gel containing gold nanorods. NIPAM gel was prepared in the presence of PEG-modified gold nanorods in a microcapillary. The center of the gel was irradiated with focused continuous-wave laser light (490 mW), after which the shrinking process was observed microscopically.

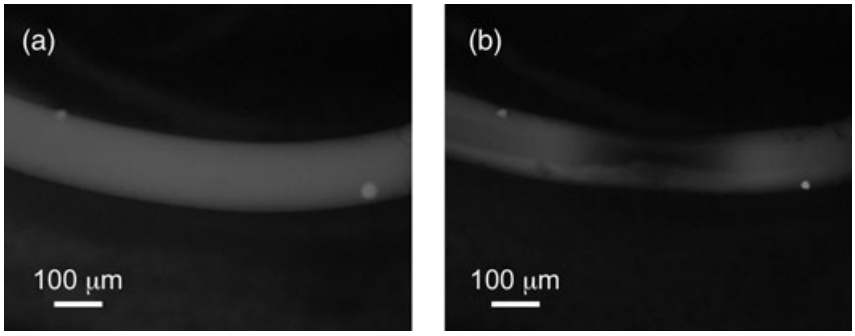

Figure 8.18 Fluorescence microscopy images of a gel containing gold nanorods and rhodamine-modified dextran. (a) Before laser irradiation, the fluorescence of rhodamine was detected uniformly in the gel; (b) After continuous-wave laser irradiation (750 mW), the release of rhodamine was observed from the irradiated site.

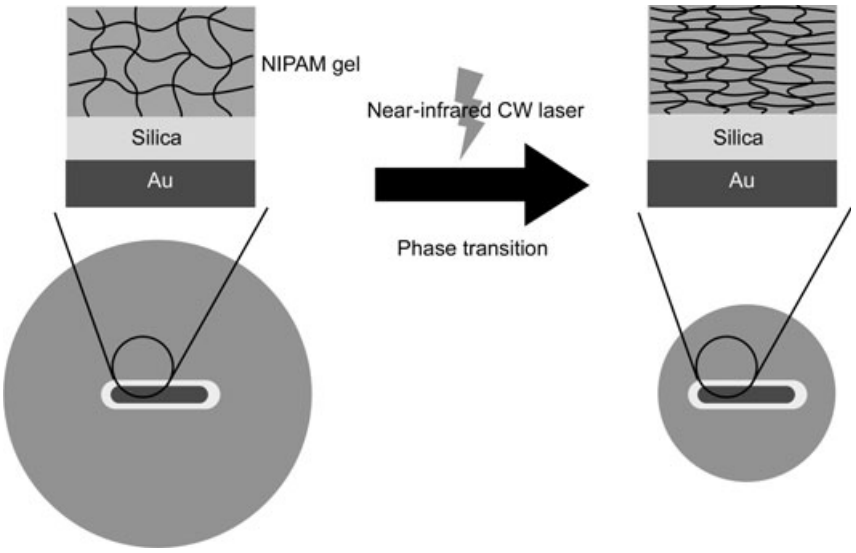

Figure 8.19 Schematic representation of the shrinking process of NIPAM gel-modified gold nanorods.

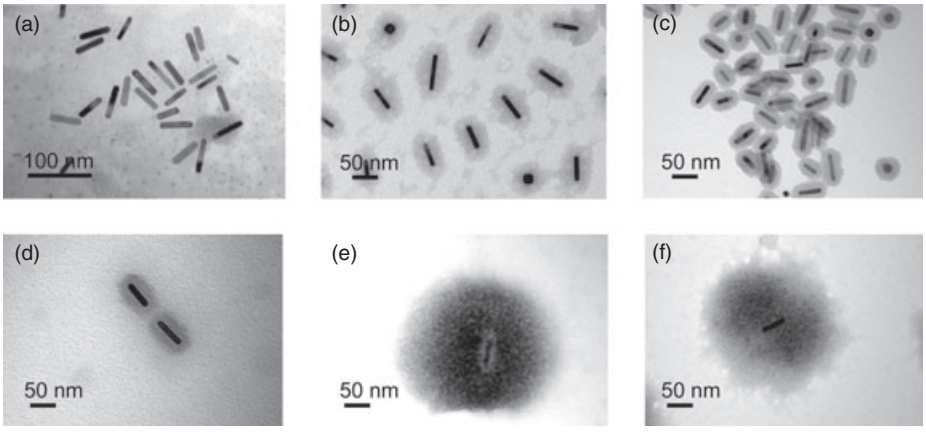

Figure 8.20 Electron microscopy images of modified gold nanorods. (a) CTAB-stabilized gold nanorods; (b) PEG_{20000}-modified gold nanorods; (c) silica-modified gold nanorods; (d) metacryl group-modified gold nanorods; (e) NIPAM gel-modified gold nanorods; (f) NIPAM gel-modified gold nanorods treated with HF to remove the silica layer.

crosslinked with *N,N′*-methylene-bisacrylamide was synthesized from the metacryl groups (Figure 8.20). The sizes of the NIPAM-modified gold nanorods were decreased by irradiating with near-IR laser light (CW diode laser, 807 nm, 1 W) (Figure 8.21), and the size of the change was reversible. These results suggested that a light-responsive drug delivery and release system could be established by

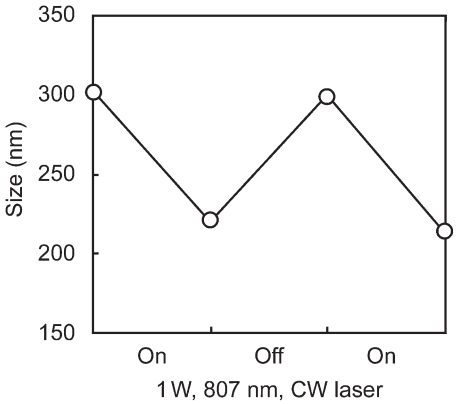

Figure 8.21 Size change of NIPAM-modified gold nanorods. The modified gold nanorods were irradiated with continuous-wave laser light (diode laser, 807 nm, 1 W), after which the sizes were monitored. The size change was seen to be reversible.

using functional nanodevices composed of a thermoresponsive polymer and gold nanorods.

8.4.6 Controller of Gene Expression

Gold nanorods can be used to control gene expression by using their photothermal effect. To demonstrate this property, Chen *et al.* prepared gold nanorods attached to a PCR-amplified DNA fragment encoding enhanced green fluorescence protein (EGFP) for the remote control of gene expression in cultivated cells. After irradiating with femtosecond near-IR laser light, the gold nanorods underwent a change in shape to a spherical form, resulting in a release of the plasmid DNA (Figure 8.22). The complex of gold nanorods and plasmid DNA was transfected into HeLa cells, after which a limited area was irradiated with femtosecond near-IR laser light. As a result, induced GFP expression was observed specifically in cells that were locally exposed to near-IR laser irradiation [58]. The remote control of gene expression limited to a specific area with external stimulation is a key to successful gene therapy; indeed, gold nanorods are likely to be powerful tools for gene therapy during the next generation of these investigations.

A complex was also constructed between the PC-modified gold nanorods, the surface charge of which was positive (zeta-potential = +15 mV), and negatively charged plasmid DNA. After confirming that all of the DNA was bound to the gold nanorods (by using agarose gel electrophoresis), the complex was irradiated with near-IR laser light (Nd : YAG laser, 1064 nm, 160 mJ per pulse, 10 Hz, 120 s). The DNA subsequently released from the nanorods was detected by agarose gel

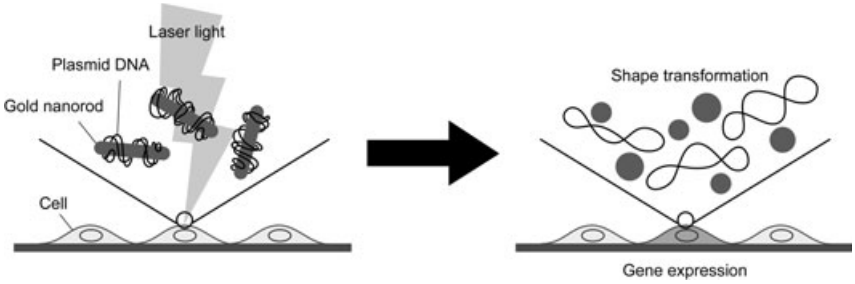

Figure 8.22 Schematic representation of the release of plasmid DNA from gold nanorods, mediated by a photothermal reshaping of the nanorods.

electrophoresis and by the assay of luciferase activity that expressed the plasmid DNA in a cell-free transcription and translation kit. Unfortunately, the efficiency of DNA release was very low, with only 1.2% of the plasmid DNA being released from the complex with the gold nanorods, while 0.5% of the plasmid DNA was active for gene expression [59]. These results indicated that half of the released DNA was inactive, in turn suggesting that photothermal damage of the DNA should be considered to optimize the conditions for controlling gene expression.

8.5
Other Anisotropic Gold Nanoparticles

Other recently reported examples of anisotropic gold nanoparticles include gold nanoprisms (triangles) [60–65] and tetrapods [66, 67]. In particular, gold nanoprisms have attracted much attention because they have strong surface plasmon bands at the near-IR light region, which suggests that they might be useful as contrast agents in near-IR light imaging, as a photosensitizer for photothermal therapy, and in drug delivery devices which respond to the near-IR light that can deeply penetrate tissues (as described above). However, most current studies focus on controlling the size and shape of nanoprisms by changing conditions such as seeding and the strength of the reducing agents [61–63]. By contrast, natural compounds have also been reported as effective reducing agents. For example, Sastry's group showed that an extract of the lemongrass plant (*Cymbopogon flexuosus*), when reacted with aqueous chloroaurate ions, yielded a high percentage of gold nanoprisms [60, 64]. Use of the extract of the *Aloe vera* plant is also effective as a reducing agent for preparing gold nanoprisms [65]. Modifications with functional molecules such as biocompatible molecules, ligands for targeted delivery and various drugs should spur developments in the use of gold nanoprisms in medical nanodevices.

8.6 Conclusions

Although, gold nanoparticles have a long history of use as medications, the scientific application of gold nanoparticles to medicine has commenced only during the past decade. In particular, the combination of photothermal effect and near-IR light that is able to penetrate deep into tissues has attracted much attention. Gold nanoparticles are both easy and inexpensive to prepare, and their surfaces may be modified with a variety of molecules. With regards to safety issues, metallic gold is inert under physiological conditions – that is, it demonstrates no acute liver or kidney toxicity, neither is any cytokine-related inflammatory response observed after local or systemic injection of biocompatible gold nanoparticles modified with hydrophilic polymers and natural lipids. By using the unique optical and chemical characteristics of gold nanoparticles, intelligent medical technology not only for diagnosis but also for minimally invasive therapy will be developed in the future. Finally, in order to achieve such a major undertaking, it is essential that research groups from a wide array of areas such as medicine, pharmacy, chemistry, physics and engineering should collaborate for the future success of this technology in applications to improve human health.

Acknowledgments

These studies were supported by a Grant-in-Aid for Exploratory Research (No. 18650124) and a Grant-in-Aid for Scientific Research (B) (No. 19300172) from the Japan Society for the Promotion of Science (JSPS), a Grant-in-Aid for Scientific Research in the Priority Area 'Molecular Nano Dynamics' (No. 17034049) from the Ministry of Education, Culture, Sports, Science and Technology (MEXT), and a Grant-in-Aid from PRESTO, Japan Science and Technology Corporation.

References

1 Hayat, M.A. (1989) *Colloidal Gold, Principles, Methods, and Applications*, Academic Press, San Diego, USA.
2 Mahdihassan, S. (1985) Cinnabar-gold as the best alchemical drug of longevity, called Makaradhwaja in India. *The American Journal of Chinese Medicine*, **13**, 93–108.
3 Mahdihassan, S. (1984) Tan, dinnabar, as drug of longevity prior to alchemy. *The American Journal of Chinese Medicine*, **12**, 50–4.
4 Richards, D.G., McMillin, D.L., Mein, E.A. and Nelson, C.D. (2002) Gold and its relationship to neurological/glandular conditions. *International Journal of Neuroscience*, **112**, 31–53.
5 Mukherjee, P., Bhattacharya, R., Patra, C.R. and Mukhopadhyay, D. (2007) Nanogold in cancer therapy and diagnosis, in *Nanotechnologies for the Life Sciences, Volume 7, Nanomaterials for Cancer Diagnosis* (ed. C.S.S.R. Kumar), Wiley-VCH Verlag GmbH, pp. 86–120.
6 Schmidt, G. (1992) Large clusters and colloids. Metals in the embryonic state. *Chemical Reviews*, **92**, 1709–27.

7 Rigobello, M., Folda, A., Baldoin, M., Scutari, G. and Bindoli, A. (2005) Effect of auranofin on the mitochondrial generation of hydrogen peroxide. Role of thioredoxin reductase. *Free Radical Research*, **39**, 687–95.

8 Kim, I., Jin, J., Lee, I. and Park, S. (2004) Auranofin induces apoptosis and when combined with retinoic acid enhances differentiation of acute promyelocytic leukaemia cells in vitro. *British Journal of Pharmacology*, **142**, 749–55.

9 Shaw, C.F., III (1999) Gold-based therapeutic agents. *Chemical Reviews*, **99**, 2589–600.

10 Han, G., Ghosh, P., De, M. and Rotello, V.M. (2007) Drug and gene delivery using gold nanoparticles. *NanoBiotechnology*, **3**, 40–5.

11 El-Sayed, I.H., Huang, X. and El-Sayed, M.A. (2005) Surface plasmon resonance scattering and absorption of anti-EGFR antibody conjugated gold nanoparticles in cancer diagnosis: application in oral cancer. *Nano Letters*, **5**, 829–34.

12 El-Sayed, I.H., Huang, X. and El-Sayed, M.A. (2006) Selective laser photo-thermal therapy of epithelial carcinoma using anti-EGFR antibody conjugated gold nanoparticles. *Cancer Letters*, **239**, 129–35.

13 Kattumuri, V., Vijaya, K., Katti, S., Bhaskaran, E.J., Boote, S.W., Casteel, G.M., Fent, D.J., Robertson, M., Chandrasekhar, R., Kannan, K. and Katti, V. (2007) Gum arabic as a phytochemical construct for the stabilization of gold nanoparticles: *in vivo* pharmacokinetics and X-ray-contrast-imaging studies. *Small*, **3**, 333–41.

14 Liu, Y., Shipton, M.K., Ryan, J., Kaufman, E.D., Franzen, S. and Feldheim, D.L. (2007) Synthesis, stability, and cellular internalization of gold nanoparticles containing mixed peptide-poly(ethylene glycol) monolayers. *Analytical Chemistry*, **79**, 2221–9.

15 Gannon, C.J., Patra, C.R., Bhattacharya, R., Mukherjee, P. and Curley, S.A. (2008) Intracellular gold nanoparticles enhance non-invasive radiofrequency thermal destruction of human gastrointestinal cancer cells. *Journal of Nanobiotechnology*, **6**, 2.

16 Kogan, M.J., Bastus, N.G., Amigo, R., Grillo-Bosch, D., Araya, E., Turial, A., Labarta, A., Giralt, E. and Puntes, V.F. (2006) Nanoparticle-mediated local and remote manipulation of protein aggregation. *Nano Letters*, **6**, 110–15.

17 Mukherjee, P., Bhattacharya, R., Bone, N., Lee, Y.K., Patra, C.R., Wang, S., Lu, L,, Secreto, C., Banerjee, P.C., Yaszemski, M.J., Kay, N.E. and Mukhopadhyay, D. (2007) Potential therapeutic application of gold nanoparticles in B-chronic lymphocytic leukemia (BCLL): enhancing apoptosis. *Journal of Nanobiotechnology*, **5**, 1–13.

18 Ohsaki, M., Okuda, T., Wada, A., Hirayama, T., Niidome, T. and Aoyagi, H. (2002) *In vitro* gene transfection using dendritic poly(L-lysine). *Bioconjugate Chemistry*, **13**, 510–17.

19 Okuda, T., Kidoaki, S., Ohsaki, M., Koyama, Y., Yoshikawa, K., Niidome, T. and Aoyagi, H. (2003) Time-dependent complex formation of dendritic poly(L-lysine) with plasmid DNA and correlation with *in vitro* transfection efficiencies. *Organic and Biomolecular Chemistry*, **1**, 1270–3.

20 Kawano, T., Okuda, T., Aoyagi, H. and Niidome, T. (2004) Long circulation of intravenously administered plasmid DNA delivered with dendritic poly(L-lysine) in the blood flow. *Journal of Controlled Release*, **99**, 329–37.

21 Niidome, T., Nakashima, K., Takahashi, H. and Niidome, Y. (2004) Preparation of primary amine-modified gold nanoparticles and their transfection ability into cultivated cells. *Chemical Communications*, 1978–9.

22 Kawano, T., Yamagata, M., Takahashi, H., Niidome, Y., Yamada, S., Katayama, Y. and Niidome, T. (2006) Stabilizing of plasmid DNA *in vivo* by PEG-modified cationic gold nanoparticles and the gene expression assisted with electrical pulses. *Journal of Controlled Release*, **111**, 382–9.

23 Oldenburg, S.J., Jackson, J.B., Westcott, S.L. and Halas, N.J. (1999) Infrared extinction properties of gold nanoshells. *Applied Physics Letters*, **75**, 2897–9.

24 Weissleder, R. (2001) A clearer vision for *in vivo* imaging. *Nature Biotechnology*, **19**, 316–17.

25 Hirsch, L.R., Stafford, R.J., Bankson, J.A., Sershen, S.R., Rivera, B., Price, R.E., Hazle, J.D., Halas, N.J. and West, J.L. (2003) Nanoshell-mediated near-infrared thermal therapy of tumors under magnetic resonance guidance. *Proceedings of the National Academy of Sciences of the United States of America*, **23**, 13549–54.

26 O'Neal, D.P., Hirsch, L.R., Halas, N.J., Payne, J.D. and West, J.L. (2004) Photo-thermal tumor ablation in mice using near infrared-absorbing nanoparticles. *Cancer Letters*, **2**, 171–6.

27 Loo, C., Lowery, A., Halas, N., West, J. and Drezek, R. (2005) Immunotargeted nanoshells for integrated cancer imaging and therapy. *Nano Letters*, **4**, 709–11.

28 Yu, Y.-Y., Chang, S.-S., Lee, C.-L. and Wang, C.R.C. (1997) Gold nanorods: electrochemical synthesis and optical properties. *Journal of Physical Chemistry B*, **101**, 6661–4.

29 Link, S., Mohamed, M.B. and El-Sayed, M.A. (1999) Simulation of the optical absorption spectra of gold nanorods as a function of their aspect ratio and the effect of the medium dielectric constant. *Journal of Physical Chemistry B*, **103**, 3073–7.

30 Li, C.-Z., Male, K.B., Hrapovic, S. and Luong, J.H.T. (2005) Fluorescence properties of gold nanorods and their application for DNA biosensing. *Chemical Communications*, 3924–6.

31 Eustis, S. and El-Sayed, M. (2005) Aspect ratio dependence of the enhanced fluorescence intensity of gold nanorods: experimental and simulation study. *Journal of Physical Chemistry B*, **109**, 16350–6.

32 Alekseeva, A.V., Bogatyrev, V.A., Dykman, L.A., Khlebtsov, B.N., Trachuk, L.A., Melnikov, A.G. and Khlebtsov, N.G. (2005) Preparation and optical scattering characterization of gold nanorods and their application to a dot-immunogold assay. *Applied Optics*, **44**, 6285–95.

33 Zhu, J., Huang, L., Zhao, J., Wang, Y., Zhao, Y., Hao, L. and Lu, Y. (2005) Shape dependent resonance light scattering properties of gold nanorods. *Materials Science and Engineering: B*, **121**, 199–203.

34 Wang, H., Huff, T.B., Zweifel, D.A., He, W., Low, P.S., Wei, A. and Cheng, J.-X. (2005) *In vitro* and *in vivo* two-photon luminescence imaging of single gold nanorods. *Proceedings of the National Academy of Sciences of the United States of America*, **102**, 15752–6.

35 Huff, T.B., Hansen, M.N., Zhao, Y., Cheng, J.-X. and Wei, A. (2007) Controlling the cellular uptake of gold nanorods. *Langmuir*, **23**, 1596–9.

36 Connor, E.E., Mwamuka, J., Gole, A., Murphy, C.J. and Wyatt, M.D. (2005) Gold nanoparticles are taken up by human cells but do not cause acute cytotoxicity. *Small*, **1**, 325–7.

37 Takahashi, H., Niidome, Y., Niidome, T., Kaneko, K., Kawasaki, H. and Yamada, S. (2006) Modification of gold nanorods using phosphatidylcholine to reduce cytotoxicity. *Langmuir*, **22**, 2–5.

38 Niidome, T., Yamagata, M., Okamoto, Y., Akiyama, Y., Takahashi, H., Kawano, T., Katayama, Y. and Niidome, Y. (2006) PEG-modified gold nanorods with a stealth character for *in vivo* applications. *Journal of Controlled Release*, **114**, 343–7.

39 Quintana, A., Raczka, E., Piehler, L., Lee, I., Myc, A., Majoros, I., Patri, A.K., Thomas, T., Mulé, J. and Baker, J.R., Jr (2002) Design and function of a dendrimer-based therapeutic nanodevice targeted to tumor cells through the folate receptor. *Pharmaceutical Research*, **19**, 1310–16.

40 Myc, A., Majoros, I.J., Thomas, T.P. and Baker, J.R., Jr (2007) Dendrimer-based targeted delivery of an apoptotic sensor in cancer cells. *Biomacromolecules*, **8**, 13–18.

41 Arap, W., Pasqualini, R. and Rouslahti, E. (1998) Cancer treatment by targeted drug delivery to tumor vasculature in a mouse model. *Science*, **279**, 377–80.

42 Shadidi, M. and Sioud, M. (2003) Selective targeting of cancer cells using synthetic peptides. *Drug Resistance Updates*, **6**, 363–71.

43 Dharap, S.S., Wang, Y., Chandna, P., Khandare, J.J., Qiu, B., Gunaseelan, S., Sinko, P.J., Stein, S., Farmanfarmaian, A. and Minko, T. (2005) Tumor-specific targeting of an anticancer drug delivery system by LHRH peptide. *Proceedings of the National Academy of Sciences of*

the United States of America, **102**, 12962–7.

44 Schrama, D., Reisfeld, R.A. and Becker, J.C. (2006) Antibody targeted drugs as cancer therapeutics. *Nature Reviews Drug Discovery*, **5**, 147–59.

45 Shukla, R., Thomas, T.P., Peters, J.L., Desai, A.M., Kukowska-Latallo, J., Patri, A.K., Kotlyar, A. and Baker, A.J.R., Jr (2006) HER2 specific tumor targeting with dendrimer conjugated anti-HER2 mAb. *Bioconjugate Chemistry*, **17**, 1109–15.

46 Huang, X., El-Sayed, I.H., Qian, W. and El-Sayed, M.A. (2006) Cancer cell imaging and photothermal therapy in the near-infrared region by using gold nanorods. *Journal of the American Chemical Society*, **128**, 2115–20.

47 Takahashi, H., Niidome, T., Nariai, A., Niidome, Y. and Yamada, S. (2006) Gold nanorod-sensitized cell death: Microscopic observation of single living cells irradiated by pulsed near-infrared laser light in the presence of gold nanorods. *Chemistry Letters*, **35**, 500–1.

48 Takahashi, H., Niidome, T., Nariai, A., Niidome, Y. and Yamada, S. (2006) Photothermal reshaping of gold nanorods prevents further cell death. *Nanotechnology*, **17**, 4431–5.

49 Mohamed, M.B., Volkov, V., Link, S. and El-Sayed, M.A. (2000) The "lightning" gold nanorods: fluorescence enhancement of over a million compared to the gold metal. *Chemical Physics Letters*, **317**, 517–23.

50 Imura, K., Nagahara, T. and Okamoto, H. (2004) Plasmon mode imaging of single gold nanorods. *Journal of the American Chemical Society*, **126**, 12730–1.

51 Xu, M. and Wang, L.V. (2006) Photoacoustic imaging in biomedicine. *Review of Scientific Instruments*, **77**, 041101.

52 Allen, T.J. and Beard, P.C. (2006) Pulsed near-infrared laser diode excitation system for biomedical photoacoustic imaging. *Optics Letters*, **31**, 3462–4.

53 Eghtedari, M., Oraevsky, A., Copland, J.A., Kotov, N.A., Conjusteau, A. and Motamedi, M. (2007) High sensitivity of *in vivo* detection of gold nanorods using a laser optoacoustic imaging system. *Nano Letters*, **7**, 1914–18.

54 Sershen, S.R., Westcott, S.L., Halas, N.J. and West, J.L. (2000) Temperature-sensitive polymer-nanoshell composites for photothermally modulated drug delivery. *Journal of Biomedical Materials Research*, **51**, 293–8.

55 Sershen, S.R., Westcott, S.L., West, J.L. and Halas, N.J. (2001) An opto-mechanical nanoshell-polymer composite. *Applied Physics B–Lasers and Optics*, **73**, 379–81.

56 Gorelikov, I., Field, L.M. and Kumacheva, E. (2004) Hybrid microgels photoresponsive in the near-infrared spectral range. *Journal of the American Chemical Society*, **126**, 15938–9.

57 Shiotani, A., Mori, T., Niidome, T., Niidome, Y. and Katayama, Y. (2007) Stable incorporation of gold nanorods into N-isopropylacrylamide hydrogels and their rapid shrinkage induced by near-IR laser irradiation. *Langmuir*, **23**, 4012–18.

58 Chen, C.-C., Lin, Y.-P., Wang, C.-W., Tzeng, H.-C., Wu, C.-H., Chen, Y.-C., Chen, C.-P., Chen, L.-C. and Wu, Y.-C. (2006) DNA Gold nanorod conjugates for remote control of localized gene expression by near infrared irradiation. *Journal of the American Chemical Society*, **128**, 3709–15.

59 Horiguchi, Y., Niidome, T., Yamada, S., Nakashima, N. and Niidome, Y. (2007) Expression of plasmid DNA released from DNA conjugates of gold nanorods. *Chemistry Letters*, **36**, 952–3.

60 Shankar, S.S., Rai, A., Ankamwar, B., Singh, A., Sastry, A. and Ahmad, M. (2004) Biological synthesis of triangular gold nanoprisms, *Nature Materials*, **3**, 482–8.

61 Millstone, J.E., Park, S., Shuford, K.L., Qin, L., Schatz, G.C. and Mirkin, C.A. (2005) Observation of a quadrupole plasmon mode for a colloidal solution of gold nanoprisms. *Journal of the American Chemical Society*, **127**, 5312–13.

62 Ah, C.S., Yun, Y.J., Park, H.J., Kim, W.-J., Ha, D.H. and Yun, W.S. (2005) Size-controlled synthesis of machinable single crystalline gold nanoplates. *Chemistry of Materials*, **17**, 5558–61.

63 Millstone, J.E., Metraux, G.S. and Mirkin, C.A. (2006) Controlling the edge length of gold nanoprisms via a seed-mediated

approach. *Advanced Functional Materials*, **16**, 1209–14.

64 Singh, A., Chaudhari, M. and Sastry, M. (2006) Construction of conductive multilayer films of biogenic triangular gold nanoparticles and their application in chemical vapour sensing. *Nanotechnology*, **17**, 2399–405.

65 Chandran, S.P., Chaudhary, M., Pasricha, R., Ahmad, A. and Sastry, M. (2006) Synthesis of gold nanotriangles and silver nanoparticles using *Aloe vera* plant extract. *Biotechnology Progress*, **22**, 577–83.

66 Sau, T.K. and Murphy, C.J. (2004) Room temperature, high-yield synthesis of multiple shapes of gold nanoparticles in aqueous solution. *Journal of the American Chemical Society*, **126**, 8648–9.

67 Hao, E., Bailey, R.C., Schatz, G.C., Hupp, J.T. and Li, S. (2004) Synthesis and optical properties of "branched" gold nanocrystals. *Nano Letters*, **4**, 327–30.

9
Approaches to Synthesis and Characterization of Spherical and Anisotropic Palladium Nanomaterials

Ruel G. Freemantle, Minghong Liu, Wen Guo and Sherine O. Obare

9.1
Introduction

Palladium (Pd) is among the most widely used transition metals in industrial applications. Catalysis has been by far the most common use for palladium, with carbon–carbon coupling reactions such as the Stille reaction, Suzuki reaction, Heck reaction and hydrogenation reactions being amongst the most prominent. More recently, palladium has also been found to play a fundamental role in several processes related to the life sciences. These applications have included its use as a catalyst to manufacture pharmaceuticals and agricultural herbicides [1], in the degradation of harmful environmental pollutants [2, 3], and as a sensor [4] for the detection of various analytes. While the uses of palladium are extensive, there remain several additional applications yet to be uncovered as the metal is reduced to the nanoscale.

The pioneering studies of Ostwald [5] and Turkevitch [6] have provided a better understanding of the nucleation, growth and agglomeration processes of metallic nanoparticles. This has led to substantial progress towards the development of synthetic procedures to produce size-controlled Pd nanoparticles. Catalysis – a significant application of palladium particles – involves only surface atoms, which is directly related to the particle size. Thus, controlling particle size is of paramount importance for catalytic applications. As the particle size decreases, the relative number of surface atoms increases, and the activity increases. In many instances, the turnover frequency (TOF; i.e. the activity per surface atom) in palladium-catalyzed reactions increases as the particle size decreases, this being due to favorable changes in the electronic properties of the surface atoms. As advancements have been obtained in the synthesis of shape-controlled palladium nanoparticles, such progress has opened new avenues for the investigation of structure–property relationships of palladium nanoparticles. The quantum size effects associated with the specific shapes of these nanometer-sized particles may exhibit unique electronic, magnetic, optical, mechanical or thermal properties suitable for a wide range of applications. Several characterization techniques have been employed to

Metallic Nanomaterials Vol. 1. Edited by Challa S. S. R. Kumar

ISBN: 978-3-527-32151-3

elucidate the size, shape, topography and morphology of the nanostructures. Understanding the differences in the properties of isotropic and anisotropic nanoparticles has been made possible through elaborate synthetic and characterization methods.

In this chapter we describe the synthetic procedures that have been developed to create spherical and anisotropic palladium nanostructures with controlled size and shape. A discussion of the characterization techniques used to study both the chemical and physical properties of these particles is included. Finally, some details will be provided on the applications of palladium nanoparticles as they relate to the life sciences.

9.2 Synthesis

Bönnemann [7] showed that a metal salt, a stabilizer and a reducing agent were required to form metallic particles according to the equation:

$$MX_n(NR_4)_m + (n-m)\mathrm{Red} \rightarrow M_{NP} + (n-m)\left(\mathrm{Red}^+X^-\right) + m\left(NR_4^+X^-\right) \qquad (9.1)$$

where M represents a metal (from Groups 8–10), X is Cl or Br, R is an alkyl group and Red is an effective reducing agent.

Reduction of the metal salt initiates the nucleation and growth processes of the nanoparticles [8]. By carefully controlling the choice of metal salt, reducing agent and stabilizer, this method has been manipulated to obtain palladium particles with nanoscale dimensions and controlled size and shape. The stabilizer not only prevents the particles from growing uncontrollably and maintaining uniformity but can also serve as a template for shape-control of the nanoparticles. In some cases the stabilizer may play the role of both reducing agent and stabilizer. In the following section we discuss some of the most significant advances towards the synthesis of Pd nanoparticles using wet-chemical preparation methods.

9.2.1 Synthesis of Isotropic Palladium Nanoparticles

Although several reports exist describing a variety of synthetic approaches for isotropic palladium nanoparticles, a major challenge exists in the ability to produce well-defined and monodisperse Pd nanoparticles. For wet-chemical methods used in the preparation of palladium nanoparticles, both organic and inorganic Pd compounds have been used as precursors. The oxidation state of the Pd compounds largely dictates the reaction conditions under which the synthetic procedure will ensue. For example, the decomposition of zerovalent organometallic Pd complexes is usually performed in an air-free environment with well-controlled

reaction conditions. For Pd salts with oxidation states of (II) or (IV), a reducing agent must be used. The suitability of a precursor is also jointly considered with the choice of stabilizing and reducing agent, as all these components must be appreciably soluble in the solvent applied. Among the most popular sources of Pd used are palladium(II) acetate ($Pd(C_2H_3O_2)_2$), the water-soluble disodium tetrachloropalladate(II) (Na_2PdCl_4), and potassium hexachloropalladate(IV) (K_2PdCl_6). Colloidal palladium has also been successfully fabricated using palladium(II) chloride ($PdCl_2$), tetra amine palladium (II) chloride monohydrate ($Pd(NH_3)_4Cl_2 \cdot H_2O$), bis(acetonitrile)dichloropalladium(II) ($PdCl_2(CH_3CN)_2$) and tris-μ-[dibenzylideneacetone] dipalladium ($C_{51}H_{42}O_3Pd_2$ or $Pd_2(dba)_3$). Polymers, thiols, dendrimers, thioethers, phosphines, surfactants, DNA and RNA have all been used as stabilizers for spherical Pd nanoparticles. In the remainder of this section we describe the synthetic procedures developed using the above-mentioned stabilizers, and the requirements for the reaction conditions and resulting particle morphology.

9.2.1.1 Synthesis Using Polymer Stabilizers

In 1992, Henglein reported the first synthetic procedure for the generation of Pd colloids [9]. Here, $Pd(NH_3)_4Cl_2$ was reduced by γ-radiolysis in the presence of the polymer poly(ethyleneimine) (PEI) as a stabilizer. These studies provided a foundation that several research groups have followed and modified to obtain Pd nanoparticles of desired sizes.

Miyake and coworkers developed a procedure to synthesize Pd nanoparticles with a narrow size distribution using the polymer poly(*N*-vinyl-2-pyrrolidone) (PVP) as a stabilizer [10]. In a typical reaction, the palladium precursor H_2PdCl_4 (synthesized from the reaction of $PdCl_2$ with HCl) and PVP were refluxed in an ethanol/water solution for 3 h in air to provide PVP-protected Pd nanoparticles. In this reaction, the alcohol serves as a reducing agent, while PVP functions as a stabilizer [11]. Variations in the amount of PVP relative to Pd^{2+} resulted in the ability to control the size of the Pd nanoparticles; thus, the higher the PVP concentration, the smaller the nanoparticles formed. In addition, higher PVP : Pd ratios resulted in narrower size distributions of the particles. Since the alcohol serves as a reducing agent, its selection is of great importance. Miyake demonstrated the use of three alcohols in order of increasing boiling point: methanol, ethanol and 1-propanol, and found that the alcohol with a higher boiling point produced nanoparticles of smaller diameter and narrow size distribution relative to when an alcohol with a low boiling point was used in the reaction. This trend was attributed to: (i) a lower reduction potential for ethanol and propanol relative to methanol; and (ii) the alcohol with the higher boiling point produced more Pd nuclei in a shorter period (thus, a fast reduction rate) and suppressed the particles growth. Furthermore, an increase in the reducing agent concentration increased the reduction rate and resulted in particles with, on average, smaller diameters. The particles prepared using this method had a narrow size distribution with average

diameters ranging from 1.7 to 3.0 nm. Since, by using the one-step approach, particles larger than 3.0 nm could not be obtained, Miyake developed a stepwise growth reaction in which the smaller nanoparticles were used as nucleation sites in three subsequent reactions. In the first growth reaction, H_2PdCl_4 was reacted with Pd-PVP in ethanol : water (2 : 3, v/v) followed by 3 h of refluxing. The resultant particles, which were up to 6 nm in diameter, were used in two subsequent reactions.

El-Sayed reported the synthesis of PVP-stabilized Pd nanoparticles [12] that had been synthesized using the precursor H_2PdCl_4, prepared by a reaction between $PdCl_2$ and HCl with ethanol as solvent. The PVP-Pd nanoparticles, prepared by refluxing H_2PdCl_2, water, PVP and HCl for 3 h, were uniform in size and had an average diameter of 2.1 ± 0.1 nm. Meier *et al.* [13] used star-shaped block copolymers with poly(ethylene oxide) (PEO) core and a poly (ε-caprolactone) (PCL) corona as templates for the synthesis of palladium nanoparticles. Palladium acetate in *N*,*N*′-dimethylformamide was reduced using sodium borohydride, and the resultant Pd nanoparticles were ~4 nm in diameter and uniform in size. A number of other reports have demonstrated the effectiveness of polymers in the synthesis of nanoparticles, their preparation being similar to the above descriptions [14–17]. In general, well-defined Pd nanoparticles can be produced in simple steps using polymers as stabilizers.

9.2.1.2 **Synthesis Using Thiol Stabilizers**

In 1999, Yee *et al.* described a one-phase synthesis procedure for Pd nanoparticles using octadecanethiol (ODT) as stabilizing ligands and tetrahydrofuran (THF) as the solvent [18]. Palladium (II) acetate trimer (Pd_3 $(C_2H_3O_2)_6$) was used to fulfill the need of having a precursor that was soluble in the same solvent as the stabilizing ligand and the reducing agent. ODT and the precursor were reacted in a 3 : 1 ratio; the result was a brown solution that turned black on addition of the reducing agent lithium triethylborohydride (superhydride). Advantageously, this reaction was carried out at an ambient temperature, and the Pd nanoparticles were purified by centrifugation. The particle size distribution was found to be broad (ranging from 1–4 nm), with an average of 2.25 nm. Later, Murray showed that Pd nanoparticles with a narrower size distribution could be prepared using hexanethiolate or dodecanethiolate ligands [19]. The resultant Pd particles were influenced by the thiol : Pd ratio used in the reaction mixture. For example, when a 1 : 1 ratio or less was used, metallic Pd(0) clusters were formed, yet when a 2 : 1 ratio was used either extremely small Pd(0) clusters or a form of Pd(II) alkanethiolate complex resulted. Others have also shown the effectiveness of thiols as stabilizers, although the ability to obtain monodisperse Pd nanoparticles remains unclear [20, 21].

Thiols have also been used in an elaborate fashion to prepare spherical, hollow Pd nanoparticles. Hyeon's group reported the fabrication of uniform hollow Pd spheres using thiols as stabilizers and silica particles as templates [22]. The template-assisted method used (see Scheme 9.1) first involves the synthesis of uniform silica spheres which were then refluxed with mercaptopropyltrimethoxysilane in toluene in order to functionalize the silica surface with mercaptopropylsilyl (MPS)

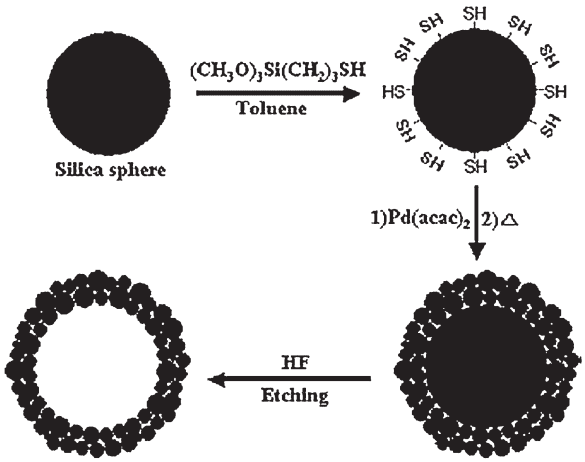

Scheme 9.1 Synthesis of hollow Pd nanoparticles.

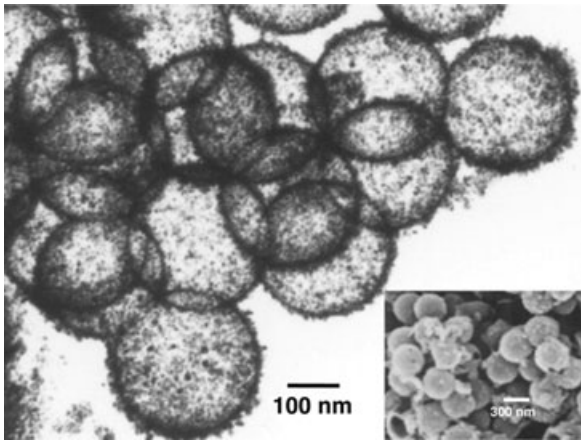

Figure 9.1 Transmission electron micrograph and scanning electron micrograph (inset) of hollow palladium spheres. Reproduced with permission from Ref. [22]; © 2002 American Chemical Society.

groups. Palladium acetylacetonate ($Pd(acac)_2$) was added, which absorbes to the MPS-functionalized silica spheres. The mixture was heated to 250 °C for 3 h, during which the decompositions product, carbon monoxide, serves as the reducing agent. Concentrated HF was then used to etch away the silica spheres, leaving ~300 nm-sized palladium spheres with a vacant central core (see Figure 9.1). Transmission electron microscopy (TEM) analysis revealed a palladium shell thickness of ~15 nm. Closer inspection revealed that the palladium shell was actually composed of palladium nanoparticles, approximately 10 nm in diameter. Hyeon and colleagues noted that the thickness of the metallic shell and the sphere

size could be controlled by altering the quantity of $Pd(acac)_2$ and varying the size of the silica spheres used.

9.2.1.3 Synthesis Using Dendrimer Stabilizers

Dendrimers, which were first reported in 1978 by Vögtle [23], have well-defined structures that make them attractive as stabilizers for nanoscale materials. In 1998, three groups reported independently the efficient use of dendrimers for the stabilization of metal nanoparticles [24–26]. A major advantage of using dendrimers is that the nanoparticles produced have narrow size distributions and thus have significant applications in catalysis, chemical sensing, magnetism and optoelectronics. Dendrimers are able to stabilize the nanoparticles either by encapsulating the metal within the dendrimer, or by having several dendrimers stabilize the nanoparticles. It is well known that both the interior and exterior functional groups of dendrimers can complex metal ions through various interactions, including covalent bonds, electrostatic interactions and complexation reactions [27–31]. The correct selection of the dendrimer structure for a specific synthetic procedure allows control of the nanoparticle size, composition and structure. It has also been shown that dendrimer generation does not affect the particle size; rather, the nanoparticle size can be controlled by varying the metal ion to dendrimer ratio [32]. Crooks and coworkers first described the synthesis of dendrimer-encapsulated Pd nanoparticles in 1999 [27], since which time several reports on the synthesis and characterization of dendrimer-encapsulated Pd nanoparticles have appeared [33–46]. In general, Pd nanoparticles are synthesized by complexing Pd^{2+} ions within the dendrimers and then reducing the composites to yield zerovalent metal particles within the dendrimer. This typically occurs in aqueous solution, although via exchange reactions the dendrimers can be driven to the organic phase. Fourth-generation, hydroxyl-terminated poly(amidoamine) (PAMAM) dendrimers have been used for this purpose, the palladium precursor typically being K_2PdCl_4. In a standard procedure, 0.1 ml of 10.0 m*M* aqueous K_2PdCl_4 and 25.0 ml of a 1.0 m*M* solution of G4-OH are added to 10 ml of water; this results in the encapsulation of about 40 Pd^{2+} ions per dendrimer (G4-OH$(Pd^{2+})_{40}$). Upon adding a tenfold excess of $NaBH_4$, the Pd^{2+} ions are reduced to Pd^0, thus providing G4-OH(Pd_{40}). Pd nanoparticles have also been synthesized within fourth-generation amine-terminated PAMAM dendrimers (G4-NH_2). Because of the tendency of Pd^{2+} ions to crosslink with the dendrimer amine groups, the particles aggregate and thus precipitate. One way to avoid such aggregation is to control the solution pH during the synthetic reaction. The reaction is most efficient between pH 2 and 5 because within this range the amine groups are protonated. An advantage of preparing nanoparticles in amine-terminated dendrimers is that, because the amines are highly reactive they can be easily functionalized or used as linkers to several surfaces, including polymers, biological molecules or various other surfaces. In order to overcome these pH limitations, Crooks and coworkers synthesized Pd nanoparticles within fourth- and sixth-generation quaternary ammonium-terminated dendrimers to prepare Pd nanoparticles. High-resolution TEM images

revealed that the encapsulated Pd nanoparticles were almost monodisperse and had an average diameter of 1.7 ± 0.3 nm [47]. Because the dendrimer surfaces were positively charged, however, they did not aggregate or precipitate.

9.2.1.4 Synthesis Using Thioether Stabilizers

With the exception of dendrimers, very few procedures yield metallic nanoparticles in high yield that are monodisperse. In 2007, Obare and coworkers reported a straightforward procedure for the synthesis and size-control of Pd nanoparticles [48]. In this approach, thioethers were found to be effective ligands for the preparation of Pd nanoparticles via a one-step procedure. Palladium acetate was used as the precursor and reacted with thioethers in a 1 : 5 Pd^{2+}: thioether ratio. Here, the thioether played two roles: (i) as a reducing agent for the Pd nanoparticles; and (ii) as a stabilizer for the nanoparticles formed. In this way, uniform Pd nanoparticles with diameters of 1.7 ± 0.2, 1.9 ± 0.2, 2.5 ± 0.1, 3.5 ± 0.1 and 4.1 ± 0.1 nm were obtained in a one-step procedure at 99% yield, and required no size selection process. Selected images to illustrate the uniformity of the nanoparticles obtained by this procedure are shown in Figure 9.2.

The modulation of reaction conditions during nanoparticle synthesis plays a significant role in controlling particle size and shape. Obare and coworkers investigated the effects of reaction temperature and reaction time on the pyrolysis of $[Pd_3(OAc)_6]$ to form thioether-stabilized Pd nanoparticles [48]. Both conditions were found to have a profound influence on nanoparticle size, as well as size distribution. A 1 h period of pyrolysis of a toluene solution containing a 1 : 5 ratio of $[Pd_3(OAc)_6]$ to *n*-dodecyl sulfide was carried out at temperatures of 95, 100, 110, 120, 130 and 140 °C, and yielded monodisperse Pd nanoparticles with sizes of 1.7 ± 0.2, 2.1 ± 0.2, 2.2 ± 0.2, 2.3 ± 0.1, 2.4 ± 0.1 and 2.5 ± 0.1 nm, respectively. The graph in Figure 9.3a shows the effect of temperature on Pd nanoparticle growth; increasing the reaction temperature was found to result in an increased particle size, accompanied by a narrower size distribution. In addition, the effect of reaction heating time was investigated; a plot of nanoparticles size as a function of reaction time is shown in Figure 9.3b. The data revealed that the average Pd nanoparticles size increased between 0 and 3 h of the reaction, but then leveled off. This effect was consistent with Ostwald ripening during the first 3 h, which results in a leveling off of the particle growth due to the depletion of smaller Pd nanoparticles, as well as any free Pd atoms that may be present in solution. Both results indicated that particle growth was consistent with an Ostwald ripening procedure, whereby a prolonged reflux time or heating time results in nanoparticles with larger diameters [5].

9.2.1.5 Synthesis Using Phosphine and Bisphosphine Stabilizers

Phosphine-based ligands are well known to coordinate to palladium and form inorganic compounds. However, their use as stabilizers for Pd nanoparticles has not been extensively utilized. In 2003, Hyeon's group investigated the use of phosphine ligands as stabilizers for Pd nanoparticles [49] by preparing a

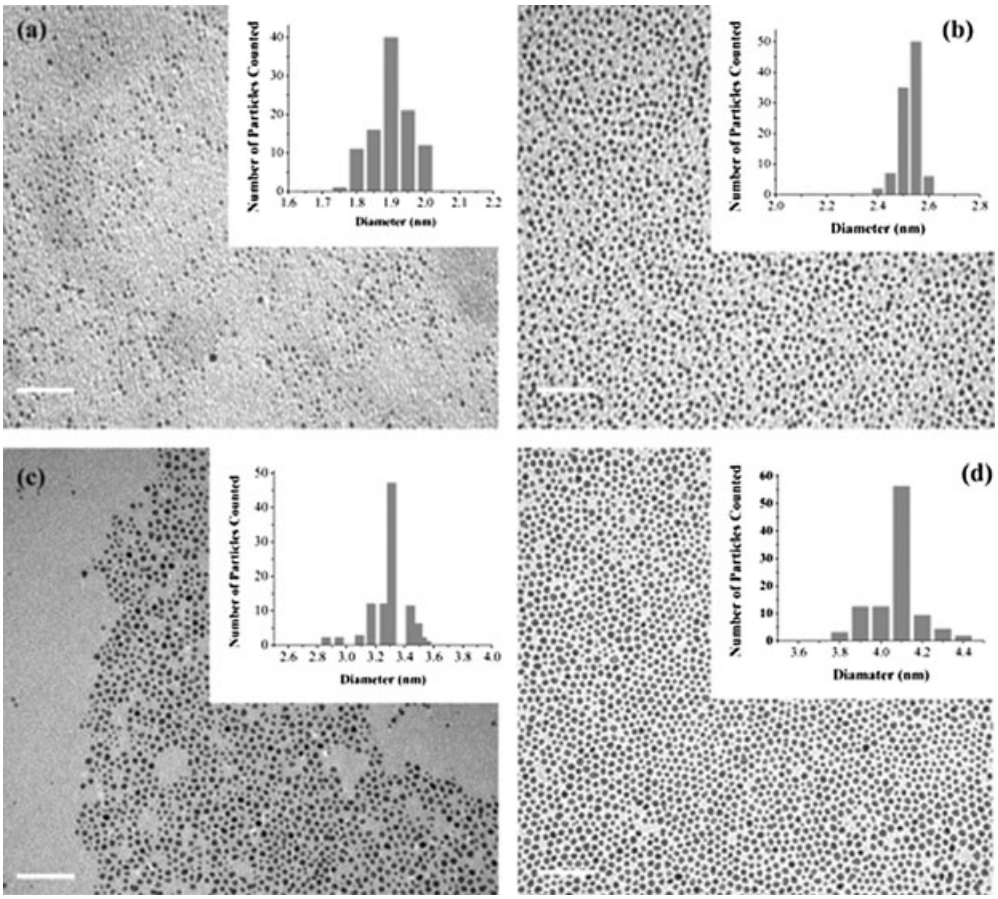

Figure 9.2 Transmission electron micrographs and size distribution histograms (insets) for *n*-dodecyl-sulfide-stabilized palladium nanoparticles. (a) 1.9 ± 0.2 nm; (b) 2.5 ± 0.1 nm; (c) 3.3 ± 0.1 nm; (d) 4.1 ± 0.1 nm. All images were acquired without a size-selection process. Scale bar = 50 nm. Reproduced with permission from Ref. [48]; © 2007 American Chemical Society.

Pd-trioctylphosphine (TOP) complex using palladium(II) acetylacetonate as a precursor. By heating the complex to 300 °C and aging for 30 min in the presence of free TOP, a black colloidal solution was formed. It was proposed that the CO molecules generated *in situ* from the thermal decomposition of acetylacetonate served as reductants. This procedure yielded monodisperse Pd nanoparticles of 3.5 nm or 5 nm diameter (Figure 9.4).

Chiral bisphosphine ligands have found extensive applications in asymmetric catalysis, which is an important reaction in the synthesis of natural products. In 2003, Fujihara reported the first example of bisphosphine-stabilized Pd nanoparticles [50]. 2,2′-Bis(diphenylphosphino)-1,1′-binaphthyl (BINAP), a chiral biaryl

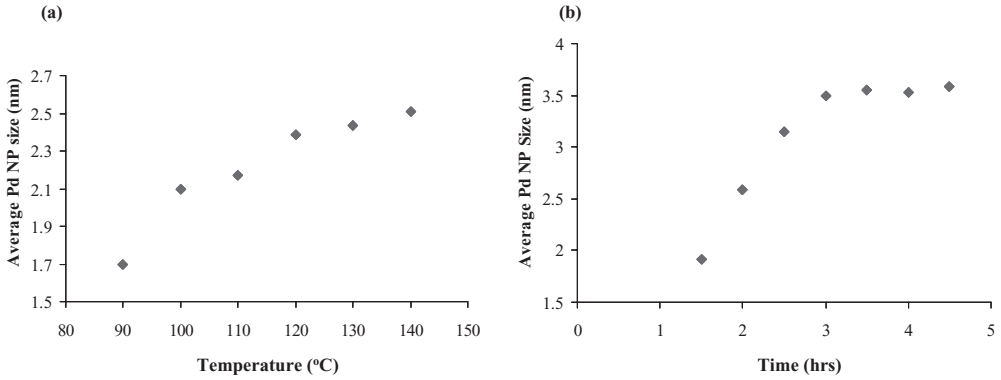

Figure 9.3 (a) Average Pd nanoparticle diameter size plotted versus temperature. An increase in synthesis temperature results in an increase in nanoparticle size, up to ~140 °C; (b) Average nanoparticle size plotted versus increase in reaction time at 95 °C; for a reaction time up to 3 h the particles continue to grow, but after this time no further growth occurs.

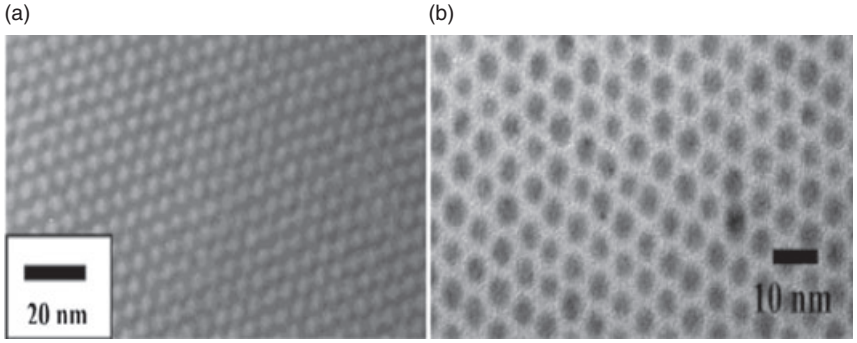

Figure 9.4 (a) TEM image of 3.5 nm-sized monodisperse Pd nanoparticles; (b) TEM image of 5 nm-sized monodisperse Pd nanoparticles. Reproduced with permission from Ref. [49]; © 2004 American Chemical Society.

ligand which is an important ligand in asymmetric catalysis, was used. In order to carry out the reaction, the solubilities of the ligand and the palladium precursor must be taken into consideration. The ligands are minimally soluble in water, while K_2PdCl_4 is water-soluble but has low solubility in most organic solvents. In a typical synthetic procedure, the Pd precursor K_2PdCl_4 was dissolved in water, while BINAP was dissolved in the organic solvent dichloromethane (DCM) in a 1 : 2.25 ratio. As DCM and water are immiscible, a phase-transfer agent, tetrabutyl ammonium bromide, was used, with $NaBH_4$ as the reducing agent. The reaction was carried out at room temperature under an argon atmosphere. The product

was washed with water until all phosphine and phase-transfer catalyst had been removed, whereupon the BINAP-Pd nanoparticles had an average diameter of 2.0 ± 0.5 nm. In comparison, when triphenylphosphine was used in a similar reaction, the resultant nanoparticles were 2.6 ± 0.7 nm in size. The authors attributed the difference in size as being due to the use of a bisphosphine versus a monophosphine ligand. The larger ligand around the phosphorus atom in BINAP may also contribute to better particle stabilization, and thus a smaller size distribution. When using C_8-BINAP, a ligand similar to BINAP – but with an alkyl chain to better stabilize the nanoparticles – was used. The C_8-BINAP, dissolved in a methanol : water (1 : 2, v/v) solution, was added to THF, and the K_2PdCl_4 reduced using $NaBH_4$ [51]. The average diameter of the resultant nanoparticles was 1.2 ± 0.2 nm.

9.2.1.6 Synthesis Using DNA Stabilizers

DNA is an attractive material for controlling the morphology of metal nanoparticles, and has been used to form palladium nanoparticles with diameters of 3 to 20 nm [52, 53], as well as to prepare particles at the surfaces. Recently, Fang *et al.* [54] reported using DNA for the synthesis of Pd nanoparticles in the range of 10 to 100 nm. For this, DNA was adsorbed onto a conductive indium tin oxide (ITO) surface via the phosphate backbone and the thiol groups, leaving the N atoms from the bases available to interact with Pd^{2+}. The ITO-coated DNA was placed in a solution of palladium acetate for 2 h to activate the DNA network. This process of activation not only involves the formation of complex bonds but also allows for the formation of Pd seeds. By applying a negative potential, Pd^{2+} was reduced to Pd^0, allowing the Pd to grow on the established seeds. The resultant nanoparticles, which were formed on the DNA duplex, were stable and used for sensor applications.

9.2.2 Anisotropic Palladium Nanoparticles

Palladium's face-centered cubic (fcc) crystal structure ensures that its nanocrystals can adopt a number of possible geometries. Similar to most noble metals, however, the fabrication of anisotropic palladium nanostructures of well-defined and controlled shapes is a major challenge and, as a result, has been heavily pursued. Although the nucleation and growth phases of anisotropic nanoparticles are not completely understood, it is believed that a careful tailoring of the formation of stable metallic nuclei of a defined crystallinity is essential. Once these nuclei have exceeded a critical size, seeds of particular crystallographic facets are realized, with the shape of such seeds being determined by the minimization of their surface energies. Continued growth of these seeds leads to a selective extension of a set of crystal faces at the expense of others. This is often accomplished through the selective adsorption of various ionic or molecular species to specific facets along the crystal, inhibiting the growth along such direction and allowing preferential growth along another, ultimately leading to the final shape assumed. It is therefore

feasible to assume that knowledge of the exposed crystal facets, and the physical and chemical parameters which permit or inhibit growth along these faces, may lead to both size and shape control.

Stabilizing ligands for anisotropic Pd nanoparticles include polymers, surfactants, coordinating ligands, specially formulated palladium–surfactant precursor complexes and RNA. Templating, corrosive pitting and etching processes have also been used. To date, spherical, cubo-octahedral, cubic, rod-like and polyhedric palladium nanocrystals have been successfully fabricated, in addition to triangular and hexagonal nanoplates, as well as low- and high-aspect ratio nanorods and nanowires.

9.2.2.1 **Nanocubes, Nanorods and Nanocages**

A seedless, templateless approach was employed by Sokolov and coworkers to fabricate cubic and rod-like single crystals of palladium [55a]. In the reaction, K_2PdCl_4 was reduced by ascorbic acid in the presence of trisodium citrate and the surfactant cetyltrimethylammonium bromide (CTAB). TEM (Figure 9.5) imaging confirmed the formation of cubes up to 32 nm in edge length and rod-like structures up to 80 nm long and 27 nm wide. The anisotropic growth of nanostructures is facilitated both by mild reducing agents (e.g. ascorbic acid) and by CTAB, which has been suggested to bind preferentially to the {100} crystal facets. The presence of trisodium citrate was also shown to trigger the formation of the geometries formed, since its absence led to the formation of spherical particles. Although the

Figure 9.5 TEM image of CTAB-stabilized Pd nanostructures prepared by the citrate reduction of K_2PdCl_4. Scale bar = 100 nm. Reproduced with permission from Ref. [55];

concentration of trisodium citrate had little effect on the ratio of morphologies observed, an increase in its concentration was found to extend the mean length and increase the aspect ratio of the rod structures.

A greater control of the diversity of nanocubes and aspect ratio structures was reported by Xia and coworkers [56]. This synthetic procedure involved the thermal reduction of Na_2PdCl_4 by ethylene glycol in the presence of potassium bromide, and PVP as the stabilizer (Na_2PdCl_4, potassium bromide and PVP were administered in a 1 : 30 : 15 mole ratio). Nanobars with aspect ratios of 8 and 2–4 were fabricated by dissolving the stabilizer in ethylene glycol (in the former case) and in water (in the latter case) prior to its injection to the pot. Nanobars of aspect ratio 1–1.2 were observed upon complete replacement of ethylene glycol with water, with the hydroxyl groups of PVP serving as a reductant. Such reaction parameters allow careful control of the reduction kinetics, which is an important factor leading to tunable anisotropic growth (Figure 9.6). The mean aspect ratio of the nanocrystals fabricated was inversely related to the rate of reduction of the metal salt. This argument was supported by replacing ethylene glycol with di ethylene glycol, which was a weaker reductant in the synthetic processes. A 20 °C increase in the reaction temperature also altered the reaction kinetics and produced nanocrystals that possessed an aspect ratio of approximately 16. Xia *et al*. also proposed that the preferential binding of bromide ions and oxidative etching play an important role in the particles' anisotropy. Br^- ions bind specifically to the Pd seed crystal surface, inhibiting its growth along all axes. Oxidative etching by O_2/Cl^- (Cl^- from $(PdCl_4)^{2-}$ and O_2 from air) reactivates the surface by displacing Br^- ions from selected regions on the seed surface, allowing the further addition of Pd atoms at specific crystallographic facets.

Xia and coworkers also followed a similar synthetic route, coupling the polyol reduction of Na_2PdCl_4 in the presence of PVP with $FeCl_3$ as an oxidative etchant [57]. $FeCl_3$ is believed to be more suited to quantitative comparative studies as the concentration of O_2 dissolved in ethylene glycol is difficult to control, when O_2/Cl^- is applied. Palladium nanocubes, of between 8 and 50 nm, as shown in Figure 9.7, were formed, with the concentration of $FeCl_3$ having a distinct effect on the sizes observed: the higher the concentration, the larger the nanocubes. Xia *et al*. rationalized that a high concentration of $FeCl_3$ reduced the quantity of Pd seeds (as the redox couple Fe^{3+}/Fe^{2+} –0.77 V was capable of oxidizing atomic palladium), leading to the formation of larger cubes.

Other interesting designs of the cubic variety have also been accomplished [57]. Pd nanoboxes and nanocages were synthesized using Na_2PdCl_4 in the presence of PVP, ethylene glycol and water. With the evolution of time, the as-synthesized 48 nm-edged Pd nanocubes were transformed, by O_2/Cl^- oxidative etching, to nanocubes (see Figure 9.8). TEM studies showed a localized etching process which began on the cubes surface and later extended to the structures' interior. After 20 h, the cubes had become completely hollow and possessed truncated corners and walls 8 nm thick. Some 4 h later, the etching process had led to the formation of nanocages: 10 nm punctures were observed in each boxes' corner, with the wall thickness being reduced to 6 nm.

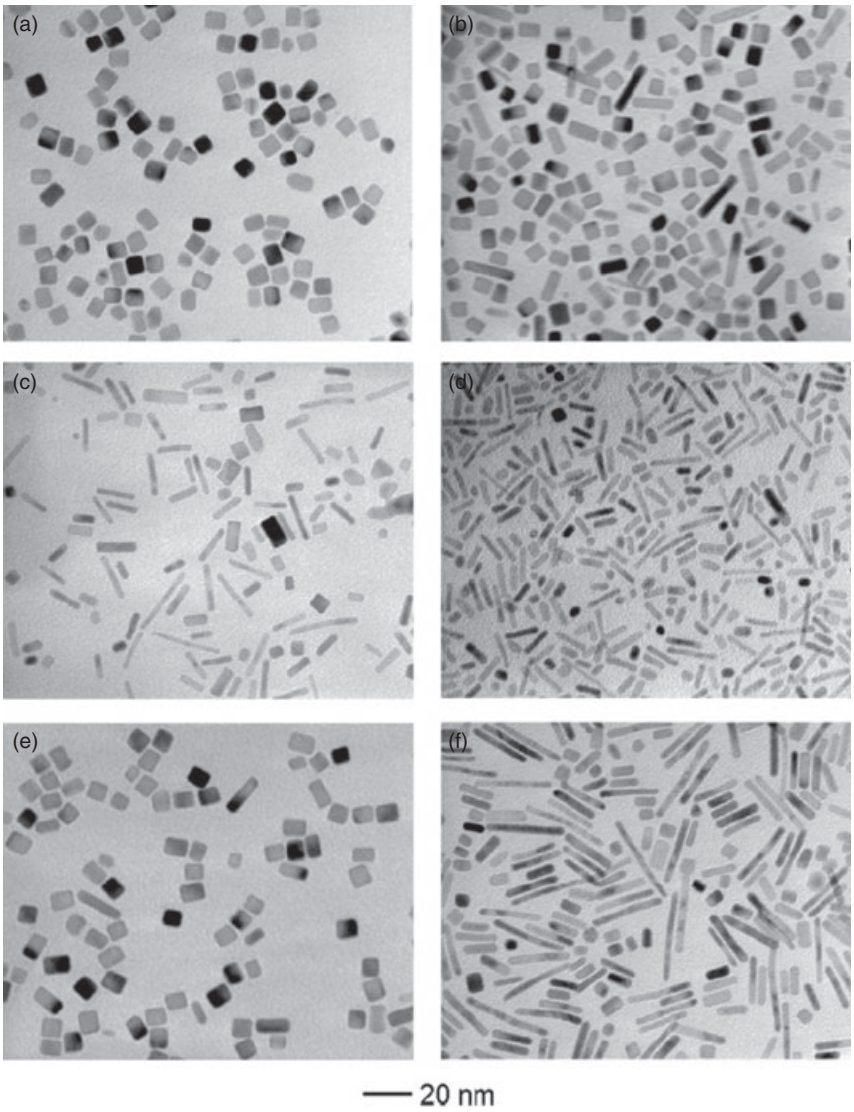

Figure 9.6 TEM images of Pd nanoparticles obtained upon the volume percent adjustment of ethylene glycol in the thermal (100 °C) reduction of Na_2PdCl_4. (a) 0%; (b) 9.1%; (c) 45.5%; (d) 72.7%; (e) Image obtained under similar conditions as (d), but ethylene glycol was replaced with di ethylene glycol; (f) Image obtained similar to (d), except that the reduction temperature was increased to 120 °C. Reproduced with permission from Ref. [56]; © 2007 American Chemical Society.

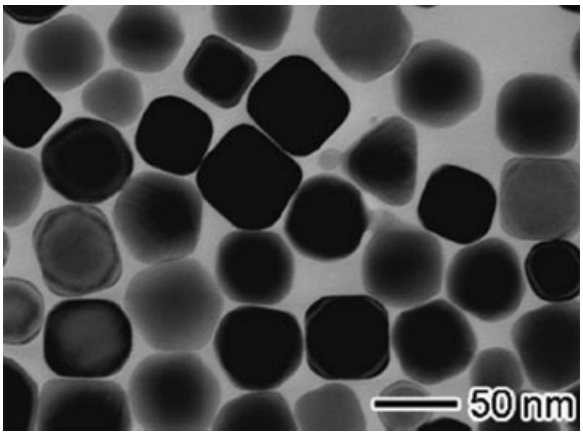

Figure 9.7 TEM image of 50 nm Pd nanocubes prepared by oxidative etching using $FeCl_3$. Reproduced with permission from Ref. [57]; © 2005 American Chemical Society.

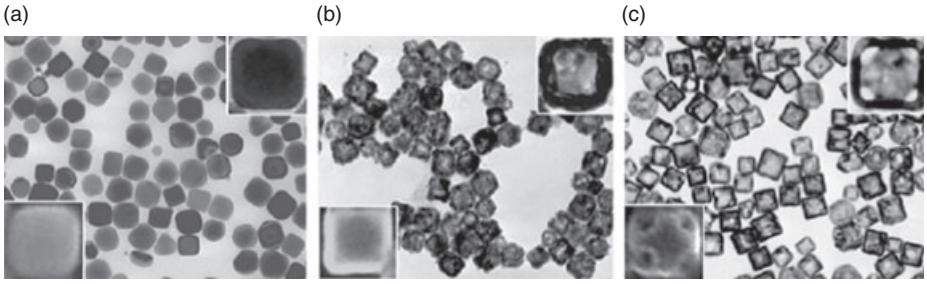

Figure 9.8 TEM images showing the progressive etching Pd nanocubes to form nanoboxes and finally nanocages. (a) t = 18 h; (b) t = 21 h; (c) t = 24 h. Reproduced with permission from Ref. [57]; © 2005 American Chemical Society.

9.2.2.2 **Triangular and Hexagonal Nanoplates**

Polyol reduction of Na_2PdCl_4, followed by oxidative etching, was used to produce triangular and hexagonal palladium nanoplates [58]. The synthesis of triangular nanoplates involved the addition of acidified (HCl) Na_2PdCl_4 and PVP to a pre-heated, 85 °C solution of ethylene glycol and $FeCl_3$. Some 70% of the morphologies were triangular plates of approximately 28 nm edge length and about 5 nm thickness (see Figure 9.9). The formation of hexagonal nanoplates followed a similar procedure, with twice the amount of $FeCl_3$ being added. The reduction rate of the metal salt must be retarded for these anisotropic features to form. The cumulative effective of both $FeCl_3$ and O_2/Cl^- were crucial to the reaction kinetics, while the addition of HCl enhanced the etching power of O_2/Cl^-. By varying the concentra-

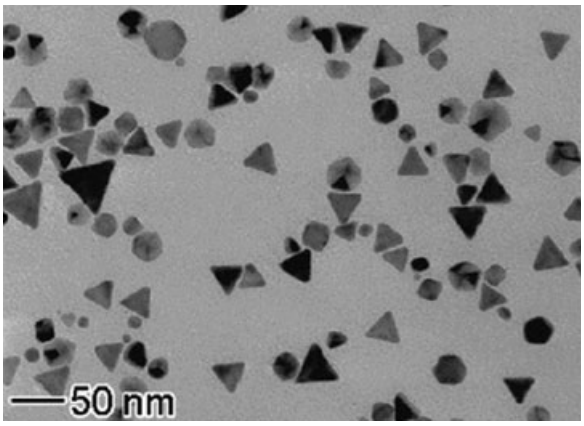

Figure 9.9 TEM image of triangular nanoplates prepared at 85 °C in the presence of HCl and the etchant $FeCl_3$ and molar ratio of stabilizer to palladium salt as 5 : 1.

tion of $FeCl_3$ the quantity of triangular nanoplates could be controlled; indeed, a twofold increase in concentration led to a doubling in the number of plates observed. If the concentration of $FeCl_3$ exceeded this threshold, however, hexagonal plates were the major products observed. Although the etching power of the O_2/Cl^- pair may be significantly enhanced by increasing the concentration of acid, it was shown that a variation in such concentration was disadvantageous to the formation of uniform nanoplates. It was also shown that relatively low reaction temperatures led to an increase in the yield of nanoplates. The percentage of triangular nanoplates in the final product, as well as the morphologies observed, were also found to be dependent on the molar ratio between the stabilizer and the Pd precursor. A ratio of 5 : 1 produced 70% triangular nanoplates, whereas any increase or decrease in the ratio led to a significant decline in the proportions observed.

The hydroxyl functionality of PVP has been shown to act as a very mild reducing agent to kinetically control the reduction process [59]. As a result, hexagonal and triangular plates can be formed. The fabrication procedure involved the addition of Na_2PdCl_4 to an 80 °C aqueous solution of PVP, and the solution was allowed to reflux for 5 h. The reduction kinetics was controlled by varying the molar ratio of PVP to Na_2PdCl_4 and the molecular weight of the PVP. A 5 : 1 molar ratio and a PVP molecular weight (MW) of 55 000 led to 70% hexagonal plates of average edge length 45 nm and an estimated thickness of 8 nm. By comparison, palladium triangular nanoplates of average edge length 50 nm were produced when the molar ratio was adjusted to 15 : 1 and PVP of molecular weight 10 000 was used.

A biologically driven approach to the formation of palladium crystals was demonstrated by Eaton and coworkers, who discovered that selected modified RNA sequences could effectively mediate the growth of hexagonal palladium

nanoparticles [60]. It was proposed that RNA possessed catalytic capabilities in the construction of inorganic particles due mainly to its ordered structure, and its ability to be folded reproducibly into complex three-dimensional arrangements. Furthermore, the positioning of the nucleotides at selected loci make RNA extremely attractive as a biopolymeric stabilizer for the size or shape control of nanoparticles.

An *in vitro* selection technique was applied to evolve a collection of catalytically active family of RNA sequences, with 5-(4-pyridylmethyl)-uridine 5′ triphosphate (*UTP) being used to provide additional metal–RNA coordination sites (beyond the nitrogen-containing heterocycles available in the native RNA structure). The RNA is then incubated with the zerovalent metal complex, tris-(dibenzylideneacetone) dipalladium(0) ($(Pd_2dba)_3$) in an aqueous medium, for 2 h at ambient temperature.

Eaton and colleagues recognized four families of evolved RNA sequences capable of catalyzing the formation of hexagonally shaped Pd plates, or Pdases (families 1–4 contained 14, 6, 2 and 2 members respectively, and were categorized by their conserved regions) (Figure 9.10) [61]. Five pyridyl-modified RNA sequences, representing each of the different catalytically active families, were found to form hexagonal plates ($1.24 \pm 0.57\,\mu m$), while another unrelated pyridyl-modified RNA sequence was found exclusively to produce cubes ($0.10 \pm 0.05\,\mu m$), under similar conditions.

The synthesis of nanoparticles in aqueous solutions is particularly attractive from an environmental perspective. Multifaceted palladium nanoparticles (Figure 9.11) were synthesized using a solution of Na_2PdCl_4, PVP and citric acid, and heating the reactants at 90 °C for 26 h [62]. The concentration of Na_2PdCl_4 and citric acid were modulated to control the morphology of the particles produced. A ratio of 5 : 1 (PVP to Na_2PdCl_4) led to the formation of smooth-faced and sharp-cornered palladium octahedra of edge length ~20 nm and in approximately 90% abundance (Figure 9.12). The relationship between particle anisotropy and palladium precursor was observed when the concentration of Na_2PdCl_4 was reduced by 20%, where-

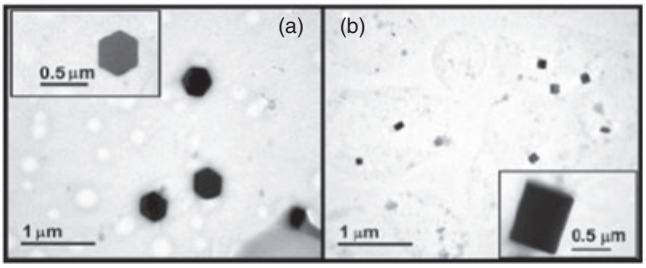

Figure 9.10 TEM images of (a) hexagonal and (b) cubic palladium particles formed in the presence of two pyridyl-modified RNA sequences (Pdases 17 and Pdase 34, respectively). Reproduced with permission from Ref. [61]; © 2005 American Chemical Society.

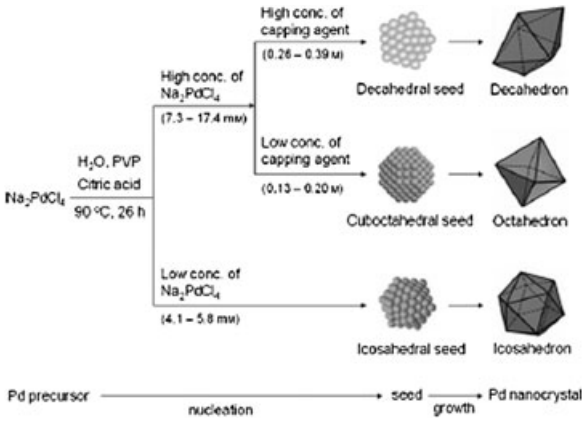

Figure 9.11 Summary of reaction conditions required for the formation of decahedron-, octahedron- and icosahedron palladium nanoparticles. Reproduced with permission from Ref. [63]; © 2007 Wiley Interscience.

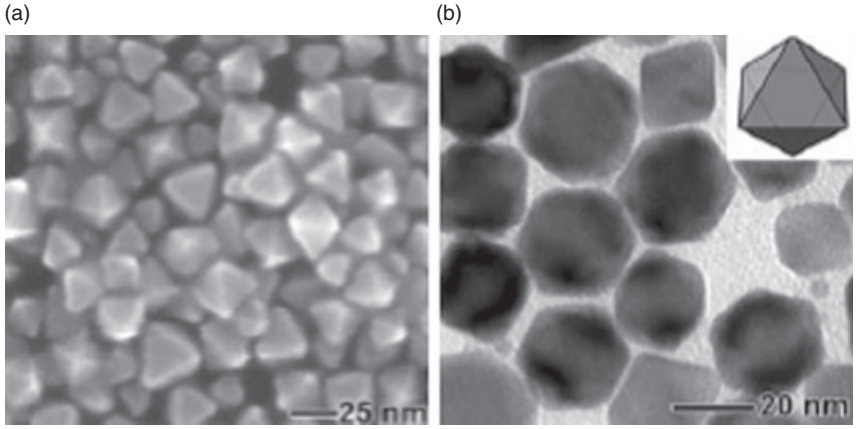

Figure 9.12 (a) SEM image and (b) TEM image of octahedral Pd nanoparticles. Reproduced with permission from Ref. [63]; © 2007 Wiley Interscience.

upon an 80% abundance of icosahedral palladium nanoparticles was formed (Figure 9.13). Pd decahedra were synthesized in high yield (>80%) when the concentration of precursor and citrate was increased beyond the threshold responsible for octahedral and icosahedral symmetry. In addition, it has also been reported that at relatively high concentrations of citrate, the abundance of decahedra approaches 90% (Figure 9.13).

Reetz's group discovered that certain tetra-*n*-octylammonium carboxylates function as both reductants and stabilizers, and could be used to synthesize triangular palladium nanostructures (Figure 9.14) [64]. This preparation involves the addition

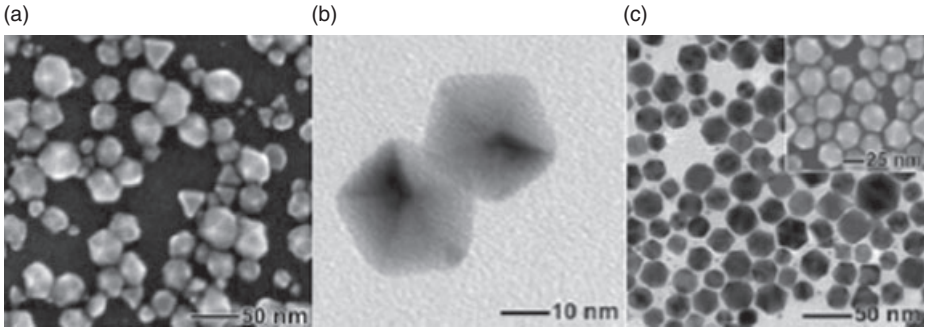

Figure 9.13 (a, b) SEM and TEM images, respectively, of decahedral Pd nanoparticles; (c) TEM and SEM image (inset) of icosahedral Pd nanoparticles. Reproduced with permission from Ref. [63]; © 2007 Wiley Interscience.

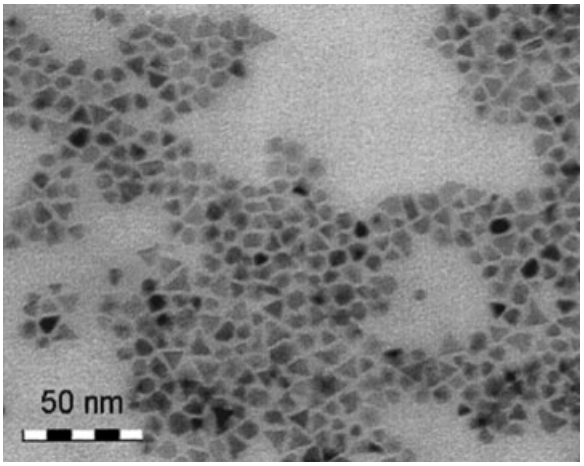

Figure 9.14 TEM image of glycolate-stabilized palladium nanoparticles with a high abundance of triangular nanostructures. Reproduced with permission from Ref. [64]; © 2000 American Chemical Society.

of $Pd(NO_3)_2$ to tetraoctylammonium glycolate in THF. Refluxing at 66 °C for 6 h led to the formation of trigonal palladium nanoparticles of edge length ~3.6 nm in 40–50% abundance.

9.2.2.3 **High-Aspect Ratio Pd Nanoparticles**

Wehrspohn and coworkers fabricated palladium nanotubes (Figure 9.15) through a template-assisted process [65] whereby dichloromethane or chloroform was used to form a solution of poly(D,L-lactide) (PDLLA) and palladium acetate. The solution was added to porous alumina in a 1 : 1 ratio under ambient conditions. Vaporization of the solvent resulted in the formation of $Pd(OAc)_2$/PDLLA tubes, followed by annealing at 200 °C which degraded the precursor to elemental palladium. Further pyrolytic treatment at 3500 °C removed PDLLA, while the alumina tem-

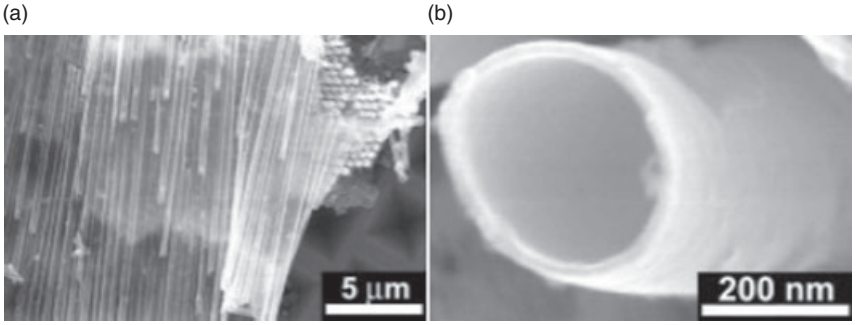

Figure 9.15 Scanning electron micrographs of Pd nanotubes (pore diameter 400 nm, pore depth 100 µm) obtained by wetting porous alumina and after annealing at 200 °C for 6 h and removing both the template and poly(D,L-lactide (PDLLA). (a) An array of aligned palladium nanotubes; (b) Cross-sectional view of an individual nanotube. Reproduced with permission from Ref. [62]; © 2007 Wiley Interscience.

plate was dissolved by aqueous KOH solution. The shape and length of the template determined the size of the tube formed. The structure of DNA had also inspired its use as a biological scaffold, functioning as a surface for the depositions of metals, to form nanowires. Filoramo an coworkers demonstrated the fabrication of palladium coated nanowires via the metallization of DNA immobilized on a silicon wafer [66]. The process involved two steps: the slow, selective precipitation of PdO, and the subsequent reduction of the metal oxide. The DNA strand was first combed onto a bexamethyldisiiazane (HMDS) coated Si substrate followed by its incubation in a solution of palladium chloride. Since the deposition of PdO on the DNA scaffold is slow, adjustments in the incubation time and temperature have been shown to produce wires of specific aspect ratios. Higher incubation temperatures encourage the increased deposition of PdO on the DNA scaffold, owing to the decreased solubility of PdO at elevated temperatures. Finally, the wafer containing the PdO-coated DNA, is immersed in a slightly alkaline, millimolar solution dimethylaminoborane – the reducing agent. The process produces wires ranging in mean width from 20–65 nm and up to 1 µm in length.

Mirkin and coworkers have applied dip-pen nanolithography (DPN) to produce a thin resist layer of palladium, patterned into controllable features [67]. An oxidized silicon wafer was first cleaned and dried in nitrogen, after which the substrate surface was coated with a 1 nm-thick adhesion layer of titanium, via thermal evaporation. A 20 nm layer of palladium was then deposited as a thin film by similar means. The prepared metal substrate was then patterned with 1-octadecanethiol by DPN with 1-octadecanethiol thermally evaporated onto a Si_3N_4 cantilever at 65 °C. After patterning with 1-octadecanethiol, the palladium substrate was immersed in a solution of a $FeCl_3$-based etchant for 10–30 s (the role of the etchant is to remove unprotected palladium from the surface of the silicon wafer). Immersion in a HF solution for 10–15 s effectively removed the 1 nm titanium layer exposed after etching. The explanation given was that the monolayer of 1-octadecanethiol adsorbed to the metallic substrate beneath acted as a resist, preventing such loci from being removed in the etching process. Subsequently,

DPN was used to produce Pd nanowires of uniform width (39 nm) when a write speed of 0.13 μm s^{-1} was used (Figure 9.16).

Minko and colleagues have used a straightforward chemical route to fabricate wire-like Pd structures from a single synthetic polycation, poly(methacryloyl) oxyethyldimethylbenzylammonium chloride (PMB-Cl) (Figure 9.17) [68]. The preparation of such structures is based on the deposition of Pd-clusters on single PMB-Cl molecules adsorbed onto a silicon wafer from an aqueous solution. Minko *et al*. found that the length and diameter of the underlying polymer chain determined the length and diameter of the wire formed. The procedure involved the actual synthesis of the polycation designated using methacryloyloxyethyldimethylbenzylammonium chloride and 2,2′-azobis (2-amidinepropane) hydrochloride. After thoroughly cleaning a highly polished silicon wafer, PMB-Cl was deposited on the surface by immersion in a solution of the polycation for 1 min, at ambient temperatures. The coated wafer was then immersed in a saturated and acidified aqueous solution of palladium acetate for 1 min, also at ambient temperatures. Finally, an aqueous solution of dimethylamine borane was used to reduce the palladium to its elemental state; the resultant Pd nanowires appeared as interconnected clusters of the metal.

He and coworkers have devised a simple, templateless solution-phase fabrication of one-dimensional, ribbon-shaped palladium nanoassemblies [69]. Palladium nanoparticles were first synthesized; this involved the dissolution of $Pd_3(OAc)_6$, and tetraoctadecylammonium bromide (TOAB) in a 5 : 1 (v/v) toluene–THF mixed solvent system, followed by the addition of absolute ethanol and refluxing the solution for 12 h at 75 °C. Colloidal Pd was then precipitated with excess absolute ethanol, after which the sample was dried by mild heating. The TOAB-stabilized Pd nanoparticles (4.5 ± 0.2 nm) were then used to construct the palladium nanoribbons (Figure 9.18). The formation of these nanostructures was accomplished by dispersing the Pd nanopowder in toluene, and incubating the sample at room temperature for designated periods of time. He and colleagues showed that an

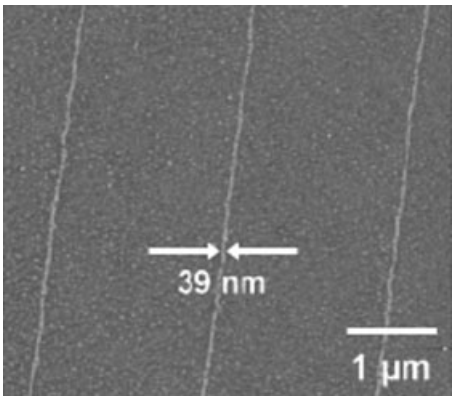

Figure 9.16 Atomic force microscopy (AFM) image of Pd nanostructure on a silica wafer, written at a speed of 0.13 μm s^{-1} with 1-octadecanethiol. Reproduced with permission from Ref. [67]; © 2004 American Chemical Society.

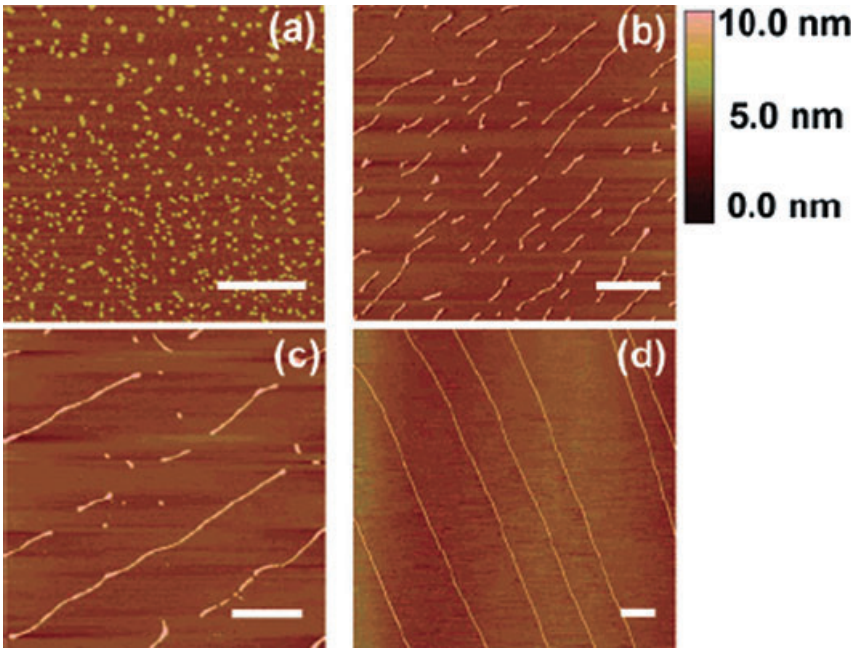

Figure 9.17 AFM images of (a) tetraoctadecylammonium bromide-stabilized palladium nanoparticles. Palladium nanoribbons of varying length have been produced by altering incubation times: (b) 4 h; (c) 6 h; (d) 24 h. Scale bar = 1.5 µm. Reproduced with permission from Ref. [68]; © 2002 American Chemical Society.

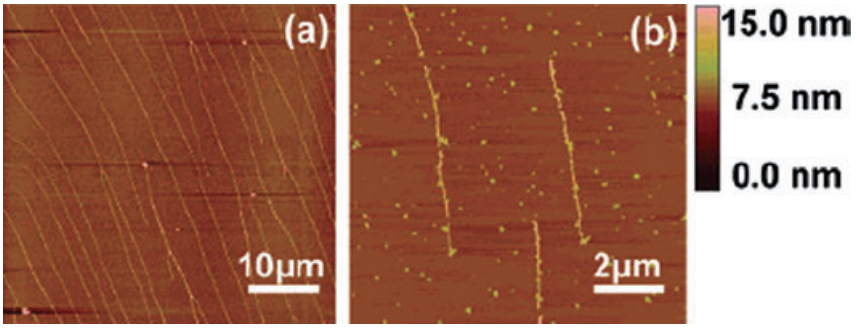

Figure 9.18 AFM images of palladium nanoribbons. (a) 24-day incubation of TOAB-stabilized palladium nanoparticles in toluene; (b) 24-day incubation in toluene, with 1-hexadecanethiol added on day 6. Reproduced with permission from Ref. [68]; © 2002 American Chemical Society.

increase incubation time led to the formation of longer ribbons (there was a limit, however, where further incubation led to instability of the overall structure). There were no significant changes in height and width (7.0 ± 1.0 nm and 75.0 ± 15.0 nm respectively) of the nanoribbons as time evolved. He's group also highlighted the fact that the width and height remained appreciably uniform throughout the length of the ribbon (height 6–8 nm; width 60–90 nm). When the addition of 1-hexadecanethiol was shown to impede the nanoribbon's growth, He *et al*. rationalized that the thiol was binding strongly to the surface of palladium, and was not easily desorbed. The TOAB ligand which passivates the palladium nanoparticles in the original synthesis, however, may be easily displaced, an effect which caused the individual metal particles to increase the forces of attraction among themselves, allowing them to align in an ordered fashion.

Wang and coworkers were able to synthesize palladium nanotubes via electroless deposition (Figure 9.19) [70]. The template used was a track-etched polycarbonate filter, coated with PVP to increase its hydrophilicity. Before deposition of the elemental palladium, the polycarbonate membrane was first sensitized and activated by immersion in a solution of tin chloride and trifluroacetic acid; these reagents are added to encourage the tethering of Sn^{2+} to the wall of the membrane pores. After thoroughly rinsing in methanol, a solution of $AgNO_3$ in ammonia was administered. On addition of Ag^+ ions, a redox reaction occurred whereby the surface-bound Sn^{2+} was oxidized to Sn^{4+} and Ag^+ reduced to elemental Ag. The nanosized silver aggregates acted as nucleation sites and catalysts for the deposition and growth of palladium on the polycarbonate membrane. After rinsing in methanol, the activated membrane was transferred to a solution containing $PdCl_2$, disodium EDTA and N_2H_4. The chelating agent,

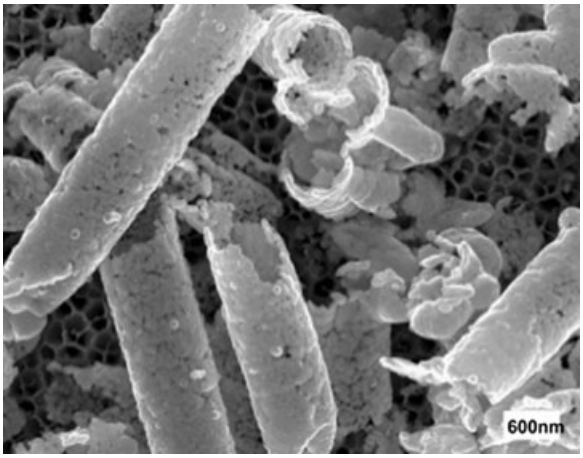

Figure 9.19 Scanning electron micrograph of palladium nanotubes after the polycarbonate membrane has been removed by rinsing the sample in methylene chloride. Reproduced with permission from Ref. [70]; © 2005 American Chemical Society.

disodium EDTA, sequesters Pd^{2+} ions to form $[Pd(EDTA)]^{2-}$, which is slowly reduced at room temperature by N_2H_4 in the following reaction:

$$[Pd(EDTA)]^{2-}_{(aq)} + N_2H_{4(aq)} + 4OH^-_{(aq)} \rightarrow Pd_{(s)} + 2EDTA^{4-}_{(aq)} + N_{2(g)} + 4H_2O_{(1)} \quad (9.2)$$

Jones and colleagues have also synthesized hollow Pd nanostructures using freshly prepared cobalt nanoparticles as sacrificial templates (Figure 9.20) [71]. The $NaBH_4$ reduction and citric acid stabilization of $CoCl_2$ in a nitrogen-filled atmosphere led to the formation of cobalt nanoparticles, with the resultant colloid immediately being added to a stirring solution of H_2PdCl_4 at room temperature. The TEM analysis of a centrifuged sample indicated the formation of hollow, raspberry-like spheres, the shell of which (~15 nm thickness) was composed of small, individual palladium nanoparticles, while the complete sphere possessed a mean diameter of 80 nm. One-dimensional tube-like, ~60 nm-diameter nanostructures were also synthesized with the addition of one-tenth the amount of citric acid. Jones *et al.* suggested that these hollow Pd nanostructures had been synthesized via a replacement reaction between elemental cobalt (nanoparticles) and the administered palladium salt:

$$Co + PdCl^{2-}_4 \rightarrow Pd + Co^{2+} + 4Cl^- \quad (9.3)$$

The respective differences in the redox potentials of the Co^{2+}/Co (–0.277 V vs. SHE) and $PdCl^{2-}_4/Pd$ (0.591 V vs. SHE) couples provide the thermodynamic driving force to encourage the aforementioned reaction, with $PdCl^{2-}_4$ being immediately reduced upon its addition to the colloidal mix of elemental cobalt. As this replacement reaction proceeds, the reduced palladium atoms nucleate, forming a thin perimeter of nanoparticles around a cobalt core. Removal of the cobalt metal

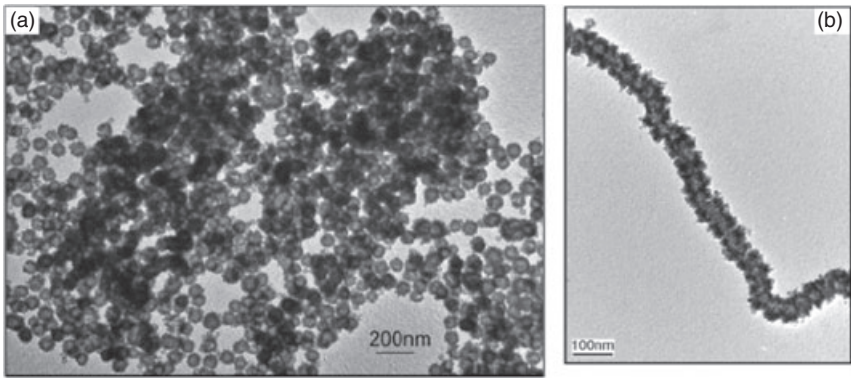

Figure 9.20 TEM images of: (a) hollow, raspberry-like palladium nanoparticles and (b) a nanotube-like palladium nanostructure. Reproduced with permission from Ref. [71]; © 2008 American Chemical Society.

core is believed to occur by the Kirkendall effect, in which the rate of diffusion of two components at an interface leads to a net directional flow. If the diffusion of cobalt atoms occurs at a faster rate compared to that of Pd atoms, then at the newly formed partition a net flow of Co atoms from the core occurs, and these are immediately oxidized by the incoming $PdCl_4^{2-}$ species. The eventual diffusion of Co atoms leads to the hollow central cavity being observed. The formation of tube-like nanostructures is related to the single magnetic dipole character that this one-dimensional structure adopts to minimize its magnetostatic energy. Thus, the reaction between chain-like cobalt nanoaggregates and $PdCl_4^{2-}$ allows the formation of nanotube-like 1-D structures.

The preparation of anisotropic palladium nanoparticles has also been accomplished by Berhault and coworkers, using an aqueous phase seeding synthesis approach (Figure 9.21) [72]. Spherical seeds were first synthesized upon the reduction of Na_2PdCl_4 by $NaBH_4$, and passivation of the nascent particles by the surfactant CTAB. The freshly prepared seeds were stirred for another 15 min and used

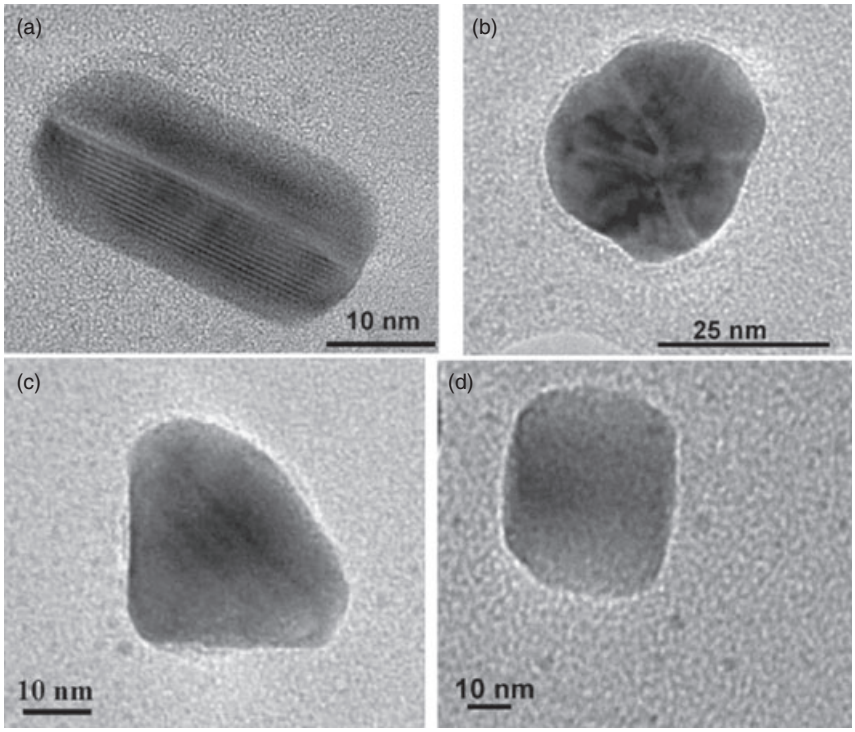

Figure 9.21 TEM images of palladium (a) nanorods of fivefold symmetry; (b) polyhedric nanoparticles formed from six tetrahedral subunits; (c) round-edged tetrahedral particles; and (d) round-edged nanocubes. Reproduced with permission from Ref. [72]; © 2007 Elsevier.

only after 2 h had expired (to ensure the decomposition of excess borohydride species). In order to synthesize anisotropic palladium nanoparticles, a growth solution of Na_2PdCl_4 and CTAB was prepared at 30 °C, after which sodium ascorbate was administered followed by the injection of an aliquot of the pre-prepared palladium seeds. When the colloidal preparation had aged for 48 h, a TEM analysis revealed an assortment of morphologies. Palladium nanocubes – the most miniscule geometry observed (18 ± 3 nm) – were produced in low yield (3 ± 1%), while nanorods of aspect ratio ~2.2 were the most abundant (47 ± 4%). A significant yield of 24 ± 5 nm polyhedric morphologies was also observed (43 ± 4%), together with a small percentage (3 ± 1%) of 29 ± 1 nm tetrahedrons.

9.2.3 Characterization

Elaborate synthetic approaches have been developed that enable significant control over the size and shape of palladium nanostructures. In order to understand the properties of the materials formed based on the preparation method, several characterization techniques have been used. These include electron microscopy, scanning probe microscopy (SPM), nuclear magnetic resonance (NMR) spectroscopy, ultraviolet–visible (UV-Vis) spectroscopy, infrared (IR) spectroscopy, electrochemistry, X-ray diffraction (XRD), thermogravimetric analysis (TGA), electron diffraction, photoelectron spectroscopy, dynamic light scattering (DLS), extended X-ray absorption fine structure (EXAFS), BET surface area analysis and X-ray reflectivity (XRR). In the following section we will describe the information provided by each of these characterization techniques.

9.2.3.1 Electron Microscopy

Electron microscopy is a powerful technique for the characterization of Pd nanoparticles, and is capable of providing information of the morphology, topography and composition of the material under investigation. Here, we describe details of TEM and scanning electron microscopy (SEM), both of which are capable of providing detailed information about particle shape and size distribution.

9.2.3.1.1 Transmission Electron Microscopy (TEM) The first TEM instrument was developed in 1931 by Max Knoll and Ernst Ruska in Germany. The instrument emits an electron beam by a tungsten filament (at a voltage of 100 keV) as its source of radiation. The electron beam is transmitted through the sample and the output transmittance provides the image. TEM allows the direct visualization of particles and so has been a very important imaging tool for determining particle formation, shape and size distribution. For TEM, the specimen is placed on a mounting surface, typically a carbon coated copper grid. The sample for analysis is prepared by either quickly contacting the carbon-coated side of the grid with the Pd nanoparticles colloid, or by dropping a few microliters of the Pd colloid onto the grid. The sample is allowed to dry before being placed in the instrument for analysis. Figure 9.22 shows the TEM images of

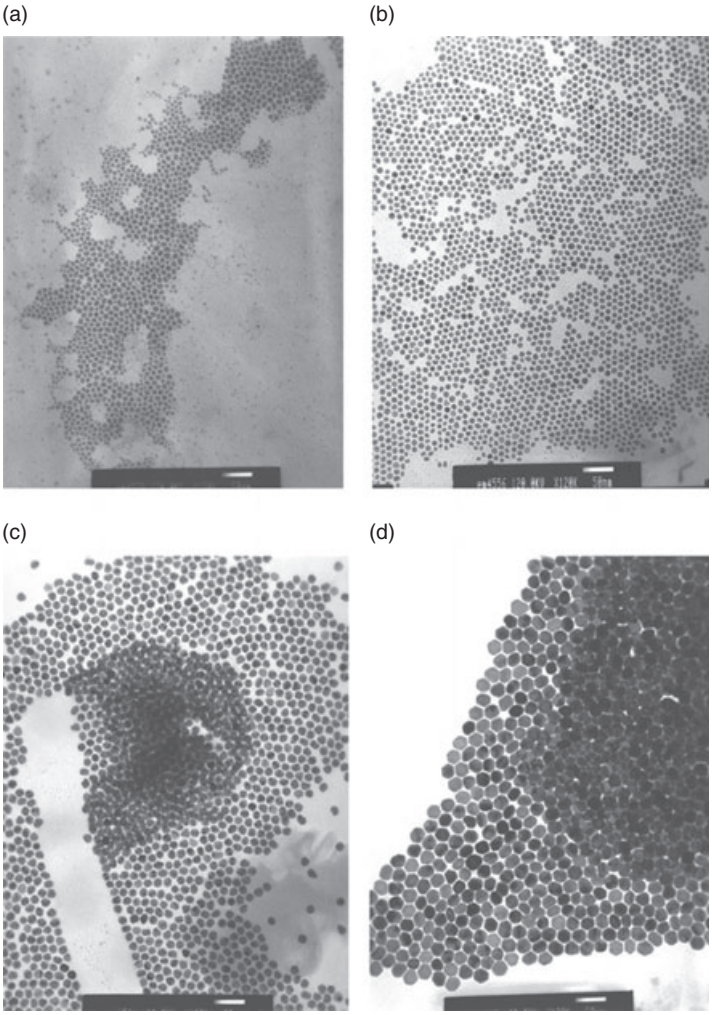

Figure 9.22 TEM images of Pd nanoparticles in *o*-xylene, reduced from precursor $Pd(fod)_2$ and stabilized by several ammonium salts $[R(CH_3)_3]^+Br^-$ (surfactants). (a) Dodecyltrimethylammonium bromide (DTAB); (b) Meristyltrimethylammonium bromide (MTAB); (c) Cetyltrimethylammonium bromide (CTAB); (d) octadecyltrimethylammonium bromide (OTAB). Reproduced with permission from Ref. [73]; © 2004 Institute of Physics.

Pd nanoparticles [73]; here, only the Pd core provides a contrast and not the surrounding ligand, such that TEM allows the determination of size distributions for each Pd NP sample.

Advancements in electron microscopy have led to the development of high-resolution transmission electron microscopy (HRTEM), which allows the analysis of nanoparticles with resolution up to 0.8 Å. This is made possible by using a

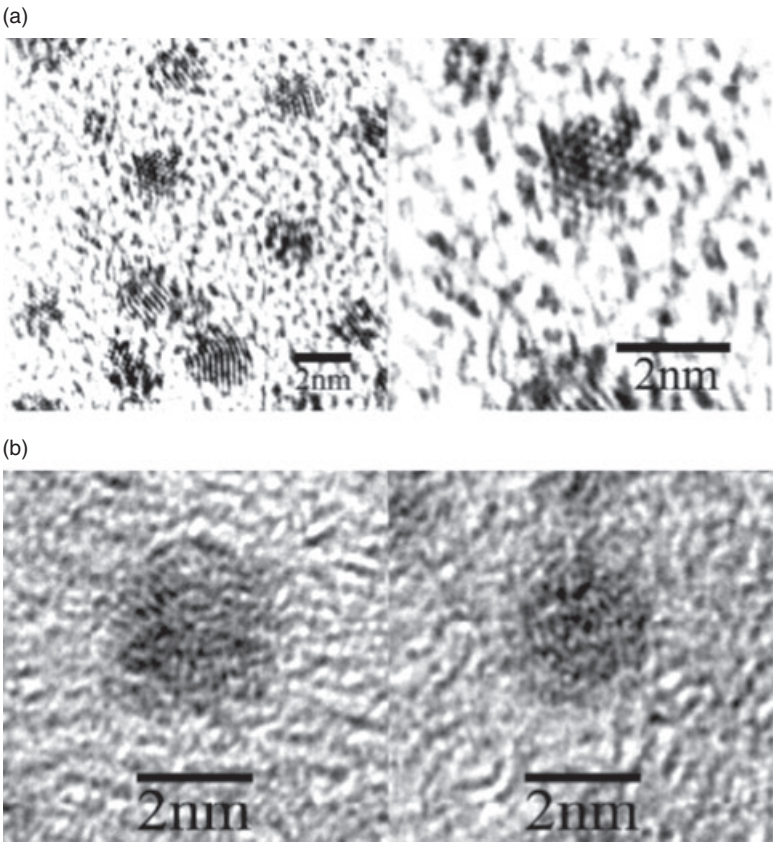

Figure 9.23 (a) HRTEM images of crystalline Pd nanoparticles in two different magnifications. These have quasi-hexagonal shape and a clear hexagonal lattice; (b) HRTEM images of amorphous Pd nanoparticles exhibit a round shape and shell-like structures. Reproduced with permission from Ref. [74]; © 2003 American Chemical Society.

high-voltage (200–300 keV) power supply for the electron beam. HRTEM also allows structural features which are only a few angstroms in size to be imaged, so that the crystal structure can also be investigated. A HRTEM image of Pd nanoparticles is shown in Figure 9.23. Consistent with the lattice spacing of Pd (111), a lattice fringe of 2.2 Å in Pd–C-passivated nanoparticles (2–4 nm) was observed using HRTEM [74]. One disadvantage of using either TEM or HRTEM is that the high accelerating voltage required may decompose the surface ligand, resulting in a 'dewetting' of the particle surface that induces particle fragmentation [75].

9.2.3.1.2 **Scanning Electron Microscopy (SEM)** The operating principles of SEM are very similar to those of TEM, except that a high-voltage (a few hundred eV to

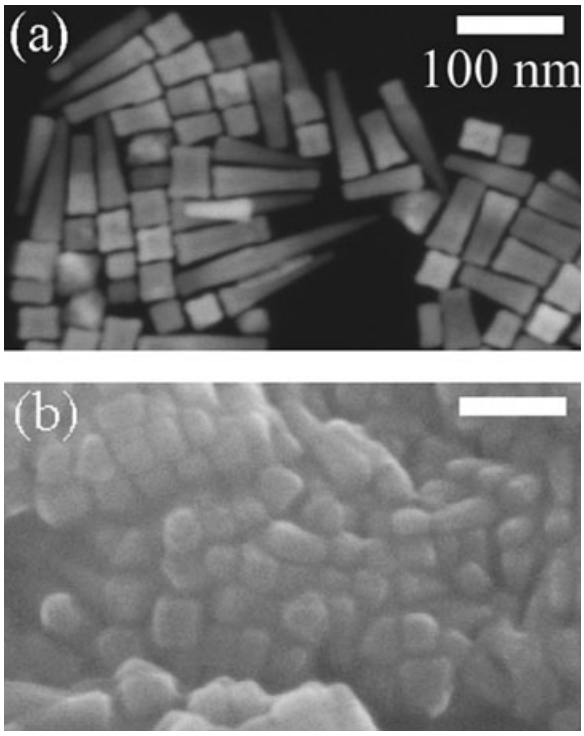

Figure 9.24 SEM images of rectangular Pd nanoparticles (a) before and (b) after tilting the silicon wafer by 45°. Both nanocube and nanorods are of rectangular shape. Reproduced with permission from Ref. [55]; © 2007 American Chemical Society.

100 keV) electron beam is used to excite the sample. The electron beam is scanned across the sample in a rastering fashion. The process creates low-energy secondary electrons which emit from the surface to form an image. The main difference between the images produced by these two methods is that TEM provides a 2-dimensional image, while SEM gives a 3-dimensional representation of the object being observed. The resolution of SEM is also about an order of magnitude lower than that of TEM.

9.2.3.1.3 **Scanning Probe Microscopy (SPM)** Atomic force microscopy (AFM) and scanning tunneling microscopy (STM) have both proved to be efficient in the characterization of palladium nanoparticles. One advantage of SPM is that it is able to resolve details of surfaces with atomic-level resolution. Both techniques operate by scanning the surface of the sample in the *xy* raster pattern, using a sharp tip that moves up and down along the z-axis. The main difference between STM and AFM is that, whereas in STM the sample being analyzed must be conductive, this is not a requirement in AFM (Figure 9.25). Several groups have

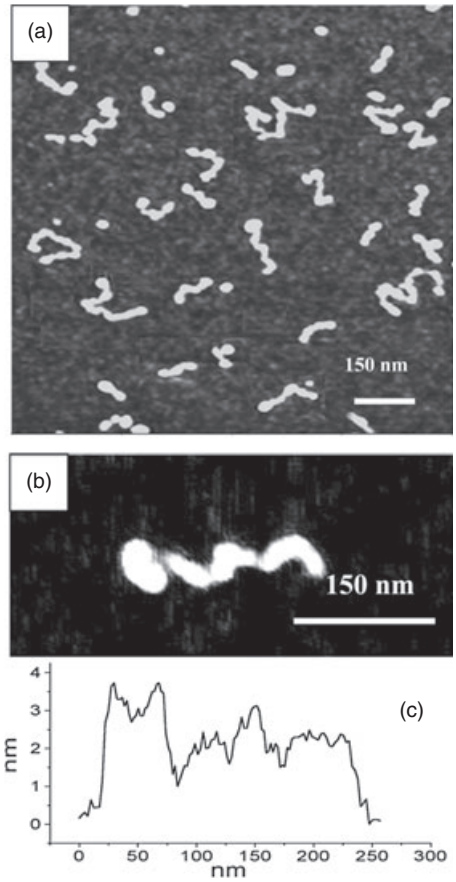

Figure 9.25 (a, b) AFM topography images of wire-shaped Pd nanostructures; (c) Cross-sectional profile along the long axis of nanowires on image (b). Pd nanowires were produced by mineralization of $Pd(OAc)_2$ in polycation molecules. Reproduced with permission from Ref. [77]; © 2004 American Chemical Society.

used SPM to analyze the morphology and topography of Pd nanostructures [68, 69, 75, 77].

9.2.3.2 Spectroscopic Techniques

9.2.3.2.1 **Infrared (IR) Spectrometry** IR spectrometry enables the determination of ligands at the surfaces of Pd nanostructures, provides information of the degree of order and relative orientation of surface-bound ligands [19, 78–82], and also plays an important role in confirming the completion of a ligand exchange reaction [74]. A number of groups have described the usefulness of IR spectroscopy in the

characterization of Pd nanostructures. For example, Yee and coworkers compared the IR spectrum of free octadecanethiol (OCT) and OCT-stabilized Pd nanoparticles [18], by observing significant changes in the symmetric and asymmetric stretching modes of the carbon adjacent to the thiol group. This occurred at a slightly lower wavenumber [$\nu_{as}(CH_2) = 2917\,cm^{-1}$; $\nu_s(CH_2) = 2849\,cm^{-1}$] when bound to the surface, relative to the stretching mode before binding ($\nu_{as}(CH_2) = 2955\,cm^{-1}$; $\nu_s(CH_2) = 2871\,cm^{-1}$]. Such shifts in the IR spectrum provide insights into the nature of the binding of the ligand to the surface. In addition, if a ligand has more than one functional group that might bind to the Pd surface, IR can be used to determine which group is actually bound to the surface. As an example, Tabuani *et al.* reported the synthesis of Pd nanoparticles supported on hyperbranched aromatic polyamides with both amino and carboxylic acid functional groups. Following fabrication of these nanostructures, IR spectroscopy showed that the carboxyl group band did not change after Pd absorption and reduction, whereas the amino groups did change. This observation suggested that only amino groups were involved in binding to the Pd surface [80]. Such analysis is particularly important when the terminal functional group is required for a subsequent reaction.

9.2.3.2.2 **UV-Visible Absorbance Spectrometry** UV-visible absorbance spectroscopy is used to characterize Pd nanoparticles in primarily two ways: (i) to monitor the palladium precursor as it is reduced to the zero-valent state, indicating formation of palladium nanoparticles; and/or (ii) to monitor the position of the palladium nanoparticles' surface plasmon resonance (SPR) peak.

UV-visible absorbance spectroscopy has often been used to reveal the completion of reduction, as the absorption for Pd(0) and Pd(II) differ significantly. Obare *et al.* monitored the change in the metal-to-ligand charge transfer (MLCT) band located at 400 nm of $Pd_3(OAc)_6$ as it was reduced from Pd^{2+} to Pd^0 [48]. The reduction was accompanied by a color change from yellow to black, as shown in the inset of Figure 9.26.

Anisotropic Pd nanoparticles appear to display well-defined absorbance peaks that have been described as being due to SPR. Xia and coworkers [58] reported that the SPR peaks for triangular (~28 nm edge length, 5 nm thickness) and hexagonal (~20 nm edge length, 10 nm thickness) nanoplate suspended in aqueous solution were located at 520 and 530 nm, respectively, and proposed that such peaks were due to the dielectric function of Pd and the thin nature of the plates. Xia's group also showed that hollow Pd nanocubes displayed a controllable increase in absorbance from blue (410 nm) to the near-infrared (1200 nm), with a decrease in particle size (Figure 9.27) [83].

9.2.3.2.3 **Nuclear Magnetic Resonance (NMR) Spectroscopy** NMR spectroscopy (most commonly ^1H NMR) has been used primarily to characterize the nature of binding of the ligand at the Pd nanoparticles' surface. For example, Ghosh [84] and coworkers observed the disappearance of phenyl proton peaks in phenol diazonium-passivated Pd nanoparticles when compared to the free ligand (see Figure 9.28). These authors proposed that the proton peaks of the ligand had

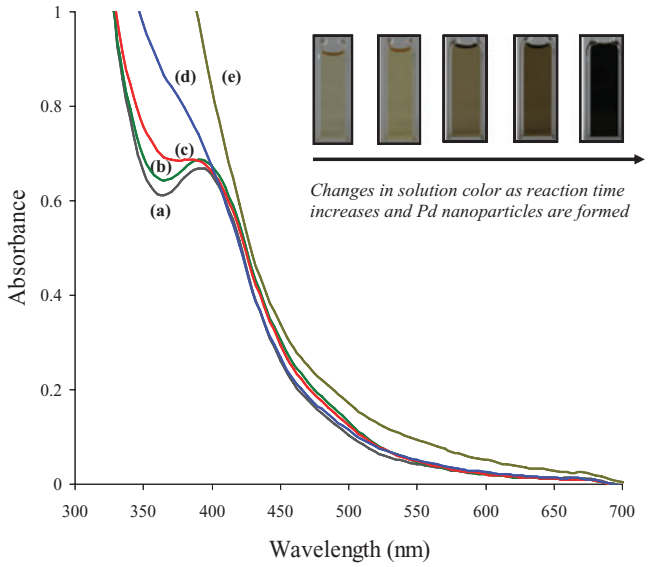

Figure 9.26 UV-visible absorbance spectra of $[Pd_3(OAc)_6]$ and *n*-dodecyl sulfide in a 1:5 molar ratio, respectively, dissolved in toluene. As the temperature is raised from room temperature to 95 °C, Pd nanoparticles begin to form, and the color of the solution changes from yellow to dark brown. At 80 °C, the solution color is dark brown, indicating the formation of Pd nanoparticles. (a) 0 min; (b) 10 min; (c) 20 min; (d) 30 min; (e) 40 min. The photograph in the inset shows the corresponding color changes associated with each spectrum. No change in UV-visible absorbance spectra was observed after 40 min, indicating Pd nanoparticle formation. Reproduced with permission from Ref. [48]; © 2007 American Chemical Society.

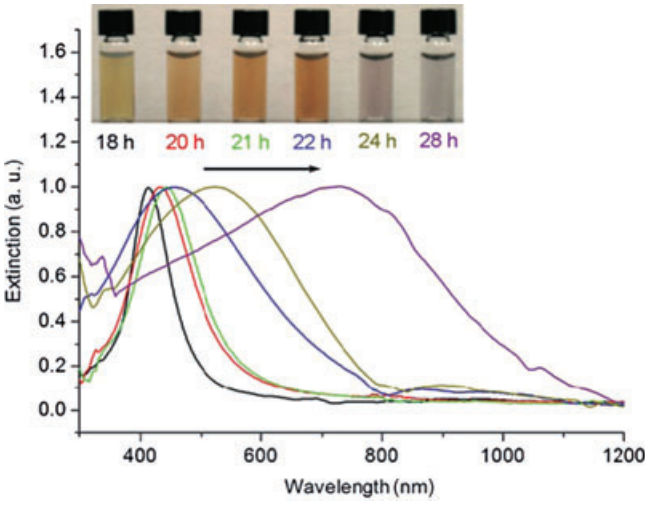

Figure 9.27 UV-visible spectra of Pd nanocubes. A longer corrosive etching time produced a thinner wall of hollow Pd nanocubes with a 48 nm edge length. The surface plasmon resonance peaks red-shift with a thinner wall. Reproduced with permission from Ref. [83] © 2005 Wiley Interscience.

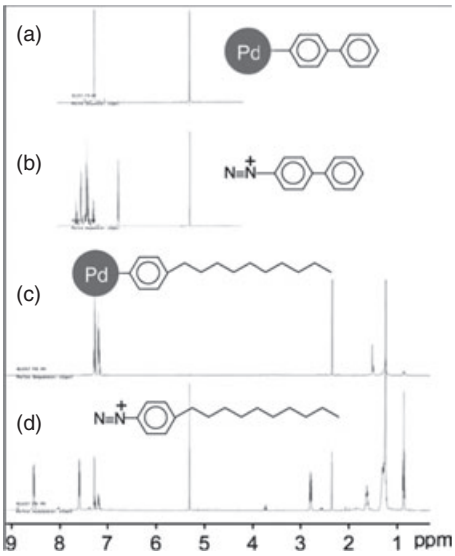

Figure 9.28 ^{1}H NMR spectra of Pd nanoparticles (a, c) and free ligands (b, d). The four phenol protons identified at 7.6 and 8.6 ppm disappear after decylphenyldiazonium (d) was bound to the Pd nanoparticles. The nine phenol protons in biphenoldiazonium (b) characterized at peaks between 7.4 and 7.7 ppm changes after binding. Reproduced with permission from Ref. [84]; © 2008 Royal Society of Chemistry.

broadened due to the slow tumbling rate of the nanoparticles, and used these data to confirm that the ligands were indeed bound to the particle surface. ^{13}C and ^{31}P NMR have also proved useful methods. For example, Son and coworkers studied the coordination chemistry of various phosphine ligands on Pd NPs using ^{31}P NMR spectroscopy [85]. Moreover, they were also able to conduct ligand-exchange reactions at the Pd surface to confirm not only the binding of different ligands but also the relative binding affinity of one phosphine ligand relative to another [86].

9.2.3.3 Chemical Analysis Techniques

9.2.3.3.1 **X-Ray Photoelectron Spectroscopy (XPS)** XPS is a surface chemical analysis technique based on the photoelectric effect, which describes the phenomenon of the ejection of electrons when photons with sufficient energy impinge upon a surface. Due to the characteristic binding energy of each element, the peaks in the resultant spectrum provide information on the chemical state and composition of the surface atoms. For the analysis of Pd nanostructures, XPS has been used primarily to examine the valent states of Pd [74, 80]. Tabuani and colleagues conducted an experiment in which they monitored the reduction of Pd^{2+} to Pd^{0} by XPS, and observed a progressive transition of Pd^{2+} (337.5 and 342.8 eV) to Pd^{0} (336.0 and 341.3 eV) [80].

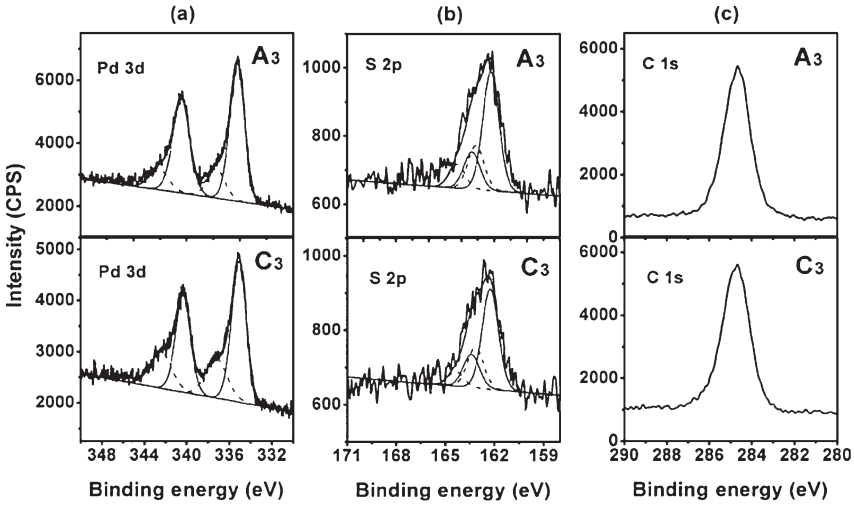

Figure 9.29 Line shapes of the high-resolution Pd 3-D core level spectra indicate that there are two types of valent states: zerovalent and nonzerovalent (PdS interphase). 337.6 and 342.8 eV are attributed to Pd $3d_{5/2}$ and $3d_{3/2}$ spin-orbit doublet peaks indicating an ionic Pd^{2+} state. Reproduced with permission from Ref. [80]; © 2003 American Chemical Society.

The ligand surrounding the Pd nanostructures influences the Pd oxidation state. For example, Lu *et al*. [74] revealed that the main component of Pd in thiol-stabilized Pd nanoparticles (either crystalline or amorphous phase) was Pd^0, which they were able to determine based on the Pd 3*d* signal with a binding energy of 335.2 eV. In addition, the presence of PdS in which the Pd 3*d* signal of 337.3 eV and S 2*p* signal of 162.3 eV (Figure 9.29) was also observed.

One limitation to XPS in the analysis of Pd nanostructures is that prolonged exposure to X-rays results in fragmentation of the particles. This problem was first observed during the TEM examination of a sample acquired after a long period of XPS analysis. However, a reduced time of X-ray analysis (<20 min) should overcome this drawback and provide an unaffected photoelectron signal [80].

9.2.3.3.2 **Energy-Dispersive X-Ray (EDX) Analysis** Similar to XPS, EDX is a technique that allows the chemical composition of a material to be determined. Here, X-ray beams are used to excite a surface, while the emission spectrum provides information on the elemental composition within the sample being analyzed, as each element provides a characteristic emission upon excitation. EDX has been coupled with electron microscopy to provide a powerful analytical tool for the chemical characterization of nanomaterials. In addition, EDX can provide quantitative data on the composition of each element contained in a sample.

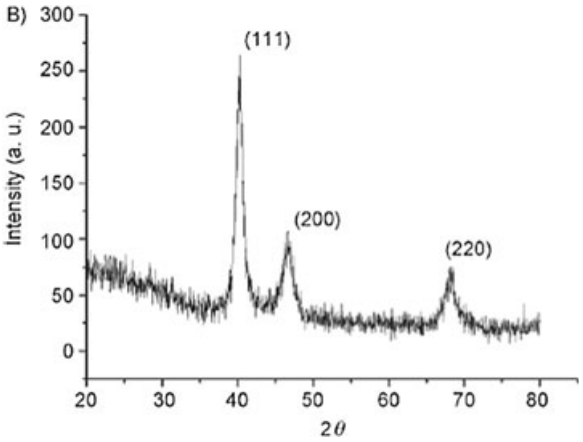

Figure 9.30 Diffractogram of 18 ± 5 nm Pd nanoparticles stabilized by high-molecular-weight ionic liquid polymer (ILP). Reproduced with permission from Ref. [87]; © 2006 Wiley Interscience.

9.2.3.4 **Physical Analysis Techniques**

9.2.3.4.1 **X-Ray Diffraction (XRD)** XRD is efficient in providing information regarding the crystallographic structure of a sample. The technique uses X-ray radiation that passes through a sample, such that the scattered beams form a diffraction pattern based on that sample. The common face-centered cubic (FCC) structure of Pd gives (111), (220) and (200) (e.g. Figure 9.30) diffraction peaks which correspond to diffraction lines at $2\theta = 40.039°$, $46.581°$, $68.047°$, respectively [87]. The particle size (d) can be calculated from the width of the (111) peak by using the Scherrer formula: [88]:

$$d = 0.9\lambda/(\beta \times \cos\theta) \tag{9.4}$$

where λ is the wavelength of the X-rays, β is the full width at half maximum (FWHM) of diffraction peak, and θ is the angle corresponding to the peak.

9.2.3.4.2 **X-Ray Reflectivity (XRR)** XRR is a surface-sensitive analytical technique used to characterize surfaces and thin films. When X-rays strike a surface at a critical angle (total reflection), the reflectivity intensity changes based on the roughness of the surface. The critical angle varies depend on the electronic density of the surface materials. At the interface between two thin layers, the reflected X-rays interfere causing the oscillation of reflectivity intensity with angle. In this way, XRR provide information on the thickness, roughness and density of thin films on a surface. XRR has been applied in the study of multilayers by Rafailovich's group, who deposited a monolayer Langmuir film of dodecanthiolate Pd nanoparticles under a pressure $7.8\,\mathrm{mN\,m^{-1}}$. A six-layer model was employed to simulate

the structure of the film by nonlinear least-squares fitting [55b]. The six layers consisted of Si substrate, SiO_2, thiol (hydrocarbon), Pd/thiol, glutathiol and air, respectively. By using XRR, the thickness of the Pd/thiol layer was determined in this case to be about 13.3 Å.

9.2.3.4.3 **Selected Area Electron Diffraction (SAED) Pattern** The selected area electron diffraction (SAED) pattern is a diffraction technique that is usually coupled with TEM to identify crystal structures and examine crystal defects. The technique is similar to XRD, but unique in that areas as small as several hundred square nanometers in size can be examined. An example is shown in Figure 9.31, in which ammonium salt-stabilized Pd nanoparticles that exhibit (111), (200), (220) and (311) ring patterns are measured and indicate the face-centered cubic (fcc) crystal structure of Pd [73]. Today, SAED is recognized as being a routine and important method for characterizing Pd nanostructures.

9.2.3.4.4 **Thermogravimetric Analysis (TGA)** TGA is a powerful technique for elucidating not only the nature of binding of surface ligands on the nanoparticles, but also the ratio of Pd atoms to stabilizing ligands. Weight loss is recorded as a function of increasing temperature and time, while a decomposition gradient accesses the thermal stability and compositions of the nanomaterial. As an example, Lee *et al.* [86] examined the dynamic and isothermal thermogravimetry of syndiotactic polystyrene (s-PS)-stabilized Pd nanoparticles. Neat s-PS was found to begin weight loss at about 330 °C, whereas for the nanocomplex the onset of

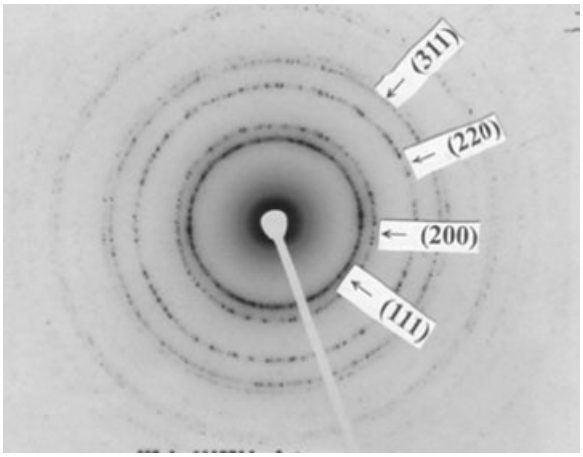

Figure 9.31 Electron diffraction pattern of Pd-surfactant complex of 14 nm size, where the stabilizing surfactant is cetyltrimethylammonium bromide (CTAB). Electron diffraction reveals crystalline structure with fcc packing arrangement. Reproduced with permission from Ref. [73]; © 2004 Institute of Physics.

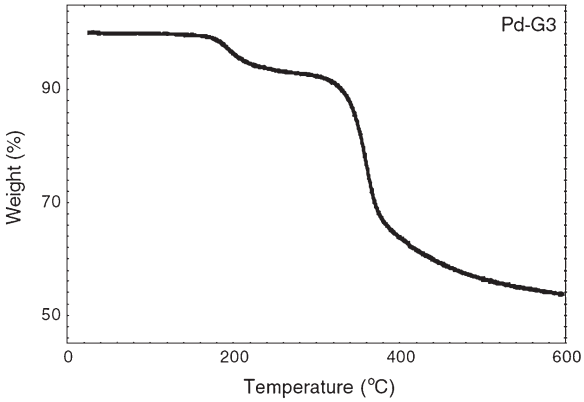

Figure 9.32 Thermogram of palladium-nanoparticle-cored dendrimer. The rate of heating was 10 °C min^{-1}. Reproduced with permission from Ref. [90] (Supplementary information); © 2003 American Chemical Society

degradation began at 360 °C. Similarly, Rao and coworkers [89] observed two distinct weight losses at 218 and 388 °C for laurylamine-capped Pd nanoparticles, with the two drops in the TGA profile indicating two possible binding modes of the amine ligand with the Pd nanoparticle surface. TGA was also carried out to estimate the total organic content of a Pd-nanoparticle-cored dendrimer (Figure 9.32) [90]. Here, the first decomposition was caused by the removal of trapped solvent and phase-transfer agent tetraoctylammonium bromide (TOBA), while the second decomposition step occurred due to volatilization of the G-3 dendron. These data showed the weight percentages of Pd and dendron to be 54 and 38%, respectively.

By combining TEM and TGA data it becomes possible to calculate the number of Pd atoms per nanoparticle by assuming that Pd clusters have the same density as bulk fcc Pd (i.e. 12.03 g cm^{-3}).

Thus, the Pd atom number in one nanoparticle can be calculated by the equation:

$$N_{Pd} = (68\,nm^{-3})(\pi/6)(D^3) \tag{9.5}$$

where D is the average diameter of the nanoparticle (in nanometers). Thus, the weight of the Pd core (W_{Pd}) is:

$$W_{Pd} = N_{Pd} \times 106.4 \text{ (where 106.4 is the atomic weight of Pd).}$$

By using this method, Gopidas *et al.* determined that their dendrimer-stabilized Pd nanoparticles had the formula $Pd_{300}G3_{14}$ [90], while Zamborini *et al.* estimated two different-sized thiol-stabilized Pd clusters of approximately 3.0 and 2.4 nm, which had 34.7% and 45% organic ligands, respectively. These data gave average formulas of $Pd_{976}C12_{274}$ and $Pd_{459}C12_{198}$, respectively [19].

9.2.3.4.5 **Dynamic Light Scattering (DLS)** DLS is an effective technique that is used to determine particle size distribution in a solution [91]. As significant synthetic approaches have been developed to control particle size, DLS has been increasingly utilized in this role. For DLS, a coherent light source (typically a laser) with a known frequency is used to irradiate particles moving under Brownian motion. As the light interacts with the particles it becomes scattered at a different frequency, depending on the particle size: small particles cause a greater shift in light frequency relative to larger particles.

9.2.3.5 Electrochemistry

Electrochemical techniques have been useful when characterizing Pd nanoparticles, where information on both the metallic component and the stabilizing ligand can be obtained. Cyclic voltammetry (CV) has been used to study the behavior of ligands at the surface [19, 92]. The quantum confinement in Pd nanoparticles has been found to influence the electron-transfer abilities of ligands at the surface. A similar technique, differential pulse voltammetry (DPV) has also been used as a characterization technique for palladium nanoparticles. The difference between CV and DPV is that, in CV, the current is measured as a function of applied potential, whereas in DPV the current at the working electrode is recorded while the pulse potential between the working and reference electrodes is swept linearly in time. Recently, the DPV of alkanethiol-stabilized Pd nanoparticles with diameters less than 5 nm displayed quantized double-layer (QDL) charging and discharging, and thus behaved in a similar manner to capacitors [19, 92]. The success of these measurement relies on the presence of uniform and small Pd nanoparticles for accurate QDL measurement. The data reveal a consistent spacing between successive peaks (ΔV), which is inversely proportional to the capacitance (sub-aF), as shown in Equation 9.6. The data allow the average size of Pd particle to be calculated.

$$\Delta V = \frac{e}{C_{MPC}} = \frac{ed}{4\pi\varepsilon\varepsilon_0 r(r+d)} \tag{9.6}$$

where e is the electron charge (1.6×10^{-19} coulombs), d is the thickness of the monolayer medium, ε is the dielectric constant of the monolayer medium around the metal core, ε_0 is the permittivity of free space [8.85×10^{-12} F m^{-1} (or C^2 N^{-1} m^2)] and r is the radius of the metal core.

By combining this equation with DPV results obtained from dendrimer-stabilized Pd nanoparticles, Crooks *et al.* [92] showed that Pd nanoparticles with 140 atoms, where the peak spacing was reflected ($\Delta V = 270 \pm 20$ mV) had a capacitance value of 0.59 aF (Figure 9.33). This value corresponded to an average diameter size of 1.6 nm yet, when using TEM this size was measured as 1.7 nm. Several reasons were proposed to explain this discrepancy. First, an interaction of the Pd nanoparticles with the TEM grid may have altered the structure of the Pd nanoparticles. Second, Pd does not provide a good contrast, which makes it difficult to resolve particles of less than 2 nm. Third, the parameters in the equation are arbi-

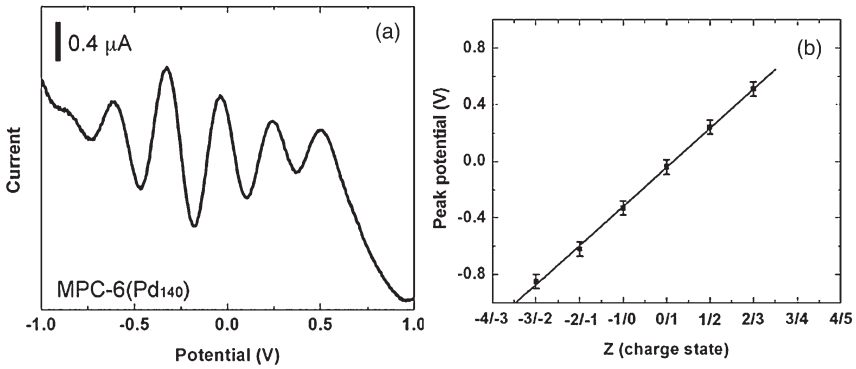

Figure 9.33 (a) Differential pulse voltammetry plots of 1.1 m*M* MPC-6(Pd140) solution; (b) Relationship between the peak potentials in (a) and the charge state of the MPCs. Reproduced with permission from Ref. [92]; © 2005 American Chemical Society.

trary in varying environmental conditions. Therefore, argument persists regarding the reliability of TEM data versus electrochemical results for particles of such small size.

9.2.3.5.1 **Scanning Tunneling Microscopy and Spectroscopy (STM/STS)** Scanning tunneling microscopy/spectroscopy (STM/STS) allows the electronic measurement of individual nanostructures by probing the local density of electronic states and the band gap of particles at the atomic scale. The experiment uses a STM tip fixed on top of a selected Pd nanoparticle, but the feedback loop is turned off. In this case, the current–voltage (I–V) curves provides information on the single-electron tunneling (SET) process that occurs in a double barrier tunneling junction (DBTJ). This consists of two capacitances between the tip and ligand-capped Pd nanoparticles and the substrate. In order to generate tunneling current, the charging energy $e^2/2C$ must exceed the thermal energy $k_B T$, and the resistances of the two tunneling junctions must be larger than the resistance quantum h/e^2 (where C is capacitance; e is the electron charge; k_B is Boltzmann's constant, T is temperature and h is Planck's constant) [74].

An ultrahigh vacuum is required to avoid the influence of atmospheric moisture. Lu *et al.* used STS to measure Pd nanoparticles at a low temperature (4.2 K) for crystalline and amorphous Pd nanoparticles, as shown in Figure 9.34. The resultant *I–V* curves display Coulomb blockade due to single-electron transfer. and Coulomb staircases where the current is zero before the voltage becomes sufficient to overcome the band gap of the Pd nanoparticle. These data show that the electronic properties differ significantly for the two phases, though this may be due to atomic ordering or disordering within the particles [74]. Although STS has not yet been fully exploited with various shapes of Pd nanoparticles, it is expected to provide much detail about the electronic properties of Pd nanostructures.

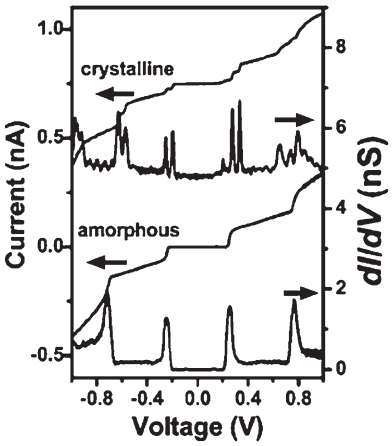

Figure 9.34 *I–V* curves and d*I*/d*V*–*V* for crystalline and amorphous Pd_{300} of ca. 2 nm diameter. The extra-fine features in each step for crystalline Pd particles are due to the discrete energy level induced by the ordered atomic structure. (The ← arrow indicates the *I–V* curves, while the → arrow represents the d*I*/d*V*–*V* curve. Reproduced with permission from Ref. [74]; © 2003 American Chemical Society.

9.3
Life Sciences-Related Applications of Palladium Nanoparticles

Whilst the primary applications of Pd nanoparticles have been in catalysis, a number of reports have described other important applications related to the life sciences. Scheme 9.2 shows several such uses of Pd nanoparticles, although for the purpose of this chapter we focus on those applications in the 'white' boxes as these relate to the life sciences. They include the role of Pd in environmental remediation, as well as in biological and chemical sensing. It is anticipated that, with the recent successes in controlling the shape of Pd nanoparticles and an improved understanding of their chemical and physical properties, a host of new applications will be discovered in the near future.

9.3.1
Catalysis

Palladium is widely used for a significant number of synthetic transformations, and has the potential to become a major influence on the synthesis of pharmaceuticals and agricultural products [93]. The key challenges in this area are not only to prepare palladium nanoparticles with controlled sizes but also to stabilize them against sintering into larger particles and leaching into solution during liquid-phase catalysis. Pd nanoparticles are known to effectively catalyze carbon–carbon (C-C) coupling reactions, including the Suzuki reaction, the Heck reaction and the Stille reaction. As shown earlier in this chapter, the synthesis of Pd

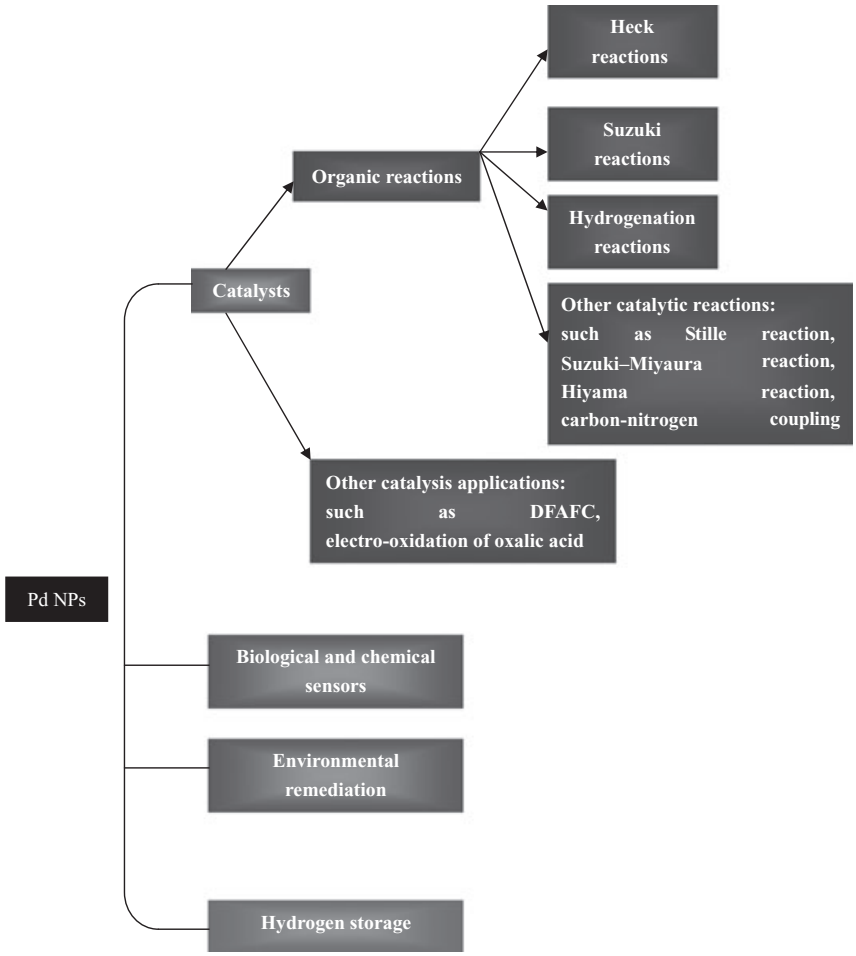

Scheme 9.2 Applications of palladium nanoparticles (NPs).

nanostructures in many cases results in colloidal particles that typically are surrounded with stabilizing ligands. The removal of stabilizing ligands from the particle surface results in particle aggregation, with a concomitant decrease in catalytic activity due to the reduction in surface area. In addition, colloidal Pd nanoparticles create complications with regards to the separation of particles from reactants and products. For this purpose, Pd nanoparticles may be immobilized on solid supports via their physical adsorption onto a range of supports, most notably polymers, charcoal, silica or alumina [94]. This immobilization creates a heterogeneous catalytic system that is reusable for several catalytic cycles.

Soluble colloidal nanoparticles present unique opportunities for homogeneous catalysis due to better activity and selectivity [95]. Palladium nanoparticles can be used as homogeneous catalysts in their colloidal state, although this is accompa-

nied by certain limitations. Obare and colleagues compared the effect of colloidal versus immobilized Pd nanoparticle catalysts in the hydrogenation of styrene to 1-ethylbenzene [48]. The catalytic activity and structures of the thioether-stabilized Pd nanoparticles with 1.7 ± 0.2 nm, 2.5 nm ± 0.1 nm and 3.5 ± 0.1 nm diameters were monitored before and after a catalytic reaction. Pd nanoparticles examined by TEM following the first catalytic cycle were found to aggregate, with the smaller 1.7 nm Pd nanoparticles forming larger-sized aggregates, relative to the larger 2.5 nm ± 0.1 nm and 3.5 ± 0.1 nm Pd nanoparticles. Both, the 2.5 nm ± 0.1 nm and 3.5 ± 0.1 nm Pd nanoparticles had similar-sized aggregates following one catalytic cycle. After the first catalytic cycle, the average reaction yields for the 1.7 ± 0.2 nm, 2.5 nm ± 0.1 nm and 3.5 ± 0.1 nm Pd nanoparticles were 98, 96 and 95%, respectively. In the second catalytic cycle, the reaction yields decreased to 12, 25 and 43% respectively, and continued to decrease with additional cycles, as shown in Figure 9.35. The 1.7 nm Pd nanoparticles showed no catalytic activity following two cycles. However, the results shown in Figure 9.35 revealed that the reactivity of the Pd nanoparticles increased with an increase in Pd nanoparticle size. This is in contrast to what might be expected – that is, the reactivity would be expected to decrease with increases in particle size, due to smaller particles having a greater percentage of their atoms on the particle surface compared to the larger particles. This observation has also been reported by others [41, 96, 97]. In addition to a loss of catalytic activity of the homogeneous Pd nanoparticles, particle recovery proved to be problematic. A second disadvantage

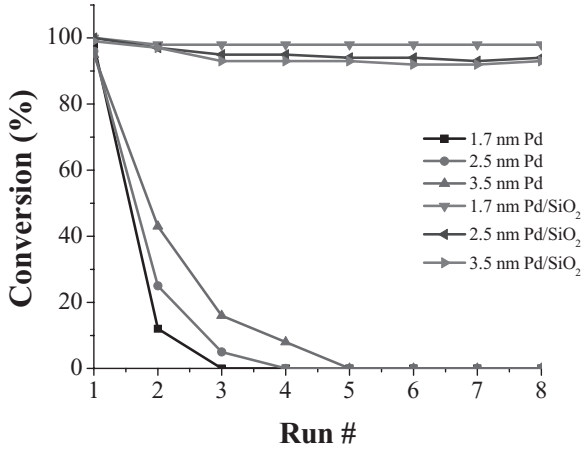

Figure 9.35 Percentage conversion plotted against the number of catalytic cycles for the conversion of styrene to 1-ethylbenzene. Comparison of colloidal and SiO_2-immobilized 1.7 nm, 2.5 nm and 3.5 nm Pd nanoparticles. For colloidal particles, the larger the size, the more reusable was the catalyst. When immobilized on SiO_2, the conversion efficiencies were highly improved compared to the colloidal counterpart; however, the smaller the particle size the better was the conversion efficiency. Reproduced with permission from Ref. [48]; © 2007 American Chemical Society.

in using homogeneous metal nanoparticle catalysts is the challenge of their recovery, and in this respect metal nanoparticle immobilization onto solid supports has become a routine, attractive and widely used approach. The advantage here is that the activity of the Pd nanoparticles can be utilized whilst simultaneously allowing the system to behave heterogeneously. Obare *et al*. further examined the catalytic activity of the 1.7 ± 0.2 nm, $2.5\,\text{nm} \pm 0.1\,\text{nm}$ and 3.5 ± 0.1 nm Pd nanoparticles immobilized on SiO_2 (Pd/SiO_2) for styrene hydrogenation, and compared the results to those obtained with nonimmobilized Pd nanoparticles. As shown in Figure 9.35, all three sizes of Pd/SiO_2 showed no loss in catalytic activity after eight reaction cycles. In addition, the 1.7 nm Pd/SiO_2 showed consistent improved conversion rates (~99%) compared to the larger 3.5 ± 0.1 nm particles. These results demonstrate the importance of immobilizing metallic nanoparticles onto solid supports for their use in catalysis.

A number of reports relating to Pd-supported catalyzed reactions are available in the literature, with many such reactions having been carried out in the organic phase. Future advancements in the use of nanoparticles for the life sciences will rely on an ability to carry out such transformations in the aqueous phase, thus creating environmentally friendly chemistries. In the following section we will showcase some notable examples of Pd-catalyzed C–C coupling reactions in the aqueous phase. It is anticipated that, based on the successes in synthetic procedures and an increased understanding of the chemical and physical properties, future progress in this area will indeed be extensive.

9.3.1.1 **Suzuki Reaction**

In addition to the well-known organic-phase transformations, the Suzuki reaction also offers methods for the crosscoupling of aryl halides with hydrophilic functional groups. These reactions therefore, require polar solvents such as water. El-Sayed's group prepared 3.6 ± 0.73 nm PVP-stabilized palladium nanoparticles and showed them to act as efficient catalysts for the Suzuki crosscouplings as colloids [15]. One limitation to this reaction was that the Pd metal precipitated during the reaction causing a decrease in catalytic activity. To investigate this effect further, a series of PVP-Pd nanoparticles of varying size was prepared to catalyze the Suzuki reaction between phenylboronic acid and iodobenzene in aqueous solution [16]. Although the results showed the catalytic activity to increase as the particle size decreased, the tendency for aggregation increased as the particle size decreased. This suggested that the reactivity of the particles was indeed 'structure-sensitive' – that is, the coordinately unsaturated vertex and edge atoms on the particle surface were each active sites for the catalysis.

El-Sayed's group also investigated the effect of three different stabilizers on the catalytic activity and stability of the Pd nanoparticles when catalyzing a Suzuki reaction in the aqueous phase [17]. Results showed that the Pd nanoparticles, when stabilized by PVP, block copolymer and G3 dendrimer, were all efficient catalysts. However, in the case of dendrimers, the strong encapsulation of Pd particles within the dendrimers resulted in a loss of catalytic activity.

In another study, Gallon *et al.* used polyaniline (PANI) nanofiber-supported palladium nanoparticles as catalysts for the coupling of aryl chlorides with phenyl boronic acid in water [98]. Typically, the aryl chlorides were ineffective in most Suzuki coupling reactions but, by substituting the aryl halide appropriately, it could be shown that Pd nanoparticles were capable of carrying out the transformation in the aqueous phase.

9.3.1.2 Heck Reaction

The Heck reaction is one of the most versatile and useful tools in organic synthesis, and provides a direct route for the synthesis of many important olefins [99]. Normally, the Heck reaction employs a palladium catalyst in the presence of phosphine ligands and a base, under an inert atmosphere. However, as polar aprotic solvents remain the major media for the Heck reaction [100], this has greatly limited the reaction's industrial application.

Very few examples have been reported of Pd-catalyzed Heck reactions being carried out in the aqueous phase. The most notable is the investigation conducted by Bhattacharya and coworkers, who used CTAB-stabilized Pd nanoparticles as catalysts [101]. In this reaction, CTAB had the dual role of providing a strong micellar effect and also acting as a stabilizer for the Pd nanocluster formation. These Pd catalysts achieved good yields for the CTAB-mediated Heck reaction in water, although some low-loading Pd catalysts also showed effective results.

9.3.1.3 Stille Reaction

Several groups have demonstrated the efficacy of Pd nanoparticles in catalyzing the Stille reaction [102–105]. In all such cases the Pd nanoparticles were immobilized on inorganic supports, such as polyoxometalates, alumina, silica and polymers, and the reactions took place in organic solvents. However, Crooks' group reported dendrimer-encapsulated nanoparticles (DENs), consisting of size-monodisperse Pd nanoparticles within poly(amidoamine) (PAMAM) dendrimers [106]. The major improvement with these highly monodisperse Pd nanoparticles as catalysts for the Stille reaction was that it was easy to achieve a high yield, at room temperature, and in water.

9.3.1.4 Hydrogenation Reactions

Crooks' group prepared monodisperse (1.7 ± 0.2 nm) palladium nanoparticles within the interiors of three different generations of hydroxyl-terminated PAMAM dendrimers [41]. This process involved encapsulation of the nonselective catalyst (the Pd nanoparticle) within a selective nanoporous cage (the dendrimer). These dendrimer-encapsulated palladium nanoparticles were used as catalysts to hydrogenate allyl alcohol and four R-substituted derivatives in a methanol/water mixture. The results showed that higher-generation dendrimer encapsulated catalysts (DECs) or larger substrates resulted in lower turnover frequencies.

9.3.2
Environmental Remediation

Halogenated hydrocarbon compounds are prevalent pollutants in the environment, and consequently several methods have been examined to identify reliable and effective ways of removing such toxic materials from the environment. Hence, Pd nanoparticles, with their excellent reducing capabilities, may represent possible candidates for this role.

Calò and coworkers reported that Pd nanoparticles catalyzed the hydrodehalogenation reactions of aryl chlorides in ionic liquids [107]. Here, molten tetrabutylammonium bromide was used as the solvent, and tetrabutylammonium acetate as the base. The results showed the Pd nanoparticles to be capable of the hydrodehalogenation of various aryl chlorides under hydrogen, at atmospheric pressure. These authors also noted that the catalyst showed only a small decrease in catalytic activity with recycling experiments, due mainly to a minor leaching of palladium from the ionic liquid phase.

In further studies, Roberts *et al.* [108] showed that 2.4 nm polysugar-stabilized-Pd nanoparticles catalyzed the hydrodechlorination of trichloroethylene, an extremely difficult pollutant to remove from the environment. Mertens and coworkers recently reported a new approach for degradation of the toxic pesticide lindane (γ-hexachlorocyclohexane; γ-HCH) through a dechlorination process catalyzed by Pd nanoparticles [109]. A heterogeneous catalyst was used in which colloidal Pd nanoparticles were immobilized onto the biomass of *Shewanella oneidensis*. The results showed that, upon interaction with the Pd nanoparticles, the dechlorination of lindane in water in a membrane reactor was highly effective. Indeed, when compared to a commercially available, powdered Pd(0) material, the immobilized Pd nanoparticles showed a high catalytic activity in the dechlorination of γ-HCH.

9.3.3
Sensing

A number of new reports have been made describing the ability of Pd nanoparticles to function as effective sensors. For example, Fang's group used Pd nanoparticles supported on multi-walled carbon nanotubes (MWCNTs) to modify a glassy carbon electrode (GCE). This material was then used in a DNA sensor system [110] where DNA hybridization processes were monitored by electrochemical measurements using the dye, methylene blue (MB) as an indicator [MB can be used to distinguish between single-stranded DNA (ssDNA) and double-stranded DNA (dsDNA)]. The results showed that Pd nanoparticles could affect the redox reaction of MB by adsorbing/releasing hydrogen; furthermore, the MWCNTs/Pd-NPs, when combined with MB, functioned as a sensitive and selective DNA sensor.

Foxx *et al.* reported the synthesis of polymer-stabilized Pd nanoparticles on carbon supports [111]. An oxidase enzyme was immobilized on the nanocomposite graphite-Pd surface to fabricate the biosensor, after which the particles were used

for sensing glucose by monitoring the oxidation or reduction of H_2O_2 (the byproduct of glucose oxidation). Lim and coworkers also reported the details of a glucose biosensor in which Pd nanoparticles and the enzyme glucose oxidase (GOx) were codeposited onto a carbon nanotube (CNT) film [112]. The results showed the Pd-GOx-Nafion CNT bioelectrode to be an efficient sensor for the oxidation and reduction of the enzymatically liberated H_2O_2, thus providing a rapid and sensitive quantification of glucose.

Huang and coworkers reported the details of biosensors based on Pd nanoparticles [113]. Here, Pd nanoparticles loaded onto carbon nanofibers (CNFs) (known as Pd/CNFs) were used to modify a carbon paste electrode (CPE) for the electrochemical-sensing of H_2O_2 and NADH. Based on these experiments, the Pd/CNF-CPE showed high sensitivity and selectivity, as well as a rapid response to H_2O_2 and NADH. These authors claimed that the presence of Pd, a good electric conductivity, a high active surface area and a high catalytic activity led to a significant improvement in the properties of the sensor.

9.4 Future Perspectives

One of the major challenges in nanoscale science is the development of straightforward synthetic approaches that produce desired nanostructures, in high yield and with uniformity in both size and shape. Over the past decade, significant advancements have been made in our understanding of the chemistry required to control the size and shape of Pd nanoparticles. Such progress has opened several avenues for the exploration of applications of Pd beyond catalysis. Quantum confinement coupled with the shape-control of Pd has demonstrated some interesting properties, including surface plasmon resonance, charge transfer and sensor applications. With additional progress devoted towards an understanding of the physical properties of Pd nanoparticles, it is expected that in future these materials will play important roles in medical applications, the environmental sciences and in electronics. Yet, the major task will be to bring together the expertise of synthetic chemists with that of physicists, biologists and engineers in order to assess the potential of these novel materials.

References

1 Markus, H., Plomp, A.J., Sandberg, T., Nieminen, V., Bitter, J.H. and Murzin, D.Y.Yu (2007) Dehydrogenation of hydroxymatairesinol to oxomatairesinol over carbon nanofibre-supported palladium catalysts. *Journal of Molecular Catalysis A–Chemical*, **274**, 42.

2 Nishihata, Y., Mizuki, J., Akao, T., Tanaka, H., Uenishi, M., Kimura, M., Okamoto, T. and Hamada, N. (2002) Self-regeneration of a Pd-perovskite catalyst for automotive emissions control. *Nature*, **418**, 164.

3 Nutt, M.O., Hughes, J.B. and Wong, M.S. (2005) Designing Pd-on-Au bimetallic nanoparticle catalysts for trichloroethene hydrodechlorination. *Environmental Science and Technology*, **39**, 1346.

4 Favier, F., Walter, E.C., Zach, P.M., Benter, T. and Penner, R.M. (2001) Hydrogen sensors and switches from electrodeposited palladium mesowire arrays. *Science*, **293**, 2227.

5 Ostwald, W. (1896) *Lehrbruck der Allgemeinen Chemie*, Vol. 2, Part 1, Leipzig, Germany.

6 Turkevitch, J. (1985) Colloidal gold. Part II. color, coagulation, adhesion, alloying and catalytic properties. *Gold Bulletin*, **18**, 86.

7 Bönnemann, H., Brijoux, W., Brinkmann, R., Dinjus, E., Fretzen, T., Joussen, B. and Korall, J. (1992) Highly dispersed metal-clusters and colloids for the preparation of active liquid-phase hydrogenation catalysts. *Angewandte Chemie-International Edition in English*, **31**, 323.

8 Jiang, Y. (2003) Forced hydrolysis and chemical co-precipitation, in *Handbook of Nanophase and Nanostructured Materials*, Vol. 59 (eds Z.L. Wang, Y. Liu and Z. Zhang), Kluwer Academic, New York.

9 Michaelis, M. and Henglein, A. (1992) Reduction of palladium (II) in aqueous solution: stabilization and reactions of an intermediate cluster and palladium colloid formation. *Journal of Physical Chemistry*, **96**, 4719.

10 Teranishi, T. and Miyake, M. (1998) Size control of palladium nanoparticles and their crystal structures. *Chemistry of Materials*, **10**, 594.

11 Reetz, M.T., Winter, M. and Tesche, B. (1997) Self-assembly of tetraalkylammonium salt-stabilized giant palladium clusters on surfaces. *Chemical Communications*, 147.

12 Narayanan, R. and El-Sayed, M.A. (2003) Effect of catalysis on the stability of metallic nanoparticles: Suzuki reaction catalyzed by PVP-palladium nanoparticles. *Journal of the American Chemical Society*, **125**, 8340.

13 Meier, M.A.R., Filali, M., Gohy, J.-F. and Schubert, U.S. (2006) Star-shaped block copolymer stabilized palladium nanoparticles for efficient catalytic Heck cross-coupling reactions. *Journal of Materials Chemistry*, **16**, 3001.

14 Piao, Y., Jang, Y., Shokouhimehr, M.D., Lee, I.S. and Hyeon, T. (2007) Facile aqueous-phase synthesis of uniform palladium nanoparticles of various shapes and sizes. *Small*, **3**, 255.

15 Li, Y., Hong, X.M., Collard, D.M. and El-Sayed, M.A. (2000) Suzuki cross-coupling reactions catalyzed by palladium nanoparticles in aqueous solution. *Organic Letters*, **2**, 2385.

16 Li, Y., Boone, E. and El-Sayed, M.A. (2002) Size effects of PVP-Pd nanoparticles on the catalytic Suzuki reactions in aqueous solution. *Langmuir*, **18**, 4921.

17 Li, Y. and El-Sayed, M.A. (2001) The effect of stabilizers on the catalytic activity and stability of Pd colloidal nanoparticles in the Suzuki reactions in aqueous solution. *Journal of Physical Chemistry B*, **105**, 8938.

18 Yee, C.Y., Jordan, R., Ulman, A., White, H., King, A., Rafailovich, M. and Sokolov, J. (1999) Novel one-phase synthesis of thiol-functionalized gold, palladium, and iridium nanoparticles using superhydride. *Langmuir*, **15**, 3486.

19 Zamborini, F.P., Gross, S.M. and Murray, R.W. (2001) Synthesis, characterization, reactivity, and electrochemistry of palladium monolayer protected clusters. *Langmuir*, **17**, 481.

20 Zelakiewicz, B.S., Lica, G.C., Deacon, M.L. and Tong, Y. (2004) ^{13}C NMR and infrared evidence of a dioctyl-disulfide structure on octanethiol-protected palladium nanoparticle surfaces. *Journal of the American Chemical Society*, **126**, 10053.

21 Chen, S., Huang, K. and Stearns, J. (2000) Alkanethiolate-protected palladium nanoparticles. *Chemistry of Materials*, **12**, 540.

22 Kim, S.-W., Kim, M., Lee, W.Y. and Hyeon, T. (2002) Fabrication of hollow palladium spheres and their successful application to the recyclable heterogeneous catalyst for Suzuki coupling reactions. *Journal of the American Chemical Society*, **124**, 7642.

23 Buhleier, E., Wehner, W. and Vögtle, F. (1978) Cascade-chain-like and nonskid-chain-like synthesis of molecular cavity topologies. *Synthesis*, 155.

24 Zhao, M., Sun, L. and Crooks, R.M. (1998) Preparation of Cu nanoclusters within dendrimer templates. *Journal of the American Chemical Society*, **120**, 4877.

25 Balogh, L. and Tomalia, D.A. (1998) Poly(amidoamine) dendrimer-templated nanocomposites. 1. Synthesis of zerovalent copper nanoclusters. *Journal of the American Chemical Society*, **120**, 7355.

26 Esumi, K., Suzuki, A., Aihara, N., Usui, K. and Torigoe, K. (1998) Preparation of gold colloids with UV irradiation using dendrimers as stabilizer. *Langmuir*, **14**, 3157.

27 Zhao, M. and Crooks, R.M. (1999) Homogeneous hydrogenation catalysis with monodisperse, dendrimer-encapsulated Pd and Pt nanoparticles. *Angewandte Chemie–International Edition in English*, **38**, 364.

28 Ottaviani, M.F., Bossmann, S., Turro, N.J. and Tomalia, D.A. (1994) Characterization of starburst dendrimers by the EPR technique. 1. Copper complexes in water solution. *Journal of the American Chemical Society*, **116**, 661.

29 Ottaviani, M.F., Montalti, F., Turro, N.J. and Tomalia, D.A. (1997) Characterization of starburst dendrimers by the EPR technique. Copper(II) Ions binding full-generation dendrimers. *Journal of Physical Chemistry B*, **101**, 158.

30 Bosman, A.W., Schenning, A.P.H.J., Janssen, R.A.J. and Meijer, E.W. (1997) Well-defined metallodendrimers by site-specific complexation. *Chemische Berichte*, **130**, 725.

31 Vassilev, K. and Ford, W.T. (1999) Poly(propylene imine) dendrimer complexes of Cu(II), Zn(II), and Co(III) as catalysts of hydrolysis of p-nitrophenyl diphenyl phosphate. *Journal of Polymer Science Part A–Polymer Chemistry*, **37**, 2727.

32 Kim, Y.-G., Oh, S.-K. and Crooks, R.M. (2004) Preparation and characterization of 1–2 nm dendrimer-encapsulated gold nanoparticles having very narrow size distributions. *Chemistry of Materials*, **16**, 167.

33 Yeung, L.K. and Crooks, R.M. (2001) Heck heterocoupling within a dendritic nanoreactor. *Nano Letters*, **1**, 14.

34 Yeung, L.K., Lee, C.T., Johnston, K.P. and Crooks, R.M. (2001) Catalysis in supercritical CO2 using dendrimer-encapsulated palladium nanoparticles. *Chemical Communications*, 2290.

35 Ooe, M., Murata, M., Mizugaki, T., Ebitani, K. and Kaneda, K. (2004) Supramolecular catalysts by encapsulating palladium complexes within dendrimers. *Journal of the American Chemical Society*, **126**, 1604.

36 Rahim, E.H., Kamounah, F.S., Frederiksen, J. and Christensen, J.B. (2001) Heck reactions catalyzed by PAMAM-dendrimer encapsulated Pd(0) nanoparticles. *Nano Letters*, **1**, 499.

37 Narayanan, R. and El-Sayed, M.A. (2004) Effect of colloidal catalysis on the nanoparticle size distribution: dendrimer-Pd vs. PVP-Pd nanoparticles catalyzing the Suzuki coupling reaction. *Journal of Physical Chemistry B*, **108**, 8572.

38 Pittelkow, M., Moth-Poulsen, K., Boas, U. and Christensen, J. (2003) Poly(amidoamine)-dendrimer-stabilized Pd(0) nanoparticles as a catalyst for the Suzuki reaction. *Langmuir*, **19**, 7682.

39 Li, Y. and El-Sayed, M.A. (2001) The effect of stabilizers on the catalytic activity and stability of Pd colloidal nanoparticles in the Suzuki reactions in aqueous solution. *Journal of Physical Chemistry B*, **105**, 8938.

40 Niu, Y. and Crooks, R.M. (2003) Preparation of dendrimer-encapsulated metal nanoparticles using organic solvents. *Chemistry of Materials*, **15**, 3463.

41 Niu, Y., Yeung, L.K. and Crooks, R.M. (2001) Size-selective hydrogenation of olefins by dendrimer-encapsulated palladium nanoparticles. *Journal of the American Chemical Society*, **123**, 6840.

42 Scott, R.W.J., Ye, H., Henriquez, R.R. and Crooks, R.M. (2003) Synthesis, characterization, and stability of dendrimer-encapsulated palladium nanoparticles. *Chemistry of Materials*, **15**, 3873.

43 Ye, H., Scott, R.W.J. and Crooks, R.M. (2004) Synthesis, characterization, and

surface immobilization of platinum and palladium nanoparticles encapsulated within amine-terminated poly(amidoamine) dendrimers. *Langmuir*, **20**, 2915.

44 Chechik, V. and Crooks, R.M. (2000) Dendrimer-encapsulated Pd nanoparticles as fluorous phase-soluble catalysts. *Journal of the American Chemical Society*, **122**, 1243.

45 Ooe, M., Murata, M., Mizugaki, T., Ebitani, K. and Kaneda, K. (2002) Dendritic nanoreactors encapsulating Pd particles for substrate-specific hydrogenation of olefins. *Nano Letters*, **2**, 999.

46 Esumi, K., Isono, R. and Yoshimura, T. (2004) Preparation of PAMAM- and PPI-metal (silver, platinum, and palladium) nanocomposites and their catalytic activities for reduction of 4-nitrophenol. *Langmuir*, **20**, 237.

47 Oh, S.K., Kim, Y.G., Ye, H. and Crooks, R.M. (2003) Synthesis, characterization, and surface immobilization of metal nanoparticles encapsulated within bifunctionalized dendrimers. *Langmuir*, **19**, 10420.

48 Ganesan, M., Freemantle, R.G. and Obare, S.O. (2007) Monodisperse thioether-stabilized palladium nanoparticles: synthesis, characterization, and reactivity. *Chemistry of Materials*, **19**, 3464.

49 Son, S.U., Jang, Y., Yoon, K.Y., Kang, E. and Hyeon, T. (2004) Facile synthesis of various phosphine-stabilized monodisperse palladium nanoparticles through the understanding of coordination chemistry of the nanoparticles. *Nano Letters*, **4**, 1147.

50 Tamura, M. and Fujihara, H. (2003) Chiral bisphosphine BINAP-stabilized gold and palladium nanoparticles with small size and their palladium nanoparticle-catalyzed asymmetric reaction. *Journal of the American Chemical Society*, **125**, 15742.

51 Tatumi, R., Tomoki, A. and Fujihara, H. (2006) Synthesis of small palladium nanoparticles stabilized by bisphosphine BINAP bearing an alkyl chain and their palladium nanoparticle-catalyzed carbon–carbon coupling reactions under room-temperature. *Chemical Communications*, 3349.

52 Richter, J., Seidel, R., Kirsch, R., Mertig, M., Pompe, W., Plaschke, J. and Schmackert, H. (2000) Nanoscale palladium metallization of DNA. *Advanced Materials*, **12**, 507.

53 Richter, J., Mertig, M., Pompe, W., Monch, I. and Schackert, H.K. (2001) Construction of highly conductive nanowires on a DNA template. *Applied Physics Letters*, **78**, 536.

54 Fang, C., Fan, Y., Kong, J.M., Zhang, G.J., Linn, L. and Rafeah, S. (2007) DNA-templated preparation of palladium nanoparticles and their application. *Sensors and Actuators B: Chemical*, **126**, 684.

55 (a) Sun, Y., Zhang, L., Zhou, H., Zhu, Y., Sutter, E., Ji, Y., Rafailovich, M.H. and Sokolov, J.C. (2007) Seedless and templateless synthesis of rectangular palladium nanoparticles. *Chemistry of Materials*, **19**, 2065; (b) Sun, Y., Frenkel, A., Isseroff, R., Shonbrun, C., Forman, M., Shin, K., Kaga, T., White, H., Zhang, L., Zhu, Y., Rafailovich, M. and Sokolov, J. (2006) Characterization of palladium nanoparticles by musing x-ray reflectivity, EXAFS; and electron microscopy. *Langmiur*, **22**, 807.

56 Xiong, Y., Cai, H., Wiley, B.J., Wang, J., Kim, M.J. and Xia, Y. (2007) Synthesis and mechanistic study of palladium nanobars and nanorods. *Journal of the American Chemical Society*, **129**, 3665.

57 Xiong, Y., Chen, J., Wiley, B., Xia, Y., Yin, Y. and Li, Z.-Y. (2005) Size-dependence of surface plasmon resonance and oxidation for Pd nanocubes synthesized via a seed etching process. *Nano Letters*, **5**, 1237.

58 Xiong, Y., McLellan, J.M., Chen, J., Yin, Y., Li, Z.-Y. and Xia, Y. (2005) Kinetically controlled synthesis of triangular and hexagonal nanoplates of palladium and their SPR/SERS properties. *Journal of the American Chemical Society*, **127**, 17118.

59 Xiong, Y., Washio, I., Chen, J., Cai, H., Li, Z.-Y. and Xia, Y. (2006) Poly(vinyl pyrrolidone): a dual functional reductant and stabilizer for the facile synthesis of

noble metal nanoplates in aqueous solutions. *Langmuir*, **22**, 8563.
60 Gugliotti, L.A., Feldheim, D.L. and Eaton, B.E. (2004) RNA-mediated metal-metal bond formation in the synthesis of hexagonal palladium nanoparticles. *Science*, **304**, 850.
61 Gugliotti, L.A., Feldheim, D.L. and Eaton, B.E. (2005) RNA-mediated control of metal nanoparticle shape. *Journal of the American Chemical Society*, **127**, 17814.
62 Xiong, Y., McLellan, J.M., Yin, Y. and Xia, Y. (2007) Synthesis of palladium icosahedra with twinned structure by blocking oxidative etching with citric acid or citrate ions. *Angewandte Chemie – International Edition*, **46**, 709.
63 Lim, B., Xiong, Y. and Xia, Y. (2007) A water-based synthesis of octahedral, decahedral, and icosahedral Pd nanocrystals. *Angewandte Chemie – International Edition*, **46**, 9279.
64 Bradley, J.S., Tesche, B., Busser, W., Maase, M. and Reetz, M.T. (2000) Surface spectroscopic study of the stabilization mechanism for shape-selectively synthesized nanostructured transition metal colloids. *Journal of the American Chemical Society*, **122**, 4631.
65 Steinhart, M., Jia, Z., Schaper, A.K., Wehrspohn, R.B., Gösele, U. and Wendorff, J.H. (2003) Palladium nanotubes with tailored wall morphologies. *Advanced Materials*, **15**, 706.
66 Nguyen, K., Monteverde, M., Filoramo, A. and Goux-Capes, L. (2008) Synthesis of thin and highly conductive DNA-based palladium nanowires. *Advanced Materials*, **20**, 1099.
67 Zhang, H. and Mirkin, C.A. (2004) DPN-generated nanostructures made of gold, silver, and palladium. *Chemistry of Materials*, **16**, 1480.
68 Kiriy, A., Minko, S., Gorodyska, G., Stamm, M. and Jaeger, W. (2002) Palladium wire-shaped nanoparticles from single synthetic polycation molecules. *Nano Letters*, **2**, 881.
69 Taratula, O., Chen, A.M., Zhang, J., Chaudry, J., Nagahara, L., Banerjee, I. and He, H. (2007) Highly aligned ribbon-shaped Pd nanoparticle assemblies by spontaneous organization. *Journal of Physical Chemistry C*, **111**, 7666.
70 Yu, S., Welp, U., Hua, L.Z., Rydh, A., Kwok, W.K. and Wang, H.H. (2005) Fabrication of palladium nanotubes and their application in hydrogen sensing. *Chemistry of Materials*, **17**, 3445.
71 Liang, H.-P., Lawrence, N.S., Wan, L.-J., Jiang, L., Song, W.-G. and Jones, T.G.J. (2008) Controllable synthesis of hollow hierarchical palladium nanostructures with enhanced activity for proton/hydrogen sensing. *Journal of Physical Chemistry C*, **112**, 338.
72 Berhault, G., Bisson, L., Thomazeau, C., Verdon, C. and Uzio, D. (2007) Preparation of nanostructured Pd particles using a seeding synthesis approach – application to the selective hydrogenation of buta-1,3-diene. *Applied Catalysis A: General*, **327**, 32.
73 Chi, P.-F. and Ho, K.-M. (2004) Size-controlled synthesis of Pd nanoparticles from β-diketonato complexes of palladium. *Nanotechnology*, **15**, 1059.
74 Lu, W., Wang, B., Wang, K., Wang, X. and Hou, J.G. (2003) Synthesis and characterization of crystalline and amorphous palladium nanoparticles. *Langmuir*, **19**, 5887.
75 Diaz-Ayala, R., Raptis, R. and Cabrera, C.R. (2005) Formation of palladium nanoparticles and other structures from molecular precursors: a microscopy and spectroscopy study. *Reviews on Advanced Materials Science*, **10**, 375.
76 Schlotterbeck, U., Aymonier, C., Thomann, R., Hofmeister, H., Tromp, M., Richtering, W. and Mecking, S. (2004) Shape-selective synthesis of palladium nanoparticles stabilized by highly branched amphiphilic polymers. *Advanced Functional Materials*, **14**, 999.
77 Imre, Á., Beke, D.L., Gontier-Moya, E., Szabó, I.A. and Gillet, E. (2004) Surface Ostwald ripening of Pd nanoparticles on the MgO (100) surface. *Applied Physics A.*, **71**, 19.
78 Mallick, K., Witcomb, M.J. and Scurrell, M.S. (2006) Fabrication of a nanostructured gold-polymer composite material. *The European Physical Journal. E. Soft Matter*, **19**, 149.

79 Nemamcha, A., Rehspringer, J.-L. and Khatmi, D. (2006) Synthesis of palladium nanoparticles by sonochemical reduction of palladium (II) nitrate in aqueous solution. *Journal of Physical Chemistry B*, **110**, 383.

80 Tabuani, D., Monticelli, O., Chincarini, A., Bianchini, C., Vizza, F., Moneti, S. and Russo, S. (2003) Palladium nanoparticles supported on hyperbranched aramids: synthesis, characterization, and some applications in the hydrogenation of unsaturated substrates. *Macromolecules*, **36**, 4294.

81 Narayanan, R. and El-Sayed, M.A. (2005) FTIR study of the mode of binding of the reactants on the Pd nanoparticle surface during the catalysis of the Suzuki reaction. *Journal of Physical Chemistry B*, **109**, 4357.

82 Horinouchi, S., Yamanoi, Y., Yonezawa, T., Mouri, T. and Nishihara, H. (2006) Hydrogen storage properties of isocyanide-stabilized palladium nanoparticles. *Langmuir*, **22**, 1880.

83 Xiong, Y., Wiley, B., Chen, J., Li, Z.-Y., Yin, Y. and Xia, Y. (2005) Corrosion-based synthesis of single-crystal Pd nanoboxes and nanocages and their surface plasmon properties. *Angewandte Chemie–International Edition*, **44**, 7913.

84 Ghosh, D. and Chen, S. (2008) Palladium nanoparticles passivated by metal–carbon covalent linkages. *Journal of Materials Chemistry*, **18**, 755.

85 Son, S.U., Jang, Y., Yoon, K.Y., Kang, E. and Hyeon, T. (2004) Facile synthesis of various phosphine-stabilized monodisperse palladium nanoparticles through the understanding of coordination chemistry of the nanoparticles. *Nano Letters*, **4**(6), 1147.

86 Lee, J.-Y., Horiuchi, S. and Choi, H.-K. (2006) Effect of palladium nanoparticles on the thermal degradation kinetics of alpha crystalline syndiotactic polystyrene. *Journal of Industrial and Engineering Chemistry*, **12**(6), 862–7.

87 Zhao, D., Fei, Z., Ang, W.H. and Dyson, P.J. (2006) A strategy for the synthesis of transition-metal nanoparticles and their transfer between liquid phases. *Small*, **2**, 879.

88 Klug, H. and Alexander, L. (1962) *X-Ray Diffraction Procedures*, John Wiley & Sons, Inc., New York.

89 Rao, C.R.K., Lakshminarayanan, V. and Trivedi, D.C. (2006) Synthesis and characterization of lower size, laurylamine protected palladium nanoparticles. *Materials Letters*, **60**, 3165.

90 Gopidas, K.R., Whitesell, J.K. and Fox, M.A. (2003) Synthesis, characterization and catalytic applications of a palladium-nanoparticles-cored dendrimer. *Nano Letters*, **3**, 1757.

91 Berne, B.J. and Pecora, R. (2000) *Dynamic Light Scattering: With Applications to Chemistry, Biology and Physics*, Dover Publications, New York, NY.

92 Kim, Y.-G., Garcia-Martinez, J.C. and Crooks, R.M. (2005) Electrochemical properties of monolayer-protected Au and Pd nanoparticles extracted from within dendrimer templates. *Langmuir*, **21**, 5485.

93 For reviews, see: (a) Tsuji, J. (1995) *Palladium Reagents and Catalysts*, John Wiley & Sons, Ltd, Chichester; (b) Malleron, J.-L., Fiaud, J.-C. and Legros, J.-Y. (2000) *Handbook of Palladium-Catalyzed Organic Reactions*, Academic Press, London.

94 Choudary, B.M., Madhi, S., Chowdari, N.S., Kantam, M.L. and Sreedhar, B. (2002) Layered double hydroxide supported nanopalladium catalyst for Heck-, Suzuki-, Sonogashira-, and Stille-type coupling reactions of chloroarenes. *Journal of the American Chemical Society*, **124**, 14127.

95 Roucoux, A., Schulz, J. and Patin, H. (2002) Reduced transition metal colloids: a novel family of reusable catalysts? *Chemical Reviews*, **102**, 3757 and references included therein.

96 Schlogl, R. and Abd Hamid, S.B. (2004) Nanocatalysis: mature science revisited or something really new? *Angewandte Chemie–International Edition*, **43**, 1628.

97 Crooks, R.M., Zhao, M.Q., Sun, L., Chechik, V. and Yeung, L.K. (2001) Dendrimer-encapsulated metal nanoparticles: synthesis, characterization, and applications to catalysis. *Accounts of Chemical Research*, **34**, 181.

98 Gallon, B.J., Kojima, R.W., Kaner, R.B. and Diaconescu, P.L. (2007) Palladium nanoparticles supported on polyaniline nanofibers as a semi-heterogeneous catalyst in water. *Angewandte Chemie–International Edition*, **46**, 7251.

99 Heck, R.F. (1985) *Palladium Reagents in Organic Synthesis*, Academic Press, London.

100 Beletskaya, I.P. and Cheprakov, A.V. (2000) The Heck reaction as a sharpening stone of palladium catalysis. *Chemical Reviews*, **100**, 3009.

101 Bhattacharya, S., Srivastavaa, A. and Sengupta, S. (2005) Remarkably facile Heck and Suzuki reactions in water using a simple cationic surfactant and ligand-free palladium catalysts. *Tetrahedron Letters*, **46**, 3557.

102 Kogan, V., Aizenshtat, Z., Popovitz-Biro, R. and Neumann, R. (2002) Carbon-carbon and carbon-nitrogen coupling reactions catalyzed by palladium nanoparticles derived from a palladium substituted Keggin-type polyoxometalate. *Organic Letters*, **4**, 3529.

103 Tatumi, R., Akita, T. and Fujihara, H. (2006) Synthesis of small palladium nanoparticles stabilized by bisphosphine BINAP bearing an alkyl chain and their palladium nanoparticles carbon-carbon coupling reactions under room temperature. *Chemical Communications*, 3349.

104 Reetz, M.T. and Westermann, E. (2000) Phosphane-free palladum catalyzed coupling reactions: The decisive role of Pd nanoparticles. *Angewandte Chemie–International Edition in English*, **39**(1), 165.

105 Pathak, S., Greci, M.T., Kwong, R.C., Mercado, K., Surya Prakash, G.K., Olah, G.A. and Thompson, M.E. (2000) Synthesis and applications of palladium-coated poly(vinylpyridine) nanospheres. *Chemistry of Materials*, **12**, 1985.

106 Garcia-Martinez, J.C., Lezutekong, R. and Crooks, R.M. (2005) Dendrimer-encapsulated Pd nanoparticles as aqueous, room-temperature catalysts for the Stille reaction. *Journal of the American Chemical Society*, **127**, 5097.

107 Calo, V., Nacci, A., Monopoli, A., Damascelli, A., Ieva, E. and Cioffi, N. (2007) Palladium-nanoparticles catalyzed hydrodehalogenation of aryl chlorides in ionic liquids. *Journal of Organometallic Chemistry*, **692**, 4397.

108 Liu, J., He, F., Durham, E., Zhao, D. and Roberts, C.B. (2008) Polysugar-stabilized Pd nanoparticles exhibiting high catalytic activities for hydrodechlorination of environmentally deleterious trichloroethylene. *Langmuir*, **24**, 328–36.

109 Mertens, B., Blothe, C., Windey, K., Windt, W.D. and Verstraete, W. (2007) Biocatalytic dechlorination of lindane by nano-scale particles of Pd(0) deposited on *Shewanella oneidensis*. *Chemosphere*, **66**, 99.

110 Chang, Z., Fan, H., Zhao, K., Chen, M., He, P. and Fang, Y. (2007) Electrochemical DNA biosensors based on palladium nanoparticles combined with carbon nanotubes. *Electroanalysis*, **20**, 131.

111 Foxx, D. and Kalu, E.E. (2007) Amperometric biosensor based on thermally activated polymer-stabilized metal nanoparticles. *Electrochemical Communications*, **9**, 584.

112 Lim, S.H., Wei, J., Lin, J., Li, Q. and You, J.K. (2005) A glucose biosensor based on electrodeposition of palladium nanoparticles and glucose oxidase onto Nafion-solubilized carbon nanotube electrode. *Biosensors and Bioelectronics*, **20**, 2341.

113 Huang, J., Wang, D., Hou, H. and You, T. (2008) Electrospun palladium nanoparticle-loaded carbon nanofibers and their electrocatalytic activities towards hydrogen peroxide and NADH. *Advanced Functional Materials*, **18**, 441.

10
Approaches to the Synthesis and Characterization of Spherical and Anisotropic Platinum Nanomaterials

Zhenmeng Peng, Shengchun Yang and Hong Yang

10.1
Introduction

Morphology plays an important role in determining the chemical and catalytic properties of platinum nanostructures, because the surface atomic arrangements and electronic configurations are largely determined by the shape of crystals [1–6]. The recent demonstration of superior catalytic property in fuel oxidation by tetrahexahedral platinum nanocrystals is one such example [7]. Shape controlled, low-dimensional nanocrystals can also be used to build hierarchical structures through self-assembly or oriented attachment [3, 8–12]. The higher-ordered nanostructures may generate additional unique functionality.

While the syntheses of nanoparticles have traditionally been conducted in aqueous solutions using colloidal methods, most of the successful strategies for controlling the shape of nanocrystals in recent years have been conducted in non-hydrolytic systems [13–15]. Such colloidal methods are also used for general platinum metal nanoparticles. The main advantages of nonhydrolytic solutions may lie in the fact that the choice of reagents and reaction conditions can be substantially broadened, because various metal precursors, stabilizing agents and reducing reagents can be identified based on the selection of solvents.

Although, in recent years, we have witnessed tremendous progresses in the shape control of metal nanoparticles, and a large variety of systems have been developed [2, 6, 16–20], silver and gold nanostructures have received a great deal of attention due to their simple synthetic approaches, chemical stability and potential applications in plasmonics, sensing, imaging, catalysis, biology and therapy [16, 17, 19, 20]. The subjects of size, shape and surface chemistry of silver and gold metal nanostructures have been reviewed by several groups. Even though the basic principles on size and shape control that have been developed for gold or silver nanoparticles should still apply to platinum, a face-centered cubic (fcc) noble metal, material systems can be very different when creating platinum nanostructures. For instance, whereas thiolates can serve as very good capping

Metallic Nanomaterials Vol. 1. Edited by Challa S. S. R. Kumar

ISBN: 978-3-527-32151-3

agents for gold and silver, amines are the preferred functional groups for platinum due to the binding strength between the capping agent and the metal surface. Today, new sets of synthetic mixtures and conditions must be determined in order to prepare platinum nanostructures with specific morphologies.

Although various topics relating to the control of platinum nanostructures have been briefly described in several recent reviews, the discussions have in general been rather generic [2, 6]. As yet, to the best of our knowledge, the shape-control of platinum nanostructures has not been systematically reviewed, in part due to the relatively small number of publications in related subjects. Those areas that have been covered well include the catalytic properties of platinum particles [1], while some degree of effort has been applied to certain aspects of the shape control of Pt nanostructures, such as multipods and dendritic nanostructures [21].

In this chapter, we examine the basic principles for the shape control of platinum nanostructures, and review state-of-the-art research data on synthetic approaches and the characterization of platinum nanostructures with different morphologies. Thermodynamic and kinetic parameters are discussed and used to understand the evolution of shape and control of uniformity during nucleation and growth processes, with emphasis on concepts related to shape control, such as defect formation. Initially, we discuss classical homogeneous nucleation theory, which centers on concepts such as excess free energy, cluster size, critical radius and nucleation rate, and describe how to design controllable experimental parameters based on theoretical analyses. The aim is to explain those aspects that can go beyond the classical LaMer concept, and which do not place emphasis on shape control; sequential growth and defect formation are also given special attention. Practical aspects of synthetic approaches to platinum nanostructures are detailed, with approaches being classified as either aqueous or nonhydrolytic phase syntheses. Colloidal and electrochemical methods by describing the choices of commonly used reagents for achieving shape control, and the choices of reagents used for nonhydrolytic systems. Representative recent examples on various shape-controlled syntheses of platinum nanostructures are outlined for aqueous and nonhydrolytic systems, respectively.

Finally, examples of synthetic and characterization approaches to zero-, one-, two- and three-dimensional nanostructured platinum are presented. Although all dimensionality for low-dimensional nanomaterials is ‘pseudo’ structures as platinum nanostructures are composed of three-dimensional unit cells, these nanostructures are classified according to convention. Simple, single crystal-based morphologies and spherical nanoparticles are categorized as zero-dimensional structures, while platinum nanomaterials with a high aspect ratio in a direction are termed one-dimensional structures. Two-dimensional nanostructures (e.g. plates and planar multipods) and three-dimensional (3D) structures (e.g. multipods, nanoflowers, hollow spheres, hollow cubes, networks) are addressed. Emerging topics on the shape control of platinum alloys and intermetallics are also provided. The chapter concludes with some recent key developments in the shape control of platinum nanostructures.

10.2
The Principles of Shape Control of Nanocrystals During Nucleation and Growth

Multiple factors can affect the morphology of platinum nanoparticles during synthesis. In order to elucidate the effects of various parameters that govern the formation of shapes, we start from the basics of nucleation and growth of nanocrystals [22–24]. In general, at beginning stage, solute atoms are not completely free of movement and bonded with molecules. Under the right conditions, these solute atoms are reduced to form zero-valence metal atoms that can collide and form meta-stable small clusters, away from thermodynamic equilibrium. Some of these unstable clusters can dissolve, while new ones form. The number of clusters at various energy levels should obey the Boltzmann distribution. When the clusters reach a critical limit in size, namely the critical size (r^*), or overcome a certain energy level called the *critical energy barrier* (ΔG^*), they become thermodynamically stable. This process is the so-called *nucleation stage*, and the thermodynamically stable clusters are called *nuclei*. The nuclei can either continue to consume free solute atoms or they can grow at the sacrifice of unstable small clusters ($r < r^*$), and eventually form crystalline particles. This whole process is complicated and – for the sake of simplicity – is often divided into nucleation and growth, despite the fact that the two stages are usually intertwined. The reaction conditions and solutes can greatly affect the kinetics for both nucleation and growth of nanocrystals. What makes this process complex is that many parameters may vary in spatiotemporal domain, which makes it difficult to separate the various factors and describe their effects accurately. In the following sections, after a brief description of the nucleation and growth processes, we will emphasize the key controllable reaction parameters that can affect the final shapes of platinum nanocrystals.

10.2.1
Nucleation

10.2.1.1 Classical Nucleation Theory

The classical nucleation theory, as pioneered by Volmer and Weber [25, 26] and by Becker and Doring [27], deals with the nucleation process based on Gibbs free energy. For a single-solute system, at the initial stage, solute atoms (A) collide and form small clusters in the solution atom-by-atom:

$$A + A \leftrightarrow A_2 \tag{10.1}$$

$$A_2 + A \leftrightarrow A_3 \tag{10.2}$$

$$A_n + A \leftrightarrow A_{n+1} \tag{10.3}$$

On average, the number of the clusters with radius r (N_r) can be obtained by the following equations [22–24]:

$$N_r = N_0 \exp\left(-\frac{\Delta G_r}{RT}\right) = N_A [C]_{eq} S \exp\left(-\frac{\Delta G_r}{RT}\right) \tag{10.4}$$

$$\Delta G_r = 4\pi r^2 \gamma + \frac{4}{3}\pi r^3 \Delta G_V \tag{10.5}$$

$$\Delta G_V = -\frac{RT \ln S}{V_m} \tag{10.6}$$

$$S = \frac{[A]_s}{[A]_{eq}} \tag{10.7}$$

where N_0 is the total number of free solute atoms per unit volume in the system, ΔG_r is excess free energy of cluster formation, γ is surface free energy per unit surface area, ΔG_V is change of free energy between solute atoms in solution and unit volume of the bulk crystal, V_m is molar volume of bulk crystal, T is reaction temperature, N_A is the Avogadro constant, R is the ideal gas constant, and S is the ratio between solute concentrations at saturation $[A]_s$ and at equilibrium $[A]_{eq}$, respectively.

The excess free energy (ΔG_r) contains two competing terms. One is usually positive, related to the creation of an interface between solute cluster and medium of solution, which is unfavorable. The other is related to the bond formation in nuclei, which can be either positive or negative according to the value of S. If the solute is not oversaturated (i.e. $S \leq 1$), ΔG_r is positive and increases with the growth of clusters. The larger the cluster size, the more thermodynamically unstable it becomes, and therefore particles cannot form in such systems. Only when the solute is saturated (i.e. $S > 1$) can ΔG_r decrease with the increase of cluster radius, and the formation of crystals is then preferable. In other words, the nucleation and growth of particles occurs when the solute is supersaturated. Under the condition $S > 1$, the relationship between ΔG_r and r can be illustrated, as in Figure 10.1.

In this relationship, the excess free energy for the formation of clusters ΔG_r, first increases then decreases with the radius of the particles, r. The critical radius, r^*, is associated with a maximum excess free energy, ΔG^*. Accordingly, there exists a critical number of atoms, n^*, in cluster A_n^* at the radius of r^*. When $r < r^*$, the system can lower its free energy by dissolution of clusters. Thus, these clusters are not thermodynamically stable and dissolve quickly, whereas some new clusters form due to spontaneous collisions. These unstable particles ($A_n < A_n^*$) are known as *clusters* or *embryos*, and their numbers follow the Boltzmann distribution and decrease exponentially with increases of ΔG_r, as described in Equation 10.4. When the radius of a cluster is larger than the critical value ($r > r^*$), it becomes stable and is referred to as a *nucleus*. Thus, the expressions of critical radius r^* and maximum excess free energy ΔG^* can be obtained mathematically when $d\Delta G_r/dr$ is equal to zero [22, 23, 28]:

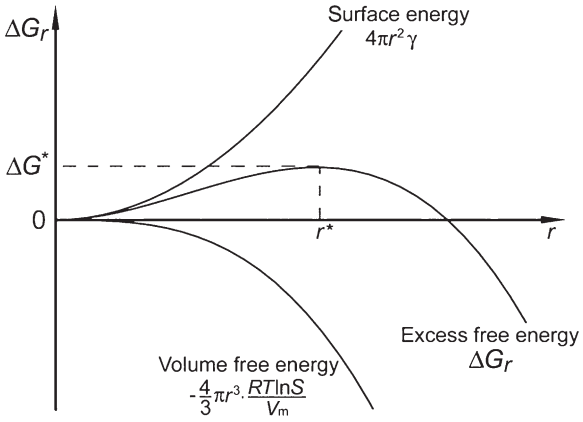

Figure 10.1 Illustration of the overall excess free energy, ΔG_r as a function of cluster size r.

$$r^* = \frac{2\gamma V_m}{RT \ln S} \tag{10.8}$$

$$\Delta G^* = \frac{16\pi\gamma^3 V_m^2}{3(RT \ln S)^2} \tag{10.9}$$

Similarly, the number of clusters that reach the critical size, N_{r^*} and nucleation rate, dN_{r^*}/dt can be given by the following two equations:

$$N_{r^*} = N_A[A]_{eq} S \exp\left(-\frac{\Delta G^*}{RT}\right) = N_A[A]_{eq} S \exp\left(-\frac{16\pi\gamma^3 V_m^2}{3(RT)^3 (\ln S)^2}\right) \tag{10.10}$$

$$\frac{dN_{r^*}}{dt} = f_0 N_A[A]_{eq} S \exp\left(-\frac{\Delta G^*}{RT}\right) = f_0 N_A[A]_{eq} S \exp\left(-\frac{16\pi\gamma^3 V_m^2}{3(RT)^3 (\ln S)^2}\right) \tag{10.11}$$

where f_0 is the ratio of critical-sized clusters becoming stable nuclei and a function containing variables such as vibration frequency of the atoms, activation energy for diffusion in liquid, and surface area of critical nuclei.

The r^*, ΔG^*, N_{r^*} and dN_{r^*}/dt values can be used to describe how easy or difficult it is for a solute to nucleate. Nuclei form easily when a system has small values of r^* and ΔG^*, since the clusters need to overcome only a small energy barrier and incorporate few atoms to become stable. In contrast, if r^* is large and ΔG^* is very positive, the formation of stable nuclei is difficult. Only a small portion of clusters can then grow into stable nuclei, and a slow nucleation rate is expected.

10.2.1.2 Controllable Parameters for Nucleation

Surface free energy (γ), reaction temperature (T), degree of supersaturation (S) and ratio of critical-sized clusters converting into stable nuclei (f_0) are the important variables that must be taken into consideration in this context, based

Table 10.1 Effects of key experimental parameters on nucleation.[a]

Experimental parameters			Effects on nucleation			
γ	T	S	r^*	ΔG^*	N_{r^*}	dN_{r^*}/dt
↑ (↓)	–	–	↑ (↓)	↑ (↓)	↓ (↑)	↓ (↑)
–	↑ (↓)	–	↓ (↑)	↓ (↑)	↑ (↓)	↑ (↓)
–	–	↑ (↓)	↓ (↑)	↓ (↑)	↑ (↓)	↑ (↓)

a The symbols '↑ (↓)' indicate the increase (decrease) of a given variable.

on the above equations of r^*, ΔG^*, N_{r^*} and dN_{r^*}/dt. f_0 is a rather complex term and cannot be readily reduced to controllable parameters experimentally. Thus, γ, T and S are the three important parameters which affect the nucleation process and can be controlled experimentally. The qualitative correlations between these variables and their effects on the nucleation are summarized in Table 10.1.

Clearly, a large surface free energy results in difficulty in nucleation, as the unstable clusters need to reach a large critical size and overcome a high energy barrier to become nuclei. As a result, a small number of clusters can reach the critical size, leading to a reduced nucleation rate. On the other hand, the reaction temperature and ratio of supersaturation have the opposite effects since, when these two variables increase, the nucleation becomes easy due to a relatively small critical size, a low energy barrier, a large number of clusters reaching the critical size, and a fast nucleation rate.

10.2.1.3 Types of Nucleation

There are three commonly known nucleation processes: homogeneous, heterogeneous, and secondary nucleation.

Homogeneous nucleation is the most common of the three, where the formation of nuclei from solute atoms can occur in the absence of any outside stimulant, such as solid interface and contaminant. The solute atoms are thermodynamically unstable when supersaturation is reached, and form stable nuclei to reduce the overall system energy. The classical nucleation theory can be used to depict a homogenous nucleation process.

In the case of *heterogeneous nucleation*, a certain amount of surface energy is released through interfaces by introducing proper foreign species. The critical value for the energy barrier is smaller than that for the corresponding homogeneous nucleation, and this results in a faster nucleation rate. The equations for describing the r^*, ΔG^*, N_{r^*} and dN_{r^*}/dt in homogeneous nucleation must be modified by adding additional terms related to the surface energy, as given below [22, 23]:

$$r^*_{het.} = \frac{2\gamma V_m}{RT \ln S} \tag{10.12}$$

$$\Delta G^{*}_{het.} = \frac{16\pi\gamma^3 V_m^2}{3(RT\ln S)^2}\cdot S(\theta) \tag{10.13}$$

$$N_{r^*,het.} = f\left(N_A[A]_{eq}S, N_{site}\right)\cdot\exp\left(-\frac{\Delta G^{*}_{het.}}{RT}\right) \tag{10.14}$$

or

$$N_{r^*,het.} = f\left(N_A[A]_{eq}S, N_{site}\right)\cdot\exp\left(-\frac{16\pi\gamma^3 V_m^2}{3(RT)^3(\ln S)^2}\cdot S(\theta)\right) \tag{10.15}$$

$$\frac{dN_{r^*,het.}}{dt} = f_0\cdot f\left(N_A[A]_{eq}S, N_{site}\right)\cdot\exp\left(-\frac{\Delta G^{*}_{het.}}{RT}\right) \tag{10.16}$$

or

$$\frac{dN_{r^*,het.}}{dt} = f_0\cdot f\left(N_A[A]_{eq}S, N_{site}\right)\cdot\exp\left(-\frac{16\pi\gamma^3 V_m^2}{3(RT)^3(\ln S)^2}\cdot S(\theta)\right) \tag{10.17}$$

where $S(\theta)$, a numerical value less than unity, is a shape factor which describes the geometric relationship between the heterogeneous nuclei and the substrate, N_{site} is the number of heterogeneous nucleation sites per unit volume, and $f(N_A[A]_{eq}S, N_{site})$ is a function of S and N_{site} depicting the number of atoms in contact with the heterogeneous nucleation sites per unit volume.

The third type of nucleation – *secondary nucleation* – refers to the formation of nuclei induced by experimental conditions such as stirring, and can continue in the growth stage of particles. As yet, no complete theory has been developed to describe secondary nucleation.

10.2.2 Growth

10.2.2.1 Uniformity Control Related to the Morphology of Nanocrystals

10.2.2.1.1 Principles for Uniformity Control Control of reaction conditions to create distinguishable nucleation and growth steps is generally required for the preparation of uniform particles. LaMer's concept [29] of a bursting nucleation followed by diffusion-controlled growth [30–32] is widely used to guide the basic experimental designs. As discussed above, three major controllable variables, namely S, γ and T, can affect the nucleation process. The surface free energy and reaction temperature can be fixed once the reaction system and conditions have been chosen, but the degree of supersaturation is usually a function of reaction time that changes throughout the nucleation and growth. This is especially the case for particle growth in solutions, where the amount of introduced solute atoms

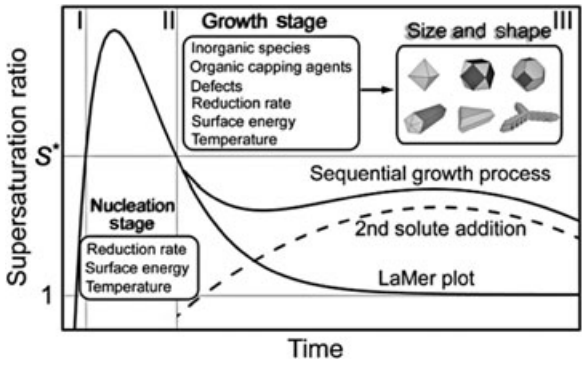

Figure 10.2 Change of supersaturation ratio as a function of time during the nucleation and growth of faceted nanoparticles.

is difficult to keep constant. Thus, the original LaMer model is modified to include those cases which involve the evolution of S with an increase in reaction time and under sequential growth conditions, as illustrated in Figure 10.2.

As indicated in Figure 10.2, the whole synthetic process can be divided into three distinguishable stages. At Stage I, free solute atoms form through either the reduction or decomposition, and the degree of supersaturation increases. When the degree of supersaturation reaches the critical value, nucleation occurs explosively, leading to the simultaneous formation of a large number of nuclei, the so-called Stage II. This process rapidly consumes solute atoms and results in a decrease in the S value. When the degree of supersaturation falls below the critical threshold value, nucleation stops and the growth stage, Stage III, becomes dominant. During this stage, formed nuclei grow at the expense of free solute atoms and unstable clusters, the radii of which are smaller than the critical value r^*.

The particle growth is usually either diffusion- or reaction-limited, although there are cases where these two processes are comparable. In a solution, a diffusion-limited process is dominant under most conditions and the rate for particle growth, $\frac{dr}{dt}$, can be depicted according to the following equation [30, 31]:

$$\frac{dr}{dt} = K\left(\frac{1}{r} + \frac{1}{\delta}\right)\left(\frac{1}{r^*} - \frac{1}{r}\right) \tag{10.18}$$

where t is the reaction time, δ the thickness of the diffusion layer, and K is a constant proportional to the diffusion constant of the solute.

10.2.2.1.2 **Size Focusing and Defocusing (Ostwald Ripening)** Based on the above expression, the diffusion-limited growth rate in a solution is strongly dependent on the particle size. The larger the particle size is, the slower the growth rate is;

while those unstable clusters with radius less than r^* disappear. Such a process leads to a narrow size distribution, and is usually called 'size focusing' [30, 31]. This occurs at the start of Stage III as described in the LaMer plot, where nucleation stops but S is still relatively high. At this stage, the size of many just-formed nuclei is only slightly larger than the critical radius r^*. These nuclei grow into particles by consuming free solute atoms and unstable clusters. On the other hand, S quickly decreases during this growth process as the solute is consumed, and as a consequence, both r^* and ΔG^* increase. Some of the stable particles with radii slightly larger than the critical size now become unstable under the condition, with decreasing S. They dissolve and reduce in number, whilst the large particles continue to grow. This process broadens the particle size distribution and is the *defocusing step* or the so-called 'Ostwald ripening' [31, 33–35].

The above theory predicts that a synthetic system with rapid nucleation followed by distinguishable growth is typically required for the preparation of uniform nanoparticles. The narrower the band for Stage II is, the more uniform particles can be. *Rapid reduction* and *hot injection* are two widely used techniques for preparing uniform nanoparticles [14, 36]. The free solute atoms are released within a very short period of time, and the degree of supersaturation (S) quickly becomes much larger than the critical value, resulting in a burst of nucleation. Consequently, most of the solute atoms are consumed and the growth stops immediately after the nucleation stage. In order to prepare large uniform nanostructures, a sequential process is usually applied. In this case, the degree of supersaturation cannot be too high – as this can result in new nucleation – or too low – which can cause Ostwald ripening. The seed particles formed at Stage II eventually grow into uniform large particles at the expense mostly of the released solute atoms.

10.2.2.2 **Shape Controls**

During the growth of nanocrystals, both thermodynamic and kinetic factors can play important roles in most cases, and either factor may be dominant under certain circumstances. In this section, we discuss the strategies of shape controls of platinum nanocrystals according to the factors in the following two major categories.

10.2.2.2.1 **Growth Habits and Defects for Shape Control** The shape control of Pt nanoparticles based on growth habits is largely governed by thermodynamic factors. As platinum metal is fcc, the low-index surfaces that are most relevant to determine the crystal shapes are (100), (110) and (111). The surface energy follows the order of (111) < (100) < (110) [37]. Pt clusters form facets with the lowest surface energy to minimize the total excess free energy, and in most cases these clusters eventually grow into nanoparticles bound by these surfaces. Figure 10.3 illustrates some common shapes based on the crystal growth habits.

The total excess free energy can further decrease by introducing *crystal defects*. *Twinning defects*, those in (111) plane for fcc metals in particular, are the most common and widely observed type in the shape control of metal nanostructures [38, 39]. The introduction of twin planes reduces the symmetry and alters the

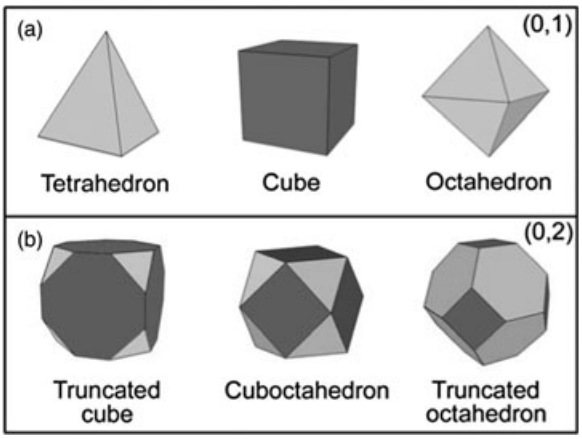

Figure 10.3 Selected common shapes of single crystalline platinum nanoparticles bound by (a) one group and (b) two groups of facets, where the notation (*n, m*) represents the number of defects, *n*, and different facets, *m*, in the crystals.

growth directions of the nanoparticles, leading to the formation of shapes that cannot exist in single crystal form [40]. Twinning in the (111) plane is preferable in comparison with that of other low-index planes, due to the relatively low surface energy and suitable inter-planar angles. Some common shapes of fcc metals containing twin planes, all of which contain either single or multiple (111) twin planes, are summarized in Figure 10.4. These shapes include bipyramid, decahedron, icosahedron, triangular plate, tripod, nanorods and nanowires.

Based on a global energy analysis, if the decrease in interfacial energy can compensate the increase in energy due to defects, the formation of a twin plane is then thermodynamically favorable. This relationship among these energy terms can be depicted in the following equation:

$$\gamma' + \gamma_{twin} + \gamma_{strain} < \gamma \tag{10.19}$$

where γ' and γ are crystal-solution interfacial energy with and without twin planes, respectively; γ_{twin} is the surface energy for the formation of twin plane, and γ_{strain} is the stain energy induced by the formation of twin plane due to lattice distortion or geometric mismatch. A decahedron is composed of five tetrahedra and is bound by ten (111) plane. As the interplanar angle of the tetrahedron is approximately 70.5°, the decahedron needs to accommodate a 7.5° gap. This geometric mismatch induces positive strain energy which increases with the expansion of the gap, and is adverse for the formation of twin planes. This mismatch can partially explain why only limited shapes containing twin planes have been observed, as a given shape must be energetically favorable and geometrically allowable. It may also attribute to the observation that large, multiple-twinned nanocrystals

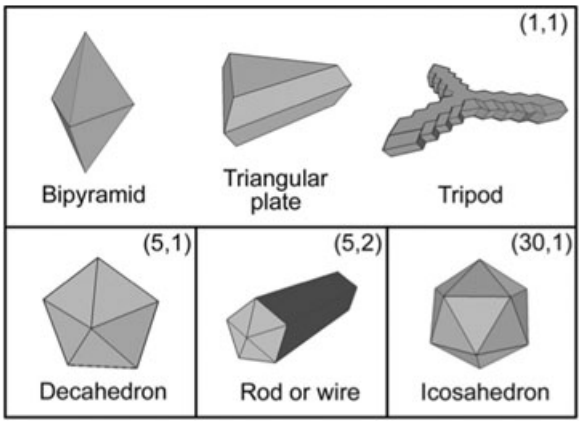

Figure 10.4 Selected common shapes of fcc metals containing twin planes, where the notation (*n, m*) represents the number of twin planes, *n*, and different types of facets, *m*.

such as icosahedrons are rarely observed [6, 41, 42] because the γ_{strain} increases rapidly with the size of particles.

The creation of energetically favored conditions for stable multiply twinned defects during both the nucleation and growth is necessary when preparing various Pt nanoparticles with symmetry-reduced shapes. According to Equation 10.19, a large difference in crystal-solution interfacial energy, with and without twin planes, favors the formation of defects. Experimentally, this difference can be generated by using proper capping reagents which interact selectively with various crystal surfaces and reduce their interfacial energy. Heterogeneous nucleation is another approach where the lattice mismatch between the two species and difference in chemical composition may help defect formation by reducing the system energy. As reported by Teng *et al.*, even a small amount of silver precursors triggered the formation of platinum multipods [43]. The shapes of multiply twinned nanoparticles can be further controlled by using inorganic species through the selective etching of certain twin planes [9, 44, 45]. Oxygen, chloride and bromide ions have been used in the growth of Ag or Pd nanocrystals. Those shapes with twin planes can be etched away, resulting in only single crystal forms if Cl^- is used [9, 45]. When a weaker etchant such as Br^- is used, however, nanoparticles with multiple twin planes can be etched, while those nanocrystals containing single twin planes survive [45].

10.2.2.2.2 **Kinetics on Shape Control**

Adsorptive Organic Capping Agents Organic capping agents, which have been widely employed to achieve shape control of Pt nanoparticles, affect particle growth mainly in three areas:

- They can stabilize the nanoparticles from aggregation by offering the proper hydrophobicity.
- Their interaction with nanoparticles reduces the surface energy, and in turn the total excess free energy, which prevents the nanoparticles from growing into bulk crystals.
- If the adsorption of a capping agent to specific crystal surfaces is favored over that of others, anisotropic growth can be achieved.

As an example, Pt nanoparticles with various shapes such as cubes or tetrahedrons can be synthesized using acrylic acid [46], polyacrylate [47] and sodium polyacrylate [48–50] as capping molecules. Tetradecyltrimethylammonium bromide (TTAB) is an effective capping agent for preparing cubic and cubo-octahedral Pt nanoparticles [4, 5]. Cubic Pt nanoparticles can also be prepared in organic solutions in the presence of oleic acid and oleylamine [51–53].

Soft Templates Soft templates include a variety of functional structures such as micelles, reverse micelles and microemulsions. Molecules that make use of such templates are usually composed of long-chain lipophilic organic fragments and hydrophilic heads. When the concentration reaches a certain value – the critical micelle concentration (CMC) – these molecules self-assemble into organized structures in order to decrease the system energy. In a microemulsion, one immiscible phase is dispersed as stable droplets in the other continuous phase. These micelles and microemulsions are thought to provide confined spaces during the synthesis of nanoparticles, where the chemical species are concentrated. This model is rather rudimentary, however, as the structures of soft templates are dynamic in solution and their stability changes with composition during the reaction [54]. However, the concept of soft templates has been used to design experiments to control the shape of nanomaterials; for example, Pt nanorods have been obtained in the presence of cetyltrimethylammonium bromide (CTAB) [55]. Some two-dimensional (2-D) and three-dimensional (3-D) Pt nanostructures have also been prepared by using liposomes [56–60].

Inorganic Ions and Molecules Recently, inorganic ions or molecules have been used instead of adsorptive organic molecules to control the shape of Pt nanoparticles (Figure 10.5). These ions or molecules can selectively adsorb onto certain surfaces to either promote or inhibit further growth. One such example is the growth of Pt nanostructures in presence of silver species [9, 61]. Here, the Ag species in the form of Ag^0 or Ag_4^{2+} are thought to adsorb more strongly onto {100} than {111} facets of Pt, which results in an enhanced growth along only one set of the directions. When different amounts of Ag ions are added into the reaction systems, Pt cubes, cubo-octahedrons and octahedrons are obtained. In a separate study, $PtCl_5(H_2O)^-$ and $PtCl_4(H_2O)_2$ were thought to form during the reaction [50]. These species, which have good oxidizing strength, preferentially adsorb onto Pt {111} facets and accelerate their growth, and this results in the formation of Pt

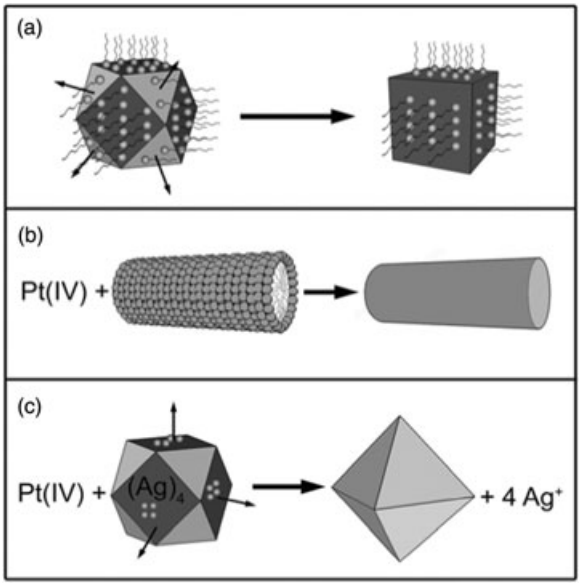

Figure 10.5 Several strategies on controlling the shape of Pt nanoparticles by using: (a) capping agents of adsorptive organic molecules; (b) soft template of micelles; and (c) inorganic ions and molecules.

nanocrystals enclosed with {100} facets. Copper ions (Cu^{2+}) have also been found effective [62]. For example, a strong effect of ion concentration on size and shape has been observed for the formation of Pt nanocubes in the galvanic displacement reaction between Cu foil and K_2PtCl_4. Nitrite ions (NO_2^-) are also thought to promote the anisotropic growth of Pt by forming complexes with Pt(II) and Pt(IV) species [63]. Fe(II) and Fe(III) ions have been used to mediate the reduction rate of Pt(IV) species in the synthesis of Pt nanorods [64, 65].

10.2.2.2.3 **Oriented Attachment** In addition to control at the atomic level, where the solute atoms are deposited continuously on the surfaces, nanoparticles can grow by aggregation with small primary particles. This process, which involves the attachment of small particles and is known as *secondary growth*, has a much higher rate of growth than normal, since the primary particles are usually small-sized and have active surfaces. Secondary growth can reduce the total surface energy and excess free energy of the system by minimizing the exposed active surfaces. A decrease in the strong electrostatic repulsion between primary particles by introducing a less-polar solvent represents one way to grow Pt wire-like nanostructures through induced attachment along preferred directions [66]. The attachment can be further controlled by selectively modifying the primary particle surfaces. For example, platinum porous nanoparticles can form from primary nanoparticles [11]; here, Pt nanoparticles form through the thermal decomposition

of platinum acetylacetonate ($Pt(acac)_2$) first. One of the key capping agents, 1-adamantanecarboxylic acid (ACA), can preferentially adsorb onto Pt surfaces [67, 68], and this results in a preferred secondary growth along ⟨111⟩ directions [11]. The so-called *single crystalline* porous Pt nanostructures have been obtained by creating an oriented attachment between (111) facets. Unfortunately, these porous structures are not thermodynamically stable, and may develop into large particles through Ostwald ripening.

10.3 General Synthetic Approaches

10.3.1 Aqueous-Phase Synthesis

10.3.1.1 Colloidal Synthesis

The term 'colloid' refers to a two-phase system where insoluble particles are dispersed in water [69] or, broadly speaking, in solvents. Some selected recent examples of the shape control of platinum nanostructures in aqueous systems are summarized in Table 10.2. The reduction of Pt salts by reducing agents in the presence of capping agents is a general method for preparing Pt nanoparticles in aqueous solutions. Hexachloroplatinic acid (H_2PtCl_6) [87–92], potassium hexachloroplatinate (K_2PtCl_6) [89] and potassium tetrachloroplatinate (K_2PtCl_4) [5, 46, 48, 49, 70, 75, 83, 108] are the widely used precursors; they can dissolve readily in water as $PtCl_6^{2-}$ and $PtCl_4^{2-}$, respectively. As the standard reduction potentials are 0.68 V for the $PtCl_6^{2-}$ anion and 0.755 V for $PtCl_4^{2-}$, they can be readily reduced by a range of reducing agents, including borohydride [87, 88, 109–112], hydrazine [91, 111, 113, 114], hydrogen [5, 48, 49], citrate [83, 115] and ascorbic acid [116, 117]. Other chemicals such as ethanol, formic acid, vitamin B_2 and potassium bitartrate have also been used to reduce Pt salts. In general, the use of a strong reducing agent results in a high S value during the nucleation stage and a high growth rate, $\frac{dr}{dt}$, during the growth stage, both of which are advantageous for the formation of uniform Pt nanoparticles. These nanoparticles typically do not possess facets due to an inability to reconstruct their surfaces during the short time spend. However, by selecting mild reducing reagents the nucleation and growth rate can be slowed down to the point where facets can develop without the generation of new nuclei. Experimentally, a two-step method is often used to control both the monodispersity and shape of Pt nanoparticles. In this process, a strong reducing reagent is first used to create uniform seed crystals, followed by the use of a mild reductant to facilitate the growth of particles.

One key factor for controlling the Pt shape during nucleation and growth is surfactant. A good surfactant should interact selectively with either Pt nanoparticles or precursors in order to confine the growth. Organic molecules, polymers

Table 10.2 Shape control of Pt nanostructures in aqueous systems.

Precursor	Reductant[a]	Surfactant[b]	Additive[c]	Condition[d]	Shape[e]	Reference(s)
K_2PtCl_4	H_2	Na[PA]	pH	RT, 12 h	C, T	[48, 49, 70, 71]
K_2PtCl_4	H_2	Acrylic acid	pH	RT, 12 h	C, T	[46]
K_2PtCl_4	H_2	poly-NIPA		LCST	C	[72]
K_2PtCl_4	H_2	poly-NEA		LCST	Tri	[73]
K_2PtCl_4	H_2	PVP, poly-NIPA, Na[PA]		RT	Tri, Sq, Hex	[74]
K_2PtCl_6	H_2	Na[PA]	HCl	RT	C, TO	[50]
K_2PtCl_6	H_2	PVP		25–45 °C	T	[75]
H_2PtCl_6, K_2PtCl_4	H_2	PVP		RT, overnight	T	[76]
K_2PtCl_4	H_2	Na_3[Cit]	NaOH	RT	C, T, Hex	[77]
H_2PtCl_6	H_2	PVP		RT, overnight	Tri, SW	[78, 79]
K_2PtCl_6	H_2	PVP		RT	Tet	[80, 81]
Na_2PtCl_4	PVP	PVP		80 °C	Tri, SP	[82]
K_2PtCl_6	Na_3[Cit]	Na[PA]		reflux, 3.5 h	SP	[83]
K_2PtCl_6	$NaBH_4$, H_2, AA	TTAB		50 °C	C, CO, PP	[4, 5]
H_2PtCl_6	$NaBH_4$	CTAB	$AgNO_3$	RT	C	[84]
K_2PtCl_6	$NaBH_4$	CTAB	HCl	RT, 12 h	DD	[85]
H_2PtCl_6	EtOH	poly-NIPA		reflux	SP	[86]
H_2PtCl_6	$NaBH_4$, H_2	Pluronic L64		RT	SP	[87]
H_2PtCl_6	$NaBH_4$	MSA			SP	[88]
$K_2[Pt(C_2O_4)_2]$ K_2PtCl_4 K_2PtCl_6	H_2		$K_2C_2O_4$, $CaCl_2$	RT or 55 °C	C, Hex	[89]

Table 10.2 *Continued*

Precursor	Reductant[a]	Surfactant[b]	Additive[c]	Condition[d]	Shape[e]	Reference(s)
K_2PtCl_4	Cu foil		Cu^{2+}		C	[62]
Na_2PtCl_6	Vitamin B_2	Vitamin B_2		RT	SP	[90]
H_2PtCl_6	Hydrazine	AOT	Isooctane	RT	SP	[91]
K_2PtCl_4	γ-Ray	CTAB	Hexanol	RT	NR	[55]
H_2PtCl_6	Hydrazine	Berol 050	Isooctane	RT	SP	[92]
K_2PtCl_4	UV, AA	SDS, Brij-35, DSPC	SnOEP, chol		SP	[56–59]
K_2PtCl_4	Ag NR				C/S	[93]
H_2PtCl_6	Co NP			95 °C	Hol	[94, 95]
H_2PtCl_6	H_2			200 °C for 4 h	Nec	[96]
H_2PtCl_6	ED			RT	SP	[97]
K_2PtCl_4	ED	AA	H_2SO_4	RT	THH	[7, 98]
K_2PtCl_6	ED		H_2SO_4	RT	NH	[99]
Na_2PtCl_6	ED		HCl	RT	NW	[100–102]
K_2PtCl_6	ED		H_3BO_3	RT	NT	[103]
H_2PtCl_6	γ-Ray		MeOH	RT	SP	[104, 105]
H_2PtCl_6	UV		MeOH	RT	NW	[106]
$PtCl_4$	Microwave		α-Glucose		SP	[107]

a PVP = poly(*N*-vinyl-2-pyrrolidone); Na_3[Cit] = sodium citrate; AA = ascorbic acid; EtOH = ethanol; NR = nanorod; NP = nanoparticle; ED = electrodeposition.

b Na[PA] = sodium polyacrylate; poly-NIPA = poly(*N*-isopropylacrylamide); poly-NEA = poly(*N*-ethylacrylamide); TTAB = tetradecyltrimethylammonium bromide; CTAB = hexadecyltrimethylammonium bromide; Pluronic L64 = $EO_{13}PO_{30}EO_{13}$ triblock copolymer; MSA = mercaptosuccinic acid; AOT = sodium bis(2-ethylhexyl) sulfosuccinate; SDS = sodium dodecylsulfate; DSPC = 1,2-distearoyl-*sn*-glycero-3-phosphocholine.

c MeOH = methanol; SnOEP = Sn(IV)-octaethylporphyrin; chol = cholesterol.

d LCST = lower critical solution temperature; RT = room temperature.

e C = cube; T = tetrahedron; O = octahedron; THH = tetrahexahedron; CO = cubo-octahedron; TO = truncated octahedron; SP = spherical particle; Tri = triangular; Sq = square; Tet = tetragonal; Hex = hexagonal; NR = nanorod; NW = nanowire; NT = nanotube; Nec = necklace structure; C/S = core/shell structure; SW = snow-like particles; DD = dendrite; PP = porous particles; NH = nanohorn; Hol = hollow structure.

and inorganic ions have all been used to control the growth of Pt nanoparticles in aqueous solutions. Polyacrylate [48, 49, 70, 71, 74], acrylic acid [46], TTAB [4, 5], poly(*N*-vinyl-2-pyrrolidone) (PVP) [76, 78–82], poly(*N*-isopropylacrylamide) [72, 74, 86], poly(*N*-ethylacrylamide) [73], mercaptosuccinic acid [88], oxalate [89], sodium citrate [77], vitamin B_2 [90], bis(2-ethylhexyl)sulfosuccinate (AOT) [91] and CTAB [55, 84, 85] are some of the capping agents used in the growth of Pt nanostructures. These can either adsorb selectively onto specific surfaces, or form micelles and liposomes that guide the growth of Pt. In addition, the growth of various low-dimensional Pt nanostructures including nanowires [96, 118, 119], nanotubes [120], hollow nanocubes [120] and hollow nanospheres [94, 95, 121], can be realized by using hard templates.

10.3.1.2 **Electrochemical Methods**

In the electrochemical method, electrons supplied externally by a power source are used to convert ions into zero-valent metals. For platinum metal made from $PtCl_6^{2-}$ and $PtCl_4^{2-}$, reduction occurs once the external potential is below about 0.68–0.75 V. Experimentally, these reactions can occur once the potential is low enough to overcome the reduction overpotential. Pt nanoparticles have been electrochemically deposited on a variety of electronically conducting supports [97, 122–126]. Pt nanowires and nanotubes have also been prepared electrochemically by introducing hard templates [100–103] or lithographically patterned templates [127]. Recently, Tian *et al*. have synthesized Pt tetrahexahedra from nanospheres electrochemically using a square-wave potential profile [7, 98]. These faceted nanoparticles are single crystalline and bound by some high-index surfaces such as (730), (210) and (520).

10.3.1.3 **Other Methods**

In addition to the above-mentioned methods, *radiation* [55, 104–106] and *sonication* [118] can be used to produce large amount of radicals that can act as strong reducing agents. *Microwaves* can also be used to create nanoparticles, by rapidly heating up the reaction mixtures [107]. Nucleation tends to occur rapidly in these cases, followed by simultaneous growth, and small nanoparticles without any characteristic facets are the normal morphology obtained in this way. A *hydrothermal method* has also been investigated for preparing Pt nanoparticles [128]; here, the reaction mixtures are heated above the boiling temperatures of the solvents in pressurized autoclaves.

10.3.2
Nonhydrolytic Synthesis

Nonhydrolytic systems refer to those using solvents other than water in the synthesis of Pt nanoparticles. While all the control principles for aqueous systems should be applicable to nonhydrolytic systems, the possible choices for solvents, Pt precursors, surfactants and reducing reagents are broaden for the latter

cases. The reaction conditions can also differ drastically for nonhydrolytic systems; notably, the reaction temperature is no longer limited to below 100 °C, the boiling temperature of water. Some recent examples of shape-controlled syntheses of platinum nanostructures in nonhydrolytic systems are listed in Table 10.3. The solvents and reactants commonly used for preparing Pt nanostructures in these nonhydrolytic systems are discussed in the following sections.

Table 10.3 Shape control of Pt nanoparticles in nonhydrolytic systems.

Precursor[a]	Surfactant[b]	Solvent[c]	Reductant[d]	Additive	Shape[e]	Reference(s)
H_2PtCl_6	PVP	EG	EG	Fe^{2+} or Fe^{3+}	BM, NW, SP	[64, 129, 130]
				$PdCl_4^{2-}$	NW	[65]
				$AgNO_3$	C, CO, O	[9]
				$NaNO_3$	SP, O, TP, OP	[63]
					NW, Pl	[64, 82, 131]
K_2PtCl_4			$K_2C_2O_4$, EG, H_2	Pt seed	NW	[132]
$Pt(acac)_2$	OAm	Toluene	H_2		C, TP, OP, MP	[51, 52]
	OAc, OAm	ODE		$Fe(CO)_5$	C	[53, 133, 134]
		OAm	OAm		NW	[135]
		[BMIM][Tf_2N]	HDD		SP	[136]
	HDA, ACA	HDA, DPE	HDD, DDD	$AgNO_3$	C, MP, F, bipod, tripod, BM.	[11, 40, 43, 137]
$Pt_2(dba)_3$		[BMI][BF_4] [BMI][PF_6]	H_2		SP	[138]
	HDA	THF, toluene	CO, H_2		SP, NW	[139]

a acac = acetylacetonate; dba = dibenzylidene acetone.

b PVP = poly(*N*-vinyl-2-pyrrolidone); OAm = oleylamine; OAc = oleic acid; HDA = hexadecylamine; ACA = 1-adamantanecarboxylic acid.

c EG = ethylene glycol; ODE = 1-octadecene; DPE = diphenyl ether; [BMIM][Tf_2N] = 1-butyl-3-methylimidazolium bis(triflylmethyl-sulfonyl) imide; [BMI][BF_4] = 1-*n*-butyl-3-methylimidazolium tetrafluoroborate; [BMI][PF_6] = 1-*n*-butyl-3-methylimidazolium hexafluorophosphate; THF = tetrahydrofuran.

d HDD = 1,2-hexanedecanediol; DDD = 1,2-dodecanediol.

e C = cube; T = tetrahedron; O = octahedron; CO = cubo-octahedron; SP = spherical particle; NW = nanowire; OP = octopod; TP = tetrapod; Pl = Plate; MP = multipod; BM = branched multipod; F = nanoflower.

10.3.2.1 Solvents

10.3.2.1.1 Ethers and Amines Ethers and amines are good solvents for many syntheses, because they have high boiling temperatures and are thermally stable. Diphenyl ether (DPE) is one of the widely used organic solvents in the preparation of Pt with controlled morphologies [11, 40, 43, 137], while oleylamine (OAm) [135, 140] and hexadecylamine (HDA) [140] are the two most commonly used amines for creating Pt nanoparticles and nanostructures. When amines are used, the amine functional groups not only interact with Pt surfaces but also function as weak reducers in the reactions. Thus, amines may often play multiple roles in the synthesis, by acting as both reducing and capping agent, as well as solvent in some cases [140].

10.3.2.1.2 Polyols Ethylene glycol (EG) is among the best known of the polyols in the synthesis of Pt nanostructures. As EG is miscible with water, the result is a mixture that has a broad range of controllable boiling temperatures and solubility for both inorganic and organometallic salts of different platinum precursors. Because of its hydroxyl group, EG can also act as mild reductant and a weak capping agent. Various progress has been made during recent years in the use of EG or its mixtures in controlling the shapes of Pt nanostructures. For example, by introducing silver ions, Yang *et al*. prepared Pt cubes, cubo-octahedrons and octahedrons in EG [9, 61]. Pt multipods and nanowires can be produced in EG in the presence of nitrite and iron ions [63–65]. $K_2C_2O_4$ has also been used to confine the growth of Pt nanowires by reducing K_2PtCl_4 in EG [132]. In addition to EG, glycerol has also been used as solvent to prepare Pt nanoparticles [141].

10.3.2.1.3 Ionic Liquids Unlike molecular solvents, ionic liquids (ILs) are composed of cation–anion pairs at room temperature. The use of ILs to control the shape of nanoparticles is a new, but potentially fruitful, research direction because of their unique solvation properties, such as extended hydrogen bonding [142–144]. Several different types of IL have been applied to the synthesis of Pt nanoparticles [116, 138, 142, 145]. In our laboratory, uniform Pt nanoparticles have been prepared in 1-butyl-3-methylimidazolium bis(triflylmethyl-sulfonyl) imide ([BMIM][Tf_2N]) as IL, using platinum acetylacetonate ($Pt(acac)_2$) as the precursor, 1,2-hexadecanediol (HDD) as the reducing agent, and oleic acid and oleylamine as capping agents [136].

10.3.2.1.4 Other Solvents Recently, *toluene* has been used as solvent to prepare Pt cubes and other nanostructures [51, 52]. Pt nanospheres, nanowires and dendrites have also been obtained in tetrahydrofuran (THF) [139, 146, 147]. Both, supercritical methanol [148] and supercritical CO_2 [149, 150] have also been used as solvents in the creation of Pt nanoparticles.

10.3.2.2 Precursors

Solubility, redox potential and thermal stability are important parameters to be considered when designing experiments, and *organometallics* are commonly used

precursors in nonhydrolytic systems. Platinum acetylacetonate ($Pt(acac)_2$) is most often used on the basis of its good solubility and thermal stability [11, 40, 43, 135, 137], and the use of platinum dibenzyl idene acetone ($Pt_2(dba)_3$) as precursor has also been reported [139]. In polyol processes – and especially those when EG is used – inorganic compounds such as H_2PtCl_6, K_2PtCl_6 and K_2PtCl_4 can also be used as metal precursors, due mainly to their good solubilities [9, 63–65, 132, 151].

10.3.2.3 **Reducing Agents**

Diols are a group of reducing agents that have attracted regular use in nonhydrolytic systems to prepare Pt nanostructures; two such examples are HDD [11, 40, 43, 137] and DDD [40, 137]. These compounds have two neighboring hydroxyl groups, and function as mild reductants at elevated temperatures in the reactions; this in turn leads to relatively slow reaction kinetics that can be controlled.

Amines also serve as weak reducing agents, as the amidocyanogen groups can be oxidized into nitriles [152, 153]. Both OAm and HDA have been used as reducing agents, besides their roles as capping agents and solvents in several studies [135, 140]. In addition, hydrogen – typically in the form of forming gas – can acts as a mild reductant in the fine control of reducing rates of Pt salts [51, 52, 139].

10.3.2.4 **Capping Agents**

A capping agent plays a key role in controlling the morphology of platinum nanostructures. Amine- [51, 52, 135, 139, 140], fatty acid- [11, 40, 43, 137] and thiol- [154] based surfactants can interact with Pt surfaces effectively, and hence are used in the control of shape. OAm has been used to prepare platinum cube, triangular prism, nanorod, multipod and dendrite forms [51, 52, 135]. 1-Adamantanecarboxylic acid (ACA) is a capping agent which is thought preferentially to be adsorbed onto Pt surfaces such that, dynamically, it can facilitate growth along given directions [11, 43]. It is often important to use several surfactants simultaneously in order to achieve a fine control of morphology. For example, when both OAm and oleic acid are used, platinum nanocubes form in octadecene [53]. ACA is often used in conjunction with amines such as HDA and long carbon chain diols to produce platinum multipods [40, 137].

10.4
Pseudo-Zero-Dimensional Pt Nanoparticles

Here, pseudo zero-dimensional platinum particles refer to those simple shapes such as spheres and highly symmetrical platonic shapes, including tetrahedrons, octahedrons, cubes, tetrahexahedrons (THHs), and their truncated forms [70, 75, 155]. Some transmission electron microscopy (TEM) images of faceted particles that have been recently obtained and categorized as pseudo-zero-dimensional nanostructures, due to their small size, symmetrical shape and single crystalline nature, are shown in Figure 10.6. Typically, spherical nanoparticles are composed

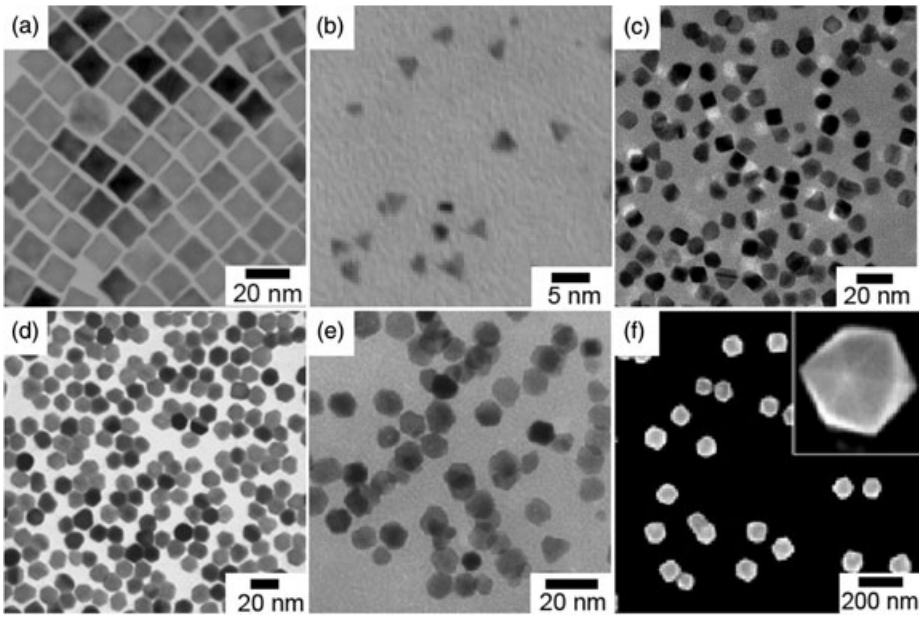

Figure 10.6 TEM images of representative (a) cubic [40], (b) tetrahedral [75], (c) octahedral [9], (d) cubo-octahedral [4], (e) truncated octahedral [81] and (f) tetrahexahedral [7] Pt nanoparticles.

of various types of undefined surfaces, while cubic platinum nanoparticles are bound by {100} facets and tetrahedrons by {111} facets. The recently discovered tetrahexahedral nanoparticles of platinum, which are composed of 24 facets with {730}, {210}, and/or {520} surfaces [7], are important as they represent a few known examples of well-defined Pt nanostructures bound by high-index facets.

10.4.1 Faceted Particles

10.4.1.1 Nanocubes

El-Sayed and coworkers were the first to report the synthesis of Pt nanoparticles of cube and tetrahedron-like shapes prepared in aqueous solutions by using sodium polyacrylate (PAA) as capping reagent and hydrogen as reductant [47–49]. In that synthesis, Pt ions in K_2PtCl_4 were reduced under mostly static conditions by hydrogen after its introduction to the reaction system. The molecular weight (MW) of PAA was found to be a key factor in the production of cubes since, by using PAA with MW 5100, about half of the population of Pt nanostructures were created in a cubic shape [71]. Subsequently, Miyazaki *et al.* synthesized platinum cubes by using a similar hydrogen reduction method [72, 156]; here, the proportion of cubes was increased to about 70% by using poly(*N*-isopropylacrylamide)

as capping reagent and controlling the reaction temperature. The type of platinum precursor was also found to be an important factor on the growth of Pt nanostructures when using the H_2 reduction method in aqueous solution [147]. Fu *et al.* compared the performance of $K_2[Pt(C_2O_4)_2]$, K_2PtCl_6 and K_2PtCl_4 as precursors in the shape control of Pt nanoparticles by using oxalate as a stabilizing reagent [89], and showed the proportion of Pt nanocubes to exceed 90% when $K_2[Pt(C_2O_4)_2]$ was used. The addition of a small amount of $CaCl_2$ could also be used to improve shape control. Ren *et al.* also recently developed a H_2 assistant decomposition method for preparing highly monodispersed Pt nanocubes [51, 52] in which $Pt(acac)_2$ was reduced under 3 bar pressure of hydrogen in toluene at 70 °C for 20 h. The concentration of $Pt(acac)_2$ may affect the size distribution.

Niesz *et al.* prepared 7.1 nm Pt nanocubes by using EG as reductant and PVP as the capping reagent, at 196 °C [117]. The groups of both Yang and Somorjai synthesized Pt cubes with well-defined morphologies by using sodium borohydride ($NaBH_4$) as reductant and TTAB as capping agent [4, 5]. In this synthesis, the formation of a stoichiometric metal–surfactant complex, $(TTA)_2PtBr_4$, before the reduction was critical. This complex could be produced from a reaction mixture of TTAB and K_2PtCl_4 at 50 °C, whereupon the platinum nuclei grew into nanocubes when the pH of the solution was approximately 12. CTAB was also used as the capping agent when $NaBH_4$ was used as the reductant [84]. When platinum acetylacetonate ($Pt(acac)_2$) and mediate agents were used, the polyol process became the method of choice for preparing faceted platinum nanocrystals. Song *et al.* reported the synthesis of Pt nanocubes from $Pt(acac)_2$ in boiling EG in the presence of a small amount of $AgNO_3$ (the $AgNO_3/Pt(acac)_2$ molar ratio was ca. 1 : 100) [9]. In addition to silver nitrate, iron carbonyl ($Fe(CO)_5$) was also found to be a useful mediating agent in the decomposition of $Pt(acac)_2$ [133, 134]. Uniform Pt nanocubes were formed in the presence of a small amount of $Fe(CO)_5$ using oleic acid and OAm as capping agents [53]. Finally, Qu *et al.* succeeded in synthesizing cubic Pt particles by galvanic displacement between an aqueous solution of K_2PtCl_4 and a Cu foil substrate [62].

10.4.1.2 Tetrahedron, Cubo-Octahedron and Octahedron

The group of El-Sayed found that, when PVP was used as the capping agent, tetrahedral Pt particles were formed preferentially, yet when PAA was used the cube was the dominant shape [70, 75, 155, 157, 158]. The reduction rate of Pt^{4+} ions was also seen to be important by others [159], with tetrahedral particles dominating when $H_2(PtCl_6)$ was reduced by H_2, but truncated octahedral particles being the main product when methanol was used as the reducing agent. The slow reduction rate of Pt^{4+} ions by hydrogen may lead to the formation of tetrahedral Pt nuclei bound by {111} facets that have a low surface energy and are thermodynamically stable. Such rapid reduction might also result in the creation of truncated octahedral nuclei, although the roles of each ingredient and the mechanism of shape control in these systems remain the subject of much debate [50, 79, 81].

The *seed-mediated approach* represents another effective strategy for the synthesis of tetrahedral Pt nanoparticles using PVP as capping agent and H_2 as reductant

in an aqueous solution. The particle size could be controlled by changing the molar ratio between the Pt precursor and seed [76]. Henglein *et al*. reported that, depending on the concentration of the stabilizing additive (e.g. citrate), Pt colloids consisting of polyhedra of different shapes (cube, tetrahedron, truncated octahedron) were formed when using H_2 as the reductant in basic aqueous solution [77]. The formation of a hydroxylated precursor, and its subsequent reduction, were the two key steps in this process. In the presence of $AgNO_3$, the polyol process could also be used to prepare cubo-octahedrons, at a $AgNO_3/Pt(acac)_2$ molar ratio of approximately 3 : 25, or octahedrons when the ratio was about 47 : 100 [9].

10.4.1.3 **Tetrahexahedron**

In addition to those Pt nanoparticles bound by low-indexed surfaces, Tian *et al*. synthesized tetrahexahedral platinum nanoparticles by using an electrochemical method [7]. Here, a square-wave potential function was used to treat Pt nanospheres supported on glassy carbon, and this led to the formation of Pt nanocrystals bound by high-indexed {730}, {210} and/or {520} facets. These particles proved to be catalytically active due to their high density of atomic steps and kinks [98].

10.4.2 **Spherical Nanoparticles**

A variety of methods exists for preparing monodispersed Pt ultrafine particles in solution phase through the reduction of Pt salts. The choice of reductant can be made from a list of reagents including hydrazine [91, 111, 113, 114], borohydride [87, 88, 109–112], ethanol [70, 86, 160], EG [63, 151], citrate [83, 115], vitamin B_2 [90], potassium bitartrate [161] and ascorbic acid [116, 117]. In aqueous solution, the typical synthetic procedure involves the addition of a reductant to a solution of platinum salt precursor and a capping reagent, with vigorous stirring. Both, Vidal-Iglesias and coworkers [111, 114] and Chen and colleagues [91] reported the synthesis of platinum ultrafine particles in reverse micellar solutions. In this case, the concentration of surfactant and oil (if used) were important in determining the particle size and size distribution. In organic solution, the polyol process becomes a common approach for producing Pt spherical nanoparticles, with the Pt precursors being reduced by polyols such as EG [63, 64] and glycerol [141], often under refluxing conditions.

Recently, ILs have been used in the synthesis and modification of nanostructured materials because of their unique properties, such as extended hydrogen bonding. Notably, platinum particles can be formed regardless of whether capping agents are used. The addition of surfactant capping agents can greatly facilitate the control of particle uniformity and dispersity in solvents. For example, Scheeren *et al*. showed that a Pt precursor could be reduced by hydrogen to produce Pt spherical nanoparticles in the presence of cyclohexene, and 1-*n*-butyl-3-methylimidazolium tetrafluoroborate ([BMI][BF_4]) or hexafluorophosphate ([BMI][PF_6]) IL

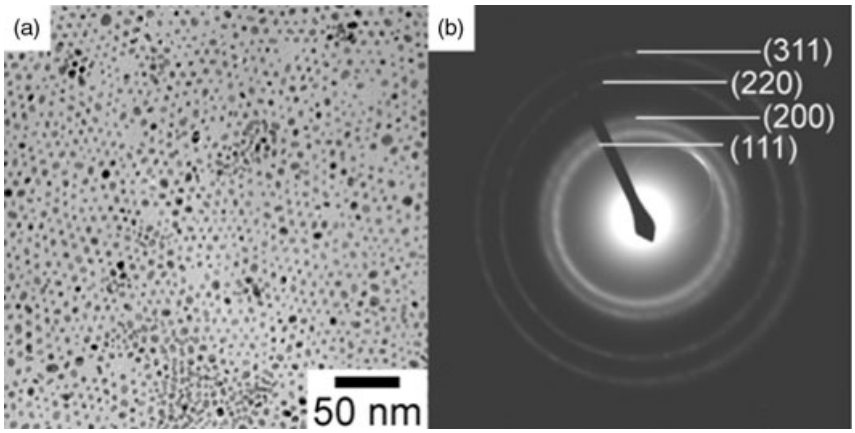

Figure 10.7 (a) TEM image and (b) electron diffraction of solvent-dispersible Pt nanoparticles prepared in [BMIM][Tf_2N] IL [136].

[138]. In another study, Wang *et al.* showed that platinum nanoparticles could be synthesized in a 1-butyl-3-methylimidazolium bis(triflylmethyl-sulfonyl) imide ([BMIM][Tf_2N]) ionic liquid, using oleic acid and OAm as the capping agents [136]. The precursor $Pt(acac)_2$ could be reduced by HDD at 230 °C. The formed Pt nanoparticles settled out from the reaction mixture of [BMIM][Tf_2N] IL, a process that greatly facilitated the separation from solvents. The spherical nanoparticles showed an excellent solvent dispersity over a range of conventional organic solvents such as hexane (see Figure 10.7).

10.5
One-Dimensional Nanostructures: Nanowires and Nanotubes

A templating approach can be important for preparing low-dimensional platinum nanostructures, as the platinum metal has a fcc cubic symmetry. In template-free solution-phase synthesis, the introduction of defects can serve as a useful strategy. Some examples of nanorods, nanowires and nanotubes of platinum prepared using different methods, with and without templates, are shown in Figure 10.8. Notably, when the diameter of nanowires becomes very small, they can exhibit excellent flexibility and form interconnected networks.

10.5.1
Nanowires

10.5.1.1 Polyol and Template-Free Synthesis

Xia and coworkers have created a variety of Pt nanowires using the polyol process [65, 129–131]. In a typical procedure, H_2PtCl_6 or K_2PtCl_6 was dissolved in EG,

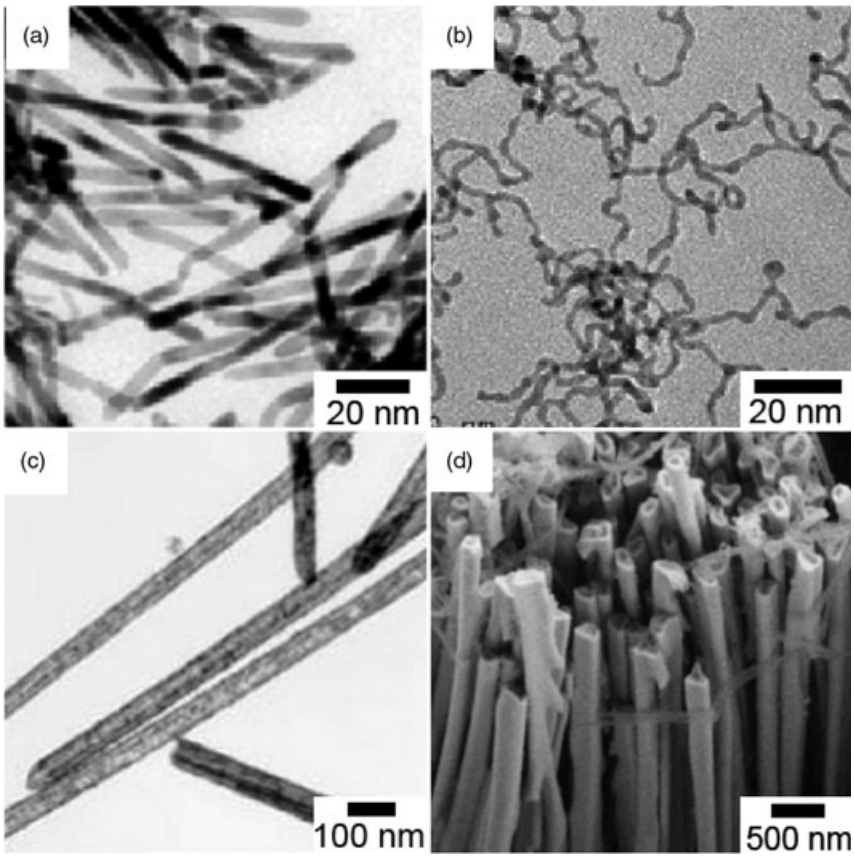

Figure 10.8 TEM images of selective 1-D Pt nanostructures. (a) Nanorods [129]; (b) nanowires [56]; nanotubes synthesized (c) by the galvanic method [162] and (d) using AAO templates [103].

which had the dual function of both solvent and reductant, in the presence of a trace amount of Fe^{2+} or Fe^{3+}. PVP was the most commonly used surface capping agent in these systems. The Pt nanowires were seen to grow on the surface of the agglomerates [129], and this procedure could be modified to grow thick and uniform sheaths made from Pt nanoparticles. Nanowires on the surfaces of polymeric and ceramic particulates could be formed by using a catalyst of palladium nanoparticles [65]. In this situation, the Pt nanowires were able to grow on the metal gauzes [130] and TiO_2 nanofibers [131]. Besides PVP, hydrogen could also be used as a reductant in order to grow Pt nanowires in polyol solutions, using a seed-mediated method [132].

Sun *et al*. demonstrated the formation of large quantities of single-crystal Pt nanowires from H_2PtCl_6 aqueous solution with formic acid, at room temperature

[163]. The spontaneous self-assembly and subsequent fusion of discrete Pt nanoparticles proved to be another template-free method for preparing long nanowires [66]. In this synthesis, ethanol was used as a weak polar solvent to assemble Pt nanoparticles into an extended nanostructure. Vitamin B_2 was another reagent used to create Pt nanorods from nanoparticles in a water/isopropanol solution [90]. Ramirez *et al.* reported that the organometallic compound platinum dibenzylideneacetone ($Pt_2(dba)_3$) could be reduced by H_2 and CO and form nanowires in organic solvents of THF and toluene, using HDA as the stabilizer [139]. The twin defect may be common among nanorods of platinum metal; for example, Yang and coworkers showed that Pt nanorods would grow out from a seed crystal with multiple twin planes [40]. These nanorods had a (111) twin plane in the center of the nanostructure, along the growth direction (Figure 10.9).

10.5.1.2 **Template Synthesis**

The deposition or confined crystallization of metal atoms may be conducted within the pores in anodic aluminum oxide (AAO) membranes [92, 101, 103, 164, 165], mesoporous silica [96, 102, 106, 166, 167], or micelles in solution [55, 56, 139]. The crystallization of metal atoms within templates can be achieved through a

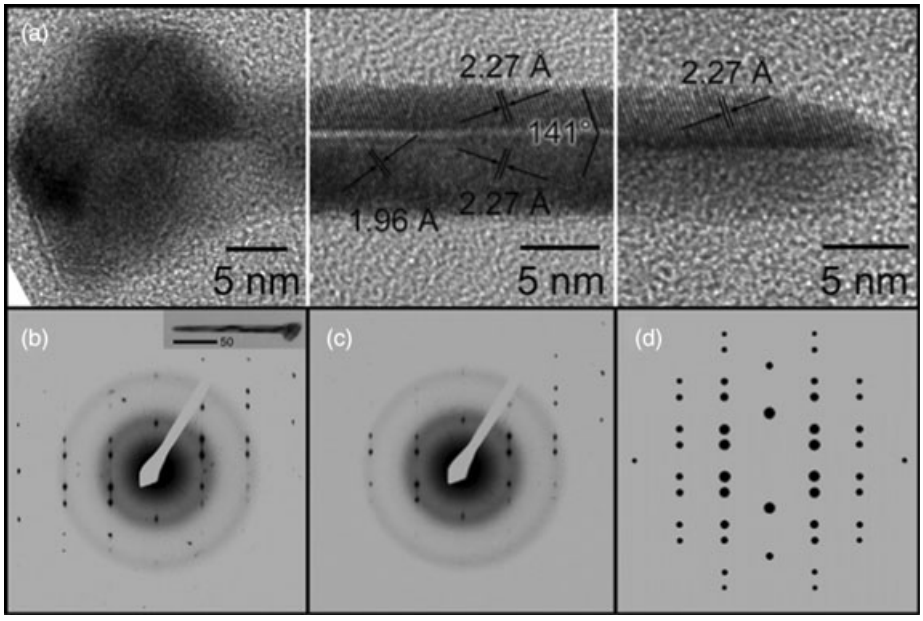

Figure 10.9 Representative Pt nanorod grown from a twin crystal seed. (a) High-resolution TEM images of the core (left), middle (center) and tip (right) regions; (b–d) Selected area electron diffraction (SAED) pattern of (b) the whole and (c) arm of the nanorod, and (d) superimposed two simulated pattern along zone axis ⟨–110⟩ offset by 141° [40]. The inset in (b) shows the nanorod used for the SAED study. Scale bar in inset = 50 nm.

direct electrodeposition inside pores followed by the *in situ* photoreduction or chemical reduction of the adsorbed metal ions in the channel of the templates. Both, wires and rods can be prepared through the confinement of physical templates. The electrodeposition of platinum is usually carried out in a three-electrode cell containing solutions of Pt ions. The aspect ratios of Pt nanowires can typically be controlled by changing the deposition conditions. Sakamoto *et al*. synthesized Pt nanowires using mesoporous silica HMM-1 impregnated with H_2PtCl_6 in the presence of adsorbed water and methanol, through photoreduction [106]. Similarly, Song *et al*. prepared platinum nanowires by the chemical reduction of a platinum complex using sodium borohydride in the presence of soft templates formed by CTAB in a water/chloroform two-phase system [56]. Later, Krishnaswamy *et al*. [55] synthesized Pt nanowires by γ-irradiation in a soft template formed by CTAB in aqueous solution.

10.5.2
Nanotubes

The generation of nanotubes replies largely on the templating approach, and both nanorods or nanowires and nanoporous structures have been explored. By using the polyol process, Xia's group was able to produce a large quantity of straight colloidal silver nanowires and, by the galvanic method, they synthesized Pt nanotubes using these silver nanostructures as sacrificial templates [120, 162, 168, 169]. Yan and coworkers prepared both Pt and Pt/Pd alloy nanotubes using a similar approach [170].

Among the porous templates for preparing nanotubes, the AAO membrane is the most frequently used. Yuan *et al*. synthesized Pt nanotube arrays by using this template via electrochemical deposition [103]. Here, the inner wall of the AAO pores was modified with 3-aminopropyltrimethoxysilane to allow the easy transpart of ionic precursors and release of the nanotubes. The electrodeposited Pt nuclei grew along the modified wall to form tubes. The Pt nanotubes were obtained after the removal the template, using chemical etching.

10.6
Two-Dimensional Platinum Nanostructures

As with the 1-D nanostructures discussed in Section 10.5, the formation of 2-D Pt nanostructures relies upon either defects in seed crystals or using templates. The most commonly encountered defects with platinum metal are those due to stacking faults, such as twin defects in (111) planes. Lipids and micelles at the interface are the types of soft template most useful for the generation of 2-D nanostructures. Some TEM images of representative, recently created 2-D Pt nanostructures are shown in Figure 10.10; these structures include planar multipods (bipods and tripods), triangular plates and dendritic sheets.

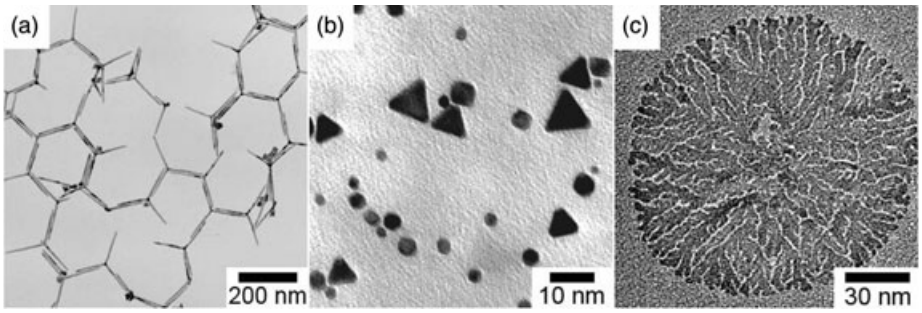

Figure 10.10 TEM images of 2-D Pt nanostructures. (a) Tripods and bipods [137]; (b) Triangular nanoplates [82]; (c) Dendritic nanosheet [58].

10.6.1 Planar Tripods and Bipods

Yang and coworkers recently developed a synthetic approach to platinum planar tripods and bipods [40, 137]. In this method, $Pt(acac)_2$ was reduced by HDD in DPE. The interaction between capping agents of ACA and HDA and the platinum growing surface was important. The optimal reactant molar ratio for producing Pt planar tripods was $Pt(acac)_2$: ACA : HDD : HDA : DPE of 1 : 3–4 : 24 : 33 : 25. In this way, nanometer-sized planar tripods with a population of about 25% could be achieved, and the length of individual branches could be controlled between 50 nm and slightly over 200 nm by varying the reaction conditions (e.g. reaction time). The average width of the branches changed correspondingly from about 6 nm to 10 nm.

The seed crystal containing a twin defect is a key for reducing the symmetry of cubic-phase platinum metal [40]. A proposed mechanism for the formation of Pt planar tripods is shown in Figure 10.11. The twin defect in the (111) plane can result in the formation of seed crystals that have two sets of growth directions in the growing plane. Those belonging to the ⟨211⟩ directions have re-entry troughs and are favored kinetically [171]. The concentration gradient generated around the tip regions of the growth front can facilitate the growth of branches [172].

10.6.2 Nanoplates

Xia and coworkers also reported that the reduction of platinum salt by hydroxyl groups of PVP could induce the formation of Pt nanoplates (see Figure 10.10b) [82]. By adjusting the molar ratio between PVP and the metal precursor, or by choosing PVP with different molecular weights, the morphology of these plates could be controlled. Nevertheless, in comparison with other shapes or other metals (such as silver and gold), colloidal Pt nanoplates are still underdeveloped.

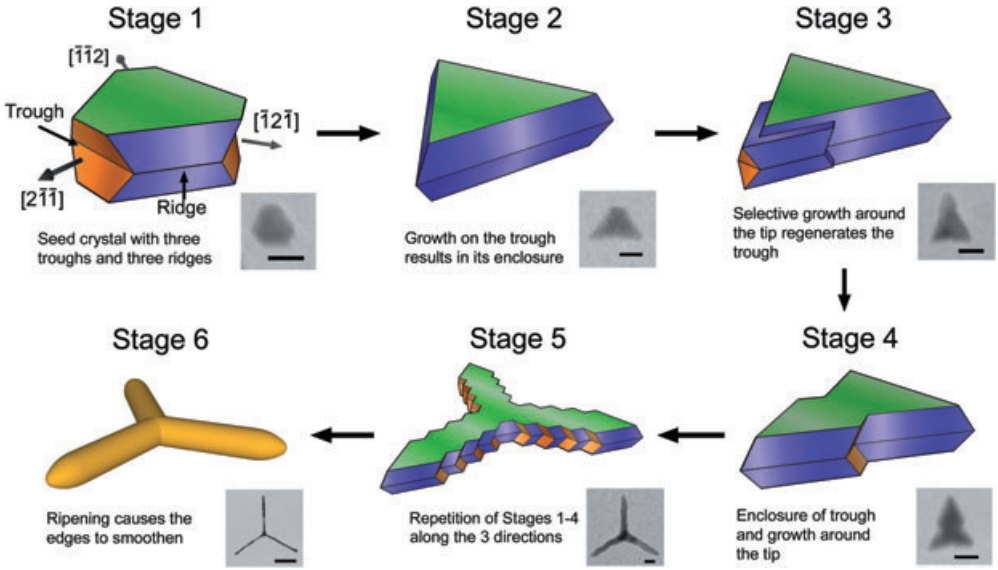

Figure 10.11 Formation of planar tripods of platinum nanostructures. The insets show TEM images where scale bars are 10 nm for Stages 1–5, and 100 nm for Stage 6 [40].

10.6.3
2-D Nanodendrites and Nanosheets

The formation of continuous or textured 2-D nanosheets often relies on soft templates, and occurs at the interface. Kijima *et al.* synthesized a 2-D network of Pt nanosheets using a mixture of lyotropic liquid crystals (LCs) which confined the growth [173]. Song *et al.* prepared 2-D dendritic Pt nanosheets using liposomal surfaces [58]; here, the nanosheets began to grow on liposomes and became attached to each other to form continuous sheets with textures at the interface. Besides the methods based on colloidal growth or soft templates, nanocrystalline Pt thin films could also be generated via metal organic chemical vapor deposition (MOCVD) [174] and cool argon sputtering techniques at the interfaces [175].

10.6.4
Porous Nanonetwork Prepared with the Langmuir–Blodgett (LB) Technique

The 2-D Pt network could be prepared at the air–water interface by using the LB deposition technique [176]. The dispersion phase used was composed of oleic acid-capped Pt nanocrystals in chloroform at a concentration of ~1 mg ml^{-1}. The Pt nanoparticles were spread at the air–water interface in the LB trough, using water as a subphase, due to the hydrophobic nature of the long-chain capping agents. However, by compressing the Pt particles onto the AAO porous membrane

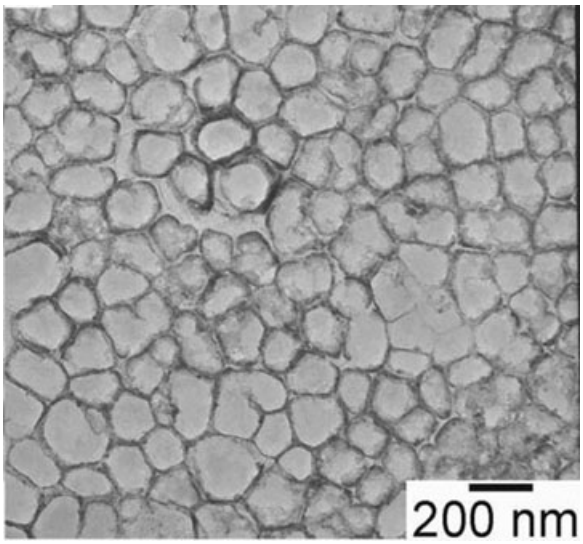

Figure 10.12 Porous Pt nanoparticle films made using the Langmuir–Blodgett technique [176].

and subsequent calcination in an argon atmosphere, the Pt particles could be produced in a carbonaceous, porous film (Figure 10.12).

10.7
Three-Dimensional Nanostructures

In this section, hyperbranched multipods, nanoflowers, hollows, foams and open networks are classified as three-dimensional (3-D) nanostructures. These 3-D nanostructures are some of the latest forms of platinum metal that can be obtained. While self-assembly and galvanic replacement play a role in the synthesis, many of these shapes are produced by using solution-phase approaches with capping agents. Besides twin defects, secondary growth from primary nanoparticles is an important pathway. If the oriented attachment is dominant during the secondary growth, then the final shapes of the Pt nanostructures may resemble those of simple platonic counterparts, but have textures.

10.7.1
Pt Multipods and Flower-Like Nanostructures

10.7.1.1 Pt Multipods

Teng *et al*. reported that Pt multipods could be synthesized by an induced anisotropic growth in the presence of HDA, ACA, DPE, and a small amount of Ag(acac) [43]. Hyperbranched Pt nanostructures with multiple high aspect ratio branches

were found in these reaction systems (Figure 10.13a). The twin defects that were seen to be important for the formation of tripods also played an essential role in the formation of platinum multipod nanocrystals [40]. In the latter case, both five- and two fold twin planes could be involved. Xia and coworkers were able to synthesize Pt tetrapods using a modified polyol method [63]. In this reaction, $NaNO_2$ was added to slow down the nucleation rate and control the growth direction of Pt nanocrystals. Tilley and coworkers also reported a preparation of tetrapods via the reduction of $Pt(acac)_2$, under 3 bar H_2 pressure, in toluene [51], with OAm being used as the surface capping agent. Besides the above approaches, a seeding-mediated growth method was also developed for preparing Pt multipods nanocrystals [177]. Here, the shape of the Pt nanostructures could be controlled by varying the ratio between the seed and the precursor.

10.7.1.2 **Nanoflowers and Dendritic Nanostructures**

Three-dimensional, flower-like nanostructures can be synthesized in DPE using $Pt(acac)_2$ as precursor and HDD as reducing agent (Figure 10.13b) [11]. In this reaction, HDA functioned as both the surface capping and solvent, while ACA was used as a co-surface capping agent that could kinetically stabilize the platinum surfaces temporarily during nucleation and growth. The reaction temperature for creating the secondary growth was 210 °C – this was higher than the temperature used for the induced growth of Pt multipods using similar reaction mixtures, but without the additives [43]. The difference interaction between capping agents and the platinum growing surfaces favored anisotropic attachment of the primary particles, while the time at which the reaction was terminated was critical for producing the flower-like Pt nanostructures.

Depending on the morphology of the primary particles and reaction conditions, other modes of attachment are also possible. Zhang *et al.* synthesized branched

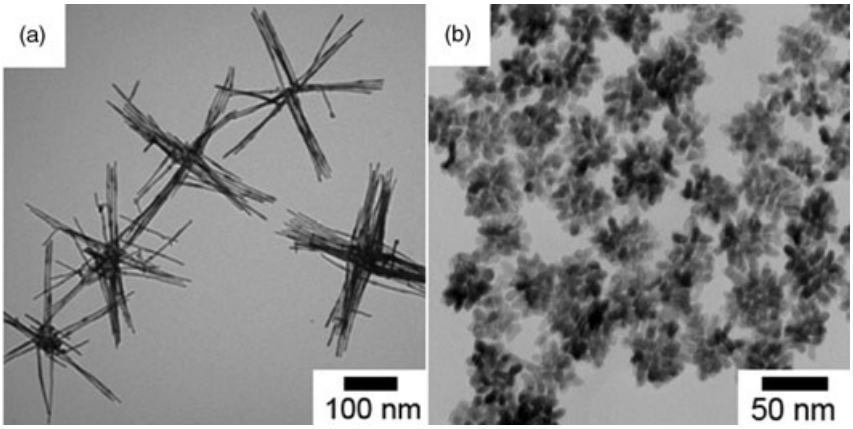

Figure 10.13 TEM images of (a) hyperbranched nanostructures and (b) nanoflowers [11].

Pt nanoparticles by directly decomposing $Pt(acac)_2$ at 250 °C in OAm [135]; here, the Pt nanostructures evolved from spherical particles to branched nanoparticles when the reaction temperature was decreased. Ullah and coworkers reported a method of using a $NaBH_4$-mediated reduction to create 3-D branched Pt nanostructures [85]. In this case, the reactant precursor CTAB–Pt(IV) complex was reduced to CTAB–Pt(0) under varying reaction conditions, including pH value. Finally, a second generation of carboxyl-cored dendrimer ([G-2]-COOH dendrimer) was successfully used as the stabilizer for preparing Pt nanodendrites at the water/toluene interface [178].

10.7.2 Hollow Nanostructures

Tan *et al.* prepared Ag@Pt core-shell nanocubes by the coreduction of Ag^+ and $PtCl_6^{2-}$ with sodium citrate [179]. The Ag cores could be removed by adding bis-(*p*-sulfonatophenyl) phenylphosphine (BSPP) solution to form hollow Pt nanocubes (Figure 10.14a). Similarly, Li *et al.* used Co nanoparticles as sacrificial templates to produce Pt hollow spheres [95], the shells of which was made primarily of Pt nanocrystallites. Galvanic replacement was also employed to create hollow spheres by Liang *et al.* (Figure 10.14b) [94]. Finally, Selvakannan and Sastry used the galvanic replacement reaction between silver nanoparticles and chloroplatinate ions in chloroform to create platinum hollow nanoparticles [180].

Besides hard inorganic metal templates, lipid molecules are used in the synthesis of foam-like nanostructures. Shelnutt and coworkers synthesized foam-like Pt nanospheres with a 2 nm-thick shell and diameters of up to 200 nm in the presence of liposomes, through either a chemical or photochemical reduction process (Figure 10.14c) [57–59]. Here, ascorbic acid was used as the chemical reducer for the platinum precursor. Alternatively, hydrophobic Sn(IV) octaethylporphyrin (SnOEP) could be used as the photocatalyst molecule under white light irradiation.

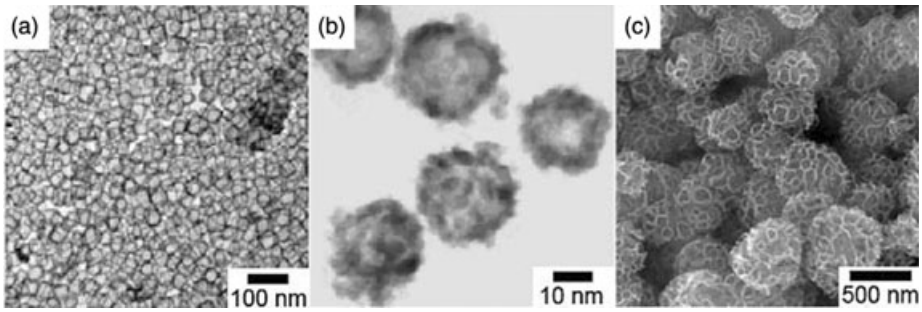

Figure 10.14 TEM images of Pt nanoparticles with hollow structures. (a) Hollow cubes [179]; (b) Hollow spheres [94]; (c) Nanofoams [59].

The dendrite-like structures were made from highly porous hollow spheres. As the SnOEP became localized at the benzene–water interface, the platinum seeds formed during the photoreduction were able to grow in autocatalytic fashion and form Pt dendrites that eventually became nanofoams [60].

10.7.3
3-D Networks

Both, templating and self-assembly approaches have been explored in order to create extended networks of 3-D nanostructures. In an initial templating method, ordered mesoporous structures such as MCM41, MCM-48 and their derivatized forms were popular templates [119, 181]. For this method it was first necessary to introduce Pt precursors into the channels of the templates through surface adsorption. The 3-D network of platinum could then be generated after reduction by hydrogen gas.

A second method was based on the direct assembly of platinum building blocks, where hyperbranched multipods with high aspect ratios could serve as the nanostructured precursors. A network of platinum nanowires directly assembled from a solution phase is shown in Figure 10.15. Unlike the networks made from templates, these assembled networks could either be disassembled into individual multipods in dispersion form, or sintered into connected networks.

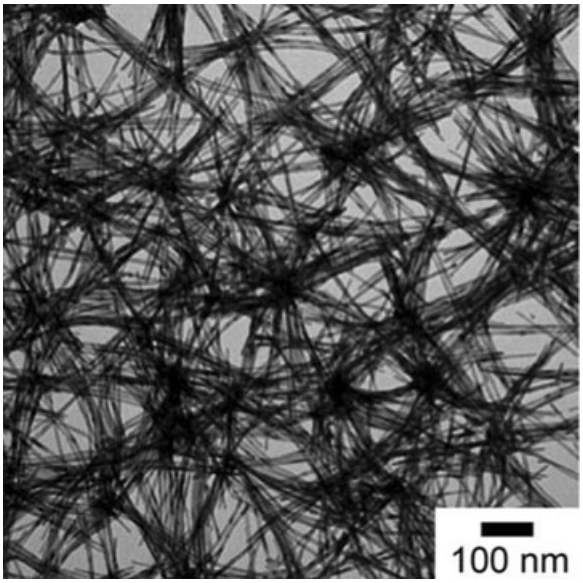

Figure 10.15 Platinum 3-D network from the self-assembly of hyperbranched multipods.

10.8
Platinum Alloys and Intermetallics

While much progress has been made in recent years on the shape control of platinum nanostructures, the number of reports relating to Pt alloys and the forms of intermetallics is somewhat limited. As an alloy has the nature of a solid solution, the control of facet formation may represent a major challenge. Nevertheless, the basic principles of shape control can often be applied to platinum alloys and intermetallics through judicious selection of the reaction precursors and conditions. A series of platinum intermetallic rods, shaped alloy dendrites and spheres that have been prepared in solution phase and in the presence of surface capping agents is shown in Figure 10.16 [12, 182, 183]. The PtPb nanorods (Figure 10.16a) were synthesized by simultaneously reducing $Pt(acac)_2$ and $Pb(acac)_2$ with a *tert*-butylamine borane (TBAB) complex in a mixture of DPE, ACA, HDA and hexadecanethiol (HDT) at 180 °C [182]. In this synthesis, ACA and HDT played key roles in the control of rod formation. As with Pt nanoflowers formed in non-hydrolytic systems, the 3-D nanodendrites of PtRu alloys could be prepared from $Pt(acac)_2$ and $Ru(acac)_2$ using HDD, 1-adamantaneacetic acid (AAA) and HDA (Figure 10.16b) [12]. At the nanometer scale, exotic alloy compositions can occasionally be generated with well-defined shapes; however, for alloys between platinum and silver the large miscibility gap which is apparent in the bulk form did not seem to affect the formation of both spheres and nanowires of PtAg alloys (Figure 10.16c) [183].

10.9
Concluding Remarks

Despite the present limitations in our ability to control the shape of platinum nanoparticles by design, tremendous progress has been made in this area

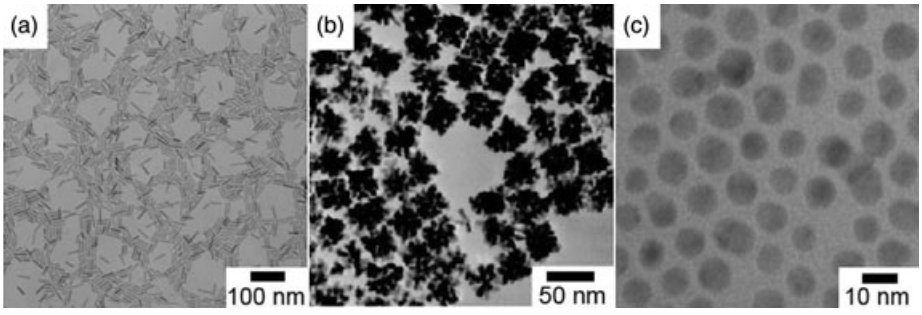

Figure 10.16 TEM images of PtM alloy and intermetallic nanostructures. (a) PtPb nanorods [182]; (b) 3-D PtRu nanoparticles [12]; (c) PtAg nanospheres [183].

during the past decade. The interaction between capping agents and various index planes of platinum surfaces – which is an important fundamental aspect – has been studied in great detail, such that uniform platinum nanocrystals can now be constructed not only in platonic shapes but also in other low-dimensional morphologies, such as rods and multipods. Indeed, it would seem that solution-phase synthesis has become the main strategy in preparing 'simple' platonic shapes such as cubes, tetrahedrons and octahedrons. Although aqueous systems are important and have been widely studied, nonhydrolytic systems involving polyols, ethers and other organic solvents have also become essential for the generation of shape-controlled platinum nanocrystals. In addition to the platinum precursors and solvents, surface capping agents and reductants can also play key roles in determining the final shapes of platinum nanoparticles.

Defects in seed crystals are often pivotal in order to produce the symmetry-reduced morphologies of platinum nanoparticles. The production of twinning in (111) planes represents a strategy that has been used widely in recent years to prepare platinum nanorods, nanowires and multipods, and both two- and five-fold twin defects have been observed in these low-dimensional shapes. Another approach which enables the control of platinum morphology is through the use of templates, the most frequently used of which include less-noble metal nanoparticles, lipid-based soft templates and porous anodic aluminum oxide membranes. Platinum hollow spheres and nanotubes can be developed through galvanic replacement reactions on templating metal nanostructures, while lipids can be used to guide the deposition of platinum metal from salt precursors through reduction reactions, resulting in the formation of foam-like structures. Those nanorods and nanotubes fabricated from AAO porous membranes tend to be made from polycrystalline platinum.

Finally, secondary growth and self-assembly can be used to produce higher-order platinum nanostructures with reduced symmetries, while flower-like nanoparticles can be generated from primary platinum nanoparticles in solution, through oriented attachments. The differences in surface properties among various low-indexed planes is the main structural reason for such anisotropic attachments. Interconnected networks and thin porous membranes of platinum nanoparticles prepared from Langmuir–Blodgett films are examples of platinum nanostructures created through self-assembly.

Acknowledgments

These studies were supported in part by the US National Science Foundation, the Environmental Protection Agency, and the American Chemical Society. We are grateful to our former colleagues, Xiaowei Teng, Yong Wang, Sean Maksimuk and others, for their contributions to the research data presented in this chapter. S.C.Y. is a visiting student from Xi'an Jiaotong University.

References

1 Wieckowski, A., Savinova, E.R. and Vayenas, C.G. (2003) *Catalysis and Electrocatalysis at Nanoparticle Surfaces*, Marcel Dekker, Inc., New York.

2 Burda, C., Chen, X.B., Narayanan, R. and El-Sayed, M.A. (2005) Chemistry and properties of nanocrystals of different shapes. *Chemical Reviews*, **105**, 1025.

3 Ozin, G.A. and Arsenault, A.C. (2005) *Nanochemistry: A Chemical Approach to Nanomaterials*, RSC Publishing, Cambridge.

4 Bratlie, K.M., Lee, H., Komvopoulos, K., Yang, P.D. and Somorjai, G.A. (2007) Platinum nanoparticle shape effects on benzene hydrogenation selectivity. *Nano Letters*, **7**, 3097.

5 Lee, H., Habas, S.E., Kweskin, S., Butcher, D., Somorjai, G.A. and Yang, P.D. (2006) Morphological control of catalytically active platinum nanocrystals. *Angewandte Chemie–International Edition*, **45**, 7824.

6 Tao, A.R., Habas, S. and Yang, P.D. (2008) Shape control of colloidal metal nanocrystals. *Small*, **4**, 310.

7 Tian, N., Zhou, Z.Y., Sun, S.G., Ding, Y. and Wang, Z.L. (2007) Synthesis of tetrahexahedral platinum nanocrystals with high-index facets and high electro-oxidation activity. *Science*, **316**, 732.

8 Milliron, D.J., Hughes, S.M., Cui, Y., Manna, L., Li, J.B., Wang, L.W. and Alivisatos, A.P. (2004) Colloidal nanocrystal heterostructures with linear and branched topology. *Nature*, **430**, 190.

9 Song, H., Kim, F., Connor, S., Somorjai, G.A. and Yang, P.D. (2005) Pt nanocrystals: shape control and Langmuir-Blodgett monolayer formation. *Journal of Physical Chemistry B*, **109**, 188.

10 Zhuang, J.Q., Wu, H.M., Yang, Y.G. and Cao, Y.C. (2008) Controlling colloidal superparticle growth through solvophobic interactions. *Angewandte Chemie–International Edition*, **47**, 2208.

11 Teng, X.W., Liang, X.Y., Maksimuk, S. and Yang, H. (2006) Synthesis of porous platinum nanoparticles. *Small*, **2**, 249.

12 Teng, X.W., Maksimuk, S., Frommer, S. and Yang, H. (2007) Three-dimensional PtRu nanostructures. *Chemistry of Materials*, **19**, 36.

13 Jeong, U., Teng, X.W., Wang, Y., Yang, H. and Xia, Y.N. (2007) Superparamagnetic colloids: controlled synthesis and niche applications. *Advanced Materials*, **19**, 33.

14 Yin, Y. and Alivisatos, A.P. (2005) Colloidal nanocrystal synthesis and the organic-inorganic interface. *Nature*, **437**, 664.

15 Jun, Y.W., Choi, J.S. and Cheon, J. (2006) Shape control of semiconductor and metal oxide nanocrystals through nonhydrolytic colloidal routes. *Angewandte Chemie–International Edition*, **45**, 3414.

16 Chen, J.Y., Wiley, B.J. and Xia, Y.N. (2007) One-dimensional nanostructures of metals: large-scale synthesis and some potential applications. *Langmuir*, **23**, 4120.

17 Murphy, C.J., Gole, A.M., Hunyadi, S.E., Stone, J.W., Sisco, P.N., Alkilany, A., Kinard, B.E. and Hankins, P. (2008) Chemical sensing and imaging with metallic nanorods. *Chemical Communications*, 544.

18 Pileni, M.P. (2007) Control of the size and shape of inorganic nanocrystals at various scales from nano to macrodomains. *Journal of Physical Chemistry C*, **111**, 9019.

19 Wiley, B., Sun, Y.G., Mayers, B. and Xia, Y.N. (2005) Shape-controlled synthesis of metal nanostructures: the case of silver. *Chemistry–A European Journal*, **11**, 454.

20 Xia, Y.N. and Halas, N.J. (2005) Shape-controlled synthesis and surface plasmonic properties of metallic nanostructures. *MRS Bulletin*, **30**, 338.

21 Yang, H., Teng, X.W. and Maksimuk, S. (2008) Multipods and dendritic nanoparticles of platinum: colloidal synthesis and electrocatalytic property, in *Metal Nanoclusters in Catalysis and Materials Science: The Issue of Size Control. Part II: Methodologies* (eds B. Corain, G.

Schmid and N. Toshima), Elsevier B.V., Amsterdam, p. 307.
22 Porter, D.A. and Easterling, K.E. (1992) *Phase Transformations in Metals and Alloys*, 2nd edn, Chapman & Hall, London.
23 Mullin, J.W. (1997) *Crystallization*, 3rd edn, Oxford University Press, Oxford.
24 Park, J., Joo, J., Kwon, S.G., Jang, Y. and Hyeon, T. (2007) Synthesis of monodisperse spherical nanocrystals. *Angewandte Chemie–International Edition*, **46**, 4630.
25 Volmer, M. and Weber, A. (1926) Keimbildung in übersättigten Gebilden. *Zeitschrift für Physikalische Chemie*, **119**, 227.
26 Volmer, M. (1939) *Kinetic der Phasenbildung*, Steinfopff, Leipzig.
27 Becker, R. and Doring, W. (1935) Kinetische behandlung der keimbildung in übersättigten dämpfern. *Annales de Physique*, **24**, 719.
28 Sugimoto, T., Shiba, F., Sekiguchi, T. and Itoh, H. (2000) Spontaneous nucleation of monodisperse silver halide particles from homogeneous gelatin solution I: silver chloride. *Colloids and Surfaces A–Physicochemical and Engineering Aspects*, **164**, 183.
29 LaMer, V.K. and Dinegar, R.H. (1950) Theory, production and mechanism of formation of monodisperse hydrosols. *Journal of the American Chemical Society*, **72**, 4847.
30 Sugimoto, T. (1987) Preparation of monodispersed colloidal particles. *Advances in Colloid and Interface Science*, **28**, 65.
31 Peng, X.G., Wickham, J. and Alivisatos, A.P. (1998) Kinetics of II-VI and III-V colloidal semiconductor nanocrystal growth: 'focusing' of size distributions. *Journal of the American Chemical Society*, **120**, 5343.
32 Reiss, H. (1951) The growth of uniform colloidal dispersions. *Journal of Chemical Physics*, **19**, 482.
33 Dadyburjor, D.B. and Ruckenstein, E. (1977) Kinetics of Ostwald ripening. *Journal of Crystal Growth*, **40**, 279.
34 Sugimoto, T. (1978) General kinetics of Ostwald ripening of precipitates. *Journal of Colloid and Interface Science*, **63**, 16.
35 Marqusee, J.A. and Ross, J. (1983) Kinetics of phase transitions: theory of Ostwald ripening. *Journal of Chemical Physics*, **79**, 373.
36 Teng, X.W. and Yang, H. (2004) Effects of surfactants and synthetic conditions on the sizes and self-assembly of monodisperse iron oxide nanoparticles. *Journal of Materials Chemistry*, **14**, 774.
37 Wang, Z.L. (2000) Transmission electron microscopy of shape-controlled nanocrystals and their assemblies. *Journal of Physical Chemistry B*, **104**, 1153.
38 Lofton, C. and Sigmund, W. (2005) Mechanisms controlling crystal habits of gold and silver colloids. *Advanced Functional Materials*, **15**, 1197.
39 Jana, N.R., Gearheart, L. and Murphy, C.J. (2001) Wet chemical synthesis of silver nanorods and nanowires of controllable aspect ratio. *Chemical Communications*, 617.
40 Maksimuk, S., Teng, X. and Yang, H. (2007) Roles of twin defects in the formation of platinum multipod nanocrystals. *Journal of Physical Chemistry C*, **111**, 14312.
41 Xiong, Y.J., McLellan, J.M., Yin, Y.D. and Xia, Y.N. (2007) Synthesis of palladium icosahedra with twinned structure by blocking oxidative etching with citric acid or citrate ions. *Angewandte Chemie–International Edition*, **46**, 790.
42 Kim, F., Connor, S., Song, H., Kuykendall, T. and Yang, P.D. (2004) Platonic gold nanocrystals. *Angewandte Chemie–International Edition*, **43**, 3673.
43 Teng, X.W. and Yang, H. (2005) Synthesis of platinum multipods: an induced anisotropic growth. *Nano Letters*, **5**, 885.
44 Xiong, Y.J., Chen, J.Y., Wiley, B. and Xia, Y.N. (2005) Understanding the role of oxidative etching in the polyol synthesis of Pd nanoparticles with uniform shape and size. *Journal of the American Chemical Society*, **127**, 7332.
45 Xiong, Y.J., Wiley, B. and Xia, Y.N. (2007) Nanocrystals with unconventional shapes–a class of promising catalysts. *Angewandte Chemie–International Edition*, **46**, 7157.

46 Petroski, J.M., Green, T.C. and El-Sayed, M.A. (2001) Self-assembly of platinum nanoparticles of various size and shape. *Journal of Physical Chemistry A*, **105**, 5542.

47 Petroski, J.M., Wang, Z.L., Green, T.C. and El-Sayed, M.A. (1998) Kinetically controlled growth and shape formation mechanism of platinum nanoparticles. *Journal of Physical Chemistry B*, **102**, 3316.

48 Ahmadi, T.S., Wang, Z.L., Green, T.C., Henglein, A. and ElSayed, M.A. (1996) Shape-controlled synthesis of colloidal platinum nanoparticles. *Science*, **272**, 1924.

49 Ahmadi, T.S., Wang, Z.L., Henglein, A. and ElSayed, M.A. (1996) 'Cubic' colloidal platinum nanoparticles. *Chemistry of Materials*, **8**, 1161.

50 Yu, Y.T., Wang, J., Zhang, J.H., Yang, H.J., Xu, B.Q. and Sun, J.C. (2007) A crucial step to platinum nanocrystals with special surfaces: control of aquo/chloro ligand exchange in aqueous $PtCl_6^{2-}$ solution. *Journal of Physical Chemistry C*, **111**, 18563.

51 Ren, J. and Tilley, R.D. (2007) Shape-controlled growth of platinum nanoparticles. *Small*, **3**, 1508.

52 Ren, J.T. and Tilley, R.D. (2007) Preparation, self-assembly, and mechanistic study of highly monodispersed nanocubes. *Journal of the American Chemical Society*, **129**, 3287.

53 Wang, C., Daimon, H., Lee, Y., Kim, J. and Sun, S. (2007) Synthesis of monodisperse Pt nanocubes and their enhanced catalysis for oxygen reduction. *Journal of the American Chemical Society*, **129**, 6974.

54 Filankembo, A., Giorgio, S., Lisiecki, I. and Pileni, M.P. (2003) Is the anion the major parameter in the shape control of nanocrystals? *Journal of Physical Chemistry B*, **107**, 7492.

55 Krishnaswamy, R., Remita, H., Imperor-Clerc, M., Even, C., Davidson, P. and Pansu, B. (2006) Synthesis of single-crystal line platinum nanorods within a soft crystalline surfactant-Pt-II complex. *Chemical Physics*, **7**, 1510.

56 Song, Y., Garcia, R.M., Dorin, R.M., Wang, H.R., Qiu, Y., Coker, E.N., Steen, W.A., Miller, J.E. and Shelnutt, J.A. (2007) Synthesis of platinum nanowire networks using a soft template. *Nano Letters*, **7**, 3650.

57 Song, Y.J., Steen, W.A., Pena, D., Jiang, Y.B., Medforth, C.J., Huo, Q.S., Pincus, J.L., Qiu, Y., Sasaki, D.Y., Miller, J.E. and Shelnuttt, J.A. (2006) Foamlike nanostructures created from dendritic platinum sheets on liposomes. *Chemistry of Materials*, **18**, 2335.

58 Song, Y.J., Yang, Y., Medforth, C.J., Pereira, E., Singh, A.K., Xu, H.F., Jiang, Y.B., Brinker, C.J., van Swol, F. and Shelnutt, J.A. (2004) Controlled synthesis of 2-D and 3-D dendritic platinum nanostructures. *Journal of the American Chemical Society*, **126**, 635.

59 Song, Y.J., Garcia, R.M., Dorin, R.M., Wang, H.R., Qiu, Y. and Shelnutt, J.A. (2006) Synthesis of platinum nanocages by using liposomes containing photocatalyst molecules. *Angewandte Chemie–International Edition*, **45**, 8126.

60 Wang, H.R., Song, Y.J., Medforth, C.J. and Shelnutt, J.A. (2006) Interfacial synthesis of dendritic platinum nanoshells templated on benzene nanodroplets stabilized in water by a photocatalytic lipoporphyrin. *Journal of the American Chemical Society*, **128**, 9284.

61 Rioux, R.M., Song, H., Grass, M., Habas, S., Niesz, K., Hoefelmeyer, J.D., Yang, P. and Somorjai, G.A. (2006) Monodisperse platinum nanoparticles of well-defined shape: synthesis characterization, catalytic properties and future prospects. *Topics in Catalysis*, **39**, 167.

62 Qu, L.T., Dai, L.M. and Osawa, E. (2006) Shape/size-controlled syntheses of metal nanoparticles for site-selective modification of carbon nanotubes. *Journal of the American Chemical Society*, **128**, 5523.

63 Herricks, T., Chen, J.Y. and Xia, Y.N. (2004) Polyol synthesis of platinum nanoparticles: control of morphology with sodium nitrate. *Nano Letters*, **4**, 2367.

64 Chen, J.Y., Herricks, T. and Xia, Y.N. (2005) Polyol synthesis of platinum nanostructures: control of morphology through the manipulation of reduction

kinetics. *Angewandte Chemie–International Edition*, **44**, 2589.
65 Lee, E.P., Chen, J.Y., Yin, Y.D., Campbell, C.T. and Xia, Y.N. (2006) Pd-catalyzed growth of Pt nanoparticles or nanowires as dense coatings on polymeric and ceramic particulate supports. *Advanced Materials*, **18**, 3271.
66 Xie, J.P., Zhang, Q.B., Lee, Y. and Wang, D.I.C. (2007) General method for extended metal nanowire synthesis: ethanol induced self-assembly. *Journal of Physical Chemistry C*, **111**, 17158.
67 Dameron, A.A., Mullen, T.J., Hengstebeck, R.W., Saavedra, H.M. and Weiss, P.S. (2007) Origins of displacement in 1-adamantanethiolate self-assembled monolayers. *Journal of Physical Chemistry C*, **111**, 6747.
68 Mullen, T.J., Dameron, A.A., Saavedra, H.M., Williams, M.E. and Weiss, P.S. (2007) Dynamics of solution displacement in 1-adamantanethiolate self-assembled monolayers. *Journal of Physical Chemistry C*, **111**, 6740.
69 Graham, T. (1861) Liquid diffusion applied to analysis. *Philosophical Transactions of the Royal Society*, **151**, 183.
70 Narayanan, R. and El-Sayed, M.A. (2004) Changing catalytic activity during colloidal platinum nanocatalysis due to shape changes: electron-transfer reaction. *Journal of the American Chemical Society*, **126**, 7194.
71 Inaba, M., Ando, M., Hatanaka, A., Nomoto, A., Matsuzawa, K., Tasaka, A., Kinumoto, T., Iriyama, Y. and Ogumi, Z. (2006) Controlled growth and shape formation of platinum nanoparticles and their electrochemical properties. *Electrochimica Acta*, **52**, 1632.
72 Miyazaki, A. and Nakano, Y. (2000) Morphology of platinum nanoparticles protected by poly(*N*-isopropylacrylamide). *Langmuir*, **16**, 7109.
73 Miyazaki, A., Yoshida, S., Nakano, Y. and Balint, I. (2005) Preparation of tetrahedral Pt nanoparticles having {111} facet on their surface. *Chemistry Letters*, **34**, 74.
74 Miyazaki, A., Balint, I. and Nakano, Y. (2003) Morphology control of platinum nanoparticles and their catalytic properties. *Journal of Nanoparticle Research*, **5**, 69.
75 Narayanan, R. and El-Sayed, M.A. (2004) Shape-dependent catalytic activity of platinum nanoparticles in colloidal solution. *Nano Letters*, **4**, 1343.
76 Kinge, S. and Bonnemann, H. (2006) One-pot dual size- and shape selective synthesis of tetrahedral Pt nanoparticles. *Applied Organometallic Chemistry*, **20**, 784.
77 Henglein, A. and Giersig, M. (2000) Reduction of Pt(II) by H-2: Effects of citrate and NaOH and reaction mechanism. *Journal of Physical Chemistry B*, **104**, 6767.
78 Tang, Z.C., Geng, D.S. and Lu, G.X. (2005) A simple solution-phase reduction method for the synthesis of shape-controlled platinum nanoparticles. *Materials Letters*, **59**, 1567.
79 Tang, Z.C., Geng, D.S. and Lu, G.X. (2005) Size-controlled synthesis of colloidal platinum nanoparticles and their activity for the electrocatalytic oxidation of carbon monoxide. *Journal of Colloid and Interface Science*, **287**, 159.
80 Yu, Y.T. and Xu, B.Q. (2003) Selective formation of tetrahedral Pt nanocrystals from $K2PtCl_6$/PVP. *Chinese Science Bulletin*, **48**, 2589.
81 Yu, Y.T. and Xu, B.Q. (2006) Shape-controlled synthesis of Pt nanocrystals: an evolution of the tetrahedral shape. *Applied Organometallic Chemistry*, **20**, 638.
82 Xiong, Y.J., Washio, I., Chen, J.Y., Cai, H.G., Li, Z.Y. and Xia, Y.N. (2006) Poly(vinyl pyrrolidone): a dual functional reductant and stabilizer for the facile synthesis of noble metal nanoplates in aqueous solutions. *Langmuir*, **22**, 8563.
83 Ghannoum, S., Xin, Y., Jaber, J. and Halaoui, L.I. (2003) Self-assembly of polyacrylate-capped platinum nanoparticles on a polyelectrolyte surface: kinetics of adsorption and effect of ionic strength and deposition protocol. *Langmuir*, **19**, 4804.
84 Hu, X.G., Wang, T. and Dong, S.J. (2006) Rapid synthesis of cubic Pt nanoparticles and their use for the preparation of Pt nanoagglomerates. *Journal of Nanoscience and Nanotechnology*, **6**, 2056.

85 Ullah, M.H., Chung, W.S., Kim, I. and Ha, C.S. (2006) pH-selective synthesis of monodisperse nanoparticles and 3D dendritic nanoclusters of CTAB-stabilized platinum for electrocatalytic O-2 reduction. *Small*, **2**, 870.

86 Chen, C.W. and Akashi, M. (1997) Synthesis, characterization, and catalytic properties of colloidal platinum nanoparticles protected by poly(*N*-isopropylacrylamide). *Langmuir*, **13**, 6465.

87 Niesz, K., Grass, M. and Somorjai, G.A. (2005) Precise control of the Pt nanoparticle size by seeded growth using EO13PO30EO13 triblock copolymers as protective agents. *Nano Letters*, **5**, 2238.

88 Chen, S.H. and Kimura, K. (2001) Synthesis of thiolate-stabilized platinum nanoparticles in protolytic solvents as isolable colloids. *Journal of Physical Chemistry B*, **105**, 5397.

89 Fu, X.Y., Wang, Y.A., Wu, N.Z., Gui, L.L. and Tang, Y.Q. (2002) Shape-selective preparation and properties of oxalate-stabilized Pt colloid. *Langmuir*, **18**, 4619.

90 Nadagouda, M.N. and Varma, R.S. (2006) Green and controlled synthesis of gold and platinum nanomaterials using vitamin B-2: density-assisted self-assembly of nanospheres, wires and rods. *Green Chemistry*, **8**, 516.

91 Chen, D.H., Yeh, J.J. and Huang, T.C. (1999) Synthesis of platinum ultrafine particles in AOT reverse micelles. *Journal of Colloid and Interface Science*, **215**, 159.

92 Rojas, S., Garcia-Garcia, F.J., Jaras, S., Martinez-Huerta, M.V., Fierro, J.L.G. and Boutonnet, M. (2005) Preparation of carbon supported Pt and PtRu nanoparticles from microemulsion–Electrocatalysts for fuel cell applications. *Applied Catalysis A: General*, **285**, 24.

93 Slawinski, G.W. and Zamborini, F.P. (2007) Synthesis and alignment of silver nanorods and nanowires and the formation of Pt, Pd, and core/shell structures by galvanic exchange directly on surfaces. *Langmuir*, **23**, 10357.

94 Liang, H.P., Zhang, H.M., Hu, J.S., Guo, Y.G., Wan, L.J. and Bai, C.L. (2004) Pt hollow nanospheres: facile synthesis and enhanced electrocatalysts. *Angewandte Chemie–International Edition*, **43**, 1540.

95 Li, J., Liang, Y., Xu, Q.C., Fu, X.Z., Xu, J.Q. and Lin, J.D. (2006) Synthesis and characterization of sub-10 nm platinum hollow spheres as electrocatalyst of direct methanol fuel cell. *Journal of Nanoscience and Nanotechnology*, **6**, 1107.

96 Fukuoka, A., Higuchi, T., Ohtake, T., Oshio, T., Kimura, J., Sakamoto, Y., Shimomura, N., Inagaki, S. and Ichikawa, M. (2006) Nanonecklaces of platinum and gold with high aspect ratios synthesized in mesoporous organosilica templates by wet hydrogen reduction. *Chemistry of Materials*, **18**, 337.

97 Chen, X.X., Eckhard, N.L.i, K., Stoica, L., Xia, W., Assmann, J., Muhler, M. and Schuhmann, W. (2007) Pulsed electrodeposition of Pt nanoclusters on carbon nanotubes modified carbon materials using diffusion restricting viscous electrolytes. *Electrochemistry Communications*, **9**, 1348.

98 Ding, Y., Gao, Y., Wanga, Z.L., Tian, N., Zhou, Z.Y. and Sun, S.G. (2007) Facets and surface relaxation of tetrahexahedral platinum nanocrystals. *Applied Physics Letters*, **91**, 121901.

99 Tian, N., Zhou, Z.Y., Sun, S.G., Cui, L., Ren, B. and Tian, Z.Q. (2006) Electrochemical preparation of platinum nanothorn assemblies with high surface enhanced Raman scattering activity. *Chemical Communications*, 4090.

100 Kong, L.B., Li, M.L., M.K., Guo, X.Y. and Li, H.L. (2003) Morphology of platinum nanowire array electrodeposited within anodic aluminum oxide template characterized by atomic force microscopy. *Chinese Physics Letters*, **20**, 763.

101 Napolskii, K.S., Barczuk, P.J., Vassiliev, S.Y., Veresov, A.G., Tsirlina, G.A. and Kulesza, P.J. (2007) Templating of electrodeposited platinum group metals as a tool to control catalytic activity. *Electrochimica Acta*, **52**, 7910.

102 Wang, D.H., Kou, R., Gil, M.P., Jakobson, H.P., Tang, J., Yu, D.H. and Lu, Y.F. (2005) Templated synthesis,

characterization, and sensing application of macroscopic platinum nanowire network electrodes. *Journal of Nanoscience and Nanotechnology*, **5**, 1904.

103 Yuan, J.H., Wang, K. and Xia, X.H. (2005) Highly ordered platinum-nanotubule arrays for amperometric glucose sensing. *Advanced Functional Materials*, **15**, 803.

104 Belapurkar, A.D., Kapoor, S., Kulshreshtha, S.K. and Mittal, J.P. (2001) Radiolytic preparation and catalytic properties of platinum nanoparticles. *Materials Research Bulletin*, **36**, 145.

105 Wang, H.D., Sun, X.Q., Ye, Y. and Qiu, S.L. (2006) Radiation induced synthesis of Pt nanoparticles supported on carbon nanotubes. *Journal of Power Sources*, **161**, 839.

106 Sakamoto, Y., Fukuoka, A., Higuchi, T., Shimomura, N., Inagaki, S. and Ichikawa, M. (2004) Synthesis of platinum nanowires in organic-inorganic mesoporous silica templates by photoreduction: formation mechanism and isolation. *Journal of Physical Chemistry B*, **108**, 853.

107 Mallikarjuna, N.N. and Varma, R.S. (2007) Microwave-assisted shape-controlled bulk synthesis of noble nanocrystals and their catalytic properties. *Crystal Growth and Design*, **7**, 686.

108 Narayanan, R. and El-Sayed, M.A. (2005) Catalysis with transition metal nanoparticles in colloidal solution: nanoparticle shape dependence and stability. *Journal of Physical Chemistry B*, **109**, 12663.

109 Kim, Y.T., Ohshima, K., Higashimine, K., Uruga, T., Takata, M., Suematsu, H. and Mitani, T. (2006) Fine size control of platinum on carbon nanotubes: From single atoms to clusters. *Angewandte Chemie–International Edition*, **45**, 407.

110 Vidal-Iglesias, F.J., Solla-Gullon, J., Montiel, V., Feliu, J.M. and Aldaz, A. (2007) Screening of electrocatalysts for direct ammonia fuel cell: ammonia oxidation on PtMe (Me : Ir. Rh, Pd. Ru) and preferentially oriented Pt(100) nanoparticles. *Journal of Power Sources*, **171**, 448.

111 Vidal-Iglesias, F.J., Solla-Gullon, J., Rodriguez, P., Herrero, E., Montiel, V., Feliu, J.M. and Aldaz, A. (2004) Shape-dependent electrocatalysis: ammonia oxidation on platinum nanoparticles with preferential (100) surfaces. *Electrochemistry Communications*, **6**, 1080.

112 Perez, H., Pradeau, J.P., Albouy, P.A. and Perez-Omil, J. (1999) Synthesis and characterization of functionalized platinum nanoparticles. *Chemistry of Materials*, **11**, 3460.

113 Solla-Gullon, J., Montiel, V., Aldaz, A. and Clavilier, J. (2002) Electrochemical and electrocatalytic behaviour of platinum-palladium nanoparticle alloys. *Electrochemistry Communications*, **4**, 716.

114 Solla-Gullon, J., Montiel, V., Aldaz, A. and Clavilier, J. (2003) Synthesis and electrochemical decontamination of platinum-palladium nanoparticles prepared by water-in-oil microemulsion. *Journal of the Electrochemical Society*, **150**, E104.

115 Xu, S.L. and Cui, H. (2007) Luminol chemiluminescence catalysed by colloidal platinum nanoparticles. *Luminescence*, **22**, 77.

116 Chen, H.J. and Dong, S.J. (2007) Self-assembly of ionic liquids-stabilized Pt nanoparticles into two-dimensional patterned nanostructures at the air-water interface. *Langmuir*, **23**, 12503.

117 Niesz, K., Koebel, M.M. and Somorjai, G.A. (2006) Fabrication of two- and three-dimensional model catalyst systems with monodispersed platinum nanoparticles as active metal building blocks. *Inorganica Chimica Acta*, **359**, 2683.

118 Lu, S.X., Sivakumar, K. and Panchapakesan, B. (2007) Sonochemical synthesis of platinum nanowires and their applications as electro-chemical actuators. *Journal of Nanoscience and Nanotechnology*, **7**, 2473.

119 Chao, K.J., Chang, Y.P., Chen, Y.C., Lo, A.S. and Phan, T.H. (2006) Morphology of nanostructured platinum in mesoporous materials–Effect of solvent and intrachannel surface. *Journal of Physical Chemistry B*, **110**, 1638.

120 Sun, Y.G., Mayers, B.T. and Xia, Y.N. (2002) Template-engaged replacement reaction: a one-step approach to the large-scale synthesis of metal nanostructures with hollow interiors. *Nano Letters*, **2**, 481.

121 Liu, J.B., Zhu, M.W., Zhan, P., Dong, H., Dong, Y., Qu, X.T., Nie, Y.H. and Wang, Z.L. (2006) Morphology-controllable fabrication of ordered platinum nanoshells with reduced symmetry. *Nanotechnology*, **17**, 4191.

122 Zoval, J.V., Lee, J., Gorer, S. and Penner, R.M. (1998) Electrochemical preparation of platinum nanocrystallites with size selectivity on basal plane oriented graphite surfaces. *Journal of Physical Chemistry B*, **102**, 1166.

123 Dominguez-Dominguez, S., Pardilla, J.A., Murcia, A.B., Morallon, E. and Cazorla-Amoros, D. (2008) Electrochemical deposition of platinum nanoparticles on different carbon supports and conducting polymers. *Journal of Applied Electrochemistry*, **38**, 259.

124 Zhou, M., Chen, S.H., Ren, H.P., Wu, L. and Zhao, S.Y. (2005) Electrochemical formation of platinum nanoparticles by a novel rotating cathode method. *Physica E*, **27**, 341.

125 Lee, I., Chan, K.Y. and Phillips, D.L. (1998) Growth of electrodeposited platinum nanocrystals studied by atomic force microscopy. *Applied Surface Science*, **136**, 321.

126 Lu, G.J. and Zangari, G. (2006) Electrodeposition of platinum nanoparticles on highly oriented pyrolitic graphite–Part II: morphological characterization by atomic force microscopy. *Electrochimica Acta*, **51**, 2531.

127 Menke, E.J., Thompson, M.A., Xiang, C., Yang, L.C. and Penner, R.M. (2006) Lithographically patterned nanowire electrodeposition. *Nature Materials*, **5**, 914.

128 Kimura, Y., Abe, D., Ohmori, T., Mizutani, M. and Harada, M. (2003) Synthesis of platinum nano-particles in high-temperatures and high-pressures fluids. *Colloids and Surfaces A–Physicochemical and Engineering Aspects*, **231**, 131.

129 Chen, J.Y., Herricks, T., Geissler, M. and Xia, Y.N. (2004) Single-crystal nanowires of platinum can be synthesized by controlling the reaction rate of a polyol process. *Journal of the American Chemical Society*, **126**, 10854.

130 Lee, E.P., Peng, Z.M., Gate, D.M., Yang, H., Campbell, C.T. and Xia, Y. (2007) Growing Pt nanowires as a densely packed array on metal gauze. *Journal of the American Chemical Society*, **129**, 10634.

131 Formo, E., Lee, E., Campbell, D. and Xia, Y.N. (2008) Functionalization of electrospun TiO2 nanofibers with Pt nanoparticles and nanowires for catalytic applications. *Nano Letters*, **8**, 668.

132 Fu, X.Y., Wang, Y., Wu, N.Z., Gui, L.L. and Tang, Y.Q. (2003) Preparation of colloidal solutions of thin platinum nanowires. *Journal of Materials Chemistry*, **13**, 1192.

133 Chen, M., Liu, J.P. and Sun, S.H. (2004) One-step synthesis of FePt nanoparticles with tunable size. *Journal of the American Chemical Society*, **126**, 8394.

134 Chen, M., Kim, J., Liu, J.P., Fan, H.Y. and Sun, S.H. (2006) Synthesis of FePt nanocubes and their oriented self-assembly. *Journal of the American Chemical Society*, **128**, 7132.

135 Zhang, H.T., Ding, J. and Chow, G.M. (2008) Morphological control of synthesis and anomalous magnetic properties of 3-D branched Pt nanoparticles. *Langmuir*, **24**, 375.

136 Wang, Y. and Yang, H. (2006) Oleic acid as the capping agent in the synthesis of noble metal nanoparticles in imidazolium-based ionic liquids. *Chemical Communications*, 2545.

137 Maksimuk, S., Teng, X.W. and Yang, H. (2006) Planar tripods of platinum: formation and self-assembly. *Physical Chemistry Chemical Physics*, **8**, 4660.

138 Scheeren, C.W., Machado, G., Teixeira, S.R., Morais, J., Domingos, J.B. and Dupont, J. (2006) Synthesis and characterization of Pt(0) nanoparticles in imidazolium ionic liquids. *Journal of Physical Chemistry B*, **110**, 13011.

139 Ramirez, E., Erades, L., Philippot, K., Lecante, P. and Chaudret, B. (2007) Shape control of platinum nanoparticles. *Advanced Functional Materials*, **17**, 2219.

140 Zhong, X., Feng, Y., Lieberwirth, I. and Knoll, W. (2006) Facile synthesis of morphology-controlled platinum nanocrystals. *Chemistry of Materials*, **18**, 2468.

141 Grace, A.N. and Pandian, K. (2007) One pot synthesis of polymer protected Pt. Pd, Ag and Ru nanoparticles and nanoprisms under reflux and microwave mode of heating in glycerol–a comparative study. *Materials Chemistry and Physics*, **104**, 191.

142 Migowski, P. and Dupont, J. (2007) Catalytic applications of metal nanoparticles in imidazolium ionic liquids. *Chemistry–A European Journal*, **13**, 32.

143 Antonietti, M., Kuang, D.B., Smarsly, B. and Yong, Z. (2004) Ionic liquid for the convenient synthesis of functional nanoparticles and other inorganic nanostructures. *Angewandte Chemie–International Edition*, **43**, 4988.

144 Huddleston, J.G., Visser, A.E., Reichert, W.M., Willauer, H.D., Broker, G.A. and Rogers, R.D. (2001) Characterization and comparison of hydrophilic hydrophobic room temperature ionic liquids incorporating the imidazolium cation. *Green Chemistry*, **3**, 156.

145 Yu, P., Yan, J., Zhang, J. and Mao, L.Q. (2007) Cost-effective electrodeposition of platinum nanoparticles with ionic liquid droplet confined onto electrode surface as micro-media. *Electrochemistry Communications*, **9**, 1139.

146 Eklund, S.E. and Cliffel, D.E. (2004) Synthesis and catalytic properties of soluble platinum nanoparticles protected by a thiol monolayer. *Langmuir*, **20**, 6012.

147 Yang, J., Deivaraj, T.C., Too, H.P. and Lee, J.Y. (2004) An alternative phase-transfer method of preparing alkylamine-stabilized platinum nanoparticles. *Journal of Physical Chemistry B*, **108**, 2181.

148 Sun, Z.Y., Fu, L., Liu, Z.M., Han, B.X., Liu, Y.Q. and Du, J.M. (2006) Synthesis of noble metal/carbon nanotube composites in supercritical methanol. *Journal of Nanoscience and Nanotechnology*, **6**, 691.

149 Wakayama, H. and Fukushima, Y. (1999) Porous platinum fibers synthesized using supercritical fluid. *Chemical Communications*, 391.

150 Wakayama, H. and Fukushima, Y. (2000) Supercritical CO_2 as a solvent for synthesis of nanoporous materials. *Industrial and Engineering Chemistry Research*, **39**, 4641.

151 Chen, M. and Xing, Y.C. (2005) Polymer-mediated synthesis of highly dispersed Pt nanoparticles on carbon black. *Langmuir*, **21**, 9334.

152 Capdevielle, P., Lavigne, A., Sparfel, D., Barannelafont, J., Cuong, N.K. and Maumy, M. (1990) *Tetrahedron Letters*, **31**, 3305.

153 Clarke, T.G., Hampson, N.A., Lee, J.B., Morley, J.R. and Scanlon, B. (1968) Argentic oxide oxidations of organic compounds. *Tetrahedron Letters*, **54**, 5685.

154 Yee, C., Scotti, M., Ulman, A., White, H., Rafailovich, M. and Sokolov, J. (1999) One-phase synthesis of thiol-functionalized platinum nanoparticles. *Langmuir*, **15**, 4314.

155 Narayanan, R. and El-Sayed, M.A. (2005) Effect of colloidal nanocatalysis on the metallic nanoparticle shape: the Suzuki reaction. *Langmuir*, **21**, 2027.

156 Miyazaki, A., Asakawa, T., Nakano, Y. and Balint, I. (2005) Nitrite reduction on morphologically controlled Pt nanoparticles. *Chemical Communications*, 3730.

157 Narayanan, R. and El-Sayed, M.A. (2004) Effect of nanocatalysis in colloidal solution on the tetrahedral and cubic nanoparticle SHAPE: electron-transfer reaction catalyzed by platinum nanoparticles. *Journal of Physical Chemistry B*, **108**, 5726.

158 Narayanan, R. and El-Sayed, M.A. (2003) Effect of catalytic activity on the metallic nanoparticle size distribution: electron-transfer reaction between Fe(CN)(6) and thiosulfate ions catalyzed by PVP-platinum nanoparticles. *Journal of Physical Chemistry B*, **107**, 12416.

159 Teranishi, T., Kurita, R. and Miyake, M. (2000) Shape control of Pt nanoparticles. *Journal of Inorganic and Organometallic Polymers*, **10**, 145.

160 Mayer, A.B.R. and Mark, J.E. (1997) Comparisons between cationic polyelectrolytes and nonionic polymers for the protection of palladium and platinum nanocatalysts. *Journal of Polymer Science. Part A-1, Polymer Chemistry*, **35**, 3151.

161 Tan, Y.W., Dai, X.H., Li, Y.F. and Zhu, D.B. (2003) Preparation of gold, platinum, palladium and silver nanoparticles by the reduction of their salts with a weak reductant-potassium bitartrate. *Journal of Materials Chemistry*, **13**, 1069.

162 Sun, Y.G., Mayers, B. and Xia, Y.N. (2003) Metal nanostructures with hollow interiors. *Advanced Materials*, **15**, 641.

163 Sun, S.H., Yang, D.Q., Villers, D., Zhang, G.X., Sacher, E. and Dodelet, J.P. (2008) Template- and surfactant-free room temperature synthesis of self-assembled 3D Pt nanoflowers from single-crystal nanowires. *Advanced Materials*, **20**, 571.

164 Piao, Y., Lim, H., Chang, J.Y., Lee, W.Y. and Kim, H. (2005) Nanostructured materials prepared by use of ordered porous alumina membranes. *Electrochimica Acta*, **50**, 2997.

165 Kyotani, T., Tsai, L.F. and Tomita, A. (1997) Formation of platinum nanorods and nanoparticles in uniform carbon nanotubes prepared by a template carbonization method. *Chemical Communications*, 701.

166 Fukuoka, A., Higashimoto, N., Sakamoto, Y., Sasaki, M., Sugimoto, N., Inagaki, S., Fukushima, Y. and Ichikawa, M. (2001) Ship-in-bottle synthesis and catalytic performances of platinum carbonyl clusters, nanowires, and nanoparticles in micro- and mesoporous materials. *Catalysis Today*, **66**, 23.

167 Sasaki, M., Osada, M., Sugimoto, N., Inagaki, S., Fukushima, Y., Fukuoka, A. and Ichikawa, M. (1998) Novel templating fabrication of nano-structured Pt clusters and wires in the ordered cylindrical mesopores of FSM-16 and their unique properties in catalysis and magnetism. *Microporous and Mesoporous Materials*, **21**, 597.

168 Sun, Y.G. and Xia, Y.N. (2004) Multiple-walled nanotubes made of metals. *Advanced Materials*, **16**, 264.

169 Xiong, Y.J., Mayers, B.T. and Xia, Y.N. (2005) Some recent developments in the chemical synthesis of inorganic nanotubes. *Chemical Communications*, 5013.

170 Chen, Z.W., Waje, M., Li, W.Z. and Yan, Y.S. (2007) Supportless Pt and PtPd nanotubes as electrocatalysts for oxygen-reduction reactions. *Angewandte Chemie–International Edition*, **46**, 4060.

171 Lee, J.-W., Chung, U.-J., Hwang, N.M. and Kim, D.-Y. (2005) Growth process of the ridge–trough faces of a twinned crystal. *Acta Crystallographica Section A*, **A61**, 405.

172 Aizenberg, J., Black, A.J. and Whitesides, G.M. (1999) Control of crystal nucleation by patterned self-assembled monolayers. *Nature*, **398**, 495.

173 Sakai, G., Yoshimura, T., Isohata, S., Uota, M., Kawasaki, H., Kuwahara, T., Fujikawa, D. and Kijima, T. (2007) Synthesis of nanogroove-network-structured platinum nanosheets and their carbon-supported forms using a mixed-surfactant templating approach. *Advanced Materials*, **19**, 237.

174 Barison, S., Fabrizio, M., Carta, G., Rossetto, G., Zanella, P., Barreca, D. and Tondello, E. (2002) Nanocrystalline Pt thin films, obtained via metal organic chemical vapor deposition on quartz and CaF2 substrates: an investigation of their chemico-physical properties. *Thin Solid Films*, **405**, 81.

175 Conoci, S., Petralia, S., Samori, P., Raymo, F.M., Di Bella, S. and Sortino, S. (2006) Optically transparent, ultrathin Pt films as versatile metal substrates for molecular optoelectronics. *Advanced Functional Materials*, **16**, 1425.

176 Teng, X.W., Liang, X.Y., Rahman, S. and Yang, H. (2005) Porous nanoparticle membranes: synthesis and application as fuel-cell catalysts. *Advanced Materials*, **17**, 2237.

177 Liang, H.P., Hu, J.S., Cao, A.M., Mu, Y.Y. and Wan, L.J. (2006) Facile synthesis of Pt multipods nanocrystals. *Journal of Nanoscience and Nanotechnology*, **6**, 2031.

178 Gao, S.Y., Zhang, H.J., Liu, X.D., Wang, X.M., Sun, D.H., Peng, C.Y. and Zheng, G.L. (2006) Carboxyl-cored dendrimer and toluene-assisted fabrication of uniform platinum nanodendrites at a water/oil interface and their potential application as a catalyst. *Nanotechnology*, **17**, 1599.

179 Tan, Y.N., Yang, J., Lee, J.Y. and Wang, D.I.C. (2007) Mechanistic study on the bis(p-sulfonatophenyl)phenylphosphine synthesis of monometallic Pt hollow nanoboxes using Ag*-Pt core-shell nanocubes as sacrificial templates. *Journal of Physical Chemistry C*, **111**, 14084.

180 Selvakannan, P.R. and Sastry, M. (2005) Hollow gold and platinum nanoparticles by a transmetallation reaction in an organic solution. *Chemical Communications*, 1684.

181 Shin, H.J., Ryoo, R., Liu, Z. and Terasaki, O. (2001) Template synthesis of asymmetrically mesostructured platinum networks. *Journal of the American Chemical Society*, **123**, 1246.

182 Maksimuk, S., Yang, S.C., Peng, Z.M. and Yang, H. (2007) Synthesis and characterization of ordered intermetallic PtPb nanorods. *Journal of the American Chemical Society*, **129**, 8684.

183 Peng, Z.M. and Yang, H. (2008) Ag-Pt alloy nanoparticles with the compositions in the miscibility gap. *Journal of Solid State Chemistry*, **181**, 1546.

11
Approaches to the Synthesis and Characterization of Spherical and Anisotropic Noble Metal Nanomaterials

Harshala J. Parab, Hao Ming Chen, Nitin C. Bagkar, Ru-Shi Liu, Yeu-Kuang Hwu and Din Ping Tsai

11.1
General Introduction

Nanotechnology represents the start of a revolutionary era, wherein the word 'Nano' has attracted enormous attention from society, and especially from the scientific community. Nanotechnology is related to the activities of materials at the nanoscopic level, whereby the integration of materials can be manipulated to create a desired range of properties through controlled, size-selective syntheses and the assembly of nanoscale building blocks. Nanotechnology, as a multidisciplinary area of research and development, has grown explosively during the past few years such that today, microtechnology – the key technology during the twentieth century – is being slowly but surely being replaced by nanotechnology. Moreover, the exponential growth of nanotechnology will continue to occur, based on the realization that new materials and devices created from nanoscale building blocks can provide access to new and improved properties and functionalities.

The essential theme of nanotechnology is the novel performance of materials at the nanoscale. Materials of nanoscopic dimensions display very different properties than they do on the macroscale, which in turn enables unique applications. Nanoparticular materials often exhibit very interesting electronic, optical, magnetic and chemical properties, which are not observed in their bulk counterparts [1–10]. For example, inert materials become catalysts (platinum and gold), insulators become conductors (silicon), stable materials become combustible (aluminum), solids turn into liquids at room temperature (gold), and opaque substances become transparent (copper). Yet, the fundamental question which arises when considering such examples is, 'how do the electronic, optical and magnetic properties of a nanoscopic particle differ from those of a bulk sample of the same material?' The principal factors responsible for such differences are quantum size effects and the surface area. As the size of matter is reduced to the nanometer scale, quantum effects cause significant changes in the optical, magnetic and electrical properties. When compared to a macrostructure, a much larger proportion of the atoms or molecules of a nanostructure lie at the surface; this greatly

Metallic Nanomaterials Vol. 1. Edited by Challa S. S. R. Kumar

ISBN: 978-3-527-32151-3

increases not only the surface area but also the surface-to-volume ratio, which is a critical factor in the case of chemical catalysis. Together, these factors lead to changes in reactivity, strength and electrical and optical characteristics. These novel structural properties of nanoscale materials will inevitably lead to their increased use in a wide variety of fields [11–32], with such applications broadly classified into four major areas: (i) basic nanostructured materials; (ii) electronics and computing devices; (iii) bionanotechnology; and (iv) energy generation and storage (see Figure 11.1). It is clear that, whilst such a wide range of applications will have a huge impact on the lifestyle of humans, it will also necessitate the development of safe and efficient synthetic strategies for nanomaterials.

In this chapter we provide an overview of the synthesis and characterization of spherical and anisotropic noble metal nanomaterials, with attention focused mainly on gold and silver nanoparticles, due to their increasing popularity in a variety of applications. In recent years, extensive studies have been conducted into the synthesis and characterization of metal nanoparticles [1–4, 9, 16, 30, 32–35], and some details of chemical and biological syntheses of spherical and anisotropic noble metal nanoparticles are provided here. Solution-phase chemical synthetic methods to produce different morphological architectures are discussed in terms of shape control, nucleation and growth mechanisms. The effects of various physical parameters on crystal growth are also described, with special focus on citrate reduction, polyol synthesis and seed-mediated synthesis, all of which allow morphology to be controlled. Recently, the use of biological materials to synthesize metal nanoparticles has attracted much attention, notably from the perspectives

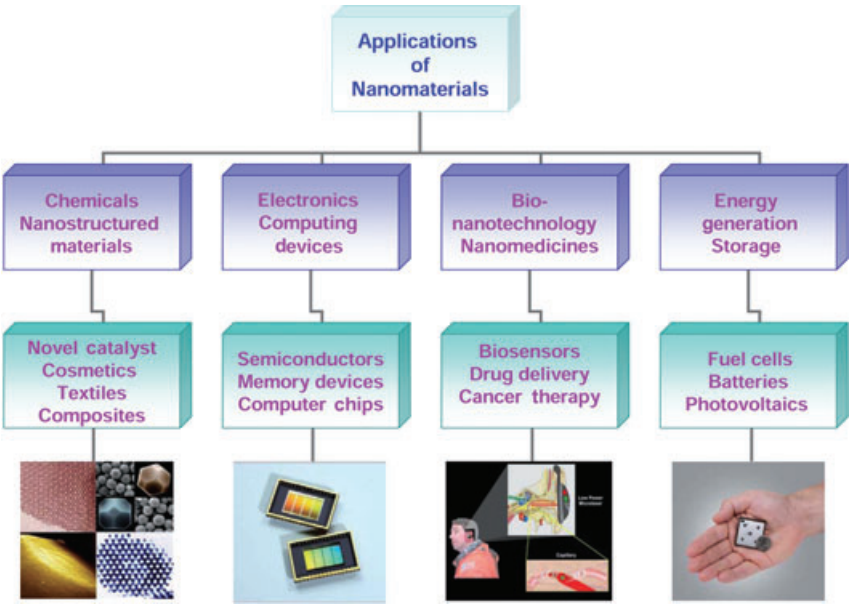

Figure 11.1 The general applications of nanomaterials.

of 'green chemistry'; thus, some recent advances in the biosynthesis of gold and silver nanoparticles are reviewed, aimed at opening new insights into nanomaterials synthesis for further applications. Finally, we outline the efforts of our own group in characterizing nanoparticles by using plasmonic measurements and X-ray absorption (XAS) techniques; hopefully, this will provide the reader with some knowledge of the mechanism of crystal growth. A brief description is also provided of the synthesis and characterization of metal nanoparticles, such that the reader may better understand the mechanistic aspects, and current progress, of crystal growth.

11.1.1 Noble Metal Nanoparticles

Recently, noble metal nanoparticles – especially of gold and silver – have attracted considerable attention owing to their unique size-dependent properties [1–4, 32–36]. The strong absorption and scattering of light by gold and silver nanoparticles, coupled with their stability, have made them popular among the other inorganic nanocrystals. Michael Faraday was the first to observe the ruby red color of a colloidal gold solution (this solution is still on display at the Faraday Museum, in London). Because of its chemical inertness, gold has been used internally in humans for biomedical applications; the earliest records of its medicinal and healing uses derive from Alexandria in Egypt where, over 5000 years ago, the Egyptians ingested gold for mental and bodily purification. Gold was mainly used in medicine for its magico-religious powers, and played almost no role in rational therapeutics until the late middle ages. During the mid-nineteenth century gold was used in syphilis therapy and, at about the same time, the Keeley Institute in the USA used gold to treat alcoholism. In recent years, gold nanoparticles (GNPs) served as molecular probes for the imaging and therapy of cancer cells, as they were found to accumulate selectively in tumor cells, where they demonstrated a bright scattering and an efficient absorption of light [37–42].

Silver is also an attractive metal to examine on the nanoscale, due to its unusual optical properties, that depend on the nanoparticle size and shape. Silver nanoparticles were demonstrated *in vitro*, to attach and prevent human immunodeficiency virus (HIV-1) from binding to host cells, through a size-dependent interaction [43]. This was the first medical study to ever explore the benefits of silver nanoparticles, and to date silver-based drugs have been used successfully in the treatment of a variety of viruses [44]. An inventory of the nanomaterials, explicitly utilized in nanotechnology consumer products, is shown in Figure 11.2 [45]. The most common material mentioned in the product description is silver, which has been used in 139 products up to October 2007. Carbon, which includes fullerenes, is the second most referenced (44), followed by zinc (including zinc oxide) (28) and titanium (including titanium dioxide) (28), silica (27) and gold (13). As shown in Figure 11.2, silver nanoparticles have been used in increasing numbers of consumer products such as food packaging, odor-resistant textiles, household

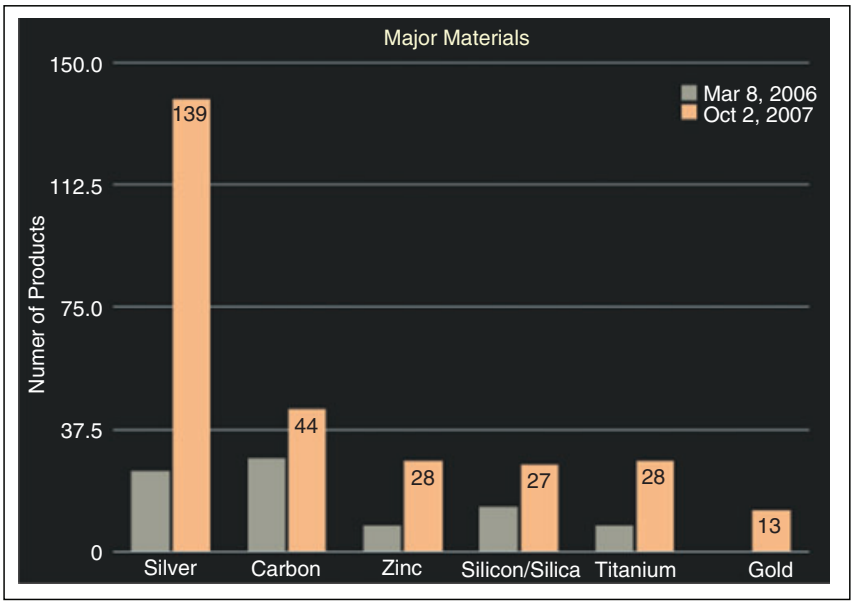

Figure 11.2 Numbers of products associated with specific materials [45].

appliances and medical devices, including wound dressings. However, the toxicity and adverse impact of these nanoparticles on the environment demands special attention since, in recent reports, concerns have been raised on the unacceptable toxicity risk posed by silver nanoparticles on human health and the environment [46–51].

The various applications of these noble metal nanoparticles stem from the unique structural properties at the nanometer dimensions, which can be further related to the surface plasmon resonance (SPR) effect (see Section 11.1.2).

11.1.2 Origin of Surface Plasmon Resonance in Noble Metal Nanoparticles

Both, the origin and evolution of SPR in noble metal nanoparticles have been studied in great detail [1–4, 33, 35]. Briefly, when the light of a wavelength much larger than the nanoparticle size interacts with that nanoparticle, it sets up standing resonance conditions, due to a collective oscillation of the electrons in the conduction band. As the wavefront of the light passes, the electron density in the particle is polarized to one surface and oscillates in resonance with the frequency of light, causing a standing oscillation. The SPR conditions strongly depend on the shape, size and dielectric constants of both the metal and the surrounding material. SPR was first calculated by solving Maxwell's equations for small spheres, interacting with an electromagnetic field [52], although later this theory was extended to ellipsoidal geometries. Modern methods, which use the discrete dipole

approximation (DDA) [4, 53], allows one to calculate the SPR absorption of arbitrary geometries. An increase in the intensity of the SPR absorption leads to an enhancement of the electric field, and this has been exploited in many applications. Noble metal particles (especially gold and silver) exhibit a strong absorption band in the visible region, giving specific colors to the solutions. For example, gold spheres have a characteristic red color at 520 nm, whereas silver possesses a yellow color at 400 nm. Figure 11.3 shows the UV-visible extinction, absorption and scat-

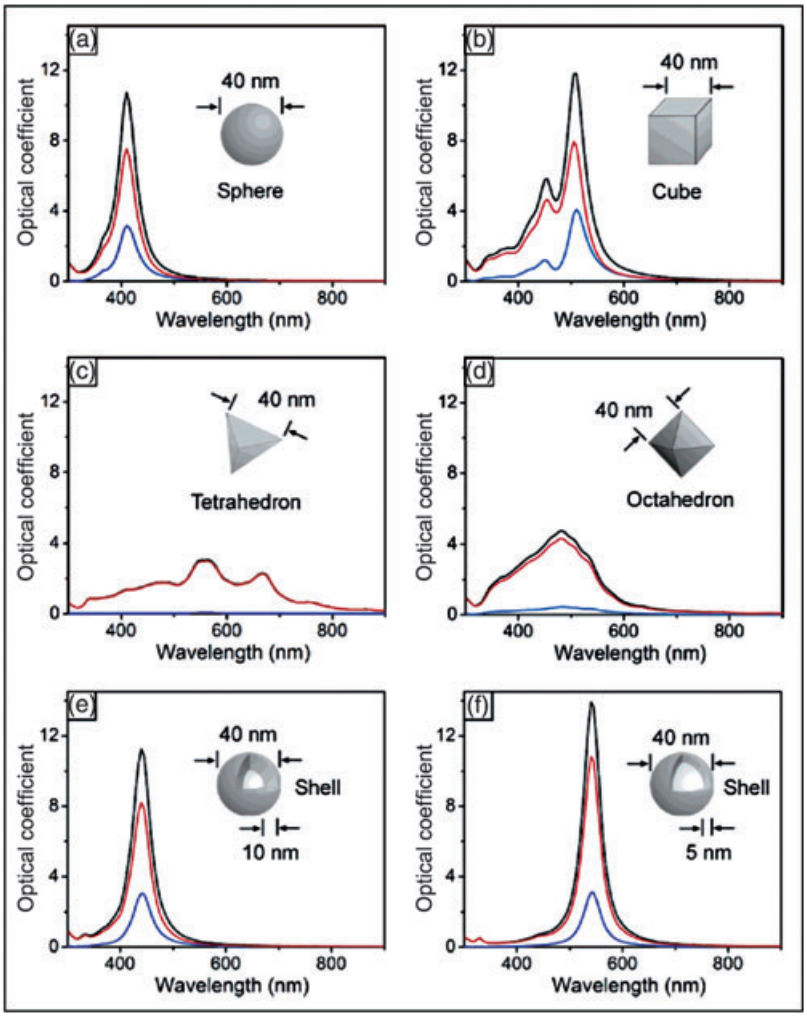

Figure 11.3 The effect of nanostructure shape on spectral properties. Calculated UV-visible extinction (black), absorption (red) and scattering (blue) spectra of silver nanostructures. Reproduced with permission from Ref. [54]; © 2006 American Chemical Society.

tering spectra for a 40-nm silver sphere in water, calculated using Mie theory [54]. It should be noted that any variation in particle size, shape or dielectric environment will cause a change in the surface polarization, and thus the resonance peak. Hence, the SPR can be tuned across a range of wavelengths in the electromagnetic spectrum by varying the size, shape or local environment of the nanoparticles, with help from a variety of synthetic strategies. The general protocols used to generate metal nanoparticles are discussed in Section 11.2.

11.2
General Synthetic Strategies

The engineering of materials at the nanoscale level with novel properties, through controlled synthesis and assembly, is an important issue. In recent years, nanotechnology has reached a stage whereby it is possible to produce, characterize and specifically tailor, the functional properties of nanoparticles. Nanoparticle synthesis has been pursued intensively not only for fundamental scientific interest but also for many technological applications [16, 30, 55–58], and the synthesis of uniformly sized (or monodisperse) nanoparticles has become a very important research area [59–63]. The two fundamentally different approaches used to synthesize nanomaterials are known as 'top-down' and 'bottom-up':

- In the 'top-down' approach, nano-objects are constructed from larger entities without atomic-level control. The process begins with a suitable starting material, and produces nanoscale structures by using machining and etching techniques. Common 'top-down' techniques include photolithography and electron-beam lithography (generation of the mask). The main disadvantage of the 'top-down' technique is the need to remove large amounts of material.
- In the 'bottom-up' approach, the materials and devices are built from molecular components, which assemble themselves chemically, by the principles of molecular recognition. In this process the nanostructured building blocks are formed first, and then assembled into the final material. The 'bottom-up' approach is a particularly attractive synthetic route for nanoparticles, because of its inherent simplicity and speed of production. In some cases, however, 'bottom-up' techniques can suffer from poor monodispersity, as growth cannot be arrested at the same point for all nanoparticles.

A schematic diagram of the two synthetic approaches, both of which have been used extensively in the formation of structural composite materials, is shown in Figure 11.4.

The choice of approach is very important with regards to any further processing of the nanomaterials for possible applications. During the past few years, 'bottom-up' techniques based on the self-assembly of building blocks have attracted considerable attention for the synthesis of anisotropic nanoparticles. The use of some popular 'bottom-up' techniques, for the rational design of spherical and highly

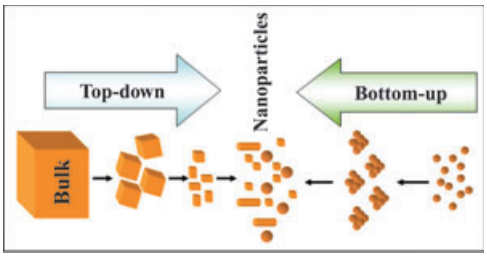

Figure 11.4 Schematic illustration of preparative methods of metal nanoparticles.

anisotropic nanoparticles, has been illustrated in Section 11.2.3. A variety of strategies have been employed in the 'bottom-up' synthesis of nanomaterials, including templating, chemical, electrochemical, sonochemical, thermal and photochemical reduction methods [34, 64–67]. Although each of these strategies has contributed to the growth of the field, the success of the synthetic strategies is found to depend on a variety of key issues:

1. Particle size distribution (uniformity): Monodispersity of the nanoparticles
2. Particle size control: Reproducibility in the synthesis
3. Shape control: High yield with the desired shape
4. Scale-up: Optimization of the synthetic strategy at large scale
5. Compatibility: Ease of the synthesis for the realistic applications

In brief, an efficient method should produce monodispersed nanoparticles in high yield, with reproducibility of the synthesis and good control over the final size and shape. The method should also be capable of optimization on the large scale, without compromising any of the above issues. Compatibility of the nanomaterials is also important, in view of their potential applications, especially in the biomedical field. Moreover, it is very important to achieve the above goals for the success of the synthesis. Shape variation, as one of the most important issues in the synthesis of nanomaterials, will be discussed in Section 11.2.1.

11.2.1 Shape Variation

The shape control of nanoparticles is a very important aspect in nanotechnology, due to the spectacular effects that structural anisotropy may have on many of the material's physical properties. Because of these size- and shape-dependent properties, much effort has been expended in controlling the morphology and assembly of nanoparticles [68–69]. The most common architecture of these nanocrystals is isotropic particles, ranging from spherical to highly faceted particles, such as cubic and octahedral. One-dimensional (1-D) anisotropic nanoparticles include uniform rods and wires, whereas two-dimensional (2-D) nanoparticles consists of nanodiscs, plates and other advanced shapes such as rod-based multipods and nanostars.

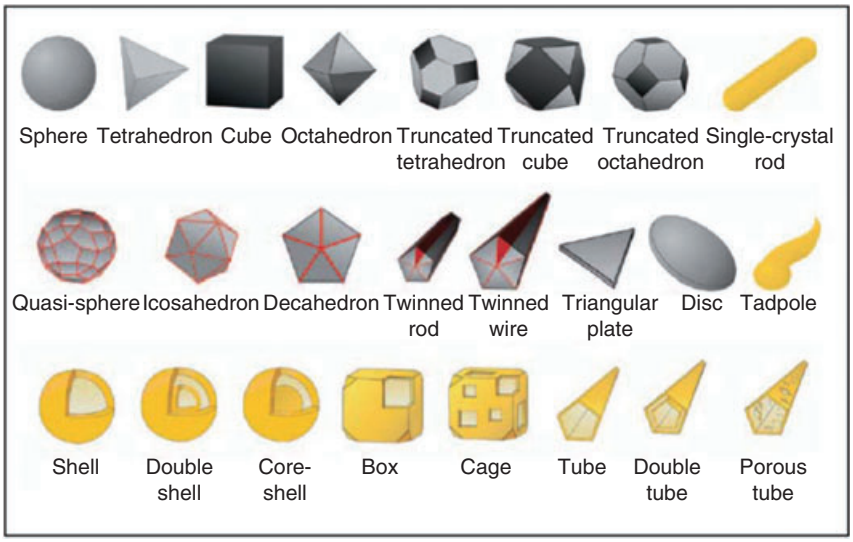

Figure 11.5 Schematic of conventional shapes of face-centered cubic (fcc) metal nanostructures. The shapes in the top row are single crystals, in the second row are particles with twin defects or stacking faults, and in the third row are gold shells. Dark facets are {100} planes, light gray are {111} planes, and {111} twin planes are shown in red. Reproduced with permission from Ref. [70]; © 2005 Materials Research Society.

The schematic shown in Figure 11.5 represents the conventional shapes of fcc metals, which are enclosed by {111} and {100} facets with a low proportion of corner and edge sites [70]. The surface energies of the different crystallographic facets decide the shapes of the fcc metals under thermodynamic considerations. Calculations of the surface energies of fcc metals suggest that the surface energies increase in the order $\gamma\{111\} < \gamma\{100\} < \gamma\{110\} < \gamma\{hkl\}$, where {hkl} represents high-index facets, with at least one h, k and l equal to 2 or more [71]. During the crystal growth, those facets with high surface energies are usually eliminated from the crystal surface as they grow much faster than others. As a result, low-index facets are enlarged at the expense of high-index facets during crystal growth. This alteration of the surface energies of various facets during nanocrystal growth is the controlling factor in deciding the final shape of the nanocrystal.

The synthesis of silver and gold nanocrystals of various shapes has been accomplished through a variety of synthetic methods. Experimental parameters such as reaction time, temperature and the concentrations of reagents play crucial roles in determining the morphology of the final product and, indeed, it is possible to achieve a much better shape control simply by adjusting these reaction parameters. The factors and mechanism responsible for shape variation, based on energy considerations, are described in the following section.

11.2.2 Nucleation and Growth

In solution-phase synthesis, the process of nanocrystal formation can be explained by nucleation and growth mechanisms, both of which can be either thermodynamically or kinetically controlled. The reduction of metal ions generally results in the formation of atoms, which aggregate to form nuclei. When the nuclei have grown beyond a critical size (referred to as 'seeds'), they will have a relatively stable crystallinity and well-defined crystallographic facets exposed on their surfaces [72–75]. The structure of a seed is determined primarily by the minimization of surface energy, which can be single-crystal, single-twinned or multiple-twinned. The nucleation stage and subsequent changes in the nuclei are critical in deciding the anisotropic shapes of the nanocrystals. Each seed will grow into a nanocrystal after the nucleation stage, with seed growth being influenced by factors such as the concentration of the metal precursor, the rate of reduction (the concentration and power of the reductant), the presence of a capping agent, and – most importantly – on the specific adsorption of a capping agent to a particular crystallographic plane. A schematic of the reactions pathways for the generation of different shapes of palladium nanostructures is shown in Figure 11.6 [76].

The growth rate can be controlled by altering the surface energies of different facets to obtain different ratios of {111} and {100} facet areas. The relative areas of the crystallographic facets that enclose the nanocrystals decide the final shape of the nanocrystal. The surfactants or capping agents interact with the different facets of fcc metals and change the order of free energies of different facets. For example, polyvinylpyrrolidone (PVP) binds most strongly to 100 facets [77, 78], whereas citrate ions bind most strongly to 111 facets [79]; this results in the formation of nanocubes and octahedrons, respectively. The capping agent plays an important role in shape guiding by chemical adsorption as it renders some facets thermodynamically favorable for crystal growth. In this way, other single crystal shapes such as octahedron, cube and tetrahedron become favorable in terms of surface energy [76–79]. As shown in Figure 11.6, twin defects (a single atomic layer in the form of a mirror plane) are formed, which are usually decahedral and icosahedral with a small surface area. The surface coverage of {111} facets is maximized because of the reduction in the surface energy, in order to compensate the extra strain energy caused by twinning. Figure 11.7 shows the crystal habits of gold and silver rods and wires derived from the decahedral particles [80]. The end faces of the nanorods are {111}-type planes, whereas the side faces are {100}-type; these can be viewed as fivefold decahedra that have been elongated parallel to the twin planes. Under kinetic control, plate-like morphologies such as triangular, hexagonal and circular are formed, where the top and bottom faces are {111} facets.

In summary, nucleation followed by kinetically controlled growth is critical for the rational design of anisotropic and highly monodisperse nanoparticles, and necessitates separation between the nucleation and growth stages. Chemical

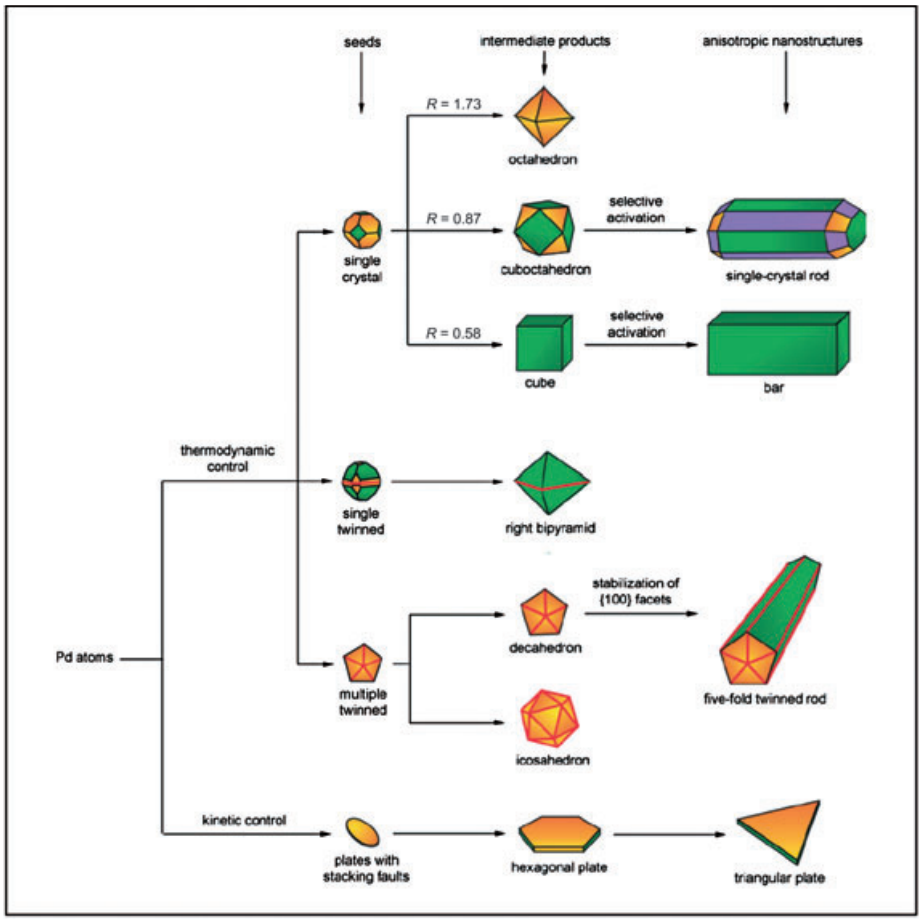

Figure 11.6 A schematic illustration of the reaction pathways that lead to Pd nanostructures with different shapes. The green, orange and purple colors represent the {100}, {111} and {110} facets, respectively. Twin planes are delineated in the figure with red lines. The parameter *R* is defined as the ratio between the growth rates along the ⟨100⟩ and ⟨111⟩ axes. Reproduced with permission from Ref. [76]; © 2007 Wiley-VCH.

methods for the synthesis of anisotropic gold and silver nanostructures are outlined in the following section.

11.2.3 Chemical Synthetic Approach

Chemical methods have been widely used to produce nanostructured materials with different strategies, not only to control the morphology of the product but also to achieve monodispersity. In general, metals (mostly with a cubic structure) tend to nucleate and grow into thermodynamically stable nanoparticles with their surfaces bound by the low-energy facets, so as to minimize the total surface energy

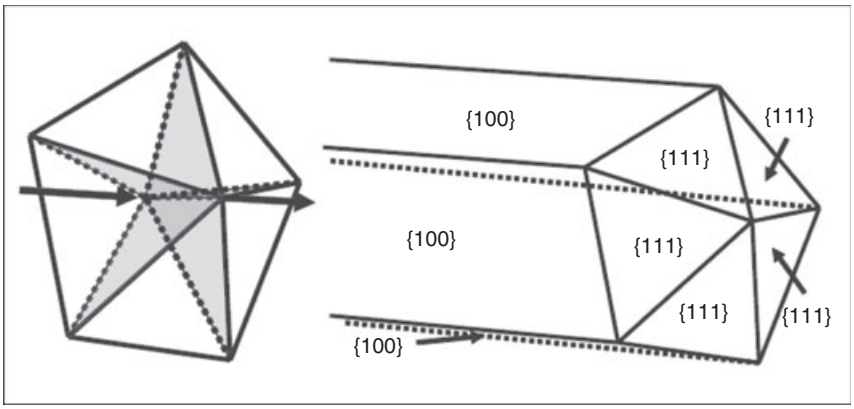

Figure 11.7 Crystal habits of the gold and silver rods and wires. Reproduced with permission from Ref. [80]; © 2005 Wiley-VCH.

[81]. None the less, highly anisotropic shapes that are not favorable from the perspective of thermodynamics have been obtained by the introduction of capping agents, stabilizers or other additives, which can alter the surface energies for the different crystallographic planes [58, 82–84]. A detailed study of the growth process has revealed that a gradual change in the morphology of the particles is directly related to the faster growth of certain crystallographic facets (see above). As the importance of capping agents, stabilizers and additives when growing nanoparticles of silver and gold has already been stressed, the major emphasis now is on citrate reduction, polyol synthesis and seed-mediated synthesis.

11.2.3.1 **Citrate Reduction**

The citrate reduction method, which was developed by Turkevitch in 1951 [85], is one of the most popular conventional techniques used to synthesize gold nanoparticles. The reaction utilizes the reduction of chloroauric acid ($HAuCl_4$) in water using sodium citrate, and leads to the production of gold nanoparticles of about 20 nm diameter. In this method, citrate plays a dual role of reductant and stabilizer in the formation of colloidal gold clusters. An excess of citrate stabilizes the particles by forming a complex multilayered assembly of anions of various oxidation states, lending an overall negative charge to the surface and thus preventing aggregation. In 1973, Frens and coworkers developed a method for the synthesis of gold nanoclusters, wherein the ratio between the reducing/stabilizing agents (trisodium citrate : gold ratio) was varied [86]. This method has proved to be useful for the synthesis of gold as well as silver nanoparticles. Recently, the role of citrate ions in the synthesis of spherical and anisotropic silver nanoparticles has been investigated [87]. Studies comparing the impact of various concentrations of citrate ions in reactions, with a constant molar concentration of silver, have shown that an excess of citrate ions dramatically slows the growth of silver nanoparticles. Although the citrate reduction method generally produces spherical nanoparticles,

by varying the reaction conditions it is possible to tailor the particle shape. A simple procedure for the synthesis of crystalline silver nanowires has been demonstrated in the presence of NaOH [88]. Here, silver nanowires were produced without using any surfactant, polymer or external seed crystallites, and the capping of citrate on certain faces of the silver facilitates the growth of nanoparticles in one direction, which is in agreement with previous reports. The quantity of NaOH used was an important factor in determining the morphology of the final product. The hydroxide ions in solution compete for the capping action with citrate, and this leads to the change in morphology of the products. Although the citrate reduction method has been found useful for the synthesis of metal nanoparticles, the need for a precise control over the morphology and greater stability of the products has led to a quest for alternative synthetic methods.

11.2.3.2 **Polyol Synthesis**

Polyol synthesis, one of the most well-known methods for the preparation of metal colloids, was first developed by Fivet and coworkers as a simple and versatile route to synthesize metallic nanoparticles [89]. In a typical polyol synthesis, the reduction of a metal salt was carried out by liquid polyol or diol in the presence of a stabilizing agent. Generally, PVP was used as the capping or stabilizing reagent owing to its excellent adsorption abilities, while ethylene glycol (EG) was commonly used as both the solvent to dissolve the metal precursor salts and the reducing agent. The highly temperature-dependent reducing power of polyol proved to be a convenient, versatile and low-cost route for the synthesis of metal and alloy particles with a quasi-spherical shape and narrow size distribution. The primary reaction of this process involves the reduction of an inorganic salt (the precursor) by polyol at an elevated temperature, which is shown in following equations [90] (shown for reduction of Au).

$$CH_2OH{-}CH_2OH \rightarrow CH_3CHO + H_2O \tag{11.1}$$

$$6\,CH_3CHO + 2\,AuCl_4 \rightarrow 2\,Au^0 + 3\,CH_3CO{-}COCH_3 + 6\,H^+ + 8\,Cl^- \tag{11.2}$$

When $AuCl_4$ is reduced by EG to generate Au^0 atoms at a sufficiently high rate, the final product will generally take the thermodynamically favored shapes (quasi-spherical). However, as the reduction become substantially slower the nucleation and growth will be kinetically controlled such that the final product may assume a range of shapes which deviate from the thermodynamic shapes. The reduction of metal ions by EG generally results in the formation of metal clusters, followed by the nucleation of seeds, and subsequent growth of seeds into different morphologies. The seminal studies of Xia and coworkers have opened up the possibility of a general methodology for shape control in metallic nanostructures by using a modified polyol process [91]. By carefully controlling the reduction kinetics, particularly at the seeding stage, the formation of these highly anisotropic structures becomes favorable in a slow reduction process. Several research groups have employed such kinetic control to obtain anisotropic nanostructures of silver and gold using a modified polyol process [92–94]. In addition, a microwave-assisted polyol process proved

to be capable of synthesizing polygonal Ag and Au nanoplates, rods and wires [95–97]. The various parameters responsible for the shape control of silver and gold nanoparticles in the modified polyol process are detailed in the following sections.

11.2.3.2.1 **The Case of Silver** In the polyol synthesis, by controlling the PVP : silver precursor ratio, it is possible to produce silver nanocubes, nanowires and quasi-spheres [98]. PVP plays a crucial role in producing silver nanostructures with good stability and size/shape uniformity, as the oxygen and nitrogen atoms of the pyrrolidone unit promote the adsorption of PVP chains onto the silver surface. The specific adsorption of PVP to the {100} facets of the seeds results in the formation of either nanocubes (for single-crystal seeds) or nanowires (for multiply twinned seeds with a decahedral shape) [77]. The overall growth process of silver nanostructures is depicted in Figure 11.8. The initial reduction of silver ions by EG results in the formation of clusters of critical sizes (nucleation); the silver atoms generated by the reduction of silver nitrate ($AgNO_3$) then diffuse to the surface of the nuclei and position themselves at active surface sites. The essence of this shape control lies in varying the molar ratio between PVP and $AgNO_3$, as this results in a modification of the thickness of the PVP coating and the location of PVP chains on the seed surface. It has been suggested that the interaction strengths between PVP and different crystallographic facets of a silver lattice are substantially different, and may therefore induce the anisotropic growth of silver.

Silver Nanocubes In polyol synthesis, silver nanocubes are the major product when the initial $AgNO_3$ concentration is high and the ratio between PVP and $AgNO_3$ is relatively low, which ensures rapid nucleation and growth of silver seeds at the expense of twin defect formation [99]. PVP plays a crucial role in reducing the twin defect formation through selective adsorption onto {100} facets, thus making available {111} facets for the addition of silver atoms [77]. The growth rate of each face of the silver nanocube will remain same after the cubic shape has

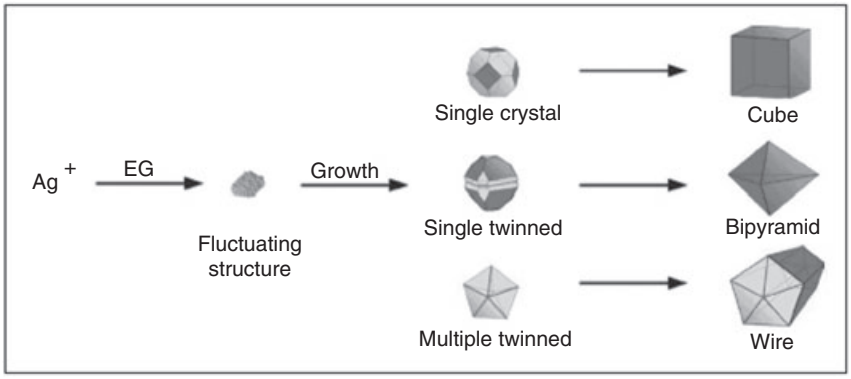

Figure 11.8 The reaction pathways leading to well-defined silver nanostructures. The growth of seeds can selectively enlarge (100) facets (dark gray) at the expense of (111) facets (light gray), resulting in the formation of cubes, bipyramids or wires. Reproduced with permission from Ref. [54]; © 2006 American Chemical Society.

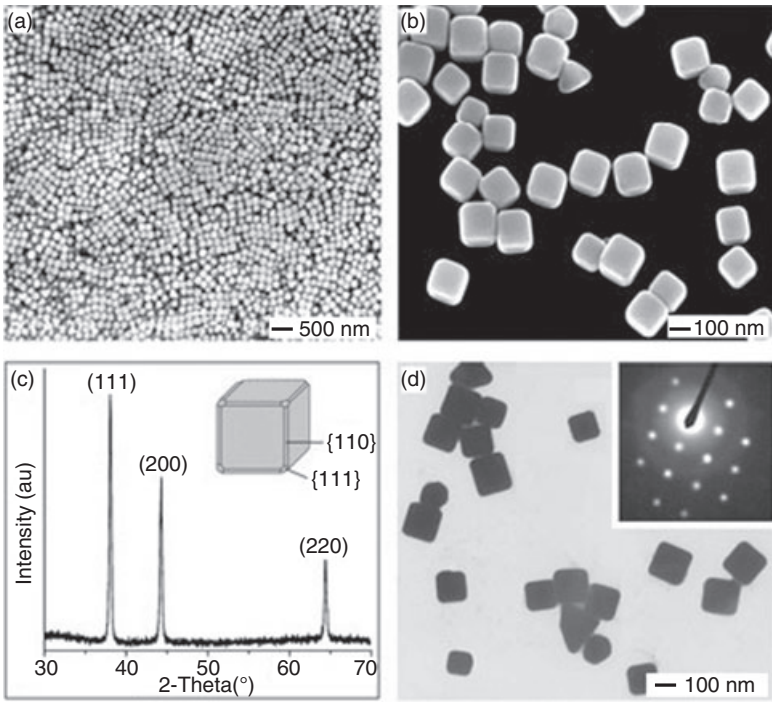

Figure 11.9 (a, b) SEM images of silver nanocubes synthesized by heating a mixture of $AgNO_3$ and PVP in ethylene glycol for 45 min. The sample stage was tilted at 20° in (b), showing that all corners and edges of each cube were slightly truncated; (c) XRD pattern obtained from the same batch of nanocubes deposited on a glass substrate. The drawing of one cube is shown as the inset. In this synthesis, the concentration of $AgNO_3$ solution was 0.25 *M* and the molar ratio between PVP and $AgNO_3$ was 1.5; (d) A TEM image of the product obtained under the same conditions as in (a), except that the concentration of $AgNO_3$ was reduced to 0.125 *M* and the growth time shortened to 30 min. The inset shows a typical electron diffraction pattern taken from any individual nanocube by directing the electron beam perpendicular to one of its square faces. Reproduced with permission from Ref. [99]; © 2005 Wiley-VCH.

been formed, and further growth will mainly increase the size with no significant morphological variation.

Scanning electron microscopy (SEM) images of the product (see Figure 11.9) indicate that this method could produce uniform silver nanocubes in high yield. The surfaces of these silver nanocubes are smooth, with all corners and edges slightly truncated. An important feature of this method is that, the size of the silver nanocubes may be varied by changing the concentration of $AgNO_3$. The selected area electron diffraction (SAED) pattern also confirms that each silver nanocube is a single crystal bound primarily by {100} facets.

Silver Nanowires In order to form the silver nanowires in high yield, control over the geometry of the seed is essential. Here, it is necessary to form multiple-twined

particles (MTP)s – which are thermodynamically stable – rather than single-crystal seeds – which are kinetically stable – in order to grow silver nanowires. Generally, the twin defect represents the highest energy site on the surface of an MTP, onto which silver atoms preferentially crystallize, leading to a uniaxial elongation of the decahedra into pentagonal rods. The pentagonal cross-section will be retained during growth of the silver nanowires.

One way to achieve the growth of MTPs is to lower the concentration of $AgNO_3$, while keeping the ratio between PVP and $AgNO_3$ constant [100]. In another modification, small amounts of sodium chloride (NaCl) and $Fe(acac)_3$ (iron acetylacetonate) were added to reaction system [101]. The role of the chloride ions was to prevent the agglomeration of seeds, which otherwise would form irregular particles. The proposal was that the chloride ions would adsorb onto the seeds and stabilize them (electrostatically) against agglomeration. The Fe(III) ions were added to prevent the etching of twinned seeds by chloride and oxygen. A SEM image of silver nanowires is shown in Figure 11.10.

Silver Right Bipyramids Right bipyramids of silver were prepared using a modified polyol process by the selective nucleation and growth of silver nanoparticles with a single {111} twin. The selective generation of single twinned seeds was facilitated by the incorporation of sodium bromide (NaBr) to a polyol synthesis [102]. Bromide ions play an important role in the formation of high yields of the single twinned seeds necessary to grow right bipyramids. As mentioned earlier, chloride ions essentially etched the nanoparticles with twinned defects, leading to the formation of single-crystal seeds. Bromide ions, which are less corrosive than chloride ions,

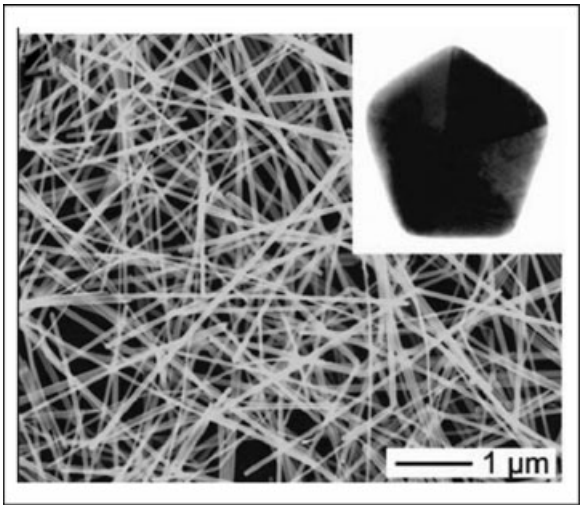

Figure 11.10 SEM image of silver nanowires. The inset shows multiply twinned pentagonal (MTP) seed. Reproduced with permission from Ref. [101]; © 2007 American Chemical Society.

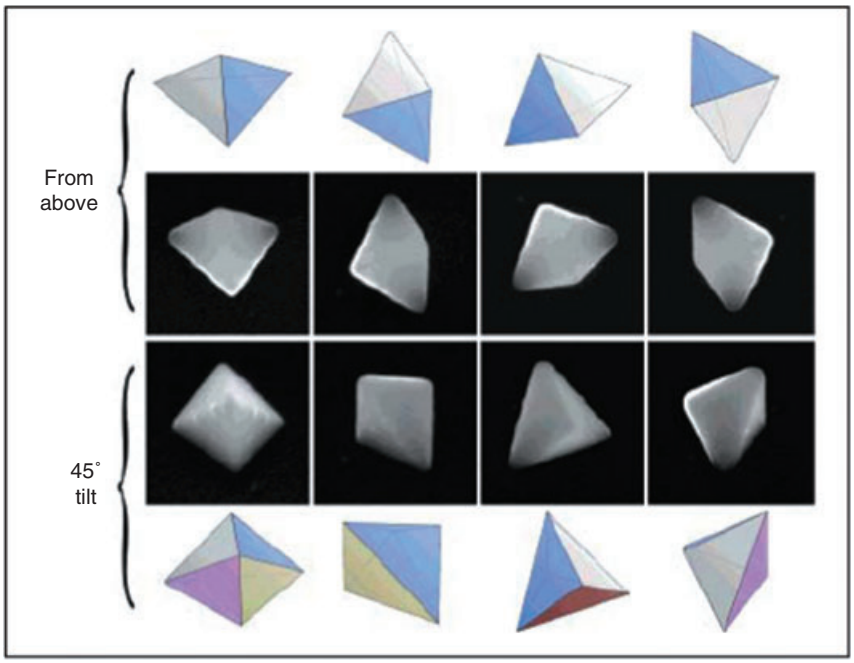

Figure 11.11 SEM image of silver right bipyramids compared with computer-aided design (CAD) model. Reproduced with permission from Ref. [102]; © 2006 American Chemical Society.

enable a moderate etching that is sufficient to eliminate any multiple twinned defects, but not single twin defects. Figure 11.11 shows the SEM image of the silver bipyramids compared to a computer-aided design (CAD) model; here, the same bipyramid is viewed under SEM from above and after a 45° tilt away from the viewer, at four different clockwise rotations. The bipyramids, with average edge length 150 nm and with corners of average radius of curvature 11 nm, were obtained with over 80% yield. Size control was possible by controlling the growth time of the silver bipyramids.

Silver Nanohexapods Silver nanohexapods (AgNHs) with a well-defined concave shape and unique structure were synthesized in almost 100% yield using a modified polyol process [103]. The rate of injection of $AgNO_3$ and PVP into EG was modified in order to form AgNHs, which had a well-defined shape and were formed within only 5 min of the initial injection of reactants into the EG. Figure 11.12 shows transmission electron microscopy (TEM) images, SAED patterns and the surface configurations of single-crystalline AgNHs along the three low-index zone axes. Each AgNH has a faceted concave shape with six branches along the {100} directions and a sharp tip of four {111} facets.

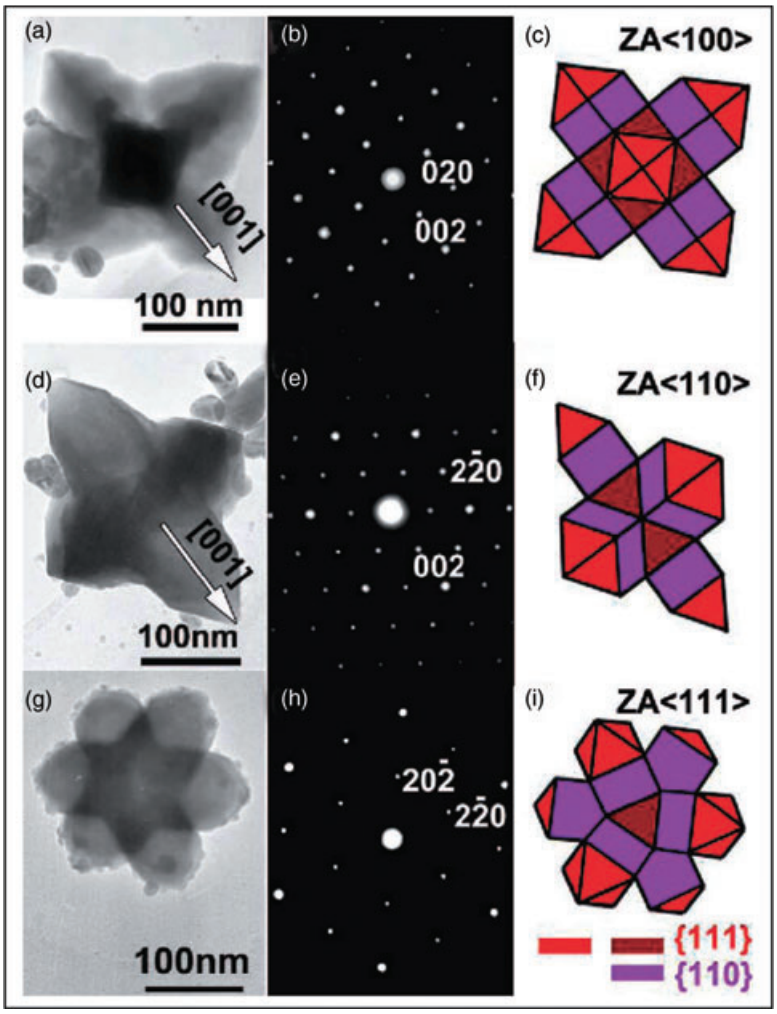

Figure 11.12 TEM images (left column), SAED patterns (center column) and surface configurations (right column) of the single-crystalline AgNHs along the three low-index zone axes (ZA): (a–c) ZA [99]; (d–f) ZA [109]; (g–i) ZA [110]. Reproduced with permission from Ref. [103]; © 2008 American Chemical Society.

11.2.3.2.2 **The Case of Gold** The synthesis of highly selective nanostructures of gold has been demonstrated using a polyol method [98]. A systematic evolution of gold nanocrystals with sizes of 100–300 nm has been achieved with a modified polyol process, where the distinct uniform shapes of tetrahedron, cube, octahedron and icosahedron were realized in high yield by using PVP and foreign ions. Here, the PVP played a dual role of stabilizer and shape-regulating polymer (i.e. essen-

tially the same role as for silver nanostructures). The reducing ability of PVP can be attributed to the hydroxyl end groups present in the polymer, when water is used as the polymerization solvent. In the presence of EG, the reduction of $AgNO_3$ takes place at a relatively high reaction temperature (160 °C); however, when water molecules are used as solvent the reducing ability of PVP is enhanced dramatically, with PVP capable of reducing $AgNO_3$ at 60 °C, or even at room temperature. The reducing ability of PVP or the reaction speed can be controlled by regulating the water content, thus improving the ability of PVP to kinetically control the growth of Au. In this regard, a novel two-phase system – water/PVP/*n*-pentanol (WPN) – has been successfully exploited to realize the highly shape-selective synthesis of anisotropic Au nanoparticles with controlled sizes and remarkable shapes, such as regular octahedrons, triangles, rods, dumbbells, belts and hexagons [104]. The synthesis conditions and factors responsible for the anisotropic growth of gold nanostructure are described in the following sections.

Gold Spheres A simple, one-step, one-phase synthetic route for spherical gold nanoparticles with a uniform size distribution by using *o*-diaminobenzene as a reducing agent in the presence of PVP has been achieved [105]. In this reaction, PVP was used as the capping agent that controlled the particle growth and stabilized the micro/nanoparticles in high yield (almost 100%). The diameter of the gold micro/nanoparticles could easily be controlled by changing the molar ratio of PVP to $HAuCl_4$.

Gold Nanocubes The size control of gold nanocubes has been achieved by a modified polyol process which involves a rapid reduction of gold precursors in refluxing 1,5-pentanediol in the presence of 1/200 equivalents of silver nitrate [106]. As PVP alone (without $AgNO_3$) was insufficient to stabilize the gold particles, $AgNO_3$ was used as a stabilizer during the growth of the nanocubes. The suggestion was that, the introduction of $AgNO_3$ might suppress the growth of a certain face at some rates, thus preventing large cluster formation and providing stability to the nanocrystals. The schematic of gold nanocube formation is shown in Figure 11.13. The first addition of gold precursors resulted in the formation of seeds of diameter

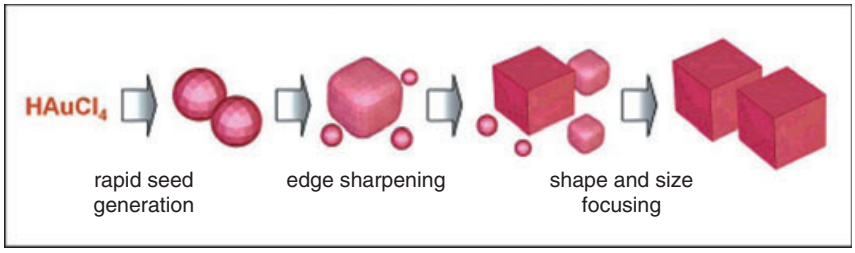

Figure 11.13 Schematic of the formation of gold nanocubes. Reproduced with permission from Ref. [106]; © 2006 American Chemical Society.

approximately 60 nm; subsequently, larger particles grew at the expense of smaller seeds, a situation typical of Ostwald ripening. The edge sharpening of the crystals, together with shape and size focusing, resulted in the formation of gold nanocubes.

Gold Octahedra Octahedral Au particles of hundreds of nanometers in size were easily synthesized by a modified polyol process, in which EG was replaced with polyethylene glycol 600 (PEG 600) [107]. In the initial stages of the synthesis, the Au octahedra were in low yield and always mixed with other types of Au nanostructure. However, the addition of $NaBH_4$ to PEG 600 dramatically increased the yield of single crystalline Au nano-octahedra, from an initial value of less than 15% to more than 90%. Here, the $NaBH_4$ acts as a strong reducing agent that directly reduces the Au^{III} ions in Au salts to Au^0 atoms. The formation of octahedral Au nanocrystals is facilitated by a preferential adsorption of PVP onto the {111} planes of Au nuclei, reducing the growth rate along the {111} direction but enhancing that along the {100} direction. The ratio of growth rates along the {100} to {111} directions has been shown to determine the geometric shape of a crystal. The shape of a cubic nanocrystal evolves from a perfect cube ($R = 0.58$) to a cubo-octahedron ($R = 0.87$), a truncated octahedron ($0.87 < R < 1.73$), and finally to a perfect octahedron ($R = 1.73$) as R increases. Figure 11.14 shows the field emission

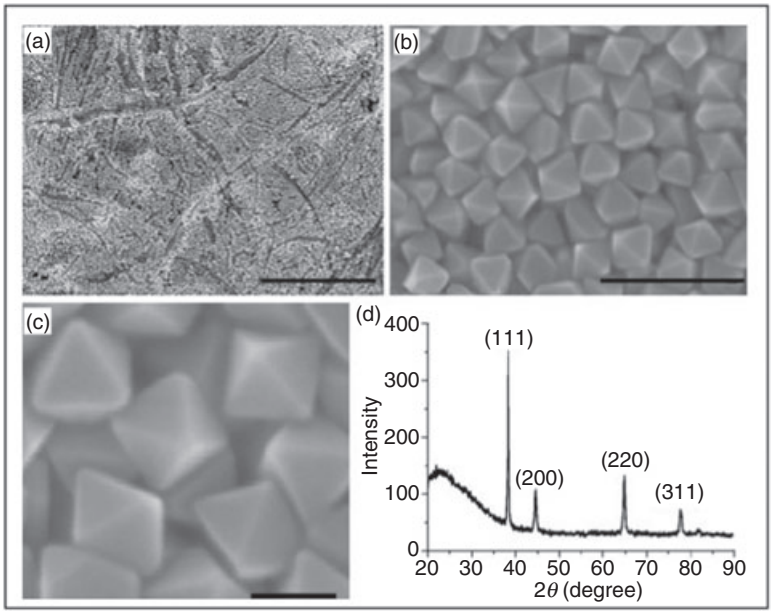

Figure 11.14 (a) Low-, (b) medium and (c) high-magnification FESEM images and (d) X-ray diffraction pattern of the Au nano-octahedra. Scale bars for (a), (b) and (c) are 2 mm, 200 nm and 50 nm, respectively. Reproduced with permission from Ref. [107]; © 2007 Wiley-VCH.

scanning electron microscopy (FESEM) images of the Au nano-octahedra and X-ray diffraction (XRD) pattern, which confirm that the products consisted of pure crystalline fcc Au nanoparticles.

In another method, regular gold octahedra were synthesized in high yield by using a modified polyol process in which Au octahedra were obtained by sequentially adding aqueous citrate and ethanol solutions of $HAuCl_4 \cdot H_2O$ to a *n*-pentanol solution of PVP [108]. In this reaction, the average edge length of the regular octahedra could be tuned by using appropriate amounts of PVP, water and sodium citrate.

Gold Nanosheets Single crystalline gold nanosheets, with triangular, hexagonal or truncated triangular shapes, have been successfully synthesized in high yield using a polyol process [109]. Both, EG and PVP in the solution play important roles in the formation of Au nanosheets. The concentrations of the precursors (PVP, $HAuCl_4$) and the reaction temperature are also crucial in determining the morphology and size of the final product. A schematic of the formation of hexagonal nanosheets and nanobelts, formed along with triangular sheets in low yields, is shown in Figure 11.15.

The formation of small triangular and truncated triangular (or hexagonal) nanosheets is attributed to the preferential adsorption of PVP onto the {111} planes of Au nuclei; this greatly decreases the surface energy of the {111} planes and leads to preferential growth along the {110} directions. It is believed that small nanosheets are connected together along the {110} lateral planes, which are of

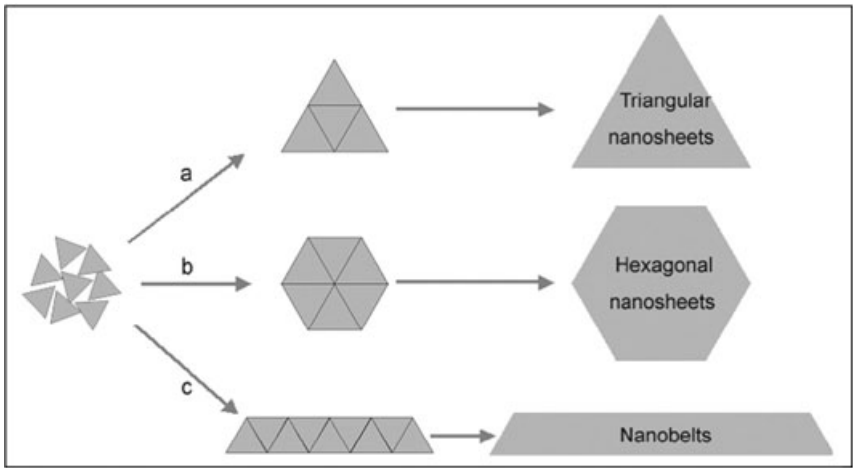

Figure 11.15 Schematic of the formation of: (a) triangular nanosheets; (b) hexagonal nanosheets; (c) nanobelts. Reproduced with permission from Ref. [109]; © 2007 Wiley-VCH.

relatively high surface energy, leading to the formation of triangular or hexagonal nanosheets (Figure 11.15a and b). Small triangular nanosheets with the same size are also connected into a long and thin nanobelt (Figure 11.15c) along the ⟨110⟩ direction. A TEM image of a single triangular nanosheet, together with the corresponding SAED pattern, are shown in Figure 11.16. Here, the surfaces of the Au nanosheets are atomically flat, as indicated by the inner sets of spots {111} pattern, originated from the 1/3{422} plane.

In brief, polyol synthesis has been successfully applied to the generation of spherical and anisotropic nanomaterials of gold and silver, with high yields. Moreover, the method exhibits good control over the morphology of the product, with quantitative reproducibility.

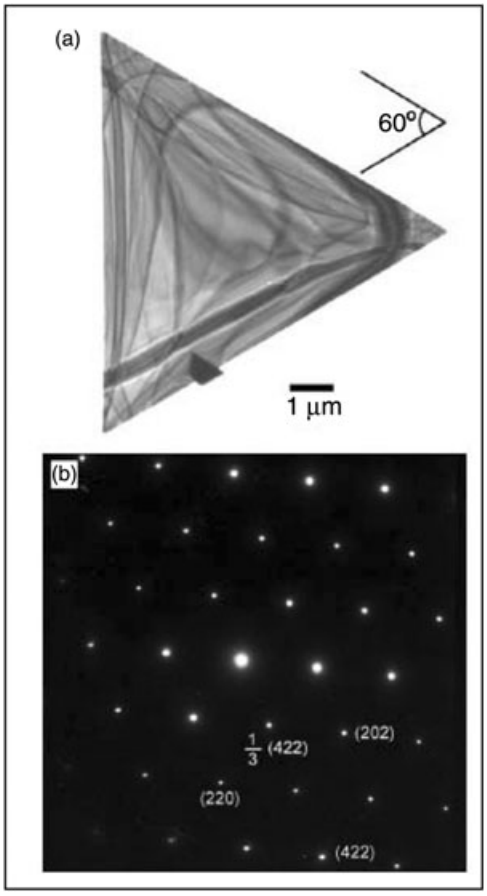

Figure 11.16 (a) TEM image and (b) SAED pattern of single triangular Au nanoplate. Reproduced with permission from Ref. [109]; © 2007 Wiley-VCH.

11.2.3.3 Seed-Mediated Synthesis

In recent years, the seed-mediated synthesis of spherical and highly anisotropic metal nanoparticles has gained much importance in the field of nanotechnology [66]. The technique facilitates the use of smaller seed particles added externally for the growth of the anisotropic nanostructures. In brief, the method is divisible into two steps: (i) seed preparation; and (ii) growth of the desired nanoparticles on the seed in the presence of a surfactant. While the seeds are generated with a strong reducing agent (e.g. $NaBH_4$), the growth solution employs a weaker reducing agent (often ascorbic acid) to reduce the metal salt. Growth is believed to be due to kinetic conditions, limiting the control over size and shape; however, the concentrations of the reagents may be adjusted to control crystal growth. The synthesis of the seed is critical (as for the polyol method) in obtaining the final product with a narrow size distribution. The particle size of the product can be manipulated by varying the ratio of seed to metal salt. Seed-mediated synthetic strategies for silver and gold nanoparticles are described in the following sections, with attention focused on the use of cetyltrimethylammonium bromide (CTAB) as surfactant. The evolution of both spherical and nonspherical particles is discussed based on recently reported data, contributing to a better understanding of the shape evolution of anisotropic nanostructures.

11.2.3.3.1 The Case of Gold

A variety of shapes of gold nanostructures has been realized using seed-mediated synthesis, and consequently the technique is regarded as a favorite where gold is concerned. Such success lies in the simplicity and ease of shape variation, it having been shown that the creation of different shapes for gold nanostructures is possible with only minor changes to the experimental conditions.

Gold Nanospheres Seed-mediated growth has been used successfully for the synthesis of gold nanospheres [110], the size of which can be tuned from 5 to 40 nm by controlling the ratio of the seed and precursor, and using CTAB as the growth medium. In this method, the seed particles are repeatedly exposed to fresh aliquots of growth solution, which yields products of greater monodispersity in terms of both size and shape. It was proposed that nucleation is a slow process at the start of the reaction, rapidly increases as the reaction progresses, and then slows and eventually stops as growth predominates. Thus, an initial slow nucleation, followed by a burst of nucleation mediated by seeds and growth, yield the final products.

In another example, a single-step citrate method was employed to prepare 30–100 nm-sized gold particles from smaller seeds, utilizing the surface-catalyzed reduction of Au^{3+} by hydroxylamine [111]. The diameter of the seed particles and the amount of Au^{3+} present in the growth solution were critical issues in controlling the physical properties of the products. Further studies revealed that the reduction of Au^{3+} was extensively catalyzed on any surface, such that other (stronger) reducing agents could be used in seeded growth methods [112]. However, as the rate of reduction at the seed surface greatly exceeded the reduction rate of

metal ions in the growth solution, the seed nanoparticles grew at the expense of nucleating new particles.

Gold Nanorods The most popular chemical method for producing gold nanorods is that of seed-mediated nanoparticle growth in the presence of surfactant, as introduced by the group of Catherine Murphy [113–116]. The most widely used surfactant is CTAB and, in a typical process, spherical gold seeds of 3.5 ~ 4 nm in diameter are prepared by reduction of a gold salt solution with a strong reducing agent, $NaBH_4$, in the presence of a capping agent such as sodium citrate. The seed was then introduced to a growth solution containing $HAuCl_4$, CTAB and a weak reducing agent (ascorbic acid) to generate gold nanorods in solution. This can be achieved either by single or multistep seeding processes. A schematic diagram for the synthesis is provided in Figure 11.17 [117], where the weak reducing agent (usually ascorbic acid) is incapable of fully reducing the metal salt at room temperature. However, upon addition of the seeds, the reaction is thought to take place on the seed surface, and being autocatalytic, to produce larger nanoparticles. The presence of a structure-directing agent is crucial to obtain nanorods, and the aspect ratio (defined as the length of an object divided by its width) of the gold nanorods can be tuned easily by using this method. The formation of other shaped particles (especially spherical) can be reduced to a significant level simply by modifying the

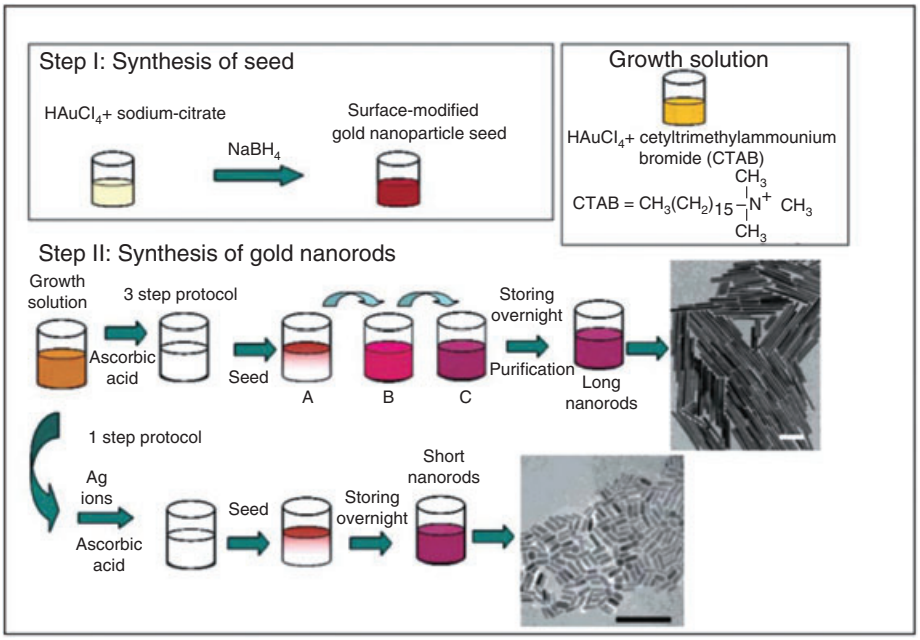

Figure 11.17 Schematic of the seed-mediated growth of gold nanorods. Reproduced with permission from Ref. [117]; © 2006 American Chemical Society.

methodology or introducing certain additives to the system. The effect of the concentrations of the seed, metal ions, reducing agents, surfactants and silver nitrate has been well studied [117–119]. It has been observed that the aspect ratio of the nanorods increases as the seed size decreases and that, in the case of negatively charged seeds, the variation in aspect ratio is more pronounced compared to that with positively charged seeds. Although the use of silver nitrate enhances the yield of the gold rods, the aspect ratio of the product remains low when compared to rods prepared in the absence of silver nitrate [118, 120]. Amongst all anisotropic structures of gold, rods have attracted considerable attention due to their highly tunable optical properties. In general, their optical spectra have been characterized by two absorption peaks, corresponding to plasmon resonances in the transverse and longitudinal directions. The peak positions can be varied by varying the aspect ratio of the rods, which find useful applications in a variety of fields; for example, the absorption of gold nanorods in the NIR region is useful for cancer imaging and therapy [37, 38, 41, 42].

An insight into the growth mechanism of gold nanorods in the presence and absence of silver ions has provided valuable information [120–123]. An electric field-directed growth mechanism for gold nanorods in an aqueous surfactant solution, in the absence of Ag^+, suggests the binding of $AuCl_4$–CTAB micelles, followed by ascorbic acid reduction of Au^{3+} to Au^+ to form $AuCl_2^-$–CTAB micelles. Gold rod-shaped growth is further kinetically controlled by the collision between CTAB-protected seed particles and $AuCl_2^-$–CTAB micelles, which is found to be higher at the tips and thus facilitates growth in one direction. Similar observations were found by Murphy and colleagues for gold nanorods prepared using citrate-capped seeds, without silver ions. The group observed that a preferential adsorption of ions to the different crystal faces of gold ({100} or {110}) inhibited growth at those faces (Figure 11.18). The role of silver in gold nanorod growth has also been described by considering the contribution from Ag^0 underpotential deposition (UPD) on the growing gold nanorods. Ascorbic acid is capable of reducing Ag^+ at the growing gold nanorod surface at a potential less than its standard reduction potential, so as to form monolayers or submonolayers of Ag^0. It was found that nanorods grown using CTAB-protected gold seeds in the presence of Ag^+ bear Au{110} faces on the sides of the rods and {100} faces on the ends. A greater positive shift in potential for silver UPD on gold surfaces is observed on {110} surfaces compared to the {100} or {111} faces, which leads to a faster deposition of silver on the sides of the rods ({110} facets) than on the ends ({100} facets). This is followed by strong CTAB binding which further inhibits gold growth on the sides of the rods and leads to a preferential growth of gold at the ends. A pictorial representation of the proposed mechanism of growth of gold nanorods in the presence of silver ions is shown in Figure 11.19 [122].

It has also been reported that long-chain surfactants produce longer rods with the higher yields than do those with short chains. The mechanism of formation of gold nanorods in a surfactant medium has been well studied [124, 125], the proposal being that the surfactant head groups can selectively bind to the specific crystallographic facets of the seeds or the growing rods. The 'tail' parts of the

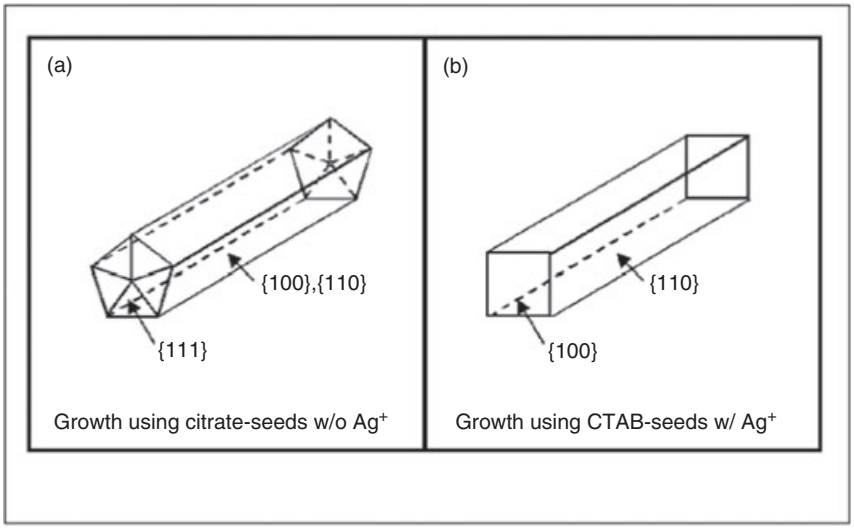

Figure 11.18 Schematic of three-dimensional morphology of gold nanorods prepared using: (a) citrate-capped seeds without Ag^+; (b) CTAB-capped seeds in the presence of Ag^+. Reproduced with permission from Ref. [122]; © 2006 American Chemical Society.

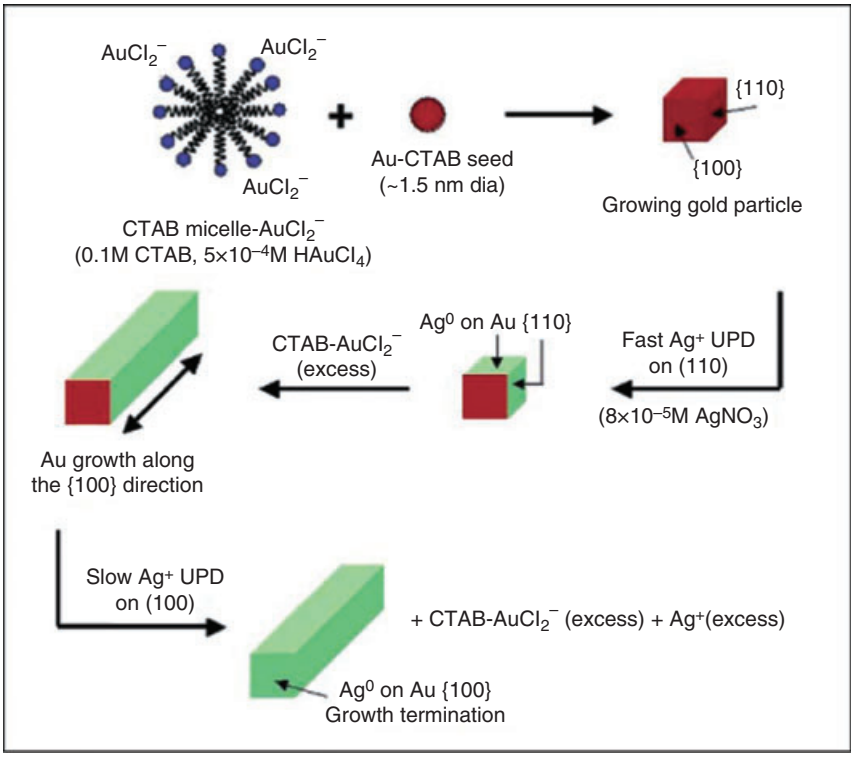

Figure 11.19 Schematic for the mechanism of nanorod growth from CTAB-protected gold seed particles in the presence of Ag^+. Reproduced with permission from Ref. [122]; © 2006 American Chemical Society.

surfactant can then form a bilayer structure with each other through van der Waals interactions, which play an important role in the structural design of nanorods. The growth of gold nanorods has also been reported [126] using the surfactants cetyltripropylammonium bromide (CTPAB) and cetyltributylammonium bromide (CTBAB), both of which have larger headgroups than CTAB and cetyltriethylammonium bromide (CTEAB). In a systematic comparison of nanorod growth using the four surfactants, the average aspect ratio of the Au nanorods increased and the nanorod growth rate decreased as the size of the headgroup became larger. The reason for the headgroup size-dependent effect on nanorod growth was due to a higher stability of the bilayers formed on the nanorod surfaces by surfactants with larger headgroups.

The direct, high-yield synthesis of high-aspect ratio gold nanorods, using a modified seed-mediated synthesis and the addition of nitric acid, has been demonstrated [127, 128]. In this approach, the citrate-capped gold seeds yielded 60–70% of nanorods with an average aspect ratio of 21–23, whereas the CTAB-capped gold seeds yielded 90% nanorods with an average aspect ratio of 19. A TEM image of the gold nanorods is shown in Figure 11.20. When using the CTAB-capped gold seeds, nanoplate formation could be reduced at the early stages of gold nanorod growth. The role of nitric acid proved to be crucial as it forms cetyltrimethylammonium nitrate (CTAN) in the reaction medium; micelles formed by CTAN showed not only a larger aggregation number and size than those formed by CTAB, but also a greater elongation effect compared to micelles formed in the absence of nitric acid.

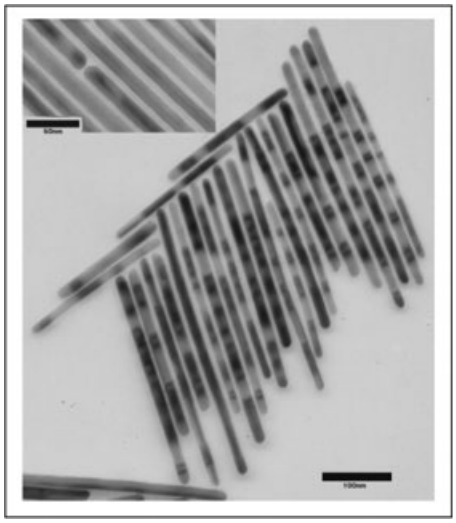

Figure 11.20 TEM image of the high-aspect-ratio gold nanorods. Reproduced with permission from Ref. [128]; © 2007 American Chemical Society.

A new method of producing gold nanowires by controlling the volume of the growth solution has been reported [129]. Here, a structural analysis clearly showed the shape to evolve from fusiform nanoparticles to 1-D rods, with nanorod shape and length being controlled by the successive addition of growth solution to the seed solution. In this way the nanorod length could be extended to 2 μm, and the aspect ratio to ~70. This investigation included a procedure whereby the [growth solution]:[seed] ratio was held constant during the reaction and played an important role in determining the final product. The evolution of shape was found to depend heavily on the volume of growth solution added. Although many methods have been developed for creating gold nanorods using a seed-mediated approach, they cannot be discussed here, for reasons of space limitation. Hence, for further details the reader is directed to an excellent review [130].

Au Bipyramids A seed-mediated synthesis has been used to grow Au bipyramids in aqueous solutions, using cationic surfactants as stabilizing agents in the presence of $AgNO_3$ [131, 132]. The multiply twinned gold seeds are mainly responsible for the growth of elongated bipyramidal nanoparticles, by preserving the initial twinned structure in the final product with the defect-free deposition assisted by Ag(I). The structural characterization revealed that, the bipyramids are penta-fold twinned around the growth axis, with the side {100} facets tilted toward the {111} facets.

CTEAB has also been used as a stabilizing agent to grow Au bipyramids [133]. The SPR wavelengths of the resultant bipyramids can be varied from 700 to 1100 nm by changing the amount of seeds, relative to that of the Au precursor. The growth of Au bipyramids has been demonstrated by using cationic surfactants with different sizes of headgroup as stabilizing agents [134]; for example, growth using CTBAB led to the production of Au bipyramids with tunable longitudinal surface plasmon (LSP) wavelengths, in high yield. When the surface-plasmon properties of Au bipyramids were investigated using the finite-difference time-domain method, the extinction cross-sections and local electric-field enhancements of Au bipyramids were found to be larger than those of Au nanorods, which possess almost similar LSP wavelengths as those of Au bipyramids.

Thorny Gold Nanostructures Three-dimensional (3-D) thorny gold nanostructures have been developed using a seed-mediated growth approach [135], wherein control over the morphology (from sphere to thorny nanostructure) was achieved by introducing different amounts of Ag^+ ions into the reaction systems of $HAuCl_4$ and NH_2OH. The synthesis was carried out in the absence of templates and surfactants. A schematic representation of the synthetic strategy for thorny gold nanostructures is shown in Figure 11.21. At too-high concentrations, the number of nanothorns on each gold nanoparticle decreased, while the central parts of the 3-D gold nanostructures (the body) expanded. The formation and structural changes of the 3-D thorny gold nanoparticles can be explained by the deposition of AgCl precipitate on the surface of the gold nanoseeds. Moreover, complicated dendrimer-like structures can be achieved by a second growth, using the thorny

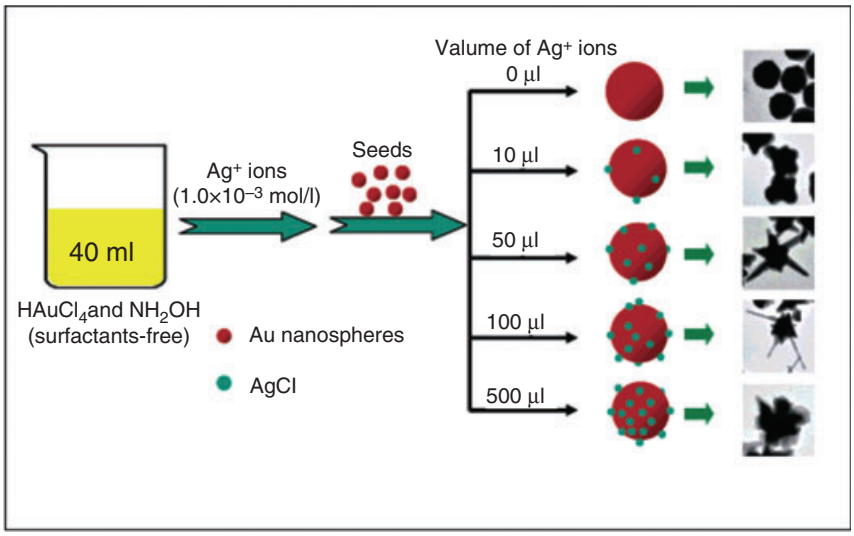

Figure 11.21 Schematic illustration of the synthetic strategy for the thorny gold nanostructures. Reproduced with permission from Ref. [135]; © 2007 American Chemical Society.

nanoparticles as seeds in the presence of Ag^+ ions (but an absence of surfactant and template).

Gold Tadpoles A simple temperature-reducing seeding approach for the synthesis of 'tadpole'-shaped gold nanoparticles in high yield, without additional capping agent or surfactant, has been reported [136]. The initial concentration of gold ions, the added seed colloids and the solution reaction temperature each played critical roles. Structural characterization of the nanoparticles at different stages of the reaction (using TEM and UV-visible spectrophotometry) revealed the formation of a special structure as a type of aggregation-based growth, including spherical aggregation at the boiling temperature and linear aggregation at reduced temperature. A pictorial representation of the formation of gold 'nanotadpoles' is shown in Figure 11.22. In another example, a simple aqueous-phase method for the synthesis of tadpole-shaped gold nanoparticles in large quantity by the reduction of chloroauric acid with trisodium citrate in the presence of a capping agent such as sodium dodecylsulfate (SDS) has been demonstrated [137]. Here, the nanoparticles possessed a well-defined shape with a maximal head width of 25.0 nm and a tail that tapered along the longitudinal axis of 115.0 nm. Both, SEM and UV-visible absorption measurements and electrophoresis experiments, showed the tadpoles to possess unusual optical and electrical properties.

Multishaped Gold Nanoparticles A novel method for the synthesis of multiple shapes of gold nanostructural architectures, such as rectangle, dogbone, peanut

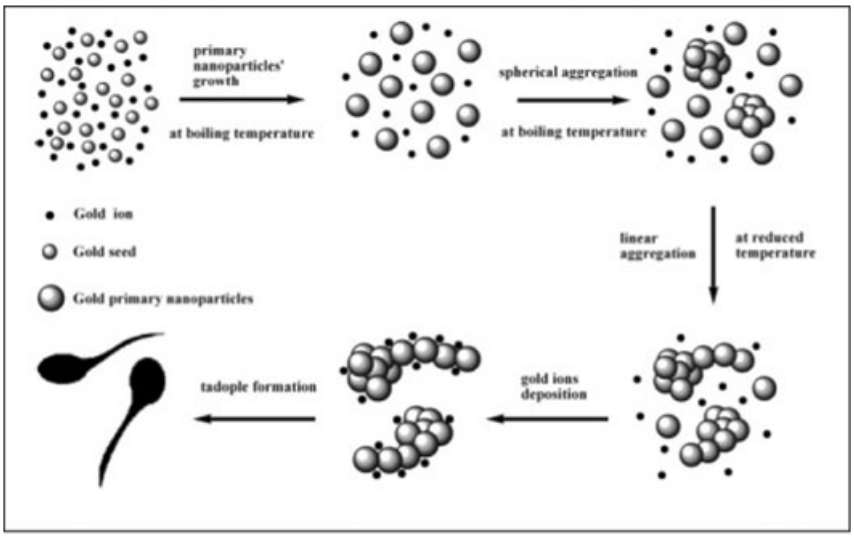

Figure 11.22 Schematic growth mechanism of gold nanotadpoles synthesized by the temperature-reducing seeding approach. Reproduced with permission from Ref. [136]; © 2007 American Chemical Society.

and branched multipods with corrugated surface, has been demonstrated by varying the pH of the reaction medium, in the presence of gold nanorods, which acted as seeds [138]. The different shapes were fabricated by varying the solution pH in the range of 3.6 to 9.6 from gold nanorods with aspect ratios of 2.9 and 2.1. The general methodology of the synthesis is shown schematically in Figure 11.23. The pH value of the growth solution is crucial in determining the shape of the final product as it strongly influences the reducing power of ascorbic acid.

A modified seed-mediated growth method to create multishaped gold nanoparticles (e.g. spherical, bipyramid, nanorod, nanowire, T- and star-shaped, triangular) by varying the experimental conditions has been demonstrated [139]. TEM images of gold nanoparticles synthesized in the presence and absence of silver ions and using a three-step seed-mediated process are shown in Figure 11.24. Structural variation in the products was observed with changes in the experimental conditions. In the absence of silver, gold nanorods with average lengths of ~59 nm and ~570 nm were obtained after the addition of second and third growth solutions, respectively. A high-resolution TEM analysis showed the structure of the shorter rods to be twinned along the long axis and to be isometric pentafold, twinned around their growth axis, for longer rods. In the presence of a mild (medium) concentration of silver ions (0.004 m*M*), gold nanorods of average length ~550 nm were formed via the formation of pentafold twinned gold bipyramids. The aspect ratio of the gold nanorods was found to be lower when synthesized in

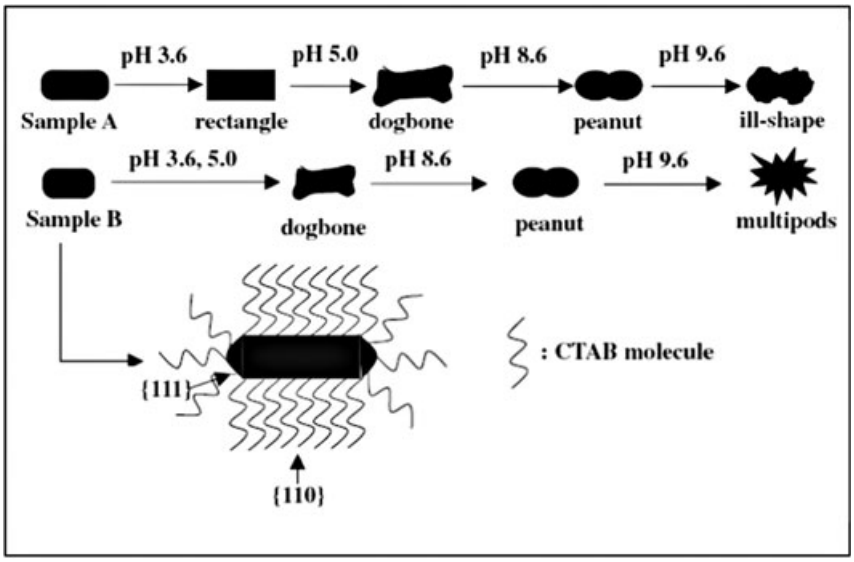

Figure 11.23 Evolution of different shapes from gold nanorod seeds at different pH values of the solution. Reproduced with permission from Ref. [138]; © 2005 Institute of Physics and IOP Publishing Limited.

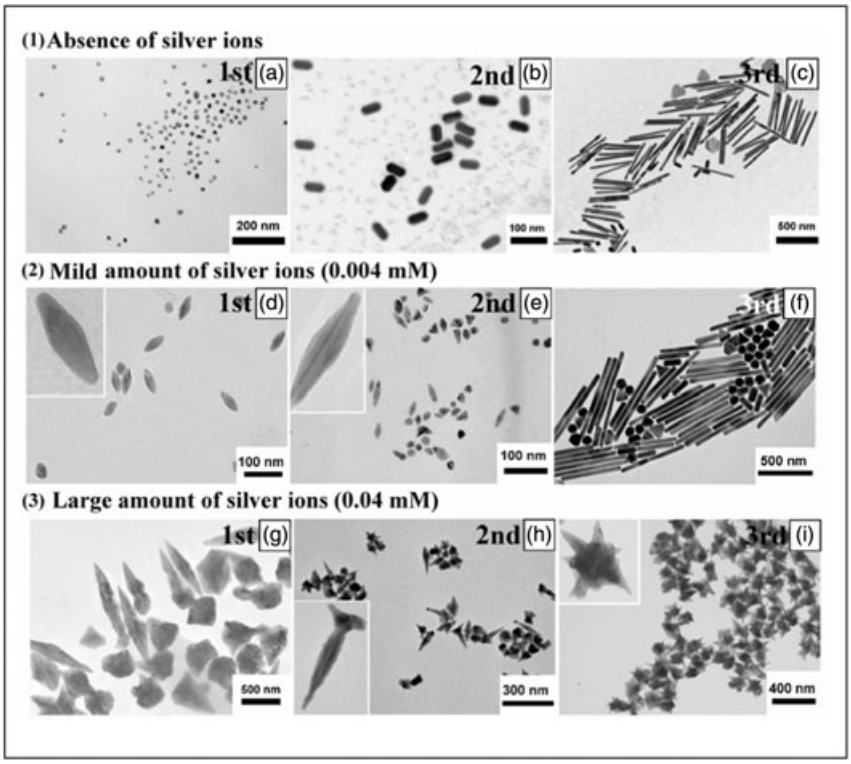

Figure 11.24 TEM images of gold resulting products synthesized at three different situations. (1) a–c: absence of silver ions; (2) d–f: presence of 0.004 m*M* silver ions; (3) g–i: presence of 0.04 m*M* silver ions. (Reproduced from Ref. [139].)

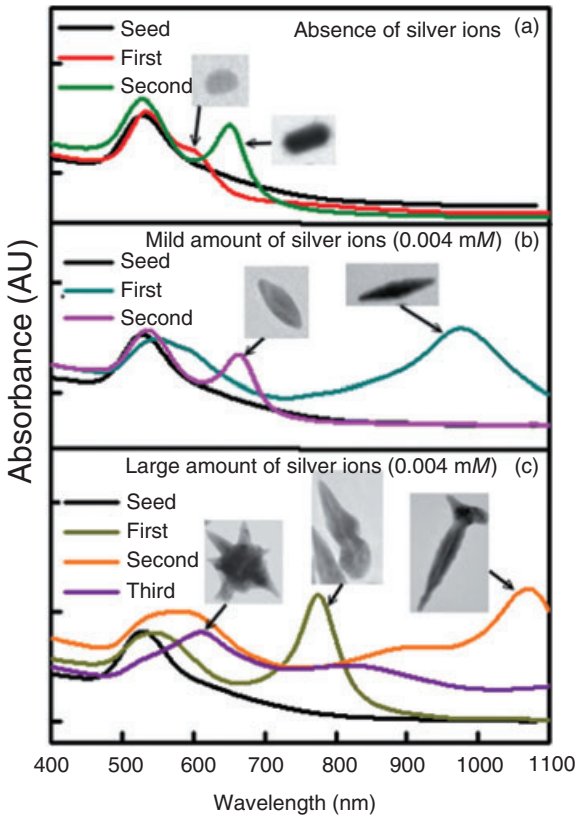

Figure 11.25 Extinction spectra of samples prepared at different conditions. (a) Absence of silver ions; (b) Presence of 0.004 m*M* silver ions; (c) Presence of 0.04 m*M* silver ions. (Reproduced from Ref. [139].)

the presence of silver. On the addition of excess growth solution (0.04 m*M*), multipod-shaped (T-shaped and branched-shaped) and star-shaped nanoparticle were formed. The absorption spectra of these gold nanomaterials, recorded under different conditions, are shown in Figure 11.25. Differences in the spectra for the various experimental conditions suggests the formation of different products; moreover, the variations in temperature over the range of 60–90 °C led to the production of triangular and hexagonal gold nanoparticles.

11.2.3.3.2 **The Case of Silver** Silver nanostructures have also attracted considerable attention owing to their highly anisotropic physico-chemical properties (similar to those of gold nanostructures). In this respect, a variety of shapes have been successfully produced using seed-mediated synthetic techniques.

Silver Nanorods and Nanowires A straightforward synthesis of silver nanorods and nanowires, with varying aspect ratio, has been demonstrated [140] wherein the chemical reduction of a silver salt was carried out in the presence of a silver seed, the micellar template CTAB, and NaOH. Ag seeds of 4 nm diameter were prepared by the chemical reduction of $AgNO_3$ by $NaBH_4$, in the presence of trisodium citrate to stabilize the nanoparticles. The concentration of seed and the Ag^+ concentration were shown to be the key factors for obtaining nanomaterials with a higher aspect ratio. For nanorods, the solution pH was slightly higher than the pK_a of the second proton of ascorbic acid (≈11.8), which suggested that the ascorbate dianion was a significant component of the solution. In the case of nanowires, the solution pH was slightly lower than this pK_a, suggesting that the monoanion of ascorbic acid (first $pK_a \approx 4.1$) was predominant in solution. The results of these studies suggested that complexes of silver ion with two different forms of the reducing agent, and with cationic CTAB and silver seed in solution, were important factors in the production of nanorods and nanowires.

Silver Nanoplates Truncated triangular silver nanoplates were prepared in large quantities, by reduction of silver ions with ascorbic acid on silver seeds in an alkaline solution of highly concentrated CTAB micelles [141]. The particles obtained were single crystals, with a (111) lattice plane as the basal plane, and were able to self-assemble into chain-like nanostructures, either by partial or close stacking of neighborhood nanoplates. In another example, the controlled synthesis of disk-like and flower-like monodisperse silver nanoplates was reported in high-yield [142]. This synthesis was carried out by reducing $[Ag(NH_3)_2]^+$ with ascorbic acid in the presence of silver seed at room temperature; the precursor $[Ag(NH_3)_2]^+$ was seen to control the reduction reaction in a mild manner.

11.2.3.4 **Other Methods**

A variety of alternative synthetic strategies has been created for the generation of metal nanoparticles, all of which make use of different ligands as stabilizers, reverse micelles, microemulsions, membranes, polyelectrolytes, and so on.

In recent years, the synthetic strategy of nanoparticles using different ligands such as thiols, amines and phosphines has gained in importance. The first report of the stabilization of AuNPs with alkanethiols was made by Mulvaney and Giersig, in 1993 [143]. A year later, the Brust–Schiffrin method for preparing dodecanethiol-stabilized nanoparticles, which described the synthesis of thermally and air-stable AuNPs of reduced dispersity and controlled size, attracted much attention among research groups in this field [144]. The Brust–Schiffrin technique utilizes thiol ligands that first bind strongly to gold and are then transferred to toluene by using tetraoctylammonium bromide (TOAB) as the phase-transfer reagent. Further reduction of the gold salt is carried out by $NaBH_4$ in the presence of dodecanethiol. Brust and coworkers subsequently extended this synthesis to *p*-mercaptophenol-stabilized AuNPs in a single-phase system [145], and this procedure in turn opened up an avenue for the synthesis of AuNPs, stabilized by a variety of functional thiol ligands [146, 147]. Although, today, many reports exist that are based on the Brust–

Schiffrin approach [148–152], the method has certain limitations with regards to the compatibility of the stabilizing thiol ligands with the other reagents.

Although, Schmid and coworkers reported the synthesis of triphenylphosphine-stabilized nanoparticles [153–155], the use of toxic chemicals such as benzene or diborane presents significant health and explosion hazards. In order to avoid this problem, Hutchison *et al.* demonstrated a safer and convenient, yet scalable, synthesis of high-quality 1.4 nm triphenylphosphine-stabilized gold nanoparticles, in which diborane was substituted with $NaBH_4$ and benzene with toluene [156]. This method makes use of a phase-transfer reagent (TOAB) to facilitate the transfer of chloroaurate ions from an aqueous solution to an organic phase (toluene) containing triphenylphosphine. The reduction is carried out using aqueous $NaBH_4$, delivered to the organic phase via complexation with TOAB. Whilst Hutchison's method provided a better yield of nanoparticles than Schmid's method, a major disadvantage lay in the tedious purification of the nanoparticle product.

A number of other reports have been made relating to the use of surfactants, reverse micelles, microemulsions, membranes and polyelectrolytes for the synthesis of noble metal nanoparticles [157–159]. This type of synthetic method generally involves a two-phase system with a surfactant, causing the formation of a microemulsion or micelle, and maintains a favorable microenvironment together with extraction of metal ions from aqueous phase to organic phase. In such cases, the surfactant not only acts as a stabilizer but also plays an important role in controlling crystal growth.

11.2.4
Bio-Based Synthetic Approach

The growing demand for environmentally benign, clean, nontoxic and eco-friendly techniques to synthesize nanoparticles has resulted in the development of biological systems capable of growing nanoscale structures. Many organisms, both unicellular and multicellular, are known to produce inorganic nanomaterials; some well-known examples of bioreduction and nanoparticle production include magnetostatic bacteria synthesizing magnetic nanoparticles [160], diatoms synthesizing siliceous materials [161] and S-layer bacteria producing gypsum and calcium carbonate layers. [162]. Biological systems have the unique ability that they can control the structure, phase and nanostructural topography of the inorganic crystals. Although biological materials have been used for many years in the remediation of toxic metals, their potential in the synthesis of nanoparticles has only recently come to light [163]. Today, a variety of inorganic nanomaterials have been synthesized using plants, algae, bacteria, yeast and fungi; a brief overview of the biological systems used to synthesize silver and gold nanostructures is provided in Tables 11.1 and 11.2, respectively [164–192].

11.2.4.1 Bacteria

An early example of nanoparticle synthesis using bacteria was reported by Beveridge and coworkers, that included the precipitation of colloidal gold of nanoscale

Table 11.1 Silver nanostructures prepared using a biosynthetic approach.

Type of biosystem	Name of biosystem	Average size/ size range obtained (nm)	Morphology of the nanoparticles	Year	Reference
Bacteria	*Pseudomonas stutzeri* AG259	200	Triangular and hexagonal	1999	[164]
	Lactobacillus strains, (common in buttermilk)	20–50	Hexagonal, triangular and other shapes	2002	[165]
	Klebsiella pneumoniae	–	–	2007	[166]
	Escherichia coli	–	–	2007	[166]
	Enterobacter cloacae (Enterobacteriacae)	–	–	2007	[166]
Fungi	*Phoma* Sp.3.2883	71.06 ± 3.46	Spherical	2003	[167]
	Fusarium oxysporum	5–15	–	2003	[168]
	Fusarium oxysporum	20–50	–	2005	[169]
	Phaenerochaete chrysosporium	–	Pyramidal	2006	[170]
	Aspergillus fumigatus	5–25	Spherical and triangular	2006	[171]
	Aspergillus flavus	8.92 ± 1.61	–	2007	[172]
Yeast	Yeast strain MKY3	2–5	Hexagonal	2003	[173]
Plants	Alfalfa	–	Spherical	2003	[174]
	Pelargonium graveolens (Geranium leaf)	16–40	Spherical and ellipsoidal	2003	[175]
	Azadirachta indica (Neem leaf broth)	5–35	Spherical and polydispersed	2004	[176]
	Aloe vera	15.2 ± 4.2	Spherical	2006	[177]
	Cinnamomum camphora (camphor leaf)	55–80	Triangular and spherical	2007	[178]
Algae	*Chlorella vulgaris*	–	Truncated triangular nanoplates; irregular particles	2007	[179]

Table 11.2 Gold nanostructures prepared using a biosynthetic approach.

Type of biosystem	Name of biosystem	Average size/ size range obtained	Morphology of the nanoparticles	Year	Reference
Bacteria	*Bacillus subtilis* 168	5–25 nm	Octahedral	1996	[180]
	Lactobacillus strains (common in buttermilk)	–	Spherical	2002	[165]
Fungi	*Verticillium* sp.	20 ± 8 nm	Spherical, triangular and hexagonal	2001	[181]
	Fusarium oxysporum	20–40 nm	Spherical and triangular	2002	[182]
	Colletotrichum sp.	8–40 nm	Spherical	2003	[183]
	Aspergillus niger	–	Triangular, hexagonal, spherical, spiral nanoplates, nanowalls, lamellar and spherical nanoagglomerates	2007	[184]
Actinomycetes	*Rhodococcus* sp.	5–15 nm	Spherical	2003	[185]
	Thermomonospora sp.	8 nm	Spherical	2003	[186]
Plant	Alfalfa	2–20 nm	Icosahedral	2002	[187]
	Alfalfa	2–20 nm	Spherical	2003	[174]
	Pelargonium graveolens (geranium leaves)	20–40 nm	Rods, flat sheets and triangular	2003	[183]
	Azadirachta indica (Neem leaf broth)	–	Triangular, hexagonal and spherical plates	2004	[176]
	Avena sativa (Oat)	–	Tetrahedral, decahedral, hexagonal, icosahedral multi-twinned, irregular and rods	2004	[188]
	Cymbopogon flexuosus (lemongrass plant)	0.05–1.8 μm	Triangular	2004	[189]
	Aloe vera	50–350 nm	Triangular	2006	[177]
	Sesbania drummondii	6–20 nm	Spherical	2007	[190]
	Cinnamomum camphora (camphor leaf)	15–100 nm	Triangular and spherical	2007	[178]
Algae	*Chlorella vulgaris*	–	Triangular, and hexagonal plates	2007	[191]
	Sargassum wightii Greville	8–12 nm	Thin planar	2007	[192]

dimensions within bacterial cells, by incubating the cells with Au^{3+} ions [180–193]. Others have shown that culture supernatants of *Klebsiella pneumonia, Escherichia coli* and *Enterobacter cloacae* (Enterobacteriacae) readily synthesize the silver nanoparticles within 5 min of contacting silver ions in a cell filtrate [166]. The advantage of the latter method is that the synthesis required much less time than have previously published biological methods.

11.2.4.2 **Plants**

The possibility of using live or dead plants to create nanoparticles has long been explored, with the first such report appearing in 2002, whereby gold nanoparticles ranging in size from 2 to 20 nm were formed in alfalfa seedlings [187]. Having grown the alfalfa plants in an $AuCl_4$-rich environment, XAS spectroscopy confirmed the gold present in the plant samples to be elemental. Likewise, atomic resolution analysis confirmed the nucleation and growth of Au nanoparticles within the alfalfa plant. Subsequently, it was shown that alfalfa also could form silver nanoparticles, when exposed to a silver-rich solid medium [174]. Sastry and colleagues showed that other plant species could also serve as useful media for nanoparticle synthesis, including geranium leaves, *Aloe vera* plant extract, Neem (*Azadirachta indica*) leaf broth, lemongrass plant (*Cymbopogon flexuosus*) extract and *Cinnamomum camphora* leaf [176–178, 189]. These studies also revealed that the concentration of reducing agent in the reaction mixture had a major impact on the yield and size of the final product, which in turn led to a significant control over the optical properties of the nanoparticulate solution. It was believed that the slow reduction of metal ions, in combination with the shape-directing effect of the plant extract constituents, were responsible for the formation of anisotropic nanoparticles in solution. Sharma and coworkers also demonstrated the uptake of large amounts of Au(III) ions by a leguminous shrub, *Sesbania drummondii*, with subsequent reduction of Au(III) ions to Au(0) inside the plant cells or tissues [190]. Moreover, the gold nanoparticle-bearing biomatrix of *Sesbania* has been further examined for its catalytic activity, aimed at reduce the hazardous and toxic pollutant, aqueous 4-nitrophenol. Most importantly, all of these reports have demonstrated the feasibility of a simple synthesis of nanoparticles from either dead or living plants.

11.2.4.3 **Fungi**

Fungi are considered to be extremely good candidates for the synthesis of nanoparticles, based on a number of advantages that include the secretion of large amounts of enzymes (this is mainly responsible for the reduction of metal ions), easy handling, economic viability and ease in scale-up of the process. Consequently, many reports have been made of nanoparticle syntheses using different types of fungi. Recently, Xie and coworkers [184] reported the use of different parts of the filamentous fungus, *Aspergillus niger*, such as cell surface (fungal biomass), secreted metabolic products (mycelia-free spent medium) and intracellular content (fungal extract), for the synthesis of gold nanocrystals with different morphologies (spherical, regular nanoplate, spiral nanoplate, nanowall, lamellar nanoagglomerate, spherical nanoagglomerate) at high yield. Xie's group noted that the shape and

size of the products could be controlled by using different parts of the *Aspergillus niger* system, and by varying the experimental conditions. Their results implied that proteins on the fungal cell walls and in the fungal extract were the primary biomolecules involved in the synthesis of gold nanocrystals. In contrast, the formation of gold nanoplates in the spent medium was mediated by an enzymatic reaction, with small molecules and enzymes serving as substrate and catalyst, respectively. The formation of these highly anisotropic structures was kinetically controlled, as shown by the dependence of both shape and size on environmental variables such as temperature and pH of the solution.

11.2.4.4 **Actinomycetes, Yeast and Algae**

Both, intracellular and extracellular syntheses of gold nanoparticles using actinomycetes, namely *Rhodococcus* sp. and *Thermomonospora* sp., have been described [185, 186]. Likewise, some reports have been made outlining the use of yeast [173] and algae [179, 191, 192] for the reduction of gold and silver ions.

The development of reliable and eco-friendly processes to synthesize metallic nanoparticles using natural resources represents an important step in the application of nanotechnology, with a variety of biomaterials having been used recently for nanoparticles synthesis. Due to the structural complexity of these biosystems, it is often difficult to understand the exact mechanism of synthesis, although in many cases the nucleation and growth of the inorganic structures are controlled by proteins and other biomacromolecules. Whilst the reduction of metal ions occurs via enzymatic processes, structural proteins are mainly responsible for the stabilization and shape control of the metal nanoparticles. The main concern when using biosystems in this role is the monodispersity of the particles and scaling-up of the process. However, if these problems can be overcome, a bio-based approach should be capable of competing with existing physical and chemical synthetic processes. Indeed, if this proves to be true, it would represent a major step in the 'green' synthesis of the nanomaterials, and perhaps even head us towards another industrial revolution.

11.3
Characterization of Anisotropic Nanostructures

It is important to study the fundamentals of growth processes, as an understanding of these aspects will lead to the development of novel material designs and increasingly sophisticated synthetic methods. The structural characterization of spherical and anisotropic nanostructures, along with the reaction intermediates, is essential in this regard. The most common techniques of characterization include UV-visible spectroscopy, X-ray diffraction and microscopic methods such as TEM and SEM. Since the majority of these have been described elsewhere in detail, we will at this point focus mainly on X-ray absorption spectroscopy, providing examples taken from our laboratory and the surface plasmon measurements of a single gold nanorod.

11.3.1
Plasmonic Measurements of Single Gold Nanorod

It is well known that, surface plasmons contribute to a variety of novel applications in nano-optics and localized field enhancement for near-field measurements [194]. In this respect it is crucial to recognize the individual optical properties of anisotropic nanostructures, and especially the relationship between the incident light and induced SPR modes on each single nanorod. Much research effort has been devoted to identify the optical properties of silver and gold nanorod arrays, by using optical extinction spectroscopy and apertured-type scanning near-field optical microscopy (SNOM). Unfortunately, the scanning probes in SNOM cause some interactions with metallic nanorods, and thus have some influence on the dispersion characteristics. Recently, possible interference was avoided by using polarization-contrast microscopy coupled with atomic force microscopy (AFM) to attain far-field optical images of the multipolar SPR modes of a single gold nanorod, as shown in Figure 11.26 [195]. The far-field scattering image of a gold

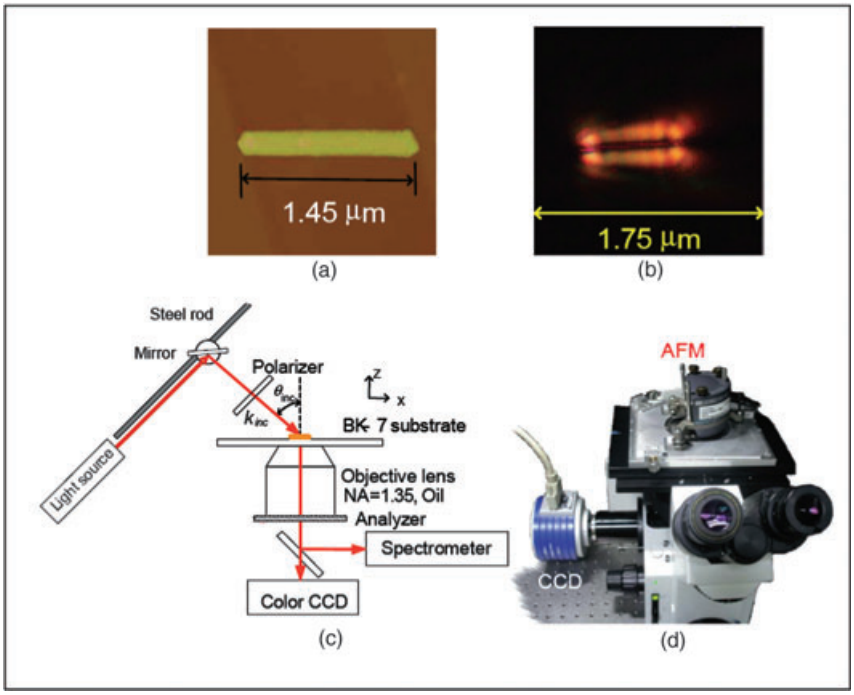

Figure 11.26 AFM image of (a) a single gold nanorod; (b) a far-field image of the single gold nanorod; (c, d) Schematic and photograph of the experimental set-up. Reproduced with permission from Ref. [195]; © 2007 The Optical Society of America.

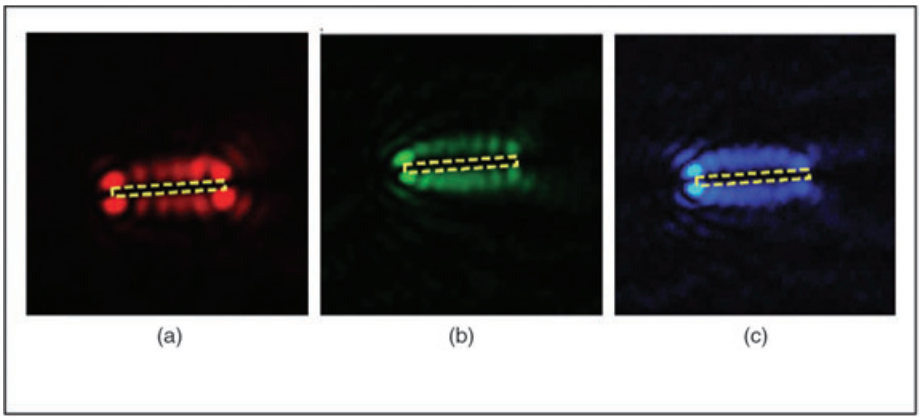

Figure 11.27 Far-field images of SPR modes of the same single gold nanorod for various incident laser light. (a) Red (658 nm); (b) Green (532 nm); (c) Blue (488 nm). Reproduced with permission from Ref. [195]; © 2007 The Optical Society of America.

nanorod in Figure 11.26b was recorded simultaneously with an AFM image by using P-polarized (parallel to the nanorod) white light as the incident source.

P-polarized red (658 nm), green (532 nm) and blue (488 nm) laser light was also used as the incident light source instead of white light source, as shown in Figure 11.27a–c, respectively, with the analyzer in the *y*-direction. The modulated standing modes for the three wavelengths can be clearly seen, with the dashed line representing the location of the measured single gold nanorod. The wave vector of longitudinal SPR modes was obtained from modulated standing modes resulting from the interference of longitudinal average distance of adjacent beats on this single gold nanorod. A linear relationship between the wave vectors of the incident light and the induced SPR modes was observed. These results demonstrate a feasible way of acquiring plasmonic optical properties from an individual single gold nanorod. In addition, polarization-contrast microcopy is capable of efficiently reducing the optical background and thus providing a simple, inexpensive and easily realized way to observe the plasmonic properties of anisotropic metallic nanoparticles. Similar experiments may be extended to acquire the individual optical properties of multishaped silver and gold nanostructures in complicated nanodevices of plasmonic nanophotonics.

11.3.2
XANES Analysis of Gold Nanoparticles

X-ray crystallography is an extremely powerful structural probe, as it provides a description of the structure in the solid state. In order to precisely understand the reaction, it is essential to confirm that the crystallographic structure accurately

represents the molecule of interest, when it is in the solution phase. One promising way to achieve this goal involves XAS techniques [196–201]. Studies of the extended X-ray absorption fine structure (EXAFS) have been particularly useful in providing local structural information about the noncrystalline state, while X-ray absorption near-edge structure (XANES) can be used to characterize the chemical bonding environment of the absorbing atoms and to derive the effective oxidation state of the metal atoms. The characterization of anisotropic gold nanostructures, using XAS techniques, is discussed below.

X-ray absorption spectroscopic analysis was carried out for different stages of the seed-mediated growth of gold nanoparticles in our laboratory, in order to understand the mechanism involved. Figure 11.28 shows the XANES Au L_3-edge analysis of the samples at each stage of the synthesis, which provide the absorption spectra of gold during the reaction [202]. The spectrum recorded after the addition of CTAB to the precursor ($HAuCl_4$) showed a significant decrease in the white line intensity. The L_3-edge white line intensity depends on the electronic charge transfer between the absorbing atoms and ligands. This result indicated a certain degree of electron transfer from bromide to gold; such transfer had occurred on account of the ligand exchange of chloride ions with bromide ions from CTAB. When ascorbic acid (as reducing agent) was added into the growth solution, a striking change occurred in the spectrum, with the white line intensity considerably decreased. Such a decrease in intensity was attributed to the fact that Au^{3+} ions were reduced to Au^0 and/or Au^{1+} by ascorbic acid. Nevertheless, it is believed that most of the Au^{3+} ions were reduced to Au^0 atoms, as the stoichiometry of the reagents was such that the amount of ascorbic acid was sufficient to reduce all of the gold salt in the solution. When seeds were mixed with growth solution, the near-edge structure was similar to that of gold foil, whereas the intensity of the

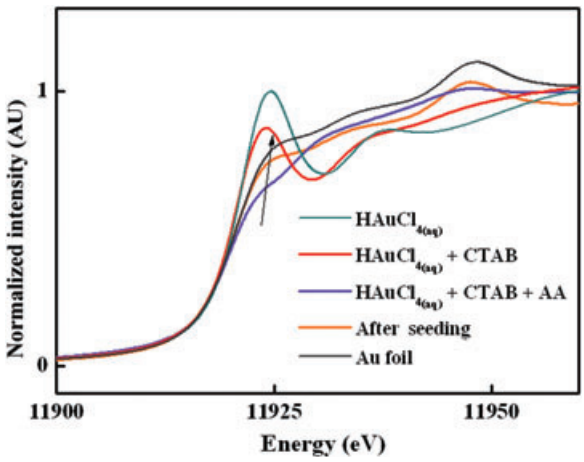

Figure 11.28 XANES spectra of Au L_3-edge for each reaction step. AA = ascorbic acid. Reproduced with permission from Ref. [202]; © 2007 American Chemical Society.

solution after seeding was clearly lower than that of gold foil, indicating a structural similarity of the product with the bulk gold.

Figure 11.29 shows the Fourier transform (FT) of the Au L_3-edge EXAFS spectra of gold at different stages of the reaction. As the solution of $HAuCl_4$ was mixed with CTAB, a strong peak appeared in the FT before phase correction, which could be attributed to the Au-complex change from ~1.9 to ~2.1 Å. This indicated that the first shell around the Au^{3+} atoms was Br atoms rather than Cl atoms. When ascorbic acid was added, the Au^{3+} atoms were reduced to Au^0, with an increase in the radius of the Au atoms. Thus, the peak appearing at ~2.6 Å before phase correction had arisen from the Au–Au scattering in ultrafine gold nanoparticles. On the other hand, the observed bond-length contraction with decreasing cluster size could also be explained by the redistribution of charge. The number of nearest-neighbor atoms was significantly less on the surface than in the bulk, which led to a reduction in repulsive interactions between nonbonding electron pairs. This resulted in a contraction of the nearest-neighbor distance, which forms the basis

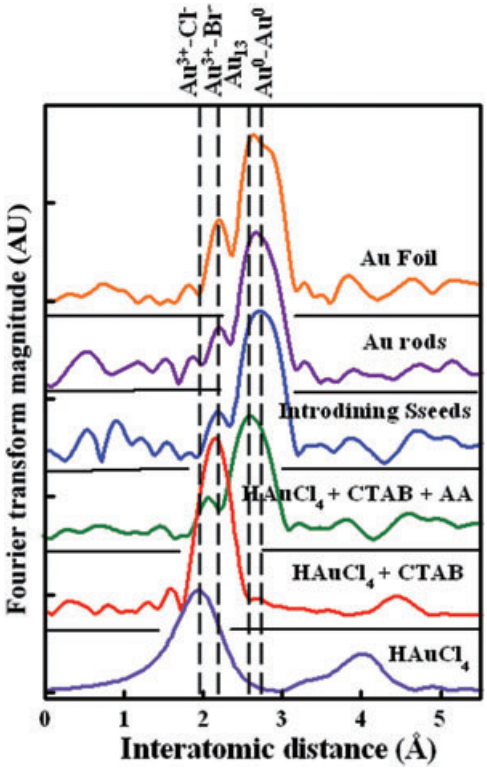

Figure 11.29 Fourier transforms of Au L_3-edge EXAFS spectra for each reaction stage. AA = ascorbic acid. Reproduced with permission from Ref. [202]; © 2007 American Chemical Society.

of both EXAFS and XANES characterization of nanostructures. The addition of seed to the growth solution showed a strong peak at ~2.7 Å, due to the scattering of Au atoms. Seed particles are believed to provide active sites for subsequent crystal growth. The peak corresponding to the scattering of the Au–Au path became sharper than after the addition of ascorbic acid, and suggested the growth of gold nanocrystals.

11.3.3 Theoretical Simulation of XANES

The structure and geometry of gold during the reaction was demonstrated more accurately by a theoretical simulation study of XANES. Theoretical simulations based on the *ab initio* relativistic self-consistent code FEFF8, have been used to show that XANES can provide considerable insight into the morphology of gold. Figure 11.30a shows the experimental data of $HAuCl_4$ and theoretical simulation spectrum based on the model in which $AuCl_4^-$ has a square-planar structure (D_{4h}). The theoretical simulation spectrum was observed to match well with the experimental spectrum, and the computed value was found to be ~2.39 Å – slightly higher than the value obtained from the quantum chemical calculation (2.36 Å) [203]. The higher value for the Au–Cl bond can be attributed to a weakening of the overlap between the orbitals of gold and those of chloride, since the $AuCl_4^-$ used in this study was not in solid phase. Rather, it may be surrounded by solvent molecules (e.g. H_2O). Figure 11.30b shows the experimental data of a mixture of $HAuCl_4$ and CTAB, and a theoretical simulation spectrum based on the model in which $AuBr_4^-$ has a square-planar structure (D_{4h}). As the CTAB was added into the $HAuCl_4$ solu-

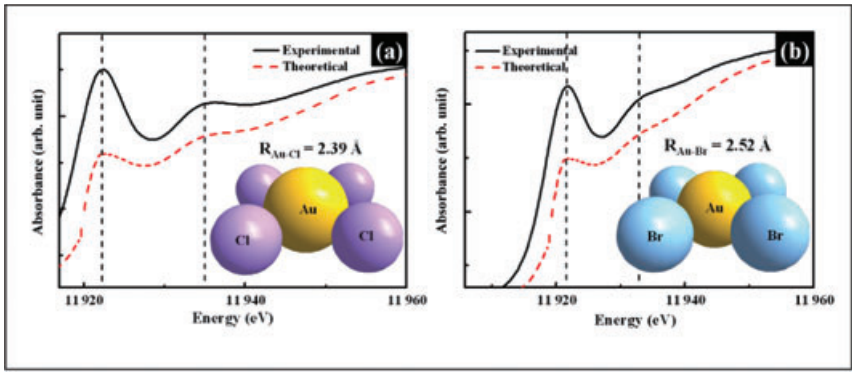

Figure 11.30 (a) Comparison between experimental spectrum and that calculated with FEFF for the Au–Cl complex; (b) Comparison between experimental spectrum and that calculated with FEFF for the Au–Br complex. Reproduced with permission from Ref. [202]; © 2007 American Chemical Society.

tion, a ligand exchange occurred and simultaneously chloride ions were replaced with bromide ions. The simulation was operated using a similar model to that of $AuCl_4^-$ molecule, and the calculated results showed the bond length for the Au–Br bond to be ~2.52 Å. This increase in bond length (0.13 Å) could be attributed to the difference in atomic radius between chloride and bromide (0.12 Å). As a result, bromide at a very high concentration (100-fold that of chloride) should strongly affect the course of the reaction and the growth of gold nanostructures.

Figure 11.31 shows the experimental data after the addition of ascorbic acid, and the theoretical simulation spectrum based on the model considering that gold atoms have a fcc structure $(Fm\bar{3}m)$. In order to investigate the cluster size effects on XANES spectra, several calculations were performed with increasing number of atoms. As shown in Figure 11.31a, the intensity of the white line varied slowly with the size of the cluster (indicated by an arrow). This is a direct consequence of the existence of unequivalent sites in small clusters, and concludes that a size effect is directly observable on the white line. Most interestingly, the intensity of the white line was increased by the addition of ascorbic acid to the gold foil (as indicated by an arrow in Figure 11.28), which is consistent with the evolution of the clusters size effect, generated by theoretical simulation. The simulation spectra exhibit an additional peak located at about 11980 eV, the intensity of which was found to increase with cluster size. Thus, a simulation spectrum of Au_{13} displays

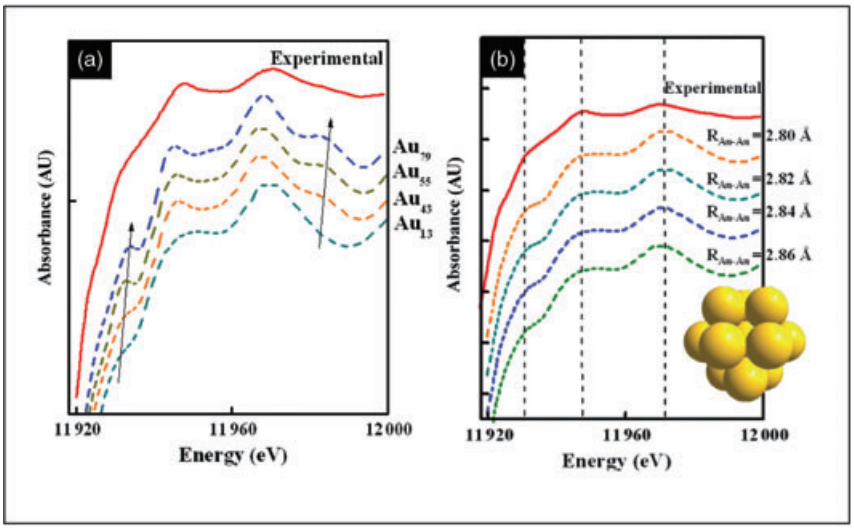

Figure 11.31 (a) Size effect on the XANES spectra for Au_{13}, Au_{43}, Au_{55}, and Au_{78}; (b) XANES spectra as calculated with FEFF for a 13-atom cluster of gold with different interatomic distances (R_{Au-Au} = 2.80 Å, 2.82 Å, 2.84 Å and 2.86 Å). Reproduced with permission from Ref. [202]; © 2007 American Chemical Society.

a feature similar to the experimental results, and the numerical simulation emphasized the formation of ultrafine clusters at this stage.

A set of calculations for 13-atom clusters of gold with different Au–Au interatomic distances was performed, in order to evaluate the modifications derived from a slight variation in the interatomic distance. It was clear that the position of resonance peaks slightly varied with the change of Au–Au bond length (Figure 11.31b), with a shift towards higher energies being attributed to a smaller interatomic distance. The results obtained for the effects of interatomic distance in XANES were in reasonable agreement, both in amplitude and relative splitting, with those of a simulation with $R_{Au\text{-}Au} = 2.82$ Å, implying the occurrence of structural contraction. Consequently, the XANES features could not be explained only in terms of cluster size; rather, the interatomic distance must also be taken into account. Nonetheless, there were clear numerical trends in the XANES analysis, which provided a semi-quantitative insight into the design of these gold cluster materials. The simulation of XANES for gold provided clear and accurate evidence verifying the presence of Au_{13} clusters, with structural contraction.

The evolution of gold has been summarized in Figure 11.32, based on the above observations. When the $HAuCl_4$ solution was mixed with CTAB as surfactant, chloride ions were replaced by bromide ions to form complex $(AuBr_4^-)$ with gold ions (Au^{3+}). As ascorbic acid was added into the $AuBr_4^-$ solution, the majority of gold ions (Au^{3+}) was reduced to Au^0 atoms and aggregated to form Au_{13} clusters. The surfactant (CTAB) acted as a stabilizer to prevent the Au_{13} clusters from further growth. After introducing the seeds into the reaction system, the Au_{13} clusters grew on the surfaces of seeds, while the presence of nanoparticles as seeds significantly enhanced the growth steps, rather than the nucleation steps. The surfactant mainly acted as a growth director to serve a 1-D environment, by the formation of rod-like micelles. The hydrophobic tail portion of the CTAB formed a bilayer on the rods, whereas the cationic headgroups of the first monolayer were

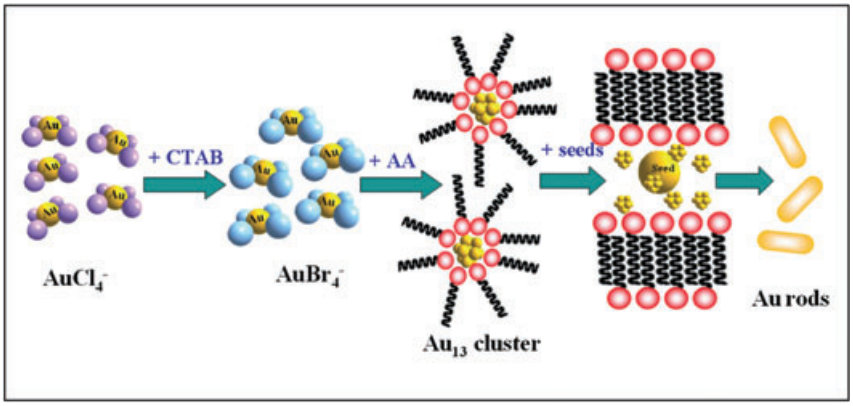

Figure 11.32 The evolution of gold at an early stage. Reproduced with permission from Ref. [202]; © 2007 American Chemical Society.

facing towards the gold surface. As a consequence of this anisotropic growth, 1-D gold nanorods were formed under these experimental conditions.

11.4 Conclusions and Future Perspectives

The ability to tailor the shapes and sizes of inorganic nanostructures is critical for modern materials chemistry, because the intrinsic properties of most nanostructures depend heavily on their shape and size. During the past few years, considerable progress has been made in the synthesis of monodisperse and well-defined structured nanoparticles. In this chapter, we have discussed a number of useful parameters that can be tuned to control the formation of anisotropic silver and gold nanostructures with a specific shape in a solution-phase synthesis. The shapes of the resultant nanostructures can be controlled by manipulating the crystallinity of seeds and the growth rates of different crystallographic facets. The crystallinity of a seed can be controlled by manipulating the reduction rate, whereas growth rates can be controlled with a capping agent, which can alter the surface energy through selective chemisorption. By using the synthetic methods described herein, a variety of well-defined anisotropic shapes of silver and gold nanoparticles can be acquired. Moreover, the methodology established for the silver and gold systems can be directly extended to other fcc metals such as Pt and Pd. In future, the discovery of a novel capping agent will be necessary to produce unconventional anisotropic nanostructures. Research in this area is rapidly expanding worldwide, and is already having a significant commercial impact, which is expected to provide a major driving force for the industry in the future, offering potential solutions to many problems. Although, for many years, this type of research has been conducted globally in the field of nanoscience, it may require a few more years to change the complete scenario at the industrial level.

Acknowledgments

The authors would like to thank the National Science Council of the Republic of China (contract numbers: NSC 96-2120-M-002-019, NSC 96-2120-M-001-009 and NSC 96-2120-M-002-017) and the Industrial Technology Research Institute for financially supporting this research.

References

1 El-Sayed, M.A. (2001) Some interesting properties of metals confined in time and nanometer space of different shapes. *Accounts of Chemical Research*, **34**, 257–64.

2 Burda, C., Chen, X., Narayanan, R. and El-Sayed, M.A. (2005) Chemistry and properties of nanocrystals of different shapes. *Chemical Reviews*, **105**, 1025–102.

3 Jain, P.K., Huang, X., El-Sayed, I. and El-Sayed, M.A. (2007) Review of some interesting surface plasmon resonance-enhanced properties of noble metal nanoparticles and their applications to biosystems. *Plasmonics*, **2**, 107–18.

4 Hao, E., Schatz, G.C. and Hupp, J.T. (2004) Synthesis and optical properties of anisotropic metal nanoparticles. *Journal of Fluorescence*, **14**, 331–41.

5 Sun, S., Murray, C.B., Weller, D., Folks, L. and Moser, A. (2000) Monodisperse FePt nanoparticles and ferromagnetic FePt nanocrystal superlattices. *Science*, **287**, 1989–92.

6 Nirmal, M. and Brus, L. (1999) Luminescence photophysics in semiconductor nanocrystals. *Accounts of Chemical Research*, **32**, 407–14.

7 Jacobs, K., Zaziski, D., Scher, E.C., Herhold, A.B. and Alivisatos, A.P. (2001) Activation volumes for solid-solid transformations in nanocrystals. *Science*, **293**, 1803–6.

8 Michler, P., Imamoglu, A., Mason, M.D., Carson, P.J., Strouse, G.F. and Buratto, S.K. (2000) Quantum correlation among photons from a single quantum dot at room temperature. *Nature*, **406**, 968–70.

9 Noguez, C. (2007) Surface plasmons on metal nanoparticles: the influence of shape and physical environment. *Journal of Physical Chemistry C*, **111**, 3806–19.

10 Murray, C.B., Kagan, C.R. and Bawendi, M.G. (1995) Self-organization of CdSe nanocrystallites into three-dimensional quantum dot superlattices. *Science*, **270**, 1335–8.

11 Michalet, X., Pinaud, F.F., Bentolila, L.A., Tsay, J.M., Doose, S., Li, J.J., Sundaresan, G., Wu, A.M., Gambhir, S.S. and Weiss, S. (2005) Quantum dots for live cells, in vivo imaging, and diagnostics. *Science*, **307**, 538–44.

12 Simo, J.M., Joven, J., Cliville, X. and Sans, T. (1994) Automated latex agglutination immunoassay of serum ferritin with a centrifugal analyzer. *Clinical Chemistry*, **40**, 625–9.

13 Bangs, L.B. (1996) New developments in particle-based immunoassays: introduction. *Pure and Applied Chemistry*, **68**, 1873–9.

14 Forster, S. and Antonietii, M. (1998) Amphiphilic block copolymers in structure-controlled nanomaterial hybrids. *Advanced Materials*, **10**, 195–217.

15 Adres, R.P., Bielefeld, J.C., Henderson, J.I., Janes, D.B., Kolagunta, V.R., Kubiak, C.P., Mahoney, W.J. and Osifchinm, R.G. (1996) Self-assembly of a two-dimensional superlattice of molecularly linked metal clusters. *Science*, **273**, 1690–3.

16 Alivasators, A.P. (1996) Semiconductor clusters, nanocrystals, and quantum dots. *Science*, **271**, 933–7.

17 Schmid, G. (1992) Large clusters and colloids. Metals in the embryonic state. *Chemical Reviews*, **92**, 1709–27.

18 Lewis, L.N. (1993) Chemical catalysis by colloids and clusters. *Chemical Reviews*, **93**, 2693–730.

19 Johnson, B.F.G. (1999) From clusters to nanoparticles and catalysis. *Coordination Chemical Reviews*, **190**(192), 1269–85.

20 Kim, S.-W., Son, S.U., Lee, S.S., Hyeon, T. and Chung, Y.K. (2001) Colloidal cobalt nanoparticles: a highly active and reusable Pauson–Khand catalyst. *Chemical Communications*, 2212–13.

21 Son, S.U., Lee, S.I., Chung, Y.K., Kim, S.-W. and Hyeon, T. (2002) The first intramolecular Pauson-Khand reaction in water using aqueous colloidal cobalt nanoparticles as catalysts. *Organic Letters*, **4**, 277–9.

22 Bönnemann, H., Brijoux, W., Siepen, K., Hormes, J., Franke, R., Pollmann, J. and Rothe, J. (1997) Surfactant stabilized palladium colloids as precursors for cis-selective alkyne-hydrogenation catalysts. *Applied Organometallic Chemistry*, **11**, 783–96.

23 Weddle, K.S., Aikin, J.D. and Finke, R.G. (1998) Rh(0) nanoclusters in benzene hydrogenation catalysis: kinetic and mechanistic evidence that a putative $[(C_8H_{17})_3NCH_3]^+[RhCl_4]^-$ ion-pair catalyst is actually a distribution of Cl^- and $[(C_8H_{17})_3NCH_3]^+$ stabilized Rh(0) nanoclusters. *Journal of the American Chemical Society*, **120**, 5653–66.

24 Reetz, M.T. and Lohmer, G. (1996) Propylene carbonate stabilized nanostructured palladium clusters as

catalysts in heck reactions. *Chemical Communications*, 1921–2.
25 Klingelhofer, S., Heitz, W., Greiner, A., Oestreich, S., Forster, S. and Antonietti, M. (1997) Preparation of palladium colloids in block copolymer micelles and their use for the catalysis of the heck reaction. *Journal of the American Chemical Society*, **119**, 10116–20.
26 Reetz, M.T. and Westermann, E. (2000) Phosphane-free palladium-catalyzed coupling reactions: the decisive role of Pd nanoparticles. *Angewandte Chemie–International Edition in English*, **39**, 165–8.
27 Zhao, M. and Crooks, R.M. (1999) Homogeneous hydrogenation catalysis with monodisperse, dendrimer-encapsulated Pd and Pt nanoparticles. *Angewandte Chemie–International Edition in English*, **38**, 364–6.
28 Colvin, V.L. (2003) The potential environmental impact of engineered nanomaterials. *Nature Biotechnology*, **21**, 1166–70.
29 Service, R.F. (2003) American chemical society meeting: nanomaterials show signs of toxicity. *Science*, **300**, 243.
30 Schmid, G. (2004) *Nanoparticles: from Theory to Application*, Wiley-VCH Verlag GmbH, Weinheim.
31 Soloviev, M. (2007) Nanobiotechnology today: focus on nanoparticles. *Journal of Nanobiotechnology*, **5**(11), 1–3.
32 Hu, M., Chen, J., Li, Z.-Y., Au, L., Hartland, G.V., Li, X., Marquez, M. and Xia, Y. (2006) Gold nanostructures: engineering their plasmonic properties for biomedical applications. *Chemical Society Reviews*, **35**, 1084–94.
33 Eustis, S. and El-Sayed, M.A. (2006) Why gold nanoparticles are more precious than pretty gold: Noble metal surface plasmon resonance and its enhancement of the radiative and nonradiative properties of nanocrystals of different shapes. *Chemical Society Reviews*, **35**, 209–17.
34 Daniel, M.-C. and Astruc, D. (2004) Gold nanoparticles: assembly, supramolecular chemistry, quantum-size-related properties, and applications toward biology, catalysis, and nanotechnology. *Chemical Reviews*, **104**, 293–346.
35 Ghosh, S.K. and Pal, T. (2007) Interparticle coupling effect on the surface plasmon resonance of gold nanoparticles: from theory to applications. *Chemical Reviews*, **107**, 4797–862.
36 Govorov, A.O. and Richardson, H.H. (2007) Generating heat with metal nanoparticles. *Nanotoday*, **2**, 30–8.
37 Jain, P.K., El-Sayed, I. and El-Sayed, M.A. (2007) Au nanoparticles target cancer. *Nanotoday*, **2**, 18–29.
38 Durr, N.J., Larson, T., Smith, D.K., Korgel, B.A., Sokolov, K. and Ben-Yakar, A. (2007) Two-photon luminescence imaging of cancer cells using molecularly targeted gold nanorods. *Nano Letters*, **7**, 941–5.
39 Kim, D., Park, S., Lee, J.H., Jeong, Y.Y. and Jon, S. (2007) Antibiofouling polymer-coated gold nanoparticles as a contrast agent for in vivo X-ray computed tomography imaging. *Journal of the American Chemical Society*, **129**, 7661–5.
40 El-Sayed, I., Huang, X. and El-Sayed, M.A. (2006) Selective laser photo-thermal therapy of epithelial carcinoma using anti-EGFR antibody conjugated gold nanoparticles. *Cancer Letters*, **239**, 129–35.
41 Huang, X., El-Sayed, I., Qian, W. and El-Sayed, M.A. (2006) Cancer cell imaging and photothermal therapy in the near-infrared region by using gold nanorods. *Journal of the American Chemical Society*, **128**, 2115–20.
42 Eghtedari, M., Oraevsky, A., Copland, J.A., Kotov, N.A., Conjusteau, A. and Motamedi, M. (2007) High sensitivity of in vivo detection of gold nanorods using a laser optoacoustic imaging system. *Nano Letters*, **7**, 1914–18.
43 Elechiguerra, J.L., Burt, J.L., Morones, J.R., Camacho- Bragado, A., Gao, X., Lara, H.H. and Yacaman, M.J. (2005) Interaction of silver nanoparticles with HIV-1. *Journal of Nanobiotechnology*, **3**(6), 1–10.
44 Cnmo, E.R.D.C. (2003) Viral pathogens and severe acute respiratory syndrome: oligodynamic Ag+ for direct immune intervention. *Journal of Nutritional and Environmental Medicine*, **13**, 109–18.

45 Nanotechnology Consumer Products Inventory at http://www.nanotechproject.org/44 (accessed 1 March 2008).

46 Hori, K., Martin, T.G. and Rainey, P. (2002) Believe it or not–silver still poisons. *Veterinary and Human Toxicology*, **44**, 291-2.

47 http://ww2.samsung.co.za/silvernano/silvernano/ (accessed 1 March 2008).

48 Eisler, R. (1996) A review of silver hazards to plants and animals, in The Fourth International Conference Proceedings: Transport, Fate and Effects of Silver in the Environment, (eds W.A Andren and W.T. Bober), Sea Grant Institute, University of Wisconsin, Madison, WI, USA, pp. 143–4.

49 Braydich-Stolle, L., Hussain, S., Schlager, J.J. and Hofmann, M.-C. (2005) In vitro cytotoxicity of nanoparticles in mammalian germline stem cells. *Toxicological Sciences*, **88**, 412–19.

50 Hussain, S.M., Hess, K.L., Gearhart, J.M., Geiss, K.T. and Schlager, J.J. (2005) In vitro toxicity of nanoparticles in BRL 3A rat liver cells. *Toxicology in Vitro*, **19**, 975–83.

51 Hogstrand, C. and Wood, C.M. (1996) The toxicity of silver to marine fish, in The 4th International Conference Proceedings: Transport, Fate and Effects of Silver in the Environment (eds W.A Andren and W.T. Bober), Sea Grant Institute, University of Wisconsin, Madison, WI, USA, pp. 109–12.

52 Mie, G. (1908) Beiträge zur optik trüber medien, speziell kolloidaler metallösungen. *Annalen der Physik* (*Leipzig*), **25**, 376–445.

53 Kelly, K.L., Coronado, E., Zhao, L.L. and Schatz, G.C. (2003) The optical properties of metal nanoparticles: the influence of size, shape, and dielectric environment. *Journal of Physical Chemistry B*, **107**, 668–77.

54 Wiley, B.J., Im, S.H., Li, Z.-Y., McLellan, J., Siekkinen, A. and Xia, Y. (2006) Maneuvering the surface plasmon resonance of silver nanostructures through shape-controlled synthesis. *Journal of Physical Chemistry B*, **110**, 15666–75.

55 Klabunde, K.J. (2001) *Nanoscale Materials in Chemistry*, John Wiley & Sons, Inc. New York.

56 Dahl, J.A., Maddux, B.L.S. and Hutchison, J.E. (2007) Toward greener, nanosynthesis. *Chemical Reviews*, **107**, 2228–69.

57 Hyeon, T. (2003) Chemical synthesis of magnetic nanoparticles. *Chemical Communications*, 927–34.

58 Pileni, M.-P. (2003) The role of soft colloidal templates in controlling the size and shape of inorganic nanocrystals. *Nature Materials*, **2**, 145–50.

59 Sun, S. and Murray, C.B. (1999) Synthesis of monodisperse cobalt nanocrystals and their assembly into magnetic superlattices. *Journal of Applied Physics*, **85**, 4325–30.

60 Murray, C.B., Norris, D.J. and Bawendi, M.G. (1993) Synthesis and characterization of nearly monodisperse CdE (E = S, Se, Te) semiconductor nanocrystallites. *Journal of the American Chemical Society*, **115**, 8706–15.

61 Peng, X., Wickham, J. and Alivisatos, A.P. (1998) Kinetics of II-VI and III-V colloidal semiconductor nanocrystal growth: 'focusing' of size distributions. *Journal of the American Chemical Society*, **120**, 5343–4.

62 Peng, Z.A. and Peng, X. (2002) Nearly monodisperse and shape-controlled CdSe nanocrystals via alternative routes: nucleation and growth. *Journal of the American Chemical Society*, **124**, 3343–53.

63 Shimizu, T., Teranishi, T., Hasegawa, S. and Miyake, M. (2003) Size evolution of alkanethiol-protected gold nanoparticles by heat treatment in the solid state. *Journal of Physical Chemistry B*, **107**, 2719–24.

64 Hulteen, J.C. and Martin, C.R. (1997) A general template-based method for the preparation of nanomaterials. *Journal of Materials Chemistry*, **7**, 1075-87.

65 Jin, R.C., Cao, Y.W., Mirkin, C.A., Kelly, K.L. and Schatz, G.C. and Zheng, J.G. (2001) Photoinduced conversion of silver nanospheres to nanoprisms. *Science*, **294**, 1901–3.

66 Murphy, C.J., Sau, T.K., Gole, A.M., Orendorff, C.J., Gao, J., Gou, L.,

Hunyadi, S.E. and Li, T. (2005) Anisotropic metal nanoparticles: synthesis, assembly, and optical applications. *Journal of Physical Chemistry B*, **109**, 13857–70.

67 Pileni, M.P. (1997) Nanosized particles made in colloidal assemblies. *Langmuir*, **13**, 3266–76.

68 Sau, T.K. and Murphy, C.J. (2004) Room temperature, high-yield synthesis of multiple shapes of gold nanoparticles in aqueous solution. *Journal of the American Chemical Society*, **126**, 8648–9.

69 Wang, C., Wang, T., Ma, Z. and Su, Z. (2005) pH-tuned synthesis of gold nanostructures from gold nanorods with different aspect ratios. *Nanotechnology*, **16**, 2555–60.

70 Xia, Y. and Halas, N.J. (2005) Shape-controlled synthesis and surface plasmonic properties of metallic nanostructures. *MRS Bulletin*, **30**, 338–48.

71 Wang, Z.L. (2000) Transmission electron microscopy of shape-controlled nanocrystals and their assemblies. *Journal of Physical Chemistry B*, **104**, 1153–75.

72 Smith, D.J., Petford-Long, A.K., Wallenberg, L.R. and Bovin, J.O. (1986) Dynamic atomic-level rearrangements in small gold particles. *Science*, **233**, 872–5.

73 Iijima, S. and Ichihashi, T. (1986) Structural instability of ultrafine particles of metals. *Physical Review Letters*, **56**, 616–19.

74 Yacaman, M.J., Ascencio, J.A., Liu, H.B. and Gardea-Torresdey, J. (2001) Structure shape and stability of nanometric sized particles. *Journal of Vacuum Science and Technology B*, **19**, 1091–103.

75 Liu, H.B., Ascencio, J.A., Perez-Alvarez, M. and Yacaman, M.J. (2001) Melting behavior of nanometer sized gold isomers. *Surface Science*, **491**, 88–98.

76 Xiong, Y. and Xia, Y. (2007) Shape-controlled synthesis of metal nanostructures: the case of palladium. *Advanced Materials*, **19**, 3385–91.

77 Sun, Y., Mayers, B., Herricks, T. and Xia, Y. (2003) Polyol synthesis of uniform silver nanowires: a plausible growth mechanism and the supporting evidence. *Nano Letters*, **3**, 955–60.

78 Xiong, Y., Chen, J., Wiley, B., Xia, Y., Yin, Y. and Li, Z.-Y. (2005) Size-dependence of surface plasmon resonance and oxidation for Pd nanocubes synthesized via a seed etching process. *Nano Letters*, **5**, 1237–42.

79 Xiong, Y., McLellan, J.M., Yin, Y. and Xia, Y. (2007) Synthesis of palladium icosahedra with twinned structure by blocking oxidative etching with citric acid or citrate ions. *Angewandte Chemie – International Edition*, **46**, 790–4.

80 Lofton, C. and Sigmund, W. (2005) Mechanisms controlling crystal habits of gold and silver colloids. *Advanced Functional Materials*, **15**, 1197–208.

81 Bastys, V., Pastoriza-Santos, I., Rodríguez-González, B., Vaisnoras, R. and Liz-Marzán, L.M. (2006) Formation of silver nanoprisms with surface plasmons at communication wavelengths. *Advanced Functional Materials*, **16**, 766–73.

82 Marks, L.D. (1994) Experimental studies of small particle structures. *Reports on Progress in Physics*, **57**, 603–49.

83 Xiong, Y., Cai, H., Wiley, B.J., Wang, J., Kim, M.J., Xia, Y., (2007) Synthesis and mechanistic study of palladium nanobars and nanorods. *Journal of the American Chemical Society*, **129**, 3665–75.

84 Xiang, Y., Wu, X., Liu, D., Jiang, X., Chu, W., Li, Z., Ma, Y., Zhou, W. and Xie, S. (2006) Formation of rectangularly shaped Pd/Au bimetallic nanorods: evidence for competing growth of the Pd shell between the {110} and {100} side facets of Au nanorods. *Nano Letters*, **6**, 2290–4.

85 Turkevitch, J., Stevenson, P.C. and Hillier, J. (1951) A study of the nucleation and growth processes in the synthesis of colloidal gold. *Discussions of the Faraday Society*, **11**, 55–75.

86 Frens, G. (1973) Controlled nucleation for the regulation of the particle size in monodisperse gold suspensions. *Nature*, **241**, 20–2.

87 Pillai, Z.S. and Kamat, P.V. (2004) What factors control the size and shape of silver nanoparticles in the citrate ion reduction method? *Journal of Physical Chemistry B*, **108**, 945–51.

88 Caswell, K.K., Bender, C.M. and Murphy, C.J. (2003) Seedless, surfactantless wet chemical synthesis of silver nanowires. *Nano Letters*, **3**, 667–9.

89 Fievet, F. and Lagier, J.P. and Figlarz, M. (1989) Preparing monodisperse metal powders in micrometer and submicrometer sizes by the polyol process. *MRS Bulletin*, **14**, 29.

90 Xiong, Y., Siekkinen, A.R., Wang, J., Yin, Y., Kimb, M.J. and Xia, Y. (2007) Synthesis of silver nanoplates at high yields by slowing down the polyol reduction of silver nitrate with polyacrylamide. *Journal of Materials Chemistry*, **17**, 2600–2.

91 Wiley, B., Sun, Y., Chen, J., Cang, H., Li, Z.-Y., Li, X. and Xia, Y. (2005) Shape-controlled synthesis of silver and gold nanostructures. *MRS Bulletin*, **30**, 356–61.

92 Zhang, W., Chen, P., Gao, Q., Zhang, Y. and Tang, Y. (2008) High-concentration preparation of silver nanowires: restraining in situ nitric acidic etching by steel-assisted polyol method. *Chemistry of Materials*, **20**, 1699–704.

93 Yang, Y., Matsubara, S., Xiong, L. and Hayakawa, T. and Nogami, M. (2007) Solvothermal synthesis of multiple shapes of silver nanoparticles and their SERS properties. *Journal of Physical Chemistry C*, **111**, 9095–104.

94 Kim, F., Connor, S., Song, H., Kuykendall, T. and Yang, P. (2004) Platonic gold nanocrystals. *Angewandte Chemie–International Edition*, **43**, 3673–7.

95 Komarneni, S., Li, D., Newalkar, B., Katsuki, H. and Bhalla, A.S. (2002) Microwave-polyol process for Pt and Ag nanoparticles. *Langmuir*, **18**, 5959–62.

96 Gou, L., Chipara M. and Zaleski, J.M. (2007) Convenient, rapid synthesis of Ag nanowires. *Chemistry of Materials*, **19**, 1755–60.

97 Tsuji, M., Hashimoto, M., Nishizawa, Y. and Kubokawa, M. and Tsuji, T. (2004) Microwave-assisted synthesis of metallic nanostructures in solution microwave. *Chemistry–A European Journal*, **11**, 440–52.

98 Sun, Y. and Xia, Y. (2002) Shape-Controlled Synthesis of Gold and Silver Nanoparticles. *Science*, **298**, 2176–9.

99 Wiley, B., Sun, Y. and Mayers, B. and Xia, Y. (2005) Shape-controlled synthesis of metal nanostructures: the case of silver. *Chemistry–A European Journal*, **11**, 454–63.

100 Wiley, B., Herricks, T., Sun, Y. and Xia, Y. (2004) Polyol synthesis of silver nanoparticles: use of chloride and oxygen to promote the formation of single-crystal, truncated cubes and tetrahedrons. *Nano Letters*, **4**, 1733–9.

101 Wiley, B., Sun, Y. and Xia, Y. (2007) Synthesis of silver nanostructures with controlled shapes and properties. *Accounts of Chemical Research*, **40**, 1067–76.

102 Wiley, B.J., Xiong, Y., Li, Z.-Y., Yin, Y. and Xia, Y. (2006) Right bipyramids of silver: a new shape derived from single twinned seeds. *Nano Letters*, **6**, 765–8.

103 Liu, X., Huang, R. and Zhu, J. (2008) Functional faceted silver nano-hexapods: synthesis, structure characterizations, and optical properties. *Chemistry of Materials*, **20**, 192–7.

104 Zhang, H., Wang, Z. and Ming, N. (2007) Shape-selective synthesis of gold nanoparticles with controlled sizes, shapes, and plasmon resonances. *Advanced Functional Materials*, **17**, 3295–303.

105 Guo, S. and Wang, E. (2007) One-pot, high-yield synthesis of size-controlled gold particles with narrow size distribution. *Inorganic Chemistry*, **46**, 6740–3.

106 Seo, D., Park, J.C. and Song, H. (2006) Polyhedral gold nanocrystals with oh symmetry: from octahedra to cubes. *Journal of the American Chemical Society*, **128**, 14863–70.

107 Li, C., Shuford, K.L., Park, Q.-H., Cai, W., Li, Y., Lee, E.J. and Cho, S.O. (2007) High-yield synthesis of single-crystalline gold nano-octahedra. *Angewandte Chemie–International Edition*, **46**, 3264–8.

108 Zhang, J., Liu, H., Wang, Z. and Ming, N. (2007) Shape-selective synthesis of gold nanoparticles with controlled sizes, shapes, and plasmon resonances.

Advanced Functional Materials, **17**, 3295–303.

109 Li, C.C., Cai, W.P., Cao, B.Q, Sun, F.Q., Li, Y., Kan, C.X. and Zhang, L.D. (2006) Mass synthesis of large, single-crystal au nanosheets based on a polyol process. *Advanced Functional Materials*, **16**, 83–90

110 Jana, N.R., Gearheart, L. and Murphy, C.J. (2001) Evidence for seed-mediated nucleation in the chemical reduction of gold salts to gold nanoparticles. *Chemistry of Materials*, **13**, 2313–22.

111 Brown, K.R. and Natan, M.J. (1998) Hydroxylamine seeding of colloidal Au nanoparticles in solution and on surfaces. *Langmuir*, **14**, 726–8.

112 Brown, K.R., Walter, D.G. and Natan, M.J. (2000) Seeding of colloidal Au nanoparticle solutions. 2. Improved control of particle size and shape. *Chemistry of Materials*, **12**, 306–13.

113 Busbee, B.D., Obare, S.O. and Murphy, C.J. (2003) An improved synthesis of high-aspect-ratio gold nanorods. *Advanced Materials*, **15**, 414–16.

114 Nikoobakht, B. and El-Sayed, M.A. (2003) Preparation and growth mechanism of gold nanorods (NRs) using seed-mediated growth method. *Chemistry of Materials*, **15**, 1957–62.

115 Pérez-Juste, J., Liz-Marzán, L.M., Carnie, S., Chan, D.Y.C. and Mulvaney, P. (2004) Electric-field-directed growth of gold nanorods in aqueous surfactant solutions. *Advanced Functional Materials*, **14**, 571–9.

116 Jana, N.R. (2005) Gram-scale synthesis of soluble, near-monodisperse gold nanorods and other anisotropic nanoparticles. *Small*, **1**, 875–82.

117 Murphy, C.J., Gole, A.M., Hunyadi, S.E. and Orendorff, C.J. (2006) One-dimensional colloidal gold and silver nanostructures. *Inorganic Chemistry*, **45**, 7544–54.

118 Sau, T.K. and Murphy, C.J. (2004) Seeded high yield synthesis of short Au nanorods in aqueous solution. *Langmuir*, **20**, 6414–20.

119 Gole, A. and Murphy, C.J. (2004) Seed-mediated synthesis of gold nanorods: role of the size and nature of the seed. *Chemistry of Materials*, **16**, 3633–40.

120 Pérez-Juste, J., Liz-Marzán, L.M., Carnie, S., Chan, D.Y.C. and Mulvaney, P. (2004) Electric-field-directed growth of gold nanorods in aqueous surfactant solutions. *Advanced Functional Materials*, **14**, 571–9.

121 Liu, M.Z. and Guyot-Sionnest, P. (2005) Mechanism of silver (I)-assisted growth of gold nanorods and bipyramids. *Journal of Physical Chemistry B*, **109**, 22192–200.

122 Orendorff, C.J. and Murphy, C.J. (2006) Quantitation of metal content in the silver-assisted growth of gold nanorods. *Journal of Physical Chemistry B*, **110**, 3990–4.

123 Rodríguez-Fernández, J., Pérez-Juste, J., Mulvaney, P. and Liz-Marzán, L.M. (2005) Spatially-directed oxidation of gold nanoparticles by Au(III)-CTAB complexes. *Journal of Physical Chemistry B*, **109**, 14257–61.

124 Gao, J., Bender, C.M. and Murphy, C.J. (2003) Dependence of the gold nanorod aspect ratio on the nature of the directing surfactant in aqueous solution. *Langmuir*, **19**, 9065–70.

125 Nikoobakht, B. and El-Sayed, M.A. (2001) Evidence for bilayer assembly of cationic surfactants on the surface of gold nanorods. *Langmuir*, **17**, 6368–74.

126 Kou, X.S., Zhang, S.Z., Tsung, C.-K., Yang, Z., Yeung, M.H., Stucky, G.D., Sun, L.D., Wang, J.F. and Yan, C.H. (2007) One-step synthesis of large-aspect-ratio single-crystalline gold nanorods by using CTPAB and CTBAB surfactants. *Chemistry – A European Journal*, **13**, 2929–36.

127 Wu, H.-Y., Chu, H.-C., Kuo, T.-J., Kuo, C.L. and Huang, M.H. (2005) Seed-mediated synthesis of high aspect ratio gold nanorods with nitric acid. *Chemistry of Materials*, **17**, 6447–51.

128 Wu, H.-Y., Huang, W.-L. and Huang, M.H. (2007) Direct high-yield synthesis of high aspect ratio gold nanorods. *Crystal Growth and Design*, **7**, 831–5.

129 Chen, H.M., Peng, H.-C., Liu, R.-S., Asakura, K., Lee, C.-L., Lee, J.F. and Hu, S.-F. (2005) Controlling the length and shape of gold nanorods. *Journal of Physical Chemistry B*, **109**, 19553–5.

130 Pérez-Juste, J., Pastoriza-Santos, I., Liz-Marzán, L.M. and Mulvaney, P. (2005) Gold nanorods: synthesis, characterization and applications. *Coordination Chemical Reviews*, **249**, 1870–901.

131 Jana, N.R., Gearheart, L. and Murphy, C.J. (2001) Seed-mediated growth approach for shape-controlled synthesis of spheroidal and rod-like gold nanoparticles using a surfactant template. *Advanced Materials*, **13**, 1389–93.

132 Liu, M.Z. and Guyot-Sionnest, P. (2005) Mechanism of silver (I)-assisted growth of gold nanorods and bipyramids. *Journal of Physical Chemistry B*, **109**, 22192–200.

133 Kou, X., Zhang, S., Tsung, C.-K., Yeung, M.H., Shi, Q., Stucky, G.D., Sun, L., Wang, J. and Yan, C. (2006) Growth of gold nanorods and bipyramids using CTEAB surfactant. *Journal of Physical Chemistry B*, **110**, 16377–83.

134 Kou, X., Ni, W., Tsung, C.-K., Chan, K., Lin, H.-Q., Stucky, G.D. and Wang, J. (2007) Growth of gold bipyramids with improved yield and their curvature-directed oxidation. *Small*, **3**, 2103–13.

135 Yuan, H., Ma, W., Chen, C., Zhao, J., Liu, J., Zhu, H. and Gao, X. (2007) Shape and SPR evolution of thorny gold nanoparticles promoted by silver ions. *Chemistry of Materials*, **19**, 1592–600.

136 Huang, L., Wang, M., Zhang, Y., Guo, Z., Sun, J. and Gu, N. (2007) Synthesis of gold nanotadpoles by a temperature-reducing seed approach and the dielectrophoretic manipulation. *Journal of Physical Chemistry C*, **111**, 16154–60.

137 Hu, J., Zhang, Y., Liu, B., Liu, J., Zhou, H., Xu, Y., Jiang, Y., Yang, Z. and Tian, Z.-Q. (2004) Synthesis and properties of tadpole-shaped gold nanoparticles. *Journal of the American Chemical Society*, **126**, 9470–1.

138 Wang, C., Wang, T., Ma, Z. and Su, Z. (2005) pH-tuned synthesis of gold nanostructures from gold nanorods with different aspect ratios. *Nanotechnology*, **16**, 2555–60.

139 Chen, H.M. and Liu, R.-S. Facile synthesis and mechanistic study of multishaped gold nanostructures. *Journal of Crystal Growth and Design* (submitted).

140 Jana, N.R., Gearheart, L. and Murphy, C.J. (2001) Wet chemical synthesis of silver nanorods and nanowires of controllable aspect ratio. *Chemical Communications*, 617–18.

141 Chen, S. and Carroll, D.L. (2002) Synthesis and characterization of truncated triangular silver nanoplates. *Nano Letters*, **2**, 1003–7.

142 Lu, L., Kobayashi, A., Tawa, K. and Ozaki, Y. (2006) Silver nanoplates with special shapes: controlled synthesis and their surface plasmon resonance and surface-enhanced Raman scattering properties. *Chemistry of Materials*, **18**, 4894–901.

143 Giersig, M. and Mulvaney, P. (1993) Preparation of ordered colloid monolayers by electrophoretic deposition. *Langmuir*, **9**, 3408–13.

144 Brust, M., Walker, M., Bethell, D., Schiffrin, D.J. and Whyman, R.J. (1994) Synthesis of thiol-derivatized gold nanoparticles in a two phase liquid-liquid system. *Journal of the Chemical Society D–Chemical Communications*, 801–2.

145 Brust, M., Fink, J., Bethell, D., Schiffrin, D.J. and Kiely, C.J. (1995) Synthesis and reactions of functionalised gold nanoparticles. *Journal of the Chemical Society D–Chemical Communications*, 1655–6.

146 Chen, S. (1999) 4-Hydroxythiophenol-protected gold nanoclusters in aqueous media. *Langmuir*, **15**, 7551–7.

147 Chen, S. and Murray, R.W. (1999) Arenethiolate monolayer-protected gold clusters. *Langmuir*, **15**, 682–9.

148 Hostetler, M.J., Green, S.J., Stokes, J.J. and Murray, R.W. (1996) Monolayers in three dimensions: synthesis and electrochemistry of ö-functionalized alkanethiolate-stabilized gold cluster compounds. *Journal of the American Chemical Society*, **118**, 4212–13.

149 Ingram, R.S., Hostetler, M.J. and Murray, R.W. (1997) Poly-hetero-ö-functionalized alkanethiolate-stabilized gold cluster compounds. *Journal of the American Chemical Society*, **119**, 9175–8.

150 Hostetler, M.J., Wingate, J.E., Zhong, C.-J., Harris, J.E., Vachet, R.W., Clark,

M.R., Londono, J.D., Green, S.J., Stokes, J.J., Wignall, G.D., Glish, G.L., Porter, M.D., Evans, N.D. and Murray, R.W. (1998) Alkanethiolate gold cluster molecules with core diameters from 1.5 to 5.2 nm: core and monolayer properties as a function of core size. *Langmuir*, **14**, 17–30.

151 Templeton, A.C., Hostetler, M.J., Kraft, C.T. and Murray, R.W. (1998) Reactivity of monolayer-protected gold cluster molecules: steric effects. *Journal of the American Chemical Society*, **120**, 1906–11.

152 Hostetler, M.J., Templeton, A.C. and Murray, R.W. (1999) Dynamics of place-exchange reactions on monolayer-protected gold cluster molecules. *Langmuir*, **15**, 3782–9.

153 Schmid, G. (1990) Hexachlorododecakis (triphenylphosphine) pentapentacontagold, $Au55[P(C_6H_5)_3]12Cl_6$. *Inorganic Syntheses*, **27**, 214–18.

154 Schmid, G., Klein, N., Korste, L., Kreibig, U. and Schoenauer, D. (1988) Large transition metal clusters–VI. Ligand exchange reactions on the gold triphenylphosphine chloro cluster, $Au55(PPh_3)12Cl_6$–the formation of a water-soluble gold (Au55) cluster. *Polyhedron*, **7**, 605–8.

155 Schmid, G., Pfeil, R., Boese, R., Brandermann, F., Meyer, S., Calis, G.H.M. and Van der Velden, J.W.A. (1981) $Au55[P(C_6H_5)_3]12Cl_6$–ein Goldcluster ungewöhnlicher Größe. *Chemische Berichte*, **114**, 3634–42.

156 Hutchison, J.E., Foster, E.W., Warner, M.G., Reed, S.M., Weare, W.W., Buhro, W. and Yu, H. (2004) Cluster and polynuclear compounds. Triphenylphosphine-stabilized gold nanoparticles. *Inorganic Syntheses*, **34**, 228–32.

157 Holmberg, K. (2004) Surfactant-templated nanomaterials synthesis. *Journal of Colloid and Interface Science*, **274**, 355–64.

158 Herrera, A.P., Resto, O., Briano, J.G. and Rinaldi, C., (2005) Synthesis and agglomeration of gold nanoparticles in reverse micelles. *Nanotechnology*, **16**, S618–25.

159 Pileni, M.P. (2006) Reverse micelles used as templates: a new understanding in nanocrystal growth. *The Journal of Experimental Nanoscience*, **1**, 13–27.

160 Lowenstam, H.A. (1981) Minerals formed by organisms. *Science*, **211**, 1126–31.

161 Mann, S. (2001) *Biomineralization: Principles and Concepts in Bioinorganic Materials Chemistry*, Oxford University Press, Oxford.

162 Pum, D. and Sleytr, U.B. (1999) The application of bacterial S-layers in molecular nanotechnology. *Trends in Biotechnology*, **17**, 8–12.

163 Gericke, M. and Pinches, A. (2006) Biological synthesis of metal nanoparticles. *Hydrometallurgy*, **83**, 132–40.

164 Klaus, T., Joerger, R., Olsson, E. and Granqvist, C.-G. (1999) Silver-based crystalline nanoparticles, microbially fabricated. *Proceedings of the National Academy of Sciences of the United States of America*, **96**, 13611–14.

165 Nair, B. and Pradeep, T. (2002) Coalescence of nanoclusters and the formation of sub-micron crystallites assisted by lactobacillus strains. *Crystal Growth and Design*, **2**, 293–8.

166 Shahverdi, A.R., Minaeian, S., Shahverdi, H.R., Jamalifar, H. and Nohi, A.-A. (2007) Rapid synthesis of silver nanoparticles using culture supernatants of enterobacteria: a novel biological approach. *Process Biochemistry*, **42**, 919–23.

167 Chen, J.C., Lin, Z.H. and Ma, X.X. (2003) Evidence of the production of silver nanoparticles via pretreatment of *Phoma Sp.*3.2883 with silver nitrate. *Letters in Applied Microbiology*, **37**, 105–8.

168 Ahmad, A., Mukherjee, P., Senapati, S., Mandal, D., Khan, M.I., Kumar, R. and Sastry, M. (2003) Extracellular biosynthesis of silver nanoparticles using the fungus *Fusarium oxysporum*. *Colloids and Surfaces. B, Biointerfaces*, **28**, 313–18.

169 Durán, N., Marcato, P.D., Alves, O.L., De Souza, G.I.H. and Esposito, E. (2005) Mechanistic aspects of biosynthesis of silver nanoparticles by several *Fusarium oxysporum* strains. *Journal of Nanobiotechnology*, **3**(8), 1–7.

170 Vigneshwaran, N., Kathe, A.A., Varadarajan, P.V., Nachane, R.P. and Balasubramanya, R.H. (2006) Biomimetics of silver nanoparticles by white rot fungus, *Phaenerochaete chrysosporium*. *Colloids and Surfaces B, Biointerfaces*, **53**, 55–9.

171 Bhainsa, K.C. and D'Souza, S.F. (2006) Extracellular biosynthesis of silver nanoparticles using the fungus *Aspergillus fumigatus*. *Colloids and Surfaces. B, Biointerfaces*, **47**,160–4.

172 Vigneshwaran, N., Ashtaputre, N.M., Varadarajan, P.V., Nachane, R.P., Paralikar, K.M. and Balasubramanya, R.H. (2007) Biological synthesis of silver nanoparticles using the fungus *Aspergillus flavus*. *Materials Letters*, **61**, 1413–18.

173 Kowshik, M., Ashtaputre, S., Kharrazi, S., Vogel, W., Urban, J., Kulkarni, S.K. and Paknikar, K.M. (2003) Extracellular synthesis of silver nanoparticles by a silver-tolerant yeast strain MKY3. *Nanotechnology*, **14**, 95–100.

174 Jorge, L., Torresdey, G., Gomez, E., Peralta-Videa, J.R., Parsons, J.G., Troiani, H. and Yacaman, M.J. (2003) Alfalfa sprouts: a natural source for the synthesis of silver nanoparticles. *Langmuir*, **19**, 1357–61.

175 Shankar, S.S., Ahmad, A. and Sastry, M. (2003) Geranium leaf assisted biosynthesis of silver nanoparticles. *Biotechnology Progress*, **19**, 1627–31.

176 Shankar, S.S., Rai, A., Ahmad, A. and Sastry, M. (2004) Rapid synthesis of Au, Ag, and bimetallic Au core–Ag shell nanoparticles using neem (*Azadirachta indica*) leaf broth. *Journal of Colloid and Interface Science*, **275**, 496–502.

177 Chandran, S.P., Chaudhary, M., Pasricha, R., Ahmad, A. and Sastry, M. (2006) Synthesis of gold nanotriangles and silver nanoparticles using *Aloe vera* plant extract. *Biotechnology Progress*, **22**, 577–83.

178 Huang, J., Li, Q., Sun, D., Lu, Y., Su, Y., Yang, X., Wang, H., Wang, Y., Shao, W., He, N., Hong, J. and Chen, C. (2007) Biosynthesis of silver and gold nanoparticles by novel sundried *Cinnamomum camphora* leaf. *Nanotechnology*, **18**, 105104, 1–11.

179 Xie, J., Lee, J.Y., Wang, D.I.C., Ting, Y.P. (2007) Silver nanoplates: from biological to biomimetic synthesis. *ACS Nano*, **1**, 429–39.

180 Southam, G. and Beveridge, T.J. (1996) The occurrence of sulfur and phosphorus within bacterially derived crystalline and pseudocrystalline octahedral gold formed in vitro. *Geochimica et Cosmochimica Acta*, **60**, 4369–76.

181 Mukherjee, P., Ahmad, A., Mandal, D., Senapati, S., Sainkar, S.R., Khan, M.I., Ramani, R., Parischa, R., Ajayakumar, P.V., Alam, M., Sastry, M. and Kumar, R. (2001) Bioreduction of $AuCl_4^-$ ions by the fungus, *Verticillium* sp. and surface trapping of the gold nanoparticles formed. *Angewandte Chemie – International Edition*, **40**, 3585–8.

182 Mukherjee, P., Ahmad, A., Senapati, S., Khan, M.I., Kumar, R., Ramani, R., Srinivas, V., Sastry, M., Ajaykumar, P.V., Alam, M. and Parischa, R. (2002) Extracellular synthesis of gold nanoparticles by the fungus *Fusarium oxysporum*. *Chemistry and Biochemistry*, **5**, 461–3.

183 Shankar, S., Ahmad, A., Pasricha, R. and Sastry, M. (2003) Bioreduction of chloroaurate ions by geranium leaves and its endophytic fungus yields gold nanoparticles of different shapes. *Journal of Materials Chemistry*, **13**, 1822–6.

184 Xie, J., Lee, J.Y., Wang, D.I.C. and Ting, Y.P. (2007) High-yield synthesis of complex gold nanostructures in a fungal system. *Journal of Physical Chemistry C*, **111**, 16858–65.

185 Ahmad, A., Senapati, S., Khan, M.I., Kumar, R., Ramani, R., Srinivas, V. and Sastry, M. (2003) Intracellular synthesis of gold nanoparticles by novel alkalotolerant actinomycetes, *Rhodococcus* sp. *Nanotechnology*, **14**, 824–8.

186 Ahmad, A., Senapati, S., Khan, M.I., Kumar, R. and Sastry, M. (2003) Extracellular biosynthesis of monodisperse gold nanoparticles by a novel extremophilic actinomycete, *Thermomonospora* sp. *Langmuir*, **19**, 3550–3.

187 Gardea-Torresdey, J.L., Parsons, J.G., Gomez, E., Peralta-Videa, J., Troian, i H.E., Santiag, P. and Yacaman, M.J.

(2002) Formation and growth of au nanoparticles inside live alfalfa plants. *Nano Letters*, 397–401.

188 Armendariz, V., Herrera, I., Peralta-Videa, J.R., Jose-Yacaman, M., Troiani, H., Santiago, P. and Gardea-Torresdey, J.L. (2004) Size controlled gold nanoparticle formation by *Avena sativa* biomass: use of plants in nanobiotechnology. *Journal of Nanoparticle Research*, **6**, 377–82.

189 Shankar, S.S., Rai, A., Ankamwar, B., Singh, A., Ahmad, A. and Sastry, M. (2004) Biological synthesis of triangular gold nanoprisms. *Nature Materials*, **3**, 482–8.

190 Sharma, N.C., Sahi, S.V., Nath, S., Parsons, J.G., Gardea–Torresdey, J.L. and Pal, T. (2007) Synthesis of plant-mediated gold nanoparticles and catalytic role of biomatrix-embedded nanomaterials. *Environmental Science and Technology*, **41**, 5137–42.

191 Xie, J., Lee, J.Y., Wang, D.I.C. and Ting, Y.P. (2007) Identification of active biomolecules in the high-yield synthesis of single-crystalline gold nanoplates in algal solutions. *Small*, **3**, 672–82.

192 Singaravelu, G.G., Arockiamary, J.S., Kumar, V.G. and Govindaraju, K. (2007) A novel extracellular synthesis of monodisperse gold nanoparticles using marine alga, *Sargassum wightii*. *Colloids and Surfaces. B, Biointerfaces*, **57**, 97–101.

193 Fortin, D. and Beveridge, T.J. (2000) Biomineralization, in: *From Biology to Biotechnology and Medical Applications* (ed. E. Baeuerien), John Wiley & Sons, Ltd, Weinheim, pp. 7–22.

194 Payne, E.K., Shuford, K.L., Park, S., Schatz, G.C. and Mirkin, C.A. (2006) Multiple plasmon resonances in gold nanorods. *Journal of Physical Chemistry B*, **110**, 2150–4.

195 Huang, H.J., Yu, C.P., Chang, H.C., Chiu, K.P., Chen, H.M., Liu, R., Optical, S. and Tsai, D.P. (2007) Properties of a single gold nano-rod. *Optics Express*, **15**, 7132–9.

196 Penner-Hahn, J.E. (1999) X-ray absorption spectroscopy in coordination chemistry. *Coordination Chemistry Reviews*, **190**, 1101–23.

197 Besenbacher, F., Chorkendorff, I., Clausen, B.S., Hammer, B., Molenbroek, A.M., Norskov, J.K. and Stensgaard, I. (1998) Design of a surface alloy catalyst for steam reforming. *Science*, **279**, 1913–15.

198 Polarz, S., Neues, F., Berg, M.W.E., Grünert, W. and Khodeir, L. (2005) Mesosynthesis of ZnO-silica composites for methanol nanocatalysis. *Journal of the American Chemical Society*, **127**, 12028–34.

199 Jensen, M.P., Dzielawa, J.A., Rickert, P. and Dietz, M.L. (2002) EXAFS investigations of the mechanism of facilitated ion transfer into a room-temperature ionic liquid. *Journal of the American Chemical Society*, **124**, 10664–5.

200 Chen, H.M., Liu, R.-S., Asakura, K., Lee, J.-F., Jang, L.Y. and Hu, S.-F. (2006) Fabrication of nanorattles with passive shell. *Journal of Physical Chemistry B*, **110**, 19162–7.

201 Nashner, M.S., Somerville, D.M., Lane, P.D., Adler, D.L., Shapley, J.R. and Nuzzo, R.G. (1996) Bimetallic catalyst particle nanostructure. evolution from molecular cluster precursors. *Journal of the American Chemical Society*, **118**, 12964–74.

202 Chen, H.M., Liu, R.S., Asakura, K., Jang, L.Y. and Lee, J.-F. (2007) Controlling length of gold nanowires with large-scale: X-ray absorption spectroscopy. *Journal of Physical Chemistry C*, **111**, 18550–7.

203 Hargittai, M., Schulz, A., Réffy, B. and Kolonits, M. (2001) Molecular structure, bonding, and Jahn-Teller effect in gold chlorides: quantum chemical study of $AuCl_3$, Au_2Cl_6, $AuCl_4^-$, AuCl, and Au_2Cl_2 and electron diffraction study of Au_2Cl_6. *Journal of the American Chemical Society*, **123**, 1449–58.

12
Biological and Biomaterials-Assisted Synthesis of Precious Metal Nanoparticles

Jason G. Parsons, Jose R. Peralta-Videa, Kenneth M. Dokken and Jorge L. Gardea-Torresdey

12.1 Introduction

The main goal in the synthesis of nanomaterials is for their ultimate application in catalysts, medicines, nanodevices, nanoelectronics, or sensors [1–6]. Literally tens of thousands of different methods have been reported for the synthesis of metallic nanoparticles, including chemical and physical methods for precious metal reduction. In recent years, however, the synthesis of metallic precious metal nanoparticles has taken a new turn to include biological synthesis or techniques using living and nonliving organisms and plant extracts [7–9]. It has been well documented that many different plant, fungal and bacterial species have the ability to reduce precious metals ions in solution to form metallic nanoparticles [7–9]. Hence, in this chapter we will discuss a variety of chemical and biological techniques used for the reduction of precious metals – such as gold, platinum, palladium and silver – to form nanomaterials. Details of the use of osmium, rhodium, ruthenium and iridium in the formation of metallic nanoparticles, employing biological materials, have been excluded from this chapter as no relevant citations could be identified.

In general, the synthesis of precious metal nanoparticles involves the use of a reducing agent and a protecting agent or surfactant to control nanoparticles growth and to provide a narrow nanoparticle size distribution. Many different chemicals have the ability to donate electrons in solution and thus induce the reduction of precious metal ions to produce metallic nanoparticles. For example, sodium borohydride, lithium hydride and hydroxylamine are all known to donate electrons to metal ions in solution to produce metallic nanomaterials [10–13]. A number of different nanoparticles have also been synthesized using these techniques, including platinum, palladium, gold and silver [10–17]. The following syntheses are commonly used to produce precious metal nanoparticles. For example, the synthesis of 5 nm platinum nanoparticles has been achieved through the use of hydrazine in ionic reversed micelle systems [18]. Alternatively, platinum nanopar-

Metallic Nanomaterials Vol. 1. Edited by Challa S. S. R. Kumar

ISBN: 978-3-527-32151-3

ticles have been synthesized under a H_2(g) atmosphere in a polyacrylate solution which had been degassed using argon; this resulted in the production of cubic platinum nanoparticles with an average diameter of 11 nm [19]. Another technique involved the use of methanol and a sodium citrate reduction to produce platinum nanoparticles with average diameters of 2–3 nm [20]. The synthesis of dodecanethiolate palladium nanoparticles was carried out using anhydrous tetrahydrofuran (THF); the result was cubo-octahedral nanoparticles with average diameters of 2–3 nm [21]. Alternatively, palladium and gold metal nanoparticles have been synthesized using polyaniline dissolved in *N*-methylpyrrolidone to yield nanoparticles ranging in size from 50 to 200 nm [22].

Although several common physical methods, including chemical vapor deposition (CVD), sonication and laser ablation [23–30], have been used to produce precious metal nanoparticles, these will not be discussed at this point.

The main factor regarding the synthesis of precious metal nanoparticles is control of their size and shape. In recent years, this has been fairly well achieved using chemical and physical means of synthesis [10–31]. The reduction of soluble gold salts to produce gold ions in solution was achieved using tin chloride as early as the seventeenth century to produce ruby-colored glass [31]. Likewise, early reports of colloidal nanoparticle synthesis using chemical means (e.g. those of Turkevick) highlighted the possibility of using different chemicals to produce nanoparticles of different sizes and shapes [31, 32]. As an example, Turkevich used hot sodium citrate solutions to produce gold nanoparticles of spherical or icosahedral shape, with an average diameter of 20 nm and a relatively small dispersion in size (ca. 12%) [31]. In the presence of sugars, however, silver ions are reduced and to produce spherical nanoparticles averaging 10 nm in diameter [33]. In the same reaction Au(III) was reduced to give gold nanoparticles with average diameters of about around 1.0 nm [33]. Platinum ions, in the presence of sugars, are also reduced to give spherical nanoparticles of average diameter of 2.0 nm, while the reduction of palladium ions in solutions containing sugars results in spherical nanoparticles of approximately 20 nm diameter [33].

The above-mentioned precious metal nanoparticle synthetic techniques use 'soft' reducing agents such as salts of citric acid, or other organic reducing agents such as sugars that are often plant-derived materials. In general, the chemical synthesis of precious metal nanoparticles involves conditions that are rather harsh and use either toxic or dangerous solvents and chemicals or energy-intensive methods in order to accomplish the metal reduction. In contrast, the synthesis of precious metal nanoparticles using biological systems requires the use of neither toxic chemicals nor energy-intensive processes. In fact, when using biomaterials to synthesize precious metal nanoparticles, a low temperature of only 100 °C is required, or even less in aqueous solution [7, 8]. This low temperature, when synthesizing precious metal nanoparticles, may become more apparent when comparing the thermodynamics of the reduction of gold on oat and wheat biomasses (see Section 12.2). At this point it should also be noted that most reports of the formation of precious metal nanoparticles consist only of a reduction on Au(III) ions to form pure metallic gold nanoparticles, with very few reports on the reduction of

platinum and palladium. Thus, this chapter will focus on the biological formation of metallic gold nanoparticles and cross-references to the use of other precious metals will be made as appropriate.

To date, reviews and book chapters on the biological synthesis of nanoparticles have focused on the size and morphology of nanoparticles created in this way [7, 8]; hence, this chapter will focus on the current characterization techniques of nanoscience, including X-ray absorption spectroscopy (XAS) techniques, scanning electron microscopy (SEM), transmission electron microscopy (TEM) and environmental scanning electron microscopy (ESEM), selected area electron diffraction (SAED) and X-ray diffraction (XRD), as applied to the biological synthesis of precious metal metallic nanoparticles. The chapter also details the growth of gold nanoparticles in thermodynamic terms which, to the authors' knowledge, has never been attempted for biological syntheses. Here, the biological synthesis of precious metal nanoparticles is categorized on the basis of the biomaterial used, including inactivated biological tissues and extracts from biological tissues, fungi, bacteria and live plants. The techniques used to characterize biologically synthesized precious metal nanoparticles, and their typical morphologies and size distributions, are also discussed.

12.2
Growth Process of Precious Metal Nanoparticles: Gold as an Example

The growth of nanomaterials consists of two distinct phases – nucleation and coagulation. In the nucleation phase, nanoparticle growth occurs in much the same way as in any other crystal growth, with the metal ions first being reduced from their ionic solutions into atomic clusters, which continue to grow over time [32]. The growth of nanoparticles has been found to follow an 'S'-shaped curve, with a short induction period for the growth [32]. The coagulation or agglomeration period occurs when the smaller nanoparticles collide with each other to create larger particles. The growth phase stops when the nanoparticle become stabilized in solution by different stabilizing agents. The chemical reduction of gold using sodium citrate in solution has been shown to be temperature-dependent, with an activation energy of 15 kcal mol^{-1} (62.8 kJ mol^{-1}) [32]. The activation energies for the reduction of gold via oat and wheat biomasses have been determined as 0.66 ± 0.07 and 4.8 ± 0.5 kJ mol^{-1}, respectively (present authors, unpublished results). These data suggest that a much lower activation energy is required for the reduction of Au(III) ions when using oat and wheat biomasses, as compared for example to sodium citrate reduction. The chemical reduction of Au(III) ions using formic acid and oxalic acid involves activation energies of 121.4 and 57.4 kJ mol^{-1}, respectively [34], while the reduction of Au(III) ions with other reducing agents has been estimated as 50.2 kJ mol^{-1} [35]. This shows, again, that the reduction of Au(III) ions with oat and wheat biomasses is a much more favorable process than with other reducing agents. The need for such a low activation energy may be due to the biomaterial providing the necessary nucleation sites for the

reduction and growth of gold nanoparticles. By comparison, when in solution, the other chemicals do not produce the nucleation sites needed, which in turn leads to an inhibition of nanoparticle formation and the higher activation energies associated with chemical reduction processes [33]. The lower activation energy of the biomass reduction of Au(III) ions when compared to chemical reduction may further explain the formation of equilibrium-shaped nanoparticles using bioreduction techniques [36].

On investigating the thermodynamics of gold reduction using oat and wheat biomasses in our laboratory, the activation energies for gold nanoparticle growth were shown to be 12 and 17 kJ mol^{-1}, respectively (present authors, unpublished results). These thermodynamics indicate that the reduction of Au(III) ions using aqueous slurries of biological materials is much more favorable due to the lower activation energy required for the process. Gold nanoparticle growth by vapor-depositing the gold onto the 110 surfaces of TiO_2 has an apparent activation energy of 6.6 kJ mol^{-1} [37], whereas the nucleation of gold onto the 100 surfaces of MgO involved an activation energy of 0.12 eV (ca. 12.0 kJ mol^{-1}) and showed a decrease in the saturation density of gold nucleation with increasing temperature [38]. For silicon nanowires, the activation energy of gold nanoparticle growth was determined as 10.54 kJ mol^{-1}, when using a plasma-chemical vaporization growth process [39].

Thermodynamic results (present authors, unpublished results) have shown the production of gold nanoparticles using biomaterials to be comparable with that using synthetic or organic materials. The growth data also indicate that the coagulation or agglomeration processes are the same for gold nanoparticles on biomaterials as on inorganic substances; however, the reduction process of Au(III) to Au(0) is much slower for biomaterials, which suggests that different nucleation processes are involved in the biological and inorganic/synthetic syntheses.

The coagulation or coalescence process is shown in Figure 12.1, which depicts the formation of an irregularly shaped gold nanoparticle grown by the reaction of

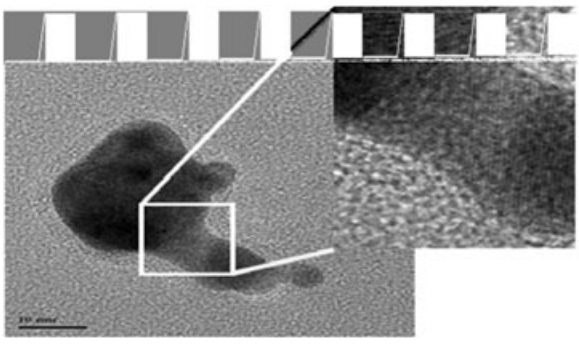

Figure 12.1 High-resolution (HR) TEM image showing the coalescence or coagulation of gold nanoparticles and the growth or joining together of two gold nanoparticles.

tetrachloroaurate with a hops biomass at pH 3 in aqueous solution. The dark and light areas of the nanoparticles represent the varying densities of Au(0) in different areas. While the expanded view of nanoparticle coalescence shows the formation of a small layer of gold between two larger gold nanoparticles. This may indicate that some nucleation of smaller nanoparticles occurs such that the larger nanoparticles are joined together. It may also represent the process of the reduction of gold by the biomass, which leads to the extremely low activation energies compared to chemical reduction techniques. The activation energy determined using oat and wheat biomass to reduce gold on the biomass may in fact be the activation energy for the sorption of gold nanoparticles by the biomass, and not the true activation energy of the reduction.

12.3 Characterization Techniques for Nanomaterials Synthesized Through Biological Means

Biologically synthesized nanomaterials may be characterized using the same instrumental techniques as for traditionally synthesized nanomaterials. The most commonly used methods for the analysis of precious metal nanoparticles include high-resolution transmission electron microscopy (HRTEM), TEM, SEM, scanning tunneling electron microscopy (STEM), XRD, electron diffraction (ED) or SAED and XAS, which incorporates extended X-ray absorption fine structure (EXAFS) and X-ray absorption near edge structure (XANES) [7, 8].

UV-Visible spectroscopy represents a basic but very important means of characterization to determine whether gold nanoparticles have been synthesized. Au(0) nanoparticles have a plasmon resonance that appears at 535 nm in the UV/Visible range, this being caused by the electronic transitions that comprise a surface phenomenon in nanoparticles [40]. The plasmon resonance for nanoparticles shifts to a lower wavelength as the synthesized nanoparticles decrease in size [41]. The plasmon resonance for gold nanoparticles synthesized using oat biomass at pH 4 and potassium tetrachloroaurate in aqueous solution is shown graphically in Figure 12.2.

The next simplest method used to determine the average size of nanoparticles is that of diffraction, which includes ED, SAED and XRD. It is well known that the broadness of a diffraction peak is related to the grain size of the nanoparticle [42]. The equation for this calculation is referred to Scherrer's equation which is shown below.

$$d = \frac{0.9\lambda}{B\cos\frac{2\theta}{2}}$$

where d is the diameter or grain size of the nanoparticles, 0.9 is a correction factor for using a Gaussian curve, λ is the wavelength of the X-rays (for copper 1.54 Å),

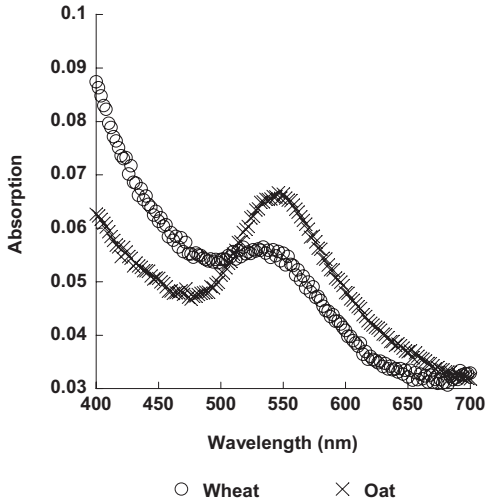

Figure 12.2 UV-visible spectra of gold nanoparticles formed in solution through the reaction of potassium tetrachloroaurate with oat and wheat biomasses at pH 4.

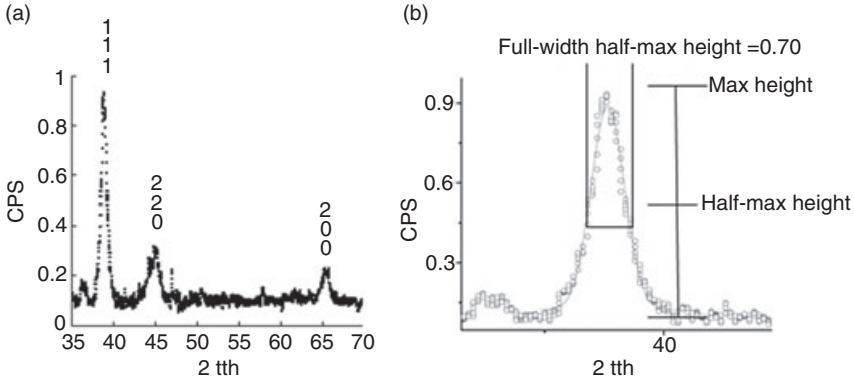

Figure 12.3 (a) X-ray diffraction of gold nanoparticles synthesized on an oat biomass using 3.0 m*M* aqueous potassium tetrachloroaurate solution and a temperature of 100 °C showing the 111, 220 and 200 diffraction planes of fcc gold; (b) An example of a Gaussian fitting of the 111 gold metal nanoparticle diffraction peak for the determination of average grain size of the biosynthesized gold nanoparticles.

B is the full width at half maximum height of the diffraction peak, and $2\theta/2$ is the peak position in 2θ divided by 2, or the peak position given in θ [42]. Scherrer's equation is applicable to all nanomaterials whether they are pure metallic, metallic oxide or organic nanoparticles. Figure 12.3(a) shows the background-corrected and normalized XRD patterns of gold nanoparticles formed on an oat biomass through

the reaction of 3.0 m*M* potassium tetrachloroaurate and oat biomass at pH 4. The biomass sample shows the gold 111, 220 and 200 diffraction peaks. The presence of a gold 111 peak also indicates that the gold nanoparticles are in a face-centered cubic (fcc) crystal structure, similar to bulk gold [43]. Figure 12.3(b) shows a calculation of the grain size of gold nanoparticles found on the oat biomass; based on the diffraction data and using the gold 111 diffraction peak, the nanoparticle size was determined as 12.0 nm. Although the ratio of peak heights between the 111 and 220 planes of gold in bulk gold has been shown as 1.9 [44], in this case the ratio was 3.03. This indicated that the gold present on the oat biomass was indeed nanoparticulate. Whilst this technique provides a bulk average distribution of the metal nanoparticles in a sample, the distribution of nanoparticle sizes can be determined via the deviations in size calculated using multiple diffraction peaks and based on the degree of anisotropy in a sample.

More exact size distributions can be determined using electron microscopy; indeed, the size distributions of nanoparticles using TEM, SEM and STEM have been well documented for nanoparticulate materials synthesized through chemical, physical and biological methods [7, 8]. Electron microscopy provides an image that allows for the determination of the morphology, size and size distribution of the nanoparticles [7]. The more recently developed technique of dark-field HRTEM has been applied to the observation of gold and silver nanoparticles synthesized through biological methods [45, 46]. Examples of dark-field and conventional HRTEM images are shown in Figure 12.4, which depicts the reduction of tetrachloroaurate with oat biomass. The dark-field HRTEM image in Figure 12.4a

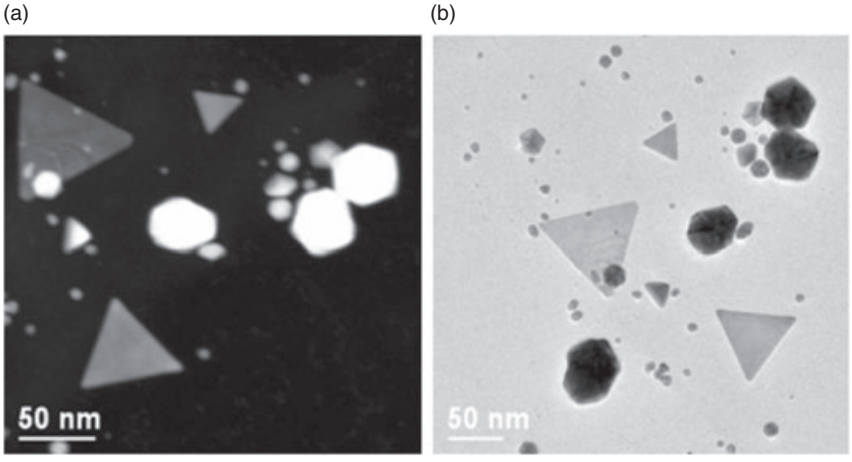

Figure 12.4 (a) Dark-field and (b) conventional HRTEM images of gold nanoparticles synthesized through the reduction of potassium tetrachloroaurate using an oat biomass. Compared to the conventional HRTEM image, the dark-field HRTEM imaging provides a better perspective of the actual shape of the nanoparticles, especially of the nonplatelet nanoparticles.

reveals bright spots which represent gold nanoparticles that have been immobilized onto the oat biomass through a reduction process.

One of the more difficult techniques used to determine nanoparticle size is that of XAS. As stated earlier, this method comprises the two complementary techniques of XANES and EXAFS, although only EXAFS is useful when determining actual nanoparticle size. The size determination of nanoparticles using EXAFS has been developed through information obtained from EXAFS spectra which provide information regarding the coordination environment of metals within the nanoparticle. More specifically, the EXAFS data provide information on the coordination number and interatomic distances between neighboring atoms. Several different EXAFS models have been developed to determine nanoparticle sizes; the majority assume a spherical shape for the nanoparticles, although some assume a cubic shape [47–52]. Although the size of nanoparticles cannot be determined using XANES analysis, other important information about nanoparticles can be obtained in this way. Figure 12.5 shows the XANES region for bulk gold (potassium tetrachloroaurate) and a sample of gold nanoparticles derived from the bioreduction of potassium tetrachloroaurate using hops biomass. The XANES of potassium tetrachloroaurate displays a feature at 11.921 keV (Figure 12.5); this so-called 'white line feature' is caused by the transition of electrons in the 5 *d*-orbital. Whilst oxidized gold has unoccupied 5 *d*-orbitals which electrons can occupy (causing this effect), Au(0) has a full 5 *d*-orbital which does not allow the white line feature to appear in the reduced gold spectrum [53]. A close observation of the gold nanoparticles shows a small white line feature at 11.921 keV, while the presence of a small white line feature and a difference in transition through the L_{III} absorption edge of the gold nanoparticle indicates that there is some unreduced gold present in the biomass sample.

Although various XAS techniques have been used to determine nanoparticle sizes, only EXAFS analysis has achieved success in this direction. Unfortunately,

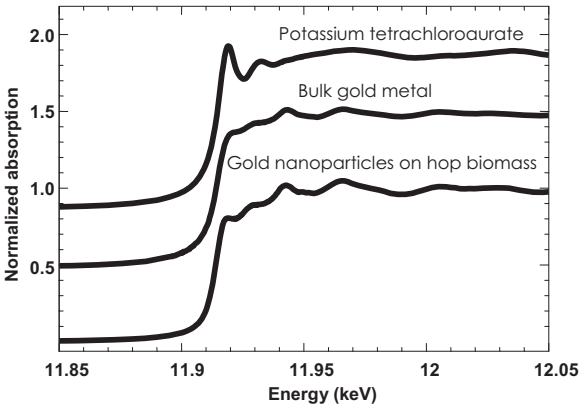

Figure 12.5 Gold L_{III} XANES region from 11.85–12.05 keV of a bulk Au(0) model compound, a potassium tetrachloroaurate model compound, and a potassium tetrachloroaurate reacted with an oat biomass at pH 4.

the use of EXAFS when determining the size of gold nanoparticles invariably leads to an underestimation in nanoparticle size, due to the nature of the technique [54–56]. The EXAFS analysis provides a bulk average of the sample, which includes both the reduced and oxidized metal contained in the sample; consequently, an averaging effect is observed in the EXAFS spectrum. This was clearly apparent when determining the mixed oxidation states of Cr(III) and Cr(VI) on an agave biomass [57]. In this case, the ligands on the biomass bound both the Cr(III) and Cr(VI), such that an arithmetic mean of the concentrations of Cr(III) and Cr(VI) was seen in the EXAFS spectrum. These concentrations were represented in the XANES of the biomass samples through calculations based on mixed standards, and the coordination numbers were determined to be averages of the bonds from the Cr(VI) and Cr(III) present on the biomass [57].

Figure 12.6 shows the Fourier-transformed EXAFS spectrum of potassium tetrachloroaurate reacted with wheat biomass and amine resin, the Au(0) foil and a potassium tetrachloroaurate model compound. Similar to results obtained for the reduction of Cr(VI) on agave biomass, the reduction of potassium tetrachloroaurate on wheat biomass (Figure 12.6a) or on an amine resin (Figure 12.6b) at pH

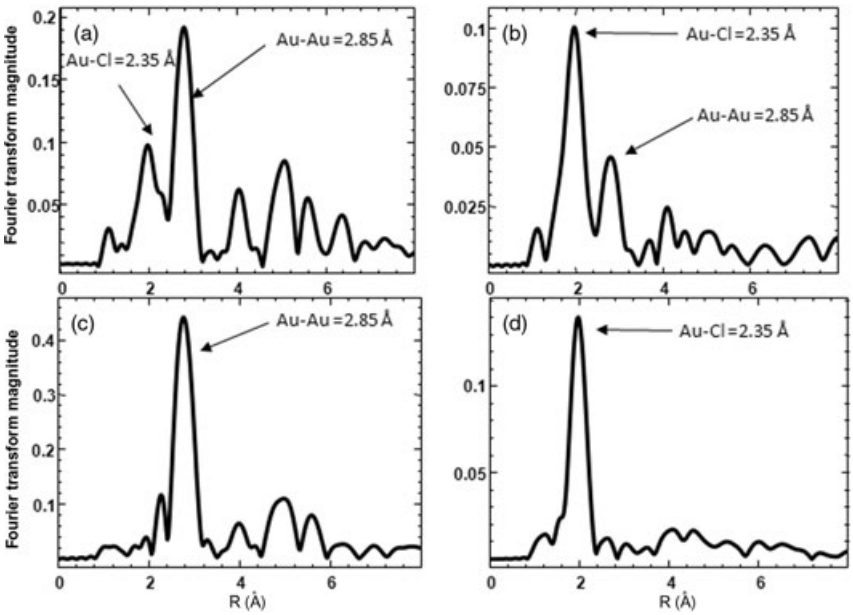

Figure 12.6 (a) Fourier-transformed gold L_{III} EXAFS of the reaction of potassium tetrachloroaurate with a wheat biomass at pH 3, showing the presence of chlorine ligands and gold–gold interactions; (b) Fourier-transformed gold L_{III} EXAFS of the reaction of potassium tetrachloroaurate with an amine resin at pH 5, showing the presence of chlorine ligands and gold–gold interactions; (c) Fourier-transformed gold L_{III} EXAFS of a Au(0) metal foil; (d) Fourier-transformed gold L_{III} EXAFS of the model compound, potassium tetrachloroaurate. R = interatomic distance.

3 was observed. Two compounds were shown to be present in the gold samples. The first compound contained Au–Cl ligands, as indicated by the interatomic distances of the first oscillation, while the second compound was gold nanoparticles, as indicated by the gold–gold interaction. Both of these interactions were present in the Fourier-transformed EXAFS, which provided an average composition of the samples, as indicated in the Cr(VI) reduction by agave biomass. Figure 12.7 shows the extracted back-transformed first shell Au–Au interaction for Au(0) in each of the samples. This showed a decrease in amplitude of the Au–Au interaction in nanoparticles synthesized both on the wheat biomass at pH 3 and on the amino resin. However, two effects were evident in the nanoparticles of both samples:

- A reduction in coordination number due to an averaging of the EXAFS oscillations of the two compounds present in the samples.
- A reduction in amplitude due to a smaller coordination in the gold nanoparticles when compared to the bulk.

In order to obtain the true coordination of the gold nanoparticles, a correction factor must be used which is based on the composition of the sample, and can be obtained from the XANES fittings of the samples. This procedure provides the true nanoparticle size. The most commonly used equation to determine the size of the Au(0) nanoparticles on biomasses, when using XAS, was developed by Borowski [50]. The equation was first developed for the size determination of small copper nanoparticles in an fcc metal, compared to the average grain size as determined by XRD [50]. The Borowski equation has been shown to be valid for all metals with a fcc packing structure, and is based on a spherical model for metal

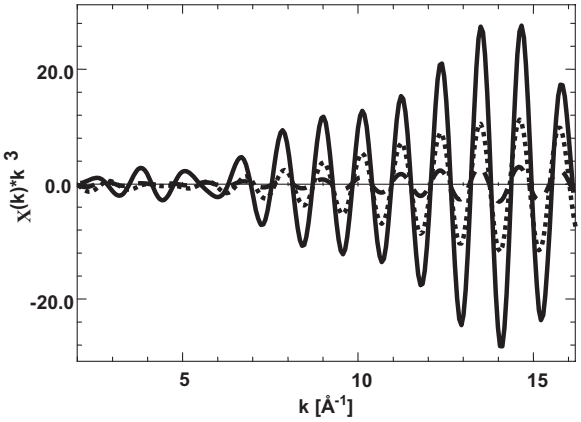

Figure 12.7 (a) Back-transformed gold L_{III} EXAFS of the reaction of potassium tetrachloroaurate with a wheat biomass at pH 3 (dotted line), and the reaction of potassium tetrachloroaurate with an amine functional group containing resin at pH 5, and a Au(0) metal foil. The solid line represents the EXAFS oscillations for the bulk gold.

nanoparticles and the partially filled first coordination sphere around the absorbing atom [50]:

$$\mathrm{FR} = R^3(N_{\mathrm{ratio}} - 1) + \frac{3}{4}dR^2 - \frac{1}{16}d^3$$

where FR is the function of the radius of the nanoparticles, N_{ratio} is the ratio of the coordination number of partially filled first coordination sphere of the nanoparticle compared to the bulk metal, d is the interatomic distance between the neighboring atoms in the first coordination sphere, and R is the radius of the nanoparticle [50].

12.4
Morphology of Biologically Synthesized Precious Metal Nanoparticles

The different structural characteristics of precious metal nanoparticles obtained via the biological reduction of precious metal ions are similar to those obtained via chemical reduction. Some different geometric types of nanoparticle obtained by the reduction of Au(III) using the inactivated tissues of biological materials are shown in Figure 12.8, while some representative nanoparticles synthesized via biological reduction techniques, including spherical (or icosahedron), decahedral, tetrahedral (nanotriangles or nanoprisms), hexagonal platelets, irregular shapes, pentagonal shapes and rods are shown in Figure 12.9. Any defects observed in nanoparticles produced by the chemical synthetic process are also visible in those

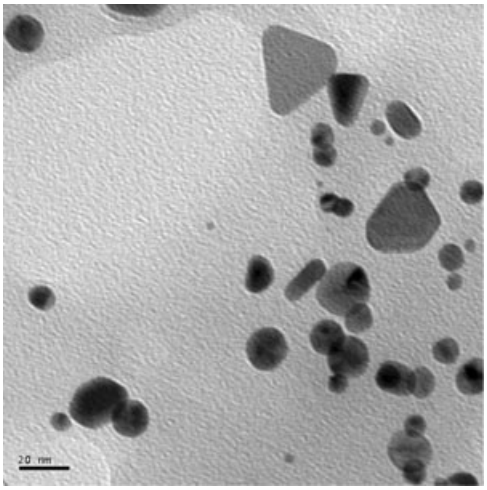

Figure 12.8 TEM image of gold nanoparticles displaying different geometries, formed on biomasses.

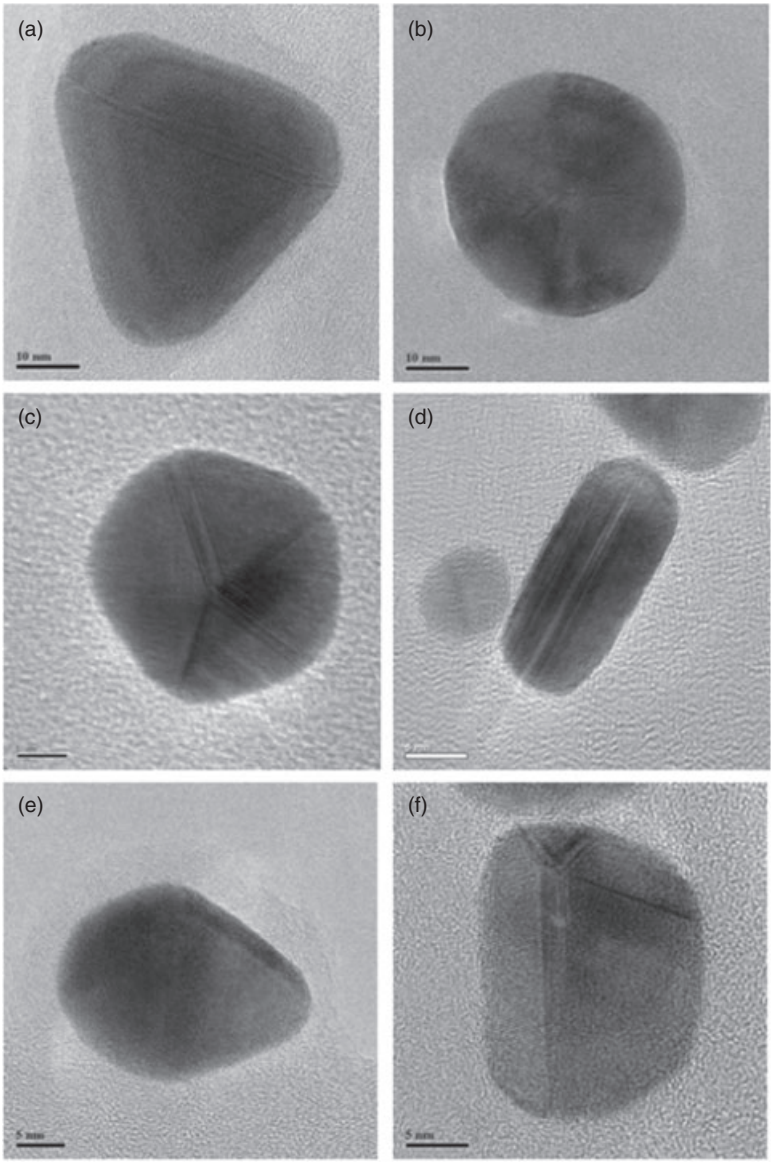

Figure 12.9 Representative geometries formed through the bioreduction of Au(III) ions using biomasses.
(a) Nanotriangle or nanoprism (tetrahedral); (b) Nanorod;
(c) Spherical (icosahedron); (d) Irregular shape;
(e) Decahedral; (f) Trapezoidal.

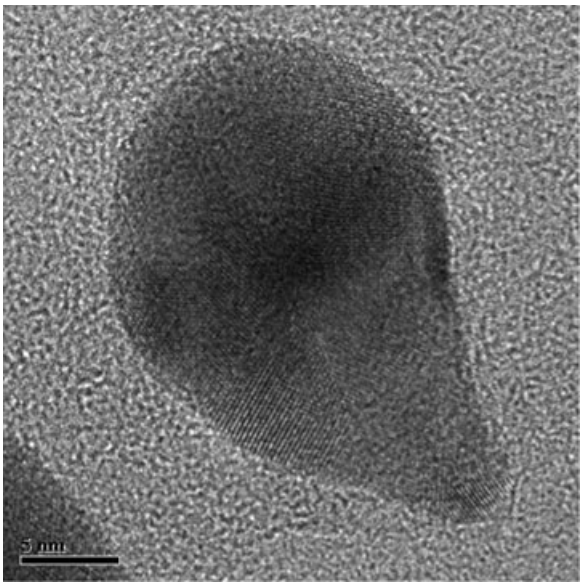

Figure 12.10 HRTEM image of an irregularly shaped gold nanoparticle formed by the reduction of potassium tetrachloroaurate with a hops biomass, resulting in a 'tadpole'-like shape.

synthesized by biological processes. For example, defects in the crystal structure, such as twinning and multiple twinning, are present in both biologically synthesized and chemically reduced gold when producing Au(0) nanoparticles.

More recently, some additional shapes reported during the chemical reduction of gold to create gold nanoparticles have been observed when using biomaterials to effect the same product. One such shape is the 'tadpole' [58]; this was created via the reduction of chloroaurate ions in the presence of trisodium citrate, using sodium dodecylsulfate (SDS) as capping agent [58]. The 'tadpole' is in fact an irregularly shaped nanoparticle formed by the coalescence of two differently shaped nanoparticles, and has been observed in the reduction of Au(III) ions using a hop biomass (see Figure 12.10).

12.5
Inactivated Biological Tissues and Extracts for Nanoparticle Synthesis

12.5.1
Synthesis Using Inactivated Biological Tissues

The reduction of metal ions to form metallic nanoparticles has been performed using inactivated tissues and extracts of several different organisms [7]. Such

reduction by biomaterials is not new, an early example being the 'silver mirror' test, in which aldehydes, ketones, amines or reducing sugars induced the reduction of silver [7]. The silver mirror test was in fact the earliest example of reducing sugars being used to synthesize nanomaterials. The experiment involved the reaction of reducing sugars with a silver nitrate solution so as to form bulk silver particles [7], with the nanoparticle synthesis being regulated by the concentration of either the silver ions or sugars in solution. Biological materials contain many different functional groups such as sugars, carboxyl acids, carbonyl groups and amine groups, all of which have the ability to reduce metal ions.

12.5.1.1 **Algal Biomass**

Several different biomasses have the ability to reduce gold and silver ions in aqueous solution to form metallic nanoparticles [7]. Among these, algal biomasses were the first to demonstrate an ability to reduce aqueous Au(III) ions from hydrogen tetrachloroaurate in aqueous solution to form colloidal gold solutions [59]. Colloidal gold formation was demonstrated using UV-visible spectroscopy and measuring the Au(0) plasmon resonance peak at 525 nm [59]. Although the actual size of the nanoparticles was not determined, the initial reduction mechanism for Au(III) colloidal or nanoparticle formation was determined [59] as follows:

Step 1. $AuCl_4 \rightarrow$ Au(I)Cl-Biomass
Step 2. Au(I)Cl-Biomass $\rightarrow Au(0)_{(s)}$-Biomass

Step 1 of the mechanism involved the rapid reduction of Au(III) ions to Au(I), this being determined by the rapid loss of three chloride ions in solution. The subsequent reduction of Au(I) to Au(0) was seen to be the rate-limiting step in the mechanism [59].

12.5.1.2 **Alfalfa Biomass**

Some years later, the synthesis of gold nanoparticles was also demonstrated on an alfalfa biomass, with Au(III) ions being reduced in aqueous solution to form Au(0) nanoparticles [60]. By using the alfalfa biomass, several studies were conducted to characterize this bioreduction process [60–62]. Based on their bioprecipitation, the gold nanoparticles were seen to consist of fcc crystal structures with structures including tetrahedral, hexagonal platelets, icosahedral multi-twinned, decahedral multi-twinned and irregularly shaped [60]. The study also showed that, at pH 2, the reaction of an aqueous solution of tetrachloroaurate with an alfalfa biomass resulted in a 40% particle distribution with an irregular shape, 25% icosahedral, 18% decahedral, 16–17% tetrahedral and 4–6% hexagonal platelet [60]. In terms of size distribution, the tetrahedral nanoparticles ranged from 20 to 300 nm, the hexagonal platelet Au(0) nanoparticles from 20 to 350 nm, the irregularly shaped nanoparticles from 15 to 110 nm, and the decahedral nanoparticles from 5 to 90 nm. The icosahedral nanoparticles had the smallest size distribution, from 10 to 80 nm [60].

The bioreduction of Au(III) ions by alfalfa biomass was also investigated, using XAS, to demonstrate the effect of pH on reduction [61]. By using slightly different

reaction conditions, nanoparticles synthesized on alfalfa at pH 2 had an average radius of 9.0 nm, but this rose to 6.2 nm when the pH was raised to 5 [61]. The average nanoparticle size was determined using the Borowski equation. When the binding and reduction of Au(III) ions by alfalfa biomass was investigated using a combination of flame atomic absorption spectroscopy (FAAS), XAS and electrochemical techniques [62], the results were similar to those obtained for the bioreduction of Au(III) ions by an algal biomass. Initially, 3 mol of Cl^- were released per mole of gold adsorbed onto the alfalfa biomass [62]. However, XAS data showed that the ligand present on the alfalfa biomass responsible for the binding and possible reduction of the Au(III) ions was either an oxygen or a nitrogen moiety, this being the only ligand clearly visible in the EXAFS spectra after 5 min of binding [62]. It was also shown that a period of up to 12 h was required to achieve complete reduction at room temperature [59]. The report also resulted in the discovery of a new, previously unobserved nanoparticle geometry in the synthesis of Au(0) nanoparticles through chemical or physical means. This so-called truncated icosahedron had an extremely low-energy geometry for Au(0) nanoparticles, and was thought to be formed as a result of the slow reduction of Au(III) to Au(0) on the biomass [36].

12.5.1.3 Oat and Wheat Biomasses

Additional biomasses capable of reducing Au(III) ions to form Au(0) nanoparticles were those of oat and wheat [63, 64]. Although an oat biomass produced gold nanoparticles with a size distribution of 10 to 80 nm in a reaction of 0.10 m*M* gold(III) solution over a pH range of 2 to 5 [63], the major proportion of the nanoparticles was in the 10 to 40 nm size range [63]. In addition, a larger number of gold nanoparticles was formed at pH 2 and 3 than at pH 4 and 5 [63], whereas at pH 6 most of the nanoparticles formed were irregularly shaped [63]. A wheat biomass proved capable of forming gold(0) nanoparticles at pH 2–6, the reactions being carried out at room temperature with an aqueous 0.3 m*M* Au(III) solution and a reaction time of 3.5 h [64]. Nanoparticles synthesized via the reduction of Au(III) ion on a wheat biomass yielded all morphologies of fcc Au(0) nanoparticles observed previously with other biomaterials, including tetrahedral, decahedral, hexagonal, icosahedral, irregular and rod [64]. Data from the wheat biomass also showed the greatest percentage of gold nanoparticles to be in the range of 10–30 nm. At pH 2, the majority was in the size range of 10 to 50 nm, with a tailing in size distribution towards larger nanoparticles, whereas at pH 3 the size distribution was greatest between 5 and 30 nm. At pH 4, nanoparticle sizes ranged between 5 and 25 nm (with the majority 10 nm), while at pH 5 the size range was 5 to 30 nm, with the highest distribution between 10 and 20 nm. A similar trend was observed at pH 6 [64].

12.5.1.4 Hops Biomass

Hops biomass has the ability to reduce Au(III) ions to form Au(0) nanoparticles [65]. XAS techniques have been used to elucidate the average nanoparticle size and to determine the binding and reduction mechanisms of Au(III). These authors

further investigated the reduction of Au(III) ions and nanoparticle formation by chemically modifying the hops biomass; this included hydrolysis or the addition of oxygen moieties to the biomass [65]. EXAFS calculations and the Borowski equation showed the nanoparticles to have an average diameter of 34.6 nm in the unmodified hops biomass [66]. However, when the biomass was hydrolyzed the Au(0) nanoparticles grew too large to be determined with this method, indicating a diameter in excess of 50 nm. Finally, an esterified biomass led to an average nanoparticle diameter of 18.4 nm [66], indicating that oxygen-containing functional groups on the biomass are fundamental in the reduction of Au(III) ions to form Au(0) nanoparticles.

12.5.1.5 *Cinnamomum camphora* Biomass

The reduction of both silver and gold ions has also been studied in the dried leaves of *Cinnamomum camphora* [67]. By using UV-visible spectrometry, these authors followed the plasmon resonance at 440 nm and 530 nm for silver and gold, respectively. The results showed an increasing absorption from 2 min through 60 min, indicating that the reduction of both metals had occurred in solution with the biomass. When the silver nanoparticles formed on the biomass were analyzed using TEM, the particle distribution was seen to range from 20 to 85 nm, although the majority was in the range of 50 to 85 nm, with the greatest proportion between 65 and 75 nm. In contrast, gold nanoparticles synthesized on the same biomass showed a spherical morphology with an overall distribution from 12 to 35 nm (greatest proportion from 15 to 22 nm). Gold nanotriangles were also observed in the reduction of Au(III) ions with this biomass, showing a size range of 25 to 200 nm, with a highest distribution between 40 and 100 nm. XRD analysis indicated that both silver and gold nanoparticles synthesized on the *C. camphora* biomass had fcc structures showing the 111, 200, 220 and 311 planes for silver and gold [67].

12.5.2 Synthesis Using Extracts from Biological Tissues

Similar to the reduction of precious metal ions on biomasses, extracts from plants have also been shown capable of reducing precious metal ions in aqueous solution [7]. Extracts from *Aloe vera*, geranium leaf, lemongrass, *Emblica officinalis* fruit extract and Neem leaf broth have been used to synthesize either Au(0), Ag(0) or gold/silver core-shell nanoparticles [68–75]. The general synthesis techniques in these types of study involve the boiling in water of fresh-cut plant materials in different proportions to create a 'broth' of organic acids and organic compounds present in the plants. This broth is then reacted with gold or silver ions at different times, temperatures or dilutions [68–75].

In the case of lemongrass extracts, aqueous solutions of tetrachloroaurate were reacted with the plant extract, which resulted in the formation of colloidal gold solutions [71]. The formation of gold nanoparticles was confirmed by UV-visible data, which showed the presence of plasmon resonance at approximately 530 nm in the reaction solutions. A TEM analysis revealed the nanoparticles to be nano-

triangles or tetrahedrals and platelets, with some spheres; however, the size distribution ranged from small nanometer to micron-sized particles, with the highest distribution around 500 nm. An atomic force microscopy (AFM) analysis showed the nanoparticles to be nanotriangles with definite dimensions and rather flat on the surface [71]. When using a geranium leaf broth, a combination of UV-visible, TEM and XRD was used to characterize the nanoparticle synthesized [69]. The plasmon resonance for silver nanoparticles was shown to be present in the UV-visible spectra of the sample and increased with increasing time. In addition, the XRD data showed the 111, 200, 220 and 311 planes for fcc silver, which were broadened and indicated the presence of nanoparticles formed by the leaf broth. Finally, TEM analysis showed the silver nanoparticles to be polydispersed from 16 nm to 40 nm, with an average size of 27 nm [69].

In a similar study, gold nanotriangles and silver nanoparticles were synthesized using *Aloe vera* plant extracts [68]. The gold nanoparticles produced were triangular in shape, with a very long edge length of 150 nm when synthesized using 1 ml of *Aloe vera* extract and 6 ml of 1.0 m*M* $HAuCl_4$ solution. The majority of the nanoparticles resembled platelets rather than tetrahedrals. However, when the reaction mixture included 4 ml of *Aloe vera* extract and 6.0 ml of gold solution the nanoparticles contained multiple shapes, including tetrahedral, but the platelets had disappeared [68]. When the reaction was performed with 0.5 ml of plant extract and 6.0 ml gold solution the nanoparticles were an agglomeration of much smaller nanoparticles. Electron diffraction was also used to corroborate the nanoparticle formation, which showed the 422, 220 and 311 lattice planes of fcc gold. With regards to the silver nanoparticles, both TEM and electron diffraction showed the nanoparticles in fact to be spherical Ag(0) nanoparticles, with electron diffraction showing the 111, 200, 220 and 311 lattice planes of fcc silver.

Extracts of the fruit of *Emblica officinalis* (Indian Gooseberry) have been shown to reduce gold and silver ions in solution to produce gold and silver nanoparticles [74]. The gold nanoparticles ranged in size from 10–20 nm, while the silver nanoparticles were between 15 and 25 nm. The same authors also performed a phase transfer of the nanoparticles from aqueous phase to an organic phase using a cationic surfactant, octadecylamine.

Silver nanoparticles have also been synthesized using *Capsicum annuum* L. (Cayenne pepper) plant extracts [76]. The plasmon resonance at 440 nm was followed (using UV-visible spectrometry) from 0 to 15 h, and showed an increasing intensity as time passed and the concentration of silver was augmented. However, XRD showed rather clean and sharp diffraction peaks in the synthesized nanoparticles corresponding to the 111, 200, 220, 311 and 222 lattice planes of fcc silver. The average grain size determined from the XRD using the Debye–Scherrer equation was 42–46 nm, depending on the reaction conditions. XPS was used to confirm the presence of Ag(0) in the samples by the presence of $Ag3d_{5/2}$ and $Ag3d_{3/2}$ peaks. The SAED analysis showed spacings of 0.236, 0.220, 0.141 and 0.121, which were indexed as the 111, 200, 220 and 311 planes of silver. Finally, a TEM analysis showed the presence of spherical nanoparticles in the extracts [76].

Extracts from Neem leaf broth have been used to synthesize gold, silver and bimetallic gold/silver core-shell nanoparticles [75]. In the individual nanoparticle

synthesis, the plasmon resonance was observed for both silver and gold at 440 and 550 nm, respectively, and was shown to augment with increasing time from 0 to 240 min. The diffraction patterns for the individual silver and gold nanoparticles showed the presence of the 111, 200, 220 and 311 diffraction planes of fcc gold and silver. A TEM analysis showed the silver nanoparticles to be spherical, with a small organic layer on the top of the nanoparticles, indicating a capping agent, whereas the gold nanoparticles varied in shape, to form spherical, hexagonal platelets, tetrahedral, rod and other common shapes. The core-shell nanoparticles showed that the gold was reduced at a faster rate in the bimetallic solution than in the monometallic solutions. It was also assumed that the silver nanoparticles were very small during this synthesis, as the plasmon resonance was found to be at 317 nm. It was inferred that the absence of 450 nm silver plasmon resonance was due to a precipitation of the gold shell on top of the silver nanoparticles. A TEM analysis showed that the size of the core-shell gold/silver nanoparticles synthesized via this method ranged from 50 to 100 nm; it was also noted that the nanoparticles were 50–70 nm, with smaller nanoparticles of 15–20 nm capping the larger nanoparticles. A further assumption was that, due to the slower reduction rate of silver, the latter was dispersed over the surface of the gold nanoparticles.

The bioreduction of chloroaurate ions by geranium leaf broth and its native fungus *Colletotrichum* sp. has been shown to produce gold nanoparticles [70]. UV-visible spectroscopy at 550 nm showed the intensity of the gold plasmon resonance to increase with reaction time, as seen with other biomass extracts. An XRD analysis showed that the nanoparticles were fcc gold metal nanoparticles with 111, 200, 220 and 311 diffraction peaks. However, a TEM analysis showed that, unlike other extracts, the nanoparticles synthesized by this plant included nanorods, but were predominately decahedral and icosahedral, with averages sizes in the range of 20 to 40 nm. The synthesis of silver nanoparticles has also been achieved using spent mushroom substrate [77], where the silver nanoparticle plasmon resonance at 436 nm was found to increase over time. The authors also used XRD to analyze the nanoparticles which showed main diffraction peaks of fcc silver between 30 and 80 in 2θ. A TEM analysis was also performed which showed the nanoparticles to be monodispersed, with sizes ranging from 25 to 35 nm. The TEM analysis also showed the presence of a small organic layer formed around the silver nanoparticles, which was considered to be the formation of a protein protective layer. These nanoparticles demonstrated good antibacterial properties when further tested against *Staphylococcus aureus* and *Klebsiella pneumonia*.

12.6
Nanoparticle Synthesis Using Fungi and Bacteria

12.6.1
Fungal Synthesis of Precious Metal Nanoparticles

Although, fungi have been shown to produce metallic nanoparticles of silver, gold and platinum [7], the majority of studies in this area have focused on the synthesis

of silver nanoparticles. The species of fungi studied include (but are not limited to) *Aspergillus niger, Aspergillus fumigates, Aspergillus flavus, Fusarium oxysporum* f. sp. *lycopersici, Fusarium semitectum, Phaenerochaete chrysosporium* and *Verticillium* [77–93]. The synthesis of silver nanoparticles using fungi has produced some very interesting results in terms of the type and size distribution of the nanoparticles created. *Fusarium semitectum* has been shown to synthesize Ag(0) nanoparticles on the cell surface and, by using UV-visible spectroscopy to follow the reduction, such synthesis has been shown to be time-related [93]. The UV-visible data showed the silver nanoparticle plasmon resonance at 440 nm to increase slowly over 120 h of reaction time. In order to further corroborate the synthesis of silver nanoparticles, the same authors used XRD analysis, which showed the 111, 200, 220 and 311 diffraction planes for metallic silver. Based on XRD data and Scherrer's equation analysis, the average grain size of the nanoparticles was determined as 35 nm. A TEM analysis of samples showed 30% of the particles to be in the 25 nm range, and 20% and 17% to be in the range of 35 and 42 nm, respectively. The remaining 33% of the nanoparticles were either <8 nm or up to 65 nm in size. The *A. fumigates*-mediated synthesis of silver nanoparticles was followed with UV-visible spectroscopy, TEM and XRD analyses. XRD showed four distinct diffraction peaks in the range of 30 to 80 in 2θ, which correspond to the 111, 200, 220 and 311 planes of fcc silver nanoparticles [80]. The UV-visible data showed that the silver nanoparticle surface plasmon resonance at 450 nm increased with increasing incubation time, from 0 to 72 h, indicating the growth and formation of silver nanoparticles. Based on a TEM analysis of the fungal mycelium, it was determined that the nanoparticles had a size range of 5 to 25 nm.

Silver nanoparticles have also been successfully synthesized using the white rot fungus *P. chrysosporium* [89]. Here, the authors used TEM, UV-visible, XRD and ESEM/SEM to investigate the synthesis of silver nanoparticles. The XRD analysis showed all major diffraction peaks of FCC silver between 30 and 80 degrees, which has low intensity and were broadened, indicating the formation of silver nanoparticles. ESEM/SEM showed the nanoparticles to be present on the outside of the fungal mycelium, while TEM showed them to have shapes consistent with pyramidal and hexagonal structures. TEM also showed that the silver nanoparticles synthesized using this technique were polydispersed.

Verticillium has also been shown to synthesize silver nanoparticles [91]. From a TEM analysis, it was determined that the Ag(0) nanoparticles synthesized via the reaction of *Verticillium* with silver ions were polydispersed, with a mean size of 25 ± 12 nm. Silver nanoparticles synthesized through the incubation of aqueous Ag(I) ions with *A. flavus* [92] were monodispersed, with an average size of approximately 9 nm ± 1.6 nm as determined by TEM. An XRD analysis of these samples confirmed the silver as fcc silver, based on the 111, 200 and 220 diffraction peaks. Again, SEM showed the silver nanoparticles to be located on the outside of the fungal mycelium. The UV-visible data showed an initial increase in silver plasmon resonance with time, but this then remained constant after 72 h. *Fusarium oxysporum* has also been shown to synthesize Ag(0) nanoparticles extracellularly [87]; here, a TEM analysis showed the nanoparticles to be polydispersed, ranging in size from 5 to 50 nm. The SAED analysis showed diffraction of the silver 311, 200

and 220 planes of fcc, which indeed indicated the presence of Ag(0) nanoparticles. As with most other fungal species, the reduction did not seem to be complete even, after 72 h of reaction time, as large increases in the silver nanoparticle plasmon resonance at 425 nm were still evident.

Colloidal gold nanoparticles synthesized using the fungus *A. niger* were found to be self-assembled on the hyphal surface of the fungus [78]. In this study, optical absorption spectroscopy showed the nanoparticles to be glutathione-protected on the fungal surface. More interestingly, one of the SEM images showed collapse of the hyphae, thus creating a tubular assembly of gold nanoparticles that may be useful to create hollow, nanoparticulate assemblies. The synthesis of gold nanoparticles has also been observed using *F. oxysporum* [88]; here, UV-visible spectroscopy analysis of the gold nanoparticle plasmon resonance at 550 nm was used to show that the fungus could synthesize gold nanoparticles over a span of 2 to 48 h. TEM analysis showed the gold nanoparticles to be in the size range of 20 to 40 nm, and to have spherical and triangular shapes. Fourier-transform infra-red (FTIR) analysis also demonstrated the presence of carbonyl stretches and amide stretches, from which the authors inferred that the stability of these nanoparticles was due to protein stabilization.

The synthesis of platinum nanoparticles has been shown to occur on *Fusarium oxysporum* f. sp. *lycopersici*, through the reaction of aqueous platinum ions and the fungal biomass [83]. A TEM analysis showed the synthesis of rectangular platinum nanoparticles ranging in size from 10 to 100 nm on the hyphal surface, whereas, under slightly different reaction conditions rectangular and cubic platinum nanoparticles were formed, with size ranges of 10 to 30 nm, after only 2 h of incubation. Interestingly, the zero-time sample had widely varying nanoparticle shapes and sizes, including irregular, cubic and rectangular.

12.6.2 Bacterial Synthesis of Precious Metal Nanoparticles

It is perhaps not surprising that bacteria are able to reduce precious metal ions in solution or growth media synthesizing metallic nanoparticles, as many bacteria have reducing properties; examples include iron-, sulfate- and nitrate-reducing bacteria [94–96]. The following bacteria (among others) have been used to synthesize gold and silver nanoparticles: *Bacillus subtilis, Shewanella* algae, *Pseudomonas stutzeri, Thermomonospora* sp., *Rhodococcus* sp., filamentous cyanobacteria (*Plectonema boryanum*), *Acidithiobacillus thiooxidans* sp. and *Rhodopseudomonas capsulata* [97–107]. However, the use of bacteria to reduce precious metal ions to form metallic metal nanoparticles is scarce, most likely due to the toxicity of elements such as platinum and silver in biological systems.

The reduction and formation of colloidal gold was observed in a study on the bioaccumulation of the gold by the filamentous cyanobacterium (*P. boryanum*) from a Au(III) chloride complex [104]. When the bacterial samples were studied using XAS, SAED and TEM, the XAS or XANES analyses showed the presence of a mixture of different types of gold compounds, including Au(I) sulfide, gold

metal, gold hydroxide and some residual Au(III) chloride complex. A TEM analysis showed the presence of commonly shaped gold nanoparticles, including tetrahedral, spherical and other geometries. The gold nanoparticles were further analyzed using SAED analysis, which showed the 400, 311, 420 and 511 diffraction planes for gold. The 220, 311 and 220 diffraction planes of fcc gold were also observed in the nanoparticles. The morphology of gold nanoparticles synthesized by this filamentous cyanobacterium from Au(I) thiosulfate and Au(III) complexes were also investigated, using TEM, SAED and XPS [106]. The XPS data suggested that the bacterium promoted growth of the gold 111 faces in the samples, confirming the presence of Au(0), whereas, the SAED analysis showed again the 400, 311, 420 and 511 diffraction planes. However, TEM analysis showed the presence of gold nanoparticles of less than 10 nm diameter inside the living cells, although in solution the gold was found to precipitate as octahedral 111 platelets with sizes of 1 to 10 nm.

Gold nanoparticles have also been synthesized using living cells of *Pseudomonas aeruginosa* [108]. In this study, the authors followed the Au(0) nanoparticle plasmon resonance, which was found to be slightly shifted to a higher wavelength compared to the normal plasmon resonance of 530 nm. A TEM analysis showed the nanoparticles to have size distributions of 40 ± 10 nm, 25 ± 15 nm and 15 ± 5 nm, possibly due to the slightly different reaction conditions and the use of varied subspecies of *Ps. aeruginosa*.

Rhodopseudomonas capsulata has also shown an ability to reduce gold ions to form Au(0) nanoparticles [107]. A TEM analysis of nanoparticles formed by this bacterium showed a size distribution between 10 and 20 nm. The shape of the nanoparticles was found to be spherical at pH 7, although at pH 4 the formation of nanoplatelets was observed with sizes in the range of 50 to 400 nm. The nanoparticles synthesized via this reaction were diffracted using X-rays and showed the common gold diffraction peaks for fcc gold nanoparticles. Another study monitoring the effects of the thiosulfate-reducing bacterium *Acidithiobacillus thiooxidans* on the stability of the gold–thiosulfate complex has shown that, over time, the complex is reduced to Au(0) nanoparticles [106]. In fact, after 75 days, the gold was found to have precipitated into gold wires or gold coils which were analyzed using XRD, TEM and SAED. The XRD spectrum showed a very broad but weak peak corresponding to the gold 111 diffraction plane; however, the SAED results showed the presence of 110, 200 and 220 planes of fcc gold. Unfortunately, the gold was also shown to be toxic towards the bacterium. Whilst a TEM analysis showed gold wires of 0.5 to 5 μm in length, a closer observation of these data suggested that these large structures were actually collections of smaller Au(0) nanoparticles. The small nanoparticles (5–10 nm) were also shown to be precipitated inside the cells.

Platinum nanoparticles have been successfully synthesized using cyanobacteria (*Plectonema boryanum*) [105], with a TEM analysis showing the nanoparticles to have spherical shapes and multiple size ranges, due mainly to the different temperatures used. The SAED analysis also confirmed that the bacterium could synthesize platinum nanoparticles showing the 111, 002, 022 and 113 diffraction

planes of fcc platinum metal. SEM images showed the platinum nanoparticles to be located on the outside of the bacterium. In addition, when an XPS analysis was used to determine the coordination of the platinum in the growth medium, reduced platinum and a composition of platinum cluster compounds (e.g. complexes with carboxyl groups and metallothioneins) was identified.

Silver nanoparticles may be synthesized via the bioreduction of silver ions, using the supernatants of cell cultures from *Klebsiella pneumonia, Escherichia coli* and *Enterobacter cloacae* [109]. Here, the Ag(0) nanoparticle plasmon resonance was observed at about 430–450 nm, giving a strong indication that reduction of the silver ions had indeed occurred. It was found that, after a 5 min reaction between the silver ions and the supernatant of *K. pneumonia*, silver nanoparticles were formed that appeared to have spherical shapes. The sizes of the nanoparticles formed in this reaction were also extremely polydispersed, ranging in size from 28 to 120 nm, with the highest distribution between 38 and 78 nm.

12.7 Nanoparticle Synthesis by Living Plants

The first report of nanoparticle production by higher plants was credited to Gardea-Torresdey *et al.*, who found that alfalfa plants (*Medicago sativa*) grown for two weeks in a Au(III)-enriched medium formed structures in the fcc configuration after reducing Au(III) to Au(0). The TEM images of reduced gold within the plant tissues showed an icosahedral structure, which is considered to be the low-energy configuration for Au(0). Subsequently, the same group germinated and cultivated alfalfa in a silver-enriched medium and found that the plant could also form silver nanoparticles [110, 111]. TEM images of stem segments showed that silver nanostructures ranging between 2 and 20 nm in size were distributed throughout the stem, in assemblies akin to nanowires. In 2005, Yates and coworkers reported that Morning glory (*Ipomoea lacunosa*) was able to form titanium nanoparticles when exposed to a titanium-enriched medium in a hydroponic solution [112]. Recently, Gardea-Torresdey and colleagues, at the University of Texas at El Paso, reported that Desert willow (*Chilopsis linearis*), a desert plant species that grows well in mine tailings, is able to absorb and reduce up to 67% of the Au(III) to Au(0), even in the presence of thiourea or thiocyanate [113]. The XAS and TEM analyses of gold-laden plant samples indicated that Desert willow could produce gold nanoparticles within its tissues (Figure 12.11). Typically, plants treated for 13 days with 160 mg $Au\,l^{-1}$ formed nanoparticles with diameters averaging approximately 8, 35 and 18 Å in the root, stem and leaf, respectively [114]. It was also reported that the average size of the Au nanoparticles formed was related to the total Au concentration in the tissues, and their location in the plant, with larger nanoparticles being found in the stems and smaller particles in the roots.

The Massey University group in New Zealand, in conjunction with the Gardea-Torresdey group, also showed that other gold-absorbing could form gold nanoparticles [115]. It was reported that Au nanoparticles of 5–50 nm diameter were

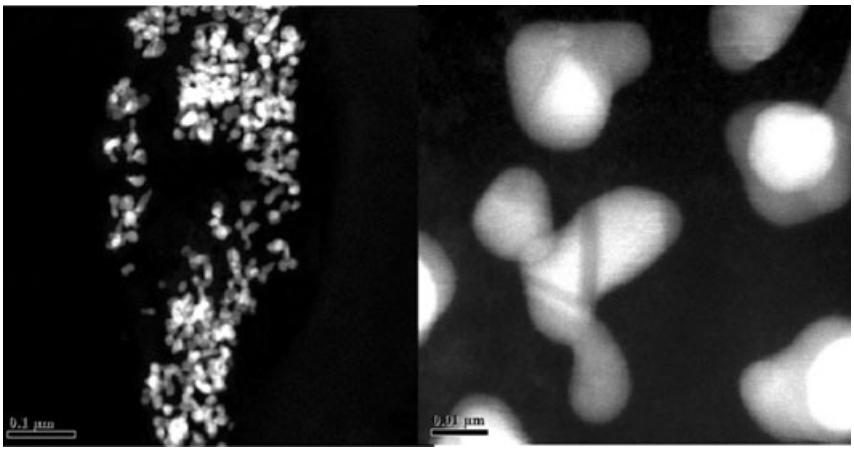

Figure 12.11 Dark-field TEM images of the stem of *Chilopsis linearis* grown for 13 days with Au (5 mg l^{-1}) and treated with isocyanate.

formed by Indian mustard (*Brassica juncea*) plants grown in soil with 22–48 mg Au kg^{-1}. However, unlike alfalfa and Desert willow – both of which reduced a high percentage of the Au(III) to Au(0) – Indian mustard produced Au(0) and Au(I) in similar proportions [115]. The group of Sahi, at Western Kentucky University [116], also in combination with Gardea-Torresdey and colleagues, reported recently that the rattlesnake plant (*Sesbania drummondii*) was able to biotransform Au(III) into Au(0) with great efficiency, thus forming Au nanoparticles with catalytic power. The gold nanoparticle-bearing biomatrix produced was shown directly to reduce 4-nitrophenol in aqueous solution, thereby demonstrating the catalytic potential of these bioformed gold nanoparticles.

More recently, the research group at Massey University showed that plants could also form mixed-metal nanoparticles [117]. In this study, Indian mustard was grown for nine weeks in soil enriched with Au, Cu and Ag, at concentrations of 48, 44 and 31 mg kg^{-1}, respectively. By using STEM and energy dispersive X-ray analysis, it was shown that the plants formed nanoparticles containing Au, Ag, and Cu at an average composition of 43, 57 and 1 atom%, respectively. It was concluded that this procedure might permit the construction of catalysts that are difficult to create using traditional methods.

Although the mechanism(s) used by plants to form metal nanoparticles remain largely unsolved, the results of a reaction between lemongrass plant extract and tetrachloroaurate led Shankar and coworkers to conclude that the reducing sugar in the extract reduced the Au(III) to Au(0), while the aldehydes/ketones of the extract induced growth of the gold nanocrystals [71]. It has been hypothesized that, in the rattlesnake plant, Au(III) is bound to the carboxylic acid moieties present in the root cell walls. Yet, the nanoparticles were observed exclusively in the cytoplasm, which is indicative of active transport [117]. In addition, Manceau *et al.*

have suggested that ascorbic acid in the roots, and the breakdown products of ascorbic acid in the rhizosphere, each participate in the reduction of copper at the soil–root interface, although unfortunately no evidence was provided of mechanistic processes inside the cells. The discovery of the mechanisms of nanoparticle formation inside plant tissues, and the way in which these nanoparticles can be harvested, should represent a major advance in the 'green' production of metal nanoparticles, and benefit environmental science as a whole.

12.8 Conclusions

During the past five years, a host of advances have been made in the biological synthesis of precious metal nanoparticles. The characteristics of these biological syntheses are, in general, similar to those of chemical syntheses, with the two systems resulting in very similar shapes, geometries and size ranges. It is perhaps not surprising that biological systems are capable of synthesizing metallic precious metal nanoparticles, as they contain similar functional groups as are used for such chemical reductions. Some examples include carboxyl and amine groups commonly used to reduce precious metal ions to form metallic nanoparticles. More recently, a variety of sophisticated techniques, including XRD, TEM, HRTEM, SEM, SAED, XAS and XPS, have been used to determine the characteristics of biologically and chemically synthesized precious metal nanoparticles, and provided essentially the same information for both materials. Likewise, the characterization of precious metal nanoparticles synthesized biologically show the same characteristics such as fcc metal structure, as determined by XRD and SAED. In some instances there have been reports of new nanoparticles arising from the biological reduction of precious metal nanoparticles, an example being the truncated icosahedron nanoparticles synthesized using an alfalfa biomass.

Acknowledgments

The authors acknowledge the STARS and LERR programs of the University of Texas System and the University of Texas at El Paso's Center for Environmental Resource Management through funding from the Office of Exploratory Research of the U.S. Environmental Protection Agency (cooperative agreement CR-819849-01). The authors also thank the National Science Foundation and the DOE Gateway Program at UTEP. Parts of this research were carried out at the Stanford Synchrotron Radiation Laboratory, a national user facility operated by Stanford University on behalf of the U.S. Department of Energy, Office of Basic Energy Sciences. The SSRL Structural Molecular Biology Program is supported by the Department of Energy, Office of Biological and Environmental Research, and by the National Institutes of Health, National Center for Research Resources, Biomedical Technology Program. Jorge Gardea-Torresdey also acknowledges the Dudley family for the Endowed Research Professorship in Chemistry. Dr. Gardea-Torresdey acknowledges the funding from the NSF-EPA funded UC Center for Environmental Implications of Nanotechnology (Grant # EF-0830117)

References

1 Marsden, C., Taarning, E., Hansen, D., Johansen, L., Klitgaard, S.K., Egeblad, K. and Christensen, C.H. (2008) Aerobic oxidation of aldehydes under ambient conditions using supported gold nanoparticle catalysts. *Green Chemistry*, **10**(2), 168–70.

2 Gatewood, D.S., Schull, T.L., Baturina, O., Pietron, J.J., Garsany, Y., Swider-Lyons, K.E. and Ramaker, D.E. (2008) Characterization of ligand effects on water activation in triarylphosphine-stabilized Pt nanoparticle catalysts by X-ray absorption spectroscopy. *Journal of Physical Chemistry C*, **112** (13), 4961–70.

3 Kairemo, K., Erba, P., Bergstrom, K. and Pauwels, E.J. (2008) Nanoparticles in cancer. *Current Radiopharmaceuticals*, **1**(1), 30–6.

4 Goddard, W.A., III (2008) Methods for first principles predictions on complex systems, with applications to catalysis, nanoelectronics, fuel cells, pharma and materials science. Abstracts of Papers, 235th ACS National Meeting, New Orleans, LA, United States, April 6–10, 2008, PHYS-226.

5 Somorjai, G.A., Tao, F. and Park, J.Y. (2008) The nanoscience revolution: merging of colloid science, catalysis and nanoelectronics. *Topics in Catalysis*, **47**(1–2), 1–14.

6 Peng, J., He, X., Wang, K., Tan, W., Wang, Y. and Liu, Y. (2007) Noninvasive monitoring of intracellular pH change induced by drug stimulation using silica nanoparticle sensors. *Analytical and Bioanalytical Chemistry*, **388**(3), 645–54.

7 Parsons, J.G., Peralta-Videa, J.R. and Gardea-Torresdey, J.L. (2007) Use of plants in biotechnology: synthesis of metal nanoparticles by inactivated plant tissues, plant extracts, and living plants. *Developments in Environmental Science*, **5**, 463–85.

8 Han, C.S., Lee, H.Y. and Roh, Y. (2006) On biologically produced nanomaterials. *International Journal of Nanotechnology*, **3**(2/3), 236–52.

9 Evstigneeva, R.P. and Pchelkin, V.P. (2006) Ligands of biologically active compounds in the nanochemistry of silver and gold (a review). *Pharmaceutical Chemistry Journal*, **40**(4), 211–21.

10 Eklund, S.E. and Cliffel, D.E. (2004) Synthesis and catalytic properties of soluble platinum nanoparticles protected by a thiol monolayer. *Langmuir: ACS Journal of Surfaces and Colloids*, **20**(14), 6012–18.

11 Chen, S. and Kimura, K. (1999) Synthesis and characterization of carboxylate-modified gold nanoparticle powders dispersible in water. *Langmuir*, **15**(4), 1075–82.

12 Niu, J., Zhu, T. and Liu, Z. (2007) One-step seed-mediated growth of 30–150 nm quasispherical gold nanoparticles with 2-mercaptosuccinic acid as a new reducing agent. *Nanotechnology*, **18**(32), 325607/1–325607/7.

13 Jurvilliers, X., Schneider, R., Fort, Y., Walcarius, A. and Ghanbaja, J. (2005) Novel single-phase and gram-scale synthesis of thiol-uncapped stable colloidal gold nanoparticles. *Journal of Nanoscience and Nanotechnology*, **5**(2), 282–7.

14 Rodriguez-Gattorno, G., Aleman-Vazquez, L.O., Angeles-Franco, X., Cano-Dominguez, J.L. and Villagomez-Ibarra, R. (2007) Cyclohexane ring opening on alumina-supported Rh and Ir nanoparticles. *Energy and Fuels*, **21**(2), 1122–6.

15 Zhang, X. and Chan, K.-Y. (2003) Water-in-oil microemulsion synthesis of platinum-ruthenium nanoparticles, their characterization and electrocatalytic properties, *Chemistry of Materials*, **15**(2), 451–9.

16 Berhault, G., Bausach, M., Bisson, L., Becerra, L., Thomazeau, C. and Uzio, D. (2007) Seed-mediated synthesis of Pd nanocrystals: Factors influencing a kinetic- or thermodynamic-controlled growth regime. *Journal of Physical Chemistry C*, **111**(16), 5915–25.

17 Wei, H., Li, J., Wang, Y. and Wang, E. (2007) Silver nanoparticles coated with adenine preparation, self-assembly and application in surface-enhanced Raman scattering. *Nanotechnology*, **18**(17), 175610/1–175610/5.

18 Hamada, K., Hatanaka, K., Kawai, T. and Kon-no, K. (2000) Synthesis of nanosize Pt particles by direct addition of hydrazine in ionic reversed micelle systems. *Shikizai Kyokaishi*, **73**(8), 385–90.

19 Ahmadi, T.S., Wang, Z.L., Henglein, A., El-Sayed, M.A. (1996) 'Cubic' colloidal platinum nanoparticles. *Chemistry of Materials*, **8**(6), 1161–3.

20 Lin, C.-S., Khan, M.R. and Lin, S.D. (2006) The preparation of Pt nanoparticles by methanol and citrate. *Journal of Colloid and Interface Science*, **299**(2), 678–85.

21 Sun, Y., Frenkel, A.I., Isseroff, R., Shonbrun, C., Forman, M., Shin, K., Koga, T., White, H., Zhang, L., Zhu, Y., Rafailovich, M.H. and Sokolov, J.C. (2006) Characterization of palladium nanoparticles by using X-ray reflectivity, EXAFS, and electron microscopy. *Langmuir*, **22**(2), 807–16.

22 Wang, J., Neoh, K.G. and Kang, E.T. (2001) Preparation of nanosized metallic particles in polyaniline. *Journal of Colloid and Interface Science*, **239**(1), 78–86.

23 Okumura, M., Nakamura, S., Tsubota, S., Nakamura, T., Azuma, M. and Haruta, M. (1998) Chemical vapor deposition of gold on Al_2O_3, SiO_2, and TiO_2 for the oxidation of CO and of H_2. *Catalysis Letters*, **51**(1, 2), 53–8.

24 Kim, H., Lee, S.J. and Jung, N.J. (2007) Chemical vapor deposition of Pt nanoparticles on carbon nanotubes. *Solid State Phenomena*, **124–6**, 1769–72.

25 Song, Z., Cai, T., Hanson, J.C., Rodriguez, J.A. and Hrbek, J. (2004) Structure and reactivity of Ru nanoparticles supported on modified graphite surfaces a study of the model catalysts for ammonia synthesis. *Journal of the American Chemical Society*, **126**(27), 8576–84.

26 Zhang, G.H., Guo, W.L., Wang, X.K. (2007) Sonochemical formation of nanocrystalline gold in aqueous solution. *Materials and Research Innovations*, **11**(4), 201–3.

27 Yang, G.-W. and Li, H. (2008) Sonochemical synthesis of highly monodispersed and size controllable Ag nanoparticles in ethanol solution. *Materials Letters*, **62**(14), 2193–5.

28 Mizukoshi, Y., Makise, Y., Shuto, T., Hu, J., Tominaga, A., Shironita, S. and Tanabe, S. (2007) Immobilization of noble metal nanoparticles on the surface of TiO_2 by the sonochemical method: Photocatalytic production of hydrogen from an aqueous solution of ethanol. *Ultrasonics Sonochemistry*, **14**(3), 387–92.

29 Navaladian, S., Viswanathan, B., Viswanath, R.P. and Varadarajan, T.K. (2007) Thermal decomposition as route for silver nanoparticles. *Nanoscale Research Letters*, **2**(1), 44–8.

30 Yu, L., Yao, J. and Fu, Z.-W. (2007) Laser ablated preparation of noble metal nanoparticles in liquid. *Wuli Huaxue Xuebao*, **23**(6), 945–9.

31 Turkevich, J. (1985) Colloidal gold. Part I. Historical and preparative aspects, morphology and structure. *Gold Bulletin (Geneva)*, **18**(3), 86–91.

32 Turkevich, J. (1985) Colloidal gold. Part II. Color, coagulation, adhesion, alloying and catalytic properties. *Gold Bulletin (Geneva)*, **18**(4), 125–31.

33 Panigrahi, S., Kundu, S., Ghosh, S., Nath, S. and Pal, T. (2004) General method of synthesis for metal nanoparticles. *Journal of Nanoparticle Research*, **6**(4), 411–14.

34 Kazakov, V.P. and Konovalova, M.V. (1968) Kinetics of the reduction of $AuBr_4^-$ by formic and oxalic acids. *Zhurnal Neorganicheskoi Khimii*, **13**(9), 2377–83.

35 Gatellier, J.P. and Disnar, J.R. (1990) Kinetics and mechanism of the reduction of gold (III) to gold (0) by sedimentary organic materials. *Organic Geochemistry*, **16**(1–3), 631–40.

36 Ascencio, J.A., Perez, M. and Jose-Yacaman, M. (2000) A truncated icosahedral structure observed in gold nanoparticles. *Surface Science*, **447**(1–3), 73–80.

37 Parker, S.C., Grant, A.W., Bondzie, V.A. and Campbell, C.T. (1999) Island growth kinetics during the vapor deposition of gold onto TiO_2 (110). *Surface Science*, **441**(1), 10–20.

38 Hojrup-Hansen, K., Ferrero, S. and Henry, C.R. (2004) Nucleation and growth kinetics of gold nanoparticles on MgO (1 0 0) studied by UHV-AFM. *Applied Surface Science*, **226**(1–3), 167–72.

39 LaLonde, A.D., Norton, M.G., Zhang, D., Gangadean, D., Alkhateeb, A., Padmanabhan, R. and McIlroy, D.N. (2005) Controlled growth of gold nanoparticles on silica nanowires. *Journal of Materials Research*, **20**(11), 3021–7.

40 Sonnichsen, C., Franzl, T., Wilk, T., von Plessen, G., Feldmann, J., Wilson, O. and Mulvaney, P. (2002) Drastic reduction of plasmon damping in gold nanorods. *Physical Review Letters*, **88**(7), 077402.

41 Bogle, K.A., Dhole, S.D. and Bhoraskar, V.N. (2007) Growth of copper and gold nanoparticles on a polyimide surface. *Radiation Effects and Defects in Solids*, **162**(3–4), 259–65.

42 Clark, G.L. (1926) X-rays and colloids. Fourth Colloid Symposium Monograph, pp. 145–73.

43 Barth, T. and Lunde, G. (1926) The lattice constants of metallic platinum, silver and gold. *Zeitschrift für Physikalische Chemie*, **121**, 78–102.

44 Guo, S. and Wang, E. (2007) One-pot, high-yield synthesis of size-controlled gold particles with narrow size distribution. *Inorganic Chemistry*, **46**(16), 6740–3.

45 Morones, J.R., Elechiguerra, J.L., Camacho, A., Holt, K., Kouri, J.B., Ramirez, J.T. and Yacaman, M.J. (2005) The bactericidal effect of silver nanoparticles. *Nanotechnology*, **16**(10), 2346–53.

46 Gardea-Torresdey, J.L., Gomez, E., Peralta-Videa, J., Parsons, J., Tiemann, K., Troiani, H. and Jose Yacaman, M. (2003) Use of XAS and TEM to determine the uptake of gold and silver and nanoparticle formation by living alfalfa plants. Abstracts of Papers, 225th ACS National Meeting, New Orleans, LA, United States, March 23-7, 2003 ENVR-246.

47 Comaschi, T., Balerna, A. and Mobilio, S. (2008) Temperature dependence of the structural parameters of gold nanoparticles investigated with EXAFS. *Physical Review B: Condensed Matter and Materials Physics*, **77**(7), 075432/1–075432/10.

48 Witkowska, A., Di Cicco, A. and Principi, E. (2007) Local ordering of nanostructured Pt probed by multiple-scattering XAFS. *Physical Review B: Condensed Matter and Materials Physics*, **76**(10), 104110/1–104110/12.

49 Calvin, S., Luo, S.X., Caragianis-Broadbridge, C., McGuinness, J.K., Anderson, E., Lehman, A., Wee, K.H., Morrison, S.A. and Kurihara, L.K. (2005) Comparison of extended X-ray absorption fine structure and Scherrer analysis of X-ray diffraction as methods for determining mean sizes of polydisperse nanoparticles. *Applied Physics Letters*, **87**(23), 233102/1–233102/3.

50 Borowski, M. (1997) Size determination of small Cu clusters by EXAFS. *Journal de Physique IV*, **7** (C2, X-Ray Absorption Fine Structure, Vol. 1), 259–60.

51 Jentys, A. (1999) Estimation of mean size and shape of small metal particles by EXAFS. *Physical Chemistry Chemical Physics*, **1**(17), 4059–63.

52 Frenkel, A.I. (1999) Solving the structure of nanoparticles by multiple-scattering EXAFS analysis. *Journal of Synchrotron Radiation*, **6**(3), 293–5.

53 Lu, Z.H., Sham, T.K., Vos, M., Bzowski, A., Mitchell, I.V. and Norton, P.R. (1992) Unoccupied d states of gold impurities in silicon as studied by X-ray absorption spectroscopy. *Physical Reviews B*, **45**, 8811–14.

54 Fauth, K. (2004) How well does total electron yield measure X-ray absorption in nanoparticles? *Applied Physics Letters*, **85**(15), 3271–3.

55 Shido, T. and Prins, R. (1998) Why EXAFS underestimated the size of small supported MoS_2 particles. *Journal of Physical Chemistry B*, **102**(43), 8426–35.

56 Clausen, B.S., Graabaek, L., Topsoe, H., Hansen, L.B., Stoltze, P., Noerskov, J.K. and Nielsen, O.H. (1993) A new procedure for particle size determination by EXAFS based on molecular dynamics simulations. *Journal of Catalysis*, **141**(2), 368–79.

57 Parsons, J.G., Dokken, K., Peralta-Videa, J.R., Romero-Gonzalez, J. and Gardea-Torresdey, J.L. (2007) X-ray absorption near edge structure and extended X-ray absorption fine structure analysis of standards and biological samples containing mixed oxidation states of chromium (III) and chromium (VI). *Applied Spectroscopy*, **61**(3), 338–45.

58 Hu, J., Zhang, Y., Liu, B., Liu, J., Zhou, H., Xu, Y., Jiang, Y., Yang, Z. and Tian, Z.-Q. (2004) Synthesis and properties of tadpole-shaped gold nanoparticles. *Journal of the American Chemical Society*, **126**(31), 9470–1.

59 Hosea, M., Greene, B., McPherson, R., Henzl, M., Alexander, M.D. and Darnall, D.W. (1986) Accumulation of elemental gold on the alga *Chlorella vulgaris*. *Inorganica Chimica Acta*, **123**(3), 161–5.

60 Gardea-Torresdey, J.L., Tiemann, K.J., Gamez, G., Dokken, K., Tehuacanero, S. and Jose-Yacaman, M. (1999) Gold nanoparticles obtained by bio-precipitation from gold (III) solutions. *Journal of Nanoparticle Research*, **1**(3), 397–404.

61 Gardea-Torresdey, J.L., Tiemann, K.J., Parsons, J.G., Gamez, G., Herrera, I. and Jose-Yacaman, M. (2002) XAS investigations into the mechanism(s) of Au(III) binding and reduction by alfalfa biomass. *Microchemical Journal*, **71**(2–3), 193–204.

62 Gardea-Torresdey, J.L., Tiemann, K.J., Gamez, G., Dokken, K., Cano-Aguilera, I., Furenlid, L.R. and Renner, M.W. (2000) Reduction and accumulation of gold (III) by *Medicago sativa* alfalfa biomass: X-ray absorption spectroscopy, pH, and temperature dependence. *Environmental Science and Technology*, **34**(20), 4392–6.

63 Lopez, M.L., Parsons, J.G., Peralta Videa, J.R. and Gardea-Torresdey, J.L. (2005) An XAS study of the binding and reduction of Au (III) by hop biomass. *Microchemical Journal*, **81**(1), 50–6.

64 Armendariz, V., Jose-Yacaman, M., Duarte-Moller, A., Peralta-Videa, J.R., Troiani, H., Herrera, I. and Gardea-Torresdey, J.L. (2004) HRTEM characterization of gold nanoparticles produced by wheat biomass. *Revista Mexicana de Fisica*, **50** (Suppl. 1), 7–11.

65 Lopez, M.L., Parsons, J.G., Peralta Videa, J.R. and Gardea-Torresdey, J.L. (2005) An XAS study of the binding and reduction of Au. (III) by hop biomass. *Microchemical Journal*, **81**(1), 50–6.

66 Huang, J., Li, Q., Sun, D., Lu, Y., Su, Y., Yang, X., Wang, H., Wang, Y., Shao, W., He, N.H., Chen, J. and C. (2007) Biosynthesis of silver and gold nanoparticles by novel sundried *Cinnamomum camphora* leaf. *Nanotechnology*, **18**(10), 105104/1–105104/11.

67 Chandran, S.P., Chaudhary, M., Pasricha, R., Ahmad, A. and Sastry, M. (2006) Synthesis of gold nanotriangles and silver nanoparticles using *Aloe vera* plant extract. *Biotechnology Progress*, **22**(2), 577–83.

68 Shankar, S.S., Ahmad, A. and Sastry, M. (2003) Geranium leaf assisted biosynthesis of silver nanoparticles. *Biotechnology Progress*, **19**(6), 1627–31.

69 Shankar, S.S., Ahmad, A., Pasricha, R. and Sastry, M. (2003) Bioreduction of chloroaurate ions by geranium leaves and its endophytic fungus yields gold nanoparticles of different shapes. *Journal of Materials Chemistry*, **13**(7), 1822–6.

70 Shankar, S.S., Rai, A., Ankamwar, B., Singh, A., Ahmad, A. and Sastry, M. (2004) Biological synthesis of triangular gold nanoprisms. *Nature Materials*, **3**(7), 482–8.

71 Rai, A., Chaudhary, M., Ahmad, A., Bhargava, S. and Sastry, M. (2007) Synthesis of triangular Au core-Ag shell nanoparticles. *Materials Research Bulletin*, **42**(7), 1212–20.

72 Shankar, S.S., Rai, A., Ahmad, A. and Sastry, M. (2005) Controlling the optical properties of lemongrass extract synthesized gold nanotriangles and potential application in infrared-absorbing optical coatings. *Chemistry of Materials*, **17**(3), 566–72.

73 Ankamwar, B., Damle, C., Ahmad, A. and Sastry, M. (2005) Biosynthesis of gold and silver nanoparticles using *Emblica officinalis* fruit extract, their phase transfer and transmetallation in an organic solution. *Journal of*

Nanoscience and Nanotechnology, **5**(10), 1665–71.

74 Shankar, S.S., Rai, A., Ahmad, A. and Sastry, M. (2004) Rapid synthesis of Au, Ag, and bimetallic Au core-Ag shell nanoparticles using Neem (*Azadirachta indica*) leaf broth. *Journal of Colloid and Interface Science*, **275**(2), 496–502.

75 Li, S., Shen, Y., Xie, A., Yu, X., Qiu, L., Zhang, L. and Zhang, Q. (2007) Green synthesis of silver nanoparticles using *Capsicum annuum* L. extract. *Green Chemistry*, **9**(8), 852–8.

76 Vigneshwaran, N., Kathe, A.A., Varadarajan, P.V., Nachane, R.P. and Balasubramanya, R.H. (2007) Silver-protein (core-shell) nanoparticle production using spent mushroom substrate. *Langmuir*, **23**(13), 7113–17.

77 Li, Z., Chung, S.W., Jwa-M., N., Ginger, D.S. and Mirkin, C.A. (2003) Living templates for the hierarchical assembly of gold nanoparticles. *Angewandte Chemie–International Edition*, **42**(20), 2306–9.

78 Sugunan, A., Melin, P., Schnurer, J., Hilborn, J.G. and Dutta, J. (2007) Nutrition-driven assembly of colloidal nanoparticles: growing fungi assemble gold nanoparticles as microwires. *Advanced Materials*, **19**(1), 77–81.

79 Bhainsa, K.C. and D'Souza, S.F. (2006) Extracellular biosynthesis of silver nanoparticles using the fungus *Aspergillus fumigatus*. *Colloids and Surfaces, B: Biointerfaces*, **47**(2), 160–4.

80 Mohammadian, A., Shojaosadati, S.A. and Rezaee, M.H. (2007) *Fusarium oxysporum* mediates photogeneration of silver nanoparticles. *Scientia Iranica*, **14**(4), 323–6.

81 Duran, N., Marcato, P.D., De Souza, G.I.H., Alves, O.L. and Esposito, E. (2007) Antibacterial effect of silver nanoparticles produced by fungal process on textile fabrics and their effluent treatment. *Journal of Biomedical Nanotechnology*, **3**(2), 203–8.

82 Riddin, T.L., Gericke, M. and Whiteley, C.G. (2006) Analysis of the inter- and extracellular formation of platinum nanoparticles by *Fusarium oxysporum* f. sp. *lycopersici* using response surface methodology. *Nanotechnology*, **17**(14), 3482–9.

83 Duran, N., Marcato, P.D., Alves, O.L., De Souza, G.I.H. and Esposito, E. (2005) Mechanistic aspects of biosynthesis of silver nanoparticles by several *Fusarium oxysporum* strains. *Journal of Nanobiotechnology*, **3**, 8–14.

84 Senapati, S., Ahmad, A., Khan, M.I., Sastry, M. and Kumar, R. (2005) Extracellular biosynthesis of bimetallic Au-Ag alloy nanoparticles. *Small*, **1**(5), 517–20.

85 Senapati, S., Mandal, D., Ahmad, A., Khan, M.I., Sastry, M. and Kumar, R. (2004) Fungus mediated synthesis of silver nanoparticles: a novel biological approach. *Indian Journal of Physics, A*, **78A**(1), 101–5.

86 Ahmad, A., Mukherjee, P., Senapati, S., Mandal, D., Khan, M.I., Kumar, R. and Sastry, M. (2003) Extracellular biosynthesis of silver nanoparticles using the fungus *Fusarium oxysporum*. *Colloids and Surfaces, B: Biointerfaces*, **28**(4), 313–18.

87 Mukherjee, P., Senapati, S., Mandal, D., Ahmad, A., Khan, M.I., Kumar, R. and Sastry, M. (2002) Extracellular synthesis of gold nanoparticles by the fungus *Fusarium oxysporum*. *ChemBioChem*, **3**(5), 461–3.

88 Vigneshwaran, N., Kathe, A.A., Varadarajan, P.V., Nachane, R.P. and Balasubramanya, R.H. (2006) Biomimetics of silver nanoparticles by white rot fungus, *Phanerochaete chrysosporium*. *Colloids and Surfaces, B: Biointerfaces*, **53**(1), 55–9.

89 Gericke, M. and Pinches, A. (2006) Biological synthesis of metal nanoparticles. *Hydrometallurgy*, **83**(1–4), 132–40.

90 Mukherjee, P., Ahmad, A., Mandal, D., Senapati, S., Sainkar, S.R., Khan, M.I., Ramani, R., Parischa, R., Ajayakumar, P.V., Alam, M., Sastry, M. and Kumar, R. (2001) Bioreduction of $AuCl_4^-$ ions by the fungus, *Verticillium* sp. and surface trapping of the gold nanoparticles formed. *Angewandte Chemie–International Edition*, **40**(19), 3585–8.

91 Vigneshwaran, N., Ashtaputre, N.M., Varadarajan, P.V., Nachane, R.P.,

Paralikar, K.M. and Balasubramanya, R.H. (2007) Biological synthesis of silver nanoparticles using the fungus *Aspergillus flavus*. *Materials Letters*, **61**(6), 1413–18.

92 Basavaraja, S., Balaji, S.D., Lagashetty, A., Rajasab, A.H. and Venkataraman, A. (2008) Extracellular biosynthesis of silver nanoparticles using the fungus *Fusarium semitectum*. *Materials Research Bulletin*, **43**(5), 1164–70.

93 McCormick, M.L., Bouwer, E.J. and Adriaens, P. (2002) Carbon tetrachloride transformation in a model iron-reducing culture: relative kinetics of biotic and abiotic reactions. *Environmental Science and Technology*, **36**(3), 403–10.

94 Sisler, F.D. and Zobell, C.E. (1951) Hydrogen utilization by some marine sulphate-reducing bacteria. *Journal of Bacteriology*, **62**(1), 117–27.

95 Sreenivasan, A. (1957) Nitrate-reducing bacteria from marine environment. *Current Science*, **26**, 392–3.

96 He, Y., Yuan, J., Su, F., Xink, X. and Shi, G. (2006) *Bacillus subtilis* assisted assembly of gold nanoparticles into long conductive nodous ribbons. *Journal of Physical Chemistry B*, **110**(36), 17813–18.

97 Konishi, Y., Ohno, K., Saitoh, N., Nomura, T., Nagamine, S., Hishida, H., Takahashi, Y. and Uruga, T. (2007) Bioreductive deposition of platinum nanoparticles on the bacterium *Shewanella* algae. *Journal of Biotechnology*, **128**(3), 648–53.

98 Konishi, Y., Nomura, T., Tsukiyama, T. and Saitoh, N. (2004) Microbial preparation of gold nanoparticles by anaerobic bacterium. *Transactions of the Materials Research Society of Japan*, **29**(5), 2341–3.

99 Klaus, T., Joerger, R., Olsson, E. and Granqvist, C.-G. (1999) Silver-based crystalline nanoparticles, microbially fabricated. *Proceedings of the National Academy of Sciences of the United States of America*, **96**(24), 13611–14.

100 Ahmad, A., Senapati, S., Khan, M.I., Kumar, R. and Sastry, M. (2003) Extracellular biosynthesis of monodisperse gold nanoparticles by a novel extremophilic actinomycete, *Thermomonospora* sp. *Langmuir*, **19**(8), 3550–3.

101 Ahmad, A., Senapati, S., Khan, M.I., Kumar, R., Ramani, R., Srinivas, V. and Sastry, M. (2003) Intracellular synthesis of gold nanoparticles by a novel alkalotolerant actinomycete, *Rhodococcus* species. *Nanotechnology*, **14**(7), 824–8.

102 Lengke, M.F., Fleet, M.E. and Southam, G. (2007) Biosynthesis of silver nanoparticles by filamentous cyanobacteria from a silver(I) nitrate complex. *Langmuir*, **23**(5), 2694–9.

103 Lengke, M.F., Fleet, M.E. and Southam, G. (2006) Morphology of gold nanoparticles synthesized by filamentous cyanobacteria from gold(I)-thiosulfate and gold(III)-chloride complexes. *Langmuir*, **22**(6), 2780–7.

104 Lengke, M.F., Fleet, M.E. and Southam, G. (2006) Synthesis of platinum nanoparticles by reaction of filamentous cyanobacteria with platinum(IV)-chloride complex. *Langmuir*, **22**(17), 7318–23.

105 Lengke, M.F. and Southam, G. (2005) The effect of thiosulfate-oxidizing bacteria on the stability of the gold-thiosulfate complex. *Geochimica et Cosmochimica Acta*, **69**(15), 3759–72.

106 He, S., Guo, Z., Zhang, Y., Zhang, S., Wang, J. and Gu, N. (2007) Biosynthesis of gold nanoparticles using the bacteria *Rhodopseudomonas capsulata*. *Materials Letters*, **61**(18), 3984–7.

107 Husseiny, M.I., Abd El-Aziz, M., Badr, Y. and Mahmoud, M.A. (2007) Biosynthesis of gold nanoparticles using *Pseudomonas aeruginosa*. *Spectrochimica Acta, Part A: Molecular and Biomolecular Spectroscopy* , **67A**(3–4), 1003–6.

108 Shahverdi, A.R., Minaeian, S., Shahverdi, H.R., Jamalifar, H. and Nohi, A.-A. (2007) Rapid synthesis of silver nanoparticles using culture supernatants of Enterobacteria: a novel biological approach. *Process Biochemistry (Amsterdam, Netherlands)*, **42**(5), 919–23.

109 Gardea-Torresdey, J.L., Parsons, J.G., Gomez, E., Peralta-Videa, J., Troiani, H., Santiago, P. and Jose-Yacaman, M. (2002) Formation and growth of Au nanoparticles inside live alfalfa plants. *Nano Letters*, **2/4**, 397–401.

110 Gardea-Torresdey, J.L., Gomez, E., Peralta-Videa, J.R., Parsons, J.G., Troiani, H. and Jose-Yacaman, M. (2003) Alfalfa sprouts: a natural source for the synthesis of silver nanoparticles. *Langumir*, **19**(4), 1357–61.

111 Yates, B.J., Myre, E., Breetz, D. and Dionysiou, D.D. (2005) Biotemplating of nanoparticles for environmental applications using phytomining techniques. Abstracts of Papers, 230th ACS National Meeting, Washington, DC, United States, August 28–September 1, 2005.

112 Rodriguez, E., Peralta-Videa, J.R., Sanchez-Salcido, B., Parsons, J.G., Romero, J. and Gardea-Torresdey, J.L. (2007) Improving gold phytoextraction in Desert willow (*Chilopsis linearis*) using thiourea: a spectroscopic investigation. *Environmental Chemistry*, **4**(2), 98–108.

113 Rodriguez, E., Parsons, J.G., Peralta-Videa, J.R., Cruz-Jimenez, G., Romero-Gonzalez, J., Sanchez-Salcido, B.E., Saupe, G.B., Duarte-Gardea, M. and Gardea-Torresdey, J.L. (2007) Potential of *Chilopsis linearis* for gold phytomining: using XAS to determine gold reduction and nanoparticle formation within plant tissues. *International Journal of Phytoremediation*, **9**(2), 133–47.

114 Marshall, A.T., Haverkamp, R.G., Davies, C.E., Parsons, J.G., Gardea-Torresdey, J.L. and Agterveld, D. (2007) Accumulation of gold nanoparticles in *Brassica juncea*. *International Journal of Phytoremediation*, **9**(3), 197–206.

115 Sharma, N.C., Sahi, S.V., Nath, S., Parsons, J.G., Gardea-Torresdey, J.L. and Pal, T. (2007) Synthesis of plant-mediated gold nanoparticles and catalytic role of biomatrix-embedded nanomaterials. *Environmental Science and Technology*, **41**(14), 5137–42.

116 Haverkamp, R.G., Marshall, A.T. and van Agterveld, D. (2007) Pick up your carats: nanoparticles of gold-silver-copper alloy produced in vivo. *Journal of Nanoparticle Research*, **9**, 697–700.

117 Manceau, A., Nagy, K.L., Marcus, M.A., Lanson, M., Geoffroy, N., Jacquet, T. and Kirpichtchikova, T. (2008) Formation of metallic copper nanoparticles at the soil-root interface. *Environmental Science and Technology*, **42**, 1766–72.

13
Spherical and Anisotropic Gold Nanomaterials in Plasmonic Laser Phototherapy of Cancer

Adela Ben-Yakar, Daniel Eversole and Ozgur Ekici

13.1
Introduction

Cancer is a major healthcare concern across the globe. United States figures alone show that slightly less than one-half of males and one-third of females will develop cancer during their lifetime, which translates to approximately 1.5 million new cases of cancer being diagnosed yearly [1]. The National Institutes of Health estimates cancer related expenditures to have cost the United States approximately $219.2 billion in 2007, spreading across the health system and other industries in part due to lost productivity [1]. These issues are of such great concern that a major goal of the National Cancer Institute is to eliminate suffering and death due to cancer by 2015 [2]. As such, there is a great need for the development of highly sensitive and cost effective technologies for the screening, diagnostic, and therapeutic treatment of cancer. The development of a multimodal tool that can combine these capabilities would be most ideal.

Nanoparticles have shown a great potential to be multimodal tools with functionality as both a contrast agent for imaging and a therapeutic agent for treatment of cancerous tissue. Several molecular imaging modalities, taking advantage of the unique optical properties of nanoparticles as contrast agents, are currently under development for cancer imaging [3–6]. While early detection can eventually reduce and even eliminate the need for expensive and time-consuming histological examinations, molecular imaging can improve the precision of cancer margin detection and the understanding of disease progression through the monitoring of biomarker overexpression. Furthermore, the nanoparticle can be utilized for the simultaneous removal of cancer. The application of nanoparticle-assisted phototherapeutics includes the removal of displasia or large scale and deep tumors, and controlled therapy of cancers with minimal impact to healthy, benign tissues.

Nanomaterials have a number of advantageous characteristics in aiding the development of *in vivo*, optically-active, biospecific probes that are highly controllable and have tunable optical properties. Among nanomaterials, noble-metal

Metallic Nanomaterials Vol. 1. Edited by Challa S. S. R. Kumar

ISBN: 978-3-527-32151-3

nanoparticles have shown great clinical potential in the fight against cancer due to their unique optical and chemical properties. Noble-metal nanoparticles have enhanced scattering and absorption properties in the visible to near-infrared (NIR) wavelength regimes that arise due to strong resonances upon excitation of conduction band electrons along the particle surface known as the plasmon resonance [7]. These electrodynamic properties render nanomaterials as bright contrast agents for imaging and highly effective tools for therapeutic applications. Among metal particles, gold nanostructures have been shown to be relatively biologically compatible, as their low or negligible cellular toxicity makes them ideal for *in vivo* clinical use [8, 9]. Gold nanoparticles can be synthesized relatively easily into a variety of geometries, including nanospheres [10, 11], nanorods [12], nanoshells [13, 14], nanocages [15], and their clusters [16, 17]. Another promising particle type with strong optical properties is carbon nanostructures [18-21].

The molecular targeting of metallic nanoparticles to specific cancer biomarkers can easily be achieved through active functionalization methods. Active methods employ molecular specific bioagents such as antibodies [22] (e.g., anti-EGFR [3] and anti-HER2 [23]), DNA sequences [24], and ligands (folate [25, 26]) conjugated to the particle surface for highly specific *in vivo* delivery and binding to a disease biomarker of choice. Functionalization enables the selective targeting of cells or tissues expressing their cognate receptor, with high specificity [4]. For therapeutic applications, nanoparticles have also been delivered to solid tumors using passive methods that involve capping the nanoparticle with, for example poly (ethylene) glycol (PEG), for increased biocompatibility, biostability, and retention within tissues [27-29].

This chapter will primarily focus on recent developments in plasmonic laser phototherapy (PLP) techniques using plasmonic gold nanoparticles as cancer therapeutic agents. For a comprehensive review of nanoparticles as imaging contrast agents for cancer diagnostics, we refer the reader to the review papers of Rebecca Richards-Kortum [30, 31]. The El-Sayed group provides a nice review discussing the use of gold nanoparticles for the enhanced photothermal therapy of cancer [32, 33]. In this chapter, we discuss particle scattering and heating processes along with extending plasmonic phototherapeutics beyond photothermal therapy to additionally include cancer-killing schemes through mechanical, chemical, and plasma-mediated ablative effects. PLP has been divided into two distinct modes in accordance to the physical interactions between laser light and nanoparticles: continuous wave (CW) and pulsed. CW laser plasmonic phototherapy utilizes nanoparticles to initiate cell death via hyperthermic means. Pulsed laser plasmonic phototherapeutic localizes laser damage to subcellular targets through the confinement of photodamage.

The chapter begins with a review of the plasmonic properties of noble-metal particles. The effects of size, geometry, and aggregation on the near- and far-field scattering and absorption properties are discussed. Second, the heating processes in both the particle and surrounding medium induced by nanoparticle absorption of laser energy are detailed. We begin with the elementary heating processes

induced by femtosecond laser pulses, and proceed to detail how simultaneous heating and cooling occur with the application of longer pulse durations and CW irradiation. Third, the uses of nanoparticles for therapy are detailed. Here, we begin with a discussion of from single cell to large-scale tissue modification utilizing CW laser irradiation and progress to pulsed irradiation therapies where subcellular photodisruptions are possible. Cellular damage due to pulsed laser light is localized through one of the following techniques: hyperthermia, bubble and overlapping-bubble formation, nanoparticle fragmentation, and nonlinear scattering and absorptive processes. Finally, we summarize a number of issues which still need to be addressed before PLP techniques can fully mature and find application in a clinical setting.

13.2
Theoretical Understanding of Plasmonic Resonance

Noble-metal nanoparticles have unique optical properties that arise due to the collective oscillation of conduction band electrons along the particle surface upon excitation by an electromagnetic field; this is known as the plasmon resonance [7]. This strong resonance is responsible for the enhanced scattering and absorption of light in the visible to NIR wavelength regimes that can be exploited in nanobiophotonics applications. In this section, we discuss the physical properties for the rise of the plasmon resonance. Particular insight is provided on the effect of particle size, geometry and aggregation on the electrodynamic properties of noble-metal nanoparticles in both the far and near-fields.

13.2.1
Origin of Surface Plasmon Resonance

As the size of a metallic material is reduced to the nanoscale, both the electronic properties and the optical response of the material are dramatically affected [7, 34–38]. Changes in material electronic properties occur due to reductions in the density of states and the spatial length scale of the electronic motion. Energy eigenstates need now to be determined by the material–substrate boundaries, making surface effects of high importance. Optically, as the size is reduced, the electrodynamic properties become size-dependent, and colors not typically associated with the original bulk material can be scattered. This optical phenomenon is eloquently demonstrated by observing stained glass windows as sunlight passes through. Metallic gold nanocrystals embedded in the glass are responsible for the brilliant reds that are seen, due to their interaction with the incident light. Simply by adjusting the size of a gold nanoparticle and the environment in which it is found, it is possible to scatter light at a variety of colors, ranging from deep violet to red [39–41].

When an electromagnetic field is incident an arbitrarily shaped noble-metal nanoparticle, the oscillating electric field perturbs the surface conduction

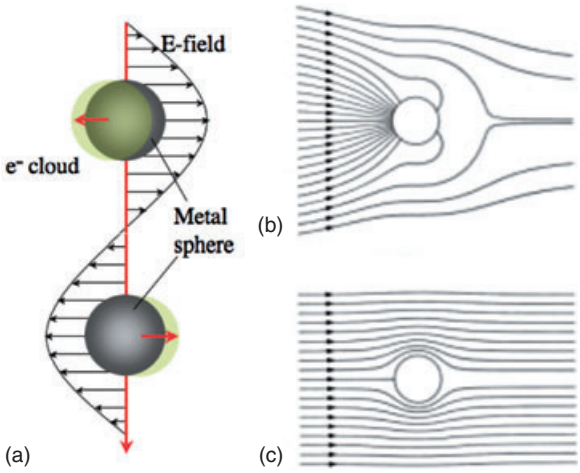

Figure 13.1 Description of the plasmon resonance. (a) Schematic of the coherent oscillations of the surface conduction band electrons induced by the oscillating electric field (reproduced with permission from Ref. [42]); (b, c) Poynting vector field lines (excluding scattering) around a small nanosphere irradiated by laser light at the resonance and off resonance, respectively (reproduced with permission from Ref. [7]).

electrons, as shown in Figure 13.1a. Conduction electrons oscillate coherently with respect to the electric field direction – a phenomenon known as surface plasmon oscillation [42]. The ability to induce these coherent oscillations allows noble-metal nanoparticles of a certain size range to strongly absorb and scatter light [7, 34–38]. When resonant conditions are met, the nanoparticle acts as a field intensifier, and its influence on the incident wave extends beyond its geometric boundaries. As such, the effective cross-sectional area of the collected light is significantly larger than the particle itself [43]. Figure 13.1b presents the field lines around the particle when the resonant conditions for electron oscillation are met; Figure 13.1c demonstrates when resonant conditions are not met. The nature at which the electrons oscillate is dependent upon the material composition, size and geometry, as well as the dielectric constant of the surrounding medium. The oscillatory behavior strongly affects particle electrodynamic properties and location and width of the plasmon bands, providing highly controllable and tunable properties.

13.2.2 Description of Absorption and Scattering Properties

For spherical, metal particles having a diameter much smaller than the incident wavelength, the electric field intensity is uniformly distributed across the particle surface, such that all conduction band electrons are equally excited. In this case, electron movement can be well approximated by the Drude free-electron model,

which assumes that the conduction band electrons can be treated independently from the ionic core and can move freely, whereas the ions act only as scattering centers [44–46]. As such, conduction band electrons have a higher polarizability and the incident electric field induces a polarization of the electrons with respect to the heavier ionic core. A net charge difference is only felt at the surface of the nanoparticle, creating a restoring force that causes the electron cloud to oscillate in phase in a dipolar fashion. In this model, retardation effects that lead to plasmon damping are negligible, and the optical cross-section is dominated by dipole absorption, which can simply be described by [47]:

$$\sigma_{abs}(\omega) = 9\frac{\omega}{c}\varepsilon_m^{3/2}V_0\frac{\varepsilon_2(\omega)}{[\varepsilon_1(\omega)+2\varepsilon_m]^2+\varepsilon_2(\omega)^2} \tag{13.1}$$

where $V_0 = (4\pi/3)a^3$ is the spherical particle volume, ω is the angular frequency of the excitation radiation, and ε_m and $\varepsilon(\omega) = \varepsilon_1(\omega) + i\varepsilon_2(\omega)$ donate the bulk dielectric functions of the surrounding material and of the particle material, respectively. The absorption resonance is dependent upon the bulk material properties and the position and shape of the resonance are governed solely by the dielectric functions. From Equation 13.1, we can deduce that a strong, yet narrow, absorption resonance appears at $\varepsilon_1(\omega) = -2\varepsilon_m$ if $\varepsilon_2(\omega)$ is small and does not vary much in the vicinity of the resonance.

In its basic expression, the Drude model does not predict that the absorption bandwidth is affected by particle size. Experimentally, colloidal systems having a weak cluster–matrix interaction show a well-established inverse correlation with respect to the plasmon bandwidth with particle size. In order to describe the bandwidth dependency on particle size, Hovel *et al*. [47] proposed a classical view of free-electron metals; here, the scattering of electrons with other electrons, phonons, lattice defects and impurities leads to a damping of the Mie resonance. Briefly, in realistic metals, the dielectric function is composed of contributions from both interband transitions and the free-electron portion [48]. The free-electron dielectric function can be modified by the Drude model to account for this dependency, giving [47–50]

$$\varepsilon(\omega) = 1 - \frac{\omega_p^2}{\omega^2 + i\gamma\omega} \tag{13.2}$$

where $\omega_p = Ne^2/\varepsilon_0 m_{eff}$ is the plasma frequency and the Drude γ is the size-dependent phenomenological damping constant. As the particle size approaches the dimensions of the mean free path of electron scattering, the dimensions of the particle physically limit electron movement, leading to an enhanced electron-surface scattering. In gold and silver, the electron mean free path is on the order of 40–50 nm [51]. Additional collision processes result in a reduced electron mean free path and increased damping. Because size effects are a function of the particle dielectric function, they are labeled intrinsic size effects [47].

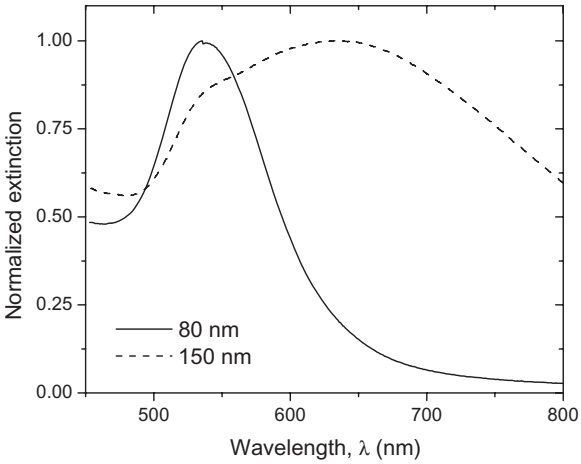

Figure 13.2 Size dependency on extinction spectra for spherical gold nanoparticles. With increasing particle size, the dipolar plasmon peak red-shifts and broadens. The formation of a quadrupole at the original plasmon peak is found for the 150 nm particle size.

As the particle size approaches the incident wavelength, scattering becomes a major contributor. Absorption effects are significantly minimized because the gold dielectric function reduces with longer wavelengths due to decreased *d*-level to *sp*-band electronic transitions. The optical response of the particle is now the superposition of both the absorption and scattering modes. Higher-order multipolar electrodynamic effects become more dominant as surface plasmons are unevenly distributed around the particle. As particle size increases, the incident electric field can no longer homogeneously polarize the surface conduction electrons, and retardation effects lead to higher order modes being excited [35]. Figure 13.2 shows how the plasmon response changes (red-shifts and broadens) with respect to particle size.

13.2.3 Near-Field Scattering Dynamics

Many common applications and experimental conditions rely on light scattering measurements made in the far field, a distance far away from the particle surface. In recent years, a number of groups have been looking to develop biological technologies that rely on near-field effects of metallic nanostructures. The scattered wave in the far field consists solely of the electric field components E_θ and E_ϕ. As the point of interest is moved closer to the particle surface, large local electromagnetic fields due to the addition of the radial electric field component E_R, are found. This can be verified in the known fact that, for free-electron metals, the electric field must radiate normally to the surface. To describe the strength of the electro-

magnetic field in the near-field regime, Messinger *et al.* [43] introduced the following term:

$$Q_{NF}(R) = \frac{R^2}{\pi a^2} \int_0^{2\pi} \int_0^{\pi} E_S \cdot E_S^* \sin\theta d\theta d\phi \tag{13.3a}$$

and

$$Q_R(R) = \frac{R^2}{\pi a^2} \int_0^{2\pi} \int_0^{\pi} E_R \cdot E_R^* \sin\theta d\theta d\phi \tag{13.3b}$$

Here, Q_{NF} represents the square of the spatially averaged electric field of the scattered wave $E_S = (E_R, E_\theta, E_\varphi)$ as a function R. The scattered field consists of all three components of the electric field vector, where the angular components, E_θ and E_ϕ, are perpendicular to the particle surface and the radial component, E_R, lies normal to the surface. This provides a measure of the ability of the sphere to convert the incident electric field intensity to a near-field intensity. Q_R is the main contribution of Q_{NF}, approximately 67%, which is due to the radial field component only and provides a measure of the sphere's ability to convert the incident electric field into a radially directed field. Because the E_R field component increases proportionally to R^{-2}, Q_{NF} will increase faster than Q_{sca}, which is only proportional to R^{-1}. As $R >> a$, Q_{NF} will approach the asymptotic value of Q_{sca}.

For the fundamental spherical particle geometry, with increasing particle size, the near-field scattering band red-shifts while its magnitude decreases and width broadens. Figure 13.3a summarizes the calculations of Q_{NF} using Equation 13.3a for varying particle diameters in an air medium irradiated with 780 nm wavelength

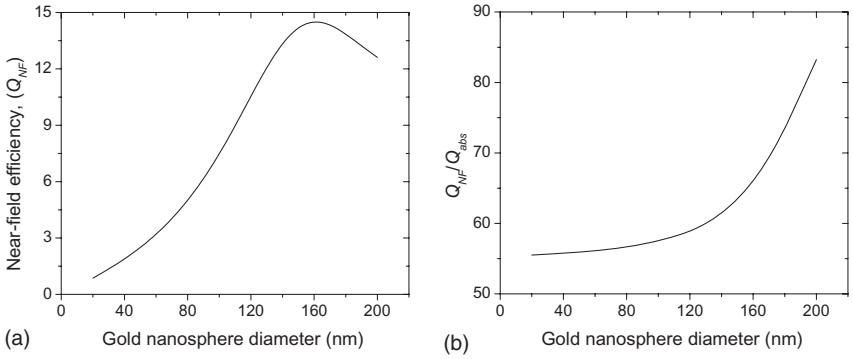

Figure 13.3 (a) Estimated near-field scattering efficiency, Q_{NF}, of a gold nanosphere in air as a function of particle diameter. Q_{NF} is a measurement of the particle's ability to convert incident electric field intensity into a near-field intensity. The efficiency term is estimated for an incident laser wavelength of 780 nm using Equation 13.3a, according to Ref. [43]; (b) Q_{NF} as compared to the degree of particle absorption, Q_{abs}, for various particle diameters.

laser light. The red-shift of the near-field scattering is apparent, with it peaking for particles of 150–170 nm in diameter. This red-shifting phenomenon is similar to that of the absorption band, but the near-field band will red-shift faster with increased particle size. This equates to particles being able to scatter intense fields with minimal absorption. To understand this mathematically, we can observe the ratio of the near-field scattering to the absorption efficiency, $\zeta = Q_{NF}/Q_{abs}$. Figure 13.3b provides a plot of this ratio over a range of particle diameters. As the particle diameter increases, the degree of near-field scattering rapidly increases over the absorption at the 780 nm wavelength. When the near-field magnitude peaks at the 150 nm particle diameter, the scattering efficiency in the particle near-field is 65-fold more than the absorption efficiency.

13.2.4 Tunable Optical Properties of Particles

The frequency, magnitude and bandwidth of the plasmonic resonance and near-field properties can be tuned through particle aggregation and variation of the particle's material composition and geometry.

13.2.4.1 Effect of Particle Aggregation

The interaction of closely spaced particles – that is, particle coupling – has a strong effect on the location and width of the plasmon resonance. Here, we will discuss coupling in two particles systems, linear chains and randomly oriented clusters. For a simple understanding of particle coupling, the dipole–dipole interaction model [52] is used to describe the plasmonic interaction of two closely spaced nanospheres [53]. As previously described, the surface plasmon response is confined along the particle surface. When certain conditions are met, the system becomes resonant and the particle strongly interacts with the incident light. Now, a second particle is placed within the oscillating field of the first particle. Upon polarization of the conduction electrons by the incident field, additional forces act upon both particles. First, let us observe a particle pair oriented such that the long axis is orthogonal to the incident electric field. In this case, the repulsive force of the surface charges is enhanced, leading to a higher resonance frequency and effectively blue-shifting the plasmon resonance to lower wavelengths. The opposite effect occurs when the electric field is parallel to the long axis of the particle pair. In this case, the plasmon band shifts and stronger enhancement will be seen in the NIR. As a quick note, particle interaction has been seen out to separation lengths of five particle diameters [54].

Linear particle chains are formed with the addition of particles along the axis of interest. When unpolarized light is incident a particle chain, the plasmon band is split into two components [55]. One maximum, relating to the absorption band of individual particles, is seen at lower wavelengths, while another maximum at higher wavelengths corresponds to strong electrodynamic coupling effects by particles along the chain axis [56]. A similar effect will be discussed with nanorods later, but chains show a much more complex longitudinal resonance. Here, the

longitudinal resonance depends upon the number of particles along the chain and the separation distance between neighboring particles. With increasing particle number and fixed particle separation, the longitudinal band red-shifts although, as the particle chain becomes too long, there will be saturation in the amplification of the absorption properties. Red-shifting of the plasmon band and increased absorption properties are also seen when the particle number is fixed and the particle separation is reduced. For all chain sizes, as the particles become too closely spaced, the primary plasmon band begins to split into several resonances, due to increased particle coupling.

The plasmon band of randomly oriented nanoparticle aggregates follows similar trends as that of particle pairs and chains [56]. With increasing aggregate size, a broadening and red-shifting of the plasmon band is observed and the primary plasmon resonance splits into several new resonances, which are directly proportional to the number of particles in the aggregate [54]. The strength of each resonance is now dependent, however, on the size and particle orientation within the aggregate.

The near-field scattering is also greatly affected by particle aggregation [54]. With particle aggregation, the near-field enhancement becomes a function of all the individually scattered wavelets from particles in the aggregate. Essentially, primary particles in the aggregate electromagnetically couple, exhibiting additional extinction features at longer wavelengths λ, where the surface plasmon is strongly decreased in single particle irradiation. At longer wavelengths, scattering processes dominate the plasmon band, whereas absorption still dominates in shorter wavelengths, but will again be negligible in the NIR regime. Because the superposition of scattered waves is responsible for the near-field enhancement, the aggregate size will have a finite limit, beyond which the maximal optical enhancement saturates [54, 57]. This limit will depend upon particle cross-talk and deconstructive interference effects.

13.2.4.2 **Effect of Particle Material Composition**

Material changes are typically the most trivial adjustment. Localized surface plasmons can arise in particles made from all noble-metal types. As such, particles can be composed of any of the noble metals or from composites of two or more noble metals. Composite systems include alloy and heterodyne particles [58, 59].

Among the noble metals, silver and gold are the most utilized in biological applications due to their low cellular toxicity. Both metal types show a strong plasmon resonance in the visible portion of the electromagnetic spectrum. In general, the silver plasmon band is found at lower wavelengths and has a stronger scattering cross-sectional area than gold. As a simple example, switching the material composition of a gold nanosphere of diameter $2a = 44\,nm$ to a silver particle of the same dimension affords a 15-fold increase in scattering at the plasmonic resonance [43].

In recent years, a variety of alloy and heterodyne particles have been developed. Nanocages are gold and silver alloy nanostructures that have a hollow interior and a thin, porous – but robust – wall [15]. By controlling the molar ratio of Ag to

chloroauric acid during production, the optical response can be tuned over a broad spectral range spanning from the visible to the NIR. Figure 13.4a describes the optical response for a nanocage having a 45 nm edge length and 3.5 nm wall thickness, with a 25% residual silver alloyed with gold [60]. Additionally, noble-metal coatings can be applied to dielectric particles to achieve strong plasmonic effects.

Nanoshells are a class of optically tunable, spherical nanoparticle consisting of a dielectric core surrounded by an ultrathin metal shell [14]. By using the ability to control the ratio of shell thickness and core radius dimensions, particles can be engineered to either absorb or scatter light over a broad spectral range spanning from the visible to the NIR. Figure 13.4b shows that, as the core-to-shell ratio is increased, the plasmon resonance red-shifts [61]. In order to adjust the core-to-shell ratio, gold shells of varying thickness were reduced onto a silica core of 60 nm radius.

13.2.4.3 **Effect of Particle Geometric Changes**

Through the introduction of particle anisotropy, the plasmon band can be engineered into the NIR regime, without the limitations associated with particle aggregation. Gold can be fashioned into a variety of particle geometries such as rods [62], triangles [63] and nanorice [64]. As the rod shape has proved most important to biomedical applications, it will be the focal point of the discussions on geometry.

Nanorods are anisotropic structures having a longitudinal and a transverse axis that splits the plasmon resonance into two bands [12]. As was observed with particle chains, a strong lower-frequency plasmon band arises due to the longitudinal oscillations of electrons, while a weak higher-frequency plasmon band arises from the transverse electron oscillations. This leads to strong, tunable absorption properties in both the visible and NIR wavelength regimes by changing the nanorod aspect ratio. For a nanorod with aspect ratio of 3.3, a small absorption peak located around 520 nm corresponds to the transverse plasmon mode, while a larger peak at 750 corresponds to the longitudinal plasmon mode [65]. As the aspect ratio increases, the energy separation between the two bands of the plasmon resonance increases. Figure 13.4c provides experimental evidence for the plasmon shift with increasing nanorod aspect ratio. Furthermore, the plasmon band in the NIR regime has a much tighter full width half maximum than is achievable with spherically shaped nanoparticles.

13.2.4.4 **Near-Field Tunability**

The near-field enhancement is strongly affected by geometric changes, sharp edges [66] and surface irregularities along the particle surface [67], which can dramatically increase the overall scattering. Especially large local enhancements are found at sharp edges. Through the understanding of near-field physics, it is feasible to generate large near-field scattering enhancements at wavelengths far from the absorption resonance. Nonfundamental particle geometries can enhance the near-field scattering. For example, Krug *et al*. [68] showed that right trigonal pyramids

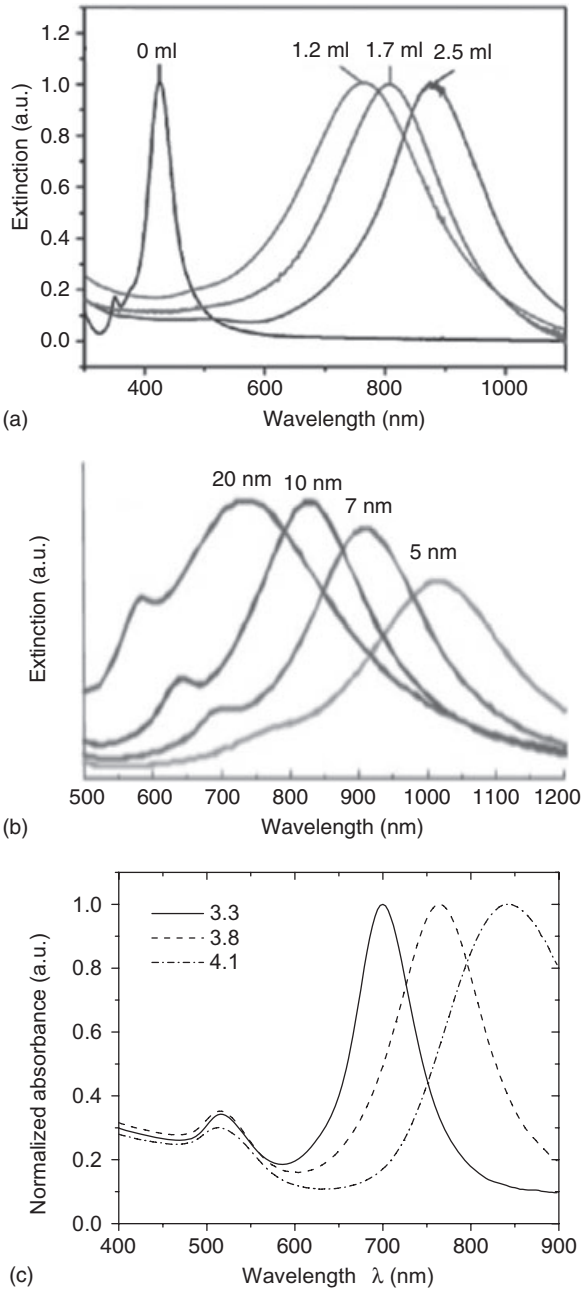

Figure 13.4 Evidence for the highly tunable nature of the plasmon resonance of gold nanostructures arising from variations in particle geometry and composition. (a) Nanocages, gold and silver alloy nanostructures, having 36.7 nm edge length and 3.3 nm wall thickness (reproduced, with permission, from Ref. [60]); (b) Nanoshells, silica and gold heterodyne nanospheres, of various gold shell thickness to a constant 60 nm silica core radius (reproduced, with permission, from Ref. [61]); (c) Gold nanorods, anisotropic nanostructures, of varying aspect ratios.

composed of gold and having a 45 ° cone angle and 675 nm long conical tip illuminated by a 825 nm wavelength plane wave can, in theory, generate intensity enhancements on the order of 7400. As particle development continues to advance, such nonfundamental shapes will be essential to nanoparticle-based techniques.

13.2.5 Plasmonic Summary

In summary, we have discussed the dynamics of the plasmon resonance and how it affects the electrodynamic properties of gold nanoparticles. Nanoparticle geometry, size and composition can be engineered to obtain a wide range of absorption and scattering resonances, ranging from the visible to the NIR. For spherical particles, we find that absorption dominates the dipolar resonance for smaller particle sizes, while scattering gains greater importance with increasing particle size. With increasing particle size, we find that both the absorption and scattering components of the plasmon band red-shift. However, the absorption peak stops red-shifting when it reaches the wavelength of approximately 600 nm, beyond which it drops off to negligible amounts. For scattering-based applications, this drop-off effect in the absorption is desirable. In contrast, absorption-based applications using spherical particles require wavelengths centered in the visible wavelength range. Other particle shapes (e.g. rods) have been engineered to red-shift the absorption band into the NIR, which will have great implications in biological applications due to greater light penetration. When observing the near-field scattering of spheres, we find that there is a continued red-shifting in the scattering plasmon band deep into the NIR. By using this information, it is possible to engineer particles specifically to a desired application.

13.3 Understanding Nanoparticle Heating Properties

The degree of metal nanoparticle heating during laser irradiation depends on their optical properties and the intensity of the incident laser pulse. In this section, we briefly describe the fundamentals of laser heating and cooling (through heat diffusion) of metal nanoparticles, and then present theoretical models for the accurate description of these processes. An understanding of the role of laser parameters in the rate of nanoparticle heating and the extent of heat diffusion to the surrounding tissue is important to fully optimize therapeutic applications of plasmonic nanoparticles.

13.3.1 Fundamentals of Laser Heating of Nanoparticles and Their Surrounding Medium

In nanoparticle-based therapeutic applications, the degree of heat confinement within the surrounding medium is directly related to the laser pulse duration. If

the pulse duration is shorter than the characteristic time scales for heat dissipation from the particle (i.e. femto- and picosecond laser pulses), the heat deposition is mostly confined within the particle during the pulse duration. Due to minimal heat loss to the surrounding water, ultrafast pulses provide the most efficient method for particle heating. Conversely, during nanoparticle heating, substantial heat loss to the surroundings occurs with the application of longer pulse durations and CW irradiation. The efficiency of particle heating reduces with heat loss, and a larger volume surrounding the particle is affected as a result of the larger energies required to reach the desired temperatures.

We will begin our discussion with the most elementary particle heating process initiated by ultrafast (femto- and picosecond) laser pulses. During exposure to an ultrashort laser pulse, electrons absorb the photon energy. These highly energetic electrons initially form a nonequilibrium energy distribution which is relaxed through electron–electron scattering on the order of 10–50 fs in metals. A negligible amount of energy exchange occurs between electrons and phonons within these time scales, and the electrons persist in high energy levels. The particle temperature begins to increase as a result of electron–phonon scattering, where the thermal equilibrium is reached on the order of 10 ps between the electrons and phonons. Meanwhile, the energy exchange between the particle and its surroundings begins to take place as a result of the elevated particle temperatures. Heat transfer across the interface occurs through the coupling of particle phonons with the phonons of the surroundings. Thermal resistance at the solid/liquid interface initially results in a large temperature jump across the boundary. The time scale to reach the thermal equilibrium across the interface is on the order of 100 ps to 1 ns, depending on the particle size and the laser pulse intensity. The fundamental processes and time scales in ultrafast laser heating of metal nanoparticles are summarized schematically in Figure 13.5. When exposed to longer pulses (e.g. nanosecond and CW irradiation), the particle will be in a thermal equilibrium during laser heating; in this case there is continual competition between the particle heating rate and the heat diffusion rate to its surrounding.

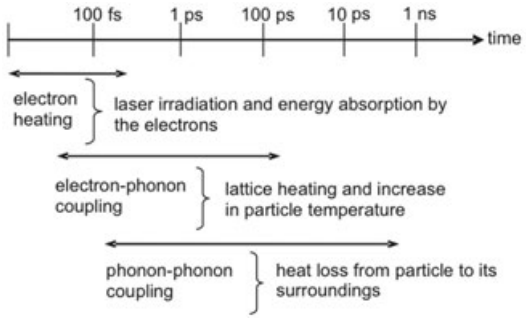

Figure 13.5 Time scales of the fundamental processes in ultrafast laser heating of metal nanoparticles.

13.3.2 Particle Heating/Cooling Models

A variety of studies have investigated the laser-induced thermal processes occurring in colloidal systems having a weak cluster–matrix interaction. Such models are important for the understanding of heating processes in and around nanoparticles for applications such as protein inactivation and membrane disruption. Through modeling, it is possible to optimize the particle size and laser duration and wavelength for the most efficient particle heating. Here, we present a brief overview of the developed heating/cooling models, and cite a number of experimental studies supported by these theoretical models.

13.3.2.1 Thermodynamic Model

To calculate the maximum particle temperature without temporal information, a simple thermodynamic model can be used:

$$m\int_{T_i}^{T_f} c_p dT = E_{abs} \tag{13.4}$$

where m is the mass of the particle, c_p is the specific heat, and the integration limits T_i and T_f are the initial and final temperatures of the particle, respectively. The laser pulse energy absorbed by the particle E_{abs} is directly correlated to the incident laser fluence and the effective cross-sectional area of the nanoparticle. This model is only valid when the time scale for heat dissipation from the particle is much larger than the heating time scale (i.e. using ultrafast laser pulses). This simple approach assumes that all of the absorbed energy is confined within the particle during the relevant time scales of the problem. As such, the thermodynamic model provides an accurate representation of the peak particle temperature with the application of femtosecond laser pulses. For example, the Hartland group [69, 70] studied symmetric breathing modes in spherical gold particles exposed to femtosecond laser pulses. When the breathing periods were calculated using the thermodynamic model to estimate particle temperature after irradiation, a reasonable agreement between the measured and calculated periods below the melting point was found.

13.3.2.2 Heat Transfer Model

A more complete approach, which is valid for heating with both pulsed and CW lasers, utilizes the heat transfer equation to describe the temporal distribution of the particle temperature and its surroundings. In the absence of phase transformations, the general form of the heat transfer equation in cylindrical coordinates is:

$$\rho(r)c_p(r)\frac{\partial T(r,t)}{\partial t} = \nabla k(r)\nabla T(r,t) + \dot{E}_{abs}(r,t), \tag{13.5}$$

where all variables are defined locally as a function of the radial coordinate r to distinguish the particle and its surroundings. $T(r,t)$ is the local temperature and

$\dot{E}_{abs}(r,t)$ is the rate of the absorbed energy per unit particle volume, which is zero for the coordinates outside of the particle. The material density ρ, specific heat c_p and thermal conductivity k are also defined locally to separate the particle from its surroundings. This general form of the heat transfer equation, however, must be modified to accommodate for the small size and short time scales involved in the pulsed laser heating of nanoparticles, including the following three issues.

First, when heat flows across an interface between two different materials (such as gold and water), there exists a temperature jump at the interface which can be estimated through knowledge of the thermal interface conductance, G. The standard assumption of equal temperatures at the boundary fails to hold in the time scales of short-laser heating of particles due to relatively long phonon–phonon coupling times. For example, the need for thermal interface conductance during the femtosecond laser heating of particles could be seen in the pump-probe spectroscopy study by Hu and Hartland [71]. In this study, a heat transfer model without the thermal interface conductance was implemented to examine the rate of energy dissipation from spherical gold nanoparticles to their surroundings. These authors measured the thermal relaxation time between the particle and its surroundings, and found that it is proportional to the square of the particle radius and is not a function of the initial particle temperature. However, the theoretical relaxation times as solved with simple heat transfer equations were found to be consistently faster than the experimentally measured ones. This discrepancy between the experimental and calculated results was attributed to the temperature boundary condition used in the heat transfer model, which assumed equal temperatures at the interface.

The values of thermal interface conductance, G, were estimated through measurement of the temperature decay at the interface. Both, Wilson *et al.* [72] and Ge *et al.* [73] measured the laser-heated particle temperature decay through time-resolved changes in optical absorption. The experimental data were used to estimate the thermal interface conductance values of Au, Pt and AuPd nanoparticles by solving the heat transfer equations in which the thermal conductance is a fitting parameter in the solution. In another study, Plech *et al.* [74] investigated the lattice dynamics of spherical gold nanoparticles in a water medium by using X-ray scattering, and estimated that the thermal interface conductance of $G = 105 \pm 15\,MW\,m^{-2}\,K$ matched well their experimental results.

Second, the initial thermal nonequilibrium between electrons and phonons during ultrafast laser heating of nanoparticles requires special attention. A two-temperature model [75] describing the particle can be used to account for the electron–phonon relaxation time of the particle. Here, the electrons and the lattice of the particle are treated separately and the coupling – that is, the heat transfer from electrons to the lattice – is realized through the electron-lattice coupling factor, g.

Third, a uniform temperature profile across the particle can be assumed considering the characteristic length scales and the heat transfer mechanisms. In support of this assumption, a typical Biot number, $Bi = G \cdot L_c/k_{gold}$, for a nanosized particle can be estimated to be on the order of 10^{-3}, which means that the temperature variation within the particle is negligible. The characteristic length L_c is

defined as the volume of the particle divided by the surface area of the particle, k_{gold} is the thermal conductivity of bulk gold, and G is the thermal interface conductance. Typically, less than 5% error is introduced by assuming a uniform temperature profile for Biot numbers less than 0.1.

By incorporating the concepts stated above, a new set of equations can be written to describe the transient temperature profiles for the particle:

$$C_e \frac{dT_e}{dt} = g(T_l - T_e) + \dot{E}_{abs} \tag{13.6a}$$

$$C_l \frac{dT_l}{dt} = g(T_e - T_l) - \frac{\dot{Q}_w}{V_p} \tag{13.6b}$$

where V_p is the volume of the particle, T_e and T_l are the electron and lattice temperatures of the particle, respectively, g is the heat transfer rate from electrons to the lattice, and C_e and C_l are the heat capacities for electrons and the lattice of bulk gold, respectively.

The rate of heat loss from the particle to its surroundings (Equation 13.6b) is calculated by taking into account the interface conductance given by:

$$\dot{Q}_w = A_{surface} \cdot G \cdot (T_l - T_{w,s}) \tag{13.7}$$

where T_l is the particle temperature (lattice temperature), $T_{w,s}$ is the water temperature at the particle surface, and G is the thermal conductance at the particle/fluid interface.

The energy equation for the surrounding aqueous medium can be written as:

$$\rho_w c_{p,w} \frac{\partial T_w}{\partial t} = \nabla (k_w \nabla T_w) \tag{13.8}$$

where the subscript w is used to denote the parameters of the surrounding medium (e.g. water).

Figure 13.6 compares the theoretical transient particle temperatures determined from the three different models discussed above: (1) the thermodynamic model (Equation 13.4); (2) the heat transfer model without interface conductance (Equations 13.6–13.8 with G = 0); and (3) the heat transfer model with interface conductance (Equations 13.6–13.8). We have calculated the temperature of an 80 nm gold nanosphere over a 1 ns time duration after the application of a 250 fs laser pulse of 50 mJ cm^{-2} average fluence and 780 nm wavelength. The results show that, both the thermodynamic model and the heat transfer model including interface conductance give similar maximum particle temperatures, while the exclusion of the interface conductance estimates slightly lower temperatures. The heat transfer model provides the exponential decay profile of the particle temperature during cooling.

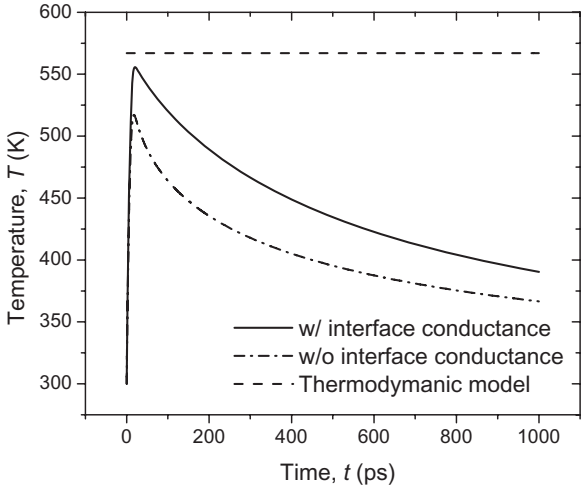

Figure 13.6 Transient temperature profiles of an 80 nm gold nanosphere irradiated with 250 fs laser pulse of 50 mJ cm^{-2} average fluence (energy per area) and 780 nm wavelength as calculated utilizing the thermodynamic model and the heat transfer model and with (w/) and without (w/o) interface conductance.

In order to demonstrate the accuracy of this heat transfer model with thermal interface conductance, we have compared our calculations of femtosecond laser heating of gold nanospheres [76] with the experimental results of Plech and coworkers [77], who investigated the lattice dynamics of spherical gold nanospheres in a water medium by using X-ray scattering and measuring the lattice expansion. Figure 13.7 shows the calculated values of lattice expansion measurements 52 nm and 94 nm gold particles at 100 ps and 1 ns after irradiation by a 1 fs laser pulse, along with data provided by Plech and colleagues as a function of laser fluence. The model predictions are found to be in very good agreement with experimental results, especially at low fluences, although beyond a certain laser fluence the data deviates from the linear line. As also discussed in detail by Plech and coworkers, we believe that the discrepancy between predicted and measured values occurs as a result of high water temperatures at the particle surface. When the water temperature rises near the critical temperature, bubbles can form and the presented heat transfer model is no longer valid.

13.3.3 Laser-Induced Phase Changes

As mentioned previously, the models presented above are valid in the absence of phase changes (of the particle or the surrounding medium). It is important to

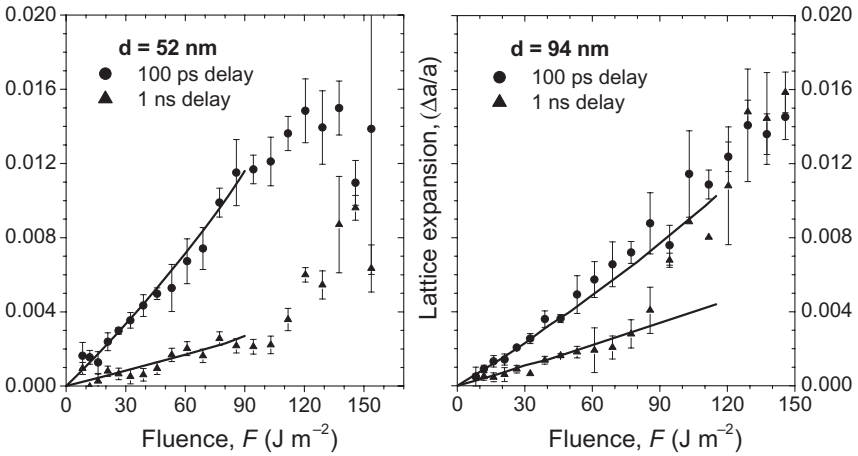

Figure 13.7 Validation of heat transfer model [76] with experimental data up to the fluence at which 90% critical temperature of water is reached. Lines are calculated lattice expansion of spherical gold nanospheres of 52 nm and 94 nm diameters as a function of peak laser fluence. Symbols are experimental data of Plech and coworkers [77].

define the critical temperature limits to identify when the phase changes in the particle and surrounding medium occur. First, the surrounding aqueous medium has two temperature limits depending on the rate of heat transfer: (i) a normal boiling temperature of water ($T = 373$ K); and (ii) a critical temperature of water ($T_{cr} = 647$ K), beyond which the water becomes thermodynamically unstable and water vapor forms. The upper temperature limit for the nanoparticle is the melting temperature ($T_m = 1337$ K, the bulk melting value for gold).

We will first discuss the phase change of the surrounding liquid as a result of the heat transfer from a laser-heated particle. A phase change induces a vapor layer around the particle, which in turn causes a drastic reduction in heat transfer at the surface. Figure 13.8 presents the pressure–temperature (P–T) diagram including the binodal (equilibrium vaporization, normal boiling) and spinodal (superheating limit) lines to illustrate the liquid–vapor phase change of water. The phase change can occur at any point between the binodal and spinodal lines, depending on the rate of heating. The rate at which the laser pulse deposits energy dictates whether the liquid temperature will heat faster than the heterogeneous nuclei will grow. Under slow heating conditions, as with CW or pulsed-lasers having long durations, the phase change occurs along the binodal line (e.g. at $T = 373$ K at atmospheric pressure). Slow heating will not allow extensive superheating past the binodal as excess energy will result in the growth of heterogeneous nuclei rather than further heating of the liquid [78]. On the other hand, in the case where high rates of energy (10^9 K s^{-1}) are deposited into the particle – as seen in short laser

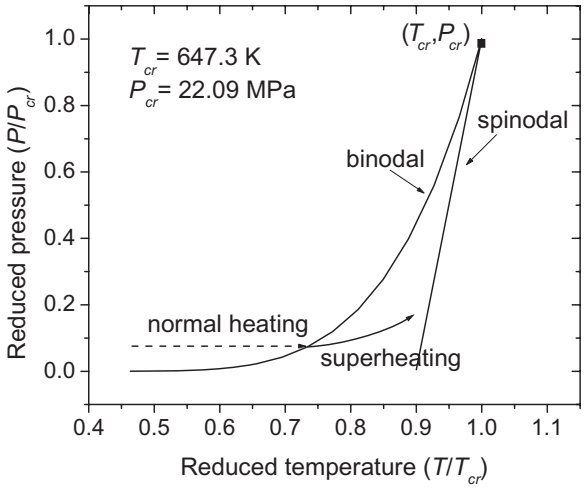

Figure 13.8 Pressure–temperature (*P–T*) diagram illustrating the liquid-vapor phase change of water.

pulse irradiation – the surface vapor pressure build up in the surrounding fluid takes place more slowly compared to the temperature rise [79]. In this case, heterogeneous nuclei will not have enough time to grow and superheating can be observed [70–72, 78]. The spinodal line forms an upper limit for the superheated liquid, and when this is reached the water becomes thermodynamically unstable and an explosive phase change (homogeneous boiling) occurs. A significant amount of vapor nuclei can be found when the temperature of the liquid reaches 90% of the critical temperature at atmospheric pressure [77, 80, 83, 85].

Laser-induced melting of the particle will affect the heat transfer properties of the nanoparticles, as well as laser–particle interactions during the subsequent laser irradiations. The governing equation describing the energy processes must incorporate changes in phase and subsequent thermophysical properties. The optical properties of particles will change due not only to melting but also to the subsequent shape transformation of nonspherical particles to the thermodynamically more stable spherical particles. In addition, it has been inferred experimentally that a surface melting phenomenon can occur at temperatures much less than the bulk melting value, such that liquid shell nanoparticles with solid cores can be generated [69].

The shape transformation of gold nanostructures in aqueous solution from ellipsoids to spheres was investigated by Inasawa *et al.* [85]. After exposure to a 30 ps single laser pulse, the required energy for shape transformation was found to be approximately 40 fJ. This value was smaller than the calculated energy for complete melting (67 fJ), a difference which was attributed to the surface melting phenomenon. El-Sayed and coworkers experimentally studied the melting

threshold of a 44×11 nm nanorod by using spectroscopy [86] and transmission electron microscopy (TEM) imaging [87]. A threshold energy of 65 fJ for complete nanorod melting (having a 30% associated error) was found to be independent of the incident wavelength [86]. In another study conducted by the same group, Link *et al.* [87] determined a complete nanorod melting threshold fluence of about $10\,\mathrm{mJ\,cm^{-2}}$ by using femtosecond laser pulses. These authors also showed that laser pulse fluences lower than the threshold fluence caused partial melting of the nanorods, whereas fragmentation of the nanorods was observed at high laser fluences ($\sim 1\,\mathrm{J\,cm^{-2}}$). Ekici *et al.* [76] investigated (on a theoretic basis) the melting fluences of nanorods 48×14 nm in size with respect to particle orientation to the laser polarization. Hence, it was found that particles melted with three orders magnitude less fluence when aligned parallel to the laser polarization rather than perpendicular.

13.3.4 Summary of Heating Dynamics

In conclusion, laser pulse duration must be considered carefully when studying particle heating dynamics since, the shorter the pulse duration the greater the confinement of heat dissipation into the surrounding water. When the pulse duration is shorter than the electron–phonon and phonon–phonon relaxation times (as in the case of femtosecond laser pulses), it is possible to calculate the maximum particle temperature by using a thermodynamic model. This approximation works quite well, since heat loss from the particle is almost negligible within the duration of the pulse and the subsequent electron–phonon coupling time. Conversely, when the pulse duration is comparable to the phonon–phonon coupling time, it is no longer valid to neglect heat dissipation from the particle. In other words, the temperature estimation for relatively long pulses requires a heat transfer model for both the particle and its surroundings in order to include a descriptive picture of energy processes occurring in the system. Another difference is observed at the particle/surroundings interface, where the temperature jump at the boundary becomes relatively significant as the time scale of interest becomes shorter. Finally, modeling of the system with laser pulse durations longer than electron–phonon coupling times requires special attention because of the changing optical properties of the nanoparticle and its surroundings during the pulse.

In addition to pulse duration, laser-induced phase changes must be considered carefully in the studies and/or models of particle heating dynamics. First, the particle melting and the subsequent shape transformation may be observed at high temperatures. Second, a phase change in the surrounding medium of the particle may be observed. Either of these phase transformation will cause drastic changes in the heat transfer properties and lead to a requirement for more complicated models (i.e. a solution for the full set of compressible equations) to represent the effects of pressure and bubble formation around the particle.

13.4 Plasmonic Laser Phototherapy (PLP)

The strong plasmon resonance of noble-metal nanoparticles has led to the development of numerous nanoparticle-based laser therapeutic treatments, termed plasmonic laser phototherapy (PLP). Through the use of molecular specific bioagents such as antibodies and ligands, various research groups have demonstrated the potential for a selective treatment of cancer cells targeted with a variety of gold nanostructures. Nanoparticle-based cancer treatment has been shown through either hyperthermal therapy or localized photodisruption of cellular membranes, with both modes having been demonstrated across the visible to NIR wavelengths of the electromagnetic spectrum. In extending beyond cancer treatment, photoactivated nanoparticles have been used to inactivate proteins [88, 89] and to perturb DNA [90] and chromatin [91] through a direct coupling of the nanoparticle to the desired structure. Additional therapeutic prospects exist in gene transfection [92], proteomics, angiogenesis, atherosclerosis, virology [93] and bacteriology [94].

As mentioned previously, two distinct modes for the selective killing of cancer cells are currently being investigated. The first PLP mode involves the generation of thermal damage through hyperthermia induced by the CW-laser heating of nanoparticles. Hyperthermia is defined as the heating of tissue to a temperature of 41–47 °C for tens of minutes [95]. Tumors have a reduced heat tolerance due to their inability to easily dissipate heat; this is a product of their disorganized and compact vasculature structure [32]. A fundamental aspect of photothermal therapy is that the incident light is tuned to the frequency of the nanoparticle absorption resonance, thus providing maximal energy absorption by the particle. Due to the strong absorption dynamics of metallic nanoparticles, large temperature rises in tissue structures can be achieved such that cancer cells can be selectively killed, with limited damage to healthy surrounding tissues [32]. Plasmonic photothermal therapy causes irreparable tissue damage through protein denaturation, coagulation and cell membrane disorganization.

The second PLP mode involves the application of pulsed lasers to induce localized photodamage to cellular membranes in the vicinity of the nanoparticle. Depending upon the laser pulse duration and fluence, a variety of photoactivated processes (i.e. photothermal and photomechanical effects/damage) including hyperthermia, bubble formation as a result of boiling or explosive boiling and particle fragmentation, can be used for the local disruption of a biological membrane. It is important to remember that, with decreasing laser pulse duration to the nanoscale and subnanoscale, photothermal and photomechanical effects/damages in the tissue can be confined to the particle near-field as a result of a greater efficiency in the heating and scattering processes. This confinement provides the possibility for membrane- and molecular-specific phototherapy, with high specificity.

Nanoparticles have highly tunable plasmon resonances that allow for therapy over the entire visible to NIR wavelengths. The fundamental, spherical particle

shape typically has a resonance from 400–600 nm [7]. Through the engineering of anisotropic (nanorods, nanocubes) and heterodyne (nanoshells) particles, the resonance is red-shifted into the NIR wavelengths. This tunability is important when accessing the size of the region of interest. For surface lesions or *ex vivo* cell treatments, where light does not need to penetrate deep within tissue, visible wavelengths could be appropriate. However, deep lesions require laser wavelengths that are not highly absorbed by water in the cells and tissues. NIR wavelengths should be used for large-scale lesions and those lesions deeply embedded within a tissue structure.

In this section, we review the various approaches of nanoparticle-based laser therapeutic treatments. We commence with a discussion of CW plasmonic photothermal therapies, with details of single cell and large tumor manipulations. We then proceed to a discussion of microscale and nanoscale manipulations of subcellular materials using pulsed lasers. To introduce the concept of confinement, the discussion begins with localized photothermal therapy for the manipulation of protein expression, and then describes how laser confinement has been used in a variety of cancer treatment methods. It is our hope that after, reading this section, the reader will begin to understand how particle shape and size and laser pulse duration and wavelength can be engineered to fulfill the parameters for a large set of cancer phototherapies.

13.4.1 Continuous-Wave Laser Plasmonic Phototherapy

The first class of nanoparticle-based phototherapy applications utilizes CW lasers. Here, the goal is to deliver a lethal dose of heat into large-scale tumor structures in which a high density of nanoparticles are embedded while causing as little damage as possible to any intervening and surrounding normal tissues. Specifically, for photothermal therapy (hyperthermia), tissue temperatures are moderately raised to 41–47 °C for several minutes, which is high enough to cause cellular membrane disorganization and protein denaturation. The details of some recent demonstrations of the PLP of cancer cells *in vitro* across the visible and NIR wavelength regimes utilizing gold nanospheres, nanorods and nanoshells are listed in Table 13.1. The discussion begins with a number of *in vitro* cells studies and works towards *in vivo* studies, where the details of two techniques for the effective delivery of particles to tumor regions are presented.

13.4.1.1 In Vitro Cell Studies

13.4.1.1.1 Nanoshells Nanoshells, which originally were developed by the Halas group [14], are a class of optically tunable nanoparticles consisting of a dielectric core surrounded by a thin gold shell, and have shown great promise for photothermal therapy applications. Since it is possible to control the ratio of the shell thickness and core radius dimensions, the resonant wavelength can be tuned from 500 nm to 2 μm [61]. Specifically, gold shells of 10 nm encasing a silica core of

Table 13.1 Summary of nanoparticle-based, continuous-wave laser phototherapies performed on cells *in vitro*.

Nanoparticle characteristics	Laser wavelength	Exposure parameters: Exposure time Total Irradiation Total energy per area	Results	Year [Reference]
Sphere				
35 nm, gold 520 nm plasmon resonance functionalized with αEGFR	514 nm	4 min $19\,W\,cm^{-2}$ $4.56\,kJ\,cm^{-2}$	Fourfold greater energy required to kill unlabeled normal cells compared to labeled malignant cells	2006 [98]
Shell				
10 nm gold shell 110 nm silica core 820 nm plasmon resonance functionalized with αHER2	820 nm	7 min $35\,W\,cm^{-2}$ $14.7\,kJ\,cm^{-2}$	Cell death was confined to the laser/nanoshell treatment area. Exposure to NIR alone did not kill cells	2003 [99]
Rod				
3.9 Aspect ratio, gold 800 nm plasmon resonance functionalized with αEGFR	800 nm	4 min $10\,W\,cm^{-2}$ $2.4\,kJ\,cm^{-2}$	Half laser energy required to kill labeled malignant cells compared to normal cells	2006 [5]

110 nm and having a peak resonance centered at 820 nm were found to be most effective in therapy due to their high particle absorption in comparison to the tissue of interest.

The research group at Rice University has primarily been responsible for much of the experimental evidence for the efficacy of photothermal therapy with nanoshells. In various proof-of-principle experiments, the group demonstrated the *in vitro* photothermal destruction of HER2-positive SKBr3 breast adenocarcinoma cells [23, 97, 98]. Here, cells bound with the anti-HER2 conjugated nanoshells were irradiated for 7 min with CW laser light operating at 820 nm wavelength with a total intensity of $35\,W\,cm^{-2}$. As shown in Figure 13.9, all labeled, malignant cells

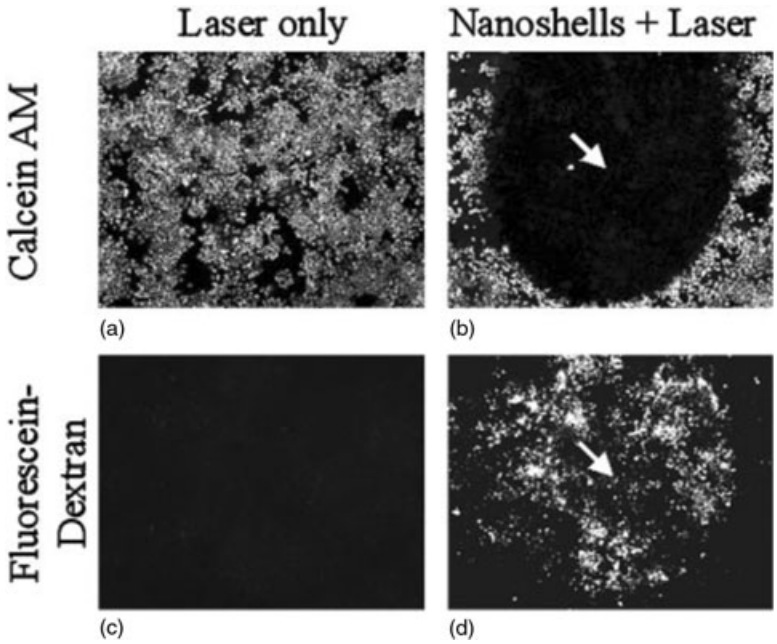

Figure 13.9 Plasmonic laser photothermal treatment of breast cancer cells (SK-BR-3) exposed to 35 W cm^{-2} laser intensity for 7 min. Unlabeled cells maintained both cell viability, as shown by (a) calcein fluorescence and (c) membrane integrity, indicated by the lack of 10 kDa FITC-dextran uptake. Cells labeled with nanoshells underwent photothermal destruction within the laser spot, as shown by (b) calcein fluorescence and (b) cellular uptake of 10 kDa FITC-dextran. (Reproduced, with permission, from Ref. [97].)

within the laser spot were photothermally damaged, whereas the unlabeled cells remained intact [97]. Stern *et al*. [99], at The University of Texas Medical Center, determined experimentally that cells must be labeled with approximately 5000 nanoshells for the most effective photothermal treatment.

13.4.1.1.2 **Nanospheres** Nanospheres, the most fundamental particle geometry, were exploited for their large resonant absorptions in the visible portion of the electromagnetic spectrum and ease of production. It has been found by several research groups that particles of 30–40 nm in size produced maximal temperatures when irradiated with light tuned to their plasmonic resonance [32]. The El-Sayed group experimentally labeled HSC 3 and HOC 313 cells (human oral squamous cell carcinomas), in an *in vitro* setting with 35 nm gold nanospheres conjugated to anti-EGFR antibodies. Dark-field microscopy was used to verify that the immuno-targeted nanoparticles bound homogeneously to the malignant cell types with a 6-fold greater affinity than nonmalignant cell types [4]. The labeled cells were irradiated with a CW, 514 nm wavelength, argon laser which overlaps the surface

plasmon absorption of the spherical nanoparticles (520 nm peak absorption wavelength). The laser light was focused to a 1 mm spot size, and the sample was irradiated for 4 min. A threshold intensity of 19 W cm^{-2} was determined to kill the labeled, cancer cells, this being less than half the laser intensity required to kill unlabeled, nonmalignant cells [98, 100].

13.4.1.1.3 **Nanorods** Gold nanorods, originally developed by the El-Sayed group [12, 64], provide great potential for photothermal ablation in the NIR wavelength regime. By tuning the ratio of the transverse to longitudinal lengths, the strong longitudinal absorption band is shifted into the NIR wavelength regime, which allows for photothermal therapy with maximal penetration of light through the tissues. This is a regime in which single gold nanospheres have shown low levels of absorption. As their size is considerably smaller than other engineered particle types (such as nanoshells), gold nanorods have the potential to penetrate more deeply into tissue structures through passive means. Albeit, there is a strong dependence on laser absorption with nanorod orientation to the incident electric field, which is currently uncontrollable with current targeting methods.

The El-Sayed group has shown evidence for the nanorod-assisted photothermal ablation of the human oral squamous cell carcinoma types HOC 313 clone 8 and HSC 3. By capping the nanorods with poly(styrenesulfonate) (PSS), it is possible to functionalize the nanorod surface; indeed, PSS-capped nanorods have a strong binding ability to molecular macromolecules. Cells labeled *in vitro* with gold nanorods conjugated to anti-EGFR antibodies were found to be irreversibly damaged after a 4 min exposure to CW Ti:sapphire laser light at 800 nm. The threshold intensity to kill cancer cells was found to be 10 W cm^{-2}, which was lower than that found for nanospheres and nanoshells, and the result of a higher particle absorption cross-section [5]. The group of Wei and Cheng has demonstrated extensive membrane damage using folate ligand-functionalized nanorods [26]. Here, *in vitro* labeled KB cells (a malignant cell line derived from oral epithelium) were irradiated for 81.4 s with a CW, 765 nm laser light. Severe blebbing, associated with Ca^{2+} influx into the cell, was found at a threshold intensity of 389 W cm^{-2}. When the nanorods were internalized into the cells, cell death required an approximate 10-fold increase in laser intensity.

13.4.1.2 **In Vivo Animal Studies**

In animal studies, Gobin *et al.* [101] studied the efficacy of both the direct injection of nanoshells into the tumor and passive accumulation of nanoshells into tumors via enhanced blood vessel permeability and retention. Female nonobese diabetic CB17-Prkd c SCID/J mice were inoculated in the right and left hind leg with canine TVT cells. PEG-passivated NIR-absorbing gold-silica nanoshells were injected interstitially 5 mm into the tumor volume, after which the nanoshell-laden tissue was exposed for 6 min to a total intensity of 4 W cm^{-2}, 30 min after injection. By using magnetic resonance thermal imaging, the temperature profile was monitored during nanoshell exposure to NIR light. Consequently, the average maximum

temperature sustained in the tissue was shown to be increased by $37.4 \pm 6.6\,^{\circ}C$, causing irreversible tumor damage [97].

The direct injection of nanoshells to the point of interest is not possible in every case, as tumors or lesions may be embedded deep within a tissue structure. Hence, the research group at Rice University investigated the uptake of nanoshells via passive accumulation from the bloodstream. During tumor formation, rapid angiogenesis causes much of the newly formed vasculature to be 'leaky', and this allows macromolecules to be extravasated preferentially into the tumor tissue. It is from this vasculature that nanoparticles may enter into the tumor via standard blood flow; indeed, nanoshells of 60–400 nm in size have been shown to extravasate and accumulate in many tumor types. Following photothermal therapy, complete tumor regression was seen in the murine model within 10 days after heat treatment, although more promising was the fact that no tumor regrowth was seen after 60 days. When compared to control studies (no treatment and laser treatment alone), the survival times for mice inoculated with nanoshells were significantly improved; some 83% of mice survived for seven weeks after nanoshell phototherapy, compared to less than 20% of controls.

13.4.2 Pulsed Laser Plasmonic Phototherapy

Pulsed laser irradiation provides a platform for the confinement of photoactivated processes. Here, we describe the various approaches taken to localize laser damage to subcellular targets. A list of reported pulsed PLP data is provided in Table 13.2. In order to introduce the concept of confinement, we begin our discussion with a presentation of heat confinement to disrupt molecular macromolecules (e.g. proteins), and then proceed to cancer treatments mediated by photoinduced hyperthermia. Next, we describe higher-energy nanoparticle irradiation where bubble formation is induced in both single and multiple particle systems. Cellular disruption through explosive particle fragmentation and nonlinear absorption mechanism is next described. Finally, we discussed the details of near-field ablation of cellular membranes.

13.4.2.1 Localized Thermal Damage (Hyperthermia)

Localized thermal damage of absorbing molecules by pulsed laser irradiation was first proposed by Anderson and Parrish [105], who showed that laser-induced thermal damage is confined to the endogenous absorbing structure when the pulse duration is shorter than the thermal relaxation time of the structure. In their original studies, these authors utilized the interaction between subcellular pigment microparticles with short pulse laser radiation to induce cell lethality. This simple concept has led to an explosion of technologies in hair and port-wine stain removal and acne reduction, for example. The manipulation of subcellular material requires irradiation by lasers with pulse durations of nanoseconds and less.

The concept of localized thermal damage was next extended to the use of exogenous micro- and nanoabsorbers for controlled subcellular and cellular membrane

Table 13.2 Summary of pulsed plasmonic laser phototherapies (PLP).

Nanoparticle characteristics	Laser parameters: Pulse duration Wavelength Repetition rate	Exposure parameters: Number of pulses Irradiation values	Results	Year [Reference]
Nanosecond pulses				
Sphere				
30 nm, gold	20 ns pulse duration 565 nm wavelength	100 pulses 500 mJ cm^{-2} per pulse	500 particles per cell 95% cell death	2003 [89]
30 nm, gold	6 ns pulse duration 532 nm wavelength	5 pulses 15 mJ cm^{-2} per pulse	68% transfection efficiency 27% cell death 1.1×10^5 particles per cell labeling	2005 [92]
Sphere aggregates				
30 nm, gold >200 nm cluster	10 ns pulse duration 532 nm wavelength	1 pulse 600 mJ cm^{-2} per pulse	Cell death only found when large clusters present; Bubble formation detected	2006 [17]
40 nm, gold >300 nm cluster	12 ns pulse duration 1064 nm wavelength	500 pulses 80 mJ cm^{-2} per pulse	Cell death only found when large clusters present	2005 [102]
Shell aggregates				
45 nm, γ-Fe_2O_3/Au 540 nm plasmon resonance	7 ns pulse duration 700 nm wavelength	1 pulse 400 mJ cm^{-2} per pulse	Observed reduced calcein AM fluorescence	2007 [103]
Rod				
5.9 aspect ratio, gold 900 nm plasmon resonance	6–9 ns pulse duration 1064 nm wavelength 10 Hz repetition rate	1200 pulses 280 mJ cm^{-2} per pulse	Studied trypan blue uptake	2006 [104]
Picosecond pulses				
Sphere				
15 nm, gold	35 ps pulse duration 527 nm wavelength 1 kHz repetition rate	10^4 pulses 50 mJ cm^{-2} per pulse	aP protein inactivation	2002 [88]

Table 13.2 *Continued*

Nanoparticle characteristics	Laser parameters: Pulse duration Wavelength Repetition rate	Exposure parameters: Number of pulses Irradiation values	Results	Year [Reference]
Cages				
45 nm edge length 3.5 nm wall thickness 3 : 1 gold : silver ratio 810 nm plasmon resonance	20 ps pulse duration 810 nm wavelength 82 MHz repetition rate	5 min exposure time 18 nJ cm^{-2} per pulse	Studied calcein AM and EthD-1 uptake	2007 [60]
Femtosecond pulses				
Sphere				
5 nm, gold	80 MHz 835 nm wavelength	3 s exposure time 15 mJ cm^{-2} per pulse (cited 56 mW and 2.5 mm spot size)	Chromatin assembly disrupted *in-vivo*	2007 [91]
80 nm, gold ~540 nm plasmon resonance	80 MHz 760 nm wavelength	10 s exposure time[a] 18 mJ cm^{-2} per pulse (20 mW with 0.95 NA lens)	Studied 10 kDa FITC-dextran uptake	2008 presented here
Sphere aggregates				
30 nm, gold 540 plasmon resonance after cellular attachment	1 kHz 800 nm wavelength	2 min exposure time 140 mJ cm^{-2} per pulse (cited 1.1 mW and 1 mm spot size)	Quadratic dependence of photothermal efficiency on laser power indicates multiphoton process	2006 [17]
Silver shell				
40 nm silver shell 20 nm gold core 400 nm plasmon resonance	800 nm wavelength 80 MHz repetition rate	Line scan 7–30 mJ cm^{-2}	Cut chromosomes	2007 [90]
Rod				
765 nm plasmon resonance	200 fs pulse duration 765 nm wavelength 77 MHz repetition rate	10 s exposure time[a] 3 mJ cm^{-2} per pulse (cited 9.7 pJ per pulse with 1.2 NA lens)	Nanorods localized on membrane; Studied Ca^{2+} intake	2007 [26]

a Laser beam is scanned.
aP = alkaline phosphatase; EthD-1 = ethidium homodimer 1.

manipulations by Lin *et al.* [106] and Huttman *et al.* [88]. These groups demonstrated thermal effects with spatial confinements of less than 50 nm by using highly absorbing polystyrene latex microspheres loaded with iron oxide and immunogold nanospheres irradiated with nanosecond and picosecond laser pulse durations.

At their plasmonic frequency, gold nanoparticles have strong absorption properties, which allows for large surface temperature generation with excitation fluences as low as 1 mJ cm^{-2}. As a quick example, we can calculate (using the heat transfer model with interface conductance) that a gold nanosphere of 30 nm diameter irradiated by a single, 35 ps laser pulse at 527 nm wavelength and fluence 1 mJ cm^{-2} will absorb approximately 10 fJ of energy, giving a maximum particle temperature of approximately 540 K (Figure 13.10a). In Figure 13.10b, it is shown – on a theoretical basis – that the particle will heat the surrounding medium with a spatial confinement of approximately 5 nm.

The concept of spatial confinement using picosecond laser-heated nanoparticles was studied via protein denaturation and subsequent inactivation. In their initial study, Huttman *et al.* [88] characterized the extent of the spatial confinement by changing the distance between the target and the particle surface. Initially, 15 nm gold nanospheres were directly coupled with the protein alkaline phosphatase (aP). The aP protein was denatured by the application of 10^4 pulses of 35 ps, 527 nm wavelength laser light of fluence 50 mJ cm^{-2}; however, when aP was indirectly coupled to the nanoparticle via an antibody linker (~5–10 nm long), irradiation of the particle system with the same parameters did not cause protein inactivation. Subsequently, questions arose as to whether the linker was inactivated rather than the protein of interest, which would result in aP becoming dissociated from the linker. However, the conclusion was reached that the aP protein would not diffuse away from the particle by any appreciable distance during the nanosecond long

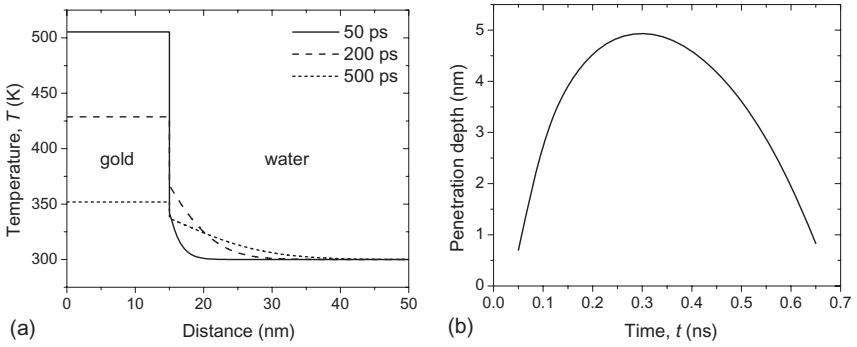

Figure 13.10 Thermal heating properties of a 30 nm spherical gold particle irradiated with 35 ps laser light at a 527 nm wavelength and fluence of 1 mJ cm^{-2}. (a) Temperature profile of the particle and water at 50, 200 and 500 ps after the application of the laser pulse; (b) Penetration depth of high temperatures (down to the 1/e value of the water temperature rise, 330 K) into the surrounding water.

heating cycle (see Figure 13.10b), and that localized heating induced by the nanoparticle was most likely responsible for aP inactivation. The photochemical generation of reactive species and surface-enhanced two-photon absorption were also cited as possible damage mechanisms.

In order to elucidate the temperature at which protein unfolding and inactivation occurred, Huttman *et al.* [107] performed a set of protein inactivation studies by laser-induced temperature jumps. They also modeled particle heating dynamics to determine whether the particle could reach sufficiently high temperatures to cause protein inactivation. Here, free chymotrypsin in water was heated via irradiation from 2.1 μm laser light of varying pulse durations, to temperatures between 370–470 K. Chymotrypsin inactivation occurred within 300 μs at a temperature of 380 K. The unfolding of chymotrypsin with respect to the generated heat followed the Arrhenius equation down to pulse durations of 330 μs. From theoretical temperature calculations of nanospheres after laser irradiation (using the model developed by Goldenberg and Tranter [108]), it was determined that temperatures generated by the particle after irradiation with picosecond and nanosecond laser pulses of fluences ranging from tens to a few hundreds of mJ cm^{-2} would indeed be sufficient to induce protein inactivation. One concern of the Goldenberg and Tranter model is that it does not take into account the interface conductance. Due to the phonon–phonon mismatch, there would be a temperature drop at the boundary and, as such, higher fluences than reported might be necessary to generate a water temperature sufficiently high to induce protein inactivation.

To verify the hypothesis that thermal processes are indeed the mechanism of protein inactivation, we should refer to studies discussing the mechanisms of explosive boiling. By using nanosecond time-resolved microscopy, Lin *et al.* [106] determined that surface tension permitted high temperatures to exist at the nanoparticle surface, without vaporizing the surrounding water. The extreme particle temperature rise occurred as a result of the high rate of energy deposition. As explained earlier, this rapid deposition can cause superheating in a thin layer of surrounding water, instead of the expected phase change at the normal boiling temperature. If the vapor pressure were to overcome the surface tension, the superheated liquid would undergo an explosive phase change. Explosive boiling typically occurs when the temperature of the liquid reaches 90% of its critical temperature (647 K) [77, 80, 83, 84]. As chymotrypsin can be denatured within 300 μs at temperatures below 380 K – which is well below the critical temperature for explosive boiling – it can be concluded that, in the above examples, protein inactivation cannot be the result of explosive boiling but is most likely due to hyperthermic processes. It was also argued that, if mechanical damage by explosive boiling were the cause, then aP proteins indirectly coupled to the nanoparticle would also be damaged during irradiation.

Pulsed photothermal therapy for targeted tumor therapy has also been demonstrated in the NIR wavelength regime using functionalized nanocages and nanorods. Chen *et al.* [60] demonstrated experimentally the photothermal destruction of SK-BR-3 cells labeled with nanocages after the application of 20 ps, 810 nm laser

light (82 MHz repetition rate) for 5 min. An average threshold intensity of 1.5 W cm^{-2}, which corresponds to a pulse fluence of 18 nJ cm^{-2}, was determined for irreversible membrane damage. Takahashi *et al.* [104] reported HeLa cell death in the presence of phosphatidylcholine-passivated gold nanorods when exposed to 2 min of 6–9 ns laser pulse of 1064 nm wavelength with a pulse fluence of approximately 280 mJ cm^{-2}. Albeit, with pulsed lasers, particle reshaping to the more thermodynamically stable spherical shape can also be induced. In further experiments, Link *et al.* [87] studied nanorod reshaping for both nanosecond and femtosecond lasers, and found that the energy threshold required for complete melting of the nanorods was two orders of magnitude less when using femtosecond laser pulses compared to that required with nanosecond laser pulses. This difference was attributed to the decreasing absorption efficiency and increased heat dissipation from the particle to the surroundings during pulse duration in the case of nanosecond laser pulses. Takahashi *et al.* [109] proposed a method of using nanorod reshaping to mediate the finality of phototherapy and found that, after applying 890 mJ cm^{-2} fluence pulses for 2 min, the nanorod was transformed to a spherical shape. The conclusion was that nanorod reshaping during therapy would prevent continued cell death in the surrounding normal tissues due to significantly reduced absorption effects in the NIR, but still cause killing of the intended targets.

13.4.2.2 **Bubble Formation**

A vapor bubble will rapidly expand around a particle if the amount of energy absorbed by the nanoparticle is sufficiently high for the initial high vapor pressure to overcome the surface tension of the liquid, which is inversely proportional to the particle size [107]. Due to low heat transfer across the vapor zone, the bulk of the surrounding material remains at ambient temperature. A shock wave and traveling high-pressure waves will be generated as a result of the expansion and the collapse of bubbles, and this is proposed to be the cause of cellular membrane disruption [110]. When cavitation bubbles form, thermal denaturation most likely plays a minor role in cellular death [89]. It has been found that damage due to cavitation is highly localized, with only those cells having internalized or membrane-bound particles being killed upon laser exposure.

Pitsillides and coworkers [89] were the first to demonstrate the use of bubble formation around nanoparticles as a means of selectively introducing exogenous macromolecules into the cellular cytoplasm through the plasma membrane. They investigated transient pore formation in the plasma membrane by irradiating 30 nm gold nanospheres with 100 pulses of 20 ns, 565 nm wavelength laser light at a laser fluence of 500 mJ cm^{-2}. When membrane permeability was assessed by monitoring the increased cellular uptake of a permeability probe (10 kDa FITC-dextran), a loading of 500 gold particles conjugated to the plasma membrane proved to be most effective by killing 95% of cells under the aforementioned laser irradiation conditions. This reported loading was approximately 10-fold less than found necessary for CW techniques and, when compared to other photoactivated therapies (e.g. photodynamic therapy), an approximately 2000-fold less cellular

loading of immunotargeted particles was required to achieve a similar level of performance [111].

The ability of pulsed laser-irradiated nanospheres to induce localized damage through nanoscale bubble formation was further studied by Yao *at al.* [92]. Their goal of this study was to inflict temporary permeability in the plasma membrane – without causing cell death – as a means of assisting gene transfection and gene therapy. To prove the concept, 30 nm particles conjugated to membrane-specific antibodies were delivered to the plasma membrane of the cancer cell lines L428 (Hodgkin's disease) and 299 (Karpas lymphoma). As a consequence, the efficient transfer of relatively small exogenous molecules in the cytoplasm was demonstrated by using 6 ns laser pulses at 532 nm wavelength. Permeabilization and resealing were also studied by varying the laser parameters, gold concentration and membrane proteins; thus, a transfection efficiency of 68% was achieved with only 27% cell death after exposure to five laser pulses of 120 mJ cm^{-2} fluence, when the cell was labeled with 1.1×10^5 nanoparticles.

With decreasing pulse duration, the energy required to heat the surrounding water to 90% of its critical temperature was reduced, thus confining the extent of heat damage. For comparison, it is possible to estimate the energies required to create bubbles around a 30 nm gold nanosphere irradiated by picosecond and nanosecond laser pulses, using the heat diffusion model described in Section 13.4.2.1. A theoretical comparison between two cases: (i) heating with a single, 35 ps laser pulse at 527 nm wavelength (conditions similar to the experiments of Huttman *et al.* [88]); and (ii) heating with a single, 20 ns laser pulse at 565 nm wavelength (conditions similar to the experiments of Pitsillides *et al.* [89]), is presented in Figure 13.11. Both cases were modeled using the heat transfer model with interface conductance. As can be seen in Figure 13.11, the application of

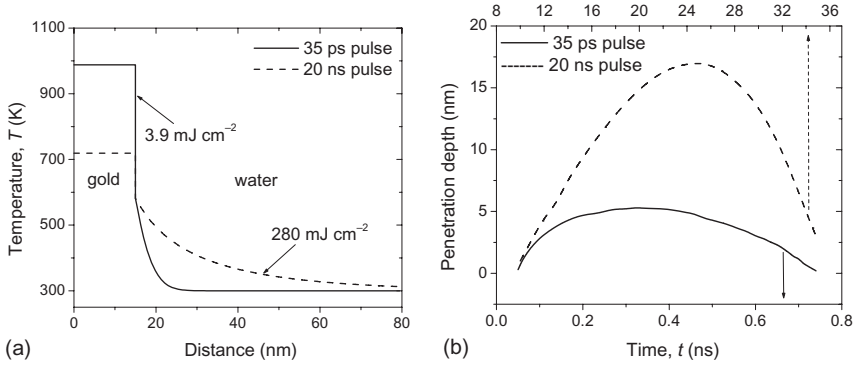

Figure 13.11 Comparison of laser fluences necessary to bring water to 90% of its critical temperature at 580 K around a 30 nm spherical gold particle exposed to picosecond (35 ps, $\lambda = 527$ nm) and nanosecond (20 ns, $\lambda = 565$ nm) laser pulses with a Gaussian temporal profile. (a) Temperature profile of the particle and water at 22 ns and 125 ps for the picosecond and nanosecond pulses, respectively, when the peak water temperature occurred; (b) Heat penetration depth as defined by the 1/e location of water temperature rise (~400 K).

picosecond laser pulses requires 72-fold less energy for the particle to reach 90% of the critical temperature of water than is required by nanosecond laser pulses. Whilst the heat confinement is approximately 5 nm for picosecond-laser-heated particles, it reaches 17 nm for nanosecond-laser-heated particles.

Finally, cell membrane disruption by cavitation bubbles can also be mediated by nanorods, due to their increased efficiency in NIR absorption and photothermal energy conversion. Tong *et al.* [26] demonstrated the photothermolysis of KB cells through the laser interaction of nanorods functionalized with folic acid to the plasma membrane. Following the application of 765 nm, 200 fs laser light at a 77 MHz repetition rate with an energy deposition rate of 9.7 pJ per pulse (for a 1.2 NA objective lens, we calculate a fluence of 3 mJ cm^{-2} per pulse) deposited during 10 s, the labeled KB cells produced clearly visible membrane blebbing. By comparison, KB cells loaded with internalized nanorods required a six-fold greater laser fluence to induce cellular damage. This large difference in fluence required for cell death between membrane-labeled and internalized nanorods emphasized the high localization of induced photodamage.

13.4.2.3 **Overlapping Bubble Formation**

Bubbles can be overlapped for the enhanced photodisruption of cancer cells. Overlapping bubbles can be created by gold nanosphere aggregates, the production of which may be achieve by a variety of methods, including: (i) clustering secondary monoclonal antibody-labeled nanospheres on a targeted single nanosphere [16, 17]; (ii) targeting naturally clustered cancer biomarkers [3, 112]; and (iii) concentrating nanoparticles with viruses and vesicles [93].

Enhanced bubble formation occurs due to overlapping bubbles from individual particles within an aggregate, generating one large bubble around the aggregate [17, 115]. Lapotko *et al.* [17] presented experimental evidence for selectively induced microbubbles in leukemia cells labeled with large aggregates, but not those labeled with individual particles and small aggregates. A bubble formation threshold of 600 mJ cm^{-2} was found for large nanoparticle aggregates under single-pulse, 532 nm, 10 ns laser irradiation conditions.

Nanoparticle aggregates also red-shift the plasmon resonance into the NIR wavelengths, leading to enhanced optical and thermal amplification. Both, Zharov *et al.* [104] and Larson *et al.* [103] provided experimental evidence for enhanced bubble formation in the vicinity of large nanosphere aggregates when irradiated by NIR laser light. Both groups showed a reduction in the bubble formation threshold from 600 mJ cm^{-2} down to 400–500 mJ cm^{-2} with the application of a single nanosecond laser pulse in the NIR. The role of multiple nanosecond laser pulses was also studied by Zharov *et al.* [104], who irradiated nanosphere-labeled cells with 500 pulses, further reducing the bubble formation threshold to 80 mJ cm^{-2}.

13.4.2.4 **Fragmentation of Nanoparticles**

The fragmentation and thermal explosion of nanoparticles is an additional mechanism that can induce localized damage (either desired or undesired) to cellular

material in the vicinity of the particles. A desired thermal explosion of particles may accompany plasma or bubble formation, further decreasing the threshold for cell death. However, undesired damage to surrounding healthy cells because of the uncontrolled nature of the extent of damage after the particle fragmentation or explosion can also occur. In addition, once the particle has been reshaped due to fragmentation, the efficiency of the PLP is greatly reduced. Shape transformations shift the peak of the plasmon resonance, significantly reducing the designed laser absorption efficiency of particles, and thus the efficacy of the PLP.

The fragmentation and thermal explosion of nanoparticles may also occur with the application of short-duration laser pulses. Here, a large degree of the absorbed energy will initially remain in the particle, heating it to very high temperatures, since the heat diffusion to the surrounding tissue is minimized during rapid heating with short-duration laser pulses. The mechanism of fragmentation, however, may differ for different pulse durations. Link *et al.* [89] have discussed the differences in fragmentation mechanisms of nanorods irradiated by femtosecond and nanosecond pulses. The TEM images produced by this group showed that the fragmented particles were mostly irregularly shaped in the case of femtosecond pulses, whereas near-spherical shapes were observed in the case of nanosecond pulses. It was suggested that the fragmentation of particles exposed to nanosecond pulses occurred as a result of thermal heating and melting processes. In contrast, when exposed to femtosecond pulses, a rapid particle explosion can occur as a result of multiphoton ionization where the lattice is still cold, and this would explain the formation of irregularly shaped fragmented particles. By applying a theoretical approach, Letfullin *et al.* [110] calculated the threshold fluence for thermal explosions of both gold nanospheres and nanorods when irradiated with nanosecond pulses at the plasmon resonance. A threshold fluence of approximately 40 mJ cm^{-2} was found for gold nanospheres, which could be reduced to 11 mJ cm^{-2} for relatively large gold nanorods.

13.4.2.5 **Nonlinear Absorption-Induced PLP**

Particles can exhibit enhanced heating properties due to nonlinear absorption effects such as two-photon absorption and second harmonic generation. The principle has been exploited by a variety of groups to achieve intracellular molecular manipulation and to locally disrupt cellular membranes. Csaki *et al.* [24] utilized two-photon absorption by silver–gold heterodyne spherical particles conjugated to single-stranded (ss) DNA strands to photodisrupt targeted chromosomal molecular material with 800 nm laser light with laser fluences of tens of mJ cm^{-2}. By using this technique, a large-scale parallelization of gene-specific molecular surgery utilizing metal nanoabsorbers can be achieved. Envisioned applications include DNA analytics as well as single cell manipulation. Mazumder *et al.* [91] targeted spherical 5 nm gold particles towards chromatin to investigate the mechanical coupling of chromatin to the nuclear architecture. Perturbation of the chromatin assembly was performed with 835 nm, pulsed laser light at 56 mW focused at the nucleus for 3 s (the corresponding fluence is 15 mJ cm^{-2} per pulse). Using the high spatial localization of nanoparticle-generated heat, the group's findings showed the direct

differential coupling of heterochromatin to specific cytoskeletal network elements. Huang *et al.* [100] found that with large particle loading on the plasma membrane of HSC oral cancer cells, the formation of large particle aggregates led to enhanced, nonlinear absorption processes and reduced the threshold fluence to cause a 20-fold increase in the number of cells killed.

13.4.2.6 Plasmonic Laser Nanosurgery

Femtosecond laser pulses can initiate plasma-mediated ablation with only a few tens of nJ of energy, due to their high peak intensities [114–117]. Ablation with very-low pulse energies becomes especially important when dealing with live cells and organisms having minimal tolerance to temperature increases. The intense near-field scattering effect of gold nanoparticles in the NIR wavelength regime can be used to induce plasma formation in the vicinity of the particle for high precision cellular membrane disruption.

Figure 13.12 shows the first experimental evidence of the concept of plasmonic laser nanoablation (PLN), where the enhanced plasmonic scattering in the near-field of gold nanoparticles can be used to vaporize both solid materials and biological structures with nanoscale resolution. Eversole *et al.* [118] showed experimentally the nanocrater formation on silicon by enhanced ultrafast laser scattering in the near-field of 150 nm gold nanospheres. As shown previously in Figure 13.3a, the chosen particle size maximizes near-field scattering at the 780 nm laser wavelength, while minimizing absorption effects (the ratio of near-field scattering to linear absorption is approximately 60, as shown in Figure 13.3b). Figure 13.12b and c provide experimental evidence of material removal after the plasmonic laser ablation of silicon. The generated crater follows the theoretical scattering pattern,

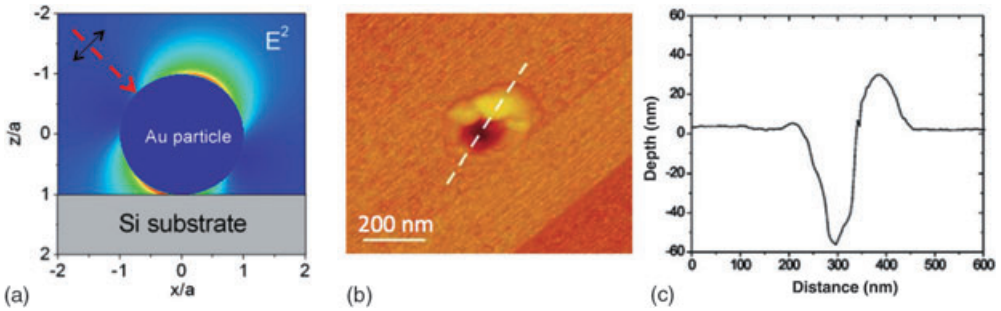

Figure 13.12 Plasmonic laser nanoablation (PLN) technique proposed by Ben-Yakar's group. (a) Theoretical calculations showing the field intensity around a gold nanosphere deposited on silicon substrate. The large enhancement of the ultrafast laser scattering in near-field of a gold nanoparticle can be used to ablate the silicon substrate immediately underneath the particle; (b) Experimental evidence for PLN showing nanocraters on silicon ablated using a 150 nm, spherical, gold nanoparticles; atomic force microscopy image of nanocrater generated by a 88 mJ cm^{-2} average fluence laser pulse at 780 nm having p-polarization at 45° incident angle; (c) Corresponding cross-section along the dotted white line in panel (b).

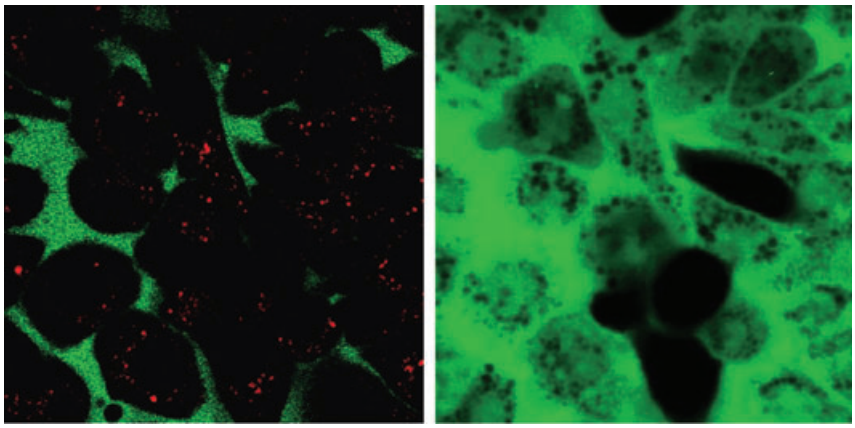

(a) (b)

Figure 13.13 Plasmonics laser nanoablation of cancer cells (MDA-MB-468) labeled with 80 nm gold nanoparticles functionalized with anti-EGFR antibodies. (a) Nanoparticles in red, imaged at 850 nm wavelength through multiphoton luminescence, and cell membrane-impermeable dye (10 kDa FITC-Dextran) in green, imaged at 760 nm wavelength; (b) Fluorescence images show reduced membrane integrity, as seen by the intake of FITC-Dex, after the application of 80 MHz laser pulses of 18 mJ cm^{-2} for 10 s.

confirming that crater generation is indeed the result of near-field scattering effects.

The Ben-Yakar laboratory group is currently extending plasmonic laser nanoablation to cellular membrane ablation. In their initial studies, MBA-MB-468 epithelial breast cancer cells were labeled with 80 nm gold nanospheres functionalized with anti-EGFR antibodies. Figure 13.13a shows a multiphoton luminescence image of labeled cells at 850 nm, which provides only a weak autofluorescence signal relative to the luminescence from the particles. Labeled cells, irradiated with 80 MHz repetition rate pulses of 18 mJ cm^{-2} fluence for 10 s at 760 nm wavelength, showed reduced membrane integrity, as seen by the uptake of 10 kDa FITC-dextran (Figure 13.13b). Unlabeled cells required eight times more laser fluence for the membrane integrity to be reduced. As linear absorption by the particle is negligible at the laser wavelength (the ratio of near-field scattering to linear absorption is approximately 55), membrane disruption can be attributed to the formation of free electrons and the resultant low-density plasma in the particle near-field due to the intense near-field scattering.

13.4.3
Summary of Plasmonic Laser Phototherapy

We have summarized the plasmonic phototherapy of biological materials, and indicate how this approach can be utilized for a highly selective treatment of

cancer. For the most part, plasmonic phototherapy has centered on the use of the strong absorption properties of gold nanostructures to kill cancer via hyperthermia, bubble formation, particle and fragmentation. Some more recent technology has begun to exploit the intense near-field scattering properties of gold nanoparticles for plasma-mediated ablation. By changing particle geometry and composition, applications across the visible and NIR wavelength regimes have been developed. In addition, depending upon the pulse duration, the region of photodamage can be controlled. Continuous-wave irradiation allows for large-scale tissue destruction, while short pulses can be yielded to manipulate finer structures in tissues and cells. With further refinements in cell labeling and laser delivery to the tissues, various nanoparticle-based laser phototherapies – including photothermal, photomechanical (bubble formation or particle fragmentation) and photoablation (plasma-mediated) techniques – have strong prospects for becoming the 'gold standards' of various cancer treatments.

13.5 Summary

Noble-metal particles have highly tunable optical properties and, as such, have shown great promise as highly sensitive and cost-effective multimodal tools for the screening, diagnosis and therapy of cancer. In this chapter we have primarily discussed the role of PLP as a novel nanoparticle-based laser cancer treatment. Research studies have shown that, by conjugating molecular-specific bioagents (e.g. antibodies and ligands) to the particle surface, a variety of potential cancer targets exist. Likewise, by using nanoparticles of different sizes, geometries and compositions, therapies can be tuned to a variety of laser wavelengths ranging from the visible to NIR regions of the electromagnetic spectrum. The fundamental spherical particle strongly absorbs laser light in the visible wavelength range, and in order to shift the plasmon resonance to NIR wavelengths – where light penetration into the tissues is maximized – both heterodyne and asymmetric particles have been developed. The treatment of surface lesions would benefit most from lower wavelength laser light, while large-scale tumors require NIR laser light (light penetration on the order of several centimeters, depending on the tissue type). Additionally, varying the laser pulse durations has allowed investigators to define the degree of heat confinement around the particle during treatment. Continuous-wave lasers are typically used to treat bulk tissue structures, while pulsed lasers can be used to confine any thermal and subsequent thermomechanical effects/damages to the cellular level. Hence, by employing variations of each of these parameters, it should be possible to develop a wide range of cancer therapies for a variety of tissues.

With CW lasers, *in vivo*, large-scale tumor reduction was verified using nanoshell phototherapy, with complete tumor regression being found at 10 days after treatment, and no regrowth after 60 days. By using active methods to bind nanoparticles to cancer cells, the thresholds for photodestruction were determined as

35 W cm^{-2} for nanoshells, 19 W cm^{-2} for nanospheres and 10 W cm^{-2} for nanorods. With pulsed lasers, the manipulation of proteins, organelle membranes and DNA has been achieved. Large amounts of energy are absorbed by the particle within a short time duration, significantly reducing the required fluence to generate large temperature increases. Femtosecond laser pulses require fluences which are an order of magnitude smaller than those needed for nanosecond pulses. As such, heat is confined to the particle near-field, providing a platform for true *in vivo* nanoscale manipulation of biological substances. With both CW irradiation and pulsed laser techniques, PLP has shown great promise for the selective treatment not only of cancer but also of other diseases. Indeed, it is anticipated that, in the near future, the technique will be successfully applied to the clinical setting as the operational parameters are optimized.

13.6 Future Perspectives

PLP – a novel, nanoparticle-based laser technology used not only for the elimination of cancer cells, viruses and bacteria but also for genetic manipulations – has matured well over the past few years. Nonetheless, a number of operational parameters still require optimization (see Table 13.3) before the technique can be applied

Table 13.3 Parameters important in understanding the applications of PLP in a clinical setting.

1. Particle dynamics
   a. *Stability:* ability to circumvent physiological systems without removal from body
   b. *Biocompatibility:* no adverse chemical reactions with physiological environment
   c. *Optical:* ability of particle to optimally absorb and scatter incident laser light
   d. *Clearance after therapy:* particle removal through lymphatic system
2. Particle functionalization
   a. *Stability:* dissociation of molecular-specific bioagents from particle
   b. *Delivery:* transport of particles to desired location through topical delivery or intravenous injection
   c. *Biomarker targeting:* desired location of particle in tissue/cell and distance from choice target
   d. *Spatial localization:* functional method for bringing the particle to desired distance to the target
3. Laser irradiation
   a. *Optical spatial localization:* laser parameters defining the optical localization for a given geometry
   b. *Delivery:* ability to bring laser light to desired location
   c. *Light Penetration:* light penetration in tissue to desired depth with minimal scattering and absorption
4. Multifunctionalization
   a. *Therapeutic:* use in combination with conventional photodynamic therapies
   b. *Imaging:* development of 'smart particle' for both *in vivo* imaging and therapy

effectively to a clinical setting. Both, particle and optical parameters are functions of the clinical application and must be optimized accordingly. Hence, in this section we will briefly define the possible parameter optimizations that will complement ongoing *in vitro* and *in vivo* experiments such that PLP achieves maturity.

PLP has a number of distinct advantages that make it compatible for the treatment of disease:

1. Nanoparticles spatially confine thermal and mechanical effects, providing:
   - Highly precise photodisruption of cells or subcellular targets
   - Low-fluence irradiation with minimal disruption to surrounding, normal tissue
2. Their optical properties are tunable to NIR wavelengths, allowing:
   - Deep tissue penetration
   - Possible use of nonlinear effects to improve selectivity
   - Freedom to choose between absorption and near-field scattering dynamics
3. Easy nanoparticle functionalization methods provide:
   - Enhanced targeting to cancer biomarkers with high selectivity
   - High-throughput phototherapeutic process
4. Allows for combined imaging and therapy:
   - Through scattering and bright multiphoton luminescence, nanoparticles can additionally double as image contrast agents
   - Image-guided therapy

By confining thermal and mechanical effects to the target tissue or cell, it is possible to treat a particular region of interest with high specificity – which is extremely important in cancer therapy. Particles can also be functionalized to target cancer biomarkers with high specificity. Taken together, these two properties provide the highest level of therapeutic selectivity of cancer cells. Additionally, particles can act as strong contrast agents for the differentiation of normal versus cancer cells, further allowing for use in image-guided therapy. As an example, when treating a cancer in the brain (e.g. medulloblastoma) it is vital to kill the tumor but to leave the normal, healthy brain tissue intact; in this way, important brain functions such as visual and motor control are not disrupted. Such precise phototherapy can be achieved only through image-guided therapy with the aid of plasmonic gold nanoparticles. Moreover, by varying the laser pulse duration it is possible to confine any damage to the biological material surrounding the particle. Finally, the optical response of the particle is highly tunable (visible to NIR); this is especially important for reaching tumors embedded deep within a tissue.

Today, several important parameters (see Table 13.3) still require attention in the development of PLP, many of which are defined by the biology of the clinical situation. Until now, PLP has been tested mainly in an *in vitro* setting; however, as the procedure continues to be monitored in animal models, and the particle-laser interaction is refined, it will surely become applicable to the destruction of tumors *in vivo*.

In this respect, particle design parameters – both dynamic and functional – must be optimized to meet clinical needs. First, in order for the clinical setting to become reality, the developed bioconjugates must have a sufficiently long shelf life under the ambient conditions of clinics (most current bioconjugates have shelf lives of 2–3 days at 4 °C before the bioagent dissociates from the nanoparticle surface). Studies are also required to verify the biologically inert nature of bioconjugates, such that interactions other than with cognate receptors do not occur. An inert nature can also be defined as the ability of a particle to navigate the body without intermediate removal, or accumulating nonspecifically in other tissues. The particle must be capable of traveling through the bloodstream to seek out a choice target, whilst interacting minimally with other locations in the body. Details of particle targeting and localization within tissues or cells also require investigation – from a therapeutic standpoint, it is not clear whether it is more effective to induce apoptosis or necrosis to cause cell death. As such, cancer cells can be targeted in a variety of ways, from subcellular components (e.g. DNA or proteins) to the plasma membrane. The spatial location of the particle within the cell also affects the degree of optical localization required. For example, the targeting of a molecular macromolecule would require far greater spatial confinement than would photodamage to the plasma membrane. One recently acknowledged hurdle is that of particle bifunctionalization for controlled directionality into cells and attachment to desired intracellular targets; delivery methods have still to be matured to overcome this problem. Recently, the intracellular delivery of gold nanoparticles utilizing the TAT protein from the HIV virus was demonstrated [119, 120]. Stealth-based nanoshuttles (e.g. liposomes and viruses) are also in their early stages of development for transporting nanoparticles to regions of interest [123]. Typically, these vessels must either be biodegradable or become part of the cellular membrane upon attachment to the target of interest. These nanoshuttles have the potential to deliver a large payload of nanoparticles into the target tissue or cell, with high specificity.

Laser irradiation parameters are directly related to both the particle geometry and biological setting. Each particle type has a unique absorption and scattering spectrum; thus, the laser wavelength must be chosen so as to maximize the interaction between the laser and the particle, thereby achieving the most effective therapy. The particle type and laser wavelength and duration will be a function of the tissue type and of the tumor location. Depending upon the tissue structure, a specific particle size may be necessary; for example, if a tissue has a large volume of connective tissue, then smaller particles (e.g. nanorods) may be necessary, and this will dictate the laser wavelength. The laser pulse duration will be determined by the type of disease-state present, whether solid or scattered among healthy cells. The physical delivery of laser light is also important – the probe-based technology used must minimize patient discomfort but effectively irradiate the region of interest. The delivery mode will also depend upon the location of the lesion; for example, in the oral cavity the use of an endoscopic probe or a modified dental device will be necessary.

Finally, the goal of multimodal therapy is of great importance, using combinations of therapeutic and imaging techniques. Procedures under current development include smart particles for combined imaging (MRI/optical) and photothermal therapy [122, 123], or combinations of phototherapy and photodynamic therapy [124].

To summarize, the therapeutic application of PLP has been demonstrated for the treatment of cancer in a series of *in vitro* studies. In this chapter we have provided examples of clinical applications, and discussed how the biological limits affect optical and particle parameters. The importance of understanding the physical properties of bioconjugates in order to develop the next generation of 'smart' phototherapeutic particles, was also highlighted. As these optical and particle parameters are further refined, as particle development matures, and as *in vivo* laser delivery techniques for both depth and surface applications develop, plasmonic phototherapy will surely demonstrate its clear potential to become a 'gold standard' among cancer treatments.

Acknowledgments

We would like to thank R.K. Harrison for his help computing optical cross-sections, Dr. A. Plech for providing experimental data, and Dr. B. Luk'yanchuk for nanoparticle scattering intensity modeling. Some of the investigations described in this chapter were supported by the National Institutes of Health grant RO3 CA125774 and by the Texas Higher Education Coordinating Board through The Advanced Research Program (ARP) grant and the National Science Foundation grant BES-0508266.

References

1 American Cancer Society (2008) Cancer Facts and Figures.

2 U.S. Department of Health and Human Services (2004) Cancer Nanotechnology Plan: A Strategic Initiative to Transform Clinical Oncology and Basic Research Through the Directed Application of Nanotechnology.

3 Sokolov, K., Aaron, J., Hsu, B., Nida, D., Gillanwater, A., Follen, M., Macaulay, C., Adler-Storthz, K., Korgel, B., Discour, M., Pasqualini, R., Arap, W., Lam, W. and Richartz-Kortum, R. (2003) Optical systems for in vivo molecular imaging of cancer. *Technology in Cancer Research and Treatment*, **2**(6), 491–504.

4 El-Sayed, I.H., Huang, X. and El-Sayed, M.A. (2005) Surface plasmon resonance scattering and absorption of anti-EGFR antibody conjugated gold nanoparticles in cancer diagnostics: applications in oral cancer. *Nano Letters*, **5**, 829–34.

5 Huang, X., El-Sayed, I.H., Qian, W. and Els-Sayed, M.A. (2006) Cancer cell imaging and photothermal therapy in the near-infrared region by using gold nanorods. *Journal of the American Chemical Society*, **128**, 2115–20.

6 Durr, N.J., Larson, T., Smith, D.K., Korgel, B.A., Sokolov, K. and Ben-Yakar, A. (2007) Two-photon luminescence imaging of cancer cells using molecularly

targeted gold nanorods. *Nano Letters*, **7**(4), 941–5.
7 Bohren, C.F., Huffman, D.R. (1983) *Absorption and Scattering of Light by Small Particles*, John Wiley & Sons, Inc., New York.
8 Pourbaix, M. (1984) Electrochemical corrosion of metallic biomaterials. *Biomaterials*, **5**, 122–34.
9 Lewinski, N., Colvin, V. and Drezek, R. (2008) Cytotoxicity of nanoparticles. *Small*, **4**(1), 26–49.
10 Turkevich, J., Stevenson, P.C. and Hillier, J. (1951) A study of the nucleation and growth processes in the synthesis of colloidal gold. *Discussions of the Faraday Society*, **11**, 551951.
11 Frens, G. (1973) Controlled nucleation for the regulation of the particle size in monodisperse gold suspensions. *Nature Physical Science*, **241**, 20–2.
12 Link, S. and El-Sayed, M.A. (1999) Spectral properties and relaxation dynamics of surface plasmon electronic oscillations in gold and silver nanodots and nanorods. *The Journal of Physical Chemistry B*, **34**, 8410–26.
13 Zhou, H.S., Honma, I. and Komiyama, H. (1994) Controlled synthesis and quantum-size effects in gold-coated nanoparticles. *Physical Review B*, **50**, 12052–6.
14 Oldenburg, S.J., Averitt, R.D., Westcott, S.L. and Halas, N.J. (1998) Nanoengineering of optical resonances. *Chemical Physics Letters*, **288**, 243–7.
15 Chen, J., Saeki, F., Wiley, B., Cang, H., Cobb, M.J., Li, Z.-Y., Au, L., Zhang, H., Kimmey, M.B., Li, X. and Xia, Y. (2005) Gold nanocages: bioconjugation and their potential use as optical imaging contrast agents. *Nano Letters*, **5**, 473–7.
16 Zharov, V., Galitovsky, V. and Viegas, M. (2003) Photothermal detection of local thermal effects during selective nanophotothermolysis. *Applied Physics Letters*, **83**, 4897–9.
17 Lapotko, D.O., Lukianova, E., Oraevsky, A.A. and Laser, S. (2006) Nano-thermolysis of human leukemia cells with microbubbles generated around clusters of gold nanoparticles. *Lasers in Surgery and Medicine*, **38**, 631–42.
18 Wong, N., O'Connell, M., Wisdom, J.A., and Dai, H. (2005) Carbon nanotubes as multifunctional biological transporters and near-infrared agents for selective cancer cell destruction. *Proceedings of the National Academy of Sciences of the United States of America*, **102**, 11600–5.
19 Kim, J.W., Shashkov, E.V., Galanzha, E.I., Kotagiri, N., Zharov, V.P. (2007) Photothermal antimicrobial nanotherapy and nanodiagnostics with self-assembling carbon nanotube clusters. *Lasers in Surgery and Medicine* **39**, 622–34.
20 Son, S.J., Bai, X., Lee, S. and Hollow, I. (2007) Nanoparticles and nanotubes in nanomedicine: Part 2. Imaging, diagnostics, and therapeutic applications. *Drug Discovery Today*, **12**, 657–63.
21 Shao, N., Lu, S., Wickstrom, E., Panchapakesan, B. and Molecular, I. (2007) Targeting of IGF1R and HER2 surface receptors and destruction of breast cancer cells using single wall carbon nanotubes. *Nanotechnology*, **18**, 315101.
22 Geoghegan, W.D. and Ackerman, G.A. (1977) Adsorption of horseradish peroxide, ovomucoid, and anti-immunoglobulin to colloidal gold for the indirect detection of concanavalin A, wheat germ agglutinin, goat anti-human immunoglobulin G on cell surfaces at the electron microscope level: a new method, theory, and application. *Journal of Histochemistry*, **25**, 1187–200.
23 Loo, C., Lowery, A., Halas, N.J., West, J. and Drezek, R.A. (2005) Immunotargeted nanoshells for integrated cancer imaging and therapy. *Nano Letters*, **5**, 709–11.
24 Csaki, A., Garwe, F., Steinbruck, A., Maubach, G., Festag, G., Weise, A., Riemann, I., Konig, K. and Fritzsche, W. (2007) A parallel approach for subwavelength molecular surgery using gene-specific positioned metal nanoparticle as laser light antennas. *Nano Letters*, **7**, 247–53.
25 Huff, T.B., Tong, L., Zhao, Y., Hansen, M.N., Cheng, J. and Wei, A. (2007) Hyperthermic effects of gold nanorods on tumor cells. *Nanomedicine*, **2**, 125–32.
26 Tong, L., Zhao, Y., Huff, T.B., Hansen, M.N., Wei, A. and Cheng, J. (2007) Gold

nanorods mediate tumor cell death by compromising membrane integrity. *Advanced Materials*, **19**, 3136–41.

27 Niidome, T., Yamagata, M., Okamoto, Y., Akiyama, Y., Takahashi, H., Kawano, T., Katayama, Y. and Niidome, Y.P.E. (2006) G-modified gold nanorods with a stealth character for in vivo applications. *Journal of Controlled Release*, **114**, 343–7.

28 Chem, A.M. and Scott, M.D. (2001) Current and future applications of immunological attenuation via pegylation of cells and tissue. *BioDrugs*, **15**, 833–47.

29 Harris, J.M., Martin, N.E. and Modi, M. (2001) Pegylation: a novel process for modifying pharmacokinetics. *Clinical Pharmacokinetics*, **40**, 539–51.

30 Kumar, S. and Richards-Kortum, R. (2006) Optical molecular imaging agents for cancer diagnostics and therapeutics. *Nanomedicine*, **1**, 23–30.

31 Sokolov, K., Nida, D., Descour, M., Lacy, A., Levy, M., Hall, B., Dharmawardhane, S., Ellington, A., Korgel, B. and Richards-Kortum, R. (2006) Molecular optical imaging of therapeutic targets of cancer. *Advances in Cancer Research*, **96**, 299–344.

32 Huang, X., Prashant, K.K., El-Sayed, I.H. and El-Sayed, M.A. (2007) Plasmonic photothermal therapy (PPTT) using gold nanoparticles. *Lasers in Medical Science*, **23**(3), 217–28.

33 Huang, X., Prashant, K.K., El-Sayed, I.H. and El-Sayed, M.A. (2007) Gold nanoparticles and nanorods in medicine: from cancer diagnostics to photothermal therapy. *Nanomedicine*, **2**(5), 681–93.

34 van de Hulst, H.C. (1981) *Light Scattering by Small Particles*, Dover Books, New York.

35 Kreibig, U. and Vollmer, M. (1995) *Optical Properties of Metal Clusters*, Springer, Berlin.

36 Kerker, M. (1969) *The Scattering of Light and Other Electromagnetic Radiation*, Academic, New York.

37 Jackson, J.D. (1999) *Classical Electrodynamic*, 3rd edn, John Wiley & Sons, Inc., New York.

38 Papavassiliou, G.C. (1979) Optical properties of small inorganic and organic metal particles. *Progress in Solid State Chemistry*, **12**, 185.

39 Wagner, F.E., Haslbeck, S., Stievano, L., Calogero, S., Pankhurst, O.A. and Martinek, K.P. (2000) Before striking gold in gold-ruby glass. *Nature*, **407**, 691.

40 Kerker, M. (1985) The optics of colloidal silver: something old and something new. *Journal of Colloid and Interface Science*, **105**, 297.

41 Yguerabide J. and Yguerabide, E.E. (1998) Light-scattering submicroscopic particles as highly fluorescent analogs and their use as tracer labels in clinical and biological applications I. theory. *Analytical Biochemistry*, **262**, 137.

42 Kelly, R.L., Coronado, E., Zhao, L.L. and Schatz, G.C. (2003) The optical properties of metal nanoparticles: the influence of size, shape, and dielectric environment. *The Journal of Physical Chemistry B*, **107**, 668.

43 Messinger, B.J., Ulrich von Raben, K., Chang, R.K. and Barber, P.W. (1981) Local fields at the surface of noble-metal microspheres. *Physical Review B*, **24**, 649.

44 Drude, P. (1900) Electron theory of metals–Part I. *Annales de Physique*, **1**, 556.

45 Drude, P. (1900) Electron theory of metals–Part II. *Annales de Physique*, **3**, 369.

46 Drude, P. (1902) Electron theory of metals–Correction. *Annales de Physique*, **7**, 687.

47 Hovel, H., Fritz, S., Hilger, A., Kreibig, U. and Vollmer, M. (1993) Width of cluster plasmon resonances: Bulk dielectric functions and chemical interface damping. *Physical Review B*, **48**, 178.

48 Bassani, F., Parravicini, G.P. (1975) *Electronic States and Optical Transitions in Solids*. Pergamon, New York.

49 Alvarez, M.M., Khoury, J.T., Schaaff, T.G., Shafigullin, M.N., Vezmar, I. and Whetten, R.L. (1997) Optical absorption spectra of nanocrystal gold molecules. *The Journal of Physical Chemistry B*, **101**, 3706.

50 Link, S. and El-Sayed, M.A. (1999) Size and temperature dependence of the plasmon absorption of colloidal gold nanoparticles. *The Journal of Physical Chemistry B*, **103**, 4212.

51 Ashcroft, N.W., Mermin, N.D. (1976) *Solid State Physics*. Saunders College, Philadelphia.

52 Kuhn, H. (1982) *Biophysik* (eds W. Hoppe, W. Lohmann, H. Mark and H. Ziegler), Springer, Berlin, p. 289.

53 Rechberger, W., Hohenau, A., Leitner, A., Krenn, F.R., Lamprecht, B., and Aussenegg, F.R. (2003) Optical properties of two interacting gold particles. *Optics Communications*, **220**, 137.

54 Quinten, M. (2001) Local fields close to the surface of nanoparticles and aggregates of nanoparticles. *Applied Physics B, Lasers and Optics*, **73**, 245–55.

55 Maier, S.A., Brongersma, M.L., Kik, P.G. and Atwater, H.A. (2002) Observation of near-field coupling in metal nanoparticle chains using far-field polarization spectroscopy. *Physical Review B*, **65**, 193408.

56 Khlebtsov, B., Zharov, V., Melnikov, A., Tuchin, V. and Khlebtsov, N. (2006) Optical amplification of photothermal therapy with gold nanoparticles and nanoclusters. *Nanotechology*, **17**, 5167–79.

57 Eversole, D.S. (2007) Plasmonic laser nanoablation of solid material, Masters Thesis, University of Texas at Austin.

58 Sinzig, J. and Quinten, M. (1994) Scattering and absorption by spherical multilayer particles. *Applied Physics A*, **58**, 157–62.

59 Sinzig, J., Radtke, U., Quinten, M. and Kreibig, U. (1993) Binary clusters: homogeneous alloys and nucleus-shell structures. *Zeitschrift fur Physik D*, **26**, 242–5.

60 Chen, J., Wang, D., Xi, J., Au, L., Siekkinen, A., Warson, A., Li, Z.-Y., Zhang, H., Xia, Y. and Li, X. (2007) Immuno gold nanocages with tailored optical properties for targeted photothermal destruction of cancer cells. *Nano Letters*, **7**, 1318–22.

61 Hirsch, L.R., Gobin, A.M., Lowery, A.R., Tam, F., Drezek, R.A., Halas, N.J. and West, J.L. (2006) Metal nanoshells. *Annals of Biomedical Engineering*, **34**, 15–22.

62 Mohamed, M.B., Ismael, K.Z., Link, S. and El-Sayed, M.A. (1998) *The Journal of Physical Chemistry B*, **102**, 9370.

63 Shankar, S.S., Rai, A., Ankamar, B., Singh, A., Ahmad, A. and Sastry, M. (2004) Biological synthesis of triangular gold nanoprisms. *Nature Materials*, **3**, 482.

64 Wang, H., Brandl, D.W., Le, F., Nordlander, P. and Halas, N.J. (2006) Nanorice: a hybrid nanostructure. *Nano Letters*, **6**, 827.

65 Link, S. and El-Sayed, M.A. (2000) Shape and size dependence of radiative, nonradiative, and photothermal properties of gold nanocrystals. *International Reviews in Physical Chemistry*, **19**, 409–53.

66 Specht, M., Pedarnig, J.D., Heckl, W.M. and Haensch, T.W. (1992) Scanning plasmon near-field microscope. *Physical Review Letters*, **68**, 476.

67 Boyd, G.T., Rasing, T., Leite, J.R.R. and Shen, Y.R. (1984) Local-field enhancement on rough surfaces of metals, semimetals, and semiconductors with the use of optical second-harmonic generation. *Physical Review B*, **30**, 519.

68 Krug, J.T.II, , Sanchez, E.J., Xie, X.S. and Sunney, X. (2002) Design of near-field probes with optimal field enhancement by finite difference time domain electromagnetic simulation. *The Journal of Chemical Physics*, **116**, 10895.

69 Hartland, G.V., Hu, M. and Sader, J.E. (2003) Softening of the symmetric breathing mode in gold particles by laser-induced heating. *The Journal of Physical Chemistry B*, **107**, 7472–8.

70 Petrova, H., Hu, M. and Hartland, G.V. (2007) Photothermal properties of gold nanoparticles. *Zeitschrift für Physikalische Chemie*, **221**, 361–76.

71 Hu, M. and Hartland, G.V. (2002) Heat dissipation for Au particles in aqueous solution: relaxation time versus size. *The Journal of Physical Chemistry B*, **106**, 7029–33.

72 Wilson, O.M., Hu, X., Cahill, D.G. and Braun, P.V. (2002) Colloidal metal nanoparticles as probes of nanoscale

thermal transport in fluids. *Physical Review B*, **66**, 224301.
73 Ge, Z., Kang, Y., Taton, T.A., Braun, P.V. and Cahill, D.G. (2005) Thermal transport in Au-core polymer-shell nanoparticles. *Nano Letters*, **5**, 3.
74 Plech, A., Kotaidis, V., Grésillon, S., Dahmen, C. and von Plessen, G. (2004) Laser-induced heating and melting of gold nanoparticles studied by time-resolved X-ray scattering. *Physical Review B*, **70**, 195423.
75 Kaganov, M., Lifshitz, I.M. and Tanatarov, L.V. (1957) Relaxation between electrons and crystalline lattices. *Soviet Physics–JETP*, **4**, 173.
76 Ekici, O., Harrison, R.K., Durr, N.J., Eversole, D.S., Lee, M. and Ben-Yakar, A. Thermal analysis of gold nanorods heated with femtosecond laser pulses. *Journal of Physics D: Applied Physics*, **41**, 185501.
77 Kotaidis, V., Dahmen, C., von Plessen, G., Springer, F. and Plech, A. (2006) Excitation of nanoscale vapor bubbles at the surface of gold nanoparticles in water. *The Journal of Chemical Physics*, **124**, 184702.
78 Willis, D.A. and Xu, X. (2002) Heat transfer and phase change during picosecond laser ablation of nickel. *International Journal of Heat and Mass Transfer*, **45**, 3911–18.
79 Martynyuk, M.M. (1974) Vaporization and boiling of liquid metal in an exploding wire. *Soviet Physics–Technical Physics*, **19**(6), 793–7.
80 Xu, X. (2002) Phase explosion and its time lag in nanosecond laser ablation. *Applied Surface Science*, **197–198**, 61–6.
81 Volkov, A.N., Sevilla, C. and Zhigilei, L.V. (2007) Numerical modeling of short pulse laser interaction with Au nanoparticle surrounded by water. *Applied Surface Science*, **253**, 6394–9.
82 Dou, Y., Zhigilei, L.V., Winograd, N. and Garrison, B.J. (2001) Explosive boiling of water films adjacent to heated surfaces: a microscopic description. *The Journal of Physical Chemistry*, **105**, 2748–55.
83 Hu, M., Petrova, H. and Hartland, G.V. (2004) Investigation of gold nanoparticles in aqueous solution at extremely high lattice temperatures. *Chemical Physics Letters*, **391**, 220–5.
84 Debenedetti, P.G. (1996) *Metastable Liquids: Concepts and Principles*, Princeton University Press, Princeton.
85 Inasawa, S., Sugiyama, M. and Yamaguchi, Y. (2005) Laser-induced shape transformation of gold nanoparticles below the melting point: the effect of surface melting. *The Journal of Physical Chemistry B*, **109**, 3104–11.
86 Link, S. and El-Sayed, M.A. (2001) Spectroscopic determination of the melting energy of a gold nanorod. *The Journal of Chemical Physics*, **114**, 2362–8.
87 Link, S., Burda, C., Nikoobakht, B. and El-Sayed, M.A. (2000) Laser-induced shape changes of colloidal gold nanorods using femtosecond and nanosecond laser pulses. *The Journal of Physical Chemistry B*, **104**, 6152–63.
88 Huttmann, G., Radt, B., Serbin, J., Lange, B.I. and Birngruber, R. (2002) High precision cell surgery with nanoparticles? *Medical Laser Application*, **17**, 9–14.
89 Pitsillides, C.M., Joe, E.K., Wei, X., Anderson, R.R. and Lin, C.P. (2003) Selective cell targeting with light-absorbing microparticles and nanoparticles. *Biophysical Journal*, **84**, 4023–32.
90 Csaki, A., Garwe, F., Steinbruck, A., Maubach, G., Festag, G., Weise, A., Riemann, I., Konig, K. and Fritzsche, W. (2007) A parallel approach for subwavelength molecular surgery using gene-specific positioned metal nanoparticle as laser light antennas. *Nano Letters*, **7**, 247–53.
91 Mazumder, A. and Shivashankar, G.V. (2007) Gold-nanoparticle-assisted laser perturbation of chromatin assembly reveals unusual aspects of nuclear architecture within living cells. *Biophysical Journal*, **93**, 2209–16.
92 Yao, C.P., Rahmanzadeh, R., Endl, E., Zhang, Z.X., Gerdes, J. and Huttmann, G.J. (2005) Elevation of plasma membrane permeability by laser irradiation of selectively bound nanoparticles. *Biomedical Optics*, **10**, 064012.
93 Everts, M., Saini, V., Leddon, J.L., Kok, R.J., Stoff-Khalili, M., Preuss, M.A.,

Millican, C.L., Perkins, G., Brown, J.M., Bagaria, H., Nikles, D.E., Johnson, D.T., Zharov, V.P., Curiel, D.T. and Linked, C. (2006) Au nanoparticles to a viral vector: potential for combined photothermal and gene cancer therapy. *Nano Letters*, **6**, 587–91.

94 Zharov, V.P., Mercer, K.E., Galitovskaya, E.N. and Smeltzer, M.S. (2006) Photothermal nanotherapeutics and nanodiagnostics for selective killing of bacteria targeted with gold nanoparticles. *Biophysical Journal*, **90**, 619–27.

95 Svaasand, L.O., Gomer, C.J. and Morinelli, E. (1990) On the physical rationale of laser induced hyperthermia. *Lasers in Medical Science*, **5**, 121–8.

96 El-Sayed, I.H. and Huang, X.H. and El-Sayed, M.A. (2006) Selective laser photo-thermal therapy of epithelial carcinoma using anti-EGFR antibody conjugated gold. *Cancer Letters*, **239**, 129–35.

97 Hirsch, L.R., Stafford, R.J., Bankson, J.A., Sershen, S.R., Rivera, B., Price, R. E., Hazle, J.D., Drezek, R.A., Halas, N.J. and West, J.L. (2003) Nanoshell-mediated near-infrared thermal therapy of tumors under magnetic resonance guidance. *Proceedings of the National Academy of Sciences*, **100**, 13549–54.

98 Lowery, A.R., Gobin, A.M., Day, E.S., Halas, N.J. and West, J.L. (2006) Immunonanoshells for targeted photothermal ablation of tumor cells. *International Journal of Nanomedicine*, **1**, 149–54.

99 Stern, J.M., Stanfield, J., Lotan, Y., Park, S., Hsieh, J.T. and Cadeddu, J.A. (2007) Efficacy of laser-activated gold nanoshells in ablating prostate cancer cells in vitro, *Journal of Endourology*, **21**, 939–43.

100 Huang, X.H., Jain, P.K., El-Sayed, I.H. and El-Sayed, M.A. (2006) Determination of the minimum temperature required for selective photothermal destruction of cancer cells with the use of immunotargeted gold nanoparticles. *Photochemistry and Photobiology*, **82**, 412–7.

101 Gobin, A.M., Lee, M.H., Halas, N.J., James, M.D. and Drezek, R.A. (2007) Near-infrared resonant nanoshells for combined optical imaging and photothermal cancer therapy. *Nano Letters*, **7**, 1919–34.

102 Zharov, V.P., Galitovskaya, E.N., Johnson, C. and Kelly, T. (2005) Synergistic enhancement of selective nanophotothermolysis with gold nanoclusters: potential for cancer therapy. *Lasers in Surgery and Medicine*, **37**, 219–26.

103 Larson, T.A., Bankson, J., Aaron, J. and Sokolov, K. (2007) Hybrid plasmonic magnetic nanoparticles as molecular specific agents for MRI/optical imaging and photothermal therapy of cancer cells. *Nanotechnology*, **18**, 325101.

104 Takahashi, H., Niidome, Y., Yamada, S. and Nanorod-sensitized, G. (2006) Cell death: microscopic observation of single living cells irradiated by pulsed near-infrared laser light in the presence of gold nanorods. *Chemistry Letters*, **35**, 500–1.

105 Anderson, R.R. and Parrish, J.A. (1983) Selective photothermolysis: precise microsurgery by selective absorption of pulsed radiation. *Science*, **220**, 524–7.

106 Lin, C.P., Kelly, M.W., Sibayan, S.A.B., Latina, M.A. and Anderson, R.R. (1999) Selective cell killing by microparticle absorption of pulsed laser radiation. *Journal of Selected Topics in Quantum Electronics*, **5**, 963–8.

107 Huttmann, G. and Birngruber, R. (1999) On the possibility of high-precision photothermal microeffects and the measurement of fast thermal denaturation of proteins. *Journal of Selected Topics in Quantum Electronics*, **5**, 954–62.

108 Goldenberg, H. and Tranter, C.J. (1952) Heat flow in an infinite medium heated by a sphere. *British Journal of Applied Physiology*, **3**, 296–8.

109 Takahashi, H., Niidome, T., Nariai, A., Niidome, Y. and Yamada, S. (2006) Photothermal reshaping of gold nanorods prevents further cell death. *Nanotechology*, **17**, 4431–5.

110 Letfullin, R.R., Joenathan., C., George, T.F., and Zharov, V.P. (2006) Laser-induced explosion of gold nanoparticles: potential role for nanophotothermolysis of cancer. *Nanomedicine*, **1**, 473–80.

111 Vrouenraets, M.B., Visser, G.W.M., Stigter, M., Oppelaar, H., Snow, G.B. and van Dongen, G.A.M.S. (2001) Targeting of aluminum (III) phthalocyanine tetrasulfonate by use of internalized monoclonal antibodies: improved efficacy in photodynamic therapy. *Cancer Research*, **61**, 1970–5.

112 Miller, K., Beardmore, J., Kanety, H., Schlessinger, J. and Hopkins, C.R. (1986) Localization of the epidermal growth factor (EGF) receptor within the endosome of EGF-stimulated epidermoid carcinoma (A431) cells. *The Journal of Cell Biology*, **102**, 500–9.

113 Zharov, V.P., Letfullin, R.R. and Galitovskaya, E.N. (2005) Microbubbles-overlapping mode for laser killing of cancer cells with absorbing nanoparticle clusters. *Journal of Physics D: Applied Physics*, **38**, 2571–81.

114 Tirlapur, U.K. and König, K. (2002) Cell biology: targeted transfection by femtosecond laser. *Nature*, **418**, 290–1.

115 Yanik, M.F., Cinar, H., Cinar, H.N., Chisholm, A.D., Jin, Y. and Ben-Yakar, A. (2004) Functional regeneration after nanoaxotomy. *Nature*, **432**, 882.

116 Shen, N., Datta, D., Schaffer, C.B., LeDuc, P., Ingber, D.E. and Mazur, E. (2005) Ablation of cytoskeletal filaments and mitochondria in cells using a femtosecond laser nanoscissor. *Mechanics and Chemistry of Biosystems*, **2**, 17–26.

117 Vogel, A., Noack, J., Hüttmann, G. and Paltauf, G. (2005) Mechanisms of femtosecond laser nanosurgery of cells and tissues. *Applied Physics B, Lasers and Optics*, **81**, 1015–47.

118 Eversole, D., Luk'yanchuk, B. and Ben-Yakar, A. (2007) Plasmonic laser nanoablation of silicon by the scattering of femtosecond pulses near gold nanospheres. *Applied Physics A*, invited paper, **89**, 283–91.

119 Kumar, S., Harrison, N., Richards-Kortum, R. and Sokolov, K. (2007) Plasmonic nanosensors for imaging intracellular biomarkers in live cells. *Nano Letters*, **7**, 1338–43.

120 Kumar, S., Aaron, J. and Sokolov, K. (2008) Directional conjugation of antibodies to nanoparticles for synthesis of multiplexed optical contrast agents for both delivery and targeting moieties. *Nature Protocols*, **3**, 314–20.

121 Choi, M.R., Stanton-Maxey, K.J., Stanly, J.K., Levin, C.S., Bardhan, R., Akin, D., Badve, S., Sturgis, J., Robinson, J.P., Bashir, R., Halas, N.J., Clare, S.E. and Cellular, A. (2007) Trojan horse for delivery of therapeutic nanoparticles into tumors. *Nano Letters*, **7**, 3759–65.

122 Ji, X.J., Shao, R.P., Elliot, A.M., Stafford, R.J., Esparza-Cross, E., Bankson, J.A., Liang, G., Luo, Z.P., Park, K., Markert, J.T., Li, C. and Gold, B. (2007) Nanoshells with a supermagnetic iron oxide-silica suitable for both MR imaging and photothermal therapy. *The Journal of Physical Chemistry C*, **111**, 6245–51.

123 Kim, J., Park, S., Lee, J.E., Jin, S.M., Lee, J.H., Lee, I.S., Yang, I., Kim, J.S., Kim, S.K. and Cho, M. (2006) Designed fabrication of multifunctional magnetic gold nanoshells and their application to magnetic resonance imaging and photothermal therapy. *Angewandte Chemie – International Edition*, **45**, 7754–8.

124 Weider, M.E., Hone, D.C., Cook, M.J., Handsley, M.M., Gavrilovic J. and Russel, D.A. (2006) Intracellular photodynamic therapy with photosensitizer-nanoparticle conjugates: cancer therapy using a 'trojan horse'. *Photochemical and Photobiological Sciences*, **5**, 727–34.

14
Application of Metallic Nanoparticles in Textiles

Nadanathangam Vigneshwaran, Perianambi V. Varadarajan and Rudrapatna H. Balasubramanya

14.1
Introduction

Whilst a fashion designer often considers textiles as a base for art with purely aesthetic value, a fiber scientist sees textiles as an extended flexible surface with a huge research potential. The manipulation of nanoscale phenomena to create synergies between textiles and nanomaterials leads to the creation of novel functionalities, while preserving appearance and comfort [1]. By assembling the metal nanoparticles on the surface of textile materials, several applications could be envisioned. For example, the deposition of silver nanoparticles may impart antibacterial properties, while gold nanoparticles allow the use of molecular ligands to detect the presence of biological compounds in the environment. Most often, these nanomaterials are impregnated onto textile materials without even significantly affecting their texture or comfort. An additional benefit of using metal nanoparticles is the presence of surface plasmons; these are strong optical extinctions that can be tuned to different colors by varying their size and shape. For example, silver nanoparticles can be used to create a shiny metallic yellow to dark pink color while simultaneously imparting antibacterial properties to the textile materials. Likewise, platinum and palladium nanoparticles may impart catalytic properties such as the decomposition of harmful gases or toxic industrial chemicals. Some recent reports [2, 3] have described the coating of textile fabrics with a variety of nanoparticles such as metal, metal oxides, organic and biomaterials to impart functional properties. However, in this chapter we will concentrate only on the functionalization of textiles with metal nanoparticles, the methods of application onto textile materials, and their evaluation. The impact of nanotechnology on commercial textile industries, together with their environmental concerns, are also discussed.

Metallic Nanomaterials Vol. 1. Edited by Challa S. S. R. Kumar

ISBN: 978-3-527-32151-3

14.2 Metal Nanomaterials

Size provides an important control over the physical and chemical properties of nanoscale materials, including conductivity, catalysis and fluorescence [4]. Today, metal nanoparticles are attracting increasing attention and importance in a variety of scientific fields. Whenever size is reduced below the particular level, the band structure of metals begins to disappear and discrete energy levels become dominant, and quantum mechanical rules must replace those of classical physics [5]. The structural anisotropy of metal nanomaterials show substantially different optical properties, including light absorption, light scattering and surface-enhanced Raman spectroscopy (SERS) [6]. According to Mie's theory [7], small spherical nanocrystals (Ag or Au) exhibit a single surface plasmon band, whereas anisotropic particles exhibit two or three bands, depending on their shape. In the case of a nonspherical geometry, they show different modes (transverse and longitudinal) of oscillations in the presence of electromagnetic radiation, and a splitting of the surface plasmon resonance (SPR) absorption bands takes place [8].

The differential light scattering of anisotropic metal nanoparticles probes has been already exploited in the development of many biodiagnostic applications [9, 10]. The anisotropic growth of metal nanoparticles is attributed to one of the following mechanisms [11]:

- Different facets in a crystal have different growth rates
- The presence of imperfections in specific crystal directions
- A preferential accumulation or poisoning by impurities on specific facets.

The geometric shape of a nanoparticle plays a major role in determining the SPR of metals exhibiting spectrum red-shifts with increasing particle size. In addition, a simple heat treatment can modify a particle shape, resulting in a change in its optical plasmon resonant properties [12]. The remarkable size-, surface- and shape-dependence of the physical, chemical and optical properties of nanomaterials make them excellent candidates in modern chemistry. Indeed, today our interest in, and the importance of, anisotropic nanoparticles continue to grow, based on the following reasons [13]:

1. Their synthesis has motivated experimental progress in understanding the intrinsic shape-dependent properties of metal and semi-conductor nanocrystals.
2. Some of these structures feature optical and electrical properties that make them desirable for emerging applications entailing biolabels, photovoltaic behavior, chemical sensing and SERS.
3. The particle growth mechanism is amenable to study in some cases, which in turn makes possible the prediction and systematic manipulation of the final nanocrystal structure.
4. These nanoparticles provide new template materials for the generation of different nanostructures.

14.3 Nanotechnology in Textiles

With the advent of science and technology, a new era has emerged in the realm of textile processing. Apart from the regular finishing, functional properties such as antimicrobial, UV-resistance, stain and water repellency, wrinkle resistance, flame retardancy, moisture control and drug delivery need to be imparted through novel finishes. The modification of the surfaces of textiles and clothing through nanocoating represents a novel approach to the production of highly active surfaces to impart UV-blocking, antimicrobial and self-cleaning properties [14, 15]. Among the various metal salts, silver nitrate is the most commonly used antibacterial agent [16, 17], and indeed has long been used as an antiseptic agent. The proposed mode of action is that the silver nitrate molecules bind to bacterial proteins, thus inhibiting cellular metabolism and leading to a termination of microorganism growth. An additional benefit of using metal nanoparticles is the presence of surface plasmons; these are strong optical extinctions that can be tuned to different colors by varying their size and shape. For example, silver nanoparticles can be used to create a shiny metallic yellow to dark pink color, while simultaneously imparting antibacterial properties to the textile materials. The major disadvantage of using silver nitrate is that everything it comes into contact with is stained brown-black when exposed to light [18]. Silver nanoparticles, on the other hand do not cause staining but still retain their antibacterial properties.

14.3.1 Textile Finishing Processes

Textile wet processing consists of three different stages: (i) pretreatment/preparation; (ii) coloration/dyeing; and (iii) finishing. Finishing, as the final step, imparts any functional and/or novel properties to the base textile material. Finishes are mostly applied to fabrics such as wovens, nonwovens and knitwear, while other categories such as yarn finishings are used for specific purposes. Among the two types of finishings – namely mechanical and chemical – the application of nanomaterials (nanofinishing) falls under the realm of chemical finishing. Some of the functional finishes [19] and the corresponding chemical groups employed in the process are listed in Table 14.1.

A schematic diagram for the simple pad–dry–cure process by which a typical wet chemical finishing process is carried out is shown in Figure 14.1. The chemical bath containing the colloidal suspension of nanomaterials in a suitable solvent is used for padding, followed by a squeezing out of the excess solution. The padded fabric is dried and cured at an appropriate temperature to remove the solvent. The nanomaterials are generally mixed with polymer binders to increase the durability of the finished product. Typically, pad applications of chemicals yield wet pickups in the 70–100% range; these high pickups necessarily require the removal of large amounts of solvent during drying. It should be noted that an uncontrolled evaporation of the solvent during drying can lead to an uneven distribution of the finish due to a migration phenomenon. But, a too-low a wet pickup can be equally

Table 14.1 Typical conventional chemical finishing for various functional properties.

Serial no.	Functional properties	Chemicals used
1.	Soft handle	Silicones, cationic, anionic and nonionic surfactants
2.	Repellents	Fluorocarbons, paraffins, silicones
3.	Flame retardants	Phosphorus- and halogen-based compounds, borates, alumina trihydrate and calcium carbonate
4.	Easy-care and permanent press finish	*N,N′*-Dimethylol-4,5-dihydroxyethylene urea (DMDHEU); *N,N′*-Dimethyl-4,5-dihydroxyethylene urea (DMeDHEU); 1,2,3,4-Butanetetracarboxylic acid (BTCA)
5.	Antimicrobial property	Triclosan, quaternary ammonium salts, organo-silver compounds, silver zeolites, polyhexamethylene biguanide and chitosan
6.	Ultraviolet protection	Phenyl salicylates, benzophenones, benzotriazole derivatives and oxalic acid dianilide derivatives
7.	Antistatic property	Esters of phosphoric acid, polyamines reacted with polyglycols
8.	Soil-release/anti-soiling	Fluorocarbons, derivatives of starch and cellulose, carboxy- and ethoxy-based finishes
9.	Non-slip finishes	Silicic acid sols with softeners or silicone-based water repellents

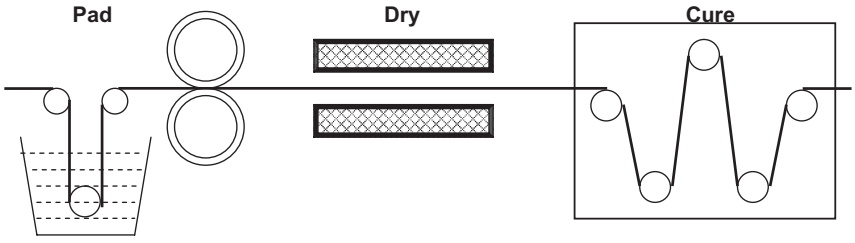

Figure 14.1 The pad–dry–cure process for the wet-finishing of textile materials.

Table 14.2 Low wet pickup finish application methods.

Type of method	Technique
Saturation–removal	Vacuum extraction
	Porous bowl technique
	Air-jet ejectors
	Transfer padding (squeeze–suck technique)
Topical application	Kiss-roll
	Loop transfer system
	Engraved roll
	Nip padding system
	Spray system
	Foam application

problematic and lead to an uneven finish distribution if the liquid phase is discontinuous. The concept of critical application value (CAV) is relevant when discussing optimal wet pickups [20]. The CAV is defined as the minimum amount of finish liquid that can be applied to a given cotton fabric, without producing a nonuniform distribution of finish after drying and curing. Cellulosic fibers, because of their inherent hydrophilicity, have CAVs in the range of 35–40% wet pick up, whereas hydrophobic fibers such as polyester may have CAVs of less than 5%. The details of some low wet pickup finishing application techniques are listed in Table 14.2 [21].

14.3.2 Textile Finishing Using Silver Nanoparticles

Many disinfectants composed of metals/organic compounds are used for the antimicrobial finishes of polymers and fibers [22, 23]. Silver is a very useful antiseptic material which binds with protein molecules, inhibits cellular mechanism, and finally eradicates microbes [24]. Nanosilver is highly reactive with proteins due to its high affinity towards sulfur-containing amino acids; in fact, when nanosilver comes into contact with bacteria and fungi it will adversely affect the cellular metabolism of the organisms and inhibit their cell growth. Nanosilver will also suppress respiration, the basal metabolism of the electron transfer system, and the transport of substrates into the microbial cell membrane. Furthermore, it inhibits the multiplication and growth of those bacteria and fungi which cause infection, odor, itchiness and sores. When both scanning electron microscopy (SEM) and transmission electron microscopy (TEM) were used to study the biocidal action of this nanoscale material [25], the results confirmed that treated *Escherichia coli* cells were damaged and showed the formation of 'pits' in the bacterial cell wall, while silver nanoparticles were found to accumulate in the bacterial cell membrane. As a membrane with such morphology exhibits a significant increase in permeability, the result is a rapid death of the cell.

On account of its nontoxic nature, nanosilver is biocompatible and can be used with great effect to reduce bacterial counts on nonwoven materials such as air-filters, water-filters, medical clothing and textile woven fabrics that come into direct contact with human skin [26, 27]. Silver is also familiar in the molecular biology laboratory, where it is used as a stain for proteins in polyacrylamide gels. Here, the silver in the stained proteins is in the reduced form of silver (nanosilver) [28]. Initially, Ag(I) binds to a denatured protein (primarily to histidine residues); this is then followed by stabilization of the polymeric Ag center, with multiple Ag reduction events. Today, silver in its different forms is used in silver-coated catheters [29], silver-coated wound bandages [30], water purification systems [31] and dental amalgams [32]. The microbiocidal activity of silver derives from the silver ions being released from compounds such as silver nitrate and silver sulfadiazine. This results in a development of Ag(I) resistance to pathogens by efflux pumping [33, 34] and occasionally also to bioaccumulation and biotransformation [35].

In an earlier study [36] the details were reported of a novel, one-pot synthetic route to prepare silver nanoparticles, reduced and stabilized by starch on the surface of cotton fabrics. The thus-formed nanoparticles imparted color to the fabrics due to their SPR (Figure 14.2). Figure 14.3 shows a SEM image of silver nanoparticles deposited on the surface of cotton fabrics. These silver nanoparticle-

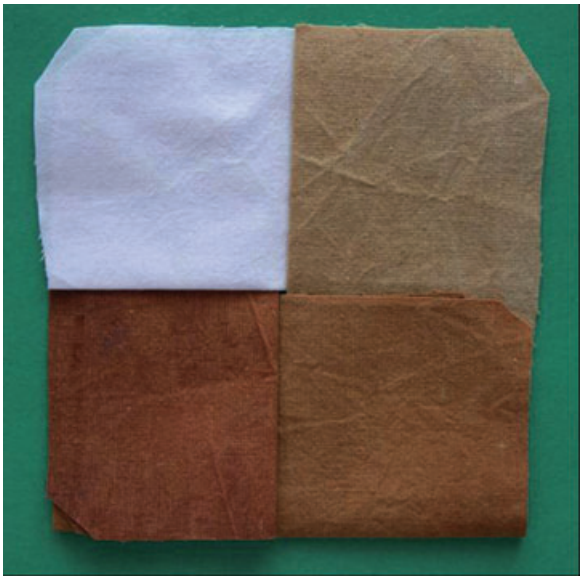

Figure 14.2 Cotton fabrics treated with increasing concentrations of silver nanoparticles. Before treatment the fabric is white; the color changes from light to dark brown with increasing silver concentrations.

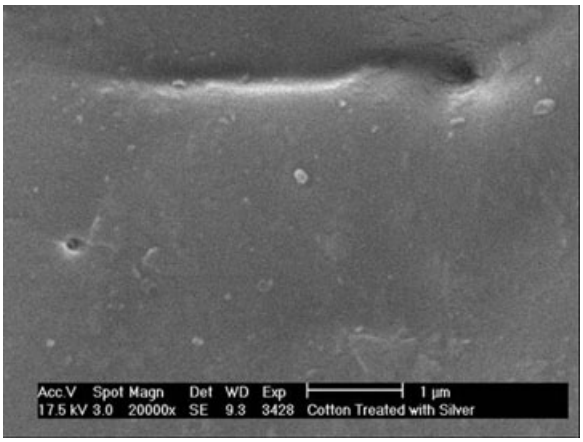

Figure 14.3 Scanning electron microscopy (SEM) image of a cotton fiber coated with silver nanoparticles.

impregnated cotton fabrics have been shown to possess excellent antibacterial activity against *Staphylococcus aureus*, and bacteriostatic activity towards *Klebsiella pneumoniae*. The nanosilver-coated fabrics, owing to their absorption in the near-UV region, exhibited better protection against UV radiation, and Gorensek and Recelj [37] observed a similar increase in UV-absorption when preparing a functionalized cotton fabric with commercial nanosilver. These authors treated cotton fabrics with commercially available silver nanoparticles (80 nm diameter; Ames Goldsmith Corp) to inhibit the growth of *Streptococcus faecalis* and *S. aureus*.

A group from the Hanyang University, Korea [38], while investigating the padding of colloidal silver solution onto textile fabrics made from cotton, polyester, cotton/polyester and cotton/spandex blended fabrics, also reported efficient antibacterial activities against both *S. aureus* and *K. pneumoniae*; moreover, the fabrics showed good laundering durability. A colored, thin film which possessed antimicrobial properties [39] was prepared using a layer-by-layer deposition method of application by the sequential dipping of nylon or silk fibers in dilute solutions of poly(diallyldimethylammonium chloride) and silver nanoparticles capped with poly(methacrylic acid). Duran *et al.* [40] demonstrated the dip-coating of silver nanoparticles synthesized by a fungus (*Fusarium oxysporum*) onto cotton textiles. Here, the silver ions were reduced extracellularly by the fungus to generate stable silver nanoparticles in water, after which the nanoparticles were coated onto the cotton fabrics by dip-coating. The coated fabrics thus produced showed excellent antibacterial activities; some typical SEM images of these fabrics are shown in Figure 14.4.

Other uses of nanosilver particles include the widespread application to socks in order to prevent the growth of odor-causing bacteria, and also to a range of

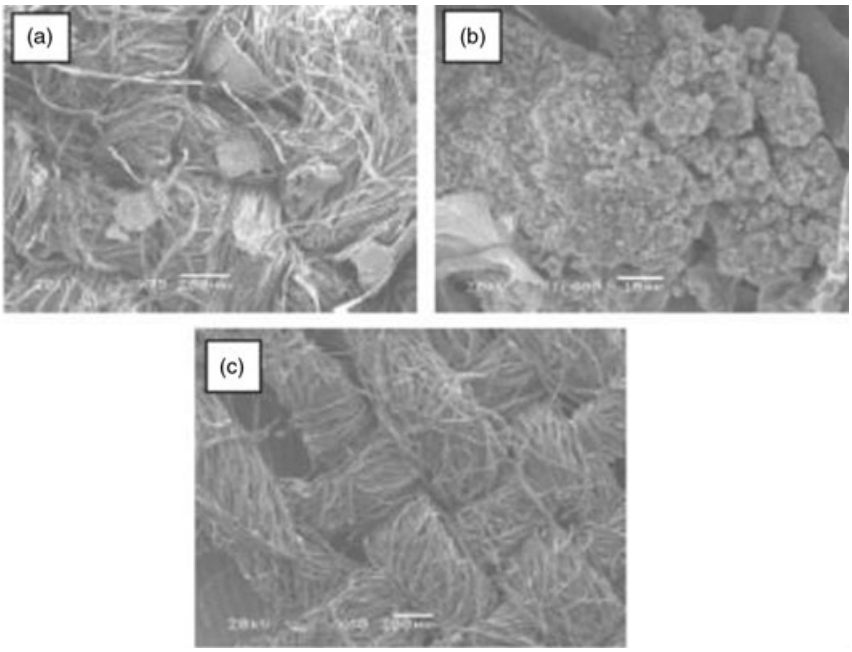

Figure 14.4 SEM images of the cotton fiber. (a) Without silver nanoparticles (control), original magnification ×75; (b) Without silver nanoparticles (control), original magnification ×1400; (c) Containing silver nanoparticles, original magnification ×60.

other healthcare products such as dressings for burns, scalds and skin donor and recipient sites. A SEM image of silver nanoparticles used for the impregnation of healthcare products is shown in Figure 14.5 [41].

Plasma treatment, as a dry and eco-friendly technology, offers an attractive alternative to adding new functionalities to textile materials. The cosputtering of silver during plasma polymerization enables a controlled incorporation of silver nanoparticles into a functional plasma polymer matrix such as a C:H:N in a one-step process, thereby inducing an antibacterial activity. A homogeneous size and spatial distribution of the nanoparticles were obtained by plasma polymerization/cosputtering (Figure 14.6) to achieve antimicrobial activity [42].

14.3.3 Textile Finishing Using Other Metal Nanoparticles

Qufu Wei [43] investigated the preparation and uses of copper nanocomposite textiles by first coating the basic textiles with copper (using magnetron sputter coating) and then characterizing them using atomic force microscopy (AFM). The surface conductivity of the textiles coated with copper nanostructures was signifi-

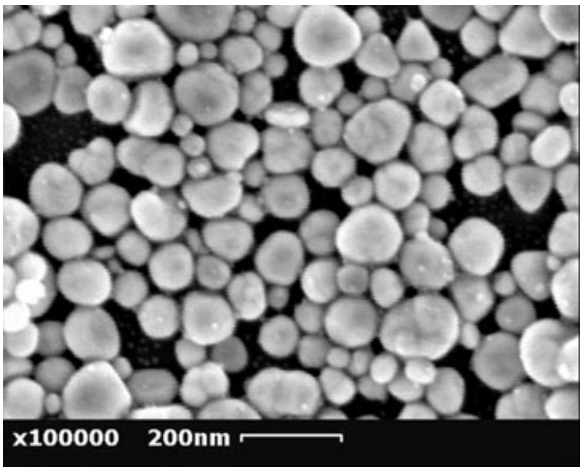

Figure 14.5 Scanning electron microscopy image of silver nanoparticles.

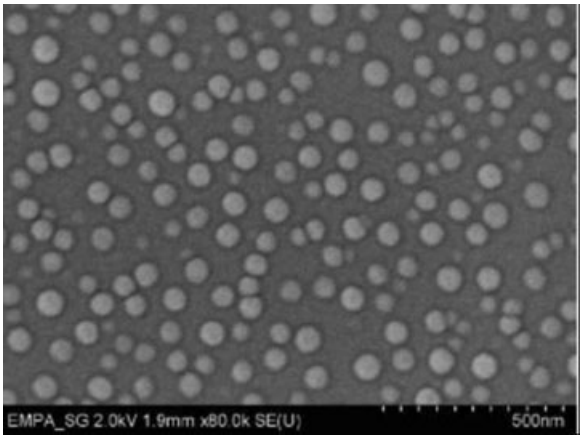

Figure 14.6 Nanosilver deposited on the textile surface by cosputtering during plasma polymerization.

cantly increased compared to the uncoated textiles. Moreover, they also exhibited an improvement in UV and visible light shielding effects. At the Victoria University of Wellington, Johnston has explored the possibility pf utilizing gold nanoparticles as stable colorants on fabrics, and particularly of wool in high-fashion garments [44]. These gold nanoparticles are red in color when their sizes range from 2–5 nm, but the color shifts through orange to yellow to violet as the particle size increases. It has also been noted that the gold nanoparticles neither fade nor denature in light, and also exhibit antimicrobial and catalytic functionalities. Platinum and palladium nanoparticles, when coated onto textiles, impart catalytic

properties such as the decomposition of harmful gases or toxic industrial chemicals.

Although the use of other metallic nanoparticles such as Cu, Fe, Co and Ni is envisaged in textile finishing, the synthetic routes for Cu, Fe, Co and Ni nanoparticles have yet to be improved upon [45]. Synthesis in inverse micelles and via the sonochemical decomposition of metal carbonyls have each been reported for the preparation of nanosized colloids of Co [46], Fe [47] and Ni [48]. However, these methods yield (in most cases) polydisperse particles and are perhaps not suited for scale-up due to problems with reproducibility at high volumes and high concentrations. Various attempts have been made to synthesize Cu nanoparticles by chemical reduction in solution [49], but these have yielded particles of irregular shapes and wide size distributions. The research group at the Pacific Northwest National Laboratory (PNNL) have grown never-before-seen configurations of metal crystals on cotton that show promise as components in biosensors, biological imaging, drug delivery and catalytic converters [50]. By using acid-treated cellulose fibers from cotton as a natural template, the PNNL team has been able to grow gold, silver, palladium, platinum (see Figure 14.7), copper, nickel and other metal-oxide nanocrystals quickly; moreover, the crystals were of a uniform size. In this process, the acid converts the cellulose to a large, stable crystallized molecule that is rich in hydroxyl groups that, predictably, are spaced along the long chemical chains that comprise the cellulose molecule's backbone. When most metal salts dissolved in solution were added in a pressurized oven and heated at 70–200 °C

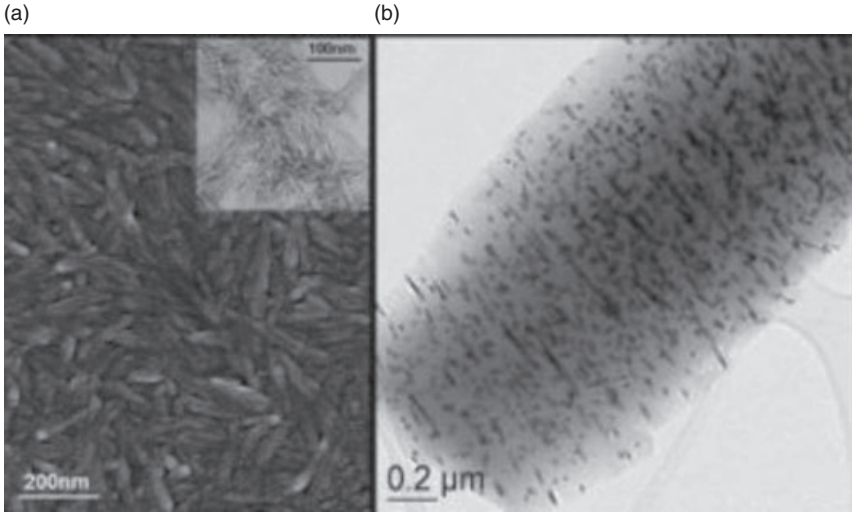

Figure 14.7 (a) Transmission electron microscopy (TEM) image of platinum, deposited on cellulose. The inset shows crystalline cellulose without the metal; (b) TEM image showing the pattern of platinum clustering along hydroxyl sites on the cellulose surface.

Table 14.3 AATCC test methods useful for evaluation of nanofinished textiles.

Serial no.	AATCC test method no.	Title	Comments
1.	147	Antibacterial activity of textile materials: parallel streak method	Qualitative
2.	100	Antibacterial finishes on textile materials, assessment of	Quantitative
3.	30	Antifungal activity, assessment on textile materials: mildew and rot resistance of textiles	Both qualitative and quantitative
4.	174	Antimicrobial activity assessment of carpets	Both qualitative and quantitative
5.	183	Transmittance or blocking of erythemally weighted UV radiation through fabrics	Quantitative
6.	76	Electrical resistivity of fabrics	Quantitative
7.	115	Electrostatic clinging of fabrics: Fabric to metal test	Quantitative
8.	134	Electrostatic propensity of carpets	Quantitative

(or higher) for 4–16 h, uniform metal crystals were seen to form at the hydroxyl sites. Details of important AATCC test methods used to evaluate nanofinished textiles are listed in Table 14.3.

14.3.4
Metallic Versus Nonmetallic Nanoparticles in Textiles

Metal oxide nanoparticles such as TiO_2, Al_2O_3, ZnO and MgO possess photocatalytic and antibacterial activity and UV absorption properties. Textile materials treated with these nanoparticles have been proved to impart antimicrobial, self-decontaminating and UV-blocking functions for both military protective clothing and civilian health products [51].

New-generation medical textiles represent an important and rapidly growing field that requires functional properties such as bacteriostatic, antiviral, fungistatic, nontoxic, high-absorbent, nonallergenic, breathable, hemostatic and biocompatible. Thus, apart from metal and metal oxide nanomaterials, nanoscale biological materials such as enzymes and drugs are required in order to add specific functionality to medical textiles [52]. Specialized nanomaterials functionalized

with ligands can be introduced onto the surface of cotton textiles, the aim being to adsorb odors, to provide strong and durable antibacterial properties, and to ease pain and relieve irritation. Such value-added textiles may also be of immense use in tissue engineering, drug delivery and protective clothing. As an example of the latter role, Nyacol Nanotechnologies Inc. has been the world's leading supplier of colloidal antimony pentoxide, which is used to produce a flame-retardant finish in textiles. The company supplies colloidal antimony pentoxide as a fine-particle dispersion for use as a flame-retardant synergist with halogenated flame-retardants.

Recently, a simple, low-cost method was developed that allowed the conversion of low-frequency vibration/friction energy into electricity using piezoelectric zinc oxide nanowires grown radially around textile fibers. By entangling two fibers and brushing the nanowires rooted on them with respect to each other, mechanical energy could be converted into electricity, owing to a coupled piezoelectric–semiconductor process. These studies establish a methodology for scavenging light-wind energy and body-movement energy using fabrics [53].

Apart from silver nanofinishing for antimicrobial finishes, nanoparticles consisting of a drug which is either surrounded by a synthetic, polymer shell or contained within a synthetic, three-dimensional polymer matrix (both micrometric to nanometric in size) can be used for drug delivery in medical textiles. Encapsulation can be achieved by using several methods, including interfacial polymerization, microemulsion polymerization, precipitation polymerization and diffusion. As a general procedure, the drug is brought into contact with a set of monomers, oligomers or polymers which then assemble around the payload; polymerization will lead to the creation of the final particles. An alternative approach would be to prepare the nanoparticle in the absence of a drug, which would then be adsorbed by the nanoparticles [54].

Another interesting investigation at the Massachusetts Institute of Technology is that of a cloth which links nanoparticles of gold in solution with strands of DNA, and which is coded to change color when exposed to the DNA of a biological agent. In this way, a shirt could detect low doses of harmful chemicals in the air, or a dressing gown could diagnose viruses such as influenza or severe acute respiratory syndrome (SARS).

Hofmann *et al.* [55] have created a bioactive cellulose surface where the nonwoven cellulose (regenerated, oxidized) fabrics were coated with hydroxy-carbonated apatite, using a procedure based on a biomimetic method (Figure 14.8). A simulated body fluid with a high degree of supersaturation was applied to accelerate the biomimetic formation of bonelike apatite on the cellulose fabrics. These materials are under consideration as attractive candidates for scaffolds in bone tissue engineering.

14.4
Commercial Use of Nanotechnology in Textiles

Today, the use of nanotechnology-based finishes in enhancing the performance of textiles made from natural fibers including cotton, wool and silk, and from also

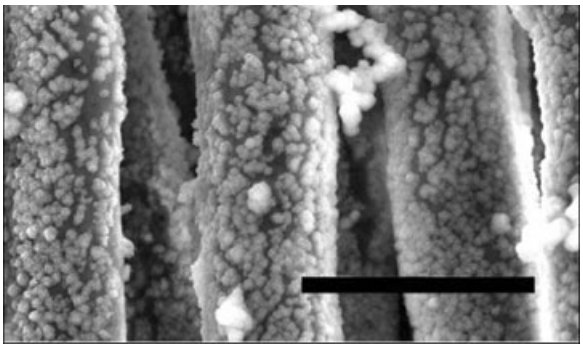

Figure 14.8 Nonwoven cellulose (regenerated, oxidized) fabrics coated with hydroxy-carbonated apatite. Scale bar = 20 μm.

synthetic fibers such as polyester and nylon, is growing rapidly. The 'lotus effect' (a super-hydrophobic and self-cleaning property found in the leaves of the lotus plants) has been emulated in synthetic textile using nanotechnology. In the 'Nano-care' technology developed by Nano-Tex, the textile is embedded with billions of nanowhiskers, each 10 nm in length, that cover the textile material and make it so dense that it can barely be penetrated by liquids. In the 'nanosphere' technology developed by Schoeller, a special 3-D surface structure of nanospheres, ranging from 1 to 100 nm in diameter, is created in the textile, thus limiting the available contact surface to which dirt particles can attach. Some important commercial organizations involved in the nanofinishing of textiles include:

- Nano-Tex, LLC, USA.
- Texcote Technology Ltd., Sweden
- Schoeller Textiles AG, Switzerland
- Beijing Zhong-Shang Centennial Nano-Tech Co. Ltd., China.

To date, each of the 20 largest textile mills worldwide has acquired Nano-Tex licensing technology.

Nanotechnology, although still at its infancy, is already proving to be an innovative tool in enhancing the performance of textiles. The Burlington Industries subsidiary, Nano-Tex, is one of such leading commercial organizations to acquire additional revenue from adding performance and value to textiles. Branded as one of the 'coolest' products in 2003 by *Time Magazine*, Nano-Tex is providing clothing manufactures such as Levi, Eddie Bauer, GAP and Old Navy the means to make their products more durable, water- and oil-repellent, stain-resistant and with a reduced need for washing, without simultaneously altering the feel of the fabric. Their chemical formulation and application technology, which can easily be adopted by existing textile mills, alters the fabric itself at the molecular level, embedding it with tiny, floppy, hair-like fibers that themselves are attached to a common spine. These 'nanowhiskers' in the chemical mix keep any stains away from the garment. Nano-Tex is said to have plans to expand its product range to include stain-proof mattresses, boat covers and hotel bedding markets.

Another company in the field is Schoeller Textiles AG, a Swiss textile company and producer of 'NanoSphere', a finishing process that renders fabric water-repellent, dirt-repellent and anti-adhesive. The use of this technology leads to the creation of a special 3-D structure, thus limiting the available contact surface to which dirt particles can attach. When considering our previous definition of 'nanotechnology', it could be argued that Nano-Tex's technology is not really nanotechnology but rather is 'improved chemistry'. However, the company is today achieving a profit while other 'proper' nanotechnology companies are still waiting and dreaming.

Toray Industries, Inc. has developed a new nanoscale processing technology that allows the necessary molecular arrangement and molecular self-assembly required to develop a new breed of advanced functionalities in textile processing. This technology – named 'NanoMATRIX' – involves the nanoscale coating of a functional material onto each of the monofilaments that forms a woven or knitted fabric. The application of this technology is expected to lead to the development of newer and complex functionalities, in turn bringing about remarkable improvements in the existing functions (quality, durability, etc.) and expansion of use in materials/application, without the fabric losing any of its textural properties.

14.5 Environmental Concerns

Since the onset of the Industrial Revolution, environmental law has steadily increased in popularity due to an interest in public health and safety and the environment [56]. As the environmental concerns regarding a novel material cannot be addressed by existing health and safety legislation, there is a clear need to develop fully fledged norms and regulations not only for the use of nanomaterials but also for their disposal in the environment. In the case of textiles, both the finished product and effluent are likely to be of major concern. As textile products have the closest interaction with the human body, they must be evaluated in terms of their toxicology and levels of tolerance. Similarly, the quantities of nanomaterials that leach into the effluent during a finishing process should be reduced and maintained within permitted limits. During the past few decades, there has been increased interest in reducing the availability of commercial textiles containing antibacterial agents, so as to limit environmental pollution. As silver is a good antibacterial agent, is nontoxic, and is also a natural inorganic metal, it appears to be an interesting material for use in different types of textile fiber. Likewise, as microbes become increasingly involved in systems for the synthesis and accumulation of metal nanoparticles, these too must be removed from the effluent. In one study, it was found that silver nanoparticles in an effluent from a cotton nanofinishing process could be removed efficiently by using *Chromobacterium violaceum* [40], a microorganism which is capable of absorbing, metabolizing and/or storing metal ions, thereby preventing damage to the environment. Very recently, a study

was carried out to analyze the risk to freshwater ecosystems caused by the release of silver from nanoparticles incorporated into textiles and plastics [57]. In this case study, which focuses on the river Rhine in 2010, biocidal plastics and textiles are predicted to account for up to 15% of the total silver released into water in the European Union. However, due to a lack of information on the toxicity of environmentally relevant silver species, only a limited risk assessment is possible at this time, although no risk is predicted for microbial communities in sewage treatment plants.

14.6 Conclusions

Today, the use of nanotechnology has allowed textiles to become 'multifunctional', and the first commercial entries of nanotechnology have recently been made into the 'textile arena'. The emergence of an ability to create, alter and improve textiles at the molecular level, and to enhance their durability and performance beyond those of existing textile products, is already clearly visible. Yet, in order to continue this favorable trend, the global textile industry must not only contribute generously to research efforts in nanotechnology, but also intensify its collaboration with other disciplines. Nanotechnology represents a means of adding value to a product, and may also serve as a valuable tool in generating extra revenue for an already hard-pressed textile industry. The twofold focus of nanofinishing in textiles will be: (i) to upgrade the existing functions of textile materials; and (ii) to develop 'smart' textiles with unprecedented functions. Wearable solar cell and energy storage, information acquisition and storage, sophisticated protection and detection, healthcare and wound healing function are just a few of the many functionalities of textiles that are likely to be developed in the near future.

References

1 Hinestroza, J.P. (2007) Can nanotechnology be fashionable? *Materials Today*, **10**(9), 56.

2 Marino, E., Huijser, T. and Creyghton, Y. (2007) Coating of textile fabrics with nanoparticles, 1st International Conference on Nanopolymers, Berlin, Germany, June 12–13, Paper no. 18, 1–10.

3 Luzinov, I., Brown, P., Chumanov, G., Drews, M., Minko, S. and Fibres, U. (2007) Lotus Approach. National Textile Center Research Briefs, NTC Project: C04-CL06.

4 Alivisatos, A.P. (1996) Semiconductor clusters, nanocrystals, and quantum dots. *Science*, **271**, 933–7.

5 Schmid, G. (2001) Metals, in *Nanoscale Materials in Chemistry* (ed. K.J. Klabunde), John Wiley & Sons. Inc., pp. 15–59.

6 Jin, R., Cao, Y.W., Mirkin, C.A., Kelly, K.L., Schatz, G.C. and Zheng, J.G. (2001) Photoinduced conversion of silver nanospheres to nanoprisms. *Science*, **294**, 1901–3.

7 Mie, G. (1908) Beitrage Zur Optik Truber Medien, Speziell Kolloidaler

Metallosungen. *Annales de Physique*, **330**, 377–445.
8 Penninkhof, J.J., Graf, C., Dillen, T.V., Vredenberg, A.M., Blaaderen, A.V. and Polman, A. (2005) Angle-dependent extinction of anisotropic silica/Au core/shell colloids made via ion irradiation. *Advanced Materials*, **17**, 1484–8.
9 Schultz, S., Smith, D.R., Mock, J.J. and Schultz, D.A. (2000) Single-target molecule detection with non bleaching multicolor optical immunolabels. *Proceedings of the National Academy of Sciences of the United States of America*, **97**, 996–1001.
10 Taton, T.A., Gang, L. and Mirkin, C.A. (2001) *Journal of the American Chemical Society*, **123**, 5164–5.
11 Cao, G. (2004) *Nanostructures & Nanomaterials – Synthesis, Properties & Applications*, Imperial College Press, London.
12 Mock, J.J., Barbic, M., Smith, D.R., Schultz, D.A. and Schultz, S. (2002) Shape effects in plasmon resonance of individual colloidal silver nanoparticles. *The Journal of Chemical Physics*, **116**(15), 6755–9.
13 Hao, E., Schatz, G.C., Hupp, J.T. (2004) Synthesis and optical properties of anisotropic metal nanoparticles. *Journal of Fluorescence*, **14**(4), 331–41.
14 Bozzi, A., Uranova, T.Y. and Kiwi, J. (2005) Self-cleaning of wool polyamide and polyester textiles by TiO_2 rutile modification under daylight irradiation at ambient temperature. *Journal of Photochemistry and Photobiology A: Chemistry*, **172**, 27–34.
15 Qian, L. (2004) Nanotechnology in textiles – recent developments and future prospects. *AATCC Review*, **4**, 14–16.
16 Purwar, R. and Joshi, M. (2004) Recent developments in antimicrobial finishing of textiles: a review. *AATCC Review*, **4**, 22–6.
17 Ramachandran, T., Rajendrakumar, K. and Rajendran, R. (2004) Antimicrobial textiles – an overview. *Institution of Engineers (India) Journal*, **84**, 42.
18 Parikh, D.V., Fink, T., Rajasekharan, K., Sachinvala, N.D., Sawhney, A.P.S. and Calamari, T.A. (2005) Antimicrobial silver/sodium carboxymethyl cotton dressings for burn wounds. *Textile Research Journal*, **75**, 134–8.
19 Schindler, W.D. and Hauser, P.J. (2004) *Chemical Finishing of Textiles*, Woodhead Publishing Ltd and CRC Press LLC.
20 Heaps, S.A. (1979) Consideration of the critical add-on and the uniformity of crosslinking. *Textile Research Journal*, **49**, 150.
21 Greenwood, P. and Holme, I. (2003) *Textile Finishing* (ed. D. Heywood), Society of Dyers and Colourists, Bradford, pp. 61–100.
22 Conner, C.J., Danna, G.S., Cooper, A.S. and Reeves, W.A. (1966) Durability of zirconium-based antimicrobial treatments on cotton. *Textile Research Journal*, **36**, 359–67.
23 Lin, J., Qiu, S., Lewis, K. and Klibanov, A.M. (2003) Mechanism of bactericidal and fungicidal activities of textiles covalently modified with alkylated polyethylamine. *Biotechnology and Bioengineering*, **83**, 168–74.
24 Joeger, T.K., Joeger, R., Olsson, E. and Granqvist, C.G. (2001) Bacteria as workers in the living factory: metal-accumulating bacteria and their potential for materials science. *Trends in Biotechnology*, **19**, 15–20.
25 Sondi, I. and Salopek-Sondi, B. (2004) Silver nanoparticles as antimicrobial agent: a case study on *E. coli* as a model for Gram-negative bacteria. *Journal of Colloid and Interface Science*, **275**, 177–82.
26 Tiller, J.C., Liao, C.J., Lewis, K. and Klibanov, A.M. (2001) Designing surfaces that kill bacteria on contact. *Proceedings of the National Academy of Sciences of the United States of America*, **98**, 5981–5.
27 Vigo, T.L., Benjaminison, A.M. (1981) Antibacterial fibre treatment and disinfection. *Textile Research Journal*, **51**, 454–65.
28 Heukeshoven, J. and Dernick, R. (1985) Simplified method for silver staining of proteins in polyacrylamide gels and the mechanism of silver staining. *Electrophoresis*, **6**, 103–12.
29 Dasgupta, K.M. (1997) Silver-coated catheters in peritoneal dialysis. *Peritoneal Dialysis International*, **17**(2), S142–5.
30 Becker, R.O. (1999) Silver ions in the treatment of local infections. *Metal-Based Drugs*, **6**, 297–300.

31 Bell, F.A. (1991) Review of effects of silver impregnated carbon filters on microbial quality of water. *Journal of the American Water Works Association*, **83**, 74–9.

32 Brune, E. (1986) Metal release from dental biomaterials. *Biomaterials*, **7**, 163–75.

33 Gupta, A., Matsui, K., Lo, J.F. and Silver, S. (1999) Molecular basis for resistance to silver cations in *Salmonella*. *Nature Medicine*, **5**, 183–8.

34 Silver, S. (2003) Bacterial silver resistance: molecular biology and uses and misuses of silver compounds. *FEMS Microbiology Reviews*, **27**, 341–53.

35 Slawon, R.M., Trevors, J.T. and Lee, H. (1992) Silver accumulation and resistance in *Pseudomonas stutzeri*. *Archives of Microbiology*, **158**, 398–404.

36 Vigneshwaran, N., Kathe, A.A., Varadarajan, P.V., Nachane, R.P. and Balasubramanya, R.H. (2007) Functional finishing of cotton fabrics using silver nanoparticles. *Journal of Nanoscience and Nanotechnology*, **7**(7), 1–5.

37 Gorensek, M. and Recelj, P. (2007) Nanosilver functionalized cotton fabric. *Textile Research Journal* **77**(3), 138–41.

38 Lee, H.J., Yeo, S.Y. and Jeong, S.H. (2003) Antibacterial effect of nanosized silver colloidal solution on textile fabrics. *Journal of Materials Science*, **38**, 2199–204.

39 Dubasa, S.T., Kumlangdudsanab, P. and Potiyarajb, P. (2006) Layer-by-layer deposition of antimicrobial silver nanoparticles on textile fabrics. *Colloids and Surfaces A: Physicochemical and Engineering Aspects*, **289**(1–3), 105–9.

40 Duran, N., Marcato, P.D., Souza, G.I.H., Alves, O.L. and Esposito, E. (2007) Antibacterial effect of silver nanoparticles produced by fungal process on textile fabrics and their effluent treatment. *Journal of Biomedical Nanotechnology*, **3**, 203–8.

41 Wong, Y.W.H., Yuen, C.W.M., Leung, M.Y.S., Ku, S.K.A. and Lam, H.L.I. (2006) Selected applications of nanotechnology in textiles. *AUTEX Research Journal*, **6**(1), 1–8.

42 Hegemann, D., Mokbul Hossain, M. and Balazs, D.J. (2006) Nanostructured plasma coatings to obtain multifunctional textile surfaces. *Progress in Organic Coatings*, **58**(1–2), 237–40.

43 Wei, Q. (2008) Preparation and characterization of copper nanocomposite textiles. *Journal of Industrial Textiles*, **37**(3), 275–83.

44 Wilson, A. (2007) A golden age of luxurious fibres. *ATA–Journal for Asia on Textile and Apparel*, **2** (access available only online).

45 Hyeon, T. (2003) Chemical synthesis of magnetic nanoparticles. *Chemical Communications*, **8**, 927–34.

46 Petit, C., Taleb, A. and Pileni, M.P. (1999) Cobalt nanosized particles organized in a 2D superlattice: synthesis, characterization and magnetic properties. *The Journal of Physical Chemistry B*, **103**, 1805–10.

47 Suslick, K.S., Fang, M. and Hyeon, T. (1996) Sonochemical synthesis of iron colloids. *Journal of the American Chemical Society*, **118**, 11960–61.

48 Chen, D.H. and Hsieh, C.H. (2002) Synthesis of nickel nanoparticles in aqueous cationic surfactant solutions. *Journal of Materials Chemistry*, **12**, 2412–15.

49 Dhas, N.A., Raj, P.C. and Gedanken, A. (1998) Synthesis, characterisation and properties of metallic copper nanoparticles. *Chemistry of Materials*, **10**, 1446–52.

50 Shin, Y. (2002) New metal crystals, formed on a cotton assembly line, http://www.physorg.com/news94131885.html (accessed April 5, 2008).

51 Kim, Y.K. (2002) Nanocomposite Fibres, National Textile Center Annual Report MOO-MD08.

52 Petrulyte, S. (2008) Advanced textile materials and biopolymers in wound management. *Danish Medical Bulletin*, **55**(1), 72–7.

53 Qin, Y., Wang, X. and Wang, Z.L. (2008) Microfibre–nanowire hybrid structure for energy scavenging. *Nature*, **451**, 809–13.

54 Soane, D.S., Osford, D.A., Ware, W., Jr, Linford, M.R., Green, E. and Lau, R. (2001) Worldwide Patent, WO 0106054 A1.

55 Hofmann, I., Müller, L., Greil, P. and Müller, F.A. (2006) Calcium phosphate nucleation on cellulose fabrics. *Surface and Coatings Technology*, **201**, 2392–8.

56 Theodore, L. (2006) *Nanotechnology: Basic Calculations for Engineers and Scientists*, Wiley-Interscience, USA.

57 Blaser, S.A., Scheringer, M., Macleod, M. and Hungerbuhler, K. (2008) Estimation of cumulative aquatic exposure and risk due to silver: contribution of nano-functionalized plastics and textiles. *Science of the Total Environment*, **390**(2–3), 396–409.

Index

Metallic Nanomaterials Vol. 1. Edited by Challa S. S. R. Kumar

ISBN: 978-3-527-32151-3